C 901

Bibliotheek Hoofdkantoor TNO
's-Gravenhage
11 DEC. 1972

CENTRAAL LABORATORIUM
COMMUNICATION No. **471**

THERMALLY STIMULATED DISCHARGE OF POLYMER ELECTRETS

by

J. van TURNHOUT

Thesis Leiden (1972)

CENTRAAL LABORATORIUM TNO, P.O. BOX 217, DELFT, THE NETHERLANDS

TNO
9506

Bibliotheek Hoofdkantoor TNO
's-Gravenhage
11 DEC. 1972

THERMALLY STIMULATED DISCHARGE OF POLYMER ELECTRETS

A STUDY OF NONISOTHERMAL DIELECTRIC RELAXATION PHENOMENA

C 314.

Bibliotheek Hoofdkantoor TNO
's-Gravenhage

11 DEC. 1972

STELLINGEN

I

De bewering van Pillai c.s. en Natarajan, dat de diëlektrische konstante van wel en niet geëlektretiseerde polymeren signifikant zou verschillen, wordt niet gestaafd door hun metingen.

P.K.C. Pillai, V.K. Jain en M. Kamdar, *J. Electrochem. Soc. 118*, 465-469 (1971).
S. Natarajan, *Indian J. Pure Appl. Phys. 8*, 174-176 (1970).

II

In hun verklaring voor de pyro-elektriciteit van polymeerfilms zien Furukawa c.s. voorbij aan het feit dat de films niet zijn opgeladen.

T. Furukawa, Y. Uematsu, K. Asakawa en Y. Wada, *J. Appl. Polym. Sci 12*, 2675-2689 (1968).

III

Het is zeer de vraag of het door Bhatnagar c.s. gevonden magneto-elektreet effekt door het aangelegde magnetische veld ontstaat; gezien de lage oplading kan het evengoed een kontakt- of wrijvingsoplading zijn.

C.S. Bhatnagar, *Indian J. Pure Appl. Phys. 2*, 331-332 (1964).
M.L. Khare en C.S. Bhatnagar, *ibid. 8*, 700-703 (1970).
P.K.C. Pillai, K. Jain en V.K. Jain, *J. Electrochem. Soc. 118*, 1676-1677 (1971).

IV

Het door Filippova gemeten verschil in dubbele breking van wel en niet geëlektretiseerde polymeren is veeleer een gevolg van een mechano- dan van een elektro-optische dubbele breking.

K.B. Filippova, *Bull. Acad. Sci. USSR, Physic. Series* (vertaling: *Izvest. Akad. Nauk. SSSR Ser. Fiz.*) *22*, 340-347 (1958).

V

Wanneer de studie van dipoolrelaxaties door middel van een ε'' vs. T meting door geleidingsverliezen wordt bemoeilijkt, biedt de bepaling van $d\varepsilon'/dT$ vs. T vaak nieuwe mogelijkheden; dit komt omdat de waarde van ε' niet door de geleiding wordt beïnvloed.

Dit proefschrift, Fig. 10-26.

VI

Om meetfouten t.g.v. een onvolledige oplading te vermijden, moet de oplaadtijd in diëlektrische stap-responsiemetingen aanmerkelijk groter zijn dan de ontlaadtijd, hierdoor vergen deze interessante laagfrekwentmetingen veel tijd. Ze kunnen evenwel aanzienlijk worden bekort door tijdens de oplading van het monster de temperatuur tijdelijk te verhogen.

Dit proefschrift, blz. 87

VII

De elektrostatische oplaadbaarheid van een stof is geen intrinsieke materiaaleigenschap, maar is een funktie van het systeem waarvan deze stof deel uitmaakt.

VIII

De retentie van een sigarettenfilter kan sterk worden verbeterd door de vezels van het filter te polariseren met een elektrisch veld. Deze verbetering vergt weinig energie en kan met een "vestzak"-generator worden verwezenlijkt.

IX

De preventieve werking van nikkelchloraat op putvorming bij het elektrochemisch bewerken van nikkellegeringen wordt door Boden c.s. op onjuiste wijze verklaard, omdat ze ten onrechte stellen dat de oplosbaarheid van nikkelchloraat in water gering is.

P.J. Boden, P.A. Brook en J.M. Evans, *Proceedings Electrochemical Engin., Symposium*, maart-april 1971, Univ. New Castle.

X

De koncentratie-afhankelijkheid van de molekulaire interakties van een opgelost polymeer kan men het beste aan de hand van het verloop van de gereduceerde (dimensieloze) evenwichtskompliantie vs. de koncentratie bestuderen. Het uitzetten van de evenwichtskompliantie zelf, zoals Einaga c.s. doen, is weinig zinvol.

J. Einaga, K. Osaki, M. Kurata en M. Tamura, *Macromolecules 4*, 87-92 (1971).
H. Janeschitz-Kriegl, *Adv. Polymer Sci. 6*, 170-318 (1969).
U. Daum en J.L.S. Wales, *J. Polymer Sci. B 7*, 459-462 (1969).

XI

Schwarzl's formules om uit een gemeten isothermische ontlaadstroom de laagfrekwent waarden van het reële deel van de dynamische diëlektrische

konstante te berekenen, verdienen de voorkeur boven de door Adamec voorgestelde konversieformule.

F.R. Schwarzl, *Rheol. Acta 8*, 6-17 (1969).
Dit proefschrift, blz. 90
V. Adamec, *Proc. IEE (GB) 116*, 1119-1121 (1969).

XII

Van de analytische methoden die zijn voorgesteld om meetresultaten met een som van e-machten te benaderen, voldoet de methode die in principe reeds door Prony werd beschreven, het best.

R. Prony, *J. École Polytechn. Cah. 3*, 27-57 (1796).
F.B. Hildebrand, *"Introduction to Numerical Analysis"*, McGraw Hill, New York, 1953, blz. 378.
J. van Turnhout, *Advances in Static Electricity 1*, 56-81 (1971). (*Proc. 1st Intern. Conf. on Static Electricity*, Vienna, May 1970, W.F. de Geest Red., Auxilia, Brussel).

XIII

Het verdient aanbeveling in Nederland een centrale opslag te realiseren van algorithmen die men op snelle wijze als subprogramma kan inlezen op de eigen rekenmachine.

XIV

De bezwaren die Springer tegen de invoering van een patiëntenbijsluiter voor op recept verstrekte geneesmiddelen aanvoert, zijn prematuur en wegen niet op tegen de grote voordelen die een dergelijke bijsluiter voor de patiënt zou meebrengen.

M.P. Springer, *Medisch Contact 27*, 281-285 (1972).

XV

Het nut om middelbare scholieren een snelschrift aan te leren, wordt te weinig onderkend in de huidige opleidingen van ons onderwijsstelsel.

J. van Turnhout, 21 december 1972

THERMALLY STIMULATED DISCHARGE OF POLYMER ELECTRETS

A STUDY ON NONISOTHERMAL DIELECTRIC RELAXATION PHENOMENA

PROEFSCHRIFT

Ter verkrijging van de graad van Doctor in de Wiskunde en Natuurwetenschappen aan de Rijksuniversiteit te Leiden, op gezag van de Rector Magnificus Dr. A. E. Cohen, Hoogleraar in de Faculteit der Letteren, volgens besluit van het College van Dekanen te verdedigen op donderdag 21 december 1972 te klokke 15.15 uur

door

J. VAN TURNHOUT

natuurkundig ingenieur
geboren te Dordrecht in 1937

PRINTED BY KRIPS REPRO B.V. – MEPPEL
1972

PROMOTOR : PROF. DR A.J. STAVERMAN

I can do all things in him who strengthens me

Phil. 4:13

To Fietje,
Marjolein and Jurgen,
in gratitude for their support,
patience and understanding.

ACKNOWLEDGEMENTS

The research described in this thesis has been carried out at the Centraal Laboratorium TNO, Delft, Netherlands. I am much indebted to the present director of this institute, Dr A. Schors, for his permission to publish this work as a thesis. His encouragement, together with that of the former director, Professor Dr A.J. Staverman, and the deputy director, Dr Ir J. Heijboer, are gratefully acknowledged. My discussions with Mr Heijboer on the choice of the polymers and the molecular interpretation of the data of Sect. 10:2 have been very instructive. Thanks are also extended to Ir D. Kleis and Ir W.H. Iding (N.V. Philips' Gloeilampenfabrieken, Eindhoven) for their advice on the work reported in Sect. 10:8.

Many others have contributed to the realization of this thesis. The head of the physical department, Dr F.R. Schwarzl, has stimulated me with his continued interest and advice. In particular, the close cooperation with my colleague, Dr P.H. Ong, has been of great help to me. Moreover, Drs Schwarzl and Ong have kindly read and commented on the manuscript. The author has also benefited from useful comments made by Mr G.P.M. Léger.

Special thanks are due to my assistants, Mr G. Roozendaal, Mr P.J. Nederveen and Mr P.J. Droppert, and to my former assistants, Mr M.B.C. Mangelsdorf and Mr L.G. van Staalduinen, their skilful experimental work has been indispensable in completing this thesis. Thanks are also due to Miss M.P. van Duijkeren for preparing most of the polymers.

The help of the photographer, Mr R. van Dijk and the valuable services rendered by the secretariat, workshop, and drawing office, under the supervision of respectively Mrs T.J. Schepp, Mr R. Nauta, and Mr M.W. van Wijk, are greatly appreciated.

The author is also grateful to Mr J.B.A. Nijssen for linguistic corrections in the draft, and to Mrs H.E. Koot and Mrs F.M. van Veenendaal for their help in preparing the manuscript for the press.

Finally, he is much indebted to Ir G. Akos, director of the Computing Centre of the University of Technology, Delft, for permission to use the I.M.B.-360 computer of this institute.

CONTENTS

List of Symbols xv
Structures of Polymers and Abbreviations of Polymer Names xviii

1. GENERAL INTRODUCTION 1
1:1 Definition of an Electret and Historical Notes 1
1:2 The Formation of Polymer Electrets 2
1:3 Number of Dipoles and Charges Contained in an Electret 5
1:4 Experimental Methods for Studying the TSD of Electrets 5
1:5 Survey of the Mechanisms Responsible for TSD 7
5.1 Representative TSD Current Thermograms 10
5.2 Representative TSD Charge Thermograms 11
1:6 Measuring Efficiency of the Decay Processes in Current TSD 13
6.1 Current TSD of Shorted Electrets 13
1a Pecularities of excess charge decay in shorted electrets 15
6.2 Current TSD of Electrets with an Adjacent Air Gap 17
2a Examples of current TSD with an air gap 17
1:7 Methods to Unravel the Various Decay Processes 18
7.1 Choice of Polymers for TSD 18
7.2 Effect of the Forming and Storage Conditions 19
7.3 The Use of Various Experimental Techniques 21
1:8 Applications of TSD 23
1:9 Scope of this Thesis 23

THEORETICAL PART

Introduction 25

2. CURRENT TSD BY DIPOLE REORIENTATION IN SHORTED ELECTRETS 26
2:1 Electrets with a Single Dipole Relaxation 27
1.1 The Charging Process 27
1a Resistivity curves of several polymers 28
1.2 The Discharging Process 31
1.3 Calculation of TSD Model Thermograms 34
2:2 Electrets with a Distribution in Dipole Relaxation Times 38
2.1 Charging and Discharging of Polymers with Continuous Distributions 40
2.2 Some Distribution Functions for Dielectric Relaxations 43
2.3 TSD Model Thermograms of Gevers's Distribution in Natural Frequencies 44

2.4 Model Thermograms of Distributions with a Finite Range of Activation Energies 49
2.5 Model Thermograms of Distributions Extending over an Infinite Interval 51
5a Analogy between an isothermal discharge and TSD 56
2.6 Conclusions 58

2:3 The Resolution of TSD Measurements 59
3.1 Multi-Stage TSD Experiments 61

3. EVALUATION OF DATA PERTAINING TO CURRENT TSD BY DIPOLE REORIENTATION 66
3:1 Calculation of the Parameters of a Debye Relaxation 66

3:2 Fitting of TSD Data to Specific Distribution Functions 71
2.1 Calculation of A from the Initial Current Rise 71
2.2 Calculation of A from the Lower Half-Width Temperature 74
2.3 Simultaneous Calculation of A and m by the Least-Squares Method 75

3:3 Calculation of Dipolar Distribution Functions 76
3.1 Calculation of a Distribution in Natural Frequencies 77
3.2 Calculation of a Distribution in Activation Energies 81

3:4 Outline of a General Computer Programme 82

4. RELATION BETWEEN CURRENT TSD BY DIPOLE REORIENTATION AND ISOTHERMAL DIELECTRIC MEASUREMENTS 83
4:1 Relation to Step-Response Measurements 83

4:2 Relation to Sinusoidal Measurements 88
2.1 Review of the Conversion of Isothermal Discharge Currents 88
2.2 Conversion of Current TSD Data into ε' and ε'' Data 91

5. CURRENT TSD BY THE MOTION OF EXCESS CHARGES AND BY OHMIC CONDUCTION IN SHORTED ELECTRETS 97
5:1 Charge Transport Equations and Boundary Conditions 98

5:2 Differences Between Current TSD of Excess Charges and Dipoles 100

5:3 SCL Drift of Spatially Uniform Excess Charges 101
3.1 Basic Equations for TSD by SCL Drift and Ohmic Conduction in Mono-Electrets 103
3.2 Current and Charge Release of Mono-Electrets with a Uniform Charge Profile 104
3.3 Model Thermograms of Mono-Electrets with a Uniform Charge Distribution 111
3a Location of the TSD current maximum 112
3b Ultimate charge released by weakly conducting mono-electrets 115

3c Charge release of a bipolarly charged electret 119
3.4 Evaluation of SCL-Drift Data of Mono-Electrets 120

5:4 SCL Drift of Spatially Nonuniform Excess Charges 122
4.1 Model Calculations on Nonuniform Excess Charges in Mono-Electrets 123
4.2 Model Calculations on Nonuniform Excess Charges in Hetero-Electrets 127

5:5 Diffusion of Excess Charges 131
5.1 Ultimate Charge Released for Blocking Electrodes 133
5.2 Basic Equations for TSD by Diffusion 133
5.3 TSD by Diffusion in Homo-Electrets 135
5.4 TSD by Diffusion in Hetero-Electrets 136

6. CURRENT TSD BY THE MAXWELL-WAGNER EFFECT IN SHORTED HETEROGENEOUS ELECTRETS 138
6:1 MW Effect in Nonpolar Laminates 140
1.1 The Charging Process 140
1.2 Current TSD of a Nonpolar Laminate 142

6:2 MW Effect in a Polar Polymer with an Adjacent Air Gap 146
2.1 Charging of the Air-Gap Set-up 146
2.2 Current TSD of the Air-Gap Set-up 149
2.3 Experimental Results on the MW Charging and Discharging of Polymers 150

7. CURRENT TSD BY DIPOLE REORIENTATION AND OHMIC CONDUCTION IN ELECTRETS SHORTED TOGETHER WITH AN ADJACENT AIR GAP 153
7:1 One-sided Metallized Hetero- and Homo-Electrets 154
1.1 Model Thermograms of TSD with an Air Gap 159
1.2 Special Model Thermograms Calculated Analytically 163
2a Conduction peak of homocharged nonpolar polymers 163
2b Dipole peak of homocharged polar polymers 166
1.3 Experimental Results and Their Evaluation 168

7:2 Two-sided Metallized Electrets 170

8. CHARGE TSD OF FOIL ELECTRETS IN OPEN CIRCUIT 174
8:1 Charge Decay by Dipole Reorientation and Ohmic Conduction 175
1.1 Some Experimental Results on PET Foil 177

8:2 Charge Decay by SCL Drift and Ohmic Conduction 178
2.1 Model Thermograms of Charge TSD by SCL Drift and Ohmic Conduction 181
2.2 TSD Charge and Current Transitions in Mono-Electrets 183
2.3 Additional Model Thermograms for Uniformly Charged Mono-Electrets 184

EXPERIMENTAL PART

9. DESCRIPTION OF THE EXPERIMENTAL SET-UP 189
9:1 Automated Equipment for Current TSD 189
1.1 Thermostat and Electrode Systems 190
1.2 PID Temperature Controller 192
1.3 Auxiliary Equipment 194
9:2 Automated Equipment for Charge TSD on Foils 195
9:3 Equipment for Conventional Dielectric and Mechanical Measurements 197
9:4 Measuring Errors of Current TSD 198
9:5 Choice of the Polymers 200
10. DISCUSSION OF EXPERIMENTAL RESULTS 202
10:1 Introduction 202
10:2 Relationship between Current TSD and Molecular Structure 203
2.1 Thermograms of Hetero-Electrets of Methacrylic Homopolymers 204
2.2 Thermograms of Hetero-Electrets of Methacrylic Copolymers 211
2.3 Current Thermograms of Hetero-Electrets of Halogen Homopolymers 220
2.4 Current Thermograms of Hetero-Electrets of Commercial Foils 222
2.5 Heterocharge Storage Capacity of Various Polymers 225
2.6 Current Thermograms of Homo-Electrets 228
6a Possible trapping sites in homocharged polymers 228
6b Experimental results on corona-charged and electron-bombarded foils 230
10:3 Influence of Formation Conditions on Current TSD 235
3.1 Thermograms of Electrets Formed by Special Techniques 239
10:4 Influence of Storage Conditions on Current TSD 241
10:5 Current TSD of Polymers Containing Additives 244
10:6 Sectioning of Electrets to Reveal Internal Charge Distributions 246
10:7 Results of Current TSD with an Air Gap 256
7.1 Air-Gap Thermograms of Nonmetallized Electrets 257
7.2 Air-Gap Thermograms of One-Sided Metallized Electrets 259
10:8 Charge TSD of Electret Foils in Open Circuit 262
10:9 Conclusions 269

Appendix I

11. CURRENT TSD BY RELEASE OF TRAPPED EXCESS CHARGES IN SHORTED ELECTRETS 271

11:1 Short Outline of the Energy-Band Model 273

11:2 General Equations for a Single Trapping Level 273

2.1 Analytical Solution for Fast Recombination and Fast Retrapping 275

2.2 Fast Recombination in Uniformly Charged Mono-Electrets 276

2.3 Fast Retrapping in Uniformly Charged Mono-Electrets 277

11:3 General Numerical Solutions 278

3.1 Model Calculations for a Single Trap Level Based on Monteith's Approximation 280

3.2 Model Calculations for a Continuous Distribution of Traps 283

Appendix II

SUPPLEMENTS TO CHAPTERS 2, 5, 6 AND 7 287

2:4 Current TSD of Shorted Electrets with a Spatial Nonuniform Dipole Relaxation 287

5:6 Estimates for Hetero- and Homocharging by Space Charges 289

6.1 Estimates for Heterocharging 289

6.2 Estimates for Homocharging 290

5:7 Particle Flow Lines for Uniform Charge Profiles in Current and Charge TSD 292

7.1 Flow Lines for SCL Drift in Current TSD of Shorted Mono-Electrets 292

7.2 Flow Lines for SCL Drift in Charge TSD of Mono-Electrets 294

5:8 SCL Drift of Uniform Excess Charges in Shorted Electrets with Blocking Electrodes 295

5:9 Finite-Difference Schemes for the Solution of the PDE's for SCL Drift and Ohmic Conduction 295

9.1 LWR Scheme for Solving Hyperbolic PDE's 297

9.2 WT Scheme for Solving Hyperbolic PDE's 299

9.3 Programming of the Boundary Conditions 300

6:3 Injection of Homocharges by Townsend Breakdown, Treated as a MW Charging 302

3.1 Homocharging of Nonpolar Polymers 302

3.2 Homocharging of Polar Polymers 303

7:3 Current TSD of Nonmetallized Electrets Sandwiched Between Two Air Gaps 307

7:4 Air-Gap Current TSD of Electrets with Multiple Dipole Relaxations 308
7:5 Air-Gap Current TSD by SCL Drift of Excess Charges 312

REFERENCES 317

SUMMARY 325

SAMENVATTING 332

LIST OF SYMBOLS

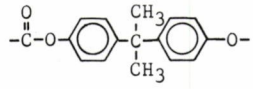
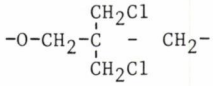
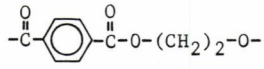
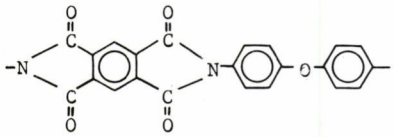
$a(T)$	shift factor of dipole relaxation frequency, $a(T) = \alpha(T)/\alpha_r$
A	activation energy for dipole relaxation; area
B	activation energy for SCL drift
C	activation energy for ohmic conduction; capacitance
c_n	capture coefficient of traps
$D(T)$	diffusion constant
E	internal electric field
E_e	external electric field in air gap
E_f	Fermi level
E_1	exponential integral, $E_1(z) = \int_z^\infty t^{-1}e^{-t}dt$
E_t	energy level of traps
$FS(\alpha_r)$,$FS(A)$	filling state of subpolarizations, i.e. correction to dipolar distribution functions due to incomplete filling
$f(\alpha_r)$	distribution function of dipolar natural frequencies
g	width of air gap
$g(A)$	distribution function of activation energies
G'	shear storage modulus
G''	shear loss modulus
$H(x)$	polynomial appearing in Hasting's approximation to the exponential integral, Eq. 2.19
j	isothermal current density
j_r	released current density during TSD
k	Boltzmann's constant, $k = 1.38 \times 10^{-23}$J/°K or 8.616×10^{-5} eV/°K
l	thickness of the sample
$L(\alpha_r)$	logarithmic distribution function of natural frequencies
m	shape parameter of dipolar distribution functions
p_s, n_s	total positive and negative space charge density
p_e, n_e	equilibrium parts of p and n, which are responsible for ohmic conduction
p, n	part of p and n due to excess charges
n_t	density of trapped electrons
N_t	density of trapping states
P_s	slowly reacting part of dipole polarization
P_o	ultimate value of P_s, $P_o = \varepsilon_o(\varepsilon_s - \varepsilon_\infty)E$
q	induced charge density; released charge density during isothermal measurements
q_r	released charge density during TSD
q_s	stored charge density
q_{se}	stored charge density as measured by the charge detecting system
Q	total excess charge density
r	penetration depth
r_o	initial penetration depth
R	resistance; recombination constant
s	inverse heating rate, $s = dt/dT$
t	time
t_d	time at which TSD is started
t_e	equivalent time for conversion of TSD to isothermal dielectric data

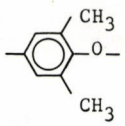
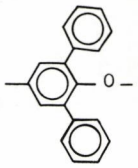
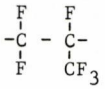
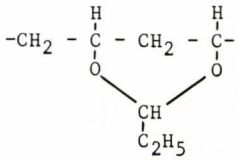
t_f	time at which isothermal formation ends
t_s	time at which isothermal storage begins
T	absolute temperature
T_c	characteristic temperature for the current maximum of ohmic conduction: $sT_c\beta(T_c) = C/kT_c$; conversion temperature for relating TSD to isothermal dielectric data
T_d	temperature at which TSD is started
T_D	characteristic temperature for the current maximum by SCL drift: $sT_D\delta(T_D) = B/kT$
T_f	isothermal forming temperature
T_g	glass-rubber transition
T_G	characteristic temperature for the current maximum by diffusion: $sT_G\delta_G = A/kT_G$, where $\delta_G = \pi^2 D(T_G)/l^2$
T_h	half-width temperature
T_r	room temperature
T_s	isothermal storage temperature
T_t	characteristic temperature for the current maximum by charge release from traps: $sT_t\nu(T_t) = E_t/kT_t$
T_u	ultimate release temperature at which $j_r \simeq 0$
T_λ	transit temperature at which the first excess charges reach the collecting electrode
u	dipolar distribution parameter, $u = \ln \alpha_r/\alpha_o$ or $u = (A-A_o)/kT$
V	voltage
V_a	applied voltage
V_b	breakdown voltage of the air
V_c	compensation voltage in charge TSD
V_e	extinction voltage of the air
w	width of a dipolar distribution function
x	position
$\alpha(T)$	relaxation frequency of dipoles
α_r	natural frequency of dipoles, or ultimate value of $\alpha(T)$
$\beta(T)$	ohmic relaxation frequency, $\beta(T) = \gamma(T)/\varepsilon_o\varepsilon$
β_r	ultimate value of $\beta(T)$, $\beta_r = \gamma_r/\varepsilon_o\varepsilon$
β_g	reduced ohmic relaxation frequency in an air-gap system
$\gamma(T)$	ohmic conductivity
$\delta(T)$	relaxation frequency of SCL drift
δ_r	ultimate value of $\delta(T)$, $\delta_r = \mu_o p_o/\varepsilon_o\varepsilon$
ε_o	permittivity of vacuum, $\varepsilon_o = 8.854 \times 10^{-12}$ F/m
ε_s	static dielectric constant
ε_∞	high frequency dielectric constant
ε'	real part of dielectric constant
ε''	imaginary part of dielectric constant or dielectric loss factor
ζ	blocking factor or discharge parameter of electrodes
$\eta(T)$	reduced time of ohmic conduction: $\eta(T) = s\int_0^T c(T)dT$, where $c(T) = \beta(T)/\beta_r$
κ	ratio of gap width to sample thickness, $\kappa = g/l$
λ	transit time of excess charges to reach the collecting electrode
$\mu(T)$	mobility of charge carriers
ν	frequency
$\nu(T)$	escape frequency of excess charges from traps

$\xi(T)$	reduced time of dipole relaxations: $\xi(T) = s\int_0^T a(T)dT$
ρ	space charge density
σ	surface charge density
$\tau(T)$	relaxation time of dipoles
τ_r	ultimate value of $\tau(T)$; recombination time
$\Psi(T)$	reduced time of SCL drift: $\Psi(T) = s\int_0^T b(T)dt$, where $b(T) = \delta(T)/\delta_r$
ω	angular frequency

FREQUENTLY USED ABBREVIATIONS

BFG	Bucci-Fieschi-Guidi
LWR	Lax-Wendroff-Richtmyer
MW	Maxwell-Wagner
ODE	ordinary differential equation
PDE	partial differential equation
SCL	space-charge limited
TSD	thermally stimulated discharge
WLF	Williams-Landel-Ferry
WT	Wendroff-Thomée
ZFP	zero-field point

Name	Abbreviation	Structure $-\underset{H}{\overset{H}{C}}-\underset{y}{\overset{x}{C}}-$
polyacrylonitrile	PAN	x = H, y = CN
poly-t-butyl methacrylamide	PtBMAm	x = CH_3, y = $CONHC_4H_9$
poly-2-chloroethyl methacrylate	P2CEMA	x = CH_3, y = $COOC_2H_4Cl$
polyethyl methacrylate	PEMA	x = CH_3, y = $COOC_2H_5$
polycyclohexyl methacrylate	PcHMA	x = CH_3, y = COO–(H)
polydimethyl itaconate	PdiMIt	x = CH_2COOCH_3, y = $COOCH_3$
polymethyl methacrylate	PMMA	x = CH_3, y = $COOCH_3$
polypropylene	PP	x = H, y = CH_3
polyphenyl methacrylate	PPhMA	x = CH_3, y = COO–(C$_6$H$_5$)
polystyrene	PS	x = H, y = (C$_6$H$_5$)
polybisphenol A carbonate (Makrofol-n)	PC-n	
chlorinated polyether viz. polydichloromethyl-oxacyclobutane (Penton)	ChPEth	
polyethylene terephthalate (Mylar)	PET	
polyimide (Kapton-H)	PI	

Name	Abbreviation	Structure
poly-2,6-dimethyl-1,4-phenylene-oxide	PPO	
poly-2,6-diphenyl-1,4-phenylene-oxide	PPPO	
polytetrafluoroethylene	PTFE	
polyhexafluoropropylene	PHFP	
polyvinyl butyral	PVB	

CHAPTER 1

GENERAL INTRODUCTION

1:1 Definition of an Electret and Historical Notes

It is a well-established truth that an action causes a reaction. The reaction, however, need not occur instantaneously. Examples of delayed responses to stimuli are numerous in several fields of human experience. The best known, in the field of physics, are mechanical and dielectric relaxation phenomena.

This thesis is devoted to a study of the nonisothermal dielectric relaxation behaviour of polymers. These exhibit a spectacular relaxation phenomenon, since they can be permanently charged by exposing them to a field-temperature treatment. Polymers, or rather dielectrics, bearing a *persistent* charge are called *electrets*. Carrying opposite charges on two sides, electrets are the analogues of magnets. It has been our aim to clarify, theoretically and experimentally, the mechanisms responsible for the decay of their frozen-in charge.

Dielectric relaxation is due to hindrance of the motions of the permanent dipoles and free charges of the polymer by frictional forces. Therefore, upon the application or removal of an electric field, a polar polymer is neither charged, nor discharged immediately. Only part of its polarization, namely that originating from electron and ion displacements within the atoms and molecules, responds almost instantaneously.

Since internal friction depends exponentially on temperature, the response time of permanent dipoles and free charges changes markedly with temperature. By heating, the response is accelerated and by cooling it is slowed down. In polymers, the response time changes e.g. sharply near the glass-rubber transition, T_g, where the conformational motions of main-chain segments set in. Hence, polymers having their T_g above room temperature can be permanently charged by subjecting them to a field-temperature treatment.

In some dielectrics the charging can also be excited by light, or by radioactive radiation instead of by heating; we then obtain photo-electrets and radio-electrets respectively. In this thesis, however, we shall restrict ourselves to "thermo-electrets".

The first thermo-electrets were made from carnauba wax in 1922 by Eguchi. After 1951 electrets were obtained from plastics and ceramics. They have meanwhile been the subject of extensive research, to which important contributions were made by many workers e.g. Antenen, Eguchi, Feaster, Gemant, Groetzinger, Gubkin, Murphy, Perlman, Sessler, Stranathan, Swann and Wiseman, but the main advances must be credited to Gross. The early work has been reviewed in the bibliographies by Johnston (Jo 62), and Gross (Gr 64), in the books by Euler (Eu 64) and

Fridkin et al. (FZ 61), and in the research reports by Wiseman (Wi 55). For more recent work we refer to the comprehensive survey by Perret (Pe 70) and to Baxt and Perlman (BP 68) who edited the papers of the first electret conference in 1967.

Electrets create a strong external field of about 30 kV/cm*, which can be utilized for various purposes. Yet, the practical potentialities for electrets had not seemed promising before Sessler and West (SW 66) successfully developed the foil-electret microphone. This microphone was taken into commercial production in 1970 by Sony (Japan). Further applications are to be expected, now that electrets of nonpolar polymers, such as Teflon-FEP**, have become available with decay times of many years.

These successful developments awakened renewed interest in electrets, but although many of our efforts were directed towards applications (NT 66, Tu 67), we shall here deal with a more fundamental aspect of electrets, namely their restoration to the neutral state by a *thermally stimulated discharge* (TSD). Study of this phenomenon has led to a better understanding of the charging and discharging processes. A fair knowledge of TSD therefore seems essential in promoting the wider use of electrets. Before discussing this technique in more detail we first describe the formation.

1:2 The Formation of Polymer Electrets

A scheme for the formation of a thermo-electret is depicted in Fig. 1-1. The polymer is heated to above T_g, by which the permanent dipoles and free charges are mobilized. Next, at time t_o, an electric field of about 30 kV/cm is applied, which causes an alignment of permanent dipoles, and a drift of free charges to the electrodes. The forming field drives the positive charges to the cathode, and the negative charges to the anode. After about one hour, say at time t_f, the charged polymer is

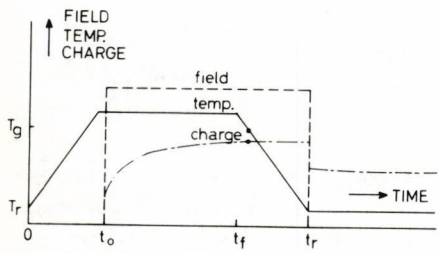


FIG.1-1 Field and temperature programme for the formation of polymer electrets. The charge remaining after the removal of the forming field at t_r, is the semi-permanently frozen-in charge.

* This field cannot exceed the breakdown strength of the air, otherwise sparking would occur that would neutralize part of the electret charge.

** A copolymer of 89 TFE and 11 HFP, DuPont de Nemours, U.S.A.

cooled to room temperature, T_r, by which the main chains of the polymer are immobilized, so that most of the permanent dipoles and charges are frozen in. As a result, they do not respond when the field is switched off at t_r; only the instantaneously reacting part of the polarization disappears. Thus, when the electret is removed from the formation unit, the charge stored at T_f, which amounts to about 10 nC/cm^2, is largely retained; in polymers of low ohmic conductivity and high T_g even for years.

We have mentioned that an electret is the electrical counterpart of a magnet. However, the analogy fails in that electrets, besides having an internal dipole and space charge polarization, can be charged by an *external* process as well. When the contact between the electrodes and the polymer is imperfect, as is usually the case for "laid-on" electrodes, there are air spaces between them, in which at high field strengths Townsend breakdowns will occur (Gr 50), so that ions or electrons from the air are *injected* into the polymer; this is shown in Fig. 1-2. Accordingly, the net charge on each side of a bare electret often consists of two opposite charges, which, in view of their polarity with respect to the adjacent forming electrodes, are called *hetero- and homocharge*.

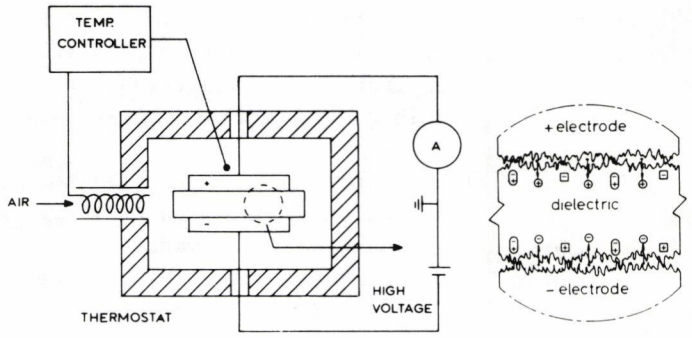


FIG.1-2 Electret forming unit (schematic). On the right, the injection of homocharges ⊕ , ⊖ from the dielectric-electrode interfaces is illustrated on an enlarged scale. The internal heterocharging by dipole orientation ⊕ ⊖ and ion migration ⊡ , ⊡ is also shown.

To increase the external field created by the bilaterally charged electrets, those intended for practical use are *metallized* in advance on *one side* (Fig. 1-3). This metallization reduces the electret from a macroscopic dipole to a monopole, because the image charges induced in the adhering metal layer effectively compensate the adjoining charges of the electret. Typical examples are the one-sided metallized electret

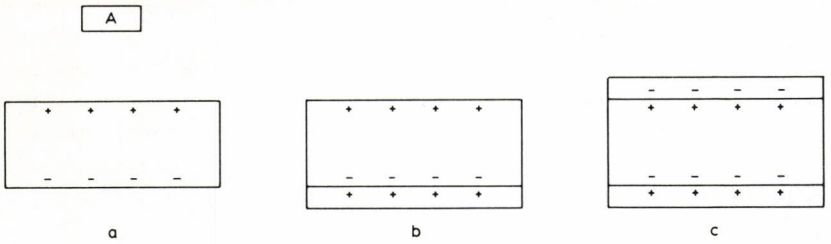


FIG.1-3a Open electret, the upper and lower net charge of which counteract each other, giving an opposite induction on metal plate A.

b One-sided metallized electret; this is the configuration most commonly used for applications, because it behaves as a unipolarly charged object, and therefore creates the strongest external field.

c Two-sided metallized electret; this is as a whole neutral and is mainly of interest for fundamental work.

films that are employed on a large scale in electret microphones. It is also worth mentioning that the homocharging by breakdown of the air is deliberately intensified in the manufacture of these electrets. This development is logical, because the deposition of homocharges from the air is a much faster process than the heterocharging by dipole orientation and space charge motion within the polymer. Moreover, in avoiding the heterocharging, nonpolar films can be used, which have a very low electrical conduction, so that the implanted homocharges are extremely persistent, even under severe environmental conditions. Note that the homocharge of such electrets is in fact a unilateral and unipolar one (mono-electrets).

For fundamental studies it is preferable to metallize the samples on *both* sides (Fig. 1-3c), for instance by evaporation of silver or gold in a vacuum. Then, homocharging is excluded and we are left with heterocharging*, the creation and decay of which are closely linked to the dielectric properties of the polymer. Most of our work has therefore been concentrated on *two-sided* metallized electrets. Such hetero-electrets are permanently charged capacitors; they have no external field, and so their decay can only be determined by *current* measurements.

For practical applications homo-electrets are more important, because they have a better long-term stability than hetero-electrets. Hence, we have studied the decay of one-sided metallized homo-electrets as well. For these a choice can be made between *current* and *charge* measurements.

* The injection of homocharges from evaporated electrodes is ruled out by this statement, which may not be strictly true for high forming fields, because of Schottky emission.

1:3 Number of Dipoles and Charges Contained in an Electret

It seems interesting to have an indication of the charge densities on a molecular scale. Let the polymer have a specific weight of 10^3 kg/m^3 with monomeric units of a molecular weight of 100. Then per cm^3 there are 6×10^{21} monomeric units, (particles for short), which may either bear, say, one dipole or one electron charge. The average radius of the particles is about 3.5 Å, and therefore their number on the polymer surface amounts to 7×10^{13} particles/cm^2.

As mentioned above, the effective surface charge density, q, found on the open side of an electret is of the order of 10 nC/cm^2. This net charge may arise from a dipole polarization, a surface charge, and from space charges.

Now, if q arises from dipoles only, and if we suppose these to have a moment of 10^{-29} Cm (3 Debyes), 10^{19} dipoles/cm^3, would have to be aligned. Substantially, there are 6×10^{21} dipoles/cm^3 available, and so *1 in 600* should remain lined up to account for the charges observed. On the other hand, if q would be due to a mere surface charge, we should need 0.6×10^{11} electrons/cm^2. This implies that *1 in 1200* surface particles must be charged.

If, finally, the charge would originate from space charges that are uniformly stored up to a depth of 5 µm, a space density of 1.3×10^{14} electrons/cm^3 would be required. Then only *1 in* 2×10^6 particles must be charged. This is a very large number, compared to that for dipole charging. Obviously, space charge polarization is much more effective than dipole polarization. This is so, because the former consists of a layer of unipolar charges, whereas the latter is built up of an array of bipolar charges (dipoles). Hence, we may expect significant TSD current peaks for a relatively small number of space charges. On the contrary surface charging, which merely consists of a monolayer of charges, is not revealed at all in current TSD. In fact, all surface charges are neutralized when the open side of the electret is metallized before TSD.

1:4 Experimental Methods for Studying the TSD of Electrets

Since spontaneous discharge of electrets takes several years at room temperature, Frei and Groetzinger (FG 36) proposed a thermal stimulation of the decay, to enhance the mobility of the frozen-in dipoles and charges, so that the decay experiment could be done within a reasonable time. Their technique consists in slowly heating the electret between two electrodes, connected to a sensitive ammeter that measures the discharge current.

This technique has later been extensively practised by Gross, Murphy and Gubkin and their associates (Gr 49, MC 63, GM 62). At that time, the temperature rise was not programmed, since interest lay chiefly in the ultimate charge released. As was already pointed out by Von Altheim (Al 36) charge release is controlled by molecular motions, which depend strongly on temperature. It is therefore advisable to measure the ensuing current as a function of temperature. For this reason, we raised the temperature linearly, at a rate of 1 °C/min, as advocated by Bucci et al. (BF 66) for inorganic dielectrics. In this modified form the technique has made encouraging progress in several laboratories (CP 70,

TF 70, Ma 70, LH 70, La 70, KK 70, Tu 70).

We shall refer to Frei's method, which we have applied to two-sided metallized electrets, as *current TSD of shorted electrets*, since the voltage drop across the ammeter is almost *zero* (Fig. 1-4a). Owing to the virtual short-circuit the mean electric field, E, and the mean ohmic conduction current within the electret are minute, so that it only generates a displacement current. In other words, the external current will be due to image charges escaping from the evaporated electrodes, where they were previously induced by the dipoles and space charges.

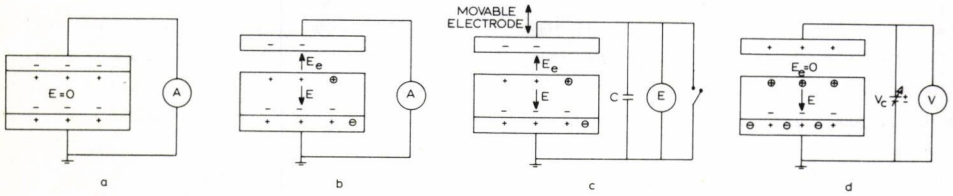


FIG.1-4a Current TSD with two evaporated electrodes. Since the electret is short-circuited, field E is zero.

b Current TSD with an air gap, which blocks the flow of a conduction current and only conveys a displacement current. In this set-up the electret itself is not shorted, so that $E \neq 0$. Note that the upper charges induce part of their image charges on the lower electrode. This loss of induction is indicated by the charges encircled.

c Charge TSD by transferring the charge induced on the upper electrode to an electrometer E. This is done periodically by moving the electrode away from the electret.

d Charge TSD based on automatic cancellation of the external field of the electret by a self-adjusting bias voltage V_c. Thus the upper electrode is virtually floating and so this system works in open circuit.

To study the decay of one-sided metallized homo-electrets, we have modified this method by introducing an *air gap* adjacent to the non-metallized side (Fig. 1-4b). When this two-layer assembly is heated in short-circuit, a displacement current is generated by image charges released from the noncontacting electrode. A marked difference from current TSD without air gap is, that the electret is *no longer* shorted. As a result, the electric field within the electret may become quite large. The air gap also prevents the electret charges from recombining with the image charges of the upper electrode, or what is the same, it will block any transport of charge carriers and therefore will only convey a displacement current.

The presence of an air gap also allows charge measurements to be made. Several methods for this have recently been surveyed (Tu 70 a). A common method (Gr 49) is to move the nonadhering electrode periodically away, in order to transfer the image charges induced on it to an integrating electrometer (Fig. 1-4c). Unfortunately, no continuous record

of the charge decay is obtained. Therefore we have preferred the *current* measurement for TSD with an air gap. This also reveals more distinctly the temperature of fastest decay, for the current then reaches a maximum.

However, there is an important group of electrets for which current measurements are less favourable, i.e. the one-sided metallized homoelectret *foils*. For these, the ratio between the air gap and the thickness of the electret, cannot easily be made small. This implies that the current measurement suffers a large induction loss, which occurs because the decaying electret induces most of its image charges on the grounded, adhering electrode instead of on the probing electrode.

In view of their application in electret microphones it is of major importance to study the decay of these electret foils. Now, for practical purposes charge decay is much more interesting than current release. We have therefore developed a novel version of the air-gap charge measurement, which allows a *continuous* monitoring of the charge (Fig. 1-4d). It is based on the field-cancelling principle (RP 68, Tu 70a), according to which the external field of the foil is nullified by driving the noncontacting electrode with an adjustable bias voltage of the same value and polarity as the equivalent voltage of the electret. It is typical of this system that the *external* current is *zero*; we shall therefore refer to it as to *charge TSD in open circuit*.

The characteristics of the three methods elaborated can be summarized as follows:

current TSD with shorted electrets	$\int_0^1 E dx = 0$	$j_r^* \neq 0$
current TSD with an adjacent air gap	$\int_0^{1+g} E dx = 0, \quad \int_0^1 E dx \neq 0$	$j_r^* \neq 0$
charge TSD in open circuit	$V_c^* = \int_0^{1+g} E dx = \int_0^1 E dx$	$j_r = 0$

where we have labeled the quantities measured by an asterisk.

1:5 Survey of the Mechanisms Responsible for TSD

The processes taking place during TSD are similar to those occurring during charging. Generally speaking, they only behave in an opposite way. It is for this reason that we have not reviewed the charging processes separately.

Let us first specify the nature of the charge stored. The net charge of an electret usually arises from *aligned dipoles* and space charges. The latter are *excess charges*, which cause the electret to be not locally neutral. However, before the electret formation the neutral polymer

already contained free charges; they manifest themselves in a conduction current when a field is applied. So in addition to the excess charges there must be free *equilibrium* charges in the electret. These do not contribute to its net charge, but are responsible for its (intrinsic) ohmic conductivity.

It are equilibrium charges, because their positive and negative densities are *time*-independent*. Moreover, it is assumed that these charge densities are always equal and *space*-independent, so that electric neutrality is everywhere preserved during the charge transport by the field. The adjective "ohmic" before conductivity accentuates that this motion gives a current that varies *linearly* with the field. By contrast, the TSD current due to the conductional motion of the excess charges will vary *nonlinearly*. This is so, because the excess charges provide not only the carriers, but also the driving field. For this reason we shall hereafter consider the decay of the excess charges by these two conductional motions separately. This makes the mathematics easier and allows one to attribute part of the excess charge decay to a known material constant, viz. the ohmic conductivity.

In hetero-electrets the excess charges are *intrinsic and bipolar*. They originate from those charges that first took part in the conduction and where next accumulated near the electrodes during the formation. This field motion has been opposed by diffusion, moreover during their transport part of the charges has been lost by recombination with opposite carriers. Incidentally, in *heterogeneous* hetero-electrets of e.g. partially-crystalline polymers, the intrinsic excess charges will mainly pile up at the phase boundaries (Fig. 1-5). They are supplied

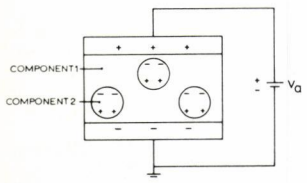


FIG.1-5 Charging of a heterogeneous polymer by the Maxwell-Wagner effect. Component 1 is assumed to be less conductive than component 2, and the embedded particles are therefore charged heteropolarly.

there by the unequal ohmic conduction currents within the two components or phases (interfacial or *Maxwell-Wagner* charging). In homo-electrets the excess charges, which are injected into the nonmetallized side, will be *extrinsic and unipolar* (mono-electrets).

The decay of the net charge of an electret during TSD will result from: *dipole reorientation, excess-charge motion and ohmic conduction*. The first process will be clear; the thermal agitation will reorient the aligned dipoles at random. The motion of excess charges originates

* This implies that the loss resulting from their conductional transport to the electrodes, must continuously be compensated by a supply of new equilibrium charges, which are (thermally) generated by the dissociation of neutral (impurity) centres.

from space charge limited (SCL)* *drift* and *diffusion*. The first motion is due to the local electric fields forcing the mobilized excess charges to drift towards opposite charges, whereby electric neutrality is restored. The excess charges will eventually recombine either with their opposed image charges, or with opposite excess charges within the polymer**. Whichever is the case, their gross motion should generate a discharge current opposed to the charging current. We shall show in Chap. 5 that SCL drift releases a current which depends *quadratically* on the excess charge stored.

The motion of the excess charges resulting from *diffusion* hardly needs comment. It arises from the tendency of the excess charges to eliminate their concentration gradients, by leaving the electret and by spreading uniformly over it. When the charges meet an opposite charge during this motion, they will again recombine to a neutral entity.

Not only the excess charges, but also the equilibrium charges are driven forward by the local electric field. This leads to local *ohmic conduction* currents, which neutralize part of the excess charges by supplying opposed equilibrium charges. This ohmic conduction can only be observed in *non*shorted electrets. Since the ohmic conductivity is space-independent, it passes unnoticed in a shorted (homogeneous) electret, although it does dissipate part of its excess charges.

In general, the decay of excess charges in heterogeneous systems is ascribed to ohmic dissipation alone; any motion of the excess charges is neglected. The excess charges are considered to be neutralized by opposed carriers replenished at the phase boundaries by the unequal ohmic conduction currents (MW discharging).

All the decay processes are *thermally activated*, i.e. their relaxation times depend exponentially on temperature. Hence, the processes are considerable accelerated during TSD, and will generate an appreciable discharge current of some pA/cm^2 for a stored charge of 10 nC/cm^2.

Actually, one may expect the temperature dependence of the dipole reorientation to differ from that of the motion of excess charges. The latter will conform closely to that of ohmic conduction, from which the charges often originate. In particular, we may expect the current maximum for dipole reorientation to occur at a lower temperature than that of the excess-charge motion. The first process requires only a rotational motion of molecular groups, whereas the latter process involves a motion of molecular groups (ions) over macroscopic distances.

* SCL refers to the fact that any drift to a certain position is limited by kindred excess charges having previously arrived at that position.

**Note that the final annihilation of the charges by recombination does not create a current.

1:5.1 Representative TSD Current Thermogram

The results on the current TSD of a shorted PMMA hetero-electret shown in Fig. 1-6 confirm the foregoing argument. As depicted in the figure, PMMA has a polar ester sidegroup $-COOCH_3$ with a dipole moment of 5.3×10^{-30} Cm (1.6 Debye), which can rotate *with* and *without* the main chain segments $-C-CH_2-$. The thermogram gives the reduced current density vs. the programmed temperature. To study the release in a broad temperature range we have frozen-in to -180 °C instead of to room temperature. For increasing temperature we found three maxima, designated: β, α and ρ.

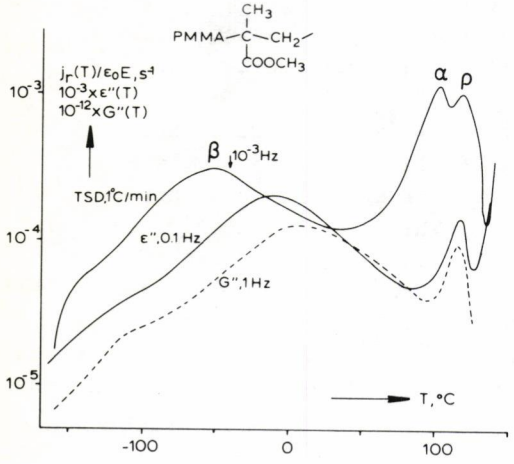


FIG.1-6 Comparison between current TSD and ε" and G" data for PMMA. The electret was formed at 140 °C - 75 kV/cm - 1.5 h. Note that the ρ peak is absent in the ε" and G" results.

The β peak, which occurs at -51 °C in the glassy state of the polymer, is ascribed to the reorientation of the polar sidegroups by local motions around the C-C bond. The α peak, found at 102 °C, is due to the joined reorientation of the polar sidegroups with adjacent main chain segments. The temperature location of this peak neatly corresponds to the glass-rubber transition, T_g, known from dilatometric measurements. This is not coincidental, because TSD studies the macromolecular relaxations at a similar slow heating rate. The two *dipolar* reorientation peaks also manifest themselves in sinusoidal dielectric measurements, this can be seen from the inserted ε" data at 0.1 Hz.

However, the ρ peak is now missing, and instead increasing conduction losses are found. This suggests that the TSD ρ peak should be attributed to the decay processes most closely related to conduction i.e. the motion of excess charges by SCL drift and diffusion. These TSD processes are transient ones, and give rise to a peak, because the moving charges gradually disappear. In contrast, in sinusoidal measurements the moving charges are not exhausted, for they are replenished by the external voltage. In this case the conduction losses do not level off but increase continuously.

This shows that TSD gives more information than conventional measurements do. Moreover, compared with the ε"peaks, these of TSD are shifted to a lower temperature and are better separated. Obviously, TSD probes the molecular relaxations at a lower frequency and therefore has a higher resolving power.

1:5.2 Representative TSD Charge Thermogram

Fig. 1-7 shows a charge thermogram obtained with the automated field-cancelling meter. The results pertain to Teflon-FEP foil bombarded with 20 keV electrons in vacuum. They thus correspond to the decay of a well-defined charge carrier. Nevertheless, the charge does not decay at a simple rate, for after a fast decay at about 170 °C, the decay rate is seen to diminish. This prompted us to perform a two-stage TSD, by making a 1st run up to 200 °C, then cooling to room temperature and starting the TSD anew with the persistent charge left.

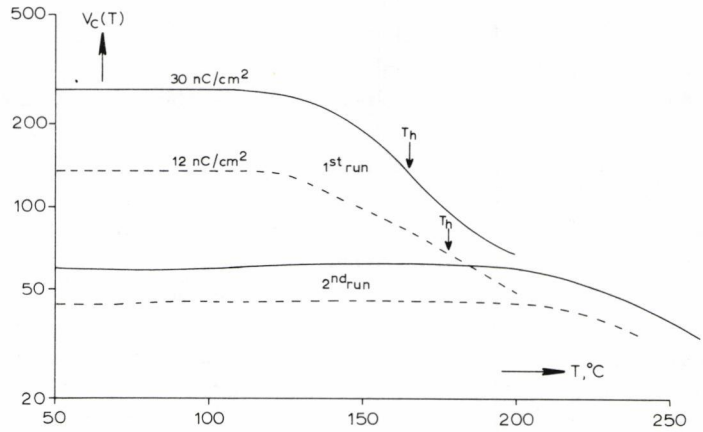


FIG.1-7 Increase in thermal stability of two electron-bombarded Teflon FEP-a foils after a partial heating. The foils were bombarded with 12 and 30 nC/cm² at 20 keV. We see that the lower charged foil has the higher half-value temperature, T_h, because the field that drives the electrons towards the back-electrode is 2.5 times smaller.

Surprisingly, the charge remains almost constant up to 200 °C during the 2nd run. This indicates that dissipation of the electrons by ohmic conduction is not the main decay process, otherwise the charge would begin to decrease at the same temperature as in the first run. For the same reason diffusion cannot dominate.

Only SCL drift of the electrons can explain the results obtained. In charge TSD all electrons are drifting towards the adhering back-electrode where they neutralize with their image charges. Now the fewer electrons are left, the lower their drift rate will be, because it are the electrons remaining that determine the driving field. Hence, this

decay process shows a stabilizing effect, but it cannot be expected to the extent we found.

We therefore generalize our concept of SCL drift and presume that the injected electrons have been *trapped* in the polymer at *different* energy levels. The electrons must then first be released from these traps before they can drift away. Electrons in shallow traps will be released first. Consequently, after the first TSD run we are mainly left with electrons in *deep* traps, and these can be expected to persist up to the final heating temperature of the first run, when the TSD is restarted.

So far we have assumed that the SCL drift involves excess charges with a thermally activated mobility, which have to surmount a certain energy barrier in order to be transported. Now the scope of our discussion is extended to include excess charges that are captured in *traps*. In this case, it is primarily the number of excess charges partaking in the drift that is thermally activated. Typical of trapping is that the freed carriers drifting along may be *retrapped* in empty traps. This retrapping may be fast or slow. If it is fast there is no formal difference with the concept of carriers having a thermally activated mobility.

In view of the various processes acting, we may expect the theory of the TSD of excess charges to be intricate, the more so since the variables will be time and space dependent giving rise to partial differential equations. The theory of dipole reorientation seems to be less complex. However, we must remember from Fig. 1-6 that the dipolar β and α peaks are broad, especially the former. This implies that we are not dealing with two single dipole relaxations, but with a vast number of them. As a result, the dipolar TSD response cannot be described by a single ordinary differential equation (ODE), but must be treated with a set of simultaneous ODE's, or for continuous distributions even with Laplace transforms.

The potentially large number of processes makes TSD experiments as fascinating as ordinary dielectric measurements, where most of the foregoing processes also occur, although some may appear less pronounced than in TSD.

The following table enumerates all possible TSD mechanisms.

Process	TSD peak	Occurrence	Remarks
dipole reorientation	α , β, γ	polar polymers	as a rule distributed
SCL drift of excess charges	(α), ρ	all polymers	for homocharges only of importance in nonpolar polymers; then often accompanied by trapping
diffusion of excess charges	"	"	revealed for blocking electrodes only*
ohmic conduction	"	"	observed when electret is not shorted (air gap systems)
Maxwell-Wagner effect	"		partially crystalline polymers

* The need of blocking electrodes for the generation of an external current by diffusion will be explained in the next section. These electrodes prevent the neutralization of the incoming electret charges by the image charges.

1:6 Measuring Efficiency of the Decay Processes in Current TSD

In charge decay all mechanisms are alike in determining the thermogram. This is not so in current TSD of shorted electrets; here only *part* of the excess charges originally stored may be recovered. For conductive polymers this deficit may partly arise from the unnoticed charge loss by ohmic conduction, but even for nonconducting polymers the charge release may be incomplete, because the internal current flow is *bi*directional, so that only part of the image charges previously induced are freed from the electrodes, while those remaining will recombine with the incoming electret charge.

1:6.1 Current TSD of Shorted Electrets

The current TSD of shorted electrets gives the simplest current thermogram, because only the dipole reorientation and the motion of the excess charges are observed. Now, for every dipole reorientating an image is liberated from the electrodes. This implies that the current release by *dipole reorientation* has an *efficiency of 100 %*.

Charge release due to the motion of excess charges by SCL drift is less efficient (Fig. 1-8a). Only part of the image charges originally induced are liberated when the excess charges become neutralized within the polymer and at the electrodes. This is so, because the image charges actually take part in this neutralization. Hence, most of them do not leave the electrodes to flow through the ammeter to ground. It is the unidirectional gross motion of the excess charges preceding their neu-

tralization that releases some of the image charges. For near-surface charges that have penetrated to a relative depth of r_o/l, we shall show in Chap. 5 that the ultimate charge released is only $r_o/2\ l$ times the charge initially stored. Similar conclusions hold when SCL drift is accompanied by trapping.

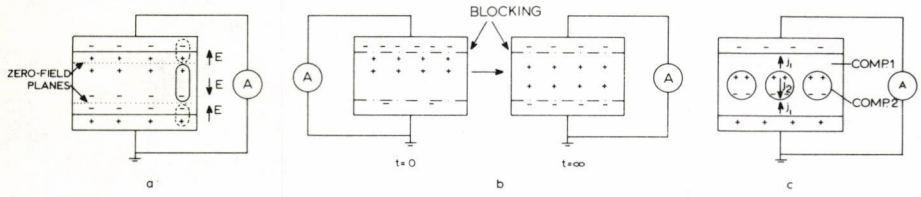


FIG.1-8a SCL drift in a hetero-electret. There are two zero-field planes. The charges confined within these planes are driven towards each other, whereas the outermost charges are swept towards the electrodes, where they recombine with most of the image charges. As a result only a small part of the image charges becomes free to flow through the ammeter.

b The diffusive motion of charges only releases a current if the electrode contacts prevent the stored charges from recombining with the image charges of the electrodes. A unipolar charge, stored near the upper electrode at t = 0, therefore will eventually spread out uniformly without loss of charge.

c The decay of interfacial charges is due to a recombination with opposite charges supplied to the interfaces by ohmic conduction currents $j_{1,2}$ flowing through the two components or phases.

Current release by the diffusive motion may also be measured inefficiently. If the evaporated electrodes are *open*, i.e. if they do not hinder the recombination between the electret charges and the image charges, diffusion will *not* generate a current at all; for the charges diffusing towards the neutralizing electrodes will be equal in number to those diffusing away from them. Accordingly, there is no gross motion of excess charges, so that all the image charges will remain bound to the electrodes, and be finally neutralized by the incoming excess charges.

Only when the *charge transfer* at the electrodes, between the electret charges and the image charges, is *completely* or *partly* blocked an average diffusion current will arise (JL 53). The blocking may be due e.g. to an insulating oxide layer; an adjacent air gap also gives a perfect blocking. For completely blocking electrodes the excess charges tend to move away from the electrodes, thus filling the sample uniformly (Fig. 1-8b). This gives a unidirectional gross motion, and as a consequence, part of the image charges earlier induced by the migrating excess charges are released. One readily verify that for electrets with thin unipolar or bipolar charge layers the efficiency will be 50 and 100 % respectively of the charge originally stored. For partly blocking electrodes, the efficiency will lie between 0 and 50-100 %. The rate of charge-exchange at the electrodes is thus crucial for current release

by diffusion. It is hard to predict, even for evaporated electrodes we found that they may not be completely open; this will be illustrated in Sect. 6:1.1.

Similar to the current release by dipole reorientation that of SCL drift does *not* depend on the charge-exchange rate at the electrodes; only the final distribution of the excess charges will differ. For open electrodes all excess charges will have disappeared at the end, whereas for blocking electrodes they are not able to neutralize the image charges and will pile up near the electrodes as two surface charges, provided that the polymer is perfectly insulating.

These surface charges do not alter, however, the internal field, for they are exactly compensated by the nearby image charges. As a result the current release by SCL drift will be the same for open and blocking electrodes.

The measuring inefficiency of excess-charge decay also appears in heterogeneous electrets. It arises, because the excess charges stored at the phase boundaries will be neutralized by conduction currents of *opposite* direction (Fig. 1-8c). This may result in a weak average current over the sample, especially when the conductivities of the components are almost equal. In this case, current efficiency will be poor, because it is the average current that equals the external current. On the other hand, if one of the components is a perfect insulator, all of the image charges previously induced will be released, and the efficiency will be 100 %.

As a résumé of the measuring efficiencies of the various TSD processes we obtain:

dipole reorientation	100 %
SCL drift of excess charges	0 - 15 %
diffusion of excess charges	25 - 50 % , homo-electrets (monopolar)
	50 - 100 % , hetero-electrets
Maxwell-Wagner discharging	0 - 100 %

The quoted maximum efficiencies of the last three processes only hold when the excess charges are not simultaneously dissipated by ohmic conduction.

1:6.1a Pecularities of Excess Charge Decay in Shorted Electrets

So far any interaction between the various processes has been ignored. However, in practice current release may be further lowered by the fact that some decay processes may counteract each other in releasing *opposite* currents. The direction of a specific discharge process can easily be predicted; it should generate a current of a polarity opposite to that of the charging current.

In shorted unipolar homo-electrets, the excess charges will move

back mainly to the near electrode on the injection side. The homocharge motion thus *attracts* image charges to this electrode, rather than liberating them. Consequently, when homocharging is attended in polar polymers by orientation of dipoles, the TSD current resulting from their reorientation will *oppose* that of SCL drift. On the other hand, in hetero-electrets these currents always have the *same* polarity, because the intrinsic excess charges move away from the electrodes (compare the α and ρ peak of PMMA in Fig. 1-6).

A similar thing happens for the combined decay by diffusion and SCL drift. These processes will enhance each other's flow in hetero-electrets, whereas in unipolar homo-electrets they may weaken each other. This is exemplified in a current thermogram of electron-bombarded Teflon FEP (bilaterally metallized). The positive current in Fig. 1-9 corresponds to SCL drift, and the weak negative current presumably arises from diffusion due to a partial blocking of the electrodes.

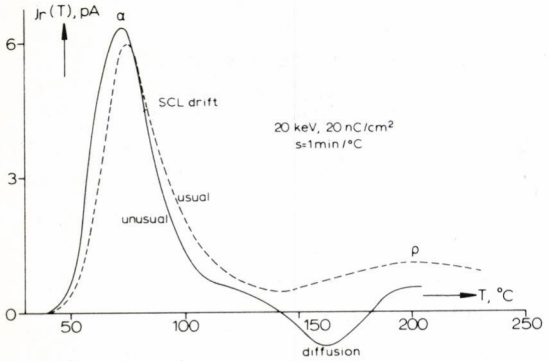


FIG.1-9 Current thermograms of metallized Teflon-FEP foils charged unipolarly by electron bombardment with an energy of 20 keV. We usually observed a unidirectional current, and only in a few cases diffusion induced a current reversal. By integrating the current the ultimate released charge, $s\int_0^\infty j_r dT$, is found to be much less than the injected charge of 20 nC/cm². The measuring area was 17.4 cm².

Yet such current reversals are rather exceptional; we usually found a unidirectional current in the direction of SCL drift. This means that *evaporated* electrodes are *hardly*, or at least not strongly, blocking. It is interesting to note that the current maximum due to SCL drift of the electrons occurs just at the glass-rubber transition of the polymer;this indicates, that the mobility of extrinsic carriers depends on temperature and free volume in a way similar to that of the chain segments of the host polymer.

Finally, the unnoticed decay of excess charges by the ohmic conduction of the polymer has a striking consequence, which has first been pointed out by Gross (Gr 70).He has stated that the *ultimate* charge released may *vary* with heating rate. This can be explained as follows. The thermally activated processes will respond the sooner the slower the heating. Now, when the temperature dependencies of ohmic conduction, SCL drift and diffusion are dissimilar, the internal charge loss may *slightly* differ for two heating rates, and the ultimate charge re-

leased will vary. A similar effect occurs in heterogeneous electrets, when the temperature dependencies of the ohmic conduction of the components differ.

1:6.2 Current TSD of Electrets with an Adjacent Air Gap

Since the air gap blocks any charge exchange, all image charges previously induced on the noncontacting electrode will be released when the electret decays. Hence, as regards the outflow of the image charges, all decay processes will have an efficiency of 100 %. However, this does not mean that the net charge of the electret is released. This also induces part of its image charges on the adhering metal layer (Fig. 1-4b). The fraction of image charges lost in this stray induction depends on the ratio of the capacitances of air gap and electret, and so for an optimal efficiency, the air gap should be relatively narrow.

Since all processes contribute we may expect the current thermogram for TSD with an air gap to be more complex than that without. In particular, the electret is *not* shorted, so that there is a mean electric field in the sample. This field may be quite large; for a charge of 10 nC/cm^2, $g/l = 1$, and $\varepsilon = 3$, we find $E(0) = 30$ kV/cm. It may therefore lead not only to an appreciable ohmic conduction within the sample, but it may also orient the permanent dipoles anew. Especially, in polar polymers the release by ohmic conduction will be pronounced. In this case, SCL drift and diffusion, which both assist current release by conduction, are relatively less important.

1:6.2a Examples of Current TSD with an Air Gap

Fig. 1-10 shows the air-gap thermograms of PVC charged by friction and corona at room temperature. We may expect these electrets to bear only a homopolar surface charge, since its dipolar C-Cl groups had no chance to orientate themselves. Then they may do so in the temperature-dependent internal field during TSD. This, however, requires them to respond at a lower temperature than the ohmic conduction, otherwise the internal field has vanished before they are able to orientate. This orientation will be such that it lowers the internal field created by the homocharge. Moreover, it will only be temporary, for when at high temperatures the ohmic conduction comes into action, the internal field will soon collapse and the dipoles will quickly randomize. As a result the TSD current peak due to the ohmic decay of the homocharge, will be preceded by a transient current peak of the same polarity, owing to the orientation of permanent dipoles.

Similarly when we start with a hetero-electret, in which there is only a dipole orientation, the ohmic conduction of the electret will respond during TSD by forming a temporary surface charge at the air gap interface, of such a polarity that it weakens the internal field created

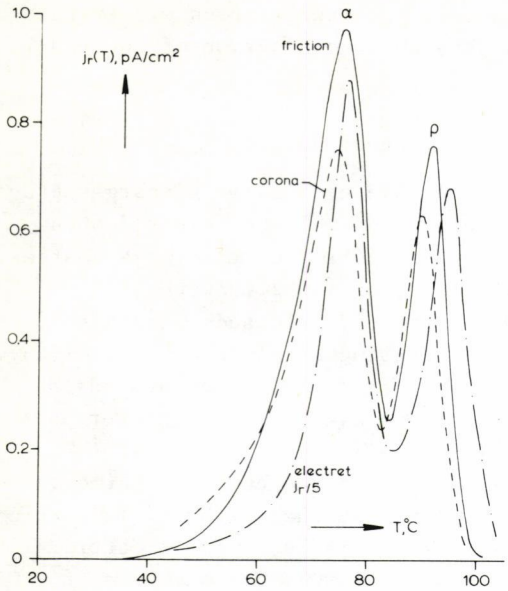


FIG.1-10 Air-gap thermograms of PVC charged by friction, and corona discharge. The thermograms are very similar, exhibiting a dipole peak, α, and a conduction peak, ρ_c. For comparison, a thermogram of a metallized PVC hetero-electret, formed at 100° - 2.5 kV/cm - 1 h, is shown. The heating rate was 1.2 °C/min, and the reduced air-gap g/l = 1; data of Ong (On 72).

by the dipoles. In practice, this homocharge reaction will be small, since dipole reorientation generally responds earlier than the charge motion by ohmic conduction. However, if it occurs, it releases a small current opposite to that of dipole reorientation.

The air-gap set-up may further elucidate the coexistence of a hetero- and homocharge on bare electret faces. For such electrets the set-up always will release a current that reverses in sign when most of the dipoles have been reoriented and the ohmic conduction starts to consume the homocharges. This concomitantly proves that homocharges are more persistent than (dipolar) heterocharges.

1:7 Methods to Unravel the Various Decay Processes

TSD depends on the properties of the polymer, the forming conditions and the TSD measuring technique.

1:7.1 Choice of Polymers for TSD

By the choice of the polymer we can change, in particular, the dipole contribution and the ohmic conduction. There are two obvious choices, viz. *polar* and *nonpolar* polymers. When the polymer is polar, we will have a distinct dipole reorientation, whereas in a nonpolar polymer we will have none. Moreover, polar polymers show a high ohmic conduction, since this arises partly from absorbed water, which may amount to a few per cent in polar materials. The high polarity will also enhance the formation of free carriers by facilitating the dissocia-

tion of impurities. Part of these carriers will be piled up near the electrodes during the formation and so form excess charges. Consequently, in polar polymers we might expect storage of dipoles and excess charges. Their high concentration often enables the excess charges to contribute discernibly to the TSD of shorted electrets, despite the fact that most of them may be dissipated, unnoticed by ohmic conduction. That they actually give a ρ peak was demonstrated in Fig. 1-6.

Their high conductivity makes polar polymers not suitable for studying TSD of injected homocharges. For this purpose nonpolar polymers are much better. In these polymers the decay by ohmic conduction will be low, whence SCL drift of the excess charge will dominate; this was shown in Fig. 1-7 for Teflon-FEP. For this reason, nonpolar polymers make the most stable homo-electrets known to-day. The homocharges may be injected by Townsend breakdown, corona discharge and electron bombardment. The latter is the most attractive, because the carrier and injection energy are well defined, whereas in negative, corona or Townsend breakdown, besides electrons, negative ions may be deposited.

By adding strongly polar or semi-conductive materials to the polymer, we obtain *composites* in which MW charging will occur. This charging may likewise be expected in partially crystalline polymers. We also investigated a simple two-layer system of heat-sealed foils, the TSD of which is more easier to analyze.

1:7.2 Effect of the Forming and Storage Conditions

The forming conditions may also be exploited to change the contribution of the various decay modes. There are three forming parameters, temperature T_f, time t_f, and field E_f. By varying T_f, we can easily detect whether a hetero-electret contains a distributed dipole polarization or not. For a single dipole relaxation the current will be lowered when T_f is decreased, but the position of its maximum will remain the same. However, for a distributed polarization the maximum will *shift* with T_f, unless T_f is chosen above the transition temperature involved. This is illustrated in Fig. 1-11 for the distributed polarization of a PMMA hetero-electret. When T_f is low, only the fast subpolarizations will be filled, and the TSD current will be cut off on the high temperature side, because of the unactivated slow polarizations. When T_f is raised, more subpolarizations will be activated, and the current maximum will rise and simultaneously shift to a higher temperature. Only when all subpolarizations are filled the dipolar current maximum is seen to appear at the actual transition temperature T_g. We observe that a decrease in T_f also markedly affects the ρ peak. Obviously, at a low T_f, the conduction is low, so that fewer carriers are available to accumulate; this weakens the space charge peak. Strikingly, its position is not changed, however, which indicates that the carriers are not trapped at different energy levels.

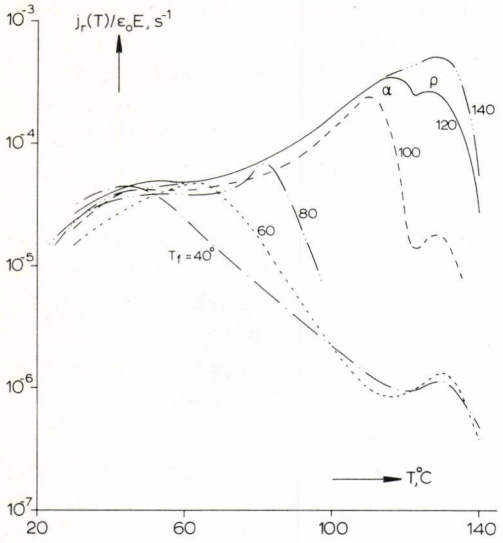


FIG.1-11 Current thermograms of a PMMA hetero-electret formed at various temperatures. For low forming temperatures, T_f, the thermograms are cut off beyond T_f, so that the dipolar current peak does not emerge at the proper glass-rubber transition, α. By contrast, the space charge or ρ peak is always there, though not prominent. We chose E_f = 100 kV/cm, t_f = 1.5 h and s^{-1} = 0.5 °C/min.

The polarization time t_f has a similar effect as T_f, but this must be changed logarithmically to obtain changes of the same magnitude.

By varying E_f, we may distinguish between dipole peaks and space charge peaks. The former increase linearly with E_f, the latter non-linearly. However, the deviations from linearity will not be very large.

The storage truncates the thermograms of a distributed polarization on the low-temperature side, since during a long storage it is mostly the fast polarizations that discharge first.

For homo-electrets T_f will mainly influence the penetration depth of the injected carriers; penetration will increase with temperature. Furthermore, by changing the polarity of the injection voltage we can inject negative or positive carriers, which can have different drift mobilities, retrapping and recombination rates. For Teflon FEP we have found the charge decay of positive carriers to be much faster than that of the negative ones. This polymer should therefore be charged *negatively* to obtain electrets with a long life time. We have also observed that the positive carriers hardly penetrate at room temperature, whereas the negative ones do, although not much. This makes it likely that electrons contribute significantly in a negative injection.

To distinguish between homocharge decay by ohmic conduction and SCL drift in an open-circuit, we can change the magnitude of the homocharge by varying the injection voltage. Decay by ohmic conduction is independent of the initial charge, but SCL drift is not. A high initial charge will enhance the drift, because it increases the field that drives the charges to the adhering back electrode (cf. Fig. 1-7).

1:7.3 The Use of Various Experimental Techniques

We have indicated in Fig. 1-6 that there is a strong resemblance between TSD thermograms of hetero-electrets and ε'' vs. T curves of conventional dielectric measurements. These conventional measurements may help in assigning the molecular origin of the TSD peaks, because much progress has been made their interpretation (Cu 60, HS 62, CR 67, Is 69, He 69, He 72). In making this comparison, we should realize that the TSD peaks occur at a lower temperature, because the equivalent frequency of TSD is low (of the order of 10^{-3} Hz). TSD measurements can therefore be best compared with results of the isothermal step-response discharge. Unfortunately, these are scarce in the current literature, and we often have to be content with results from sinusoidal experiments.

The comparison with ε'' data also reveals whether the peaks are of a dipolar or space charge origin, for in Fig. 1-6 we have shown that only the dipolar TSD peaks can be traced back to sinusoidal data. Instead of a ρ peak, increasing conduction losses are found, because dielectric measurements cannot be made in short-circuit.

When a TSD-ρ peak indeed emerges it is interesting to see whether it is related to the molecular parameters of ohmic conduction. This can best be revealed by current TSD with an air gap. In fact, this enabled us to prove that the ρ peak of shorted hetero-electrets corresponds well with the peak due to ohmic dissipation of homocharges in an air-gap set-up.

Further evidence was obtained by performing a current TSD with an air gap on *two-sided* metallized hetero-electrets. Even when these contain only a dipole polarization, we will find a pronounced TSD conduction peak. This can be explained as follows. Due to the metallization we start with a *neutral* object, because the dipoles will have induced image charges on the adhering metal layers, which makes the external field zero at t = 0. When the assembly is heated, the dipoles are reorientated and part of the image charges are free to charge the capacitor formed by the electret. Hence, there appears a field in the air gap, and the dipole reorientation will generate a current. The freed image charges are short-lived, however, for when at high temperatures ohmic conduction beccmes high enough, they will be dissipated. This dissipation will generate a current of opposite polarity to that of the dipolar current. Moreover, it will be of the *same magnitude* as the dipolar current, to make the integral $\int_0^\infty j_r dt$ zero, in accordance with the fact that we started with a neutral object.

This argument was confirmed by experimental results; we actually found a marked conduction peak in this set-up, and it was interesting to see that its position agreed well with the TSD ρ peak of the shorted electret (see Fig. 10-62).

To obtain further support for the view that the charges partaking in

the ρ peak of hetero-electrets are of the same molecular origin as the charges participating in ohmic conduction, we designed a *special MW experiment*. It consists in the charging and discharging of a polymer with an adjacent air gap, at such low voltages that no air breakdown occurs. Then an interfacial heterocharge will be formed at the blocking air gap. It originates from carriers supplied by the ohmic conduction of the polymer. This charge attains a final value when it has lowered the field within the polymer to zero. Accordingly, when the assembly is heated under a constant voltage, a current peak will arise. Similarly, when the system is subsequently discharged in short-circuit, an opposed peak of the same magnitude will be observed when the interfacial charge is neutralized. The ρ peak of the corresponding shorted electret agreed well with this artificially obtained conduction peak. Note that for polar polymers the conduction peak will be preceded by a dipolar peak. The two peaks will have the same polarity, since the dipoles and interfacial charge are both heteropolar (see Figs 6-8 and 6-9).

So far, we have not been able to separate the contributions to the ρ peak of SCL drift and diffusion, presumably because the two processes give a similar gross motion of the excess charges and therefore have about the same temperature dependence.

Strong evidence that part of the heterocharge arises from space charges was obtained by *sectioning* of the electrets. This technique was first introduced by Gross and his co-workers (GM 62, Gr 71).It consists of cutting an electret into slices and studying the current TSD of these. The faces of the slices are metallized when necessary; this has the advantage that frictional charges created during the cutting are eliminated. In this way, we found for PMMA and ChPEth electrets, that the outer sections release a higher current than the middle section; this points to an appreciable storage of excess charges near the electrodes.

Finally, for nonpolar homo-electrets we should like to clarify the contributions of SCL drift and ohmic conduction. This can be done by a multi-stage TSD. For SCL drift the decay will then stabilize during the later runs, whereas for ohmic conduction it will not. In this way, we proved that SCL drift dominates in the charge decay of Teflon FEP electrets (Fig. 1-7). A similar behaviour can be expected in current TSD of (metallized) shorted homo-electrets. The current maximum now gradually shifts to a higher temperature during the subsequent TSD runs when SCL drift prevails.

A salient feature of SCL drift of unipolar homo-electrets is that the transition temperatures in charge and current TSD will be *different* for low penetrations. This is caused by the difference in migration distance; in current TSD the excess charges move towards the nearest electrode, whereas in charge TSD they move towards the farthest (compare Fig. 1-4d). Only when ohmic conduction dominates, the transition tempe-

ratures will be the same.

1:8 Applications of TSD

The information that TSD provides is manifold. First of all, it elucidates the decay mechanisms, and reveals the thermal stability of an electret in about four hours. As the TSD processes are often the reverse of these occurring during the formation, TSD also gives insight into the charging processes. The latter are difficult to investigate on their own, for they are often masked by a strong ohmic conduction. Clearly, TSD is a powerful method for finding and developing better electret materials.

In a similar way, air-gap TSD can be utilized to study the decay of electrostatically charged polymers, about the decay of which little is known, because the results available pertain to room temperature, at which the decay times are long. Extensive knowledge of this decay is needed to properly combat the nuisance of electrostatic charging in several industrial processes.

Since TSD is governed by relaxation phenomena specific to the polymer, TSD can conversely be used to study molecular motion in dielectrics. This is an interesting development, because the dielectric behaviour of polymers is complex, so one is inclined to search for information over vast ranges of frequency and temperature. Up to now, low-frequency behaviour, which is of paramount interest for several applications of polymers, was difficult to access and it is just in this range (10^{-4} Hz) that TSD works. The only technique previously available has been that of isothermal step-response measurements, which are very time-consuming. Dielectric measurements with TSD also partly reveal the conduction properties of the polymer owing to the presence of the ρ peak. By the way, these new dielectric measurements are, of course, not restricted to polymers. They can be applied to all kind of dielectrics, even to frozen liquids.

TSD experiments are not more complicated than ordinary dielectric measurements. The basic equipment needed is rather simple; the key instrument is a sensitive electrometer. However, the interpretation of TSD results is more involved, since time and temperature are varied simultaneously, whereas in conventional measurements only one of these parameters is changed at a time.

1:9 Scope of This Thesis

The aim of this investigation was to deduce the molecular decay processes that underly the phenomena occurring during TSD of electrets. To unravel the various decay processes, attention has been paid to all the methods reviewed in Sect. 1:7. We have further looked into the application of TSD for dielectric research purposes.

The work reported consists of a theoretical and an experimental part. The theoretical part gives a *detailed* descriptive analysis of all the decay mechanisms surveyed in Sect. 1:5. Several interesting effects to be expected in the use of TSD are *quantitatively* elucidated by *model* thermograms, which were calculated on a digital computer.

We have also been able to relate TSD results to data from ordinary dielectric and mechanical measurements; this considerably facilitates the interpretation of TSD data. Our theoretical work has been focused on the three experimental methods outlined in Sect. 1:4. Several aspects of the theory developed are checked with the experimental results obtained,

In the experimental part, we first describe the equipment for the current and charge measurements. Next, we present several thermograms, in particular of methacrylic polymers. To demonstrate the applicability of TSD to the molecular spectroscopy of dielectrics we studied polymers in which the molecular structure had been systematically varied by Heijboer and his co-workers of this laboratory. Moreover, we abandoned the use of a freezing temperature of 25 °C, and extended the temperature range down to -180 °C. We also investigated several copolymers, which were found to store higher charges than homopolymers. By elaborating the air-gap technique, and by performing sectioning experiments on electrets, clear evidence has been obtained that the formerly unknown ρ peak is due to the motion of excess charges. Finally, results of charge-TSD measurements on homocharged foils used for electret microphones will be discussed.

THEORETICAL PART

Introduction

In general, an electret contains aligned dipoles, and excess charges. These decay by various processes, which often have a different temperature dependence. Accordingly, the TSD current thermograms exhibit peaks that can be attributed to specific decay processes. For this reason we shall discuss the various decay modes separately. This makes the treatment more comprehensible without loss of generality, because most of the physical quantities involved in the processes are straightforwardly additive, as will be shown in our discussion on current TSD with an air gap (Chap. 7), in which we had to study the decay modes together.

Since the polymer has a "memory", the discharge current depends on the forming conditions. The theory about the TSD of a particular process will therefore be preceded by a description of the charging.

We shall confine ourselves in this theoretical part to electrets and electrode systems of a *plane* geometry, and we shall neglect edge effects and surface conduction. All the formulae will be given in the rationalized MKS system. The symbols most frequently used have been listed on the front pages.

In passing we note that for practical applications of electrets their isothermal discharge is important. Clearly, isothermal decay is a special case of the non-isothermal theory given below. For this special case all rate parameters are constant, which considerably simplifies the mathematics (Fe 53, Pe 68, Tu 70a).

Chapter 2

CURRENT TSD BY DIPOLE REORIENTATION IN SHORTED ELECTRETS

This chapter deals with the TSD of nondistributed and distributed dipole relaxations, and as such it is of interest to the TSD α and β peaks of methacrylic polymers, cf. Fig. 1-6. Since we assume the TSD experiment to be done on shorted, bilaterally metallized electrets, we can only observe the released current. The persistent polarization, which is the other relevant quantity, must be calculated from the released charge or the current-time integral.

Current TSD of dipoles with a single relaxation time has first been formulated by Bucci et al. (BF 66). It is worth mentioning that this theory is mathematically related to other non-isothermal methods, for instance the analysis of thermoluminiscent and photoconductive glow curves (Br 63, DB 67), differential scanning calorimetry (WB 65), and thermogravimetric analysis (Br 69). The classical theories of annealing and vitrification of glasses are also similar (BW 34, To 46).

The theory of Bucci et al. has independently been generalized by Gross (Gr 68, Gr 69) and by the author (Tu 68, Tu 70) to a polarization with a distribution of relaxation times. However, the actual thermograms for a distributed polarization have not been given. In the meantime, we managed to solve the pertinent Laplace transforms with a computer; the results will be discussed in Sect. 2:2. The calculations were done for the distribution functions of Gevers,Gross,Wagner,Cole-Cole and Fuoss-Kirkwood. Salient differences between their model thermograms will be pointed out and we shall analyze their compatibility with experimental results. The dependence of the model thermograms on the forming and storage conditions will also be illustrated; this work is of interest to the experimental results given in Sects 10:2 and 10:3.

Although we have found that all dipole relaxations in polymers are distributed, we shall first outline in Sect. 2:1 the TSD behaviour for dipoles with a single relaxation time. This section merely serves as an introduction to the new work reported in Sect. 2:2. Sect. 2:3 finally discusses the resolving power of TSD for proximate relaxations and it describes multi-stage TSD to resolve overlapping current peaks by partial heatings.

To simplify the treatment we suppose the polymer to be free of charge carriers, so that the internal electric field and the dipole polarization will be *space independent*. In practice, however, dipole polarization is often accompanied by space charge polarization, by which it is made non-uniform. We shall show in the supplementary Sect. 2:4 (App. II) that in this case the *mean* value of the local polarizations is observed. This means that the theory described in this chapter is generally valid, provided the electric field and the polarization are considered to be averaged over the thickness of the polymer.

2:1 Electrets with a Single Dipole Relaxation

2:1.1 The Charging Process

Referring to Fig. 2-1, we first describe the charging process that lasts from time zero to t_s. The permanent dipoles, although hindered in their rotation by viscous forces, are gradually orientated by the forming field E. For a dipole relaxation frequency $\alpha(T)$, a polarization

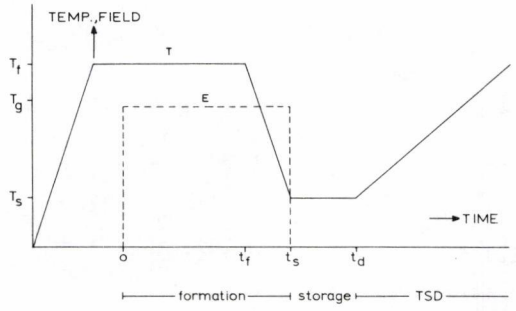


FIG.2-1 Final time-temperature scheme, showing the relevant times and temperatures, during formation, storage and TSD of electrets.

will be created that satisfies

$$dP_s(t)/dt + \alpha(T)P_s(t) = \varepsilon_o(\varepsilon_s - \varepsilon_\infty)_T\alpha(T)E \qquad (2.1)$$

In this well-known Debye equation, t is the time, T the absolute temperature, and ε_o the permittivity of a vacuum, while ε_s and ε_∞ denote the static and optical dielectric constants, respectively. Debye actually derive Eq. 2.1 for constant temperatures, but we postulate that it also holds for varying temperatures. The subscript s designates that $P_s(t)$ is the slowly reacting part of a total polarization that also contains an instantaneously reacting part, which cannot be frozen-in.

We indicated that α and $\varepsilon_s - \varepsilon_\infty$ depend on temperature. For polymers the relaxation strength $(\varepsilon_s - \varepsilon_\infty)_T$ is approximately given by

$$(\varepsilon_s - \varepsilon_\infty)_T \simeq N\mu^2/3\varepsilon_o kT \qquad (2.2)$$

where N is the number of the permanent dipoles per unit volume, μ is their dipole moment and k is Boltzmann's constant. As we shall see later, $\alpha(T)$ depends exponentially on 1/T. Thus, it varies much more strongly than $(\varepsilon_s - \varepsilon_\infty)_T$. To proceed analytically we take $\varepsilon_s - \varepsilon_\infty$ to be temperature-independent.

Since the initial value $P_s(o)$ is zero, the solution of Eq. 2.1 reads

$$P_s(t) = \varepsilon_o(\varepsilon_s - \varepsilon_\infty)E\{1 - \exp(-\int_o^t \alpha(T)dt\} \qquad (2.3)$$

Putting dt = sdT, where s is the reciprocal heating rate, we find for the resulting polarization during the cooling phase of the charging period

$$P_s(T) = \varepsilon_o(\varepsilon_s - \varepsilon_\infty)E\{1 - \exp(-\alpha(T_f)t_f - s\int_{T_f}^{T} \alpha(T)dT)\} \qquad (2.4)$$

where T_f is the forming temperature and t_f the isothermal part of the forming time. Note that the value of s is negative during cooling.

It is interesting that in Eq. 2.4 the contribution of the cooling phase does not formally differ from that of the isothermal charging period at T_f. For brevity, we shall replace the integral in Eq. 2.4 by a *reduced time* $\xi(T,T_f)$

$$\xi(T,T_f) = s \int_{T_f}^{T} a(T)dT \qquad (2.5)$$

Here a(T) is the temperature shift of the dipolar relaxation frequency, i.e.

$$a(T) = \alpha(T)/\alpha_r$$

where α_r denotes the relaxation frequency at $T = \infty$ or *natural frequency* for short, which is taken to be temperature-independent.

As we shall see later, a(T) varies exponentially with 1/T. Hence the main contribution to the exponential in Eq. 2.4 derives from the isothermal polarization at T_f; the increase of the polarization during the cooling phase can often be neglected. This is true in particular for polymers, when T drops below T_g. Furthermore, we see that the polarization obtained increases linearly with the forming field E and relaxation strength $\varepsilon_s - \varepsilon_\infty$, which means that the more polar polymers can store higher polarization. We also note that the time-temperature schedule enters in the exponential and in making this small by choosing T_f and t_f high enough, the ultimate polarization of $\varepsilon_o(\varepsilon_s - \varepsilon_\infty)E$ is reached.

2.1.1a Resistivity Curves of Several Polymers

Generally, the charging current is measured during a formation. When the current spike, caused by the instantaneous polarization, has died out, the current density becomes

$$j(t) = dP_s(t)/dt + \gamma(T)E \qquad (2.6)$$

where $\gamma(T)$ represents the ohmic conductivity of the polymer. At room temperature $\gamma(T)$ is low, but it increases exponentially with temperature, and above T_g the conduction current exceeds the polarization current dP_s/dt after some time. Consequently, the charge supplied by the voltage source is much larger than $P_s(t)$. This implies that dipole relaxations cannot be properly studied by measuring charging currents; in virtue of its short-circuit TSD is much more attractive.

Nevertheless, current measurements during the formation remain important in assessing the stability of the charges retained in the electret; for the higher $\gamma(T)$, the sooner the stored charge will later be neutralized by ohmic conduction. Now, during freezing the polarization current, dP_s/dt, has vanished and $\gamma(T)$ can be found directly from the charging current data. The results obtained at a cooling rate of 0.5 °C/min are given in Figs 2-2 to 2-4 ; note that the volume resistivity, i.e. $1/\gamma$, is plotted. The low-temperature tail of these resistivity curves of low activation energy, is attributed to impurity conduc-

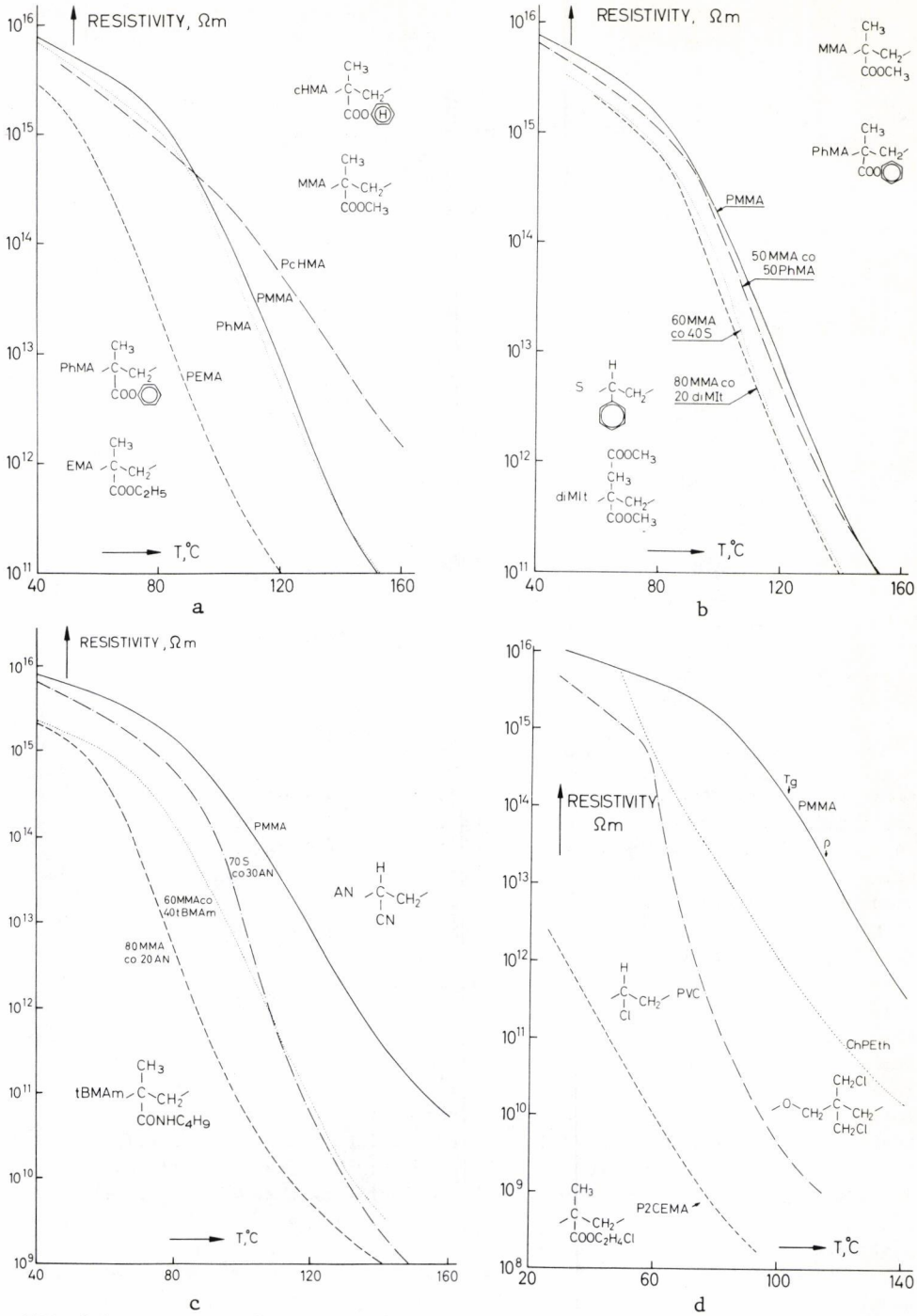


FIG. 2-2 Temperature dependence of the volume resistivity of several methacrylic homo- and copolymers. In each plot, the curve for PMMA is shown as a reference. In Fig. d the positions of T_g and the TSD ρpeak of PMMA are indicated; two graphs of commercial polymers, viz. PVC and ChPEth (Penton) are also given.

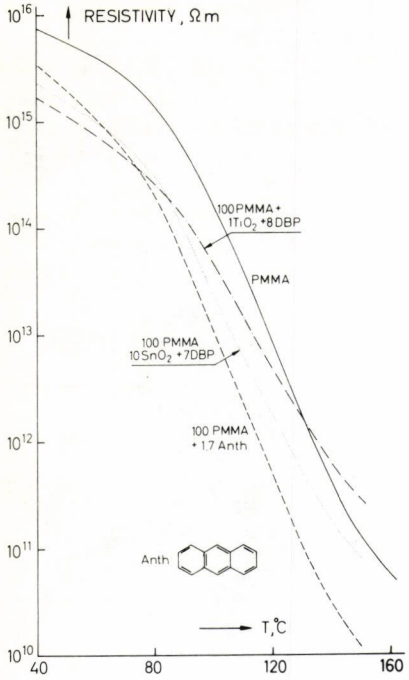


FIG.2-3 The effect of additives on the resistivity curve of PMMA. The plasticizer DBP lowers not only the resistivity, but also the activation energy of PMMA.

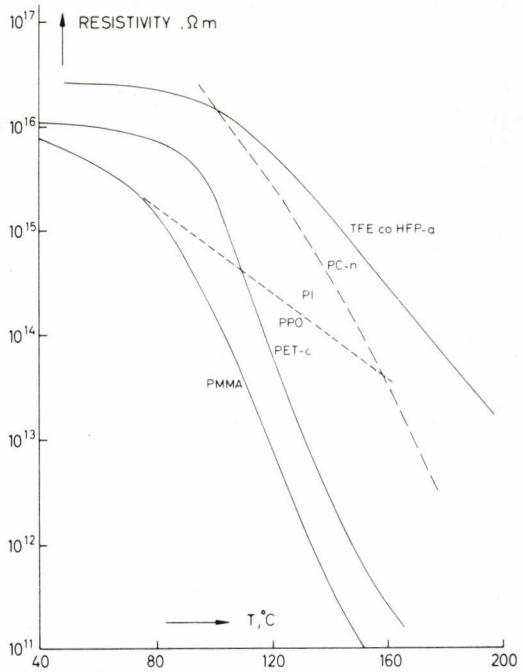


FIG.2-4 Temperature dependence of the resistivity of some commercial foils having a much higher resistivity than PMMA.

tion; the high-temperature region, with a high activation energy, arises from intrinsic conduction. According to Ioffe (Io 60) the difference in activation energies is due to the higher dissociation energy to form the carriers for intrinsic conduction. As a rule the bend in the plots occur before T_g. Thus ohmic conduction normally becomes significant near and at T_g.

Since the resistivity curves exemplify the temperature dependence of the ohmic relaxation time, $\varepsilon_o\varepsilon/\gamma(T)$, it is instructive to compare the curve of PMMA with that of the shift factor of its volumetric relaxation time as given in Fig. 2-5. There is a close resemblance, but the resistivity curve extends over a smaller number of decades.

A detailed analysis of all resistivity curves is beyond the scope of this thesis. We confine ourselves here to noting that there are marked differences in the values of the resistivity; it increases when the polymers are more polar; typical examples are PVC and P2CEMA. Moreover, copolymers clearly exhibit a lower resistivity than homopolymers. This is self-evident for copolymerization with polar groups such as AN and tBMAm, but it is striking that the copolymer of PMMA with the highly insulating PS also has a lower resistivity. In Sect. 10:1 we shall see that the enhanced conductivity of copolymers leads to a higher TSD ρ peak. This is understandable, because there are more carriers available for accumulation near the electrodes. Since the ohmic relaxation frequency, $\beta(T) = \gamma(T)/\varepsilon_o\varepsilon$, is lower than the dipole relaxation frequency at T_g, the ρ peaks generally emerge above T_g. For PMMA e.g. we have $\alpha(T_g) = 2.2 \times 10^{-5}$ Hz and $\alpha(T_g) =$

5.5×10^{-3} Hz.

As might be expected, semi-conductive organic and inorganic additives were found to lower the resistivity of a polymer, see Fig. 2-3. From Fig. 2-4 it appears that polymer foils have a much higher resistivity than a thick PMMA sample. It is therefore not surprising that electret foils perform so well. In particular, electrets of Teflon FEP-a, made of 89 TFE co 11 HFP, show excellent stability, see Fig. 10-66.

Furthermore, Figs 2-2 to 2-4 are of interest to our discussion of the results on the TSD ρ-peaks. In view of this we have calculated the activation energy of the resistivity in the high-temperature range; the results are compiled in Table 2-1. The average value amounts to about 2 eV or 46 kcal/mol.

TABLE 2-1 Activation Energy (eV) of the Resistivity of Several Homo- and Copolymers

Homopolymers		Copolymers		PMMA with additives	
P2CEMA	1.4	80 MMA co 20 AN	2.6	100 MMA + 1.7 Anth	1.9
PcHMA	1.3	60 MMA co 40 tBMAm	2.4	100 MMA + 7 DBP + 10 SnO_2	1.7
PEMA	1.7	80 MMA co 20 diMIt	2.0	100 MMA + 8 DBP + 1 TiO_2	1.7
PMMA	1.9	50 MMA co 50 PhMA	2.0		
PPhMA	1.6	60 MMA co 40 S	2.2		
ChPEth	1.5	80 S co 20 AN	3.2		
PC-n	2.2	89 TFE co 11 HFP-a	1.3		
PET-c	2.2				
PI	1.3				
PVC	3.1				

2:1.2 The Discharging Process

Let us now turn to the discharge behaviour during TSD. Usually, the electret will be stored for a short time, say $t_d - t_s$, before a TSD measurement is made. Fig. 2-1 illustrates the final nonisothermal charging and discharging scheme. We supposed the internal field after the short-circuit to be zero, neglecting the voltage drop across the ammeter that measures the discharge current.

Because of this ideal short-circuit, Eq. 2.1 reduces to

$$dP_s(t)/dt + \alpha(T)P_s(t) = 0 \qquad (2.7)$$

during storage and TSD. The initial value of P_s in the discharge experiment equals the value of $P_s(t)$ at the end of the charging period. Thus the solution of Eq. 2.7 is given by

$$P_s(t) = P_s(t_s) \exp\left(-\int_{t_s}^{t} \alpha(T)dt\right) \qquad (2.8)$$

which is identical to the formula of Bucci et al. (BF 66), who did not relate $P_s(t_s)$ to the formation conditions, however.

Substituting into this equation $P_s(t_s)$ from Eq. 2.4 we finally find that during TSD

$$P_s(T)/\varepsilon_o E = FS(\varepsilon_s - \varepsilon_\infty)\ \exp\{-\alpha_r \xi(T,T_d)\} \qquad ...(2.9)$$

where $\xi(T,T_d) = s \int_{T_d}^{T} a(T)dT$ and

$$FS = \left[1-\exp\{-\alpha(T_f)t_f - \alpha_r \xi(T_f,T_s)\}\right] \exp\{-\alpha(T_s)(t_d - t_s)\} \qquad (2.10)$$

Here, the last exponential accounts for the decay during storage. This means that in Eq. 2.8 we have separated the isothermal decay from the nonisothermal decay during TSD, in which we are more interested.

Obviously, the factor FS characterizes the *filling state* of the electret. It depends on the forming and storage conditions and is equal to the ratio of $P_s(t_d)$ to the maximum attainable polarization $\varepsilon_o(\varepsilon_s - \varepsilon_\infty)E$. By charging the polymer completely, i.e. by making FS = 1, we achieve that the thermogram of the normalized retained polarization, $P_s(T)/\varepsilon_o E$, is solely determined by the experimental parameter s and such *material constants* as $\alpha(T)$ and $\varepsilon_s - \varepsilon_\infty$. In general, it is advisable to plot $P_s(T)/\varepsilon_o E$ on a logarithmic scale, for then the shape of the thermogram is not affected by an inaccurate choice of T_f, t_f and t_d. Interestingly, the relaxation strength appears only in $P_s(t_s)$, so its *temperature dependence*, which we have neglected, is *not* relevant to TSD.

The decay of $P_s(t)$ generates externally a depolarization current, and since there is no ohmic conduction current, owing to the short-circuit, the released TSD current density becomes

$$j_r(t) = dP_s(t)/dt = -\alpha(T)P_s(T) \qquad ...(2.11)$$

The released charge density follows from integrating Eq. 2.11

$$q_r(t) = \int_{t_d}^{t} j_r(t)dt = P_s(t) - P_s(t_d) \qquad ...(2.12)$$

At the end all retained polarization will have disappeared. As a result, the ultimate released charge equals, apart from its sign, the polarization initially stored. This equality is typical of dipole reorientation, as it does not hold for the other decay processes. It implies, according to Gross (Gr 70), that a Debye model is charge-invariant, i.e. $q_r(\infty)$ is *independent* of the heating schedule, so that it does not change for various heating rates.

By differentiating Eq. 2.11 with respect to t, it is easily verified that the current maximum occurs at

$$d\tau(T)/dt = -1 \quad \text{or} \quad d\ 1/\alpha(T) = -sdT \qquad (2.13)$$

where $\tau(T) = 1/\alpha(T)$ is the relaxation time. The position of this maximum, T_m, is characteristic for the polymer and does *not* depend on the filling state of the electret, i.e. on T_f, t_f and t_s.

In order to indicate the shape of the thermograms, we have to specify the relaxation frequency $\alpha(T)$. Now, in polymers various dipole relaxations are possible and the temperature dependence of $\alpha(T)$ is not unique.

For TSD β relaxations due to *local* motions of polar side-groups and taking place in the glassy state far below T_g, an Arrhenius equation is appropriate

$$\alpha(T) = \alpha_r \exp(-A/kT) \tag{2.14}$$

where A is the activation energy and α_r is, as before, the natural frequency. Alternatively, polar groups may move *cooperatively* with the main chains. This relaxation, which results in the TSD α peak, occurs at the onset of the conformational rearrangements of the main chains, when the polymer reaches its glass-rubber transition T_g. Since the motions of the bulky main chain segments require some unoccupied or free volume, this relaxation shifts according to the WLF equation*

$$\alpha_v(T) = \alpha_g \exp\{c_1(T-T_g)(c_2+T-T_g)^{-1}\} \quad , T > T_g \tag{2.15}$$

where v refers to free volume and $\alpha_g = 7 \times 10^{-3}$ sec^{-1}, $c_1 \doteq 40$ and $c_2 = 52$ °C for amorphous polymers.

To emphasize the similarity to Eq. 2.14, we convert Eq. 2.15 into

$$\alpha_v(T) = \alpha_w \exp\{-A_w/k(T - T_\infty)\} \quad , \quad T > T_g \tag{2.16}$$

where $\alpha_w = \alpha_g \exp 40 \simeq 1.6 \times 10^{15}$, $A_w = c_1c_2k = 0.18$ eV and $T_\infty = T_g - c_2$. This shows that a WLF thermogram is identical to an Arrhenius thermogram, the axis of which is down-scaled to $T - T_\infty$ and which has *one prescribed* activation energy A_w. Note that $\alpha_v \to 0$, when $T \to T_\infty$, which suggests that the WLF equation looses its validity *below* T_g. This is well known experimentally (see also Fig. 2-5), hence Eqs 2.15 and 2.16 can only be applied for temperatures above T_g.

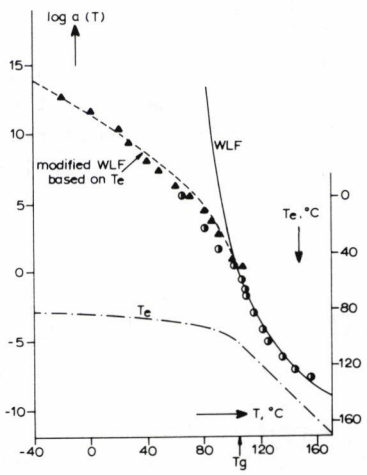


FIG.2-5 Temperature dependence of the shift factor a(T) for the α relaxation of PMMA, as found by Rush (Ru 68) from volumetric measurements. The dashed line gives a theoretical fit according to Eq. 2.15, for $T = T_e$. The course of the effective temperature T_e used, is also shown.

*WLF stands for Williams, Landel and Ferry

Below T_g part of the unoccupied or free volume is frozen, in a way similar to the polarization. To account for this nonequilibrium behaviour Rush (Ru 68) replaced T in Eq. 2.15 by an "effective temperature" T_e. In doing so he extended the applicability of the WLF equation to below T_g.

Fig. 2-5 shows the course of the shift factor $a(T) = \alpha_v(T)/\alpha_g$, for the main chain relaxation of PMMA. The experimental points are marked by triangles and shaded circles. The curves calculated for a normal WLF shift $\alpha(T)$ and a modified WLF shift $\alpha(T_e)$ are also shown, the latter is seen to fit the data reasonably well below T_g. The figure also gives the T_e values used by Rush, which remain well above the real temperature for $T_e < T_g$. It is for this reason that $a(T_e)$ increases less sharply below T_g than does Eq. 2.15. Actually, below T_g the measured shift-factor closely resembles an Arrhenius shift. As advocated by Macedo et al. (ML 65), we can therefore likewise represent the data by a hybrid of Eqs 2.14 and 2.15.

2:1.3 Calculation of TSD Model Thermograms

To see what thermograms can be expected experimentally, we first substitute an Arrhenius shift, $a(T) = \exp(-A/kT)$, in the reduced time of Eq. 2.9. Unfortunately, the integral resulting for $\xi(T,T_d)$ is not elementary. However, by partial integration it can be expressed in the exponential integral $E_1(A/kT)$, for which an asymptotic expansion is known (AS 65). In this way we obtain

$$\int_0^T \exp(-A/kT)\,dkT/A = e^{-z}/z - E_1(z) = e^{-z}z^{-2}(1-2!z^{-1}+3!z^{-2}..) \qquad (2.17)$$

where $z = A/kT$. For most polymers $z > 40$ and it is legitimate to truncate the series after the 2nd term.

For more accurate work we used a rational approximation for $E_1(z)$ due to Hastings (Ha 55)

$$E_1(z) \simeq e^{-z}z^{-1}(z^2 + a_1z + a_2)(z^2 + b_1z + b_2)^{-1},\ 1 \leq z \leq \infty \qquad (2.18)$$

where $a_1 = 2.334733$, $a_2 = 0.250621$, $b_1 = 3.330657$, and $b_2 = 1.681534$.

Substitution of Eq. 2.18 into the second identity of Eq. 2.17 gives

$$\int_\infty^z e^{-z}d\,1/z \simeq e^{-z}z^{-2}H(z) \qquad (2.19)$$

where $H(z) = \{b_1-a_1+(b_2-a_2)z^{-1}\}(1+b_1z^{-1}+b_2z^{-2})^{-1}$

The value of Eq. 2.19 at T_d can often be neglected, in that case we finally obtain for the reduced time during TSD

$$\xi(T,T_d) \simeq (skT^2/A)\exp(-A/kT)H(A/kT) \qquad (2.20)$$

For a WLF shift we get the same expression, except that A becomes A_w, while T must be replaced by $T-T_\infty$ or rather $T_e - T_\infty$.

The persisting polarization and released current for an Arrhenius shift are plotted as a function of the heating temperature in Fig. 2-6. Reduced units are introduced, by normalizing to $P_o = P_s(t_d)$ and $j_m = j(T_m)$.

The polarization is seen to drop to zero in a narrow temperature range, especially for high activation energies, i.e. when kT_m/A is low. At a temperature T_m, where the polarization decreases most rapidly, the current reaches its maximum. The current rises more slowly than it falls, giving the graphs an asymmetric appearance with respect to T_m. The current rise is clearly due to the increasing mobility of the dipoles. This rise cannot continue, however, because the number of aligned dipoles soon becomes exhausted, so that the current starts to fall above T_m. On a semilog plot log j_r vs 1/T, cf. Fig. 3-1, the current rises linearly, because of its proportionality to $\alpha(T)$. Therefore, A can be deduced from this initial rise. We shall show in Sect. 3:1 that A can also be found from the half-width of a current thermogram.

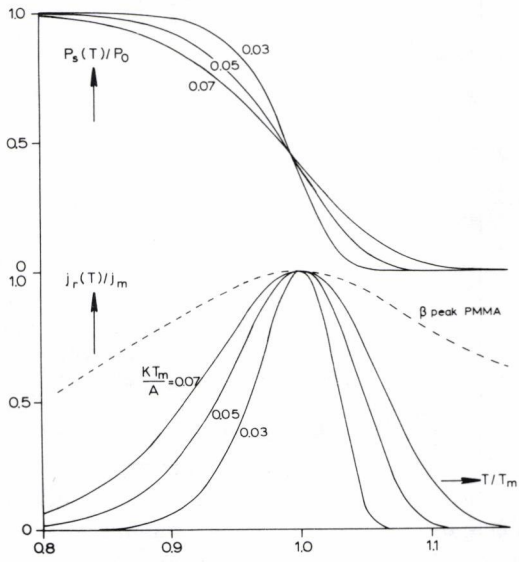


FIG.2-6 TSD thermograms of the retained polarization and released current for an Arrhenius shift. The trend is shown for three activation energies. For comparison, an experimental TSD β peak of PMMA is also plotted. Notice that $P_s(T)$ cannot be observed with metallized electrets, but that it can be deduced from the released charge (see Eq. 2.12).

For comparison we have inserted in the figure results of the TSD β peak of PMMA. We see that this peak is very broad; it would correspond to $kT_m/A = 0.18$, where $T_m = 222$ °K. This means that its activation energy A would amount to 2.5 kcal/mol, which is much lower than the value of 18 kcal/mol found from the frequency shift of the maximum in isothermal dielectric measurements. Obviously, it is incorrect to describe this TSD peak by a single relaxation time. A continuous set of relaxation times has to be considered; this will be done in Sect. 2:3.

From Eq. 2.13 it is easily verified that the current maximum occurs at

$$sT_m\alpha_m = A/kT_m \qquad (2.21)$$

where $\alpha_m = \alpha(T_m)$*. Combining Eqs 2.20 and 2.21 we find from Eqs 2.9 and 2.11 for the polarization and current density at T_m

$$P_s(T_m)/P_o = j_r(T_m)/\alpha_m P_o = \exp\{ - H(A/kT_m)\} \qquad (2.22)$$

where $H(A/kT_m) \simeq 1 - 2kT_m/A$ or roughly 1. The P_s-curves therefore attained a value of about e^{-1} at T_m in Fig. 2-6.

Fig. 2-7 shows the course of the reduced time $\xi(T)$, for $A/kT_m = 20$.

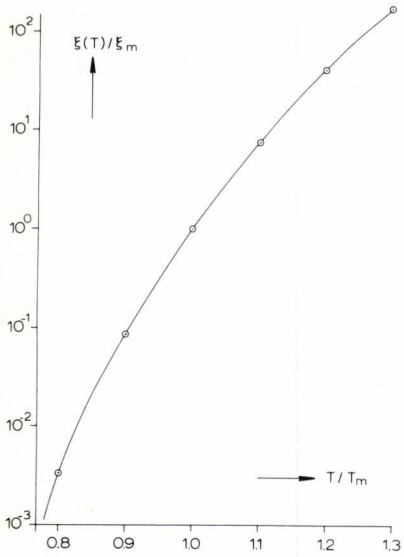


FIG.2-7 The reduced time as a function of temperature, for $A/kT_m = 20$. For the encircled points $H(A/kT_m)$ was simply taken as equal to 1.

It varies strongly, extending over several decades in a narrow temperature range. The full line was calculated using Eq. 2.20. An approximation in which H = 1 is also shown, the differences with the exact curve are hardly noticeably. Obviously, the way in which the exponential integral is approximated is not very critical. We observe that the course of $\xi(T)$ can roughly be described by $\log \xi(t) \propto T$; consequently a TSD experiment corresponds to an isothermal discharge experiment in which the time is varied logarithmically.

The important *experimental parameter* is the heating rate, s^{-1}; this affects the height and the position of the thermograms. From Fig. 2-8, in which α_m and T_m relate to s_o, we see that the current peak increases

*It is interesting to compare Eq. 2.21 with the condition for the ε'' maximum in isothermal dielectric measurements:

$$\alpha_m = \omega$$

here, ω is the angular frequency, which should obviously have a value of

$$\omega_e = A/skT_m^2$$

if the maxima are to occur at the same temperature. Now at s = 1 min/°C we have, for the α peak of PMMA, $\alpha_m = 2.2 \times 10^{-3}$ Hz, hence the equivalent frequency of TSD appears to be low.

and broadens with heating rate. This is so because, if s^{-1} is higher, the same charge has to be released in a shorter time*. It is only the initial slope proportional to $\alpha(T)$ that remains the same. The dashed line shows that the current maximum varies almost proportionally to the heating rate**. At the same time, it shifts to a higher temperature, because the polymer responds less quickly to a higher heating rate.

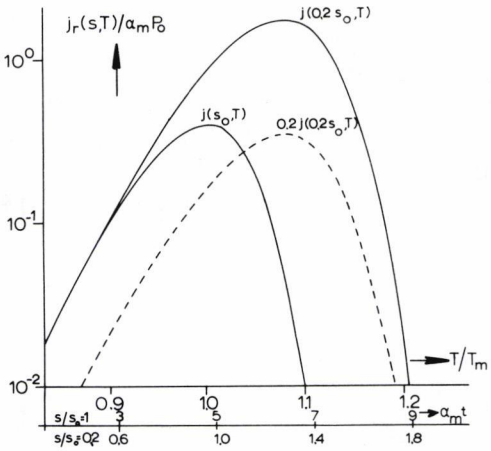


FIG.2-8 The effect of a fivefold increase in heating rate on the current thermograms. On the abscissa the reduced times spent in the two heating runs have been indicated. The calculations were made for $A/kT_m = 20$.

To verify the effects analytically, we consider two reciprocal heating rates $s_{1,2}$. Designating the corresponding current maxima and their temperatures by $j_{1,2}$ and $T_{1,2}$, respectively, we obtain from Eqs 2.21 and 2.22

$$s_1 T_1^2 \alpha(T_1) = s_2 T_2^2 \alpha(T_2) \tag{2.23}$$

$$j_1(T_1)/j_2(T_2) = \{\alpha(T_1) e^{-H(A/kT_1)}\}\{\alpha(T_2) e^{-H(A/kT_2)}\}^{-1} \tag{2.24}$$

$$\simeq s_2 T_2^2 / s_1 T_1^2 \simeq s_2/s_1$$

The first equation gives the temperature shift as a function of heating rate. It, conversely, allows one to calculate the activation energy if the temperature shift is known for a particular change in heating rate. Similarly, the equality in Eq. 2.24 can be used to find the activation energy from a measured current ratio. For further details we refer to Sect. 3:1.

Furthermore the ratio of the released charges is given by

* The reduced times indicated on the lower abscissa were calculated from $\alpha_m t = (sA/s_o kT_m)(T-T_d)/T_m$, for $T_d/T_m = 0.76$

**The approximate proportionality of $j_r(T)$ to s^{-1} has an important consequence. It means that the shape of a TSD thermogram, plotted on semilog paper, is not influenced by small changes in the heating rate; this implies that the linear temperature programming is not too critical.

$$\frac{q_r(s_1,T)}{q_r(s_2,T)} = \frac{1 - \exp\{-s_1 \int_{T_d}^{T} \alpha(T)dT\}}{1 - \exp\{-s_2 \int_{T_d}^{T} \alpha(T)dT\}} \qquad (2.25)$$

Evidently, for the release of the same ultimate charge, the upper temperature limits must differ; and as shown in Fig. 2-8 the thermograms become higher and broader with increasing heating rate.

We now turn to the calculated thermogram of the modified WLF shift to see whether it is compatible with the TSD peak of PMMA. The results shown in Fig. 2-9 are disappointing. The theoretical thermogram, based on Rush's T_e-values (Ru 68) and T_g = 105 °C, c_1 = 38.5 and c_2 = 55 °C, is much sharper than the experimental curve. The fit for the normal WLF shift is even poorer.

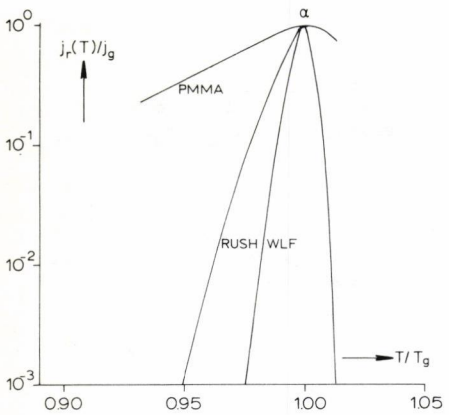


FIG.2-9 Comparison of thermograms for a normal and a modified WLF shift (Rush) with experimental results for the α peak of a PMMA electret. The thermograms calculated relate to a single Debye relaxation.

A plausible explanation for the broadness of the measured thermogram is that the typical structure of polymers admits of different conformations for the dipoles. Their β and α polarizations therefore seldom relax at a single frequency. A distribution over a number of discrete or even a continuous range of relaxation frequencies is more likely. And at the glass-rubber transition, these subpolarizations may actually shift according to the modified WLF equation.

2:2 Electrets with a Distribution in Dipole Relaxation Times

To begin with we shall briefly describe two experiments, which further support the view that the dipolar TSD β and α peaks involve distributed polarizations. First of all, we have determined the shift of the TSD β peaks of PMMA and PEMA with heating rate. The results are shown in Fig. 10-1; we see that the peaks shift only by 4 °C, whereas for an activation energy of 2.5 kcal/mol, as found from the initial current rise, the shift would have been 21 °C. The measured shift cor-

responds well to the activation energy of 18 kcal/mol, known from ordinary dielectric measurements. This proves that the β peaks are not broad because of a low activation energy, but rather because they are due to a distributed polarization.

Further evidence for this was obtained by studying the TSD for various forming temperatures T_f. Results pertaining to the α peak of PMMA were given in Fig. 1-11. They show that the current maximum shifts to T_f, when this is lower than T_g. According to Eq. 2.21, this would not have happened for a non-distributed polarization. We recall that the ρ peak due to the motion of excess charges does not shift either, though it is strongly diminished.

Analyzing the current release for a distributed polarization, we shall assume the distribution to arise either from variations in the natural frequency or from variations in the activation energy of the subpolarizations. In the literature, several distribution functions have been suggested. It seems worthwhile to derive their model thermograms, and to find out whether they can fit the experimental results. In doing so we can start from the relevant parameter values known from ordinary dielectric measurements on polymers and cited in the literature. A more general way is not to prescribe any distribution, but to deduce it from the TSD data; this will be done in Sect. 3:3. In the following we shall also examine the influence of the forming conditions on the model thermograms.

Let us first consider a polarization with a *discrete* distribution of relaxation times. For such a polarization each individual polarization $P_{si}(t)$ reacts with a particular relaxation frequency $\alpha_i(T)$, so that a set of simultaneous Debye equations like 2.1 and 2.7 result. These can be solved separately and summed afterwards to give that

$$P_s(t) = \sum_{i=1}^{n} P_{si}(t_d) \exp \{- \int_{t_d}^{t} \alpha_i(T)dt\} \qquad (2.26)$$

during TSD. By differentiating this equation we find the series for the released current, the individual terms of which can be worked out as indicated in Sect. 2:1.3. Note that, if the number of subpolarizations is large, the individual TSD current peaks will accumulate to a broad peak, the low temperature tail of which will be due to the reorientation of the fast reacting dipoles, whereas the high-temperature tail will be caused by the reorientation of the slowly reacting dipoles.

At this point it may be illustrative to describe dielectric response by an electrical model. Fig. 2-10 shows the parallel networks for one and n relaxation frequencies. The relaxation branches representing the permanent dipoles consist of a storage capacitance $(\varepsilon_s - \varepsilon_\infty)_i$, in series with a resistance $(\varepsilon_s - \varepsilon_\infty)_i \alpha_i(T)$, which determines the charging and discharging rate of the former. The resistance $1/\gamma(T)$ represents the ohmic conduction of the polymer,

and the capacitance ε_∞ stands for the instantaneous polarization; this has no series resistance and is therefore instantly charged and discharged.

Charging and discharging can be accomplished by putting switch S in position 1 or 2. It is in the latter position that during TSD the decay of the polarization stored in the capacitances $(\varepsilon_s - \varepsilon_\infty)_i$ of the short-circuited relaxation branches is studied. To stimulate this decay their series resistances are lowered by heating. Clearly, the storage capacitances with the lower series resistances will discharge first, while those with the higher resistances will preserve their charge up to high temperatures.

We remark that the released charge may leak to ground, either through the ammeter or through the ohmic resistor $1/\gamma$. Thus, if most of the charge is to pass through the ammeter, this should have a low input resistor.

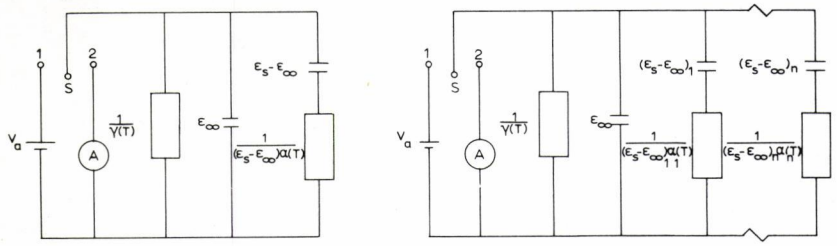


FIG.2-10 Model representation of a dielectric with one relaxation frequency (left) and n relaxation frequencies (right). For charging and discharging S is switched to position 1 and 2 respectively.

We have not yet specified the source of the various dipole relaxation frequencies within the TSD β and α peaks. If we assume the subpolarizations to shift according to an Arrhenius equation, the distributions may arise from differences in the *natural frequency* α_r, or the *activation energy* A, of the dipole groups. The more complicated case of the twofold distribution in α_r and A will be excluded from the following. The origin of differing natural frequencies lies in the different size and shape of the dipoles, whereas variations in the activation energy appear when the dipoles experience a different attraction from other molecular groups, i.e. when the arrangement of the nearest neighbours is not the same for all dipoles.

There is a striking difference between the two distributions, because to account for a broad TSD peak we need a much larger range in α_r than in A. This is directly obvious from Eq. 2.14. The likelihood of both distributions for the various dipolar relaxations in polymers is discussed in the introduction to Sect. 3:3.

2:2.1 Charging and Discharging of Polymers with Continuous Distributions

For a *continuous distribution* there is an infinite set of Debye equations, and the finite sum of Eq. 2.26 will change to an integral. The most convenient integration variables are α_r and A, for these determine

the distributions in question.

Let us first consider the *isothermal response* at a temperature T_o of a distribution arising from variations in the *natural frequency* α_r. We then have for the Debye equation of the dipole groups responding at a particular natural frequency α_r,

$$\partial p_s(t,\alpha_r)/\partial t + \alpha(T_o)p_s(t,\alpha_r) = \varepsilon_o(\varepsilon_s - \varepsilon_\infty)f(\alpha_r)\alpha(T_o)E \qquad (2.27)$$

where $p_s(t,\alpha_r)$ is the strength, at time t, of the subpolarizations labelled with α_r, while $f(\alpha_r)$ is the relative contribution to the total relaxation strength, $\varepsilon_s - \varepsilon_\infty$, of the subpolarizations between α_r and $\alpha_r + d\alpha_r$. According to this definition $f(\alpha_r)$ is normalized, and so $\int_0^\infty f(\alpha_r)d\alpha_r = 1$. The integral over all subpolarizations with α_r between 0 and ∞, leads to a total polarization.

$$P_s(t,T_o) = \int_0^\infty p_s(t,\alpha_r)d\alpha_r \qquad (2.28)$$

Now for the isothermal response to a step function in field E, the solution of Eq. 2.27 reads

$$p_s(t,\alpha_r) = \varepsilon_o(\varepsilon_s - \varepsilon_\infty)Ef(\alpha_r)\{1 - e^{-\alpha(T_o)t}\}$$

and so we finally get for the total polarization

$$P_s(t,T_o) = \varepsilon_o(\varepsilon_s - \varepsilon_\infty)E \int_0^\infty f(\alpha_r)\{1 - e^{-\alpha(T_o)t}\}d\alpha_r \qquad (2.29)$$

Similarly, we have, at temperature T_1

$$P_s(t,T_1) = \varepsilon_o(\varepsilon_s - \varepsilon_\infty) \int_0^\infty f(\alpha_r)\{1 - e^{-\alpha(T_1)t}\}d\alpha_r$$

We easily verify that these polarizations become identical if

$$P_s(t,T_o) = P_s\{a(T_1,T_o)t,T_1\}$$

where $a(T_1,T_o) = \exp(-A/kT_1 + A/kT_o)$.

Accordingly, the polarization at T_1 can be found from measurements at T_o, simply by shifting the latter along the time axis by a factor of $a(T_1,T_o)$. Staverman and Schwarzl (SS 52) have suggested to call such a behaviour *thermorheologically simple* and they pointed out that such relaxation behaviour is likely to be shown by amorphous polymers with nonpolar or weakly polar groups. Much experimental evidence for it has indeed been obtained; in particular, the much quoted results on the α relaxation of polyisobutylene are convincing (SS 56). Obviously, isothermal measurements on such polymers at various frequencies can be superimposed to a single *master curve*. In other words, distributions in the natural frequency obey the *time-temperature superposition principle**. This is not so for distributions in the activation energy.

*Actually, the natural frequencies need not shift according to an Arrhenius equation; the time-temperature superposition holds also for a WLF shift.

Nevertheless, we shall show that the TSD thermograms for the two distributions are hardly different, unless they become very broad.

Let us next turn to the *nonisothermal* charging and discharging of electrets. We then have, for $t \leq t_s$

$$\partial p_s(t,\alpha_r)/\partial t + \alpha(T)p_s(t,\alpha_r) = \varepsilon_o(\varepsilon_s - \varepsilon_\infty)f(\alpha_r)\alpha(T)E \qquad (2.30)$$

and for $t \geq t_s$

$$\frac{\partial p_s}{\partial t}(t,\alpha_r) + \alpha(T)p_s(t,\alpha_r) = 0 \qquad (2.31)$$

with the accompanying initial conditions $p_s(o,\alpha_r)$ and $p_s(t_s,\alpha_r)$ respectively. Solving Eq. 2.31 by invoking Eq. 2.28 gives for the persistent polarization during TSD

$$P_s(T)/\varepsilon_o E = (\varepsilon_s-\varepsilon_\infty)\int_0^\infty FS(\alpha_r)f(\alpha_r)e^{-\alpha_r\xi(T,T_d)}d\alpha_r \qquad ...(2.32)$$

where the filling state $FS(\alpha_r)$, which depends on the formation and storage conditions, is defined by Eq. 2.10. The released TSD current density follows from differentiating Eq. 2.32

$$j_r(T)/\varepsilon_o E = (\varepsilon_s-\varepsilon_\infty)a(T)\int_0^\infty FS(\alpha_r)\alpha_r f(\alpha_r)e^{-\alpha_r\xi(T,T_d)}d\alpha_r \qquad ...(2.33)$$

The filling state, FS, being a function of α_r, has been written under the integral sign. This implies that it is not the original distribution function $f(\alpha_r)$ which is active during TSD, but an *effective* one, viz. $FS(\alpha_r)f(\alpha_r)$. As a result the shape of the current thermogram will *depend on the forming and storage conditions*, even if it is plotted on semilog paper. In other words, the current will not only be lowered for an incomplete formation, but also its *maximum* will be *shifted* from its proper temperature; this was not the case for a nondistributed polarization. This difference enables one to distinguish experimentally, between both polarizations. Moreover, current release of a distributed polarization will be typical of the polymer investigated only if $FS(\alpha_r)$ is made unity by charging the polymer completely through a proper choice of T_f and t_f.

Eqs 2.32 and 2.33 were already given in (Tu 68, Tu 70). Similar formulae have been derived by Gross (Gr 69), who considered a distribution in activation energies. However, he related the TSD less formally to the formation conditions. For a distribution in *activation energies*, which we shall denote by g(A), Eqs 2.32 and 2.33 take the form

$$P_s(T)/\varepsilon_o E = (\varepsilon_s - \varepsilon_\infty)\int_0^\infty FS(A)g(A)e^{-\alpha_r\xi(T,T_d)}dA \qquad ...(2.34)$$

and

$$j_r(T)/\varepsilon_o E = (\varepsilon_s-\varepsilon_\infty)\alpha_r\int_0^\infty FS(A)g(A)\exp\{-A/kT - \alpha_r\xi(T,T_d)\}dA \qquad ...(2.35)$$

2:2.2 Some Distribution Functions for Dielectric Relaxations

In the literature several distribution functions have been suggested. Most of these have been compiled by Gross (Gr 53) (see also (Bö 52); those applicable to dielectric relaxations are listed in Table 2-2. The quantities m and u denote the distribution width and distribution variable, respectively.

TABLE 2-2 Some Dielectric Distribution Functions

Name	f(u)du	Limits
Gevers	$(u_2 - u_1)^{-1}du$	$u_1 < u < u_2$
Wagner	$(m/\sqrt{\pi})\ \exp\ (-m^2u^2)du$	$-\infty < u < \infty$
Cole-Cole	$\frac{\sin(m\pi)du}{2\pi\{\cosh(mu) + \cos(m\pi)\}}$	"
Fuoss-Kirkwood	$\frac{m\cos(m\pi/2)\cosh(mu)du}{\pi\{\cos^2(m\pi/2)+\sinh^2(mu)\}}$	"

In particular, $u = \ln \alpha_r/\alpha_o$ or $u = (A-A_o)/kT$, where the references α_o and A_o are the most probable values of α_r and A respectively, except for the box distribution of Gevers, for which $\alpha_o = \sqrt{\alpha_1\alpha_2}$ and $A_o = (A_1 + A_2)/2$, where $\alpha_{1,2}$ and $A_{1,2}$ denote the limits of the distribution. Fig. 2-11 illustrates the shape of the distribution functions. Those of Cole-Cole and Fuoss-Kirkwood look very much the same. They are sharper than Wagner's distribution in the vicinity of α_o, and their tails extend further. The width of the distributions has been chosen as to give similar current thermograms (cf. Fig. 2-19). This was done

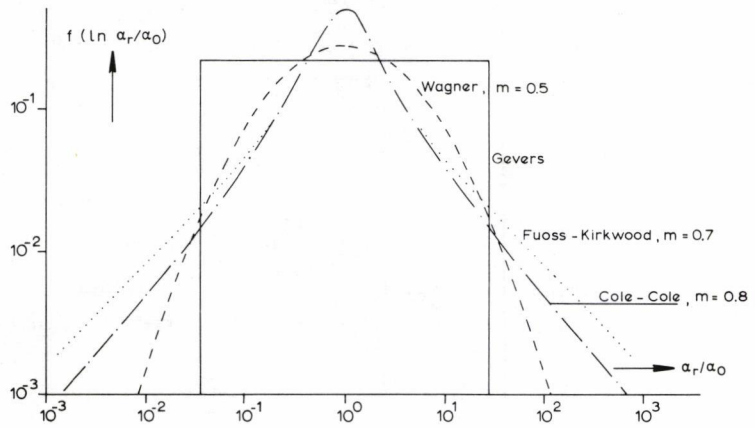


FIG.2-11 Shape of four well-known distribution functions in natural frequencies.

by considering those distributions for which $\int_{-\infty}^{\infty} f(u)du$ was nearly the same. A better choice of the appropriate widths can be made, by requiring that the sinusoidal response be similar (see (OT 72)). From Fig. 2-19 we see, however, that $j_r(T)$ does not depend strongly on the shape of the distribution. This is obvious, because the differences are levelled off by the integration with respect to α_r.

Of the distributions given that of Wagner has a sound physical basis. For it is plausible that the natural frequency or activation energy is normally distributed around a most probable value. The other distributions were derived empirically, and are easy to manipulate for sinusoidal dielectric measurements. For instance, the parameter m of a Cole-Cole distribution can be directly found from a plot of $\varepsilon''(\omega)$ vs. $\varepsilon'(\omega)$. Wagner's distribution does not give simple expressions for ε' and ε'', and has fallen into discredit*. For TSD the situation is quite different, since with the exception of Gevers's distribution in α_r, all integral equations have to be solved numerically, in which case it is tempting to prefer Wagner's distribution. However, we found from our model calculations that its initial current-rise, being equal to that of a single Debye relaxation, is too high. This again makes it less suitable for fitting TSD data.

2:2.3 TSD Model Thermograms of Gevers's Distribution in Natural Frequencies

Let us consider Gevers's manageable distribution in α_r more closely. After substituting its $f(\alpha_r)$ into Eqs 2.32 and 2.33 we find

$$P_s(T)/\varepsilon_o E = \frac{\varepsilon_s-\varepsilon_\infty}{\ln \alpha_2/\alpha_1}\left\{\int_{x_1}^{x_2} \frac{e^{-x}}{x}\,dx - \int_{y_1}^{y_2} \frac{e^{-y}}{y}\,dy\right\} \qquad (2.36)$$

$$j_r(T)/\varepsilon_o E = -\frac{(\varepsilon_s-\varepsilon_\infty)a(T)}{\ln \alpha_2/\alpha_1}\left\{\frac{e^{-x_2}-e^{-x_1}}{x_1/\alpha_1} - \frac{e^{-y_2}-e^{-y_1}}{y_1/\alpha_1}\right\} \qquad (2.37)$$

Here, $x_{1,2}$ depend on the proceeding TSD and on the previous storage, while $y_{1,2}$ are mainly determined by the forming and freezing conditions. In fact

$$x_{1,2} = \alpha_{1,2}\{a(T_s)(t_d - t_s) + s\int_{T_s}^{T} a(T)dT\}$$

and

$$y_{1,2} = x_{1,2} + \alpha_{1,2}\{a(T_f)t_f + s\int_{T_f}^{T_s} a(T)dT\},$$

where $\alpha_{1,2}$ are the extremes of α_r.

The integrands in Eq. 2.36 are those of the exponential integral, i.e.

$$\int_{x_1}^{x_2} e^{-x}\,x^{-1}\,dx = E_1(x_1) - E_2(x_2)$$

*Recently, though, some interesting approximations, which make these expressions more manageable have been suggested by Petrosyan (Pet 71).

Approximations to $E_1(x)$ have been given in Eqs 2.18 and 2.17, however, at low temperatures $x_{1,2}$ may become less than 1. We then use a polynomial approximation (AS 65)

$$E_1(x) \simeq -\ln x + a_0 + a_1 x + a_2 x^2 + a_3 x^3 + a_4 x^4 + a_5 x^5 \qquad (2.38)$$

where $a_0 = -0.57721566$, $a_1 = 0.99999193$, $a_2 = -0.24991055$, $a_3 = 0.05519968$, $a_4 = -0.00976004$ and $a_5 = 0.00107857$.

In Fig. 2-12 the *complete response, throughout the formation and subsequent TSD*, of a distribution in natural frequencies is compared with that of a Debye relaxation. We considered the Gevers distribution of Fig. 2-11, with $\alpha_2/\alpha_1 = 100$, and for normalizing we chose $P_o = \varepsilon_o(\varepsilon_s - \varepsilon_\infty)E$, which is the highest value $P_s(T)$ can ever reach. Owing to its fast subrelaxations, the initial charging and discharging currents of the Gevers distribution exceed those of Debye, so that its TSD current maximum appears at a *lower* temperature. But eventually Debye's polarization is filled sooner and also discharged sooner than that of Gevers. We further see that the freezing causes the charging currents to drop sharply. Likewise, the discharge currents during the isothermal storage are low; the discharge response mainly occurs during TSD when the dipole reorientations are stimulated. The contributions of the va-

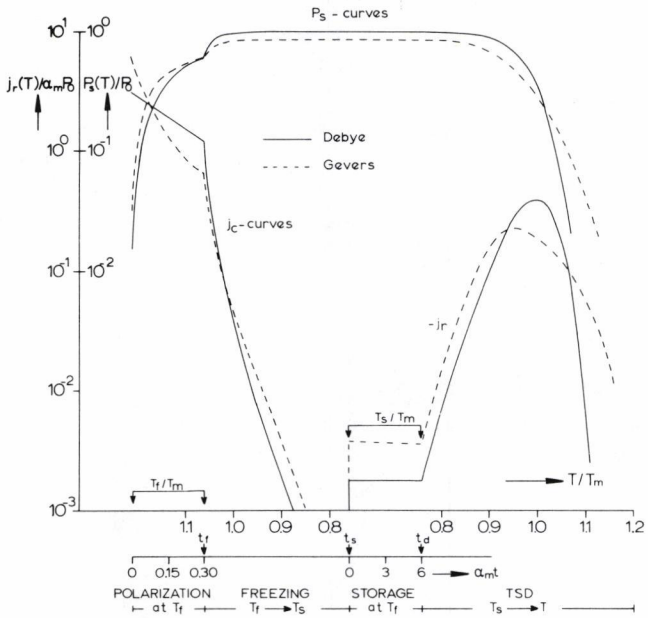


FIG.2-12 Polarization and current flow for a Gevers distribution compared with those for a Debye process during formation, storage and TSD, according to the schedule of Fig. 2-1. The two scales along the abscissa give the reduced temperature, T/T_m, and the reduced time, $\alpha_m t$. The absolute values of the charging and discharging current have been plotted; in fact they have opposite polarities. We took $A/kT_m = 20$, $T_f/T_m = 1.06$ and $T_s/T_m = 0.76$.

rious fast and slow relaxations make Gevers's thermogram broader and its maximum lower than that of Debye.

Fig. 2-13 displays the effects of a *too low formation temperature and a too long storage on the TSD response* of a Gevers distribution with $\alpha_2/\alpha_1 = 16$. Marked differences appear in comparison with the response of a completely filled polarization. (For the complete filling we took $A/kT_m = 20$, $T_f/T_m = 1.16$, $T_d/T_m = 0.76$, $\alpha_m t_f = \alpha_m t_s = 0$, and we simulated the too short formation with $T_f/T_m = 0.92$, $\alpha_m t_f = 1$ and the too long storage with $\alpha_m t_s = 1$.) Particularly, at high temperatures the polarization and the current of a too low T_f are lower than those of a complete filling. The curves are then even surpassed by those of a too low storage, the response of which differs most significantly from that of the completely filled state in the low temperature range. As expected, the current maximum for a *too low* T_f is displaced to a *lower* temperature, whereas that of a *too long* storage is shifted to a *higher* temperature. In the former case it appears at 0.97, which is somewhat above the inaccurately chosen forming temperature of $T_f/T_m = 0.92$. Note that the electret is virtually stabilized after the storage; this is important for applications.

To clarify these phenomena, we have inserted in Fig. 2-13 the effective distribution function $f^*(u) = FS(u)f(u)$. For the solid curves we have $FS(u) = 1$ and a uniform distribution results. At a too low T_f, this box is disturbed for low relaxation frequencies, since most of the slow subpolarizations have hardly been filled. On the other hand, at a too long storage the fast polarizations have mainly been discharged, and the distribution deforms for high relaxation frequencies.

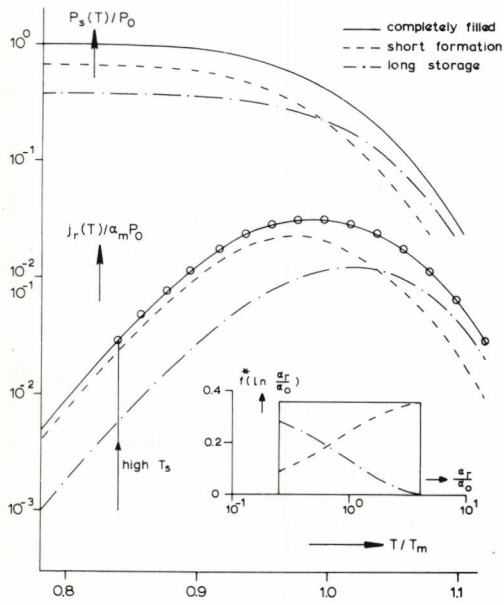


FIG.2-13 Changes caused by a too short formation, a too long storage and a too high storage temperature T_s (circles) in the thermograms of an electret with a Gevers distribution. The insert gives the effective distribution function at the beginning of TSD.

By contrast, the TSD response of a Debye relaxation would only have been *diminished* by an incomplete filling prior to TSD. But the location of its current maximum would have remained the same.

Incomplete filling of a polarization occurs also in isothermal measurements, in which it is even more difficult to avoid, except when the polarization temperature is *temporarily* raised. Yet the phenomenon is hardly noted in current literature, probably it has been overlooked by most writers, because the isothermal effects do not show up very clearly. It is also astonishing that hardly any attention has been paid to the numerical solution of the relevant integral expressions; only MacDonald has done some very interesting work in this field (Ma 63).

The circles in Fig. 2-13 finally demonstrate the effect of a too high initial depolarization temperature, $T_d/T_m = 0.84$. We assumed the polymer to be charged completely, owing to an efficient formation. The TSD current almost jumps to the correct value, after which it follows the normal TSD current very closely. In practice such a jump might occur when the freezing is cut off at room temperature, especially for polymers with a β relaxation. One should be careful not to interpret this effect as a false peak. Fig. 10-37 illustrates this truncation for the α peak of PMMA; the hump at 55 °C is certainly not a masked relaxation peak. Similarly, in the low temperature range, some peaks may be deformed by this effect (compare for instance the γ peak of P2CEMA in Fig. 10-22).

The effect of the *distribution width* on a Gevers thermogram is illustrated in Fig. 2-14. We assumed the polarization to be completely filled and took $A/kT_m = 20$. As might be expected, the broader the distribution, the broader the thermograms; their tails therefore exceed those of a Debye thermogram. Along with their shift to lower temperatures, the current maxima gradually decrease with an increasing α_2/α_0

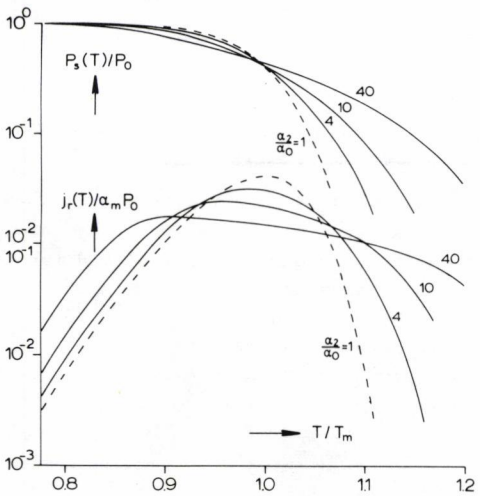


FIG.2-14 Gevers's thermograms for various distribution widths. The curves of $\alpha_2/\alpha_0 = 1$ correspond to a Debye relaxation. All current curves have the same initial slope, which exactly corresponds to $A/kT_m = 20$.

ratio. However, the initial rise of the Gevers currents hardly seems to depend on the distribution width; they all rise in the same way as the Debye current, which is at variance with the experimental results on methacrylic polymers. A high initial rise does not necessarily appear for the other distributions (see Eq. 2.45 and Fig. 2-19).

One of the curves, viz. that of $\alpha_2/\alpha_0 = 10$, closely resembles the narrow γ peak of PcHMA (cf. Sect. 3:3). The very broad distribution of $\alpha_2/\alpha_0 = 40$ has a rather peculiar shape, because it does not noticeably fall off above its maximum. In contrast with the two other Gevers's thermograms, it is also typified by having almost the same difference as a Debye curve between the lower half-width temperature and that of the current maximum. Yet, we found such odd thermograms for the broad β peaks of partially crystalline polymers such as ChPEth, PC and PET (see Figs 10-22 and 10-25). In general, however, this distribution is *not* compatible with most of the TSD dipolar peaks.

There is one final aspect to be mentioned. In Fig. 1-6 we showed that $j_r(T)$ thermograms resemble $\varepsilon''(\omega_o,T)$ thermograms; their exact relation will be derived in Chap. 4. In anticipation of this, we can state for the current ratio of the Gevers and Debye maxima

$$j_{mG}/j_{mD} \simeq \varepsilon''_{mG}/\varepsilon''_{mD}$$

of which the ε''_m ratio is given in the literature (CR 67) and so we finally get

$$j_{mG}/j_{mD} \simeq u_2^{-1}\arctan(\sinh u_2) \qquad (2.39)$$

with $u_2 = \ln \alpha_2/\alpha_o$. The actual current ratios obtained from Fig. 2-14 and those predicted by Eq. 2.39 are compiled in Table 2-3. We see that this equation is almost satisfied.

TABLE 2-3 Comparison Between Current Maxima of Gevers's Thermograms

α_2/α_o	j_{mG}/j_{mD} calculated	j_{mG}/j_{mD} predicted
1	1	1
4	0.79	0.78
10	0.61	0.60
40	0.44	0.41

When a particular relaxation peak is not only studied with TSD, but also with dielectric measurements, then the relations given enable one to *predict* the required *width* of the Gevers distribution. As an example we calculated for the β peak of PMMA $\varepsilon''_{mG}/\varepsilon''_{mD} = 0.2$, which yields $\alpha_2/\alpha_o = 2500$ or $\alpha_2/\alpha_o = 6.25 \times 10^6$; this is a tremendous range implying a difference in dipole radii of 200. This cannot easily be imagined and so a distribution in activation energies seems to be more probable. Actually, we could prove the existence of this by a multi-stage TSD (OT 72), see also Sect. 2:3.1.

2:2.4 Model Thermograms of Distributions with a Finite Range of Activation Energies

Let us once more justify our interest in a distribution in activation energies, since we know that this disobeys the time-temperature superposition principle, and therefore seems less attractive. Fig. 2-15 shows ε'' results of a set of isothermal dielectric measurements on the γ peak of P2CEMA, which is due to an intramolecular relaxation of the 2-chloroethyl side group. We see that the ε'' maximum *increases* from 0.101 to 0.126 with temperature, and simultaneously the peak becomes *narrower*. Clearly, the results cannot be superposed to give a master curve, and so this γ relaxation does *not* behave thermorheologically simply*. If we fit the data to a Wagner distribution in $\ln \alpha(T_o)$, we find, for the three curves depicted in the insert, that m (-98°) = 0.20, m (-108.8°)= 0.17 and m (-129°) = 0.14. This means that $m \propto T_o$, which according to Nowick et al. (NB 61) is just that which is expected of a distribution in activation energies**. Such a distribution was also proved to exist

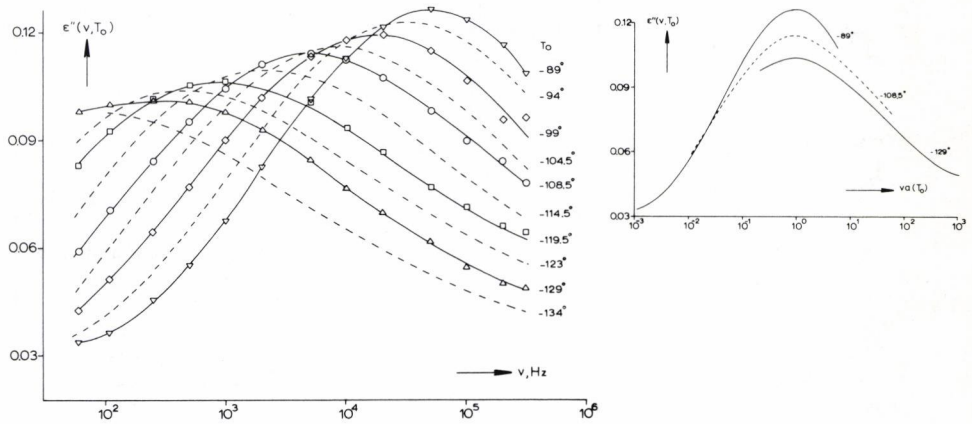


FIG.2-15 The frequency dependence of the dielectric loss factor for the γ peak of P2CEMA at various temperatures. This peak does *not* behave thermorheologically simply, because the curves do not superimpose when shifted along the frequency axis by a factor a(T); this is shown on the right for three temperatures. (The corresponding activation energy is 7.2 kcal/mol.) Measurements by Dr Ong of this laboratory.

for the γ peak of PcHMA and the β peak of PMMA by a multi-stage TSD experiment (cf. Sect. 2:3.1). The low-temperature TSD peaks, which originate from local-mode relaxations of polar side groups thus seem to have a distribution in activation energies, rather than a distribution in natural frequencies.

* I am indebted to Ir L.C.E. Struik for drawing my attention to this fact.

**The actual distribution might even be a combined one in natural frequencies and in activation energies, because m plotted vs. T does not pass through the origin (NB 61).

Most of the TSD phenomena described in the foregoing section also occur for a distribution in activation energies. In this case, during TSD, the dipolar groups with the lower activation energies are the less resistant. Hence, these reorientate first, while the dipoles with the higher activation energy remain lined up for the longest time.

For Gevers's distribution, we obtain from Eqs 2.34 and 2.35

$$P_s(T)/\varepsilon_o E = \frac{(\varepsilon_s - \varepsilon_\infty)}{A_2 - A_1} \int_{A_1}^{A_2} FS(A)g(A)e^{-\alpha_r \xi(T,T_d)}dA \qquad (2.40)$$

$$j_r(T)/\varepsilon_o E = \frac{(\varepsilon_s - \varepsilon_\infty)\alpha_r}{A_2 - A_1} \int_{A_1}^{A_2} FS(A)g(A)e^{-A/kT-\alpha_r \xi(T,T_d)}dA \qquad (2.41)$$

where FS(A) is given by Eq. 2.10. These integral transforms must be solved numerically; we applied the fast integration method of Romberg*. This method makes use of extrapolations and in order not to calculate these anew for each temperature, we implemented a modification suggested by Rabinowitz (Ra 66). The adaptive Simpson integration described by Keeman (Ke 62), also works fast.

Results of Gevers's distribution in activation energies and natural frequencies are compared in Fig. 2-16.The distribution widths chosen,

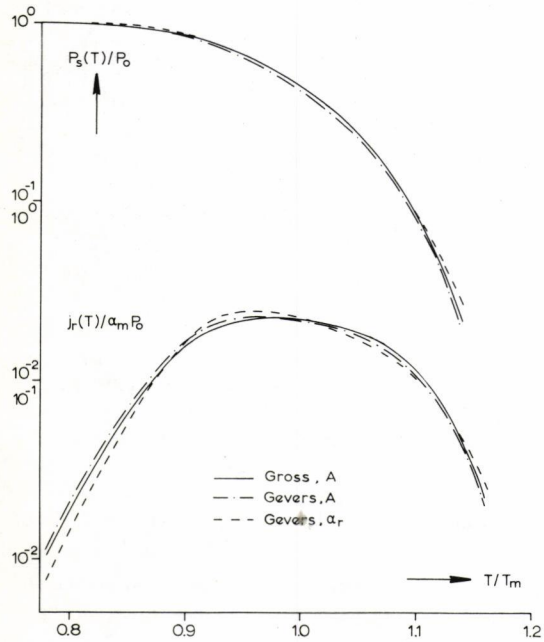


FIG.2-16 Comparison between the thermograms of an electret with a polarization distributed in activation energy, A, and natural frequency, α_r. We put $A_o/kT_m = 20$, $A_2-A_1 = 0.23\ A_o$ and $\alpha_2/\alpha_1 = 100$.

correspond to $\ln \alpha_2/\alpha_1 = (A_2-A_1)/kT_m$ and we assumed the polarizations to be completely filled, i.e. FS(A) = 1. The thermograms look quite similar.

*Romberg's Integration, Fortran-Subroutine Quatr., IBM Scientific Subroutine Package, Version 3, 1968, pp 297-298.

This is not surprising; to make them identical one should put according to Eqs 2.32 and 2.34

$$f(\alpha_r)d\alpha_r = g(A)dA \tag{2.42}$$

Now Eq. 2.14 yields, upon differentiation,

$$d \ln \alpha_r = -dA/kT$$

so that we should have in fact

$$f(\ln \alpha_r) = -kTg(A) \tag{2.43}$$

Obviously, the results become identical only if one of the distributions is forced to be temperature dependent. For instance, if g(A) is temperature independent, $f(\ln \alpha_r)$ must be proportional to kT. Besides the height, the width of $f(\ln \alpha_r)$ should change as well. For if g(A) ranges from $A_o - \Delta A$ to $A_o + \Delta A$, the natural frequencies must lie between $\alpha_o \exp(-\Delta A/kT)$ and $\alpha_o \exp(\Delta A/kT)$. Since the adjustments required for an identity are rather *small*, only minor differences appear in Fig. 2-16. As pointed out by MacDonald (Ma 62), the interconversion according to Eq. 2.43 can only be made for a Gevers and a Wagner distribution.

Fig. 2-16 also shows the current thermogram of an exponential distribution in activation energies, recently proposed by Gross (Gr 69)

$$f(u)du = \frac{e^u du}{e^{u_2} - e^{u_1}} \qquad u_1 < u < u_2 \tag{2.44}$$

where $u = A/A_o$. Again we used the Romberg-Rabinowitz method to solve the corresponding integral equation. The approximate solution method suggested by Gross was found to be rather crude. As is seen, apart from their shift to a slightly higher temperature, Gross's thermograms strongly resemble those of Gevers's distribution in A. This is understandable, because exp(u) remains almost constant in the integration interval considered.

2:2.5 Model Thermograms of Distributions Extending over an Infinite Interval

Fig. 2-17 shows the *filling* and *emptying* of a Cole-Cole distribution during isothermal polarization, freezing, isothermal storage and TSD. Neither the freezing nor the storage (at low temperatures) produce much effect. The largest changes take place during the high-temperature formation, and during TSD. As for Gevers's distribution the fast relaxations respond the earliest, so that they are soon filled during formation, and easily discharged during storage. The TSD is in this case started with an effective distribution function, which is *deprived* of subpolarizations at both sides of the relaxation-frequency scale. In the course of TSD the fast polarizations are released first; the slow polarizations disappear less readily; they are liberated only at much

higher temperatures.

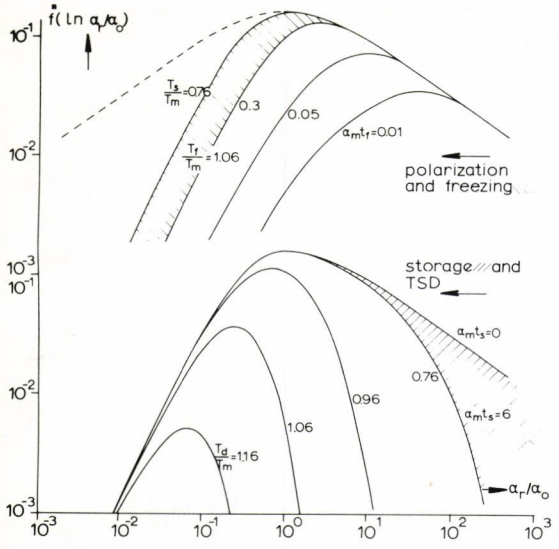


FIG.2-17 Filling and emptying of the subpolarizations of a Cole-Cole distribution at various stages during charging and discharging. The dashed curve, gives the completely filled electret state. We chose m = 0.5 and A/kT_m = 20.

The numerical solution of the Laplace transforms (Eqs 2.32 and 2.33 or 2.34 and 2.35) for distributions incorporating an infinite integration interval is more complicated. We first tried to evaluate these with the integration formulas of Gauss-Legendre and Gauss-Hermite. The results were disappointing, even for a complete filling. We then turned again to Romberg's integration. This, however, requires a finite interval, so we truncated the interval to limits where the integrands decrease to 10^{-5} of their maximum value. To illustrate the method, the integrands

$$\ln(P_s) = FS(\alpha_r)f(\alpha_r)e^{-\alpha_r \xi(T,T_d)}$$

$$\ln(j_r) = \alpha_r \ln(P_s)$$

are plotted in Fig. 2-18. The calculations were made for a Wagner polarization with $FS(\alpha_r) = 1$, m = 0.5 and $A/kT_m = 20$. The higher the release temperature, the more of the faster subpolarizations have been discharged and the smaller the integration interval can be. Three intervals have been chosen to cover the usual temperature range. It is obvious that different intervals are used for the polarization and the current.

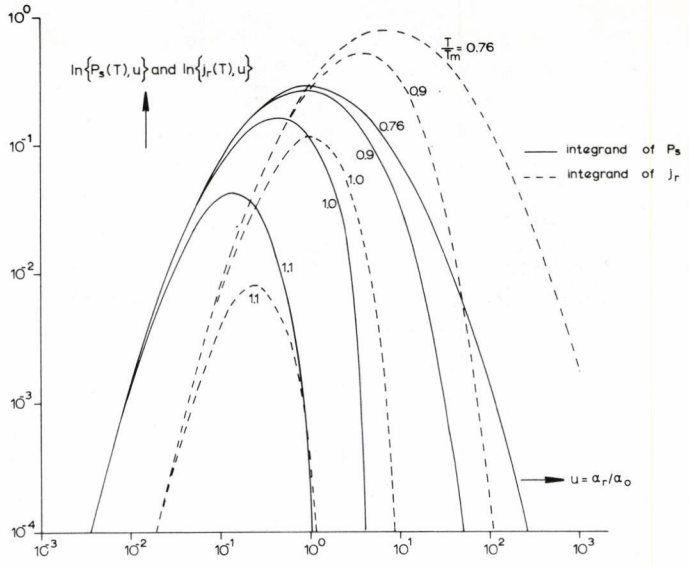


FIG.2-18 Integrands of the integral transforms for the polarization and current of an electret with a Wagner distribution at various release temperatures during TSD.

Calculated TSD thermograms for a Wagner, Cole-Cole and Fuoss-Kirkwood distribution are given in Fig. 2-19. The current thermograms of these monotonous distributions run more symmetrical than that of Gevers. They show slight differences at both temperature extremities, which originate from differences in the tails of their distributions, as in-

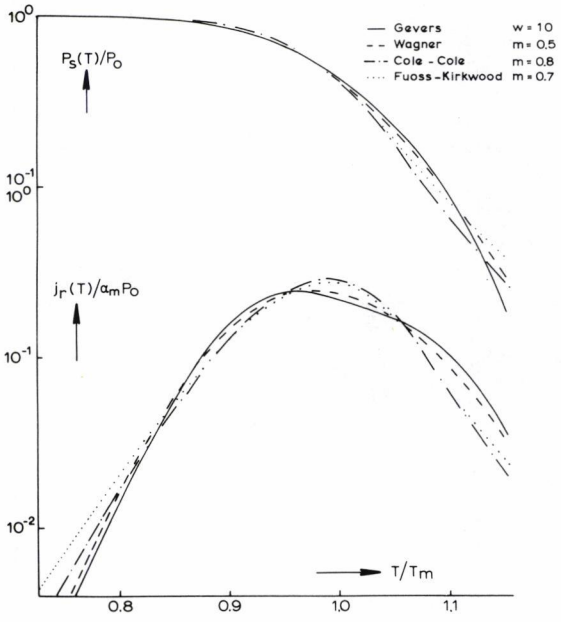


FIG.2-19 Polarization and current thermograms for the four distribution functions in natural frequencies shown in Fig. 2-11. We took $A/kT_m = 20$. The initial current slopes of the distributions of Cole-Cole and Fuoss-Kirkwood are lower than those of Gevers and Wagner, which are equal to A/kT_m.

dicated in Fig. 2-11.

Obviously, their *initial current rise* is not solely determined by A/kT_m, since this was taken the same for all distributions; their shape and width seem to be of importance too. The current thermograms of Cole-Cole and Fuoss-Kirkwood display the least rise. We shall show in Sect. 3:2 that up to the lower half-width temperature we can put

$$d \ln j_r(T)/d\, 1/T \simeq - cA/k \qquad ...(2.45)$$

where c = 1 for the Wagner and Gevers distribution and c = m for the Cole-Cole and Fuoss-Kirkwood distribution. Thus the former distributions both have the same initial slope as a Debye thermogram. This makes them much *less* attractive to describe actual data.

As an example we consider the initial rise of the TSD β peak of PMMA, which gives an activation energy of only 2.5 kcal/mol, whereas normally a value of 18 kcal/mol is quoted. This would imply that c or rather m = 0.14. Recalling that for a Fuoss-Kirkwood distribution $m = 2\varepsilon''_m(\varepsilon_o-\varepsilon_\infty)^{-1}$, we shall deduce in Sect. 4:2 for the converted TSD β peak of Fig. 1-6 that m = 0.15, which is almost equal to the value just mentioned. Clearly, to this peak only the Cole-Cole and Fuoss-Kirkwood distribution can be applied. Likewise for most of the other polymer relaxations; these distributions seem to be the most favourable. It goes without saying that Eq. 2.45 allows one to calculate the activation energy of distributed polarizations in a simple way, provided that m is known, e.g. from dynamic dielectric measurements or from the literature. Its use will be illustrated more extensively in Sect. 3:2.

Further inspection of Fig. 2-19 shows that the distributions with the infinite interval have their current maxima located close to T_m. Gevers's box distribution, which contains by its very nature too many fast polarizations, gives a current maximum at a much lower temperature.

Some relevant quantities of the four current thermograms are compiled in Table 2-4. As for Eq. 2.39, we have invoked the formulas for $\varepsilon''_{max}/\varepsilon''_{mD}$ (CR 67, Pet 71), to predict j_{max}/j_{mD}. These formulas read

Cole-Cole	$j_{max}/j_{mD} = \tan m\pi/4$	
Fuoss- Kirkwood	$" \quad = m$	(2.46)
Wagner	$" \quad = m(m^2 + 0.367)^{-\frac{1}{2}}$	

TABLE 2-4 Some Relevant Quantities of the Current Thermograms of Distribution Functions

	m	j_{max}/j_{mD} calculated	j_{max}/j_{mD} predicted	T_{max}/T_{mD} calculated	$\Delta h_D/\Delta h$ calculated	$\Delta h_D/\Delta h$ predicted
Debye		1	1	1	1	1
Cole-Cole	0.8	0.72	0.73	0.99	0.77	0.8
Fuoss-Kirkwood	0.7	0.60	0.70	0.99	0.77	0.7
Wagner	0.5	0.62	0.64	0.975	0.76	0.6-0.8
Gevers	w=10	0.61	0.60	0.95	0.91	

The calculated results for j_{max}/j_{mD}, derived from Fig. 2-19, and those predicted by Eq. 2.46 are almost the same. The columns headed $\Delta h_D/\Delta h$ give the ratio $(T_{mD}/T_{hD}-1)/(T_{max}/T_h-1)$, where T_{hD} is the lower half-width temperature of the Debye thermogram and T_h that of the other thermograms. Dielectric theory provides for this ratio the following estimates

$$\text{Cole-Cole and Fuoss-Kirkwood: } \Delta h_D/\Delta h = m \qquad (2.47)$$

$$\text{Wagner} \simeq m/0.632^*, \; m < 0.5$$

The actual values and predicted ones agree fairly well. This justifies the use of Eq. 2.47 to calculate the activation energy of distributed polarizations from the lower half-width temperature in a simple way. This subject will be taken up in Sect. 3:2.

Fig. 2-20 illustrates an attempt to fit the TSD α peak of PcHMA to a Fuoss-Kirkwood thermogram, the distribution width and activation energy of which were derived from dielectric measurements at medium frequencies. The curves overlap only in part. We believe that a better fit would have been obtained if a WLF shift had been used. The deviations may partly be due to the fact that this particular peak does not

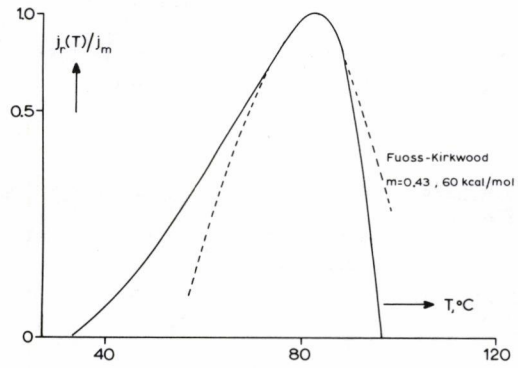


FIG.2-20 Experimental TSD α peak of PcHMA (full line), compared with a calculated thermogram for a Fuoss-Kirkwood parameter of m = 0.43 and an activation energy of 60 kcal/mol (broken line).

*This approximation has been taken from Nowick et al. (NB 61).

obey the time-temperature superposition principle, for we noticed from the isothermal dielectric measurements that its distribution width was not constant.

Finally, the consequences of an incomplete filling of a Cole-Cole distribution by a too low forming temperature T_f are portrayed in the calculated TSD current thermograms of Fig. 2-21. When T_f is chosen below the characteristic peak temperature of 400 °K, the maximum is scaled downwards in magnitude and in temperature, and appears somewhat above T_f. This is in qualitative agreement with the experimental results of Fig. 1-11. To record the peak properly up to its high-temperature tail, T_f should be taken 450 °K or higher, since from that temperature onwards the electret is fully charged.

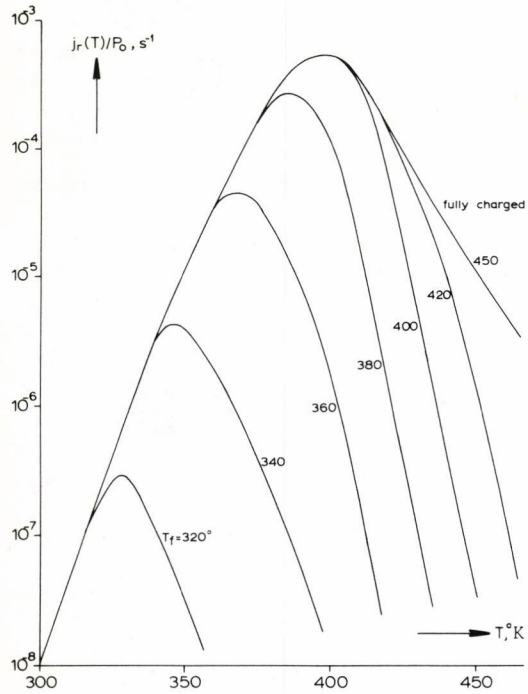


FIG.2-21 Illustration of the high-temperature distortion caused by an inaccurate choice of the forming temperature, T_f. Calculations of Ong on a Cole-Cole distribution with m = 0.5, A = 60 kcal/mol, T_m = 400 °K, s^{-1} = 1.2 °C/min and t_f = 1 h.

2:2.5a Analogy Between an Isothermal Discharge and TSD

In reference (Tu 68) we have described a method to obtain the thermograms of a distributed polarization without solving the Laplace transforms numerically. It is based on the analogy between isothermal and TSD measurements and presupposes a complete filling FS = 1. For the isothermal discharge current we have

$$j(t)/\varepsilon_o E = (\varepsilon_s - \varepsilon_\infty)a(T) \int_0^\infty \alpha_r f(\alpha_r) e^{-\alpha_r a(T) t} d\alpha_r \qquad (2.48)$$

whereas for TSD

$$j_r(T)/\varepsilon_o E = (\varepsilon_s - \varepsilon_\infty)a(T) \int_0^\infty \alpha_r f(\alpha_r) e^{-\alpha_r \xi(T)} d\alpha_r \qquad (2.49)$$

Apparently, both currents become identical if a(T)t replaces $\xi(T)$. Now formulas for the isothermal current have been cited in the literature (CC 42, JE 45, Gr 48). For example for a Voglis distribution (Ma 61)

$$j(t)/\varepsilon_e E = (\varepsilon_s - \varepsilon_\infty)\alpha_o a(T)\{1 + \alpha_o a(T)t\}^{\nu-1} \quad , \; 0 \leq \nu < 1 \qquad (2.50)$$

which corresponds to the well-known current-time relation of Von Schweidler, giving a straight line with a slope ν-1 on a log-log plot. To convert Eq. 2.50 to TSD, we substitute $\xi(T)$ for a(T)t and get

$$j_r(T)/\varepsilon_o E = (\varepsilon_s - \varepsilon_\infty)\alpha_o a(T)\{1 + \alpha_o \xi(T)\}^{\nu-1} \qquad (2.51)$$

Two thermograms corresponding to this equation are plotted in Fig. 2-22. Only their initial current rise appears to be reliable. Above T_m they are *unrealistic*, in giving no sign of charge exhaustion and so it would be unwise to apply this distribution to actual TSD data. This odd behaviour of Von Schweidler's empirical formula was already known from isothermal work, in which however it shows up less clearly. Gross and MacDonald (Gr 48, Ma 61) have truncated Voglis's distribution to correct for this error.

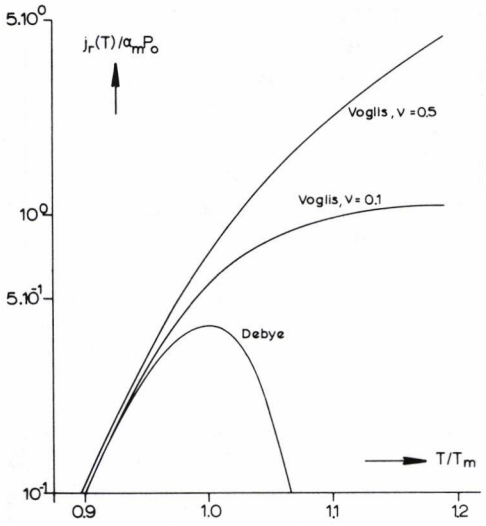


FIG.2-22 Two current thermograms of a Voglis distribution, compared with the familiar Debye thermogram; they are unreal for $T > T_m$.

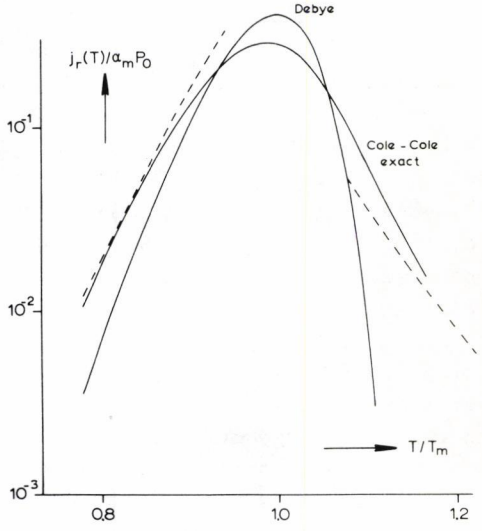


FIG.2-23 First approximations (dashed lines) to a Cole-Cole thermogram for m = 0.8 and $A/kT_m = 20$. The corresponding Debye thermogram is also shown; its initial slope is m^{-1} higher than that of Cole-Cole.

Cole and Cole have expressed their isothermal discharge current in two infinite series (CC 42). If we restrict ourselves to the first terms of these series we get the following approximations to a Cole-Cole thermogram, valid at low and high temperatures respectively

$$j_r(T)/\varepsilon_o E \simeq \frac{(\varepsilon_s - \varepsilon_\infty)e^{-A/kT}}{\Gamma(m)} \{\alpha_o \xi(T)\}^{m-1} , \qquad T < T_m \tag{2.52}$$

$$j_r(T)/\varepsilon_o E \simeq m \frac{(\varepsilon_s - \varepsilon_\infty)e^{-A/kT}}{\Gamma(1-m)} \{\alpha_o \xi(T)\}^{-m-1} , \qquad T > T_m \tag{2.53}$$

where m is the distribution width and Γ denotes the gamma-function. These approximations are compared to the exact thermogram in Fig. 2-23. At low temperatures the agreement is reasonable, but at high temperatures obviously more terms are needed for a good fit.

Differentiating Eq. 2.52 with respect to T, we find for the initial current slope

$$d \ln j_r(T)/d\ 1/T \simeq - mA/k \qquad , T < T_h \tag{2.54}$$

which proves Eq. 2.45 in expressing that the initial slope of a Cole-Cole thermogram is a factor of m less than that of a Debye thermogram. This difference is also apparent from Fig. 2-23, where m amounts to 0.8.

2:2.6 Conclusions

Model calculations were made for elucidating the TSD behaviour of polymers with distributed polarizations. These have shown that the TSD behaviour of electrets with a distributed polarization is attended with exceptional phenomena. As the most striking result, we found that their reduced current thermograms, i.e. $j_r(T)/j_m$ vs T, depend on the forming and storage conditions. So, if TSD is practised for unravelling the molecular relaxations of polymers, these should always be polarized completely* by choosing T_f and t_f properly, otherwise artifacts may be measured. On the other hand, incomplete charging enables one to distinguish between a distributed and nondistributed dipole relaxation.

The model calculations also enabled us to sort out some known distribution functions applicable to actual TSD data. Remarkably, it turned out that the distributions suggested for describing results of isothermal discharge measurements, viz. those of Voglis and Wagner, are not the most suitable. Voglis's distribution in particular, is very unsuitable, whereas Wagner's distribution is wrong only in so far that it gives a too high initial current slope. The distributions of *Cole-Cole and Fuoss-Kirkwood* were found to be much more appropriate. They are also preferable to the rectangular distribution of Gevers, which does not fit broad peaks and also has a too high initial slope. For the same reason the distribution recently suggested by Gross, which closely resembles Gevers's distribution, is not satisfactory.

So far, we have fitted experimental results to the Fuoss-Kirkwood distribution by merely taking parameter values known from dynamic di-

*A complete charging is also essential in isothermal measurements, and here leads to the inconvenience of extremely long charging times.

electric measurements. The evaluation of TSD data of dipolar peaks will be treated more extensively in Chap. 3, where we shall attempt to adjust the relevant parameters by the least-squares method. This is not an easy matter, because two parameters, i.e. the activation energy and the width of the distribution, must be evaluated simultaneously.

A more general way is not to prescribe any distribution, but to calculate it from the data. Sect. 3:3 deals with approximation methods to perform this.

2:3 The Resolution of TSD Measurements

This section describes theoretical aspects of the resolution of TSD. First, actual figures are derived for the resolving power of TSD. Next the interesting ability of a multi-stage TSD to separate overlapping peaks by partial heating is outlined; this method also allows one to distinguish between a distribution in natural frequencies and one in activation energies. Moreover, we shall point out that such a partial heating may be utilized to increase the lifetime of an electret.

With the occurrence of more relaxation peaks arises the question of their resolution. In normal dielectric measurements the resolution mostly increases on lowering the frequency. TSD measurements behave similarly, so the highest resolution is reached at low heating rates.

To elucidate this behaviour we consider in Fig. 2-24 two relaxation peaks, differing in α_r and A, at various heating rates. Peak 1 with the lower activation energy, $A_1/kT_1 = 10$, shifts slightly more with heating rate than peak 2 of the higher activation energy.

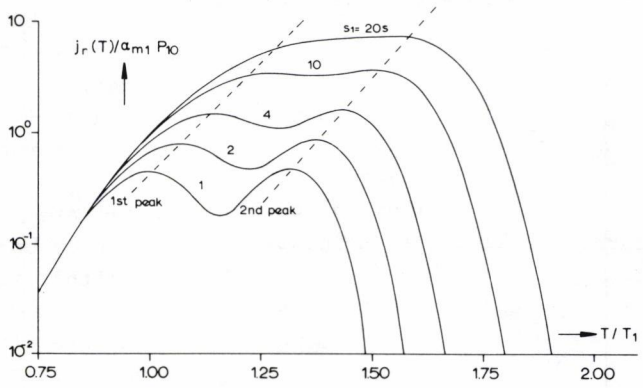


FIG. 2-24 Effect of the relative heating rate, s_1/s, on the current thermogram of two proximate polarizations of equal initial value. The ratios of the natural frequencies and activation energies were taken as $\alpha_2/\alpha_1 = 200$, $A_2/A_1 = 2$, respectively.

For a sufficiently high rate peak 1 may join peak 2. At this particular heating rate s_c^{-1}, the combined current peaks are located at the same temperature T_c, which satisfies

$$s_c \alpha_{1,2} T_c e^{-E_{1,2}} = E_{1,2} \qquad (2.55)$$

where we wrote $E_{1,2}$ for $A_{1,2}/kT_c$.

For any other heating rate the peaks separate and we have

$$s\alpha_{1,2}T_c e^{-E_{1,2}x_{1,2}} = E_{1,2}x_{1,2}^2 \tag{2.56}$$

where $x_{1,2} = T_c/T_{1,2}$. Combination of both equations yields, for the locations, $x_{1,2}$ of the two current maxima

$$x_{1,2}^2 e^{E_{1,2}x_{1,2}} = (s/s_c)e^{E_{1,2}} \tag{2.57}$$

From this formula we can calculate $x_{1,2}$ as a function of heating rate. We readily verify that if the heating rate is lowered, so that s exceeds s_c, $x_{1,2}$ increase, though differently. As a result the temperature differences between the peaks become larger, as is demonstrated in Fig. 2-24. The same conclusion applies when only A or α_r differ, except that a fusion of the peaks does not occur, because they then shift to the same extent.

It is interesting to note from Fig. 2-24 that the separation of the peaks becomes not only smaller, but also less distinguishable for higher heating rates. Since both current peaks increase with heating rate, and at the same time become broader, they finally merge into a broad hump. This effect lowers the attainable resolution considerably and makes a high heating rate much less attractive. Moreover, the sample cannot follow the change in temperature fast enough at high heating rates.

Let us now indicate the resolving power at a given s. We consider either a difference in natural frequency or in activation energy, and presume equal initial polarizations. We then have for the TSD current

$$j_r(T)/P_o = \sum_{i=1}^{2} \alpha_i e^{-A/kT-\alpha_i \xi(T)} \tag{2.58}$$

and

$$j_r(T)/P_o = \sum_{i=1}^{2} \alpha_r e^{-A_i/kT-\alpha_r \xi_i(T)} \tag{2.59}$$

respectively and we seek to know the minimum values of α_2/α_1 and A_2/A_1 that will give distinct current peaks. Let the quotient of the temperatures of the two maxima be $x = T_1/T_2$. The value of x will depend on α_2/α_1 and A_2/A_1, by invoking the condition of the current maxima we find as interrelationships

$$\alpha_2/\alpha_1 = x^2 e^{(x-1)A/kT_1} \tag{2.60}$$

and

$$e^{(1-xA_2/A_1)A_1/kT_1} = x^2 A_2/A_1 \tag{2.61}$$

We must now define a resolution criterion. A sound physical criterion could not be derived, and we therefore studied the thermograms visually

for different x values. Fig. 2-25 illustrates the choice of the admissible x value. We see that at x = 0.93 the maxima unite, while for x = 0.92 they start to separate, because the current exhibits an inflexion point. In excepting this value as a lower limit we find from Eq. 2.60 for $\alpha_2/\alpha_1 = 5.8$. For normal ε'' measurements the permissible α_2/α_1 amounts to $3 + 2\sqrt{2}$, which is also equal to 5.8. Likewise, we found a resolving limit of $A_2/A_1 = 1.09$ for a two level distribution in activation energy, for which $A_1/kT_1 = 20$.

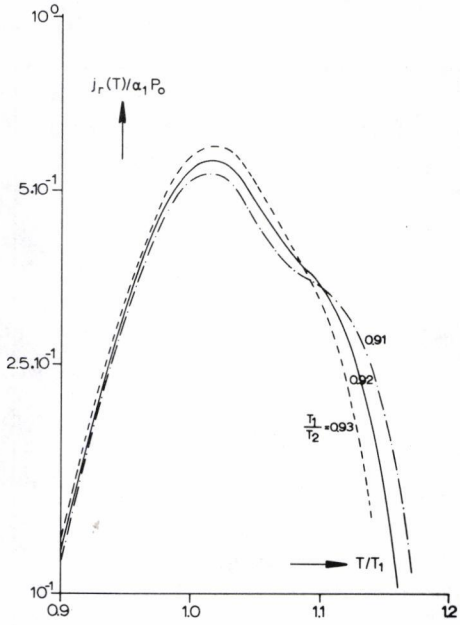


FIG.2-25 Illustration of the resolution limit for two overlapping dipole relaxations differing in natural frequency and for which $A/kT_1 = 20$.

2:3.1 Multi-Stage TSD Experiments

We mentioned already that a high resolution requires a low heating rate. The choice of s is limited, however; for low rates result in low currents and long measuring times. Normally, we took a rate of 1 °C/min at which most relaxation regions were resolved well.

But when proximate peaks do occur, they can still be decomposed, because TSD has the exceptional ability to resolve overlapping peaks (BF 66). There are two ways in which this can be done; the first being based on not filling the 2nd peak by choosing T_f at the temperature of the valley T_v, the second involving thermal cleaning of the 1st peak by a partial discharge up to T_v. In the last case we have during the 2nd run

$$j_r(T) = \sum_{i=1}^{2} P_{si}(T_v)\alpha_i(T)e^{-\alpha_i \xi_i(T,T_d)} \qquad (2.62)$$

where

$$P_{si}(T_v) = P_{si}(T_d)e^{-\alpha_i \xi_i(T_v,T_d)}$$

Note that $P_{s1}(T_v) \simeq 0$ and $P_{s2}(T_v) \simeq P_{s2}(T_d)$; for polarization 1 is almost empty after the first heating run, whereas polarization 2 is still filled.

There is *no* analogue of this interesting technique in ordinary dielectric measurements. Fig. 2-26 shows how effective the thermal cleaning is. A genuine ρ peak appears in the 2nd run, of which the initial rise no longer seems to be disturbed by the α relaxation. Thus, its activation energy can safely be calculated from this rise. In doing so, we found A = 2.0 eV, which agrees well with the activation energy of 1.9 eV for the ohmic conduction of PMMA.

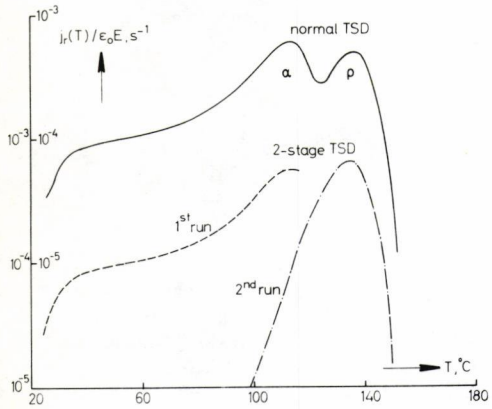


FIG.2-26 Isolating the ρ peak of a PMMA electret from its α peak by a two-stage TSD.

Creswell and Perlman (CP 70) have recently advocated a multi-stage cleaning to find the activation energies, $A_{1,2}$, of two proximate peaks. They use a programme with repeated heating an subsequent cooling, like 25° ↑ 40° ↓ 25° ↑ 45° ↓ 25° ↑ 50° ↓ 25°,....., in which the upper temperatures are steadily increased.

Their idea is that during the various TSD runs, the low temperature tail of the current is determined by A_1 and the high temperature tail by A_2. The curves of Fig. 2-27 calculated for $A_1/kT_1 = 10$, $A_2/kT_1 = 30$, $T_1/T_2 = 0.95$, $P_{s1}/P_o = 0.2$ and $P_{s2}/P_o = 0.8$, show that this hypothesis is true. Hence, the method enables one to determine $A_{1,2}$ several times. It should be noted from the lower part of the diagram that the method only works well for two relaxation peaks of different heights, for which $j_2 > j_1$.

Fig. 2-28 illustrates the results when Creswell and Perlman's method is applied to a *distributed* polarization. The calculations were done for a Gevers distribution in natural frequencies (full lines) and one

in activation energies (dashed lines); we took ln $\alpha_2/\alpha_1 = (A_2-A_1)/kT_m$ = 4.6 and $A_o/kT_m = 20$. Examining the distribution in natural frequencies first, we see from the insert that the "initial" effective distribution functions change gradually during the successive heating runs, the fast subpolarizations, in particular, becoming exhausted. Owing to the remaining slow subpolarizations, the decreasing current maximum gradually shifts to a *higher* temperature. Such a shift does not occur in a single Debye process, as can be inferred from Fig. 2-27. Hence, a multi-stage TSD provides another means of distinguishing between distributed and nondistributed polarizations.

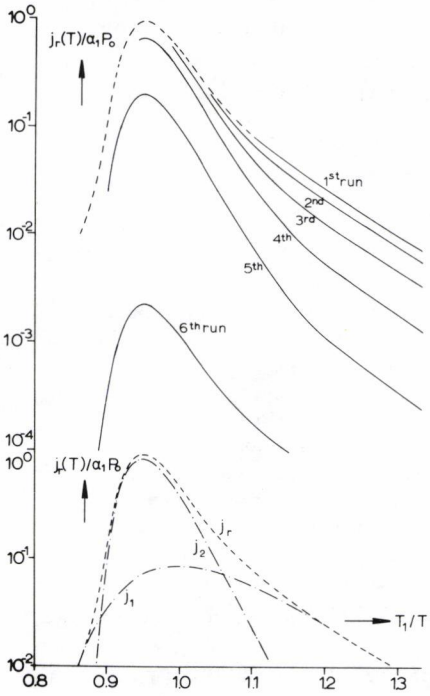


FIG.2-27 Multi-stage TSD for finding the activation energy of two proximate relaxations, as suggested by Creswell and Perlman. The lower curves give the uninterruped TSD current, j_r, and its two components, $j_{1,2}$.

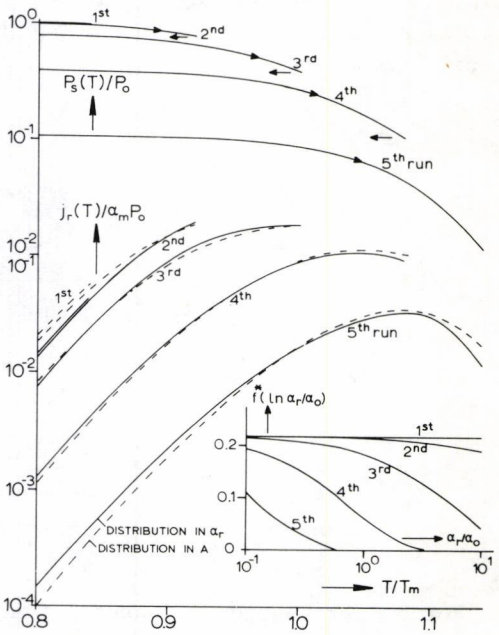


FIG.2-28 Calculated polarization and current thermograms during multi-stage TSD of an electret with a distributed polarization of Gevers. The full lines represent the results of a distribution in natural frequencies and the dashed lines those of a distribution in activation energies. The insert shows the effective distribution function $FS(\alpha_r/\alpha_o)f(\ln \alpha_r/\alpha_o)$.

It is even more useful, in enabling one to differentiate between a distribution in natural frequencies and one in activation energies. Comparing the full and dashed lines in Fig. 2-28, we see that the initial slope of the former remains *constant* whereas that of the latter *increases*

steadily, viz. from A/kT_m = 17.9 to 21.3. This change is clearly due to the increasing number of subpolarizations with a higher activation energy.

Studying the multi-stage TSD of the broad β peak of PMMA, Ong and the author (OT 72) have found such an ever increasing initial current rise, and so this peak indeed seems to arise from a distribution in *activation energies*. The consecutive thermograms are represented in Fig. 2-29. The apparent activation energies, deduced from the various initial slopes, range from 4.2 to 11 kcal/mol. The latter value is found just beneath the maximum of the uninterrupted thermogram. Here we expected to find a value of 18 kcal/mol, as found from the frequency shift of the ε" maximum in traditional dielectric measurements. We cannot yet explain this discrepancy conclusively, but it might well be that the actual distribution is a double one in activation energies and in natural frequencies.

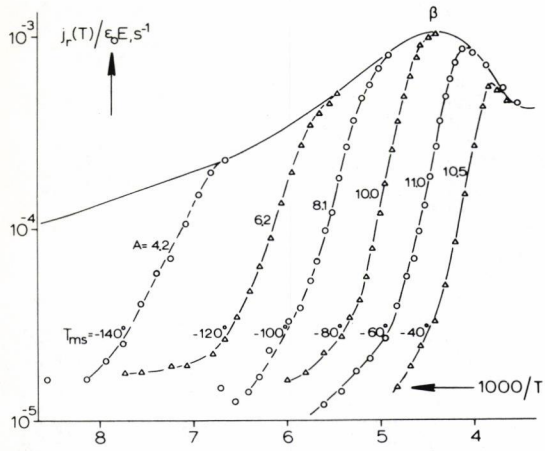


FIG.2-29 Results of a multi-stage TSD for the dipole β peak of PMMA. They show that the initial current slope *increases* progressively; the corresponding activation energies are indicated. The successive preheating temperatures T_{ms}, at which the electret was kept for 1 hour, are also given. The electret was formed at 20°-8 kV/cm-1 h and the heating rate was 3 °C/min.

For a distribution in natural frequencies, on the contrary, all dipoles have the same activation energy and the slope is unlikely to change. This is not strictly true for the distributions in natural frequencies of Cole-Cole and Fuoss-Kirkwood. These do change their initial slope in a multi-stage TSD, albeit only in the *first* heating run. Thereafter it remains constant at -A/k, instead of at -mA/k, as given by Eq. 2-54. This rise in the apparent activation energy is due to the fact that the extended high-frequency tails of these broad distributions are cut off (cf. Fig. 2-17), and so their tails now more resemble Wagner's distribution and to a lesser extent Gevers's distribution, both of which have an initial current slope of -A/k. This phenomenon enables one to find the activation energy of polarizations distributed in natural frequencies, without knowledge of the distribution parameter m. For some applications of the interesting possibilities of multi-stage

TSD we refer to (OT 72).

Another aspect worth mentioning is that from the upper curves of Fig. 2-28 we can observe that the polarization decreases less sharply with temperature in the successive heating runs. Due to the relative increase of the slow relaxations, the polarization retained is stabilized. Hence, at the expense of some charge loss the electret becomes more stable at room temperature. A partial thermal discharge therefore offers an interesting possibility to *increase the lifetime* of polymer electrets.

Chapter 3

EVALUATION OF DATA PERTAINING TO CURRENT TSD BY DIPOLE REORIENTATION

The aim of an evaluation of TSD data is to deduce the pertinent molecular parameters, and since during TSD several decay processes may concurrently take place, there is a wealth of information to be gained. For dipolar relaxations we are interested in the temperature shift or activation energy, the relaxation frequency, the relaxation strength and the distribution function, while for SCL drift the relevant quantities are the mobility, the spatial distribution and the penetration depth of the carriers. Finally, for trapped carriers we wish to know the trapping parameters.

Since we have not yet discussed the theory of the TSD ρ peak, we shall in this chapter only present some evaluation methods for the dipolar TSD peaks. However, part of this work is directly applicable to the evaluation of the ρ peak, and this will therefore not be treated separately, but will only be outlined in the proper places in Chaps 5, 6 and 7.

The evaluation methods elaborated are similar to those applied in isothermal dielectric measurements. However, there is a fundamental difference, in that for TSD we merely have *one* recorded curve, while in isothermal measurements many curves are available for different frequencies and temperatures. Now, there are *two* unknowns, viz. the distribution function and the activation energy, and it is a complicated problem to evaluate these from a single TSD curve. These complications can be circumvented by either prescribing the distribution function and calculating the activation energy, or vice versa. The former problem is studied in Sects 3:1 and 3:2, and the latter in Sect. 3:3.

In Sect. 3:1 we assume the distribution function to be a delta function, and so in this section we evaluate the parameters for a single Debye relaxation. Sect. 3:2 deals with the more interesting case of peaks due to distributed polarizations of a specific shape. Special attention is paid to the distributions of Gevers and Fuoss-Kirkwood, and besides the activation energy we calculate their width. This is done for Gevers's distribution by a least squares method. For a direct calculation of the distribution function, i.e. without presupposing its shape, we modify (Sect. 3:3) higher-order approximations first suggested by Staverman and Schwarzl (SS 52a) for isothermal measurements. Finally, Sect. 3:4 briefly describes a general computer programme, which incorporates some of the methods presented.

3:1 Calculation of the Parameters of a Debye Relaxation

This evaluation is the simplest, but unfortunately it is not applicable to the dipolar TSD peaks of polymers, which usually are distributed. Nevertheless, it is here included, not only as an introduction to the

new work of Sects 3:2 and 3:3, but also because it can often be applied in a slightly modified form to the ρ peaks.

The *activation energy* can be calculated in several ways. To begin with we can take the initial rise or one of the half-width temperatures of the current graphs (see Fig. 3-1). If the relaxation frequency shifts

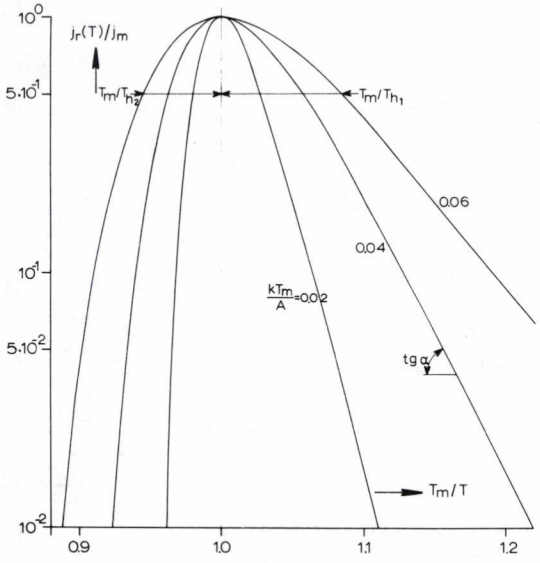


FIG.3-1 Two commonly used methods for calculating the reduced activation energy, A/kT_m, from TSD data. They are based on the initial current rise and the half-width temperature of the current thermogram.

according to an Arrhenius equation we respectively obtain

$$d \ln j_r / d\, 1/T \simeq -A/k \qquad \text{if } T < T_h \tag{3.1}$$

$$kT_m/A = 0.69117\ h_1 + 0.90887\ h_1^2 + 2.1414\ h_1^3 \tag{3.2}$$

$$kT_m/A = 1.0151\ h_2 + 0.18182\ h_2^2 \tag{3.3}$$

$$kT_m/A = 0.40843\ H + 0.24099\ H^2 \tag{3.4}$$

where $h_1 = 1 - T_{h1}/T_m$, $h_2 = T_{h2}/T_m - 1$ and $H = h_2 - h_1$, in which $T_{h1,2}$ are the half-width temperatures. Equations 3.2 to 3.4 are accurate to within less than 0.5 % for $0 \leq kT_m/A \leq 0.2$. They were derived from the implicit expression

$$j_r(T_{h1,2}) = \tfrac{1}{2}\, j_m$$

or rather

$$\alpha(T_{h1,2}) \exp\{-s \int_0^{T_{h1,2}} \alpha(T)dT\} = \tfrac{1}{2}\, \alpha_m \exp\{-s \int_0^{T_m} \alpha(T)dT\}$$

from which $T_{h1,2}$ were solved for various A values by means of the iterative method of Wegstein (We 60), after which the results were fitted to the polynomials just given. Often the upper half-width temperature is too close to T_m, and Eq. 3.2 or 3.4 is to be preferred. When we apply Eqs 3.1 and 3.2 to the TSD γ peak of PcHMA, which is the narrowest di-

polar peak we ever observed, we find A/kT_m = 10.0 and 13.2 respectively, where T_m = -119 °C and so A is 3.1 and 4.1 kcal/mol.

A qualitative method to find A, which involves the whole graph, is to use a family of calculated thermograms, such as those shown in Fig. 3-1, as a nomogram.

A more sophisticated method also based on all data and suggested by Eq. 2.11 is to calculate the temperature shift from

$$\alpha(T) = j_r(T)/P_s(T) \tag{3.5}$$

This method, which is not restricted to an Arrhenius shift, was already advocated by Bucci et al. (BF 66) and has extensively been employed by Perlman et al. (CP 70). However, it requires a knowledge of the retained polarization, $P_s(T)$, which can be found from the time integral over the current

$$P_s(T) = \int_t^\infty j_r(t)dt = -s \int_{T_u}^{T} j_r(T)dT \tag{3.6}$$

where T_u denotes the ultimate temperature at which the current has virtually become zero. This integral can readily be calculated numerically by Simpson's rule. When there are more current peaks, they must be well separated, for otherwise $P_s(T)$ cannot be subdivided over the different peaks.

A linearized BFG plot for the TSD γ peak of PcHMA is shown in Fig. 3-2. The slope of the straight line that passes through the points corresponds to a reduced activation energy of A/kT_m = 12.1, which yields A = 3.7 kcal/mol. Although the deviations are small, we note that the

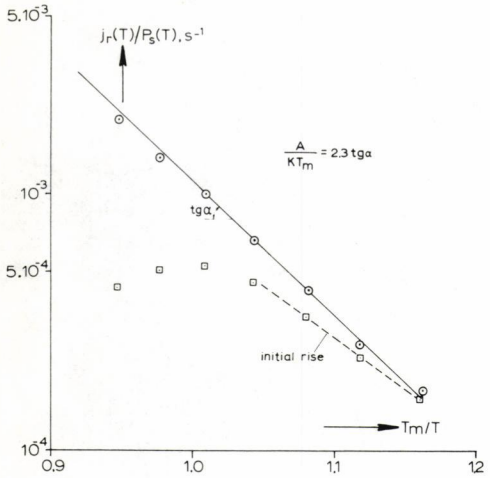


FIG. 3-2 Linearized BFG plot (solid line) and initial rise (broken line) used to calculate the activation energy of the TSD γ peak of a PcHMA electret.

two points below T_m/T = 1 do not fit properly. This gives an indication that we are dealing with a *distributed* polarization, for which Eq. 3.4 fails to give a straight line, if $T \simeq T_m$ or larger. Likewise, Eqs 3.1 to 3.4 do not hold for distributed polarizations.

Finally, A can be deduced from a least squares fit. This is the most reliable method, because it uses all the current data available without transforming them first as in Eq. 3.6. Moreover, the method even works with partly overlapping peaks. To obtain an equation in which A is the only unknown left, we eliminate $P_s(T_d)$, s and α_r from Eq. 2.11. To this end, we first divide the experimental data, $j_r(T)$, by their maximum value $j(T_m)$, this removes $P_s(t_d)$. Next we get rid of s and α_r by invoking the condition for the location of T_m, Eq. 2.21.

These operations result in

$$\ln\{j(x)/j(T_m)\} = -a/x + a - x^2 \exp(-a/x + a)H(a/x) + H(a) \qquad (3.7)$$

where $a = A/kT_m$ and $x = T/T_m$. Obviously, we are faced with a nonlinear least squares approximation. This can be linearized, however, by starting a Taylor expansion from an estimate of A/kT_m obtained by one of the previous methods. In this way, we solved A/kT_m using a standard ACM algorithm (Sp 67). Our method resembles the iterative method suggested by Cowell and Woods (CW 67), which is not based on a Taylor expansion, however, and which converges much more slowly. Results of a least squares fit to the γ peak of PcHMA are shown in Fig. 3-3. Starting from $A/kT_m = 13.2$ we found in two iterations $A/kT_m = 10.9$. Yet the fit is not a close one; in particular at low temperatures it deviates from the observed data.

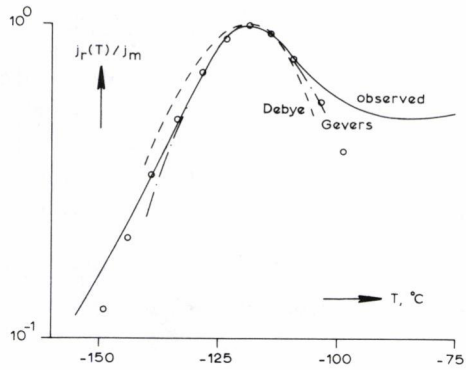


FIG.3-3 Accuracy of the least squares method for evaluating the activation energy. The figure shows a Debye fit and a Gevers fit to the TSD γ peak of a PcHMA electret. The circles represent a trial fit for a Fuoss-Kirkwood distribution with m = 0.4 and A = 8.4 kcal/mol.

This discrepancy shows once more that even this relatively narrow γ peak, which originates from the intra-molecular chair-chair flipping of the cyclohexyl ring, has a distributed polarization. We therefore see that Gevers's distribution and in particular Fuoss-Kirkwood's distribution give a closer fit; this will be further discussed in Sect. 3:2.

We can conclude that all the methods for a single Debye process invariably give a too *low* activation energy for polymer relaxations. To deal with distributed polarizations we shall therefore modify them in the following section. The occurrence of a distributed polarization al-

so explains why the various values found for A, although mutually consistent, do not agree with the value of 11.3 kcal/mol found by Heijboer (He 72), from the frequency shift of the G"-maximum in isothermal measurements.

In Sect. 2:2 we already showed that the current maximum shifts in temperature and varies in magnitude with the heating rate (cf. Eqs 2.23, 2.24 and Fig. 2.8). The variations observed depend on the activation energy A. Conversely, A can be found from the temperature shift* or from the current ratio. Indexing the quantities at the maximum for fast heating with f, and for slow heating with s, we have for a heating ratio of *two*

$$kT_f/A = 3.7795 - 8.9771\ t + 5.1977\ t^2 \qquad (3.8)$$

$$kT_f/A = 2.8482 - 4.9998\ c + 2.1518\ c^2 \qquad (3.9)$$

where $t = T_f/T_s$ and $c = j_f/2j_s$. Eqs 3.8 and 3.9 hold for $0 < kT_f/A \leq 0.1$, with maximum errors of 0.4 % and 0.8 % respectively. They were derived in a similar way as Eqs 3.2 to 3.4 by solving the implicit expressions of Eqs 2.23 and 2.24. The heating-rate method can be used only when activation energies are low; otherwise the differences between T_f and T_s become too small, because large differences in heating rate are *not* permitted owing to possible temperature lags; the maximum admissible change is 5. Even for the β peaks of polymers, its accuracy is rather low.

A typical example is given in Fig. 10-1. For a two-fold increase in heating rate the β peaks of PMMA and PEMA are seen to shift hardly. For PMMA we have $T_f = -51$ °C and $T_s = -54.5$ °C, from which we find by means of Eq. 3.8, $A/kT_f = 42$. Similarly, we obtain for the PEMA peak, which shifts from -45° to -49.5 °C, $A/kT_f = 33$. These values, the accuracy of which is not better than ± 10, are roughly compatible with the value A = 20 kcal/mol, often cited in the literature (CR 67). This value of A would result in $A/kT_f = 43$.

From the final value of the integral in Eq. 3.6 we can calculate one of the other relevant quantities, viz. the dipolar relaxation strength, $\varepsilon_s - \varepsilon_\infty$

$$\varepsilon_s - \varepsilon_\infty = P_s(T_d)/\varepsilon_o E \qquad (3.10)$$

This equation even holds for a distributed polarization, provided that the polymer is *fully* charged. For the peak of PcHMA we found $\varepsilon_s - \varepsilon_\infty = 0.13$, the values for the other polymer relaxations are listed in Table 10-4

*This method is similar to one mostly used in isothermal measurements, in which A is deduced from the shift of a relaxation peak with frequency. The frequency can readily be changed over several decades. Heijboer and coworkers (He 72) e.g. measured over 10 decades to obtain the activation energy of 11.3 kcal/mol for the γ relaxation of PcHMA.

The final quantity in which we are interested is the natural frequency α_r. This can be deduced from the condition for the current maximum (see Eq. 2.13). For an Arrhenius shift this leads to Eq. 2.21, from which we obtain for the γ peak of PcHMA ($\alpha_r = 2 \times 10^2$ Hz) if we take $A/kT_m = 12$, $T_m = 154$ °K and $s = 1$ min/°C. This value for α_r is much lower than that predicted by Eyring's rate theory for $\alpha_r = kT_m/2\pi h$, which would amount to 5×10^{12} Hz. This again shows that the actual activation energy of the maximum is much higher than 4 kcal/mol. We therefore obtain a much better agreement by inserting Heijboer's value of 11.3 kcal/mol; this yields $\alpha_r = 1.5 \times 10^{13}$ Hz.

The temperature for which Eq. 2.13 holds in the glass-rubber transition of a polymer is defined as T_g-point by Volkenshtein and Ptitsyn (VP 57). For a WLF shift, which can often be applied to the TSD α relaxation, this equation becomes

$$\{s(T_m - T_\infty)^2/c_1c_2\}\alpha_v(T_m) = 1 \qquad (3.11)$$

Putting $T_m = T_g$, we find from this equation for the relaxation time at T_g

$$\tau_v(T_g) = c_2 s/c_1 = 1.25 \text{ s} \qquad (3.12)$$

which gives $\tau_v(T_g) = 75$ sec, at $s = 1$ min/°C.
Apparently, the glass point is a dynamic quantity, which depends on the heating rate. This fact was already emphasized by Staverman in 1959 (St 59).

3:2 Fitting of TSD Data to Specific Distribution Functions

The standard distribution functions are characterized by a single parameter, namely their width parameter m (see Table 2-2). In fitting TSD data to specific distributions, we therefore have to solve for two unknowns simultaneously, viz. the width of the distribution, m, and the activation energy, A*. The most rigorous way is to find them from the integral expression 2.33 by a non-linear least-squares method. This can be done by starting from estimates given in the literature or derived from dynamic dielectric or mechanical measurements on the polymer in question. However, such a fitting procedure is intricate and time-consuming. Fortunately, if the distribution width is known, there is a much simpler way to calculate A; this will be discussed first.

3:2.1 Calculation of A from the Initial Current Rise

In Eq. 2.54 we indicated how to modify the initial-rise method for a Cole-Cole distribution. To find the modifications for the other dis-

*Note that we restrict ourselves in this paragraph to relaxations with a thermorheologically simple behaviour, i.e. to distributions in *natural frequencies*.

tributions we make use of the similarity between $j_r(T)$ and $\varepsilon''(\omega_o,T)$ as we have done successfully in Sect. 2:2. Moreover, in anticipating Chap. 4 we venture to put for the initial current slope

$$d \ln j_r(T)/d\ 1/T \propto d \ln \varepsilon''(\omega_o,T)/d\ 1/T \qquad (3.13)$$

in which the dependence on A of the last derivative can easily be derived from the formulas for $\varepsilon''(\omega_o,T)$ known from the literature (CR 67, Pet 71). At low temperatures, when $\omega\tau > 1$, these are considerably simplified, yielding the following results.

distribution	$\varepsilon''(\omega_o,T)$	$d \ln j_r(T)/d\ 1/T$ from ε''	$d \ln j_r(T)/d\ 1/T$ calculated
Debye	$C(\omega\tau)^{-1}$	$-A/k$	$-A/k$
Cole-Cole	$C(\omega\tau)^{-m}$	$-mA/k$	$-mA/k$
Fuoss-Kirkwood	$C(\omega\tau)^{-m}$	$-mA/k$	$-mA/k$
Wagner	$C(\omega\tau)^{-\kappa}$	$-\kappa A/k$	$-A/k$
Gevers	$C \arctan(\omega\tau)^{-1}$	$-A/k$	$-A/k$

Here C is a constant and $\kappa = m(m^2 + 0.367)^{-\frac{1}{2}}$. The last column gives the relations between the initial current rise and A as obtained from model calculations (see Fig. 3-4); they are consistent with the theoretical predictions derived from ε'', except for Wagner's distribution. For this the prediction is too low. Inspection of Fig. 3-4 shows that such a low

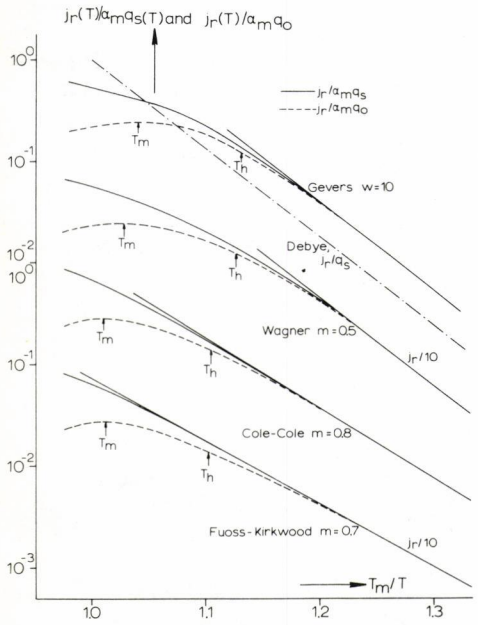


FIG.3-4 BFG plot and initial current-rise for four distribution functions. Those of Gevers and Wagner have the same initial rise as a Debye thermogram. The maximum temperature and lower half-width temperature are also indicated.

value is reached only in the vicinity of the half-width temperature.

In conclusion, we obtain from the initial current rise A directly, or the product mA. The first value, A, is found for the distributions of Gevers and Wagner, which have short tails, whereas the distributions of Cole-Cole and Fuoss-Kirkwood, which have long tails, give mA. This value is lower than A, since $m < 1$.

The figure also gives the course of $j_r(T)/q_s(T)$ for the various polarizations. These BFG plots have the same initial slope as the $j_r(T)/q_o$ curves, because at low temperatures $q_s(T) \simeq q_o$. However, when the temperature approaches the current maximum, the plots for the distributed polarizations bend downwards. Gevers and Wagner's distributions, in particular, soon begin to deflect from the straight line. Nonetheless, the BFG plots remain *straight* up to higher temperatures than do the current plots, and this enables one to find a more reliable value for the apparent activation energy.

This behaviour is demonstrated in Fig. 3-5 for the current and BFG plots of the α peak of PcHMA; they yield respectively mA = 0.63 and 1.15 eV. Now from traditional dielectric measurements we deduced that m = 0.43, which, according to the BFG plots, gives A = 2.7 eV. This value is consistent with that used in Fig. 2-20, and also with the value of 2.6 eV found from traditional dielectric measurements. Thus, the apparent activation energy of 1.15 eV obtained from the straight part of the BFG plot actually is the more reliable.

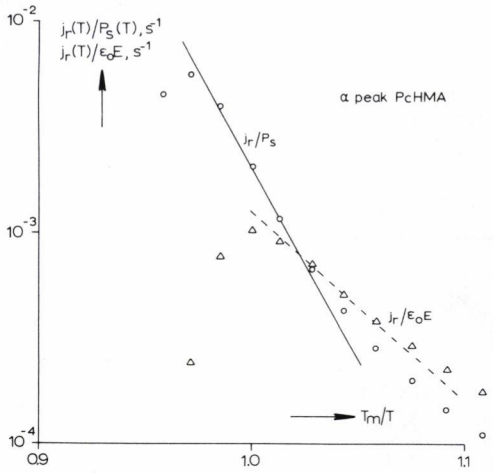


FIG.3-5 BFG plot and initial current-rise of the α peak of PcHMA.

Mechanical measurements by Heijboer enable us to check the validity of Eq. 3.13 for the γ peak of PcHMA. From his $G''(\omega_o,T)$ diagrams (which are very similar to those of ε''), we derived mA = 4 kcal/mol. This is in accord with our value of 3.7 kcal/mol, found from a BFG plot (see Fig. 3-2). If we further take Heijboer's value of 0.44 for m, we obtain as the activation energy of the TSD peak A = 8.5 kcal/mol. This agrees

fairly well with Heijboer's value of 9.2 kcal/mol for the low-temperature side of this peak. However, at the maximum of this peak, which, according to Heijboer, is due to a distribution in activation energies, we should have A = 11.3 kcal/mol. This value would require m = 0.33. Apparently, the formulae given in the 4th column of the table need a correction when they are applied to a distribution in activation energies. In the present form they can only be used for a distribution in natural frequencies.

3:2.2 Calculation of A from the Lower Half-Width Temperature

Next, we shall modify Eq. 3.2 for distributed polarizations and, as before, we shall consider only distributions in *natural frequencies*. It is well known that for a Debye relaxation the activation energy, A can be calculated from the lower half-width temperature of a $\varepsilon''(\omega_o,T)$ curve, as follows:

$$A/kT_m = 0.572/\Delta h_D \tag{3.14}$$

A similar equation holds for TSD (Tu 68)

$$A/kT_m \simeq 1.44/\Delta h_D \tag{3.15}$$

Here $\Delta h_D = T_h/T_m - 1$, where the subscript D refers to Debye.

According to dielectric theory (CR 67, NB 61) Eq. 3.14 can also be applied to distributed polarizations, provided that A is multiplied by a correction factor, and Δh_d is replaced by Δh, i.e. by $T_h/T_{max} - 1$ of the actual thermogram. The modified formulae are compiled in the following table.

distribution	modified Eq. 3.14
Cole-Cole	$mA/kT_m \simeq 0.572/h$
Fuoss-Kirkwood	$mA/kT_m = 0.572/h$
Wagner	$mA/0.632\ kT_m \simeq 0.572/h$

In view of the similarity between Eqs 3.14 and 3.15, we might expect that these corrections can be used also for TSD. This has in fact been checked in Table 2-4, where we have shown that $\Delta h_D/\Delta h$ agrees reasonably well with the correction factors just given. However, Eq. 3.15 is less accurate than Eq. 3.2, and so it is better to introduce the corrections into the latter. Hence, this formula becomes

$$kT_m/mA = 0.69117\ h_1 + 0.90887\ h_1^2 + 2.1414\ h_1^3 \tag{3.16}$$

for a Cole-Cole and Fuoss-Kirkwood distribution. By applying Eq. 3.16 to model calculations of Ong on the former distribution, we found the following results. The table gives the ratio of the effective activation energy A_{CC} to the Debye value A_D, which indeed scarcely differs from m.

m	A_{CC}/A_D
1	1
0.8	0.78
0.6	0.56
0.4	0.35
0.2	0.16

3;2.3 Simultaneous Calculation of A and m by the Least-Squares Method

We tried this method for the most manageable distribution in natural frequencies, viz. that of Gevers, which possesses an analytical expression for $j_r(T)$. Assuming a completely filled polarization and introducing the reduced time $\xi(T) = s \int_{T_d}^{T} a(T)dT$, and the width of the distribution, $w = \alpha_2/\alpha_0 = \alpha_0/\alpha_1$ we can rewrite Eq. 2.36 as

$$\frac{j_r(T)}{\varepsilon_0(\varepsilon_s - \varepsilon_\infty)E} = -\frac{a(T)}{2 \ln w} \frac{e^{-w\alpha_0\xi(T)} - e^{-w^{-1}\alpha_0\xi(T)}}{w^{-1}\alpha_0\xi(T)} \qquad (3.17)$$

where $a(T) = \exp(-A/kT)$.

Obviously, this equation has four unknowns: A, w, α_0 and $\varepsilon_s - \varepsilon_\infty$. To eliminate the relaxation strength $\varepsilon_s - \varepsilon_\infty$ we normalize on the experimental current maximum, which appears at the temperature T_B (B denotes a broad peak). This normalization gives

$$\frac{j_r(T/T_B)}{j_r(T_B)} = -\frac{a(T)\xi_B(T_B)}{a(T_B)\xi(T)} \frac{e^{-w\alpha_0\xi(T)} - e^{-w^{-1}\alpha_0\xi(T)}}{e^{-w\alpha_0\xi(T_B)} - e^{-w^{-1}\alpha_0\xi(T_B)}} \qquad (3.18)$$

Furthermore, we remove the most probable natural frequency α_0 by using the expression for its Debye maximum, which we suppose to occur at T_m (Eq. 2.21). With the aid of this equation and Eq. 2.20 we can replace $\alpha_0\xi(T)$ by

$$\alpha_0\xi(T) = x^2\{a(x)/a(1)\}H(g/x) \qquad (3.19)$$

Here $g = A/kT_m$ and $x = T/T_m$. A similar equation holds for $\alpha_0\xi(T_B)$, except that $x_B = T_B/T_m$ replaces x.

We now recognize that to eliminate α_0 it is better to refer the measured current to T/T_m, and no longer to the experimentally known temperature ratio T/T_B. This does not change Eq. 3.18, however, except that T must be exchanged for x and T_B for x_B.

The location of the Debye maximum T_m, needed to calculate x is not known in advance, but it can be calculated from T_B. By differentiating Eq. 3.18, we can derive that their ratio, x_B, satisfies

$$\frac{e^{g/x_B - g}}{x_B^2} = \frac{1}{\alpha_o \xi(x_B)} + \frac{we^{-w\alpha_o\xi(x_B)} - w^{-1}e^{-w^{-1}\alpha_o\xi(x_B)}}{e^{-w\alpha_o\xi(x_B)} - e^{-w^{-1}\alpha_o\xi(x_B)}} \qquad (3.20)$$

The only unknown in this non-linear equation is x_B, since estimates of g and w are given.

After these rearrangements, we are left with two unknowns in Eq. 3.18 namely $g = A/kT_m$ and w. We approximated the measured current according to this equation in the sense of a least squares fit, using a damped non-linear least squares method (Sp 67). During the computations we took care to adjust x_B properly after each change in g and w. To solve Eq. 3.20 for x_B we applied the iterative method of Wegstein (We 60).

We checked the complete procedure by calculating the activation energy and width of a theoretical Gevers thermogram. The true values were g = 20, w = 4; we started with g = 17, w = 3.5 and found g = 20 and w = 3.9, which means that the convergence is good. Next, we evaluated the γ maximum of PcHMA, and found $A/kT_m = 21.1$ and w = 9.7. An earlier fit to a single Debye relaxation yielded only a reduced activation energy of $A/kT_m = 10.9$. From Fig. 3-3 we see that a Gevers relaxation fits the data much better than does the Debye relaxation and so we are certainly dealing with a distributed polarization. However, the improved value of A/kT_m is still lower than Heijboer's value of 36. This discrepancy is partly due to the shortcomings inherent to Gevers's distribution.

We therefore decided to fit the data to the more adaptable Fuoss-Kirkwood distribution. We kept A = 11.3 kcal/mol ($A/kT_m = 36$) and adjusted m by trial and error. The final results are plotted as circles; they correspond to m = 0.34 and accommodate the data better than the results of Gevers's distribution. Nevertheless, m is lower than the value of 0.44 found by Heijboer from mechanical measurements. Presumably, a closer agreement would have been obtained, for a Fuoss-Kirkwood distribution in activation energies. These calculations will be undertaken at a later stage.

3:3 Calculation of Dipolar Distribution Functions

In the previous section we prescribed the shape of the distribution function and in this way obtained an analytical expression for the dipolar distribution in question. Since the data sometimes do not fit the standard distribution functions, it is often preferable not to impose a distribution on the polymer, but to calculate it from the data. In (Tu 70) we discussed first-order methods to compute the distribution functions. We shall now discuss higher-order approximations, based on the approximations derived by Staverman and Schwarzl for isothermal measurements.

It should be mentioned that the use of TSD for evaluating distribution functions has the advantage that in TSD the *complete* response is determined, whereas isothermal discharge experiments often have to be stopped before the response is completed.

In Sect. 2:2 we already mentioned that there may be two distributions, one in natural frequencies $f(\alpha_r)$, or one in activation energies $g(A)$. For α relaxations the former is the more likely, since they involve configurational rearrangements of the main chains and we can imagine that the partaking macromolecular groups of various sizes and shapes, will move at very different speeds when the polymer becomes rubbery.

For the γ and β relaxations, on the other hand, a distribution in activation energies is more likely. A strong argument in its favour is that such a distribution requires comparatively small differences in A, whereas a distribution in natural frequencies implies a vast range of α_r's, which is less plausible, since we know that these relaxations involve only local motions of relatively small and well-defined polar side-groups. These rotating groups will, however, experience various restoring forces due to spatial fluctuations in the interactions between neighbouring chains. A theoretical account of this has been given by Yamafuji et al. (YI 67). Experimental evidence for a distribution in A for the γ peak of PcHMA was obtained by Heijboer (He 72) and also by the author, who used multi-stage TSD (cf. Fig. 10-13). By this technique a distribution in activation energies was similarly found for the β peak of PMMA (see Fig. 2-29).

3:3.1 Calculation of a Distribution in Natural Frequencies

First, we consider the calculation of $f(\alpha_r)$. Such a distribution implies a thermorheologically simple behaviour, all subrelaxations having the same temperature shift. This shift must be known, for otherwise $f(\alpha_r)$ cannot be solved. To obtain a simple notation we change over from $f(\alpha_r)$ to a calculation of $f(\tau_r)$, where $\tau_r = \tau(T)/a(T)$. Assuming the polarization to be totally filled and writing P_o for $\varepsilon_o(\varepsilon_s - \varepsilon_\infty)E$, we obtain instead of Eq. 2.33

$$P_s(T) = P_o \int_0^\infty f(\tau_r) e^{-\xi(T)/\tau_r} \, d\tau_r \qquad (3.21)$$

where $\xi(T) = s \int_0^T a(T)dT$, which takes the form of Eq. 2.20 for an Arrhenius shift. Eq. 3.21 can be conceived as a Laplace transform, with $\xi(T)$ as the transform variable. Hence, the evaluation of $f(\tau_r)$ merely is a Laplace-transform inversion. This inversion has to be performed numerically.

An attractive method, advocated by Schwarzl and Staverman (SS 52a) for viscoelastic measurements, is the inversion method of Widder and Post. It is based on taking derivatives of P_s and becomes the better, the higher the derivatives involved. However, for experimental data it may not be justified to differentiate more than twice. We shall there-

fore discuss only first and second-order approximations.

Let us first recall these approximations for an isothermal discharge experiment at a temperature T_o; writing τ for $\tau(T_o)$, we then have

$$P_s(t,T_o) = P_o \int_0^\infty f(\tau)e^{-t/\tau}\, d\tau \tag{3.22}$$

for which Schwarzl and Staverman derived

$$P_o f_1(\tau) \simeq -\{dP_s(t,T_o)/dt\}_{t=\tau} \simeq \{j(t,T_o)\}_{t=\tau} \tag{3.23}$$

and

$$P_o f_2(\tau) \simeq \{td^2P_s(t,T_o)/dt^2\}_{t=2\tau} \simeq \{tdj(t,T_o)/dt\}_{t=2\tau}$$

Here, the subscripts 1,2 refer to the order of the approximation. Since in actual discharge measurements, we determine the time derivative of $P_s(t,T_o)$ directly as a current, we have introduced on the right-hand side the current density.

The approximations are strikingly simple. By considering the discharge current at various times t, we obtain by elementary operations values for $f_{1,2}(\tau)$ at different τ's that are equal to either t or 0.5 t. Nevertheless, the two approximations give satisfactory results, unless the distributions are narrow. This can be seen from Fig. 3-6, where we compared their results with the exact curve of a Wagner distribution with m = 0.5. Obviously, the curve SS2 representing Staverman and Schwarzl's 2nd approximation yields the best results, yet its maximum

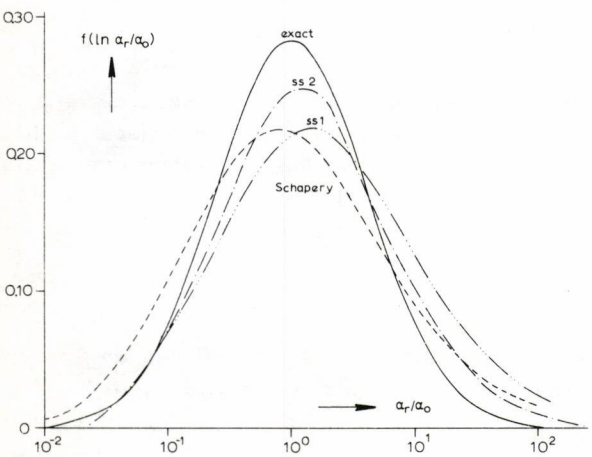


FIG.3-6 Accuracy of some approximations, derived from artificial TSD data, to the distribution function of a distributed dipole polarization. The calculations were made for a Wagner distribution in natural frequencies, for which the width parameter m = 0.5.

is still too low and its tails are slightly too high. In the figure we also drew a first-order approximation due to Schapery (Sc 61)

$$P_o f_1(\tau) \simeq \{j(t,T_o)\}_{t=0.56\tau} \tag{3.24}$$

which runs somewhat more symmetrically with respect to the exact values than does the curve SS1 corresponding to Staverman and Schwarzl's 1st

approximation.

To extend Eqs 3.22 and 3.23 to TSD experiments, we should take the derivatives with respect to $\xi(T)$. Remembering that $d\xi(T)/dt = a(T)$, we easily verify that

$$P_o f_1(\tau_r) \simeq \{j(T)/a(T)\}_{\xi(T)=\tau_r} \tag{3.25}$$

and

$$P_o f_2(\tau_r) \simeq -t_e(T)\left\{\frac{d\{j(T)/a(T)\}}{sdT}\right\}_{\xi(T)=2\tau_r} \simeq \left\{P_o f_1(\tau_r) - \frac{t_e(T)dj(T)}{a(T)sdT}\right\}_{\xi(T)=2\tau_r} \tag{3.26}$$

where τ_r follows from $\xi(T)$ by means of Eq. 2.20 and where $t_e(T)$ is the equivalent time, which for an Arrhenius shift equals $\xi(T)/a(T)$, or approximately skT^2/A. The near-identity on the right-hand side of Eq.3.26 holds also for this particular shift. This identity clearly shows the improvement of the first approximation by the second.

The use of Eq. 3.26 calls for smooth current data. To remove any noise, which may occur in the beginning of a thermogram, we smoothed our data by cubic splines. We mostly applied an algorithm of Reinsch (Re 67), but when the data strongly fluctuated, we used a more sophisticated spline programme, which was kindly sent to us by Dr M.J.D.Powell from AERE, Harwell, England (Po 67).

Up to now, we have assumed a completely filled polarization. The formulae remain valid for an incomplete filling as well, provided that $f(\tau_r)$ is replaced by $FS(\tau_r)f(\tau_r)$, which implies that from the data the effective distribution function is found.

Instead of $f(\tau_r)$ the use of the logarithmic distribution, $L(\tau_r) = f(\ln \tau_r) = \tau_r f(\tau_r)$, is often preferred, not only because a log scale for τ_r is more convenient, but also because it is the distribution $L\{\tau(T_o)\}$ that merely shifts with a change in temperature T_o, if the material shows thermorheologically simple behaviour. When τ_r is normalized to the most probable relaxation time τ_o, the first and second approximation for $L(\tau_r/\tau_o)$ become

$$P_o L_1(\tau_r/\tau_o) \simeq \{t_e(T)j(T)\}_{\xi(T)=\tau_r} \tag{3.27}$$

and

$$P_o L_2(\tau_r/\tau_o) \simeq \{P_o L_1(\tau_r/\tau_o) - t_e^2(T)dj(T)/sdT\}_{\xi(T)=2\tau_r} \tag{3.28}$$

In deriving these equations we have used $t_e(T) = skT^2/A$.

To evaluate the normalized relaxation time τ_r/τ_o, we invoke Eq. 2.20, and upon defining a temperature T_m, such that τ_o satisfies the condition of a Debye maximum, we obtain

$$\tau_r/\tau_o = c\xi(T)/\tau_o \simeq cT^2a(T)/T_m^2a(T_m) \tag{3.29}$$

where c must be chosen properly, viz. 1 or 0.5 depending on the order of the approximation. This completes our set of equations to calculate approximations to the distribution function of a polymer.

It is seen, however, that the use of Eqs 3.27 and 3.28 requires besides the knowledge of A, that of $P_o = \varepsilon_o(\varepsilon_s - \varepsilon_\infty)E$. To eliminate P_o we normalize $L(\tau_r/\tau_o)$ to its value at the current maximum; labelling the latter with the subscript B, we have

$$L_1(\tau_r/\tau_o)/L_B(\tau_r/\tau_o) \simeq \{T^2 j(T)/T_B^2 j_B\}_{c=1} \tag{3.30}$$

and

$$\frac{L_2(\tau_r/\tau_o)}{L_B(\tau_r/\tau_o)} \simeq \left\{ \frac{L_1(\tau_r/\tau_o)}{L_B(\tau_r/\tau_o)} - \frac{T^2 d\{j(T)/j_B\}}{T_B^2 sdT} \right\}_{c=0.5} \tag{3.31}$$

In Fig. 3-7 we show the calculated distributions in relaxation times for the β peak of PMMA and the γ peak of PcHMA. We recall that the former peak is due to local motions of the polar $-COOCH_3$ side-groups, while the latter peak arises from the chair-chair transition of the flexible $-C_6H_{11}$ side-group itself. The evaluation was accomplished by means of Eq. 3.30.

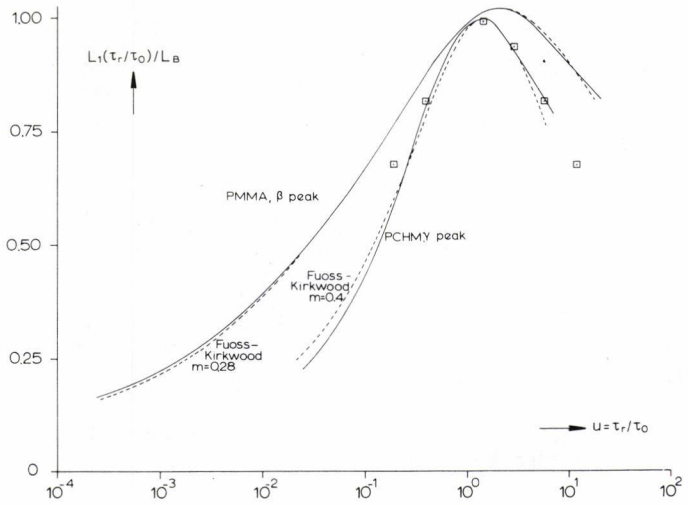


FIG.3-7 Distributions in *natural frequencies* of the β peak of PMMA and the γ peak of PcHMA calculated from TSD data, using the approximation of Eq. 3.25. We assumed $A/kT_m = 20$ and 21.1, for the β and γ peak, respectively. The distributions found can be represented fairly well by two Fuoss-Kirkwood distributions.

The two distributions are almost symmetrical. For PMMA we find a broad distribution extending over 6 decades, which is typical of most β relaxations of amorphous polymers. As might have expected the distribution of the intramolecular γ relaxation of PcHMA is much narrower. The figure also shows two Fuoss-Kirkwood distributions of width m = 0.28 and 0.4 (dashed lines). They agree rather well with the distributions calculated (full lines). This explains why we obtained fairly consistent results in applying this particular distribution to the experimen-

tal data in Sect. 3:2. The two values are also comparable with those given earlier. For the β distribution we mentioned m = 0.2 (from ε'' measurements) and for the γ distribution m = 0.44 (from G'' measurements by Heijboer). The squares, which only fit the top of the distribution in Fig. 3-7, finally correspond to a Fuoss-Kirkwood distribution of m = 0.33. In Sect. 3:2 this width turned out to be the best for calculating the activation energy.

3:3.2 Calculation of a Distribution in Activation Energies

Finally, we shall show how to calculate a distribution in activation energies, which for the two distributed relaxations just mentioned, is even more likely to occur. To solve this problem the natural frequency α_r common to all subrelaxations must be known.

For a distribution in A, Eq. 3.21 takes the form

$$P_s(T) = P_o \int_0^\infty g(A) e^{-\alpha_r \xi(T,A)} dA \tag{3.32}$$

where we have hinted that the reduced time depends on A, so that the Laplace transform variable now appears in an implicit form. To derive a first-order approximation we use Alfrey's method (AD 45) and approximate the kernel $\exp\{-\alpha_r \xi(T,A)\}$ by

$$\begin{aligned} \exp\{-\alpha_r \xi(T,A)\} &\simeq 1 \quad \text{if} \quad \alpha_r \xi(T,A) \leq 1 \\ &\quad\ 0 \quad \text{if} \quad \alpha_r \xi(T,A) \geq 1 \end{aligned} \tag{3.33}$$

This approximation reduces Eq. 3.32 to

$$P_s(T) \simeq P_o \int_{A_o(T)}^\infty g(A) dA \tag{3.34}$$

in which A_o being a function of T forms the border line for the truncation in Eq. 3.34, i.e. $\alpha_r \xi(T,A_o) = 1$. Consequently, $A_o(T)$ satisfies the nonlinear equation

$$A_o(T) \exp\{A_o(T)/kT\} = s\alpha_r kT^2 \tag{3.35}$$

By differentiating Eq. 3.34 we obtain $g(A_o)$ explicitly

$$P_o g(A_o) \simeq -dP/dA_o \tag{3.36}$$

By changing the differentiation to T one obtains

$$P_o g(A_o) = \frac{sj(T)}{k} \frac{1 + kT/A_o(T)}{2 + A_o(T)/kT} \simeq \frac{sTj(T)}{A_o(T)} \tag{3.37}$$

where $A_o(T)$ is related to T by Eq. 3.35. This again is a simple formula. Equations similar to 3.36 and 3.37 were derived by Vand and Primak (Va 43, Pr 60) for the evaluation of annealing experiments.

To eliminate the inverse heating rate s, $g(A_o)$ should be normalized on its value at the current maximum, T_B

$$g(A_o)/g_B = A_B T j(T)/A_o(T) T_B j_B \tag{3.38}$$

and plotted against the ratio $A_o(T)/A_B$, which follows from

$$A_o(T)e^{A_o(T)/kT}/A_B e^{A_B/kT_B} = T^2/T_B^2 \qquad (3.39)$$

Fig. 3-8 shows distributions in activation energy calculated for the same TSD peaks as in Fig. 3-7. As expected the differences in A are relatively small, in particular for the γ peak of PcHMA. Heijboer found similar differences from isothermal mechanical measurements. His values were centred around A_o = 11.3 kcal/mol and varied from 9.4 to 13.4 kcal/mol.

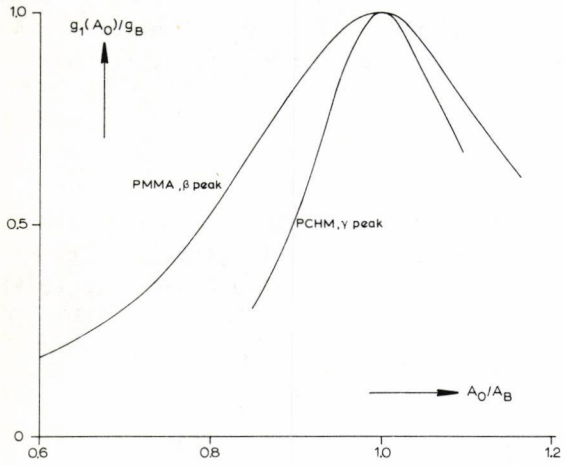


FIG. 3-8 Distributions in *activation energies* of the β peak of PMMA and the γ peak of PcHMA calculated from TSD data, using the approximation of Eq. 3.37. We assumed A_o/kT_m = 20 and 21.1, for the β and γ peak respectively.

3:4 Outline of a General Computer Programme

A general Fortran programme, based on the procedures described above, was worked out for the IBM-360 computer of the University of Technology at Delft. For reason of brevity we shall not present it here. However, its listing can be obtained from the author. The programme first smoothes the punched current and temperature data by *cubic splines* (Re 67), and next converts the temperature values from mV into °C, using a polynomial approximation for the mV - °C curve of our thermocouple. From the coefficients of the local spline polynomials the derivative of the current was found, which yields local values of the activation energy by means of Eq. 3.1. The activation energy is also computed from the half-width temperatures using Eqs 3.2 to 3.4.

After normalizing the current values to $j(T)/\varepsilon_o E$, they are numerically integrated with Simpson's rule to obtain the reduced charge, $q_r(T)/\varepsilon_o E$. The ultimate value of which $q_r(T_u)/\varepsilon_o E$, yields the relaxation strength $\varepsilon_s - \varepsilon_\infty$. Further, the course of the persisting charge is computed by substracting $q_r(T)$ from $q_r(T_u)$. Finally, the normalized current $j(T)/j(T_m)$ and temperature T/T_m for each peak are calculated, to find A from nomograms like Fig. 3-1. We also exploited the facility to plot $j/\varepsilon_o E$ vs. T, $q/\varepsilon_o E$ vs. T and j/j_m vs. T_m/T on a Calcomp plotter.

For obvious reasons, the more advanced evaluation techniques have not been incorporated in this general computer programme. However, we store the smoothed current and temperature values on punched cards, so that the calculations can readily be repeated with other computer programmes.

Chapter 4

RELATION BETWEEN CURRENT TSD BY DIPOLE REORIENTATION AND ISOTHERMAL DIELECTRIC MEASUREMENTS

We have shown on several occasions that TSD current thermograms reflect the molecular relaxations of a polymer, and more evidence for this will be given in Chap. 10. Relaxation phenomena can also be studied with other techniques. Two well established methods are measurement of the storage and loss moduli, and measurement of the dielectric constant and loss factor, cf. Fig. 1-6. Most of these traditional measurements are done at medium frequencies. TSD, to the contrary, provides information at very low frequencies, and this extension of the scope of dielectric measurements is important for various applications of dielectrics.

To make the best use of the new information thus obtained, we shall set forth the exact relation between TSD results and ordinary ε' and ε'' results. This interconversion may also ease the molecular interpretation of TSD thermograms, because there is an extensive literature on the interpretation of conventional results. In (Tu 70) we have already sought to relate TSD with the older measuring techniques. Here we shall derive more accurate interconversion formulae. This will be done for dipolar relaxations that show thermorheologically *simple* behaviour, and so we suppose the subpolarization to have the *same* activation energy and to vary only in natural frequency.

In attempting to establish a relation, one should realize that conventional methods are performed either isothermally or isochronously, while in TSD time and temperature change simultaneously. Nevertheless, we shall show that TSD thermograms will strongly resemble the temperature dependence of conventional *isochronous* data, provided that such data are taken at the proper frequency (or time), namely about 10^{-3} Hz.

Fig. 1-6 illustrated that only the dipolar peaks appear in sinusoidal ε'' measurements. The TSD ρ peak, due to the motion of excess charges, is absent; instead, one finds, owing to the external voltage, increasing conduction losses. There is only one conventional experiment that is done like TSD in short-circuit, viz. the *DC step-response technique*. This method actually is the isothermal analogue of TSD, because it determines the discharge current at constant temperatures instead of at varying temperatures. It will be demonstrated (for ChPEth) that this technique *also reveals* the ρ peak.

4:1 Relation to Step-Response Measurements

In view of the interesting fact that isothermal step-response measurements may reveal the ρ peak, we shall not restrict ourselves in this section to dipolar peaks.

Let us first outline how a single dipole peak behaves in the two experiments. According to Eq. 2.11, we have for the TSD current density of a Debye relaxation

$$j_r(T) = \alpha(T)P_o \exp\{-\alpha_r \xi(T)\} \tag{4.1}$$

In fact, j_r is a function of time t and temperature T. However, since $T \propto t$, the current can equally well be visualized as a function of T alone. We recall that $\xi(T)$ is the reduced time; it equals $s \int_{T_d}^{T} \alpha(T)dT$.

Similarly, the isothermal discharge current following a step response taken at a constant temperature T_o, is given by

$$j(t,T_o) = \alpha(T_o)P_o \exp\{-\alpha(T_o)t\} \tag{4.2}$$

Obviously, the trend of the two currents is quite different, because the TSD current is measured vs. T, whereas $j(t,T_o)$ is measured vs. t. However, if the isothermal current is determined as a function of time at *various* temperatures, the data can be combined to a j vs. T plot at a prescribed time t_o. We then obtain

$$j(t_o,T) = \alpha(T)P_o \exp\{-\alpha(T)t_o\} \tag{4.3}$$

This equation is easily combined with Eq. 4.1, because it contains T as the only variable. To make the two currents identical, we must consider the isothermal values at a *temperature dependent* equivalent time $t_e(T)$

$$t_e(T) = \alpha_r \xi(T)/\alpha(T) = \xi(T)/a(T) \tag{4.4}$$

where a(T) is the temperature shift of the relaxation frequency $\alpha(T)$. We know from Eq. 2.20 that for an Arrhenius shift, with activation energy A, Eq. 4.4 can be written as

$$t_e(T) \simeq (skT^2/A)\{1-T_d^2\alpha(T_d)/T^2\alpha(T)\} \simeq skT^2/A \tag{4.5}$$

where the latter approximation holds for $T >> T_d$.

Summarizing, a TSD current is equivalent to the following *quasi-isochronous* isothermal discharge current

$$j_r(T_c) = j\{t_e(T_c),T_c\} \tag{4.6}$$

where T_c denotes the conversion temperature and $t_e(T_c)$ the corresponding conversion time. The equation shows that the conversion from isothermal currents to TSD and vice versa is rather simple. Both currents are equal as functions of temperature, provided that t_e is continually readjusted. However, since $t_e(T_c)$ varies only quadratically with T_c, it even makes sense to compare a TSD thermogram directly with an isochronous j vs. T plot, although it is then advisable to consider j at a constant t_e value centred at the temperature of the TSD peak T_m, as follows

$$j_r(T) \simeq j\{t_e(T_m),T\} \tag{4.7}$$

With s = 1 min/°C, $t_e(T_m)$ amounts to about 330 and 180 sec for the side-group and main-chain relaxation of amorphous polymers, respectively.

A theoretical TSD thermogram and the isochronous j vs. T plot corresponding to it are shown in Fig. 4-1; both thermograms are almost identical. This clearly indicates that the approximate conversion of Eq. 4.7

is almost as good as the exact conversion of Eq. 4.6. From Eqs 2.48 and 2.49 we easily verify that both conversions can also be applied to a distributed polarization, provided that this shows thermorheologically simple behaviour. TSD can be correlated to mechanical creep data in a similar way (cf. Fig. 1-6), since mechanical and dielectric relations of polymers are closely related (HS 62, Cu 60, CR 67, WS 65, SO 63).

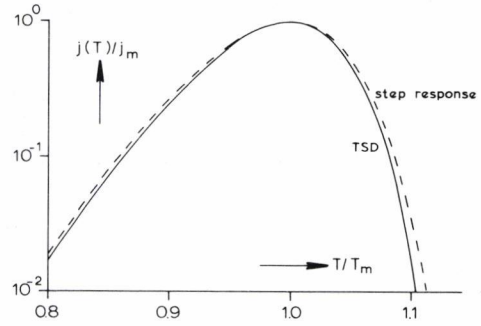


FIG.4-1 Relationship between step-response data and TSD results for a single dipole relaxation. The plots of the two artificial discharge currents vs. temperature are almost identical. The step-response data refer to a T-traverse at a constant equivalent time $t_e(T_m)$. We took $A/kT_m = 20$.

Although it turns out that current TSD and DC step-response match closely, they are experimentally quite different. To make the required T-traverse of Eq. 4.3, we must perform *many* time-consuming charging and discharging experiments at various temperatures. Current TSD, on the other hand, gives the discharge current directly as a function of temperature, and therefore works much *faster*. Of course, this is at the expense of some information, for we now find the current at only one time, which is slightly temperature dependent.

An experimental check of Eq. 4.7 for the β peak of PET is given in the lower curves of Fig. 4-2. The step-response currents are plotted

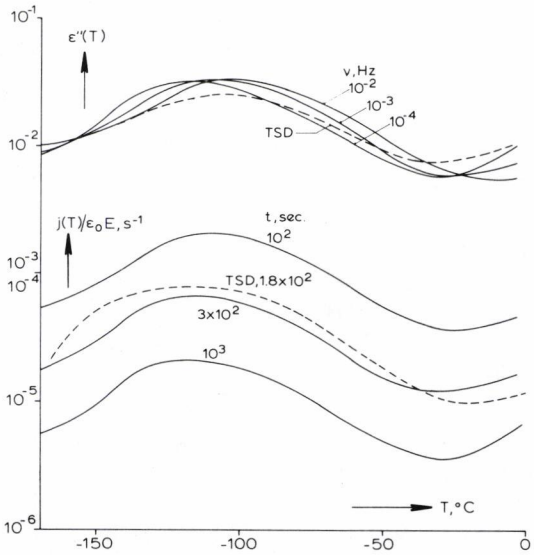


FIG.4-2 Relation between current TSD at $s^{-1} = 1.2$ °C/min (dashed lines) and DC step-response data (full lines) for the β peak of PET (measurements by Ong). The ε'' curves (top) were calculated with Hamon's conversion formula.

for three times. We see that the TSD results, which correspond to t_e = 2×10^2 sec, neatly fit in. From the shift of the current maxima of the step-response currents we obtained an activation energy of 0.6 eV or 13.4 kcal/mol, which agrees well with the value of 12.9 kcal/mol, quoted by McCrum et al. (CR 67). In the upper curves the currents have been converted to ε'' values in the frequency domain. This conversion will be discussed in the next section.

We now come to the conversion of the *TSD ρ peak*. We mentioned in Chap. 1 that this may arise form the motion of excess charges by SCL drift and/or diffusion. For both processes the TSD current and step-response current can be converted into each other in the same way as described above. This means that the conversion formula 4.6 remains valid. This equation can easily be applied to the formulae that will be derived in the next chapter for the current release of the two processes, and so we will not comment on it here.

Similarly, we may expect the approximate conversion formula (Eq.4.7) to be satisfied. However, we were anxious to see to what extent this would be the case, and we therefore made a model calculation for SCL drift. The results are presented in Fig. 4-3. These calculations were made for a polymer with and without ohmic conduction. In the former

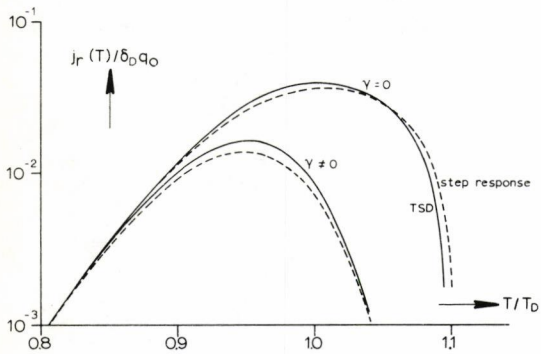


FIG.4-3 Theoretical relation between current TSD and step-response measurements at various temperatures for SCL drift of a unipolar and uniform excess-charge layer. The calculations were done for a perfectly insulating polymer (γ = o) and a slightly conductive one ($\gamma \neq$ o). As in Fig. 4-1 the step-response data refer to a T-traverse at a constant time $t_e(T_m)$. We took $B/kT_D = C/kT_c$ = 20, r_o/l = 0.5 and $T_D = T_c$.

case ($\gamma \neq$ o) we assumed the activation energies for SCL drift, B, and ohmic conduction, C, to be the same. Moreover, we assumed their ultimate conductivities, $\mu_o p_o$ and γ_o, to be equal (this corresponds to $T_c = T_D$) and we finally took as the reduced initial thickness of the charge layer r_o/l = 0.5. For both types of polymer there is a strong resemblance between the results for current TSD and isothermal step-response.

This close similarity convinced us that the ρ peak should also be found in isothermal step-response measurements, although the results published so far hardly substantiated this view. We have found only two references that report an unknown peak above T_g. Hersping (He 70) observed such a peak for PET and Adamec (Ad 71) for PMMA. Moreover,

these few results did not seem conclusive, because Adamec failed to find the ρ peak of PVC, and Hersping actually found two unknown peaks for PET. It should also be mentioned that their results are in conflict with earlier measurements by Reddish (Re 58), who did not find any ρ peaks for the two polymers.

We therefore decided to do our own step-response measurements on the ρ peak. The results for ChPEth (Penton) are shown in Fig. 4-4. They strongly support our prediction, for the ρ peak is indeed clearly observed in the step-response results. Furthermore, these results closely correspond to the TSD current, which has an equivalent time of 480 sec. In performing the step-response measurements we took care to charge the polymer completely; we therefore charged it always at a high temperature (110 °C) and thereafter cooled the sample to the appropriate discharge temperature*. This was not done by the other authors, and it may for this reason that they found conflicting results. From the shift of the current maximum of the step-response measurements we calculated an

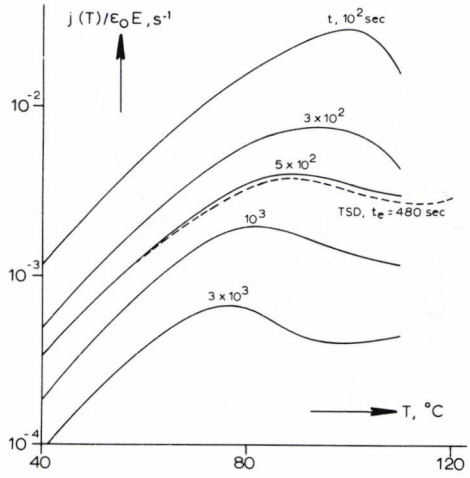


FIG.4-4 TSD current thermogram of the ρ peak of ChPEth compared with a family of step-response thermograms, compiled for various discharge times t. In both experiments the polymer was always charged at 110 °C - 7.2 kV/cm - 1.5 h and for TSD s was 1 min/°C.

activation energy of 35 kcal/mol, which is exactly equal to the activation energy for ohmic conduction. This is understandable, because the excess charges accumulated originate from carriers that previously took part in the conduction process, and therefore they have the same activation energy.

In the meantime we have likewise found the ρ and α peak of poly-n-propyl methacrylate by step-response measurements; these results will be published elsewhere.

Summarizing we found that current TSD can easily be related to dielectric and mechanical step-response data. Unfortunately, these are

*Such a charging procedure also shortens the measurements, because the charging time can be taken comparatively short.

sparse because the measurements to obtain them are time-consuming. We often have to be content with results from sinusoidal measurements, from which a great deal of data have become available for polymers.

4:2 Relation to Sinusoidal Measurements

In comparing current TSD with sinusoidal observations, which only inform us on the dipolar peaks, a time-frequency transformation has to be made. This means that the dielectric constant, $\varepsilon'(\omega)$, and dielectric loss, $\varepsilon''(\omega)$, have to be calculated from the discharge current density $j(t)$, or vice versa. The exact relations between these quantities are given by Fourier transforms. Although these might be evaluated numerically by a Fast Fourier Transform method (HP 69), it is much simpler to make the conversion with an approximation method, first suggested by Ninomiya and Ferry (NF 59). Recently, Schwarzl and Struik (Sc 69, SS 67, Sc 71) have elaborated this method to an advanced state. We will now show how their results can be extended to convert TSD measurements into ε' and ε'' results.

4:2.1 Review of the Conversion of Isothermal Discharge Currents

First, let us compare the *isothermal* sinusoidal response and discharge response of a single Debye relaxation. At a constant temperature T_o, the sinusoidal response functions $\varepsilon'(\omega,T_o)$ and $\varepsilon''(\omega,T_o)$ read

$$\frac{\varepsilon'(\omega,T_o) - \varepsilon_\infty}{\varepsilon_s - \varepsilon_\infty} = \frac{1}{1 + \omega^2/\alpha^2(T_o)} = \frac{x^2}{1 + x^2} \tag{4.8}$$

$$\frac{\varepsilon''(\omega,T_o)}{\varepsilon_s - \varepsilon_\infty} = \frac{\omega/\alpha(T_o)}{1 + \omega^2/\alpha^2(T_o)} = \frac{x}{1 + x^2} \tag{4.9}$$

while the released charge and discharge current obey the relations

$$\frac{q(t,T_o)}{\varepsilon_o(\varepsilon_s - \varepsilon_\infty)E} = 1 - e^{-\alpha(T_o)t} = 1 - e^{-x} \tag{4.10}$$

$$\frac{tj(t,T_o)}{\varepsilon_o(\varepsilon_s - \varepsilon_\infty)E} = \alpha(T_o)te^{-\alpha(T_o)t} = xe^{-x} \tag{4.11}$$

where E is the charging field and $q(t,T_o) = \int_0^t j(t,T_o)dt$.

It is our aim to calculate $\varepsilon'(\omega,T_o) - \varepsilon_\infty$ step by step from an appropriate set of given values of $q(t,T_o)$ and $tj(t,T_o)$ and, similarly, to evaluate $\varepsilon''(\omega,T_o)$ point by point from a combination of given values of $tj(t)$. To centre this conversion around a time $t = 1/\omega$ we have introduced into the equations a quantity x equal to

$$x = \alpha(T_o)t = \alpha(T_o)/\omega \tag{4.12}$$

To approximate $\varepsilon'(\omega,T_o) - \varepsilon_\infty$ by a linear combination of one $q(t)$ term

and several tj(t) terms Schwarzl and Struik put

$$x^2(1 + x^2)^{-1} \simeq 1 - \exp(-\alpha_1 x) + \sum_{k=2}^{n} a_k x \exp(-\alpha_k x) \qquad (4.13)$$

Similarly, their approximation of $\varepsilon''(\omega)$ by a linear series of tj(t) terms reads

$$x(1 + x^2)^{-1} \simeq \sum_{k=1}^{n} b_k x \exp(-\beta_k x) \qquad (4.14)$$

Both approximations, the coefficients of which we shall specify in a moment, result in an n-point to 1-point conversion. For an easy computation, n should not be too large; the smaller n, however, the larger the conversion error.

In fact, Schwarzl and Struik applied their method directly to distributed polarizations, for which the quantities satisfy Fredholm integral equations. Since we are working towards the conversion of TSD data we now make the restriction that the polymer should behave *thermorheologically simply**; we then have, for all relaxation frequencies, that $\alpha(T_o) = \alpha_r a(T_o)$, and the response functions become

$$\frac{\varepsilon'(\omega,T_o) - \varepsilon_\infty}{\varepsilon_s - \varepsilon_\infty} = \int_0^\infty \frac{f(\alpha_r)d\alpha_r}{1 + \omega^2/\alpha_r^2 a^2(T_o)} \qquad (4.15)$$

$$\frac{\varepsilon''(\omega,T_o)}{\varepsilon_s - \varepsilon_\infty} = \int_0^\infty f(\alpha_r) \frac{\omega/\alpha_r a(T_o)}{1 + \omega^2/\alpha_r^2 a^2(T_o)} d\alpha_r \qquad (4.16)$$

$$\frac{q(t,T_o)}{\varepsilon_o(\varepsilon_s - \varepsilon_\infty)E} = \int_0^\infty f(\alpha_r)\{1 - e^{-\alpha_r a(T_o)t}\}d\alpha_r \qquad (4.17)$$

$$\frac{tj(t,T_o)}{\varepsilon_o(\varepsilon_s - \varepsilon_\infty)E} = \int_0^\infty f(\alpha_r)\alpha_r a(T_o) te^{-\alpha_r a(T_o)t} d\alpha_r \qquad (4.18)$$

The kernels or intensity functions of these integral equations exactly are the Debye equations just given. Schwarzl and Struik argued that by making the intensity functions identical, the results of the integral transforms also become identical. They therefore confined themselves to converting the intensity functions. Moreover, in Eqs 4.13 and 4.14 they prescribed α_k and β_k, and actually calculated a_k and b_k. This calculation is a linear approximation problem. In addition, they chose $\alpha_k = 2\alpha_{k-1}$ and $\beta_k = 2\beta_{k-1}$, which implies the use of $q(t,T_o)$ and $j(t,T_o)$ values at logarithmically equidistant times; this has the additional advantage that one can easily switch to a more accurate conversion formula.

They determined the coefficients, a_k and b_k, with an iterative method, striving for a minimum relative error.

*With isothermal measurements there is no need for such a restriction.

In (Sc 69, SS 67, Sc 71) for each of their formulas the maximum errors possible are given, expressed in appropriate dielectric parameters such as $\tan\delta = \varepsilon''/\varepsilon'$. This helps one to make the best choice as regards required computing time and attainable accuracy, but it is of course useless to raise the latter above the measuring accuracy.

Schwarzl's simplest conversion formulae, based on one to three $j(t,T_o)$ values have the following forms

$$\varepsilon_o\{\varepsilon'(\nu_c,T_o) - \varepsilon_\infty\}E \simeq q(\sqrt{2}t_c) - a'(tj)_{t_c} - b'(tj)_{2t_c} - c'(tj)_{4t_c} \quad (4.19)$$

$$\varepsilon_o\varepsilon''(\nu_c,T_o)E \simeq a''(tj)_{\frac{1}{2}t_c} + b''(tj)_{t_c} + c''(tj)_{2t_c} + d''(tj)_{4t_c} \quad (4.20)$$

the coefficients of which are specified in Table 4-1 for two approximations*. Time t_c designates the conversion time chosen and ν_c the corresponding conversion frequency; these are related by

$$\nu_c = 0.113/t_c \quad (4.21)$$

The quantity tj stands for $tj(t,T_o)$, so that for a multiple of the conversion time pt_c we have

$$(tj)_{pt_c} = pt_c j(pt_c,T_o) \quad (4.22)$$

where p takes the values $\sqrt{2}$, $\frac{1}{2}$, 1, etc.

In particular, the first approximation for calculating ε'' is remarkably simple. It merely requires a knowledge of the discharge current at various times t_c, which have to be multiplied by $1.47/\varepsilon_o E$ and by t_c, to obtain the dielectric loss factor as a function of frequency. However, this approximation, though simple, is in many cases not very accurate. From the error bounds given in Table 4-1 we see that, especially at low tan δ values, the first approximation may introduce large conversion errors. In this case, preference should be given to the second approximation, which is applied as a numerical differentiation formula. To

TABLE 4-1 Coefficients of Schwarzl's Formulae for Calculating $\varepsilon'(\omega)$ and $\varepsilon''(\omega)$ from q(t) and j(t)

Approximation	a'	b'	c'	Relat. error bound, %	a"	b"	c"	d"	Relat. error bound, %
1st		0.593		+ 14.6 tan δ - 14.6 tan δ		1.47			+8(1+1/tan δ), 26 -8(1+1/tan δ), 26/tanδ
2nd	0.261	0	0.308	+ 7.8 tan δ - 7.8 tan δ	0.628	0	1.189	-0.325	+0.7(1+1/tan δ), 23 -4, 6/tan δ

calculate one ε''value we then require current values over a time span of 3 octaves. This number increases to 5, 7 and 9 ... for the higher

*The author thanks Dr Schwarzl for kindly putting at his disposal these unpublished formulae.

approximations. These are therefore omitted, because discharge measurements seldom extend beyond 3 decades.

A one to one point formula similar to Schwarzl's approximation was already known. It had been derived by Hamon from the Fourier transform of a Von Schweidler current response, $j = j_o t^{-n}$. Hamon's equation

$$\varepsilon_o \varepsilon''(\nu_c, T_o)E \simeq 1.59(tj)_{t_c} \quad \text{with } \nu_c = 0.1/t_c \tag{4.23}$$

formed the basis of our first discussion on the conversion of TSD data (Tu 70). However, we have just seen that this may be a rather crude approximation, and we therefore proceed to modify the more accurate formulae for converting TSD results.

4:2.2 Conversion of Current TSD Data into ε' and ε'' Data

Upon multiplying both sides of Eq. 4.1 with the reduced time $\xi(T)$, the TSD current density of a Debye relaxation becomes

$$\frac{\xi(T)\{j_r(T)/a(T)\}}{\varepsilon_o(\varepsilon_s - \varepsilon_\infty)E} = xe^{-x} \tag{4.24}$$

Similarly, we have for the released charge density

$$\frac{q_r(T)}{\varepsilon_o(\varepsilon_s - \varepsilon_\infty)E} = 1 - e^{-x} \tag{4.25}$$

where $x = \alpha_r(T) = \alpha_r a(T)/\omega$. Consequently, the conversion is now centred around the equivalent time $t_e(T) = 1/\omega$. It is evident that for the conversion of TSD we must know, besides the current, the shift factor $a(T)$.

On comparing Eqs 4.24 and 4.25 with Eqs 4.11 and 4.10 respectively, it is clear that $\xi(T)$ takes the role of $a(T_o)t$. When we assume a thermorheologically simple behaviour this replacement will also apply to a distributed polarization. Hence, there is no need to give the TSD analogues of Eqs 4.15 to 4.18.

The exchange of $a(T_o)t$ for $\xi(T)$ implies that now $\xi(T)$ will differ by a factor of p in the terms on the right-hand side of the approximations 4.19 and 4.20, and so T, rather than t, becomes the pertinent variable. Thus, if T_c is the conversion temperature chosen, we shall in addition have the attendant conversion temperatures T_{pc}. This set of conversion temperatures is related to T_c by the implicit expression

$$\xi(T_{pc}) = p\xi(T_c)$$

which for an Arrhenius shift approximately reads

$$T_{pc}^2 \exp(-A/kT_{pc}) \simeq pT_c^2 \exp(-A/kT_c) \tag{4.26}$$

By replacing t_c and t_{pc} by T_c and T_{pc} respectively, we can calculate ε' and ε'' point by point as functions of temperature rather than as functions of time, and this is exactly what we want.

After these rearrangements we readily verify that for TSD, Schwarzl's 1 and 3-point approximations take the form

$$\varepsilon_o\{\varepsilon'(\nu_c,T_c) - \varepsilon_\infty\}E \simeq q(T_{\nearrow 2c}) - a'(Tj)_{T_c} - b'(Tj)_{T_{2c}} - c'(Tj)_{T_{4c}} \quad (4.27)$$

$$\varepsilon_o\varepsilon''(\nu_c,T_c)E \simeq a''(Tj)_{T_{\frac{1}{2}c}} + b''(Tj)_{T_c} + c''(Tj)_{T_{2c}} + d''(Tj)_{T_{4c}} \quad (4.28)$$

which have the same coefficients as Eqs 4.19 and 4.20 and in which we have introduced the abbreviations

$$(Tj)_{T_{pc}} = p(T_c)j_r(T_{pc})/a(T_{pc}) \quad (4.29)$$

$$q_r(T_{\nearrow 2c}) = s\int_{T_d}^{T_{\nearrow 2c}} j_r(T)dT \quad (4.30)$$

while the frequency ν_c, corresponding to T_c, is equal to

$$\nu_c = 0.113/t_e(T_c) \quad (4.31)$$

where $t_e(T_c)$ is given by Eq.4.5 for an Arrhenius shift.

To illustrate the use of the TSD conversions derived, we pick out the first approximation for ε'' and express its right-hand side in T_c

$$\varepsilon_o\varepsilon''\{\nu_c(T_c),T_c\}E \simeq 1.47\ skT_c^2j_r(T_c)/A \quad (4.32)$$

This simple formula enables us to calculate, from the TSD current at various temperatures T_c, the corresponding $\varepsilon''\{\nu_c(T_c),T_c\}$ values, provided that the activation energy A is known*. In this way we obtain a special ε'' versus T plot in which each of the ε'' values is linked to a variable frequency $\nu_c(T_c)$. However, the small frequency variations are not relevant, since changes in viscoelastic quantities are significant only when the frequency varies logarithmically. Therefore it will often be legitimate to replace $\nu_c(T_c)$ by $\nu_c(T_m)$ in Eq. 4.32.

We may even go a step further by taking as a less accurate relation between ε'' and TSD measurements:

$$\varepsilon_o\varepsilon''\{\nu_c(T_m),T_c\}E \simeq 1.47\ t_e(T_m)j_r(T_c) \quad (4.33)$$

Similarly, we may reduce the first approximation for ε' to

$$\varepsilon_o[\varepsilon'\{\nu_c(T_m),T_c\} - \varepsilon_\infty]E \simeq q_r(T_c) \quad (4.34)$$

by virtue of the fact that $T_{\nearrow 2c} \sim T_c$, and that $Tj < q_r$, owing to the smallness of ε'' as compared to ε'. In Chap. 10 we shall often use these simplified first order approximations, for they show that we can compare

*However, A can be eliminated by a simple normalization, as follows $\varepsilon''(\nu_c,T_c)/\varepsilon''(\nu_c,T_m) \simeq T_c^2j_r(T_c)/T_m^2j_r(T_m)$. Conversely, Eq. 4.32 can be used to calculate A from ε'' and j_r. In particular, we have, for a Fuoss-Kirkwood distribution of width m: $mA \simeq 2.94\ kT_m^2j_r/P_o$.

TSD thermograms directly with those of ε' and ε''. Whenever the latter have been interpreted, it will therefore be an easy matter to designate the molecular origin of the corresponding TSD current peaks.

The accuracy of the calculation of ε' and ε'' from TSD data for a single Debye relaxation is demonstrated in Fig. 4-5. We considered the 3-point conversion formulas of Eqs 4.27 and 4.28 and compared their results with the exact values of $\varepsilon'\{\nu_c(T_c),T_c\}$ and $\varepsilon''\{\nu_c(T_c),T_c\}$. The ε' values calculated from j_r are remarkable good for all temperatures. The calculated ε'' values also agree well with the exact ε'' values up to $T/T_m = 1.1$, but for higher temperatures they diverge badly. Results of the 1-point conversion are also given. It yields ε'' values which already begin to deviate near T_m, but at this temperature the differences are still acceptable; beyond $T/T_m = 1.07$ the conversion definitely becomes incorrect. We have finally inserted the ordinary ε' and ε'' versus T plots of a Debye relaxation; their values were taken at a *constant* frequency $\nu_c(T_m)$. As was expected, the ε' and ε'' diagrams calculated from j_r also agree well with these isochronous plots, but the differences at low and high temperatures are slightly larger.

Results similar to those just described were obtained for a distributed polarization, but interestingly the deviations between the actual and calculated ε'' values are less (see also (Wi 62)).

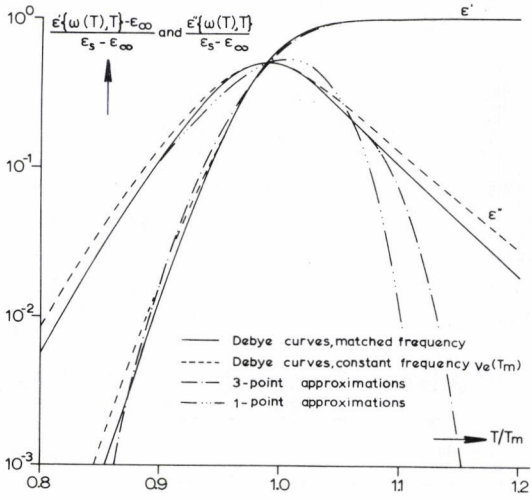


FIG.4-5 Comparison between the exact ε' and ε'' Debye plots and those calculated from a TSD current thermogram. The TSD-values were converted by modified 1- and 3-point formulae due to Schwarzl. We assumed a single dipole relaxation and took $A/kT_m = 20$.

From Eq. 4.31 we find for the side-group and main-chain relaxations of methacrylic polymers equivalent frequencies of about 3×10^{-4} and 6×10^{-4} Hz. This means that TSD enables us to find ε' and ε'' values at extremely low frequencies. Consequently, its *resolution* for various relaxation peaks will be high, which makes TSD a very attractive method for studying dielectrics. Isothermal step-response measurements also show a high resolution, but they are very time-consuming.

The high resolving power of TSD, as compared with that of conventional ε'' and G" measurements, was illustrated in Figs 1-6 for PMMA. For another example we refer to Figs 10-1 and 10-2. In the TSD thermograms the β and α peaks due to dipole relaxations of the side-group and main-chain, respectively, are distinctly better separated in particular for PEMA. The space charge or ρ peaks are absent from the ε'' thermograms, where they are displaced by the conduction losses of which only the onset is shown.

Note that for PMMA the heights of the α and β peaks in the TSD thermogram are reversed in the ε'' thermogram. This can only be partly explained with Eq. 4.32. Denoting the maxima by $T_{\alpha,\beta}$ we have since the activation energies differ also

$$\frac{\varepsilon''\{\nu(T_\alpha),T_\alpha\}}{\varepsilon''\{\nu(T_\beta),T_\beta\}} = \frac{T_\alpha^2 j(T_\alpha)/A_\alpha}{T_\beta^2 j(T_\beta)/A_\beta} \tag{4.35}$$

Substituting $\varepsilon''(T_\alpha) = 0.15$, $\varepsilon''(T_\beta) = 0.21$, $T_\alpha = 102$ °C, $T_\beta = -51$ °C, $A_\alpha = 96$ kcal/mol and $A_\beta = 18$ kcal/mol we find that $j(T_\alpha)/j(T_\beta) = 1.3$, whereas the current ratio found experimentally amounts to 3.7. We attribute this discrepancy to the fact that the α peak partly arises from the motion of space charges, which is not observed in dielectric measurements at medium frequencies. This reinforcement of the TSD α peak was later verified by sectioning experiments on PMMA electrets (see Chap. 10).

Such a reinforcement is less likely if the α and ρ peaks are well separated, or if the α peak arises at low temperatures. This is typically exemplified by PET and ChPEth. Their converted TSD results, together with those of PMMA, are collected in Table 4-2. The calculated ε'' values for the α peak of PET and ChPEth indeed scarcely differ from the measured values. The differences between the actual and calculated ε'' values of the β peaks, as found for PET and PMMA, will be explained below.

TABLE 4-2 ε''-Results at 0.1 Hz, Compared with ε''-Values Calculated from TSD (s = 1 min/°C)

Polymer	Peak	T_m, °C	A, eV	t_e, sec	ε''_{calc}	$\varepsilon''_{0.1}$
PMMA	β	- 51	0.78	330	0.15	0.21
	α	105	4.2	180	0.30	0.14
PET	β	- 114	0.59	220	0.023	0.034
	α	86	5.0	134	0.064	0.060
ChPEth	β	- 123	0.54	270	0.011	0.011
	α	- 3	3.7	104	0.033	0.035

Results of the conversion of the complete β and α peaks of PMMA are presented in Fig. 4-6. They were obtained by the simplified conversion 4.33, and they are based on the t_e values for PMMA in Table 4-2. As previously explained, we find that the converted α maximum is too high, whereas the converted β maximum is too low. Moreover, the latter is broader than the β peak of the measured ε" values. This in fact means that going to lower frequencies, the dipolar distribution of the β peak is broadened, which has also been observed by Heijboer (He 72) for the γ peak of PcHMA. Such a broadening is typical of a distribution in activation energy.

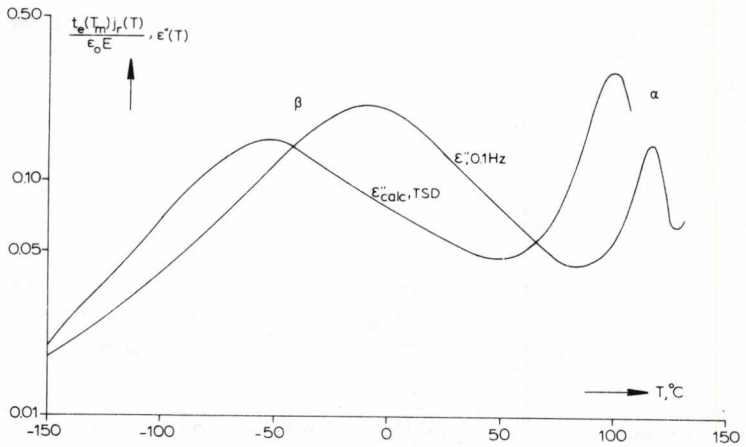


FIG.4-6 Actual ε"(T) data at 0.1 Hz of the β and α peaks of PMMA compared with ε"(T) data, calculated from current TSD measurements according to $\varepsilon''_{calc}(T) \simeq 1.47\ t_e(T_m)j_r(T)/\varepsilon_o E$.

Fig. 4-7 gives results of a more refined conversion of the TSD β peaks of PMMA and 50 MMA co 50 PhMA to ε" data. The conversion was

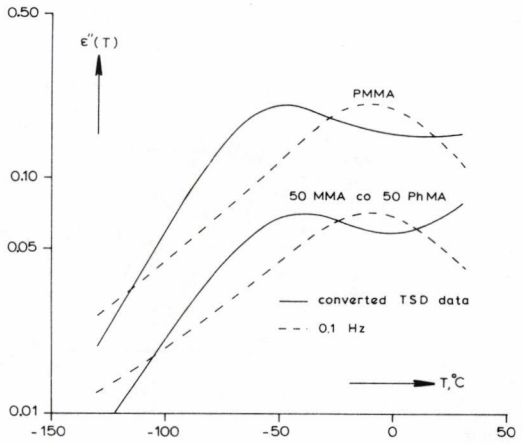


FIG.4-7 Comparison between sinusoidal ε"data, measured at 0.1 Hz, and ε" values calculated from TSD current data using the 1-point conversion formula. For both polymers the relaxation peak of the converted TSD data occur at a lower temperature, owing to the very low equivalent frequency of TSD.

carried out with the 1-point formula 4.32 and the results are again compared with ε'' data obtained by sinusoidal measurements at 0.1 Hz. As in Fig. 4-6 the calculated ε'' values are shifted to much lower temperatures owing to the extremely low equivalent frequency of TSD (3×10^{-4} Hz). The calculated and measured ε'' thermograms also differ in shape; they agree well near the maximum only. The differences may be due to the fact that the dipole relaxations are distributed in *activation energy*, and so the assumption of the thermorheological simple behaviour is violated. Accordingly, better agreement would have been obtained if we had adjusted the activation energy A in Eq. 4.32. At low temperatures we should have taken a low activation energy, and at high temperatures a high activation energy. (Note that for this broad peak, A ranges from 3 to more than 20 kcal/mol.)

Let us finally reconsider Fig. 4-2, where in the upper curves, ε'' values, calculated from step-response measurements and TSD are shown. The conversions were made with the TSD form of Hamon's approximation 4.23. The converted TSD results, corresponding to 5×10^{-4} Hz, do not fit in correctly, presumably because there is not a distribution in natural frequencies, but a distribution in activation energies. It is therefore incorrect to take A constant in Eq. 4.32. On the other hand, in the lower curves corresponding to a conversion in the time domain, A hardly plays a role in the comparison and so these curves agree much better.

Summarizing, the comparison between ε'' results from dynamic measurements and those calculated from TSD shows two interesting things. The first is that space charges may contribute to the TSD α peak, and the second that most β peaks have a distribution in activation energies rather than in natural frequencies. It therefore seems valuable to include a distribution in activation energies in the conversion of current TSD to ε' and ε'' results.

Chapter 5

CURRENT TSD BY THE MOTION OF EXCESS CHARGES AND BY OHMIC CONDUCTION IN SHORTED ELECTRETS

Besides permanent dipoles a polymer may contain mobile charges, which will migrate during the formation towards the electrodes. The charges may be ions and/or electrons and they may originate from e.g. dissociation of impurities (water, monomer, catalyst and initiator). The forming field will drive the positive carriers to the negative electrode, and the negative carriers to the positive electrode. This field drift is weakened by diffusion, while part of the moving charges is lost by recombination with opposite charges. Nevertheless, the field drift will dominate and the excess charges will gradually be built up in the vicinity of the electrodes, where they are frozen during the cooling phase.

The occurrence of such a space charge polarization requires that there be enough carriers of a sufficiently high mobility; this condition obtains only if the conduction is reasonably high. Hence, it may be inferred from the conductivity curves of Figs 2-2 to 2-4 that a significant space charge polarization is most likely to occur at forming temperatures higher than T_g.

During TSD the frozen-in excess charges are thermally activated and mobilized. They then start to move under their own field, towards the shorted electrodes (SCL drift) and also by diffusion. These two motions lead to a TSD peak, which can be expected just above T_g, when the ohmic relaxation frequency has become high enough to satisfy a condition similar to Eq. 2.21. In agreement with this, a space charge peak, or ρ peak was found above the dipolar β and α peaks in many of the current thermograms of hetero-electrets given in Chap. 10 (compare also Fig. 1-6).

Excess charges are also formed in homocharging, which today is preferred to heterocharging for preparing the films of electret microphones. The decay behaviour of such films, which are often merely near-surface charged, is of great practical importance and TSD may be of considerable help in elucidating their decay processes. Interestingly, the homocharges are injected into highly insulating, nonpolar films, in which their motion is not disturbed by dipole orientation or ohmic conduction. So it may be expected that the drift of excess charges shows up rather clearly in such foils.

The theory of the TSD motion of excess charges is more complicated than that of the preceding chapters, because the parameters are *time and space-dependent*; it thus requires the solution of nonlinear partial differential equations (PDE's), for which no general solution could be derived. We therefore restricted ourselves to the main decay processes of the excess charges, viz. their SCL drift to the electrodes or to the other excess charges of opposite sign on the one hand, and on the other to their compensation and final neutralization by opposite intrinsic

carriers supplied by the ohmic conduction of the polymer; even then we had to solve the PDE's on a computer using finite-difference schemes. An analytical solution could be given only for a *uniform* excess charge distribution. This was done by extending the work of Calderwood and Scaife on isothermal discharge by SCL drift (CS 70). The analytical and numerical solutions elaborated are discussed in Sects 5:3* and 5:4.

In Sect. 5:1 the most general form of the PDE's and boundary conditions are introduced, and Sect. 5:2 subsequently describes some differences between the decay of excess charges and dipoles. Sect. 5:5 deals with excess-charge current TSD by diffusion for blocking electrodes; part of this theory was already outlined in (Tu 70).

In this chapter we pay attention to current TSD of shorted metallized electrets. The motion of excess charges in current TSD of electrets shorted together with an adjacent air-gap, and during charge TSD in open-circuit will be discussed in Chaps 7 and 8, respectively. Appendix II includes four supplements to this chapter. These give information on e.g. estimates of hetero- and homocharging, the flowlines of the drifting particles and the finite-difference schemes used to solve the SCL drift of nonuniform excess-charge densities.

5:1 Charge Transport Equations and Boundary Conditions

The migration of positive and negative carriers is effected by the electric field and by concentration gradients (diffusion). During their migration part of the carriers are lost when they recombine into neutral species. On the other hand new carriers are formed by dissociation of neutral impurities. These four processes give rise to the following conservation laws describing carrier transport

$$\partial p_s(x,t)/\partial t = -\mu_p(T)\partial p_s(x,t)E(x,t)/\partial x + D_p(T)\partial^2 p_s(x,t)/\partial x^2 - R(T)p_s(x,t)n_s(x,t) + \delta(T)n_c(x,t) \tag{5.1}$$

$$\partial n_s(x,t)/\partial t = \mu_n(T)\partial n_s(x,t)E(x,t)/\partial x + D_n(T)\partial^2 n_s(x,t)/\partial x^2 - R(T)p_s(x,t)n_s(x,t) + \delta(T)n_c(x,t) \tag{5.2}$$

$$\partial n_c(x,t)/\partial t = R(T)p_s(x,t)n_s(x,t) - \delta(T)n_c(x,t) \tag{5.3}$$

where p_s and n_s denote the total positive and negative carrier densities, $\mu_{p,n}$ their mobility, $D_{p,n}$ their diffusion constant and R their recombination constant, n_c is the density of the neutral impurity centres and δ their dissociation constant. Of the several rate constants μ and D in particular will vary with temperature. Often they will obey an Arrhenius shift. The temperature dependence of R and δ is probably small.

*When we had completed the work of Sect. 5:3, we received from Prof. Wintle an interesting article, which also describes such an extention (Wi 71). The scopes of both extentions are, however, different, so we decided not to change the original text of Sect. 5:3, except for adding Figs. 5-18 and 5-19.

We recall from Sect. 1:5 that part of the charge densities p_s and n_s arise from the space-dependent excess charges, p and n, which constitute the electret charge, whilst the remaining portion is due to the space-independent equilibrium charges, p_e, n_e. Thus

$$p_s(x,t) = p_e(T) + p(x,t) \quad \text{and} \quad n_s(x,t) = n_e(T) + n(x,t)$$

Note that the equilibrium charges are even present in the *neutral state* and so their field drift is responsible for the space-independent *ohmic conductivity* of the polymer

$$\gamma(T) = \mu_p(T)p_e(T) + \mu_n(T)n_e(T) \tag{5.4}$$

By contrast, the field drift of the excess charges actually is an SCL drift resulting in a current that varies nonohmically i.e. nonlinearly with the field (cf. Eq. 5.19). This is so, because this field depends on p(x,t) and n(x,t) themselves.

The relation between the excess charges and the field is given by Poisson equation, which reads in the absence of permanent dipoles

$$\varepsilon_o\varepsilon\partial E(x,t)/\partial x = p(x,t) - n(x,t) \tag{5.5}$$

where we have written ε for ε_∞.

The solution of these foregoing PDE's poses our problem, they are to be solved for the appropriate boundary conditions at x = 0 and 1 and the given initial conditions at t = 0.

During TSD, when the electret is short-circuited the electric field satisfies the boundary condition

$$\int_0^1 E(x,t)dx = 0 \tag{5.6}$$

The boundary conditions for the excess-charge densities p and n depend on the electrode contact. For *blocking* electrodes which inhibit neutralization by the image charges of the incoming excess charges, these boundary conditions follow from the requirement that the particle current densities due to field drift and diffusion

$$\begin{aligned} j_p(x,t) &= \mu_p(T)p_s(x,t)E(x,t) - D_p(T)\partial p_s(x,t)/\partial x \\ j_n(x,t) &= \mu_n(T)n_s(x,t)E(x,t) + D_n(T)\partial n_s(x,t)/\partial x \end{aligned} \tag{5.7}$$

must be *zero* at x = 0 and 1. We mentioned in Sect. 1:6 that even evaporated electrodes may be partly blocking due to energy barriers to charge exchange, such as e.g. oxide layers. A typical example of a blocking electrode is an air-gap interface; this constitutes a perfect blocking.

For *open* electrodes (such as most evaporated electrodes) which do not hinder the neutralization of the excess charges, Jaffé et al. (JL 53) take

$$p_s(o,t) = p_s(1,t) = p_e(T) \quad \text{and} \quad n_s(o,t) = n_s(1,t) = n_e(T) \tag{5.8}$$

Here p_e and n_e are the uniform equilibrium densities of the neutral state. Their concentration is determined by the dissociation rate of the neutral impurities

$$p_e^2(T) = n_e^2(T) = \delta(T)n_c(T)/R(T) \tag{5.9}$$

Presumably $p_e(T)$ and $n_e(T)$ remain almost constant for varying T. Note that Eq. 5.8 implies that the *excess charge densities* are *zero* at the boundaries, because on arriving at an open electrode all excess charges recombine immediately with their image charges.

To describe *intermediate* electrode contacts, Jaffé et al. (JL 53) introduced a charge-exchange rate $\zeta(T)$ by stating

$$j_p(o,t) = -\zeta(T)\{p_s(o,t) - p_e(T)\}$$
$$j_p(1,t) = \zeta(T)\{p_s(1,t) - p_e(T)\} \qquad (5.10)$$

where $\zeta(T)$ may range from 0 to ∞ (for blocking electrodes it is zero and for open electrodes it is infinite). The temperature dependence of ζ is not known exactly, but it is likely to be small.

The total current through the sample, which equals the external current is space-independent and consists of a displacement current, $\varepsilon_o\varepsilon\partial E(x,t)/\partial t$, and the particle currents $j_{p,n}(x,t)$, or written out in full

$$j(t) = \varepsilon_o\varepsilon\partial E(x,t)/\partial t + \gamma(x,T)E(x,t) + \{\mu_p(T)p(x,t) + \mu_n(T)n(x,t)\}$$
$$E(x,t) - D_p(T)\partial p(x,t)/\partial x + D_n(T)\partial n(x,t)/\partial x \qquad (5.11)$$

Here $\gamma(T)E(x,t)$ is the local ohmic conduction current, $\{\mu_p(T)p(x,t) + \mu_n(T)n(x,t)\}E(x,t)$ is the local SCL drift current, and $-D_p(T)\partial p(x,t)/\partial x + D_n(T)\partial n(x,t)/\partial x$ is the local diffusion current.

A general solution of the nonlinear set of PDE's 5.1 to 5.5 is not known for the boundary conditions described, even for the isothermal, *steady state* they have not been solved. A general solution for non-isothermal, transient conditions is therefore out of the question; even a numerical solution is impossible since the temperature dependence of several parameters is not known explicitly. In the following we shall therefore ignore the *recombination* and *dissociation processes*. Moreover, we shall consider SCL drift and diffusion of the excess charges separately.

5:2 Differences between Current TSD of Excess Charges and Dipoles

Before dealing with the theory of the TSD ρ peak alone, we shall here mention some general aspects of the combined decay of dipoles and excess charges. We already know that the aligned dipoles are subject to thermal reorientation, whereas the frozen-in excess charges are dissipated by the ohmic conduction of the polymer, and the SCL drift and the diffusion of the charges themselves.

We shall allow the persistent polarization P_s to be *space-dependent*, which is likely in the presence of excess charges, for these distort the uniformity of the forming field. The excess charges residing in the electret may be heteropolar or homopolar or both. Owing to the metallization, surface charges will be lacking. In several polymers the mobile carriers are considered to be ions. In particular for hetero-electrets, we therefore expect the mobility and diffusion constants of positive and negative carriers not to differ very much; for convenience we put $\mu_p(T) = \mu_n(T) = \mu(T)$ and $D_p(T) = D_n(T) = D(T)$.

Generalizing Eq. 5.11 for the presence of a persistent polarization, and integrating it between x = 0 and 1 to remove the partial derivatives by introducing average values, we obtain for the discharge current

$$lj_r(t) = \varepsilon_o\varepsilon_\infty \frac{d}{dt}\int_o^1 E(x,t)dx + \frac{d}{dt}\int_o^1 P_s(x,t)dx + \gamma(T)\int_o^1 E(x,t)dx \qquad (5.12)$$
$$+ \mu(T)\int_o^1 \{p(x,t) + n(x,t)\}E(x,t)dx + D(T)\{\rho(1,t)-\rho(o,t)\}$$

where ρ denotes the excess space-charge density $\rho(x,t) = p(x,t) - n(x,t)$. On invoking the short-circuit condition $\int_0^1 E(x,t)dx = 0$ of Eq. 5.6 and the boundary conditions of Eq. 5.8, according to which $\rho(0,t) = \rho(1,t) = 0$, we can simplify Eq. 5.12 to

$$1j_r(t) = \frac{d}{dt}\int_0^1 P_s(x,t)dx + \mu(T)\int_0^1 \{p(x,t) + n(n,t)\}\, E(x,t)dx \qquad (5.13)$$

for *open* electrodes.

Obviously, the average values of the internal currents that arise from ohmic conduction and diffusion are *zero*, so that we only observe the *reorientation of the dipoles* and the *SCL drift of the excess charges*. As a result, the current TSD of shorted metallized electrets is not very complicated, giving rise to the dipolar β and α peaks and the space charge or ρ peak, as we have shown in Fig. 1-6 for a hetero-electret of PMMA. (For further experimental results on hetero-electrets we refer to Sect. 10:1.) The dipolar peaks arise from cryogenic temperatures up to T_g. In the previous chapters we have shown that these peaks involve molecular paramters only . The ρ peak emerges above T_g. This peak is less neatly reproducible, because current release by the motion of excess charges depends on many variables not typical of the polymer in question.

There are still other differences in charge release between dipoles and excess charges; for dipole reorientation releases an external charge that equals the polarization originally stored, whereas the excess charge motion releases only part of the initial excess charge. This is caused not only by the inefficiency of the release through SCL drift, but also by the fact that the excess charges are unobservably dissipated by ohmic conduction, and, to a lesser extent, by diffusion and recombination.

However, for (partly) blocking evaporated electrodes, we may have $\rho(x,t) \neq \rho(1,t)$, then the diffusive motion of the excess charges may also contribute to the ρ peak.

To obtain information about the hidden excess charge decay by ohmic conduction, which in polar polymers may be very large, we suggested the simple device of using an *air gap*. This makes $\int_0^1 E(x,t)dx \neq 0$ and also introduces one blocking electrode. As a result all processes will contribute to the charge release. However, two terms in Eq. 5.12, namely those corresponding to the capacitive current and the diffusion current, are usually small. Neglecting these, we have for the current TSD with an air gap

$$1j_r(t) = \frac{d}{dt}\int_0^1 P_s(x,t)dx + \gamma(T)\int_0^1 E(x,t)dx + \mu(T)\int_0^1 \{p(x,t) + n(x,t)\}\, E(x,t)dx$$

Thus, the main processes that are revealed by this new technique are depolarization, ohmic conduction, and SCL drift. The theory of TSD using an air gap will be discussed in Chap. 7.

5:3 SCL Drift of Spatially Uniform Excess Charges

We shall now focus on the theory of the TSD ρ peak considering the SCL drift of the unipolar excess charges which are stored in the non-polar foils used for electret microphones (Fig. 5-1). In the mass production of these mono-electrets, homocharges are injected into the non-metallized side by Townsend breakdown, corona discharge or electron bombardment. To study their current TSD we evaporated another electrode onto these foils in a vacuum. Care was taken to reduce any loss of charge during this operation.

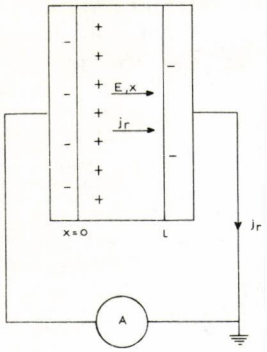


FIG. 5-1 Diagram for the current TSD of excess charges. In the mono-electret depicted, the excess charges move towards their image charges at the short-circuited electrodes by SCL drift and by diffusion or both. In the following the field E and the current j_r are taken positive, if their direction is from $x = 0$ to $x = 1$.

Experimental results will be given in Sect. 10:1. They show that in particular for the excellent homo-electrets of Teflon-FEP foil, SCL drift is indeed the main decay process, diffusion and recombination seem to play a minor rôle. Some conclusive experiments on this were discussed in Sect. 1:7, we also mentioned that the SCL drift of electrons is generally attended by trapping and retrapping. Nevertheless, we shall here assume that the injected carriers are ions or electrons whose *mobility is thermally activated* and which are virtually free to move. This assumption seems to be justified, because it is equivalent to that of the thermal release of electrons from a *single* trap level that shows *fast* retrapping. We obtained convincing evidence for fast retrapping in Teflon-FEP, which actually embodies trapping sites of various energy levels.

In restricting ourselves to SCL drift of carriers with a thermally activated mobility, we shall suppose the evaporated electrodes to be open, as is probably the case*. We also deliberately ignore dielectric absorption, because of the nonpolarity of the foils. Though these restrictions simplify the analysis substantially, no general solution could be derived. An analytical solution is only manageable for *uniform* carrier distributions, as has recently been shown by Calderwood and Scaife (CS 70) in a paper on the isothermal SCL drift of *bipolar* excess charges. Their treatment resembles earlier theories of transient SCL drift in photo-insulators under an applied voltage stress (MR 62, BS 70).

We shall adapt Calderwood and Scaife's solution to a *unipolar* excess charge and extend it to *non*isothermal conditions. Moreover, we take into account *neutralization* of the drifting carriers by intrinsic *ohmic conduction*, which may become significant at high temperatures, especially in the more polar foils (compare Fig. 2-2 to 2-4). Though its scope is limited, such an analytical solution is very useful for gaining insight into the decay processes of the much used homocharged electret foils.

*However, in Sect. 5:7 (App. II) we shall prove that for SCL drift there is no difference in current release between open and blocking electrodes. In other words, the conversion of particle currents arriving at blocking electrodes into surface charges, does not affect the external current.

5:3.1 Basic Equations for TSD by SCL Drift and Ohmic Conduction in Mono-Electrets

When diffusion, recombination and generation of carriers is negligible, the continuity equations Eqs 5.1 and 5.2 can be combined into

$$\partial\frac{\{p(x,t) - n(x,t)\}}{\partial t} = -\mu(T)\partial\frac{\{p(x,t) + n(x,t)\}E(x,t)}{\partial x} - \gamma(T)\frac{\partial E(x,t)}{\partial x}$$

where for convenience we have put $\mu_p(T) = \mu_n(T) = \mu(T)$, while the sum of the conductivities of the intrinsic equilibrium carriers has been replaced by the ohmic conductivity $\gamma(T)$ (see Eq. 5.4).

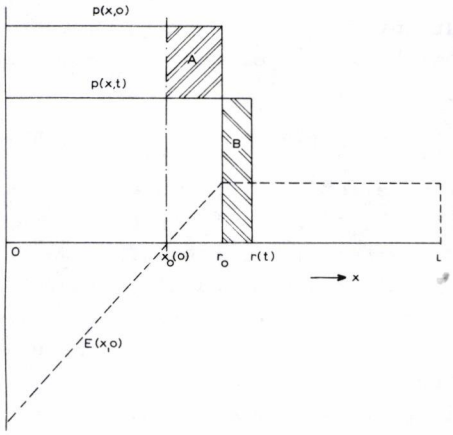


FIG. 5-2 Model for the charge distribution of an unipolar homo-electret. The excess charges initially extend up to r_o. The electric field at t = 0 and the expansion of the cloud at time t are also shown. If $\gamma = 0$, charges moving to the right are conserved reappearing in the expanded area, i.e. for infinitesimal time increments, area A = area B. In fact, we have $\{r(t) - x_o(t)\}\, dp(x_o,t) = -p(x_o,t)dr(t)$.

For our case, in which the net excess charge density is unipolar and positive (Fig. 5-2), this equation reduces to

$$\partial p(x,t)/\partial t = -\mu(T)\partial p(x,t)E(x,t)/\partial x - \gamma(T)\partial E(x,t)/\partial x \qquad (5.14)$$

Poisson's equation is also simplified to

$$\partial E(x,t)/\partial x = p(x,t)/\varepsilon_o\varepsilon \qquad (5.15)$$

Obviously, the first term on the right-hand side of Eq. 5.14 represents the loss from SCL drift of the excess charges towards the electrodes, and the second term the loss from ohmic conduction. This loss originates in the field drift of the intrinsic carriers of the polymer; since the excess charges are positive, they will repel positive intrinsic charges, and attract negative ones, with which they will eventually recombine.

Equations 5.14 and 5.15 form a set of hyperbolic PDE's of which the first is nonlinear. Starting from the initial distribution p(x,o), they have to be solved for given boundary values of p(x,t) and E(x,t). By integrating Eq. 5.15 with respect to x and using Eq. 5.6, we can derive as boundary conditions for E(x,t)

$$\varepsilon_o \varepsilon E(o,t) = -\int_o^1 (1-x/1)p(x,t)dx \qquad (5.16)$$

and

$$\varepsilon_o \varepsilon E(1,t) = \int_o^1 (x/1)p(x,t)dx \qquad (5.17)$$

For the boundary values of the excess charges at the open electrodes we have Eq. 5.8.

Actually, we are not much interested in the internal parameters p(x,t) and E(x,t); we are more anxious to know the released current and charge. After having solved p and E, we may obtain $j_r(t)$ from Eq. 5.11, which reduces to

$$j_r(t) = \varepsilon_o \varepsilon \partial E(x,t)/\partial t + \{\mu(T)p(x,t) + \gamma(T)\}E(x,t) \qquad (5.18)$$

This equation may be particularized at any x. To simplify it further, we integrate it between x = 0 and 1. With the aid of the short-circuit condition Eq. 5.6 and using Eq. 5.15, we easily find

$$j_r(t) = (\varepsilon_o \varepsilon \mu(T)/2\ 1)\{E^2(1,t) - E^2(o,t)\} \qquad ...(5.19)$$

which holds for open as well as blocking electrodes. It is exactly this equation which prompted us to designate the field drift of excess charges as SCL drift, for we see that the released current depends *quadratically* on the boundary values of E(x,t). Consequently, the current is not linearly related to the frozen-in space charge (cf. Eq. 5.24). Such an SCL behaviour differs markedly from the linear field dependence of the dipole-reorientation current.

A direct consequence of Eq. 5.19 is that distributions symmetrical to 1/2, for which E(1,t) = |E(o,t)| generate *no* external current. The charges of such distributions flow off in equal amounts to both electrodes, and their average SCL drift current is zero. This should be emphasized because ultimately all spatial distributions collapse to a (uniform) symmetrical distribution. This implies that only *part* of the original excess charge can be measured. Consequently, in current TSD, the charge decay due to SCL drift, which ends in a neutralization of the charges at the electrodes, remains partly *hidden*. The situation becomes even worse, when the excess charges are rapidly dissipated by ohmic conduction, for this decay does not contribute at all to the external current.

5:3.2 Current and Charge Release of Mono-Electrets with a Uniform Charge Profile

We shall pursue the current TSD of an initially uniform excess charge distribution, penetrated to a depth r_o. This is the simplest conceivable distribution that permits of an analytical solution. Interestingly, we found that its current release broadly exemplifies the characteristics of actual mono-electrets. This is so because current release does not depend very much on the shape of the charge distribution. The model

therefore forms a satisfactory basis for analyzing experimental data.

From Fig. 5-2 we have

$$p(x,o) = p_o, \quad 0 \leq x \leq r_o \quad \text{and} \quad p(x,o) = 0, \quad r_o \leq x \leq 1 \tag{5.20}$$

by integrating Eq. 5.15 one readily finds that this distribution creates an electric field which increases linearly up to r_o. In fact,

$$E(x,o) = E(o,o) + p_o x/\varepsilon_o\varepsilon \quad 0 \leq x \leq r_o$$

where $E(o,o)$ follows from Eq. 5.16: $E(o,o) = -(p_o r_o/\varepsilon_o\varepsilon)(1 - r_o/2\ 1)$. Beyond r_o, the field becomes space-independent, due to the absence of carriers. As Fig. 5-2 shows, this field becomes zero at x_o. This zero-field point, which gradually moves towards the middle of the foil, plays a key rôle in the solution of $p(x,t)$ and $j_r(t)$.

The field on the left of x_o is directed towards the left, that on the right of x_o points to the right. Consequently, charges on the left of x_o will be driven towards the left electrode, where they are neutralized by recombining with their image charges. Those on the right of x_o will move towards the right electrode. Thus, the distribution will diminish and expand to the right. The leading edge, however, will remain *sharp*, owing to the absence of diffusion. This can be proved by considering the motion of the carriers along their flow lines or characteristics, see Sect. 5:7 (App. II).

For the moment we shall take it for granted that the distribution remains uniform at $t > 0$. Its decrease in height can then readily be found by evaluating $p(x_o,t)$. This is a rather simple matter, for at $x = x_o(t)$ we have $E(x_o,t) = 0$ and Eq. 5.14 can be written as an *ordinary differential equation* in $p(x_o,t)$, because in view of the uniformity: $\partial p(x_o,t)/\partial t = dp(x_o,t)/dt$. After substitution of Eq. 5.15 we get

$$dp(x_o,t)/dt = -\{\mu(T)p(x_o,t) + \gamma(T)\}p(x_o,t)/\varepsilon_o\varepsilon \tag{5.21}$$

This value $p(x_o,t)$ appears everywhere between $x = 0$ and the leading front.

For an analytical solution of Eq. 5.21, $\mu(T)$ and $\gamma(T)$ should exhibit the same temperature dependence; the result will be given in Eq. 5.43*. For the moment we neglect $\gamma(T)$, which is only justified for poorly conducting polymers. If $\mu(T)$ is subjected to an Arrhenius shift with activation energy B, $\mu(T) = \mu_o e^{-B/kT}$, we then have

$$p(x_o,T) = p_o\{1 + \delta_o\psi(T)\}^{-1} \qquad \ldots(5.22)$$

where δ_o is the drift frequency of the excess charges at $T = \infty$, $\mu_o p_o/\varepsilon_o\varepsilon$, and $\psi(T)$ the reduced time for SCL drift, $s\int_{T_d}^{T} e^{-B/kT}dT$.

*Note that λ may be replaced by t.

The decay and expansion of the charge cloud (according to Eq. 5.22) during the TSD of a nonconducting polymer are illustrated in Fig. 5-3. In the beginning the carriers are hardly mobile and p(x,T) barely changes. It decays most rapidly when T approaches T_D; this is a characteristic temperature at which the current maximum occurs, see Fig. 5-8 (T_D is defined by $sT_D\delta(T_D) = B/kT_D$, which in turn is identical to the condition for a Debye maximum, Eq. 2.21). Thereafter, the decay rate decreases, because the driving field of the charges becomes too low. On the other hand, the expansion grows steadily, so that the charge cloud finally fills the entire sample. From then on the external current is zero.

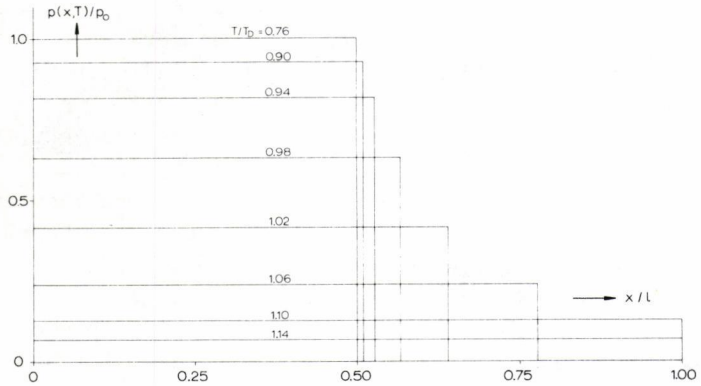


FIG. 5-3 Variations of a uniform excess-charge cloud stored in a nonconducting polymer at various release temperatures, T/T_D. As soon as the sample is entirely filled, no more current is generated, although the internal decay continues. The calculations were carried out for $B/kT_D = 20$.

If ohmic conduction dominates, one obtains instead of Eq. 5.22

$$p(x_o,T) = p_o \exp\{-\beta_o \eta(T)\} \tag{5.23}$$

where β_o is the ohmic relaxation frequency at $T = \infty$, $\gamma_o/\varepsilon_o\varepsilon$, and $\eta(T)$ the reduced time for ohmic conduction, $s\int_{T_d}^{T} e^{-C/kT}dT$. However, this case is not very interesting since at a high conductivity the space charge cloud is dissipated too quickly and can hardly expand, and $j_r(T) \simeq 0$.

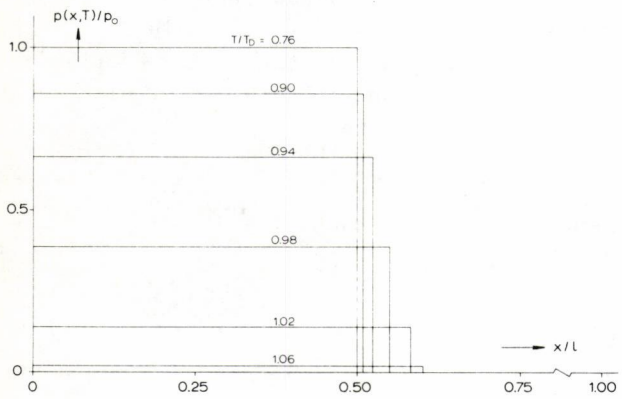


FIG. 5-4 Effect of ohmic conduction on the retained excess-charge density at various release temperatures. The charge density decreases much more rapidly and expands less far to the right than in Fig. 5-3. The calculations were done for $B/kT_D = C/kT_c = 20$ and $T_c = T_D$.

The effect of a moderate conduction on the decay and expansion of $p(x,T)$ is shown in Fig. 5-4. We assumed that the activation energies for SCL drift and ohmic conduction are the same. We also put the ultimate conductivities of the excess charges $\mu_o p_o$ and of the intrinsic carriers γ_o the same; this corresponds to $T_D = T_c$. (Like T_D, T_c is defined by $sT_c\beta(T_c) = C/kT_c$). Comparing this figure with Fig. 5-3 we see how the ohmic dissipation of the carriers increases their decay considerably. At the same time their expansion is drastically lowered by the fast decrease of the electric field at the leading front. Eventually, the leading front merely reaches $r(\infty) = 0.605\ 1$, instead of 1.

To calculate the TSD current, we eliminate $E(o,t)$ and $E(1,t)$ from Eq. 5.19 using Eqs 5.16 and 5.17; in this way we find

$$j_r(t) = -\mu(T)p^2(x_o,t)r^2(t)(1-r(t)/1)/2\varepsilon_o\varepsilon 1 \qquad ...(5.24)$$

in which the width of the charge cloud $r(t)$ is not yet specified. This quantity is determined by the drift velocity of the frontal carriers; we have

$$dr(t)/dt = \mu(T)E\{r(t),t\} = \mu(T)p(x_o,t)r^2(t)/2\varepsilon_o\varepsilon 1 \qquad (5.25)$$

An analytical solution of this equation is again not intricate when $\gamma(T) = 0$. It reads

$$1/r(T) = 1/r_o - (1/2\ 1)\ln\{1 + \delta_o\psi(T)\} \qquad ...(5.26)$$

We have seen in Fig. 5-3 that $r(T)$ is an increasing function, which cannot exceed 1. When the carrier front reaches the right electrode, the charge distribution becomes symmetrical and external current flow *ceases* abruptly. The transit temperature, T_λ, at which this happens, is given by

$$1 + \delta_o\psi(T_\lambda) = \exp\{2(1/r_o - 1)\} \qquad (5.27)$$

if $\gamma(T) \simeq 0$. This equation can be solved for T_λ by using the simple expansion of the exponential integral, Eq. 2.20.

By substituting Eqs 5.22 and 5.26 into Eq. 5.24, the generated current is found explicitly. In order to calculate the current for the *general* case that $\gamma(T)$ is *not zero* and *not proportional* to $\mu(T)$ we solved the ODE's 5.21 and 5.25 on a computer by a 4th order Runge-Kutta method, with step-size control*.

As indicated, the released current is negative, which means that it flows to the left within the sample, see Fig. 5-1. Thus it is *opposite* to the homopolar charging current, as it should be. On the other hand it has the same sign as its corresponding dipolar current, so that a homocharge virtually behaves like a heterocharge, intensifying the current of the latter whenever aligned dipoles are present. By contrast, the dif-

*Runge-Kutta's Method, Fortran-Subroutine RKGS, IBM Scientific Subroutine Package, Version 3, 1968, pp 333-335. One may also use Hamming's Predictor-Corrector Method, pp 337-341.

fusion current of a mono-electret flows in the opposite direction; this current will thus weaken the SCL current.

At the transit temperature the zero-field point (ZFP) x_o reaches its final value 1/2. Thus the ZFP moves to the middle of the polymer. This happens at a velocity which is proportional to $j_r(t)$. To prove this, we particularize Eq.5.18 at x_o

$$j_r(t) = \varepsilon_o \varepsilon \partial E(x_o,t)/\partial t$$

now $dE(x_o,t)/dt = \partial E(x_o,t)/\partial t + \partial E(x_o,t)/\partial x \; dx_o/dt = 0$ and in view of Eq. 5.15 we get

$$j_r(t) = -p(x_o,t)dx_o/dt \qquad (5.28)$$

This equation has been used, in particular in numerical work, to calculate the external current (MH 67). However, we have always preferred Eq. 5.19, because it is less sensitive to discretization errors in p(x,t) and E(x,t).

Of course, we are also interested in the released charge density

$$q_r(t) = \int_0^t j_r(t)dt \qquad (5.29)$$

The evaluation of Eq. 5.29 is straightforward when $\gamma(T) = 0$. As a function of r(t)/1 the result is given by

$$\frac{q_r(t)}{p_o r_o} = -\frac{r_o}{21}\left\{1 - \frac{r^2(t)}{r_o^2}\, e^{2(1/r(t) - 1/r_o)}\right\} \qquad ...(5.30)$$

which reduces to Eq. 5.32 (below) when r(t) becomes 1. For the general case we have obtained $q_r(t)$ numerically. A very direct way to calculate its ultimate value, $q_r(T_\lambda)$, is as follows (see Fig. 5-5).

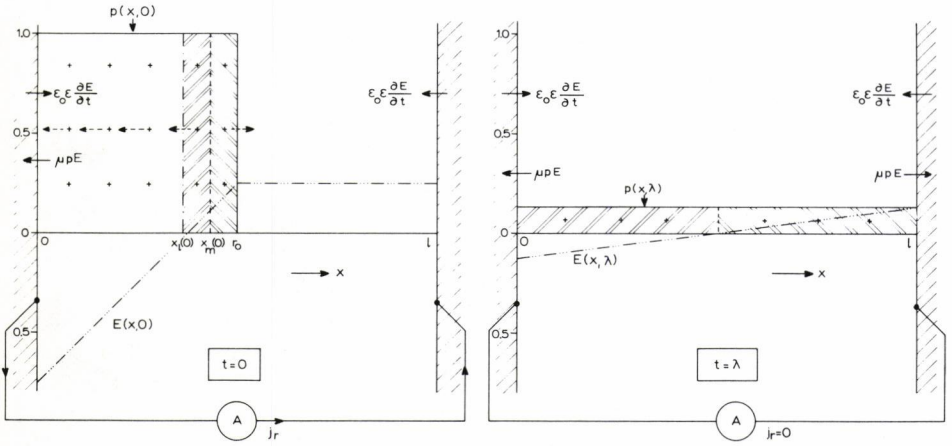


FIG.5-5 Charge release by SCL drift can best be evaluated at x = 1, where there is only a displacement current up to t = λ. Within that time, all charges between x = 0 and $x_1(o)$ have moved towards x = 0, where they are neutralized. Simultaneously, the charges between $x_1(o)$ and r_o have filled the sample uniformly ($x_1(o)$ and $x_m(o)$ are specified in Section 3:3).

As long as $T < T_\lambda$, we have $p(1,t) = 0$, so that if $\gamma(T) = 0$

$$j_r(t) = \varepsilon_o \varepsilon dE(1,t)/dt, \quad t \leq \lambda$$

Consequently,

$$q_r(\lambda) = \varepsilon_o \varepsilon \{E(1,\lambda) - E(1,o)\} \tag{5.31}$$

where λ is the transit time of the leading front of the expanding charge cloud. According to Eq. 5.17 we have $E(1,\lambda) = p(x_o,\lambda)1/2\varepsilon_o\varepsilon$, in which $p(x_o,\lambda)$ follows from Eqs 5.22 and 5.27. After some manipulations we find

$$q_r(\lambda)/p_o r_o = -(r_o/2\ 1)\{1 - (1^2/r_o^2)e^{2(1-1/r_o)}\} \quad \ldots(5.32)$$

For small penetration depths we have approximately

$$q_r(\lambda)/p_o r_o \simeq -r_o/2\ 1 \tag{5.33}$$

Since, in particular at low forming temperatures, the penetration of homocharges is no more than a few microns we may conclude from these formulas that only a current TSD based on *foils* is worthwile. Homocharges in thick electrets can hardly be observed. Clearly, if e.g. r_o = 5 μm and 1 = 25 μm, the final charge released is only 10% of the charge originally stored.

Since the initial charge $p_o r_o$ is not known experimentally, it is more logical to compare $q_r(\lambda)$ with the effective surface charge density of the foil q(o) measured just before TSD is started. This quantity can be determined with the tiny compensating charge meter described in (Tu 70a) or with the new apparatus for charge TSD of Sect. 9:1; it amounts to

$$q(o) = p_o r_o(1 - r_o/2\ 1) \tag{5.34}$$

Taking absolute values, we find for $r_o < 0.25\ 1$

$$q_r(\lambda)\{q_r(\lambda) + q(o)\}^{-1} \simeq r_o/2\ 1 \quad \ldots(5.35)$$

This is a very useful formula, because it allows one to estimate the penetration depth, r_o. Sessler and West (SW 70) and Perlman et al. (CP 71) were the first to point this out. Obviously, for larger $r_o/1$ values the exact formula Eq. 5.32 should be used.

Fig. 5-6 shows the ultimate charge density as a function of the initial penetration depth. The curve is asymmetric because if $r_o > 1/2$ the carriers are spread more quickly and less charge is measured. The maximum occurs at r_o = 0.39 1, but even then only 14% of the original charge is observed. Obviously current TSD involving SCL drift is rather inefficient, even when there is no ohmic conduction. The figure also illustrates the dependence of the current maxima on $r_o/1$. Taking the excess-charge density p_o to be constant, we have normalized to j_m $(r_o/1 = 0.1)$*.

*Note that in Fig. 5-8 (below) part of the dependence of the current on r_o is obscured by our normalization to $q_o = p_o r_o$.

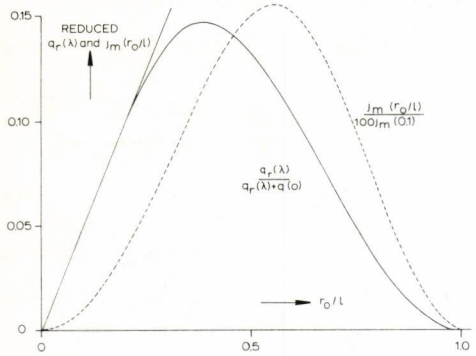


FIG.5-6 Reduced ultimate charge, released by SCL drift in a non-conducting polymer, as a function of the relative penetration depth, $r_o/1$. The dependence of the normalized current maximum on $r_o/1$ is also shown.

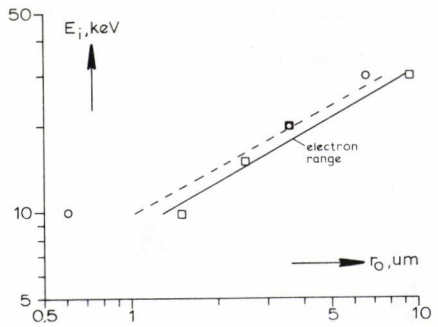


FIG.5-7 Mean penetration depth r_o of electrons shot into Teflon-FEP of 25.4 μm at energies from 10 to 30 keV. The results calculated by means of Eq. 5.33, are shown for injection into two-sided metallized Teflon-FEP (circles) and one-sided metallized Teflon-FEP (squares), and are compared with the so-called electron range known from the literature (full line).

We see that current-ratio curve extends over a similar range as the charge-ratio curve. The current ratio is low, at low as well as high penetration levels, reaching a maximum for r_o = 0.56 1. Obviously, if in a particular experiment, say electron bombardment, p_o is a constant, and the penetration depth is not, the current curve can be used to find to the ratios of the various penetrations. Because of the importance of the charge and current ratios for the evaluation of r_o from experimental data, they are given numerically at various $r_o/1$ in Table 5-1.

Fig. 5-7 shows the calculated penetration depths of electrons shot into Teflon-FEP. The values found from TSD current measurements are slightly lower than those cited for the electron range (BS 64, Fo 72). The values for injection into one-sided metallized FEP show the best agreement, because the electron-range values also pertain to non-metallized samples. The straight line corresponding to the points measured has a slope of 1.8, i.e. $r_o \propto E_i^{1.8}$, whereas the electron range conforms to $r_o \propto E_i^{1.75}$. Note that even for these high injection energies, the penetrations are low; for 20 keV we find for instance r_o = 3.6 μm.

As suggested by Sessler (Se 72) Eq. 5.35 can readily be generalized to non-uniform spatial distributions. Obviously we have quite generally

$$q_r(\lambda)\{q_r(\lambda) + q(o)\}^{-1} \simeq E(1,o)\{E(1,o) + E(o,o)\}^{-1}$$

which, by virtue of Eqs 5.16 and 5.17 becomes

$$q_r(\lambda)\{q_r(\lambda) + q(o)\}^{-1} \simeq \bar{r}/1 \qquad (5.36)$$

where $\bar{r}$ is the mean spatial depth, $\bar{r} = \int_0^1 xp(x,o)dx / \int_0^1 p(x,o)dx$. Note that for a uniform distribution $\bar{r} = r_o/2$.

TABLE 5-1 Ultimate Charge Released and Maximum Current for SCL Drift in Mono-Electrets as Functions of Penetration Depth

$\frac{r_o}{1}$	$\frac{q_r(\lambda)}{p_o r_o}$	$\frac{q_r(\lambda)}{q_r(\lambda)+q(o)}$	$\frac{j_m(r_o/1)}{j_m(o.1)}$
0.05	0.250 E-1	0.250 E-1	0.260 E-1
0.1	0.500 E-1	0.500 E-1	0.100 E+1
0.2	0.992 E-1	0.992 E-1	0.376 E+1
0.3	0.134 E+0	0.136 E+0	0.774 E+1
0.4	0.138 E+0	0.147 E+0	0.120 E+2
0.5	0.115 E+0	0.133 E+0	0.150 E+2
0.6	0.803 E-1	0.103 E+0	0.152 E+2
0.7	0.469 E-1	0.673 E+0	0.121 E+2
0.8	0.209 E-1	0.337 E-1	0.702 E+1
0.9	0.515 E-2	0.927 E-1	0.223 E+1

5:3.3 Model Thermograms of Mono-Electrets with a Uniform Charge Distribution

Thermograms of $j_r(T)$ and $q_r(T)$ are shown in Fig. 5-8 for several penetration depths. We assumed a perfect insulator, i.e. $\gamma(T) = 0$ and took $B/kT_D = 20$. Of the normalizing constants $q_o = p_o r_o$, while T_D and $\delta_D = \delta(T_D)$ are defined by Eq. 5.39 putting $T_m = T_D$. For comparison, a Debye dipole thermogram is also given. For $r_o < 0.5\ 1$, the space charge current thermograms appear to be broader and lower than the latter, only their *initial rise* being *identical*. The height of the current maxima

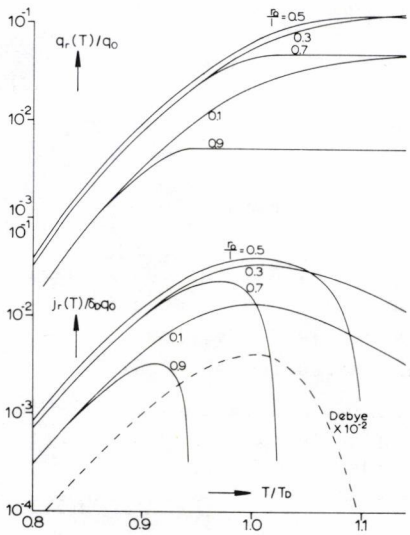


FIG. 5-8 Charge and current thermograms for SCL drift in a nonconducting polymer foil at various penetration depths, $r_o/1$; we assumed $B/kT_D = 20$. From the inserted Debye thermogram we see that the initial rise of the current thermograms is solely determined by B/kT_D.

varies with r_o/l , reaching an optimum value for $r_o = 0.45$ 1. Surprisingly, the position of the maximum, T_m, is not always characteristic of the polymer; for it is not determined by $\mu(T)$ alone, but it also depends on r_o/l. Specifically, for $r_o > 0.5$ 1, T_m departs from T_D and shifts to lower temperatures; the current flow ceasing abruptly when the transit temperature T_λ is reached. As a result the ultimate charge is reached at a lower temperature. Owing to the normalization to $q_o = p_o r_o$, the curves for r_o/l and $1-r_o/l$ rise similarly. For experimental results on the r_o/l dependence we refer to Fig. 10-35; it gives some thermograms of electron-bombarded Teflon-FEP. The currents increase with injection energy, because the penetration becomes larger (cf. Table 10-1).

5:3.3a Location of the TSD Current Maximum

On differentiating Eq. 5.24 with respect to T, we find the following condition for the location of the *current maximum*

$$2(\delta_m^* + \beta_m) - (2 - 3r_m/l)(1 - r_m/l)^{-1}\delta_m^* r_m/2l = B/skT_m^2 \qquad (5.37)$$

where $\delta_m^* = \mu_m p_m/\varepsilon_o\varepsilon$, in which m refers to T_m; thus $\mu_m = \mu(T_m)$, etc. Note that p_m follows from Eq. 5.22, while r_m is given by Eq. 5.26 and Fig. 5-9 (below). For a small intrinsic conduction, i.e. $\beta_m \simeq 0$, and $r_o < 0.5$ 1, Eq. 5.37 reduces to

$$2sT_m\delta_m^* = B/kT_m \qquad (5.38)$$

After eliminating p_m by Eq. 5.22 and approximating $\psi(T_m)$ with Eq. 2.20 in the usual way. Eq. 5.38 can be written as

$$sT_m\delta_m \simeq B/kT_m \qquad (5.39)$$

where $\delta_m = \delta_o e^{-B/kTm}$. Since Eq. 5.39 was assumed to hold *exactly* for the normalizing temperature T_D of the graphs, we have for small penetrations, $T_m \simeq T_D$, which agrees with Fig. 5-8. Consequently, in Fig. 10-35, the penetrations cannot have exceeded 0.5 1. If, conversely, an intrinsic conduction, with activation energy C, dominates we have for the location of the maximum

$$2sT_m\beta_m = C/kT_m \qquad (5.40)$$

where $\beta_m = \beta_o e^{-C/kT_m}$.

In Sect. 8:2 we will compare the location of the maxima in current TSD with those of charge TSD. It then turns out that the TSD charge transitions emerge at a higher temperature. For $B/kT_D = 40$, and $r_o/l = 0.1$ we find for example the current maximum at T_D, and the charge transition at 1.06 T_D. Whenever such a difference is found in practice, it indicates that SCL drift governs the excess-charge decay, for neither ohmic conduction nor diffusion show such a remarkable behaviour.

Fig. 5-9 illustrates how $r(T_m)$ varies with r_o/l. It is remarkable that this quantity becomes at most 20 % larger than r_o/l. Up to $r_o = 0.2$ 1, r(t) hardly exceeds r_o, because most of the charges move towards the left electrode. So for corona charged foils, which are near-surface charged, r(t) can approximately be taken constant, as was done by Creswell and Perlman (CP 70).

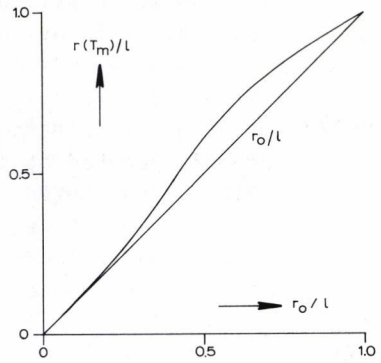


FIG. 5-9 Comparison between the reduced spatial width at T_m, and the original reduced width $r_o/1$.

Fig. 5-10 demonstrates a trial fit, based on Eq. 5.24, to the α peak of electron-bombarded Teflon-FEP. The calculated thermogram, which corresponds to 1.2 eV, coincides broadly with the data, deviating at high and low temperatures. As mentioned in Sect. 1:5, we obtained strong ev-

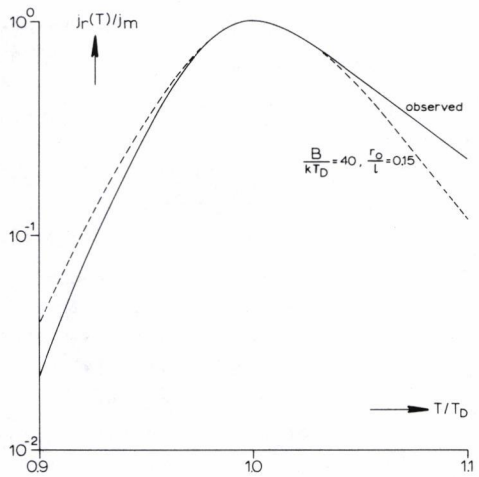


FIG.5-10 A trial fit to the α peak of electron-bombarded Teflon-FEP, charged to 20 nC/cm^2 at 20 keV. We assumed the mono-electret to be uniformly charged to $r_o/1 = 0.15$, and took as the reduced activation energy $B/kT_D = 40$, where $T_D = 353$ °K.

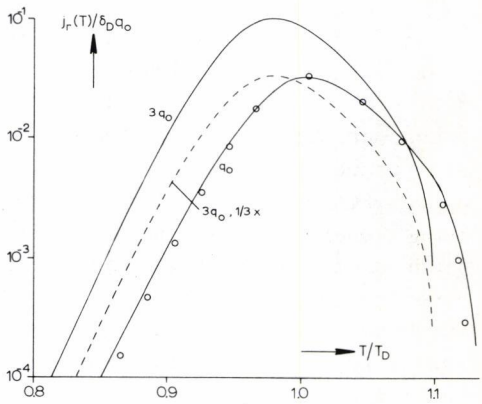


FIG.5-11 Current release of SCL drift for a threefold increase in the initial charge density. For the two full lines the current is normalized to q_o, and for the broken line and for the encircled points it is normalized to 3 q_o. The maximum of the curve for 3 q_o appears at a lower temperature than for the curve of q_o, but the actual shape of the thermogram hardly changes. This means that the current varies almost linearly with the initial charge, provided that its temperature scale is shifted properly (circles). We chose $r_o/1 = 0.3$ and $B/kT_D = 40$.

idence that the electrons are trapped in this polymer, and so their thermal release from these traps actually is the governing discharge rate. However, since retrapping in Teflon-FEP is fast, the theory described is still applicable, provided that only one trapping level is involved. The deviations indicated arise because this is not the case in FEP.

Reconsidering Eq. 5.24, we see that the TSD current depends quadratically on the charge residing in the electret, $p(x_o,t)r(t)$. This does *not* mean, however, that the entire current plot is shifted by a factor of 9 when the initial charge is three times larger. As can be seen from Fig. 5-11, this is only the case at low temperatures. At high temperatures the increase is annulled, by the faster expansion of the charge cloud, which lowers the term $1-r(t)/1$. The maximum therefore only increases by a factor of three. This could be expected, for the ultimate charge is only three times larger. For the higher initial charge, the maximum occurs at a *lower* temperature, because the field driving the carriers is higher, and the sample becomes discharged sooner. Interestingly, if the curve 3 q_o is shifted towards the curve for q_o, so that the maxima coincide both thermograms become almost the same. For experimental results on the initial-charge dependence we refer to Fig. 10-36.

So far we have neglected the ohmic conduction of the polymer. Fig. 5-12 displays how it lowers the released current and charge by dissipating the moving excess charges. At low temperatures, when the loss of excess charges is still small, the thermograms coincide with those of a non-conducting polymer. But at higher temperatures, large differences appear, in particular for r_o = 0.1 and 0.5 1; their current plots drop much sooner, so that the maxima are shifted to below T_D. From calculations on the spatial width r(T), we found that the carriers remaining never reach x = 1. By contrast, for r_o = 0.9 1 the differences for $\gamma = 0$ and $\gamma \neq 0$ are small, because then the carriers hardly have to spread to attain x = 1. The interaction between ohmic dissipation and spatial expansion is best illustrated by indicating the ultimate charges released. Referring to the curves of Fig. 5-12 they amount to 4.05, 1.40 and 0.47% of $p_o r_o$, whereas from Fig. 5-8 the respective figures are 11.5, 5.0 and 0.52% of $p_o r_o$. The calculations for $\gamma(T) \neq 0$ were done for $B/kT_D = C/kT_c = 20$, on the plausible assumption that $\mu(T)$ and $\gamma(T)$ show the same temperature dependence. We also took $T_D = T_c$; this implies that the ultimate conductivities $\mu_o p_o$ and γ_o are the same. Yet it may occur that the injected carriers have another mobility than the intrinsic carriers of the polymer. In this case the thermograms will also show only one current maximum, which occurs, e.g. just below T_D, when $T_D < T_c$. Since the carriers will first respond to the fastest process.

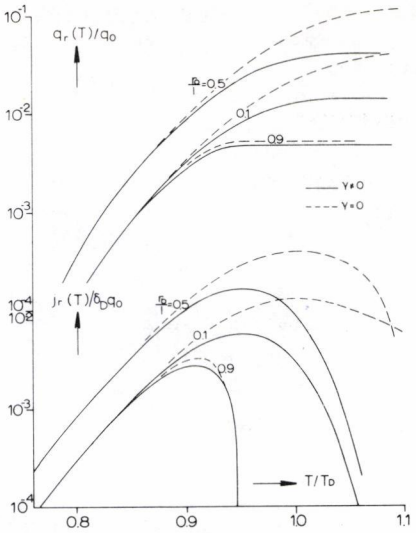


FIG. 5-12 Effect of ohmic conduction on the charge and current thermograms for SCL drift. The curves for low penetrations are most affected, in particular when ohmic conduction increases sharply, i.e. at high temperatures.

5:3.3b Ultimate Charge Released by Weakly Conducting Mono-Electrets

Of course it is of interest to estimate analytically the effect of ohmic conduction on the charge release. This can be done by supposing that the mobilities of the excess and intrinsic carriers vary identically, i.e. $\mu(T) = \mu_o a(T)$ and $\gamma(T) = \gamma_o a(T)$.

Instead of Eq. 5.31 we then have by integrating Eq. 5.18 at x = 1

$$q_r(\lambda) = \varepsilon_o \varepsilon\, E(1,\lambda) - E(1,o) + \gamma_o \int_o^\lambda a(T)E(1,t)dt \qquad (5.41)$$

Expressions for $E(1,\lambda)$ and $E(1,o)$ are readily found from Eqs 5.16 and 5.17 and we can eliminate the integral $\int_o^\lambda a(T)E(1,t)dt$ by integrating Eq. 5.25.

Substitution of the resulting expressions into Eq. 5.41 yields

$$q_r(\lambda) = p(x_o,\lambda)1/2 - p_o r_o{}^2/2\ 1 + (1-r_o)\gamma_o/\mu_o \qquad (5.42)$$

The value of $p(x_o,\lambda)$ follows from solving Eq. 5.21

$$\gamma_o/\mu_o p(x_o,\lambda) = (1 + \gamma_o/\mu_o p_o)e^{\int_o^\lambda \beta(T)dt} - 1 \qquad (5.43)$$

For the only unknown left, λ, we return to the differential equation 5.25, which after integration gives

$$e^{-\int_o^\lambda \beta(T)dt} = 1 + \{1 - e^{2(1/r_o - 1)}\}\gamma_o/\mu_o p_o \qquad (5.44)$$

By eliminating $\exp(\int_o^\lambda \beta(T)dt)$ from Eq. 5.43 and substituting $p(x_o,\lambda)$ in Eq. 5.42 we finally obtain

$$\frac{q_r(\lambda)}{p_o r_o} = \frac{q_r(\lambda)}{p_o r_o}\Big|_{\gamma = 0} + \frac{\gamma_o}{\mu_o p_o}\frac{1}{2r_o}\left(1 + e^{2(1-1/r_o)} - \frac{2r_o}{1}\right) \qquad (5.45)$$

If the intrinsic conductivity, γ_o, remains well below the excess charge conductivity, $\mu_o p_o$, Eq. 5.45 reduces to Eq. 5.32, as it should. For higher conductivities appreciably less charge is released, because most of the carriers are dissipated by ohmic conduction before they drift away.

The equations given presuppose that the carrier front reaches x = 1, which is by no means trivial. In Fig. 5-12 it only occurred for r_o = 0.9 1. At high conductivities and low penetration depths, however, it may happen that all carriers have been dissipated before 1 is ever reached. The highest value of $\gamma(t)$ for which Eq. 5.45 still holds, follows from Eq. 5.44

$$\gamma_o/\mu_o p_o \leq \{e^{2(1/r_o - 1)} - 1\}^{-1} \tag{5.46}$$

For higher conductivities, the ultimate charge is attained when t = ∞, whereby $p(x_o,\infty)$ = 0; we must then replace 1 in the last term of Eq. 5.42 by r (∞). This results in an ultimate charge density of

$$q_r(\infty) = -p_o r_o^2/2\ 1 + \{r(\infty) - r_o\}\gamma_o/\mu_o \tag{5.47}$$

in which $r(\infty)$ can be found from integrating Eq. 5.25

$$1/r(\infty) = 1/r_o - (1/2\ 1)\ \ln\ (1 + \mu_o p_o/\gamma_o) \tag{5.48}$$

The value of γ_o for which Eq. 5.46 is an identity sets an upper limit to Eq. 5.47, which is at the same time the lower limit of Eq. 5.45.

Eqs 5.45 and 5.47 can be used to check the ultimate charge reached in Fig. 5-12, for which $\gamma_o = \mu_o p_o$. Since Eq. 5.46 is violated for r_o = 0.1 and 0.5 1, we should use Eq. 5.47 for these depths, whereas for r_o = 0.9 1, Eq. 5.45 is appropriate. In this way we readily verify the figures cited for the ultimate charges in Fig. 5-12.

Fig. 5-13 illustrates a striking consequence of the combined decay of the excess charges by SCL drift and ohmic conduction. Inspection of the upper curves shows that for γ = 0 (no conduction) the ultimate charge is *independent* of the heating rate. For $\gamma \neq 0$ this is not the

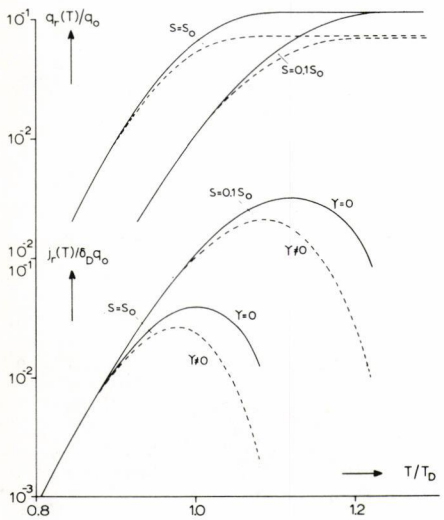


FIG. 5-13 Effect of a change in heating rate on the current and charge release for SCL drift. The upper curves show that the ultimate charge varies *slightly*, if the electret is conductive ($\gamma \neq 0$) and if the temperature dependences for SCL drift and ohmic conduction are different. We took $r_o/1$ = 0.5, $B/kT_D = C/kT_C$ = 20 and T_C/T_D = 1.05.

case, if the SCL drift and ohmic conduction have a *different* temperature dependence. Then the ultimate charge is slightly lower (viz. 4.3%) for a tenfold increase in heating rate.

This discrepancy arises from the different extent to which the responses for SCL drift and ohmic conduction are shifted to higher temperatures for higher heating rates. As a result the contribution of the unnoticed ohmic charge decay becomes relatively larger than at lower heating rates. This behaviour is typical of any excess-charge decay in which one of the decay mechanisms does not manifest itself externally. It does not occur in a dipole reorientation. Gross was the first to call attention to this phenomenon, when he discussed the TSD of lumped dielectric models (Gr 70). The lower curves in the figure, which give the current dependencies, behave like those of a Debye relaxation (cf. Fig. 2-8). They increase for the higher heating rate and shift to higher temperatures. Only the initial rate, which is solely determined by the activation energies, is the same for the two heating rates.

Experimentally we often found more than one current peak. A thermogram of a negatively charged Teflon-FEP thermo-electret is shown in Fig. 10-34. Two rather broad, but well separated, maxima appear which might be attributed to injected carriers of different mobility; either ions and/or electrons are deposited. Ions that are likely to occur in negative discharges in air have been specified by Shanin (Sh 69) and by Hayhurst et al. (HP 67). They mention e.g. NO_2^-, O_3^-, CO_3^-, $CO_3^-.H_2O$. Yet the assumption of a very broad spectrum of mobilities seems not to be justified. It is even incorrect to attribute the first peak to, e.g. electrons and the second to ions, since for positive coronas we also obtain two peaks. Moreover, by a multi-stage charge TSD we could prove that the injected carriers are specifically trapped at sites of various energies. In this case it is the thermal release of the carriers from their different traps that is the dominating rate process.

If trapping is to be favoured over the thermally activated mobility, the results of this chapter are still useful. For we shall prove in Chap. 11 (App. I) that they also hold for the *release from traps* that show *severe retrapping*.

Inspection of Fig. 5-14 shows that a two-stage current TSD actually gives evidence for trapping and retrapping in Teflon-FEP. First of all, the current maximum shifts from 85° to 96 °C after the first heating run, and concurrently the initial current slope becomes steeper giving an activation energy of 2.1 eV instead of 1.8 eV. This is understandable, because the electrons in shallow traps are released first, those in deeper traps getting their chance in the second heating run. The phenomena observed favour trapping, combined with *fast* retrapping, for they would not occur if ohmic conduction would prevail, or if recombination of the released charges would be fast (CP 70).

The change in activation energy found is typical of a distribution of traps; for a single trapping level the initial slope would not alter. This can be seen from model calculations on a multi-stage current TSD, portrayed in Fig. 5-15. Now, only the current maximum is shifted, but the initial slope does not increase. The shift of the current maximum is plausible. It occurs because the excess charges are gradually depleted, so that they create a *lower* driving field and are swept less quickly towards the electrodes.

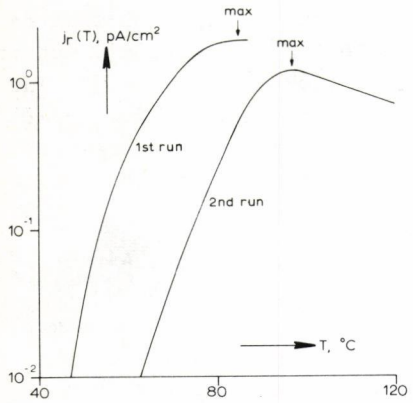


FIG.5-14 Results of a two-stage current TSD of electron-bombarded Teflon-FEP foil. They are in qualitative agreement with the predictions of Fig. 5-15. The injection energy was 30 keV and the deposited charge was 20 nC/cm^2.

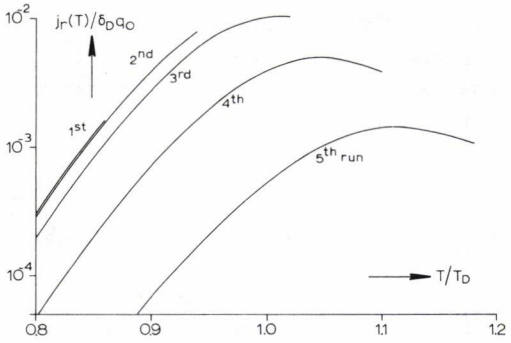


FIG.5-15 Current by SCL drift in a uniformly charged mono-electret during a multi-stage TSD. The current maximum gradually shifts to higher temperatures, so that the electret becomes more stable. We assumed $r_o/l = 0.1$ and $B/kT_D = 20$; see Fig. 5.14 for experimental results on Teflon-FEP.

The shift of the current maximum and the emptying of the shallow traps just reported for Teflon-FEP electrets are of prime importance for practical applications. They imply that the decay of these superb electrets can be further improved by *preheating*.

So far we have assumed that the excess charges occupy the foil continuously up to r_o. Another model, which can also be solved analytically, is depicted in Fig. 5-16. Similar to the distribution of Fig. 5-2 it will remain uniform for $t > 0$. This charge sheet approximately represents the charge pattern within, electron-bombarded polymer foils (SW 70). It arises, because the high-energy electrons (10 keV or more) must be slowed down before they are captured. The absence of electrons in the outer layer probably explains the stability of such foils in the presence of humidity. We also mention this case because Schumann (Sc 33) studied the motion of such charge sheets as early as 1933. Unfortunately, his calculations are in error because he ignored the spreading of the sheet. The correct solution should follow the lines just described.

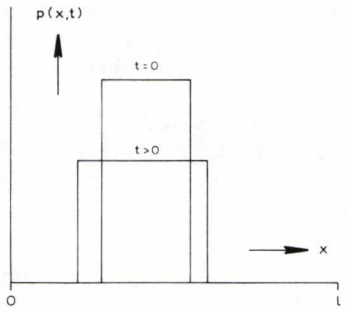


FIG.5-16 The sheet distribution as a model for electron-bombarded foils.

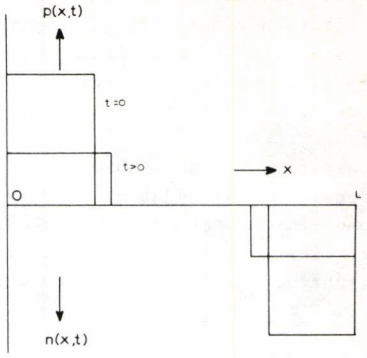


FIG.5-17 A bipolar excess charge distribution, the SCL drift of which can be solved analytically.

5:3.3c Charge Release of a Bipolarly Charged Electret

An analytical solution for a hetero-electret, which is bipolarly charged, is severely limited. Neglecting intrinsic conduction of the polymer, we then have the continuity equations

$$\partial p(x,t)/\partial t = -\mu(T)\, p(x,t)E(x,t)/\partial x$$
$$\partial n(x,t)/\partial t = \mu(T)\, n(x,t)E(x,t)/\partial x \qquad (5.49)$$

and Poisson's equation 5.5. Lately, Calderwood and Scaife (CS 70)discussed an isothermal solution of these PDE's for uniform charge distributions. They tacitly assumed that the positive and negative carriers were completely separated (see Fig. 5-17). Such a restriction, however, is *unrealistic* because it results in a discharge current flowing in the direction of the charging current; such a homopolar current contradicts common experience. Apart from this it implies an infinite recombination rate.

This unusual behaviour of separated bipolar charge distributions can be proven quite generally without solving the PDE's. The discharge current obeys

$$j_r(t) = \varepsilon_o \varepsilon \partial E(x,t)/\partial t + \mu(T)\{p(x,t) + n(x,t)\}E(x,t) \qquad (5.50)$$

Now, for positive and negative carriers of equal mobility the charge distribution is likely to be symmetrical. In this case integration of Eq. 5.50 gives

$$j_r(t) = 2\mu(T) \int_0^{1/2} p(x,t)E(x,t)dx$$

since $\int_0^{1/2} E(x,t)dx = 0$, and $p(x,t) = 0$ for $x \leq 1/2$. By eliminating $p(x,t)$ with Eq. 5.5 we finally obtain

$$j_r(t) = \{\varepsilon_o \varepsilon \mu(T)/1\}\{E^2(1/2,t) - E^2(o,t)\}$$

in which $E(o,t) > |E(1/2,t)|$. Consequently, the released current is indeed *negative*, i.e. it is directed to the left.

By contrast, we abandoned the restriction of a separated bipolar distribution for hetero-electrets, and solved the PDE *numerically*. In this way we obtained a normal heteropolar discharge current, compare Sect. 5:4.2.

Nevertheless, it seems worth indicating the ultimate released charge for the distribution of Fig. 5-17, to get an idea of the value to be expected for more realistic bipolar distributions. Furthermore, the model is representative of a bipolarly charged homo-electret. This has a discharge current of the same sign. Moreover, we can imagine that the injected positive and negative charges are well separated.

Calderwood et al. state that current flow ceases when the leading fronts of the positive and negative carriers meet at time λ, i.e. when $r_p(\lambda) + r_n(\lambda) = 1$. Beyond time λ they suppose the carriers to be annihilated by recombination.

For the uniform, symmetrically expanding distributions of Fig. 5-17 one finds a discharge current similar to that of Eq. 5.24

$$j_r(t) = -\mu(T)p^2(x_o,t)r_p^2(t)(1-2r_p(t)/1)/\varepsilon_o\varepsilon \; 1 \qquad (5.51)$$

Integrating this equation between t = 0 and λ, we obtain

$$q_r(\lambda)/p_o r_p(o) = -(r_{to}/2\; 1)\{1 - 1^2/r_{to}^2\; e^2(1-1/r_{to})\} \qquad (5.52)$$

which is identical to Eq. 5.32 except that r_o has been replaced by the total penetration depth $r_{to} = r_p(o) + r_n(o)$. Similarly, we get instead of Eq. 5.34 for the effective surface charge

$$q(o) = p_o r_p(o)(1 - r_{to}/2\; 1)$$

Consequently, Eq. 5.35 also holds, provided that r_o is replaced by r_{to}.

Assuming that $r_{po} = r_{no} < 1$, Gross has, in a heuristic way, also derived a formula for the ultimate charge released by bipolar electrets. His result (Eq. 20 in Gr 71) is a factor of two larger than the exact result.

5:3.4 Evaluation of SCL-Drift Data of Mono-Electrets

In the above, we have indicated how to calculate the penetration depth. The other relevant quantities are the initial charge density p_o, the mobility μ and the activation energy B. The penetration being known, p_o can be found from $q_r(\lambda)$ or $q(o)$ (see Eqs 5.34 and 5.35). For the mono-electret of Fig. 5-10 we had $q(o) = 17$ nC/cm^2, which gives $p_o \simeq 3\times10^{15}$ electrons/cm^3. The mobility μ can be evaluated from, e.g. the condition for the current maximum stated in Eq. 5.38, provided that B is known. For $B/kT_D = 40$ and $T_D = 353$ °K we find $\mu_o = 150$ cm^2/Vs and $\mu(25°) = 2.6\times10^{-16}$ cm^2/Vs. This is an extremely low value, which would correspond to a ridiculously low diffusion constant, according to Einstein's relation. Thus, it again appears that the injected electrons are trapped instead of being virtually free to move and so their effective mobility is in fact determined by the trapping and retrapping rates, which may be quite low.

We now come to the calculation of the activation energy. In connection with Fig. 5-8 we mentioned that the initial current slope depends solely on the activation energy. Thus the activation energy can in turn be derived from the initial slope. Unfortunately, this only gives a short straight line for low temperatures. We see from Fig. 5-18 that

this can scarcely be improved by plotting the ratio $j_r(T)/q_s(T)$, where $q_s(T) = q_r(\lambda) - q_r(T)$. According to Wintle (Wi 71) a greater improvement is obtained by plotting the charge ratio $q_r(T)/q_s(T)$. However, we shall show below that it is more accurate to map $T_D^2 q_r(T)/q_s(T)T^2$; this has been done in Fig. 5-18. We see that the latter linearization

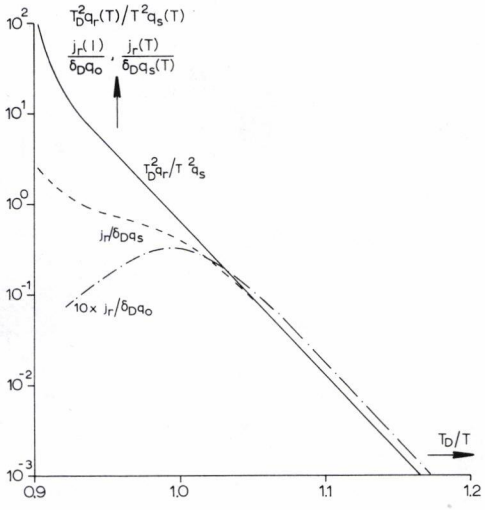


FIG.5-18 Three methods for finding the activation energy from the current thermograms of SCL drift. The longest straight line is obtained for the charge-ratio plot and so this should be preferred to the initial-rise method (j_r/q_o), and to the BFG plot (j_r/q_s). The calculations were made for $B/kT_D = 40$ and $r_o/1 = 0.3$.

is correct to temperatures as high as 1.09 T_D. This is therefore the best method for finding the value of the activation energy.

The validity of this new linearization can be proved as follows. By combination of Eqs 5.30 and 5.32 we find

$$\frac{q_r(t)}{q_s(t)} = \frac{r_o^2 - r^2(t)e^{2(1/r(t)-1/r_o)}}{r^2(t)e^{2(1/r(t)-1/r_o)} - 1^2 e^{2(1-1/r_o)}} \simeq \delta_o \psi(T) \qquad (5.53)$$

The approximation holds for $r_o < 1$ under the assumption that $r(t) \simeq r_o$ for which $T \leq T_D$, according to Eq. 5.26 and Fig. 5-9. Using the simple approximation for the exponential integral, and eliminating δ_o by means of Eq. 5.38 we can rewrite Eq. 5.53

$$T_D^2 q_r(T)/T^2 q_s(T) \simeq \exp\,(-B/kT + B/kT_D)$$

which gives precisely the linear dependence shown in Fig. 5-18.

The *linearity* of the ratio of the released charge to the stored charge is *typical* of SCL drift. It presumably occurs, because it is the stored charge that determines the decay rate of the retained charge. This is not so for the other decay mechanisms, which violate the linearity. This is illustrated in Fig. 5-19 for the model thermograms of a dipole reorientation. Now, the BFG plot, $j_r(T)/q_s(T)$ vs. T_m/T, is the only straight line. The same holds for diffusion and for the thermal

release from traps showing retrapping (CP 70). Apparently, the charge-ratio plot can be invoked for *distinguishing* thermally stimulated SCL drift (and, mutatis mutandis, also thermal release from traps with *fast* retrapping) from the other decay processes.

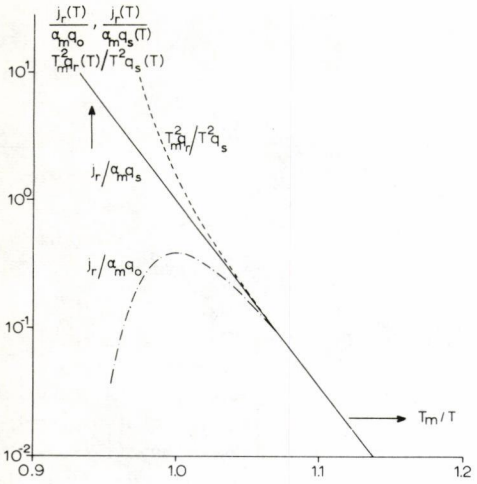


FIG.5-19 Application of the three methods of Fig. 5-18 to TSD current thermograms resulting from processes other than SCL drift, such as dipole reorientation, diffusion, and release from traps accompanied by a fast recombination. For these processes only the BFG plot (j_r/q_s) is straight. The graphs of the charge ratio (q_r/q_s) and of the normal current (j_r/q_o) begin to deviate from T_h onwards. We took $kT_m/A = 0.03$.

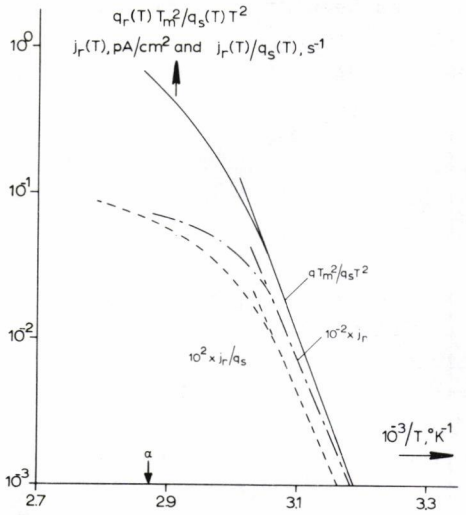


FIG. 5-20 Calculation of the activation energy from the current at the α peak of electron-bombarded Teflon-FEP (30 keV, 20 nC/cm²). The charge-ratio plot yields an activation energy A = 2.3 eV, while the initial rise and BFG plots give A = 2.0 eV.

As an example, we consider the three plots for calculating the activation energy of electron-bombarded Teflon-FEP (Fig. 5-20). We see that the charge-ratio plot deviates less from the straight line than the two other plots; this speaks in favour of fast retrapping. The activation energies found are 2.3 and 2.0 eV. The latter value agrees well with the value of 1.9 eV given by Creswell et al. (CP 71), which was also deduced from a BFG plot. An activation energy of 2.0 eV, corresponds to $B/kT_D = 65$, which is considerably higher than the value of 40 needed to fit the whole thermogram in Fig. 5-10. The discrepancy arises from the fact that there is a distribution of trapping levels.

5:4 SCL Drift of Spatially Nonuniform Excess Charges

We have seen that an analytical solution is only feasible for uniform excess charge distributions. This is a severe restriction, since neither the injected homocharge, nor the heteropolarization due to excess-

charge accumulation near the electrodes can be expected to be uniform. Furthermore, both chargings may involve carriers of different mobilities.

To cope with more general problems we solved the PDE's numerically. This was done by replacing the partial derivatives by finite differences; we tried several difference schemes. Good results were obtained with the fast two-step Lax-Wendroff-Richtmyer (LWR) scheme (RM 67), but the central Wendroff-Thomée (WT) scheme (Th 62) yielded even better results. Unfortunately, the latter requires more computer time. The modified LWR scheme proposed by Gourlay and Morris (GM 68), also performed rather well. By contrast, the leap-frog scheme (Am 69) was useless. Details of the structure and implementation of the various schemes for the present problem are given in Sect. 5:8 (App. II).

These calculations have the disadvantage that they are time-consuming, and so they are less attractive for the evaluation of actual data. It is for this reason also that we have not yet applied them to experimental results, the more so because we had no precise knowledge of the charge distribution involved. Nevertheless, it seems essential to compare, by means of model calculations, the current release of mono-electrets having a nonuniform distribution, with those having a uniform distribution, to find out what differences can be expected and whether we are justified in describing our measurements on mono-electrets with the simple model of the previous section. On the other hand, for bipolarly charged hetero-electrets, the numerical solution of the PDE's with finite-difference schemes is the only approach that leads to reliable results.

5:4.1 Model Calculations on Nonuniform Excess Charges in Mono-Electrets

Some results of our computer calculations are given in Fig. 5-21. It gives the spatial expansion during TSD for the initial distribution $p(x,o) = p_o \sin^2(2\pi x/l)$. Such a distribution may hold for electron-bombarded polymers and for homo-electrets that have been exposed to humid air, the adsorbed water having discharged mainly the outer charge layers. The calculations were performed by the LWR difference scheme neglecting ohmic conduction. It is seen that the carriers spread in moving to the electrodes, thus flattening the distribution. (It does not split into two bumps, however, as was supposed by Gross (Gr 70a)*, who tried to explain the rare current reversals in mono-electrets, cf. Fig. 1-9.) Eventually, the sample becomes uniformly filled. The current generation then stops, although the internal discharge goes on.

In Fig. 5-22 the corresponding thermograms of j_r, q_r and x_o are plotted (full lines). For comparison, the results of a uniform distribution are also given (dashed lines). Apparently, the shape of the thermograms depends markedly on the initial distribution; the current plot

*We thank Prof. Gross for sending us this preliminary report. In giving a lucid state-of-the-art survey, it inspired us to do the work reported in this chapter.

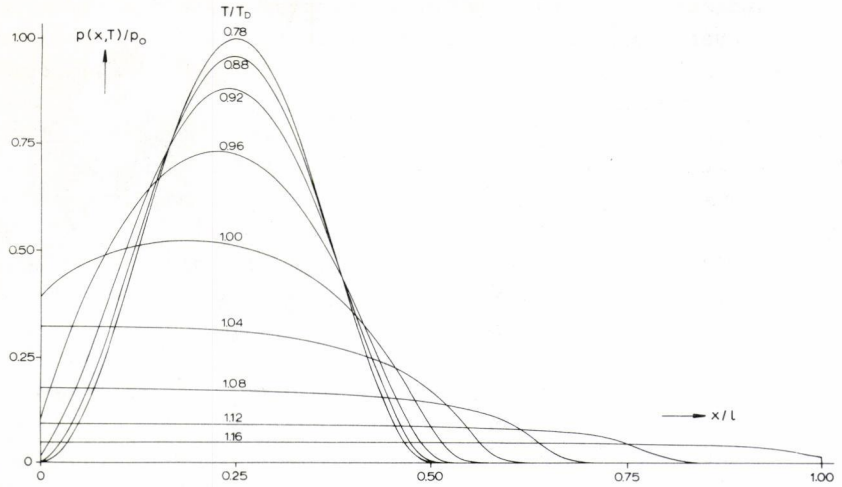


FIG.5-21 Spatial expansion of a squared sinusoidal distribution in a non-conducting polymer at various release temperatures. We assumed $B/kT_D = 20$ and took 93 grid points.

of the squared sinusoidal distribution starting lower, and extending to higher temperatures. This makes its thermogram more symmetrical and shifts its maximum to a higher temperature. However, the initial current of both distributions rises in a similar way; this means that their slopes are determined only by B/kT_D. The current maximum and released charge of the squared sinusoidal distribution appear to be lower, this is caused by normalizing them to $q_o = p_o r_o$. It would have been better

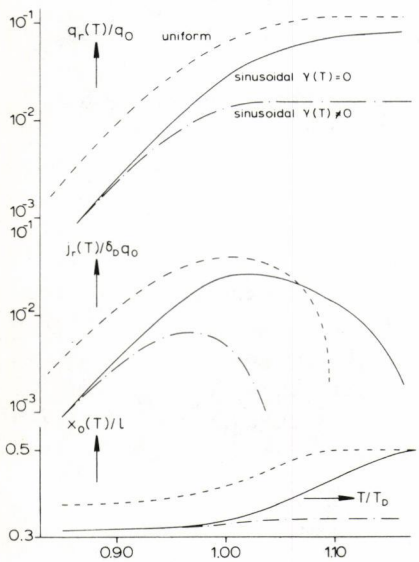


FIG. 5-22 Charge and current thermograms belonging to the squared sinusoidal distribution of Fig. 5-21. The trend is given for a conducting and a nonconducting polymer. For comparison results of a uniform distribution for $\gamma = 0$ are shown. The temperature dependence of the ZFP is given below. We took $B/kT_D = C/kT_c = 20$, $T_c = T_D$ and $r_o = 0.5$ 1.

to reduce these quantities to $q_{to} = \int_0^{r_o} p(x,o)dx = \frac{1}{2} p_o r_o$. Then the ultimate released charge would have amounted to $q_r(\lambda) = 0.162\ q_{to}^*$, which is even higher than that of the uniform distribution having $q_r(\lambda) = 0.115 \int_0^{r_o} p_o(x,o)dx$. Note that the ZFP, $x_o(T)$, of the squared sinusoidal distribution increases rather slowly, but its final value is 1/2, in accord with the collapse to a uniform distribution. (The curves for $\gamma \neq 0$ are discussed below.)

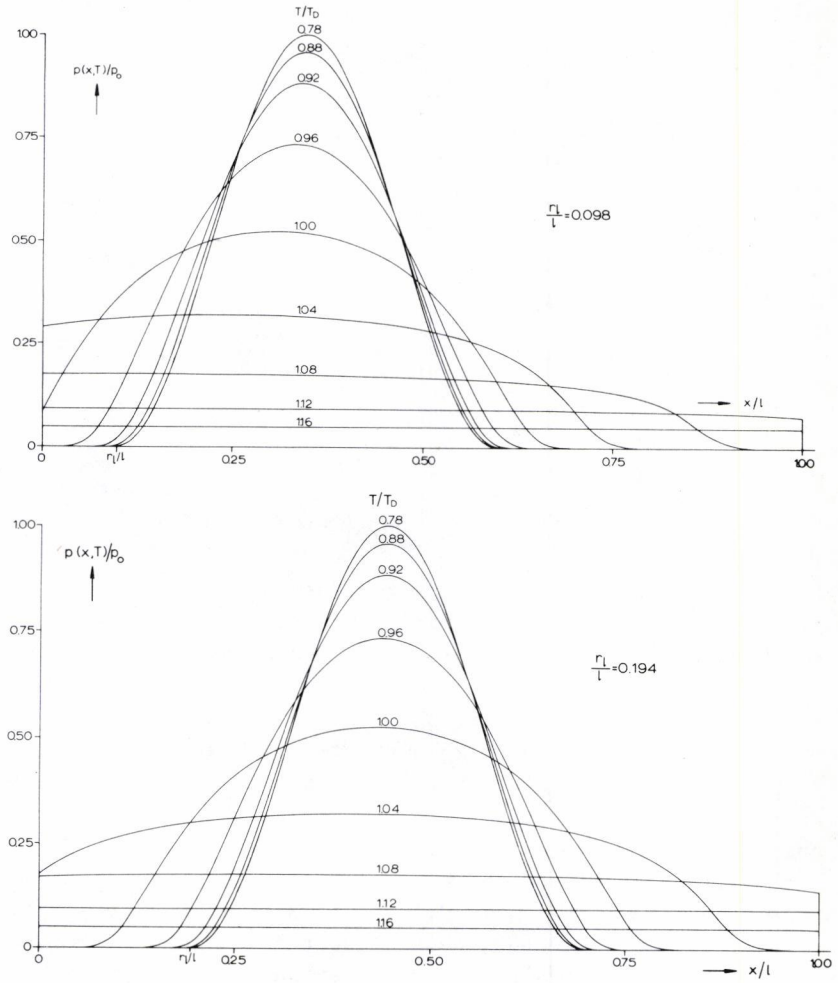


FIG.5-23 Changes in spatial expansion by starting a squared sinusoidal distribution at two different positions (compare Fig. 5-21 for which $r_1 = 0$). As the distribution starts nearer to the middle, it sooner becomes uniform, as a result of which less charge is released.

*Substituting this value of $q_r(\lambda)$ and $q(o)/p_o r_o = (3-\pi^{-2})/8$ into Eq. 5.36, we find an estimate for the average penetration depth: $\bar{r}/l = 0.183$, whereas the true value is $(1+\pi^2)/4 = 0.275$.

Fig. 5-23 shows variations in the carrier expansion when an initial squared sinusoidal distribution is gradually shifted along the x-axis. The trend is similar to that depicted in Fig. 5-21, except that, due to the higher electric field at the carrier front, the curves extend further to the right. At the end all distributions collapse into a uniform distribution, the sooner the larger $r_o/1$.

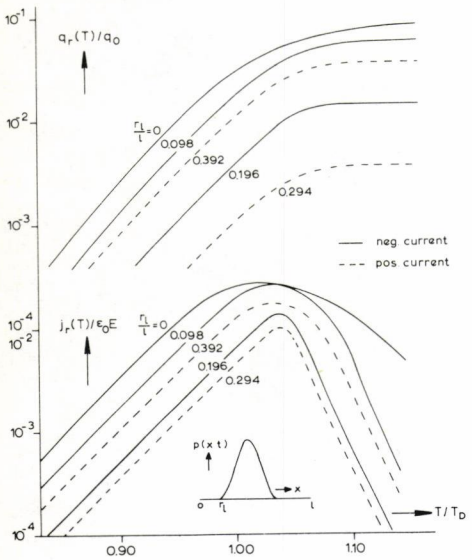


FIG. 5-24 Charge and current thermograms for the squared sinusoidal distribution shown in the insert and starting at various initial positions, $r_1/1$, for $\gamma = 0$ and $B/kT_D = 20$.

Fig. 5-24 gives the corresponding current thermograms. Note that the external current peak becomes weaker and narrower when the initial distribution becomes more symmetrical, i.e. when r_1 approaches 0.25 1. As a result, the q_r thermograms also become lower; from top to bottom they reach the ultimate values of 8.1, 5.6, 3.5, 1.4 and 0.35% of $p_o r_o$. For a distribution centred around 1/2, current flow even ceases completely. Clearly, when the initial distributions starts to the right of the middle, i.e. $r_1 > 0.25$ 1 the current flow reverses in sign, since the carriers are now mainly swept towards the right electrode.

Fig. 5-25 illustrates how ohmic conduction considerably diminishes the expansion of the space charge cloud, because it supplies oppositely charged intrinsic carriers that neutralize the drifting carriers. We observe that the cloud is already exhausted just above $T/T_D = 1.04$. From the dotted-dashed lines of Fig. 5-22, for which we assumed $C/kT_c = 20$ and $T_c = T_D$. We see that the released current and charge are also significantly lowered by the ohmic dissipation, in particular at higher temperatures. The ultimate charge released, $q_r(\infty)$, reaches only 1.55% instead of 8.1% of $p_o r_o$. Note also that $x_o(T)$ does not reach 1/2; it barely moves at all.

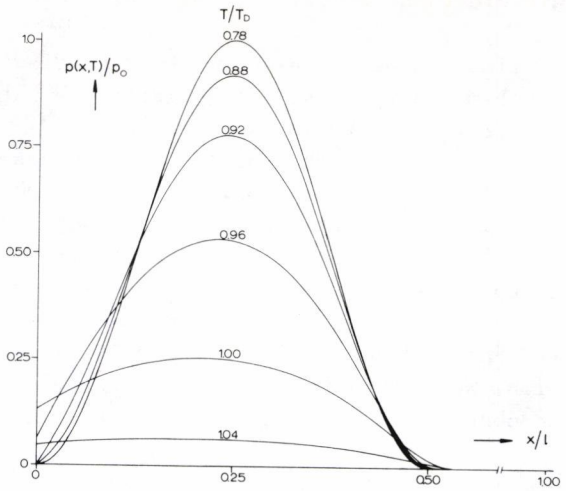


FIG. 5-25 Spatial expansion of a squared sinusoidal distribution in a conducting polymer is much less than for a nonconducting one (cf. Fig. 5-21). We considered 93 spatial grid points and put $B/kT_D = C/kT_c = 20$, and $T_c = T_D$.

5:4.2 Model Calculations on Nonuniform Excess Charges in Hetero-Electrets

In hetero-electrets, the excess charges are bipolar, and manifest themselves as the ρ-peak in the TSD current thermograms; see for instance Fig. 1-6. We have shown in Sect. 5:3.3c that the analytical solution of Calderwood et al. (CS 70) fails to describe the properties of a heteropolar discharge; this prompted us to study the numerical solution.

The relevant PDE's are Eqs 5.5 and 5.49, of which the continuity equations can, if necessary, be extended to include ohmic conduction

$$\begin{aligned} \partial p(x,t)/\partial t &= -\mu_p(T)\partial p(x,t)E(x,t)/\partial x - 0.5\gamma(T)\partial E(x,t)/\partial x \\ \partial n(x,t)/\partial t &= \mu_n(T)\partial n(x,t)E(x,t)/\partial x + 0.5\gamma(T)\partial E(x,t)/\partial x \end{aligned} \tag{5.54}$$

where we have put $\mu_p(T)p_e(T) = \mu_n(T)n_e(T) = 0.5\ \gamma(T)$. For the current equation we can derive

$$j_r(t)l = \int_0^l \{\mu_p(T)p(x,t) + \mu_n(T)n(x,t)\}E(x,t)dx \tag{5.55}$$

The velocity of the ZFP, $x_o(t)$, is again related to the current flow, and we have

$$j_r(t) = -\{p(x_o,t) - n(x_o,t)\}dx_o(t)/dt \tag{5.56}$$

At the ZFP Eqs 5.54 simplify to

$$\begin{aligned} \varepsilon_o\varepsilon\partial p(x_o,t)/\partial t &= -\{\mu_p(T)p(x_o,t) + 0.5\gamma(T)\}\{p(x_o,t) - n(x_o,t)\} \\ \varepsilon_o\varepsilon\partial n(x_o,t)/\partial t &= \{\mu_n(T)n(x_o,t) + 0.5\gamma(T)\}\{p(x_o,t) - n(x_o,t)\} \end{aligned} \tag{5.57}$$

Assuming, as before, that $\partial p(x_o,t)/\partial t \simeq dp(x_o,t)/dt$ and $\partial n(x_o,t)/\partial t \simeq dn(x_o,t)/dt$, these equations reduce to ordinary differential equations,

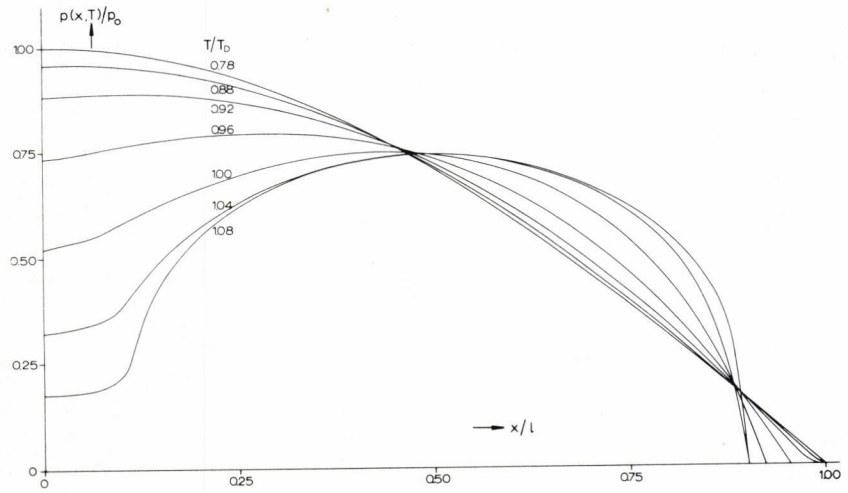
which can be solved by e.g. a 4th order Runge-Kutta method, starting from $p(x_o,o)$ and $n(x_o,o)$.

The PDE's 5.54 must be solved simultaneously. Also for this problem either the LWR scheme or the WT scheme is the most appropriate. The latter can be started from $x_o(t)$, while for the former we borrowed the boundary conditions for $p(x,t)$ and $n(x,t)$ from Thomson (He 29). Supposing that $x = 0$ was the cathode during the formation and $x = 1$ the anode, Thomson took $n(o,t) = p(1,t) = 0$, since the charging field will deplete these respective regions of n and p carriers. The carrier densities, $n(1,t)$ and $p(o,t)$, however, are kept free because these supply the ohmic field drift currents to the electrodes.

So far, we have only tried the fast LWR scheme, in which $n(1,t)$ and $p(o,t)$ were found by extrapolation. We considered 93 mesh points and took $\gamma(T) = 0$, $\mu_p(T) = \mu_n(T)$ and considered the following initial distribution

$$p(x,t) = p_o \cos(\pi x/2\ 1)$$
$$n(x,t) = n_o \sin(\pi x/2\ 1) \qquad 0 \leq x \leq 1$$

Fig. 5-26 illustrates the change of the spatial distributions of the positive carriers and of the excess charge density $\rho(x,t) = p(x,t) - n(x,t)$. The electric field at $t = 0$ is also shown. This field has such a direction that positive carriers are swept away from the electrodes and drift towards the middle of the sample. The distribution of negative carriers behaves similarly. Consequently, the excess charge density is concentrated at the electrodes, and the middle of the sample becomes electrically neutral*. The discharge current has its *normal hetero di-*



*One might expect the positive and negative carriers finally to disappear from the middle by recombination. However, in our calculations this process was not taken into account.

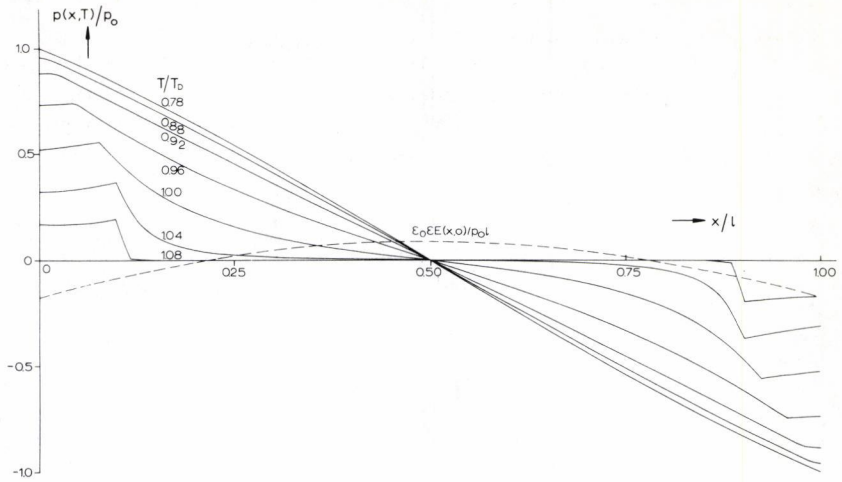


FIG.5-26 Spatial distribution of the positive carrier density, $p(x,T)/p_o$ and the excess charge density, $\rho(x,T)/\rho_o$, at various temperatures during the TSD of a non-conducting heterocharged polymer. The internal field at t = 0 is also shown. The calculations were made for 93 spatial mesh points, taking $B/kT_D = 20$.

reaction, so that in Fig. 5-27 both the ZFP's are seen to decrease to zero, i.e. they move towards the electrodes. The current and charge thermograms are also given in Fig. 5-27; they have their familiar shape. The ultimate released charge amounted to about 6% of $\int_0^1 p(x,o)dx$ and the release process is again rather inefficient. Obviously, for a ρ peak to be observed, the polymer has to contain *many* excess charges, otherwise it must exhibit a low ohmic conduction.

As pointed out by Croituru (Cr 65) the hetero excess charges will be stored nearer the electrodes, see also Fig. 5-30 and 5-31. We intend to evaluate these more realistic distributions in due course.

In Sect. 5:3.4 we showed, for uniformly charged mono-electrets, that the activation energy can best be calculated from the charge-ratio plot. This also holds for bipolarly charged electrets. The results for the high-temperature peak of 80 MMA co 20 diMIt are shown in Fig. 5-28. This peak presumably is a combined α and ρ peak to which the latter contributes most. Of the resulting activation energies of 1.8 and 1.3 eV, the former value agrees fairly well with the activation energy for ohmic conduction, which amounts to 2.0 eV. Such an agreement could be expected, because the excess charges originate in carriers that took part in the conduction during the formation. (The value of 1.3 eV derived from the BFG plot, is probably too low, because this method is most affected by the contribution of the proximate α peak.)

In practice, the excess charge peaks reproduce less nicely than dipole peaks. This is not surprising, for we have seen in this and the

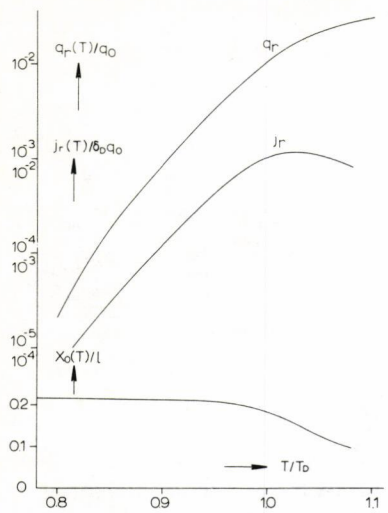


FIG.5-27 Charge and current released by SCL drift from a nonconducting hetero-charged polymer. Considering the initial positive and negative distribution, depicted in Fig. 5-26, we took $B/kT_D = 20$. The temperature dependence of both zero-field points, $x_0(T)$, is also shown.

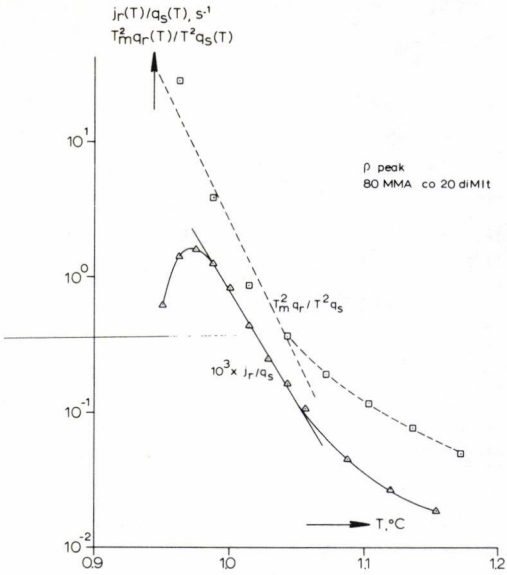


FIG.5-28 Calculation of the activation energy of the combined α and ρ peak of a hetero-electret of 80 MMA co 20 diMIt. The resulting activation energies are 1.8 eV for the charge-ratio plot and 1.3 eV for the BFG plot. The peak temperature T_m is 110 °C.

foregoing section that ρ peaks depend on many factors that are not typical of the polymer. First of all, the ρ peak will depend on the initial distribution of the excess charges. In particular, the peaks become smaller when the relative excess-charge width decreases. Moreover, excess charges actually are extrinsic, generally arising from mere impurities, such as catalyst or inhibitor molecules. Finally, diffusion, which strongly depends on the charge-exchange rate of the electrodes, may also contribute partly to the ρ peak; this topic will be discussed in the next section.

Conclusions:

In restricting ourselves to the main discharge processes, i.e.
- SCL drift of the excess charges themselves, and
- their neutralization with oppositely charged intrinsic carriers supplied by the ohmic conduction of the polymer,

we have been able to elucidate the TSD of excess charges. The numerical solution, in particular, allowed us to reveal quite complex problems.

We showed that the charge release by SCL drift of the excess charges themselves is inefficient. The carriers moving in *opposite* directions

to both electrodes, some of them only drifting a short distance before they are neutralized at the electrodes. As a result the average current, which equals the external current, is rather small; especially, when the penetration is either shallow or deep. Even for a nonconducting polymer the charge liberated amounted to at most 14% of the original charge stored. When the drifting carriers are compensated and finally neutralized by intrinsic carriers supplied by ohmic conduction, this figure becomes even less. These facts preclude the use of current TSD for homocharges shot into thick electrets; this has also recently been outlined by Gross (Gr 71). Since it was of vital importance to reveal this homocharge decay, we resorted to a current TSD with air-gap, see Chap. 7.

We also found that the thermograms depend on the initial distribution of the carriers, in particular, the relative width of the space charges is of major importance. By contrast, the initial rise of the current is typical of the polymer in question, depending only on the activation energy.

Thus, the prerequisites to observe TSD peaks by SCL drift are a high concentration of space charges and a low conduction of the polymer. The latter is especially required for homocharged foils, where the injected space charge density is fairly low; Teflon-FEP electrets having a low conductivity, therefore give good results. For heterocharged polymers a low ohmic conduction is less stringently required, because the charge densities are higher, and as a result ρ peaks were found in several polar polymers.

Looking ahead, we may hope that the numerical solution given, can be extended to include diffusion and recombination processes. Yet, the general trend found will not be much altered. We shall show in the next section that diffusion plays a minor role, merely rounding off the steep density gradients. Moreover, this only generates an external current when the electrodes are blocking. In Chap. 11 (App. I) we shall enlarge the picture to include trapping effects. It is interesting to recall that the theory of this chapter corresponds to thermal release from traps that show severe retrapping.

5:5 Diffusion of Excess Charges

So far we assumed the evaporated electrodes to be open. However, the charge-exchange rate of electrode contacts is not well known. Jaffé et al. (JL 53), and other workers in this field have assumed that even electrodes making intimate contact may partly or completely block the neutralization of the arriving excess charges. Though we have obtained experimental evidence that such electrodes evaporated onto polymers are generally open*, and do not hinder the neutralization of the excess charges, it seems worthwhile to discuss current TSD of excess

*A strong argument in favour of this is that during electret formation the charging current never drops to zero, but eventually becomes equal to the ohmic conduction current; this clearly shows that the latter is not blocked by evaporated electrodes.

charges for blocking electrodes. In mono-electrets they may introduce, by the opposed actions of SCL drift and diffusion, current reversals, which have incidentally been observed by Gross (Gr 70a) and other investigators for γ-irradiated insulators, and also by the author for electron-bombarded Teflon-FEP (cf. Fig. 1-9).

The extension of TSD to blocking electrodes is also of importance for TSD experiments in which contiguous electrodes are used. In this case there will be air inclusions between sample and electrodes, which will make part of the electrode area inaccessible to the incoming excess charges. It is also of interest to our TSD experiment, where we have introduced a finite air gap, for this yields a perfectly blocking electrode interface.

That diffusion only generates an external current for blocking electrodes is illustrated in Fig. 5-29. When the electrodes are open, we get two opposite

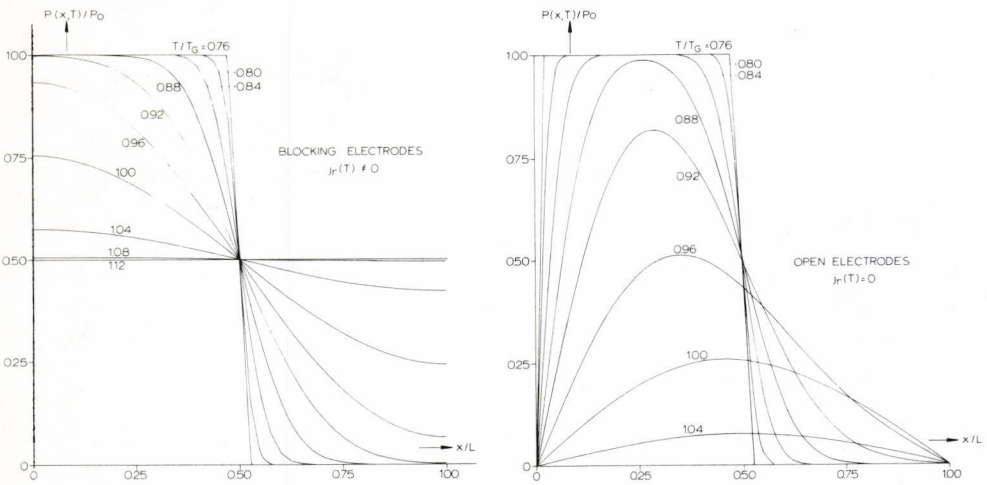


FIG. 5-29 Spreading of an uniform excess-charge layer by diffusion, for blocking and open electrodes. For the former the charges eventually spread uniformly, having no chance to recombine with their image charges at the electrodes. This is not so for open electrodes, where all charges finally flow out and recombine with their image charges. In this case no image charges are freed from the electrodes and the external current is zero. We took $A/kT_G = 20$.

diffusion currents within the sample (an outflow of charge carriers towards the left and an inflow towards the right electrode, due to the spreading into the sample). The mean value of these currents is zero, whereas for blocking electrodes, we only have a diffusion of carriers to the right, and a positive current is generated, which may partly cancel or exceed the negative SCL drift current, thus leading to the striking current reversals.

Nevertheless, it is generally accepted that diffusion plays a minor rôle (SS 67a). This can readily be verified by the following argument. For the diffusion current to be larger than the SCL current we must have

$$D(T)\partial p(x,t)/\partial x \geq \mu(T)p(x,t)E(x,t) \qquad (5.58)$$

In most hetero-electrets $p(x,t)$ can be expected to decrease exponentially with

x (see Eq. 5.79 below) and so

$$p(x,t) = p(x,o)\ \exp(-\theta x)$$

Using Einstein's relation between D(T) and μ(T): $\mu(T)/D(T) = 1.16\times10^4/T$, we can then rewrite Eq. 5.58 as

$$\theta \geq 39\ E(x,t)$$

at room temperature. According to this equation, E(x,t) must be less than 3V/cm, if $\theta = 10^4\ m^{-1}$ (which corresponds to a charge layer of about 0.1 mm). This is indeed a rather weak field.

Obviously, diffusion only becomes significant for large gradients, which may be found particularly in hetero-electrets made from polar polymers. By contrast, in homo-electrets the densities are relatively low and SCL drift will dominate. However, this is not always so in mono-electrets with blocking electrodes, where, as we shall show in Sect. 5:7, App.II) the SCL drift gradually transforms the space charges into surface charges. Clearly, this will intensify the diffusion considerably, and the final outcome may be the current reversal just mentioned.

5:5.1 Ultimate Charge Released for Blocking Electrodes

As usual we are interested in the current and charge release. Of the latter the ultimate value is of special interest. For blocking electrodes, this can be derived without solving the PDE's involved. The currents at the blocking electrode interfaces now only consist of a displacement current. Moreover, the excess charges will eventually be spread out uniformly (cf. Fig. 5-29). Let this situation be reached in a time λ; from then on the external current will be zero.

Consequently, for the ultimate charge released we obtain

$$q_r(\lambda) = \varepsilon_o\varepsilon\{E(o,\lambda) - E(o,o)\} = \varepsilon_o\varepsilon\{E(1,\lambda) - E(1,o)\} \qquad (5.59)$$

By virtue of the final symmetry at $t = \lambda$, we further have $E(o,\lambda) = -E(1,\lambda)$. Using in addition the formulae 5.16 and 5.17 for the fields E(o,o) and E(1,o), we find

$$q_r(\lambda) = \tfrac{1}{2}\int_o^1 (1 - 2x/1)\rho(x,t)dx \qquad ...(5.60)$$

For bipolarly charged electrets, which as a whole are neutral, the term $\int_o^1 \rho(x,t)dx$ in this equation will be zero.

For a monocharge of width r_o (Fig. 5-2), Eq. 5.60 yields

$$q_r(\lambda)/p_o r_o = 0.5(1 - r_o/1) \qquad (5.61)$$

This value is considerably *larger* than that for SCL drift, which for low penetrations gives $q_r(\lambda)/p_o r_o = -r_o/2$ 1. We also see that both charges are of *opposite sign*. This is so, because for SCL drift the charges move mainly to the left electrode, whereas for diffusion they move mainly to the right electrode.

Next we turn to the calculation of the complete current and charge response.

5:5.2 Basic Equations for TSD by Diffusion

A theory about isothermal discharge transients caused by diffusion has first been given by Jaffé (Ja 33) and was later generalized by Jaffé and LeMay (JL 53). In order to solve the nonlinear PDE's involved, they neglected generation and recombination of carriers and assumed the electric field to be uniform up to 1st order. Consequently, they put E(x,t) = 0 during discharge. Considering excess charges only the conservation laws, Eqs 5.1 and 5.2, then reduce to parabolic PDE's

$$\partial p(x,t)/\partial t = D(T)\partial^2 p(x,t)/\partial x^2 \tag{5.62}$$

$$\partial n(x,t)/\partial t = D(T)\partial^2 n(x,t)/\partial x^2 \tag{5.63}$$

while the particle currents obey

$$j_p(t) = -D(T)\partial p(x,t)/\partial x \quad \text{and} \quad j_n(t) = D(T)\partial n(x,t)/\partial t \tag{5.64}$$

Upon adding and integrating these equations we find for the total discharge current density

$$j_r(t) = -\{\rho(1,t) - \rho(o,t)\}D(T)/1 \tag{5.65}$$

This equation clearly shows that open electrodes, for which according to Eq. 5.8 $\rho(o,t) = \rho(1,t)$, do not generate an external current.

As discussed in (Tu 70), Jaffé and LeMay's isothermal solution can easily be adapted to TSD, when we replace t by a reduced time

$$\xi(T) = \int_o^t a(T)dt$$

where a(T) denotes the temperature shift of D(T), i.e. $a(T) = D(T)/D_o$. For convenience, however, we shall continue to use t.

Jaffé and LeMay solved Eqs 5.62 and 5.63 using the boundary conditions of Eq. 5.10 and the initial conditions p(x,o) and n(x,o). They applied the method of separation of variables and expanded the excess charge densities in terms of eigenfunctions $\chi_k(x)$. Thus, they write for the positive carriers

$$p(x,t) = \sum_{k+1}^{\infty} a_k\, e^{-\lambda_k t}\, \chi_k(x) \tag{5.66}$$

Substitution of Eq. 5.66 into 5.62 leads to an ordinary differential equation for $\chi_k(x)$

$$D(T)d^2\chi_k(x)/dx^2 + \lambda_k\chi_k(x) = 0$$

Its solution reads

$$\chi_k(x) = \cos(\nu_k x) + b_k \sin(\nu_k x) \tag{5.67}$$

where ν_k are the eigenvalues, $\nu_k = \sqrt{\lambda_k/D(T)}$. By particularizing Eq. 5.64a at x = 0 we find, in view of Eqs 5.10, 5.66 and 5.67 for b_k

$$b_k = \zeta/D(T)\nu_k \tag{5.68}$$

Similarly, the boundary condition at x = 1 yields a transcendental equation for the eigenvalues ν_k

$$\tan(\nu_k 1) = 2\zeta D(T)\nu_k\{D^2(T)\nu_k^2 - \zeta^2\}^{-1} \tag{5.69}$$

Finally, the constants a_k are determined by the initial condition p(x,o). Replacing the summation that results from Eq. 5.66 at t = 0 by a Fourier integration, we have

$$a_k = \int_o^1 p(x,o)\chi_k(x)dx / \int_o^1 \chi_k^2(x)dx \tag{5.70}$$

Let us apply the equations to the case in which the electrodes *completely* block charge transport, i.e. $\zeta = 0$. Eqs 5.68 and 5.69 then reduce to

$$b_k = 0 \text{ and } \tan(\nu_k 1) = 0,$$

so that $\nu_k = k\pi/1$, k = 0, 1, ..., ∞, while we obtain for Eq. 5.66

$$p(x,t) = p_e + \sum_{k=o}^{\infty} a_k e^{-D(T)\nu_k^2 t}\cos(\nu_k x) \tag{5.71}$$

It was with the help of this equation, and the corresponding one for open electrodes, that we calculated the course of the excess charge distribution as a function of heating temperature in Fig. 5-29.

5:5.3 TSD by Diffusion in Homo-Electrets

Now focusing on unipolarly *homocharged foils* we chose a uniform excess charge distribution up to r_o for p(x,o), see Fig. 5-2. This results according to Eq.5.70 in the following a_k values

$$a_o = p_o r_o/l \quad \text{and} \quad a_k = (2p_o/k\pi)\sin(k\pi r_o/l), \qquad k = 1, 2, \ldots, \infty$$

Substituting Eq. 5.71 into 5.65 we find for the external current density

$$j_r(t) = 2D(T)l^{-1} \sum_{k=1,3}^{\infty} a_k \, e^{-D(T)\nu_k^2 t} \qquad \ldots(5.72)$$

where a_k and ν_k take the values just given. As expected the diffusion current is indeed *positive* i.e. opposite to the SCL drift current.

In particular, if $r_o = 1/2$ we have

$$j_r(t) = (4p_o D(T)/\pi l)(e^{-t^*} - (1/3)e^{-9t^*} + (1/5)e^{-25t^*\ldots}) \qquad (5.73)$$

where $t^* = D(T)(\pi/l)^2 t$. Unless t^* is very small, the series converges rapidly. When $t^* \geq 0.3$, only one term remains.

The resulting current thermogram is plotted in Fig. 5-30. The chosen normalization temperature, T_G, is defined in the usual way by: $sT_G\delta_G(T_G) = A/kT_G$,

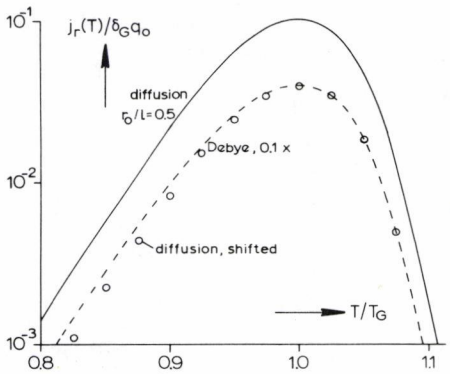


FIG. 5-30 Current release by diffusion for a uniformly charged mono-electret. The thermogram is much the same as for a single dipole relaxation. We took $A/kT_G = 20$ and $r_o/l = 0.5$.

where $\delta_G(T_G) = \pi^2 D(T_G)/l^2$, and A is the activation energy. Owing to the dominating first term in Eq. 5.73, the thermogram has almost the same initial slope as the corresponding Debye thermogram. At high temperatures, where the first term is the only one left, the resemblance even becomes perfect (compare the shifted curve). As a result, the BFG plot, $j_r(T)/q_s(T)$ vs.1/T, not shown, gives a nearly straight line over the whole temperature range. In this respect TSD by diffusion distinguishes itself from SCL drift. However, as illustrated in Fig. 5-20 the actual BFG plots for homo-electrets of Teflon-FEP are not straight. This is consistent with the view that SCL drift, rather than diffusion, predominates.

By integrating Eq. 5.72 with respect to t we obtain the released charge density

$$q_r(t) = (2/l) \sum_{k=1,3}^{\infty} \{1-\exp(-D(T)\nu_k^2 t\}a_k/\nu_k^2 \qquad \ldots(5.74)$$

Although the ultimate released charge can be found from particularizing this equation at $t = \infty$, it can be calculated more easily from Eq. 5.60. For $r_o/l = 0.5$

the result is $q_r(\infty) = p_o l/8$. This value is about two times higher than that found for SCL drift, which gave $q_r(\infty) = 0.058\ p_o l$. The spreading of the space charge will also be different. Diffusion will spread the carriers uniformly, whereas SCL drift, will pile them up near the blocking electrodes as surface charges.

In practice we have never found for homocharged metallized foils, the high release value of Eq. 5.60. Moreover, the released charge was as a rule negative. This indicates once more that for evaporated electrodes SCL drift prevails, presumably because these electrodes are open. Current reversals were observed only incidentally, in which case the electrodes must have been partly blocking.

5:5.4 TSD by Diffusion in Hetero-Electrets

To round off the discussion we next turn to the stimulated diffusion of a *heterocharged* polymer, in which the diffusion *does not* oppose the SCL drift. We first have to relate the discharge process to the charging process.

During charging the uniform field, E_o, equals V_a/l, and we have to enlarge Eqs 5.62 and 5.64 to

$$\partial p(x,t)/\partial t = D(T)\partial^2 p(x,t)/\partial x^2 - \mu(T)E_o \partial p(x,t)/\partial x \qquad (5.75)$$

$$j_r(t) = -D(T)\partial p(x,t)/\partial x + \mu(T)p(x,t)E_o \qquad (5.76)$$

The creation of an optimum charge requires that a steady state be reached, for which $dp(x,t)/dt = 0$. This state is reached at $t = \infty$, when $p(x,\infty)$ satisfies

$$D(T)d^2p(x,\infty)/dx^2 + \mu(T)E_o dp(x,\infty)/dx = 0$$

the first integral of which equals the stationary current density

$$j(\infty) = -D(T)dp(x,\infty)/dx + \mu(T)E_o p(x,\infty) \qquad (5.77)$$

Furthermore $p(x,\infty)$ obeys the boundary conditions

$$j(\partial) = \zeta\{p(1,\infty) - p_e\} = -\zeta\{p(o,\infty) - p_e\} \qquad (5.78)$$

By solving Eq. 5.77 we find

$$\frac{p(x,\infty)}{p_e} = \frac{\zeta(1-e_o) + 2\mu(T)E_o e(x)}{\zeta(1-e_o) + \mu(T)E_o(1+e_o)} \qquad (5.79)$$

where $e_o = \exp(-v) \simeq 0$ and $e(x) = \exp\{-v(1-x/l)\}$ with v being the reduced applied voltage $\mu(T)V_a/D(T)$ or, by virtue of Einstein's relation, $v = V_a/39$. Similar equations hold for the negative carrier. Fig. 5-31 gives a plot of the resulting space charge density, which is piled up in very thin layers near the electrodes. Its positive and negative parts both drop to 1/e at $\bar{r}/l = 0.05$, which is just the inverse of the value of v used.

Inserting $p(x,\infty)$ of Eq. 5.79 into Eq. 5.70 for p(x,o) we obtain for the discharge current (JL 53)

$$j_r(t) = \mu(T)p_e E_o \sum_{k=1,3}^{\infty} a_k\, e^{-D(T)\nu_k^2 t} \qquad \ldots(5.80)$$

Here $a_k = (8/v^2)\{(1+z_k^2/v^2)(1+(b^2+2b)/z_k^2\}^{-1}$ with $b = \zeta/D(T)$ and $z_k = \nu_k l$, where ν_k follows from Eq. 5.69. If negative carriers also contribute $j_r(t)$ has to be multiplied by 2. Note that the discharge current depends through a_k on the formation conditions; this dependence is not linear.

The diffusion current being positive it will *reinforce* the SCL drift current of the heterocharged electrets. This is an interesting aspect.

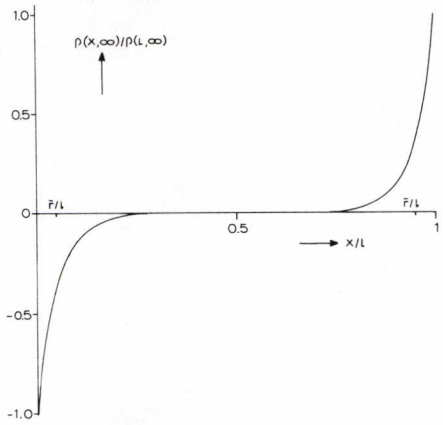


FIG. 5-31 Local space charge density accumulated, after an isothermal formation with blocking electrodes, by the opposed actions of field drift and diffusion, according to Jaffé et al. We took $\zeta = 0$ and $v = 20$.

To see what reinforcement can be expected we visualize a hetero-electret with blocking electrodes. In this case $b = 0$ and $a_k = 8(v^2 + k^2\pi^2)^{-1}$, while $\nu_k = k\pi/1$. Inserting these constants into Eq. 5.80 and writing $\gamma(T)$ for $\mu(T)(p_e+n_e)$, we obtain

$$j_r(t) = (1.22\text{x}10^4\ \gamma(T)/E_o l^2)(e^{-t^*} + e^{-9t^*} + \ldots) \qquad (5.81)$$

where $t^* = D(T)(\pi^2/l^2)t$.

Apparently, the released current *decreases* with the forming field, E_o. This is so, because the charge layers became the thinner the higher the forming field. The current further increases linearly with the ohmic conductivity $\gamma(T)$ of the polymer, and will be the lower the thicker the sample. These facts agree qualitatively with the experimental results for the TSD ρ peak. This actually is larger for the more polar polymers; compare the results of PEMA and P2CEMA in Figs 10-1 and 10-22. For results on the field and thickness dependence of PET, we refer to Figs 10-38 and 10-40.

We finally calculate the ultimate charge released from Eq. 5.60 by substituting $p(x,\infty)$ and $n(x,\infty)$ from Eq. 5.79. Noting that $\zeta = 0$ and that $v \geq 1$ we find

$$q_r(\lambda)/p_e l \simeq -4/v \quad \text{or} \quad -156/V_a$$

As could be expected from Eq. 5.81, the ultimate charge falls off for higher formation voltages.

Chapter 6

CURRENT TSD BY THE MAXWELL-WAGNER EFFECT IN SHORTED HETEROGENEOUS ELECTRETS

We mentioned in Sect. 1:5 that a prerequisite for MW charging is a heterogeneous structure, the components of which have a different dielectric constant and ohmic conductivity. The simplest composite possible is indicated in Fig. 6-1. When such a laminate is subjected to a static field, by switching S to position 1, a charge will be accumulated at the interface of the layers. The accumulated charge is supplied by the unequal ohmic conduction currents arriving at the interface. Maxwell and Wagner were the first to study this effect as a cause of dielectric relaxation phenomena.

Since the ohmic conductivities are thermally activated, the Maxwell-Wagner effect can produce a permanent charge by exposing the laminate to the temperature-field cycle of Fig. 1-1. Again the forming tempera-

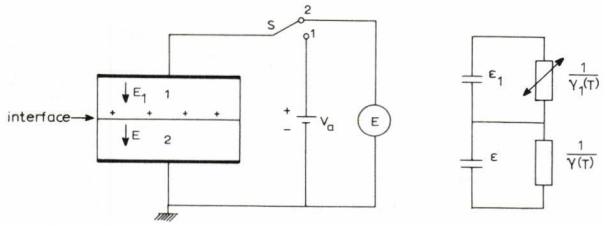


FIG.6-1 Two-layer series model as a representative for heterogeneous systems showing charge storage at the interface. This interfacial charge arises whenever the material constants ε, γ and ε_1, γ_1 are different. For homocharging, layer 1 is the air gap which has a variable conductivity $\gamma_1(T)$, owing to the alternating breakdown (cf. Sect. 6:3, App. II). Note that the fields E and E_1 have an opposite direction during current TSD.

ture should be well above T_g, for otherwise the conductivities are too low sufficiently to raise the rate of accumulation. When the laminate is next heated to study its current TSD with S in position 2 (short-circuit), the charge stored will be neutralized by new carriers of opposite polarity that are conveyed to the interface by conduction currents which are created by the interfacial charge itself. Clearly, this neutralization will be transient, thus leading to a characteristic TSD peak in the high-temperature range. Since this peak is related to the *conductive* motion of intrinsic carriers, we shall call it the ρ_c peak.

We generally studied more complex heterogeneous systems, in which MW charging occurs throughout the sample around the inhomogeneities. We investigated e.g. the current TSD of hetero-electrets made of partially crystalline polymers, the amorphous part of which has a higher (ionic) conductivity than the crystalline part. The carriers are then

accumulated at the grain boundaries. Charges injected during homocharging of crystalline foils may likewise be piled up at the crystal boundaries. We also studied the current TSD of mixtures of PMMA and metal oxides, to find out whether the heteropolar charge storage of polymers can be increased by polar or conductive additives (see Sect. 10:4).

For the appearance of a TSD MW peak, the ohmic relaxation frequency of the polymer must be high enough, so that it satisfies a condition such as Eq. 2.21. We may therefore infer from Figs 2-2 to 2-4 that the resulting TSD peak becomes apparent only above the glass-rubber transition. As such the MW effect may be responsible (in part) for the TSD ρ peaks of several heterogeneous film and disc electrets; compare, e.g., the ρ peaks in the thermograms of Figs 10-25, 10-22 and 10-34. They belong to heterocharged PET film, PC film, and ChPEth, and to homocharged Teflon-FEP film, respectively.

As we have done briefly in (Tu 70) the discussion on heterogeneous systems will be concentrated on two-layer laminates. These serve as an example for more complex models of spherical particles embedded in a polymer matrix. The mathematics of such models is very complicated. Still, this simple substitute can be expected to show the general features of actual composites.

Sect. 6:1 describes the theory of nonpolar laminates and gives experimental results for Teflon-FEP film heat-sealed to PI (Kapton H) film. In Sect. 6:2 we turn to the current TSD of a homogeneous polar polymer sandwiched between two electrodes, one of which has an adjacent *air gap*. For this we had to extend the theory to include, besides the MW relaxation, a dipole relaxation. Remarkably, in descriptions on the isothermal response of heterogeneous systems, dipole relaxations are as a rule neglected (Be 67). We shall show that this neglect is not legitimate for TSD experiments on polar polymers. These exhibit a dipole reorientation peak in front of the MW conduction peak.

The reason for studying this particular assembly of a polymer and an air gap, was to learn whether the position of its MW conduction peak coincided with the TSD ρ peak of the plain polymer electret. This turned out to be true, as will be shown by experimental results for two polymers. This substantiates our view that the ρ peak shown by shorted electrets is not an unknown dipole relaxation, but is due to the motion of excess charges by SCL drift and diffusion.

In the following we shall ignore the motion of the accumulated interfacial charges by SCL drift and diffusion, assuming that *ohmic conduction* is the main decay mechanism. Furthermore, we shall assume the interfacial charge to be a *surface charge*, so that the fields in the layers are *uniform*. More accurately, the charge stored will be a space charge, because the charges already accumulated will repel the incoming charges, i.e. the charge build-up will be space-charge limited. However, the width of the space-charge layer will be small and so it may well be

visualized as a surface charge. Note that the two assumptions are also made in current theories about the isothermal response of heterogeneous systems (see, e.g., the comprehensive review by Van Beek (Be 67)).

Before passing on to their current TSD, we shall first discuss the MW charging of nonpolar and polar laminates. Interestingly, *homocharging* due to charge injection from an ionized air gap can also be envisaged as an MW charging, although a special one, because the conductivity of the air gap is varied by the alternating ignitions and extinctions of its breakdown. This subject will be treated in Sect. 6:3 of App. II.

6:1 MW Effect in Nonpolar Laminates

6:1.1 The Charging Process

In order to relate TSD to the formation conditions, we first describe the charging. Let the two layers of the laminate have dielectric constants ε_1, ε and ohmic conductivities γ_1, γ (Fig. 6-1). The two components, being nonpolar have no permanent dipoles, and so ε_1,ε correspond to instantaneously reacting polarizations. The electric fields E_1,E are uniform, because space-charge storage is excluded.

For the current densities within the two layers we have

$$j(t) = \varepsilon_0\varepsilon_1 dE_1(T)/dt + \gamma_1(T)E_1(t) = \varepsilon_0\varepsilon dE(t)/dt + \gamma(T)E(t) \quad (6.1)$$

For convenience we ignored the temperature dependence of ε_1,ε in assuming that γ_1,γ obey an Arrhenius shift and vary much more strongly. The applied voltage will be divided across the layers according to

$$V_a = E_1(t)l_1 + E(t)l \quad (6.2)$$

At the boundary of the two layers a *surface charge* density will be built up. The continuity equation yields for its increase

$$d\sigma(t)/dt = \gamma_1(T)E_1(t) - \gamma(T)E(t) \quad (6.3)$$

Hence, the increase is determined by the difference in the ohmic conduction currents. However, since the displacement currents in Eq. 6.1 decay to zero, this difference gradually diminishes, for otherwise the spatial continuity of the total current j(t) is not preserved. The charge created therefore strengthens the lower conduction current by intensifying its driving field. For the relation between the two electric fields and $\sigma(t)$ we have Gauss's law

$$\sigma(t) = \varepsilon_0\varepsilon E(t) - \varepsilon_0\varepsilon_1 E_1(t) \quad (6.4)$$

For TSD we are mainly interested in the interfacial charge $\sigma(t)$, because it is this charge that can be frozen in. However, for homocharging we also want to know the voltage across the air gap $V_1(t) = E_1(t)l_1$, because this voltage will initiate the breakdown. In anticipation of our discussion on homocharging we therefore first derive the time dependence of $V_1(t)$. By eliminating E(t) from Eqs 6.1 and 6.2 we obtain as differen-

tial equation for $V_1(t)$

$$dV_1(t)/dt + \beta_g(T)V_1(t) = \beta(T)V_1(o) \tag{6.5}$$

where $\beta(T) = \gamma(T)/\varepsilon_o\varepsilon$ and $\beta_g(T) = \{\gamma_1(T)/l_1 + \gamma(T)/l\}/\varepsilon_o(\varepsilon_1/l_1 + \varepsilon/l)$, so the response frequency of the laminate depends implicitly on the ohmic relaxation frequencies of the components.

The initial value $V_1(o)$ is found from Eq. 6.4, noting that $\sigma(o) = 0$. According to this equation, the applied voltage V_a is capacitively divided at $t = 0$, and

$$V_1(o)/V_a = (1 + \varepsilon_1 l/\varepsilon l_1)^{-1} \tag{6.6}$$

The solution of Eq. 6.5 reads

$$V_1(t) = \{V_1(o) - V_1(\infty)\}\, e^{-\int_o^t \beta_g(T)dt} + V_1(\infty) \tag{6.7}$$

where $V_1(\infty)$ denotes the final value, which we shall specify in Eq. 6.9. $V_1(t)$ being known, we may calculate $\sigma(t)$ from Eq. 6.4, which can be rewritten as

$$\sigma(t) = \varepsilon_o(\varepsilon_1/l_1 + \varepsilon/l)\{V_1(o) - V_1(t)\} \tag{6.8}$$

The interfacial charge collected is thus proportional to the difference between the initial and actual values of $V_1(t)$.

Eq. 6.3 makes it clear that the interfacial charge eventually reaches its maximum when the ohmic currents become equal. At that time the voltage is divided according to the conductances of the layers and $V_1(t)$ attains its final value

$$V_1(\infty)/V_a = (1 + \gamma_1(T)l/\gamma(T)l_1)^{-1} \tag{6.9}$$

Substitution of Eq. 6.9 into 6.8 gives for the final charge density stored

$$\frac{\sigma(\infty)}{\varepsilon_o\varepsilon V_a/l} = \frac{1 - \varepsilon_1\gamma(T)/\varepsilon\gamma_1(T)}{1 + l_1\gamma(T)/l\gamma_1(T)} \tag{6.10}$$

Obviously, $\sigma(\infty)$ is reached only if the formation lasts long enough, so that the exponential in Eq. 6.7 becomes very small. In general, $\sigma(\infty)$ is already attained in the isothermal part of the formation at T_f, and will be frozen in during the cooling period. It is through the temperature dependences of the conductivities of the layers that the magnitude of $\sigma(\infty)$ depends on T_f. We further see that it increases *linearly* with the applied voltage.

The sign of $\gamma_1(T)\varepsilon - \gamma(T)\varepsilon_1$, determines whether $\sigma(t)$ will be positive or negative. For the upper electrode, which is positive, a positive sign means a homocharge, whereas a negative one means a heterocharge. Now $\varepsilon_1 \simeq \varepsilon$, so that a homocharge requires $\gamma_1(T) > \gamma(T)$ and the air gap (layer 1) has to be ionized. Some experimenters have tried to avoid homocharg-

ing by forming the electret in oil (GS 58). However, if $\gamma_{oil} > \gamma_{sample}$ homocharging evidently still occurs.

An electret acquires the largest MW charging when the conductivities γ_1 and γ differ significantly. Let $\gamma_1 >> \gamma$, Eq. 6.10 then reduces to $\sigma(\infty) \simeq \varepsilon_o \varepsilon V_a/l$, giving an interfacial charge that is independent of the formation temperature.

Recalling Eq. 6.9, we also have $V_1(\infty) \simeq o$, and all voltage comes across the most resistive layer. The thinner this layer, the higher the charge density for a given V_a. Consequently, the highest (homo)charges will be acquired by foils, and this makes them very suitable for applications.

6:1.2 Current TSD of a Nonpolar Laminate

Next we turn to the TSD of the two-layer model of Fig. 6-1. After disconnecting the applied voltage at time t_s, Eq. 6.5 becomes

$$dV_1(t)/dt + \beta_g(T)V_1(t) = 0 \qquad (6.11)$$

For convenience we disregard the isothermal storage and take $t_d = t_s$. The initial value at the beginning of TSD, $V(t_d)$, is then determined by the interfacial charge accumulated*;from Eq. 6.8 we obtain

$$V_1(t_d) = -\sigma(t_d)/\varepsilon_o(\varepsilon_1/l_1 + \varepsilon/l) \qquad (6.12)$$

Because V_a is absent, the solution of Eq. 6.11 simply reads

$$V_1(T) = V_1(t_d) \exp(-s \int_{T_d}^{T} \beta_g(T)dT) \qquad (6.13)$$

Substituting Eq. 6.13 into Eq. 6.1 we find for the released current density

$$j_r(T) = \{\beta_1(T) - \beta_g(T)\}\varepsilon_o\varepsilon_1 V_1(T)/l_1 \qquad ...(6.14)$$

Either a positive or a negative current (or, what is the same, a homo- or heterocurrent)may be generated. In general, however, the discharge current has the opposite direction to that of the charging current.

After eliminating $\beta_g(T)$, which is defined in Eq. 6.5, we can also write

$$j_r(t)l = \frac{\{\gamma_1(T)\varepsilon/\varepsilon_1 - \gamma(T)\}V_1(t)}{1 + \varepsilon l_1/\varepsilon l}$$

This equation shows that the TSD current is almost equal to the *difference* between the two ohmic conduction currents, which have opposite directions during TSD. This, of course, may result in a rather *inefficient* charge release. In particular, when the conductivities are similar, efficiency is low. Fortunately, this will seldom occur in practice, because the conductivity is a property which often varies significantly

*This charge need not be equal to $\sigma(\infty)$; for a short formation it will be lower than this ultimate value.

among various materials.

On the other hand, it may happen that the TSD current reverses in sign; then the interfacial charge is first dissipated by the conduction of layer 1 and later by that of layer 2, or vice versa. This remarkable situation arises when the conductivity curves of the two components intersect each other (cf. Figs 2-2). Nevertheless, this is found to be exceptional. The usual MW thermograms of nonpolar layers will show only *one* current maximum, despite the fact that the discharge current depends on two varying quantities, γ_1 and γ (see Fig. 6-2). The position of the current maximum is determined by the faster of the two ohmic dissipation rates.

We further notice that the shape of the resulting thermogram is independent of the forming temperature. This can only change the height of the thermogram via the dependences of $\sigma(t_d)$ and $V_1(t_d)$ on T_f. Such a behaviour was also found for a single Debye relaxation, but not for distributed dipole relaxations.

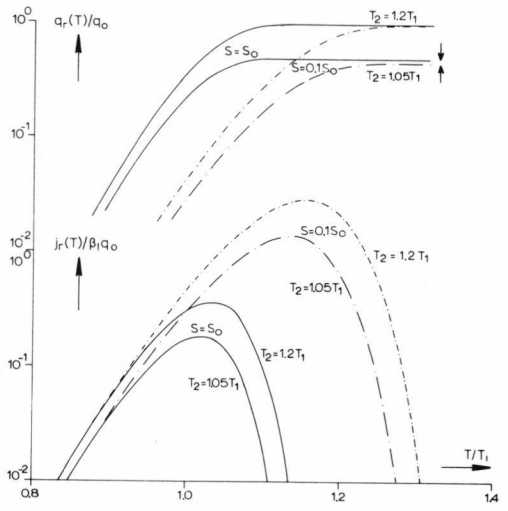


FIG.6-2 Charge and current release of a two-layer series model for two conductivity ratios, which are characterized by the temperature ratio T_2/T_1. Especially when the conductivities differ little (i.e. $T_2 = 1.05\ T_1$) the model suffers from a hidden internal charge loss, and $q_r(\infty) < q_o$. The dependence of the charge and current on the reciprocal heating rate s is also shown. In particular for $T_2 = 1.05\ T$, the ultimate charge is *not* invariant. We took $C_{1,2}/kT_{1,2} = 20$ and $\varepsilon_{1,2}/l_{1,2} = 1$.

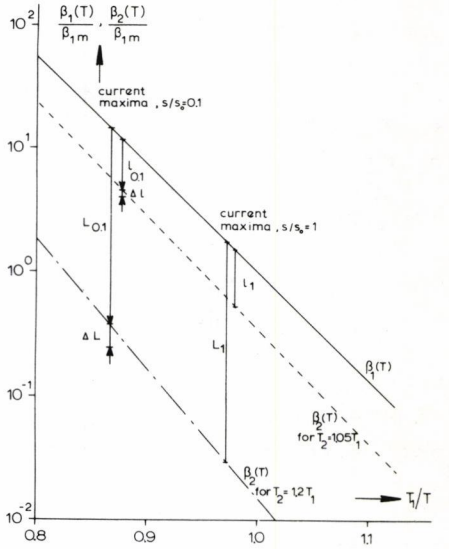


FIG.6-3 Temperature dependence of the ohmic relaxation frequencies used in the model calculations of Fig. 6-2. As indicated by the line segments Δl and ΔL, the conductivities differ less for the higher heating rate ($s = 0.1\ s_o$). This results in a higher unnoticed charge loss, which in turn, makes the ultimate charge released variable.

We just mentioned as a salient feature of this two-layer laminate that the charge release may be inefficient, as a result the ultimately released charge will generally be less than the initially induced charge on the upper electrode. The latter obeys

$$q_o = \varepsilon_o \varepsilon_1 V_1(t_d)/l_1 \tag{6.15}$$

whereas from Eq. 6.14 we have for the ultimate released charge

$$q_r(\infty) = \int_{t_d}^{\infty} j_r(t)dt =$$

$$-\varepsilon_o \varepsilon_1 V_1(t_d)/l_1 + V_1(t_d) l_1^{-1} \int_{t_d}^{\infty} \gamma_1(T) e^{-\int_{t_d}^{t} \beta_g(T)dt'} dt \quad ...(6.16)$$

Only if $\gamma_1 = o$, i.e. if the interfacial charge is solely dissipated by the conduction of layer 2, does $q_r(\infty)$ become equal to q_o, and all charge initially induced by $\sigma(t_d)$ is released.

Fig. 6-2 shows the effects quantitatively. Paying attention first to the curves for the normal heating rate, $s = s_o$, we see that if there are large differences in the conductivities, i.e. $T_1 = 1.2\ T_2$* , the unnoticed charge loss is rather small and $q_r(\infty) = q_o$. In this case the interfacial charge is chiefly dissipated by the upper layer 1, which has a conductivity 55 times higher than layer 2 (cf. Fig. 6-3). However, for $T_1 = 1.05\ T_2$ half the charge is lost, because the conductivities now only differ by a factor of 3 and the interfacial charge is dissipated in two directions by the two conduction currents. (Such a hidden loss is inherent to any excess-charge decay; we also found it in Chap. 5 for the TSD of excess charges stored in *conductive* homogeneous electrets.)

It was first noted by Gross (Gr 70) that an unobserved charge loss may imply that the charge ultimately released may differ for various heating rates, i.e., it is *not* invariant. This always occurs when the two conductivities have a different activation energy. Less charge will then be released for a higher heating rate, because the current maximum is shifted to a higher temperature where the conductivity ratio is lower (cf. Fig. 6-3).

From Fig. 6-2 we see that even for a tenfold increase in heating rate the difference in $q_r(\infty)$ is *small;* for $T_2 = 1.2\ T_1$ it is hardly discernible. In his discussion of the current TSD of lumped series and parallel networks as dielectric models, Gross has shown that a varying ultimate charge can only exist for series models or hybrids of series and parallel models. We therefore did not find it for the parallel Debye network of Fig. 2-10.

*$T_{1,2}$ are defined by the condition of their Debye maximum $sT_{1,2}\beta(T_{1,2}) = C_{1,2}/kT_{1,2}$.

Another pecularity is that the rate constant $\beta_g(T)$ depends on the elements of both relaxation branches of the laminate model, because in a series model these do not discharge independently, as do the branches of the parallel Maxwell representation for a distributed dipole polarization of Fig. 2-10, for which the relaxation frequencies are not intermixed.

In conclusion, a complete similarity between MW models and Debye dipole relaxations as advocated by Van Beek (Be 67), only holds for isothermal experiments. In TSD, where series and parallel models behave differently, the analogy is violated. But even when isothermal experiments are performed at various temperatures, MW models may show remarkable aspects, like current reversals (Gr 70-ET). This unusual behaviour precludes an extension of the simple model to more realistic models for mixtures, such as polymer matrices in which spherical particles are embedded.

We now consider the experimental results for a commercial laminate (Kapton-HF, DuPont, U.S.A.), which consists of 25 μm thick Teflon-FEP heat-sealed to 25 μm thick PI. The results, shown in Fig. 6-4, exhibit a clear MW ρ_c peak at 151 °C, which lies 30 °C below the ρ peak of the shorted Teflon-FEP hetero-electret. The height of the two peaks is also different, that of the laminate being about 80 times higher. The ultimate charge released was $q_r(\infty)/\varepsilon_o\bar{E} = 1.4$, where $\bar{E} = V_a(1 + l_1)^{-1}$. It is interesting to compare this value with that obtainable from Eq. 6.16. In this equation, γ_1 can be taken zero, since examination of Fig. 2-4 shows that the conductivity of PI is about 10 times higher than that of

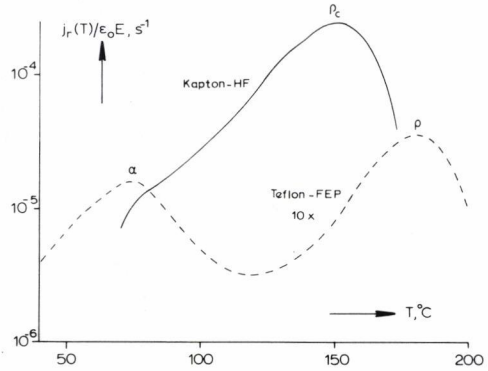


FIG.6-4 Comparison of the current TSD of Teflon-FEP and Kapton HF, which is a laminate of Teflon-FEP and PI and therefor shows a MW ρ_c peak. The two hetero-electrets were formed at 200 °C - 100 kV/cm - 1.5 h. The heating rate was 1 °C/min for Teflon-FEP and 0.45 °C/min for Kapton.

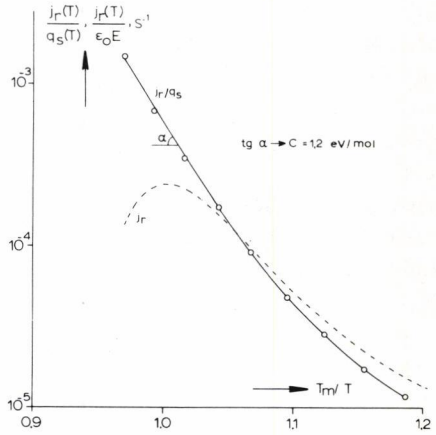


FIG.6-5 Illustration of the initial-rise method and the BFG plot for finding the activation energy for the ρ_c peak of the laminate Teflon-FEP and PI shown in Fig. 6-4.

Teflon-FEP. Hence, $q_r(\infty) = -\varepsilon_o\varepsilon_1 V_1(t_d)/l_1$. Putting $\sigma(t_d) = \sigma(\infty) = \varepsilon_o\varepsilon_1 V_a/l_1$ and using Eq. 6.12, we find theoretically: $q_r(\infty)/\varepsilon_o\bar{E} = 1.45$, in view of $1 = l_1$, $\varepsilon_1 = 2$ and $\varepsilon = 3.5$. The theoretical and experimental values for $q_r(\infty)$ are in good accord.

The similarity between Eq. 6.13 and Eq. 2.8 indicates that the activation energy of the TSD current of the laminate can be calculated in the same way as that of a Debye relaxation. We may therefore expect the BFG plot (j_r/q_s) to be straight; this is nearly so in Fig. 6-5. The corresponding activation energy amounts to 1.2 eV, which is consistent with the value of 1.3 eV for the ohmic conductivity of PI.

6:2 MW Effect in a Polar Polymer with an Adjacent Air Gap

We shall finally discuss the complete two-layer response of a homogeneous polar polymer with an air gap adjacent to its upper side at such low charging voltages that air breakdown is prevented, i.e. $\gamma_1 = 0$. In this set-up a dipole relaxation peak will appear along with the MW conduction peak. Both are typical of the polymer*. We recall that an ohmic conduction peak is *not* observed for shorted homogeneous electrets. It arises in this assembly because the conduction current flowing through the charged polymer is a transient one. It originates in the interfacial charge retained, and first increases due to the increasing conductivity, but thereafter decreases when the interfacial charge is gradually consumed. We shall show that the location of this MW ρ_c peak agrees fairly well with the ρ peak of a hetero-electret of the same polymer studied in short-circuit. This strongly supports our view (Tu 70), that the ρ peaks of shorted polymer electrets are due to the motion of excess charges, which have a similar temperature dependence as the intrinsic carriers partaking in the ohmic conduction.

6:2.1 Charging of the Air-Gap Set-Up

The equations are simpler because of the perfectly insulating air gap, and as before we neglect space-charge storage, but we include dipolar relaxation. To account for a single Debye relaxation, we introduce the persistent polarization $P_s(t)$ in the equations containing $E(t)$. The dielectric constant ε_1 and conductivity γ_1 of the air being 1 and 0, respectively, the two expressions for the current (Eq. 6.1) change to

$$j(t) = \varepsilon_o dE_1(t)/dt = \varepsilon_o\varepsilon_\infty dE(t)/dt + dP_s(t)/dt + \gamma(T)E(t) \qquad (6.17)$$

while Eq. 6.4 becomes

$$\sigma(t) - P_s(t) = \varepsilon_o\varepsilon_\infty E(t) - \varepsilon_o E_1(t) = \varepsilon_o\varepsilon_\infty V_a/1 - \varepsilon_o(1/g + \varepsilon_\infty/1)V_1(t) \qquad (6.18)$$

*When an air gap is introduced in ordinary dielectric measurements, the conduction losses can be converted into a similar MW conduction peak, which is also typical of the polymer concerned.

where $\sigma(t) - P_s(t)$ is termed the effective charge density of the polymer and the identity on the right-hand side is the modified form of Eq. 6.8.

On eliminating E(t) from Eq. 6.17 by means of Eq. 6.2 and writing g(gap) for l_1, we can readily find the new differential equation for $V_1(t)$. However, the air-gap voltage $V_1(t)$ is no longer interesting, because now the appropriate quantities are the interfacial charge $\sigma(t)$ and the dipole polarization $P_s(t)$. Changing from $V_1(t)$ to $\sigma(t)$, and using the right-hand side of Eq. 6.18, we find as the ODE for the interfacial charge $\sigma(t)$

$$d\sigma(t)/dt + \beta_g(T)\sigma(t) = \beta_g(T)P_s(t) - \gamma(T)V_a(1 + \varepsilon_\infty g)^{-1} \qquad (6.19)$$

where the relaxation frequency $\beta_g(T) = \beta(T)(1 + 1/\varepsilon_\infty g)^{-1}$.
Furthermore, the Debye relaxation equation 2.1 after expressing E(t) in V_a and $\sigma(t)-P_s(t)$ reads

$$(1+\varepsilon_\infty g)dP_s(t)/dt + (1+\varepsilon_s g)\alpha(T)P_s(t) = (\varepsilon_s-\varepsilon_\infty)\alpha(T)\{\varepsilon_o V_a+g\sigma(t)\} \qquad (6.20)$$

These two ODE's can be solved numerically to give the unknowns $\sigma(t)$ and $P_s(t)$, for the initial values $\sigma(o) = P_s(o) = 0$. Before discussing this solution, we first describe some other aspects.

From Eq. 6.3 which reduces to

$$d\sigma(t)/dt = -\gamma(T)E(t) \qquad (6.21)$$

we note that $\sigma(t)$ becomes a heterocharge which in the end reaches its maximum when the internal field E(t) becomes zero. The entire applied voltage then comes across the insulating air gap and $P_s(t)$ attains its minimum value $P_s(\infty) = 0$.
Accordingly, Eq. 6.20 gives

$$\sigma(\infty) = -\varepsilon_o V_a/g \qquad (6.22)$$

Taking V_a = 10 kV and g = 1 mm, a final heterocharge density of 8.9 nC/cm^2 results.

Inspection of the model shows that $P_s(t)$ is first built up by the increase in dipole mobility, but later destroyed by the decrease of the internal field, E(t), see also Fig. 6-6. Consequently, the maximum of $P_s(t)$ occurs at a shorter time, say at $t = \tau$. After the dipoles have passed this maximum they relax so quickly that they can follow the changes in the decreasing voltage across the polymer almost immediately. Hence, from τ on, we have

$$P_s(t) \simeq \varepsilon_o(\varepsilon_s - \varepsilon_\infty)V(t)/l$$

which agrees with Eq. 6.20, if $dP_s/dt = 0$.

Expressed in $\sigma(t)$ and $P_s(t)$ the current density during charging reads

$$j(t) = \frac{d\{P_s(t) - \sigma(t)\}/dt}{1 + \varepsilon_\infty g/l} \qquad \ldots(6.23)$$

Thus, j(t) consists of a polarization current, $dP_s(t)/dt$, and a conduction current that supplies the growing interfacial charge $\sigma(t)$. As a result *two* current peaks may appear as functions of temperature; of these peaks that due to the ohmic conduction is the true MW peak, which is also found for a nonpolar polymer. Since $\sigma(t)$ is negative, both currents have the same polarity, so that the total current will be unidirectional.

For the supplied charge we have

$$q(t) = \int_0^t j(t)dt = \{P_s(t) - \sigma(t)\}(1 + \varepsilon_\infty g/1)^{-1} \qquad ...(6.24)$$

and the charge ultimately supplied amounts to

$$q(\infty) = \frac{\varepsilon_o V_a/g}{1+\varepsilon_\infty g/1} \qquad (6.25)$$

which differs from the interfacial charge stored (Eq. 6.22), by the induction loss factor $1 + \varepsilon_\infty g/1$.

Fig. 6-6 shows results of the solution of Eqs 6.19 and 6.20 for an Arrhenius shift of $\gamma(T)$ using a 4th order Runge-Kutta method with step-size control. The trends described are clearly observed. The persistent

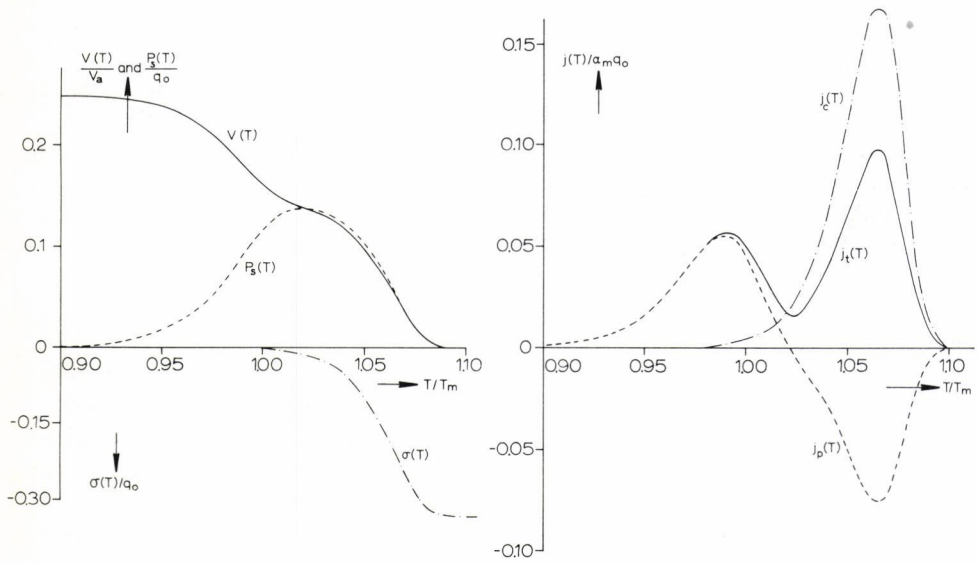


FIG.6-6 Model thermograms of the nonisothermal charging of an absorptive dielectric in series with an insulating air gap. On the left the courses of the internal parameters are given. The observable parameter j_t is shown on the right. This exhibits a dipolar peak and an ohmic conduction peak, because it is composed of, firstly, a dipolar current j_p, which on the average is zero, and secondly a transient ohmic conduction current j_c, which supplies the interfacial charge σ. We took $q_o = \varepsilon_o \varepsilon V_a/1$, $A/kT_m = 50$, $C/kT_c = 75$, $\varepsilon_s = 2\,\varepsilon_\infty = 6$, $g/1 = 1$ and $T_m/T_c = 0.95$.

polarization $P_s(T)$ actually displays a maximum, when the dipoles are neatly oriented, and it eventually vanishes when the voltage across the polymer, V(T), collapses so that finally all dipoles are reoriented at random. The initial decrease in V(T) is induced by the creation of $P_s(T)$; its further decrease is due to the increasing conduction current $j_c(T)$, which starts to build up the heteropolar surface charge $\sigma(T)$ at the air gap interface. We see that $\sigma(T)$ first grows rapidly because the ohmic conductivity increases exponentially, but this growth comes to an end when the internal field becomes zero.

Since the dipolar and conductive processes are well separated, the total current $j_t(T) = j(T)(1 + \varepsilon_\infty g/l)$, shows two peaks. The first originates from the dipole orientation and the second is due to the difference between the conduction current, $j_c(T) = d\sigma/dt$, and the opposing dipole reorientation current, $j_p(T) = dP_s/dt$.

6:2.2 Current TSD of the Air-Gap Set-Up

As soon as the interfacial charge has been created, we can freeze it by cooling the assembly to room temperature. After removing the applied field we can next perform a TSD. As a result of the presence of the air gap and the short-circuit the field in the polymer will change from zero to nonzero, owing to the induction of $\sigma(t)$ on the lower electrode. The actions of this field will be clear, $\sigma(t)$ will be destroyed by ohmic conduction, and at the same time the dipoles will again be reoriented.

The pertinent ODE's are Eqs 6.19 and 6.20, in which V_a is now zero. The initial values are $\sigma(t_d) = -\varepsilon_o V_a/g = \sigma(\infty)$ and $P_s(t_d) = 0$. Obviously, we can make the ODE's for discharging identical to those for charging, by introducing

$$\sigma^*(t) = \sigma(t) + \varepsilon_o V_a/g$$

where $\sigma^*(t_d) = 0$. Since the time dependences of σ and σ^* are the same, we may conclude that the discharging and charging currents are the *same*. Moreover, the charge released will, apart from the sign, be *equal* to the charge supplied. Consequently, Eq. 6.25 will be satisfied by the ultimate charge released, which is exactly the charge that $\sigma(\infty)$ induces on the upper electrode. This result could have been expected, since we have $\gamma_1(T) = 0$, so the stored charge is dissipated *uni*directionally, i.e. by the conduction of the polymer, which makes this particular series model loss-free and charge-invariant.

As regards the calculation of the *relevant parameters* of the resulting current thermograms we are most interested in the evaluation of the MW ρ_c peak, for we intend to relate this to the parameters of the TSD ρ peak of shorted electrets, and also to the ohmic conductivity of the polymer. The evaluation of the dipole peak will therefore not be treated, the less so, because we have based our model calculation on a single

dipole relaxation, whereas polymers always have distributed dipole relaxations. The calculation of the activation energy of the ρ_c peak of the model thermogram is illustrated in Fig. 6-7. We clearly see that the BFG plot is the most reliable, giving $C/kT_c = 74$, whereas the exact value is 75. The initial-current rise, on the other hand, is too sensitive to the contribution of the dipole current.

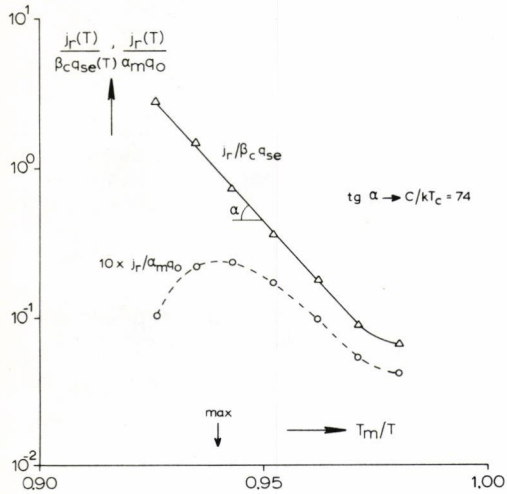


FIG.6-7 Comparison between the initial-rise and BFG method to find the activation energy for the conduction peak of the model thermogram of Fig. 6-6. (As normalization constants we took $\beta_c = \beta(T_c)$, $q_{se}(t) = q_r(\infty)$ and $q_o = \varepsilon_o \varepsilon V_a / l$.

6:2.3 Experimental Results on the MW Charging and Discharging of Polymers

In spite of the fact that the charging and discharging current ought to be the same, Ong and the author (to be published) have found for PVC* that the charging current somewhat exceeds the discharge current, see Fig. 6-8. The results relate to: a metallized sample, $V_a = 500$ V, $g = l = 2$ mm and $s = 1$ min/°C. The discrepancy found, is attributed to leakage currents during charging, because of the high voltage applied. Apart from this, it is noteworthy that the positions of the α peak and the MW ρ_c peak correspond reasonably well to those of the TSD thermogram of a metallized PVC electret, formed at 110° - 2.5 kV/cm - 1 h and discharged without air gap.

This indicates first that the TSD α peak of polymer electrets is mainly due to reorientation of dipolar main-chain segments. It further emphasizes the strong relationship between the TSD ρ peak and the MW ohmic conduction or ρ_c peak. The latter being due to the motion of intrinsic charges in the electric field of the polymer, it is likely that the ρ peak is related to a kindred motion. Obviously, this originates from the motion of excess charges which are thermally mobilized during

*Solvic 223 with 1 % w/w of an organic SnS stabilizer.

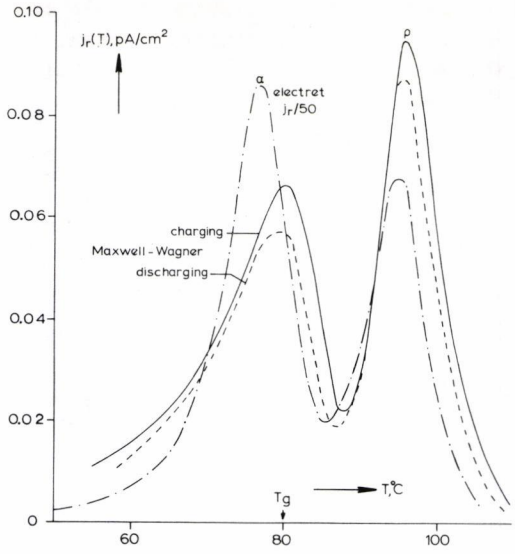


FIG.6-8 Experimental results of the nonisothermal MW charging and discharging of PVC with an adjacent air gap. The current peaks resemble those of the accompanying TSD thermogram of a short-circuited PVC electret. The α peak arises from dipole orientation (resp. reorientation) and the ρ peak from the creation (resp. dissipation) of the interfacial charge. Note that the scale of the electret thermogram has been reduced by a factor of 50.

TSD, and which drift under their own field towards the shorted electrodes. Note that the location of the α peak corresponds to the glass-rubber transition of PVC.

These assignments of the TSD α and ρ peaks of metallized polymer electrets are confirmed by results on the copolymer 80 S co 20 AN. There is again a close agreement between the related MW and TSD peaks in Fig. 6-9. In both experiments the same metallized sample was used. The MW investigations were carried out with V_a = 1 kV, g = 1.5 mm and l = 3 mm, while the electret was manufactured at 130 °C - 20 kV/cm - 1.5 h.

It is interesting to note that the charge released during TSD of the MW set-up amounts to 0.25 nC/cm^2, which agrees well with the theoretical value of 0.24 nC/cm^2, calculated from Eq. 6.25.

Fig. 6-10 finally gives the BFG plots for the three thermograms of Fig. 6-9. From the straight part of these plots we calculate an activation energy of 3.4 eV for MW charging and discharging, and of 3.1 eV for the electret. These values are fairly consistent, they are also in accord with the value of 3.2 eV found for the activation energy of the ohmic conductivity.

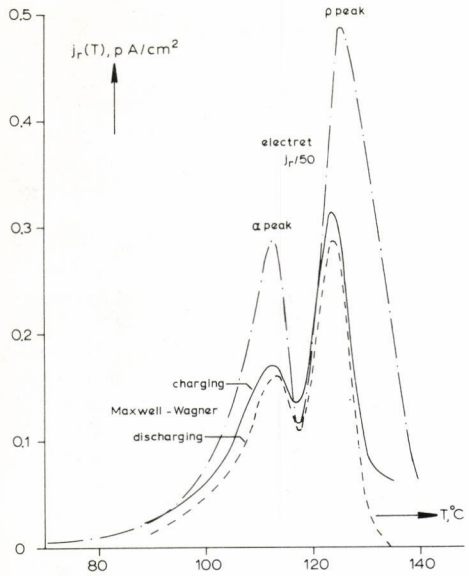


FIG.6-9 Nonisothermal MW charging and discharging currents of 80 S co 20 AN layered together with an adjacent air gap, compared with the current TSD of a shorted electret of the same polymer. The results are very similar to those of Fig. 6-8.

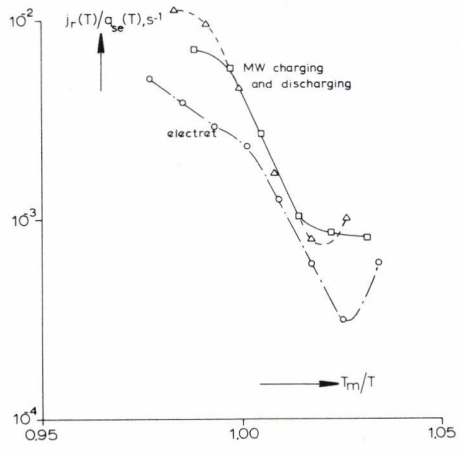


FIG.6-10 Calculation, by means of a BFG plot, of the activation energies of the ρ peak (electret) and ρ_c peak (MW charging and discharging) of 80 S co 20 AN.

Chapter 7

CURRENT TSD BY DIPOLE REORIENTATION AND OHMIC CONDUCTION IN ELECTRETS SHORTED TOGETHER WITH AN ADJACENT AIR GAP

By introducing an air gap at the upper electrodes, as shown in Fig. 7-1, we obtain a two-layer capacitor, in which the electret itself is not short-circuited, so that the average electric field within it is no longer zero, and in fact becomes quite large (Sect. 1:6.2). Consequently, the ohmic conduction current flowing through the electret produces an appreciable external displacement current, whereas in current TSD of shorted electrets it remains obscured. Accordingly, this technique enables one not only to observe the reorientation of dipoles, but also the *excess-charge decay by ohmic conduction*.

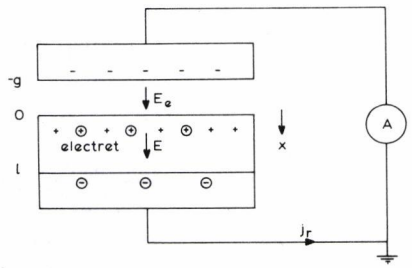


FIG.7-1 Diagram for current TSD of electrets shorted together with an adjacent air gap. The arrows indicate the positive directions of x, E and j_r. Because of the air gap the upper electret charge induces its image charges not only on the upper electrode, but also on the lower electrode, so the average field within the electret is non-zero. The lower electret charge is not shown, because this is effectively compensated by nearby image charges, induced on the adhering metal layer.

Evidently, the evaluation of a combined decay of aligned dipoles and excess charges is mathematically rather complicated. In practice, however, both decays can be separated by combining the air-gap thermograms with those of shorted electrets. In discussing this combined decay below, we assume the electret to be charged arbitrarily, and so the excess charges may be ions and/or electrons, and may be hetero and/or homopolar. They may be stored either as space charges, or as surface charges on the upper side. Apart from their ohmic dissipation, the excess charges may also disappear by SCL drift and diffusion. This decay generates a comparatively small TSD current, and will therefore be neglected.

The study of the TSD of *surface charges*, especially of homopolar ones, is very interesting, because their decay could not be observed in metallized electrets. In a TSD with an air gap, however, the surface charge remains intact, since the upper side need not be metallized. The elucidation of the TSD of heteropolar *space charges* by ohmic conduction in an air-gap system is also very interesting, for it may shed light on the origin of the TSD ρ peak in shorted metallized electrets. In particular, if the current peaks resemble each other, this would establish once more that the formerly unknown ρ peak originates from SCL drift (and diffusion) of excess charges.

In addition, the air gap and the uncovered upper side make the persistent charge of the electret accessible to a direct measurement. This prompted us to study charge TSD of homocharged foils of which we know, from Chap. 5, that TSD current measurements are far less efficient. To this end a special apparatus based on the field-cancellation principle was developed. The theory of this type of air-gap measurement will be dealt with in the next chapter.

Although this chapter is devoted to current TSD, we shall also derive the temperature dependence of the persistent charge, which is the significant quantity for the applications of electrets. This charge can be measured with a slightly modified set-up. A method incorporating a movable upper electrode and an integrating electrometer was briefly discussed in Sect. 1:4; for further details and some related methods see (Tu 70 a). Such TSD charge measurements only allow a discontinuous sampling of the electret charge, during which the actual values of the two fields are disturbed. This disturbance cannot be avoided, for otherwise the required transfer of induced image charges to the measuring equipment does not take place. We therefore paid little attention to this kind of TSD charge measurement.

In Sect. 7:1 we shall first give a theory advocated in (Tu 70), in which the combined decay of dipoles and excess charges is supposed to arise from a *single* dipole reorientation and intrinsic ohmic conduction. This description enlarges the discussion in Chap. 6 on the discharge of heterogeneous systems, in that space charges are accounted for. This work has benefited from earlier theories by Swann (Sw 50) and Gubkin (Gu 57) describing the isothermal charge decay. However, these investigators incorrectly disregarded the right-hand side of Debye's equation for dipole relaxations; this has been discussed before (Tu 70a). Sect. 7:2 modifies the theory of Sect. 7:1 to include two-sided metallized electrets. This metallization alters the current TSD considerably. We shall show that owing to the presence of image charges on the evaporated electrodes, a marked conduction peak will result, even when the electret only contains aligned dipoles. Of the addenda to this chapter in App. II, Sect. 7:3 reports on the TSD of electrets sandwiched between two air gaps, while Sect. 7:4 describes the air-gap TSD involving multiple dipole relaxations. Sect. 7:5, finally, extends the theory to excess charges that are thermally mobilized to drift under their own field (SCL drift).

7:1 One-Sided Metallized Hetero and Homo-Electrets

As shown in Fig. 7-1, we suppose that the upper face of the electret is not metallized and we assume, quite generally, a surface charge, space charge and persistent polarization to be present; we allow the latter to be *space-dependent*. The air-gap width is denoted by g, and we put x = 0 on the upper surface of the electret. The electrode evaporated

on the lower side is supposed to be open, and, therefore, to permit charge neutralization.

The decaying polarization $P_s(x,t)$, the dipoles of which we suppose to reorientate at a single relaxation frequency, will obey the following Debye equation

$$\partial P_s(x,t)/\partial t + \alpha(T)P_s(x,t) = \varepsilon_o(\varepsilon_s - \varepsilon_\infty)\alpha(T)E(x,t) \qquad (7.1)$$

in which a partial time-derivative is used, because P_s also depends on x. The ohmic conduction, on the other hand, will cause the space and surface charges to disappear according to the respective continuity equations

$$\partial\rho(x,t)/\partial t = -\gamma(T)\partial E(x,t)/\partial x \qquad (7.2)$$

and

$$d\sigma(t)/dt = -\gamma(T)E(o,t) \qquad (7.3)$$

The internal and external fields are determined by the stored charge. Their relationships are expressed by Poisson's equation and Gauss's induction law. At the boundary x = o the latter reads

$$\varepsilon_o\varepsilon_\infty E(o,t) + P_s(o,t) - \varepsilon_o E_e(t) = \sigma(t) \qquad (7.4)$$

while the former no longer takes the form of Eq. 5.5, since E(x,t) is also determined by $P_s(x,t)$. Therefore

$$\varepsilon_o\varepsilon_\infty\partial E(x,t)/\partial x + \partial P_s(x,t)/\partial x = \rho(x,t) \qquad (7.5)$$

Furthermore the short-circuit condition (Eq. 5.6) becomes

$$E_e(t)g + \int_o^1 E(x,t)dx = 0 \qquad (7.6)$$

which clearly indicates that the mean field in the sample is *not* zero.

The discharge current density arising from the decay of the polarization and the excess charges may be expressed in two forms. In the sample we have

$$j_r(t) = \varepsilon_o\varepsilon_\infty\partial E(x,t)/\partial x + \partial P_s(x,t)/\partial t + \gamma(T)E(x,t) \qquad (7.7)$$

and in the air gap we have

$$j_r(t) = \varepsilon_o dE_e(t)/dt \qquad (7.8)$$

Integrating the latter, we find for the released charge density

$$q_r(t) = \varepsilon_o\{E_e(t) - E_e(o)\} \qquad (7.9)$$

There are several ways to solve this set of equations. For practical reasons we are mainly interested in the *released current* and the *retained charge*, so we shall try to solve the equations for these quantities. By integrating Eq. 7.7 from x = 0 to x = 1 we get, in view of Eqs 7.6 and 7.8.

$$j_r(t) = (1 + \varepsilon_\infty g)^{-1}\{\frac{d}{dt}\int_0^1 P_s(x,t)dx + \gamma(T)\int_0^1 E(x,t)dx\} \quad ...(7.10)$$

Equation 7.10 shows that besides the depolarization current, there is an internal conduction, because $\int_0^1 E(x,t)dx = -E_e(t)g \neq 0$. This average conduction current clearly disappears if the air gap is reduced to zero, so that the electret itself is shorted. By replacing $j_r(t)$ with $\varepsilon_o dE_e(t)/dt$, and eliminating $\int_0^1 E(x,t)dx$ by means of Eq. 7.6, we can convert Eq. 7.10 into a differential equation for the external field, $E_e(t)$

$$dE_e(t)/dt + \beta_g(T)E_e(t) = \{\frac{d}{dt}\int_0^1 P_s(x,t)dx\}/\varepsilon_o(1 + \varepsilon_\infty g) \quad (7.11)$$

where the relaxation $\beta_g(T)$ is generally less than the ohmic relaxation frequency $\beta(T) = \gamma(T)/\varepsilon_o\varepsilon$ of the polymer, because it equals

$$\beta_g(T) = \beta(T)(1 + 1/\varepsilon_\infty g)^{-1} \quad (7.12)$$

The ODE 7.11 should be solved together with that of the total polarization $\int_0^1 P_s(x,t)dx$. Integration of Eq. 7.1 between x = 0 and 1 and elimination of $\int_0^1 E(x,t)dx$ gives

$$\frac{d}{dt}\int_0^1 P_s(x,t)dx + \alpha(T)\int_0^1 P_s(x,t)dx = -\varepsilon_o(\varepsilon_s - \varepsilon_\infty)\alpha(T)E_e(t)g \quad (7.13)$$

The solution of Eqs 7.11 and 7.13 poses our problem. The initial values are $\int_0^1 P_s(x,o)dx$ and $E_e(o)$. The latter depends on the stored charges. By integrating Poisson's equation 7.5 twice we find, on invoking Eq. 7.6 and eliminating E(o,t) by means of Eq. 7.4

$$-\varepsilon_o E_e(t)(1 + \varepsilon_\infty g) = \sigma(t)1 - \int_0^1 P_s(x,t)dx + \int_0^1 \rho(x,t)(1 - x)dx \quad (7.14)$$

Particularizing this equation at t = 0 yields $E_e(o)$.

However, we would like to proceed in another way. It will be clear that $\varepsilon_o E_e(t)$ equals the surface charge density induced on the upper electrode

$$q_i(t) = \varepsilon_o E_e(t) \quad (7.15)$$

Several methods to measure this quantity are discussed in (Tu 66, Tu 70a). From Eq. 7.14 we see that $q_i(t)$ does not consist merely of a surface charge $\sigma(t)$ but also contains contributions of $P_s(x,t)$ and $\rho(x,t)$; it is therefore called the *effective surface charge density* induced on the upper electrode. Similarly, we can introduce the effective surface charge density of the electret, which has the advantage of *not* depending on the air gap

$$q(t) = \sigma(t) - 1^{-1}\int_0^1 P_s(x,t)dx + \int_0^1 \rho(x,t)(1 - x/1)dx \quad (7.16)$$

Note that

$$q_i(t) = -q(t)(1 + \varepsilon_\infty g/1)^{-1} \quad (7.17)$$

where the factor $1 + \varepsilon_\infty g/1$ accounts for the loss of induction to the

lower electrode; this reduces to zero only if $g/l \to 0$.

Results of charge measurements during the formation of PMMA electrets are given in Fig. 6-12. Fig. 7-2 shows results of the charge TSD of a finished PMMA electret. These automated measurements were carried out by tilting the upper electrode periodically by a solenoid in order to change the gap width g and so to transfer a well-defined part of the induced charge to an electrometer-integrator system. When the upper electrode was not operated, it touched the electret, so that in fact q(t) was determined.

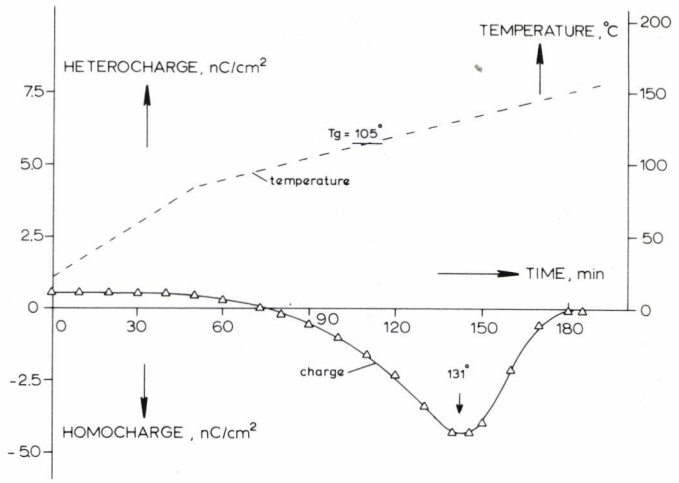


FIG.7-2 Charge TSD of a PMMA electret, formed at 140° - 20 kV/cm - 3 h. The net charge given has been measured periodically. It starts as a heterocharge, and is later transformed into a transient homocharge.

The electret had been stored for several months and we see that its initial effective charge of 0.54 nC/cm^2 is heteropolar. However, this is only part of the charge actually stored, because during TSD the effective net charge reverses in sign and becomes homopolar. At 131 °C a maximum homocharge of 4.3 nC/cm^2 is reached. Eventually, this homocharge vanishes because it is dissipated by the increasing ohmic conduction. Obviously, homocharges are generally more stable than heterocharges, which usually disappear at T_g. In ordinary dielectric measurements too, ohmic conduction operates at higher temperatures (viz. above T_g) than do the dipole relaxations of the main chains.

The induction-loss factor of Eq. 7.17 also appears in the released current density. Differentiation of this equation yields

$$j_r(t) = -(dq(t)/dt)(1 + \varepsilon_\infty g/l)^{-1} \qquad \ldots(7.18)$$

where dq(t)/dt follows from Eq. 7.20.

By integrating Eq. 7.18, or by using Eq. 7.9, we find for the ulti-

mate charge released

$$q_r(\infty) = q(o)(1 + \varepsilon_\infty g/1)^{-1} \qquad ...(7.19)$$

which indicates that this technique releases, apart from the factor $1 + \varepsilon_\infty g/1$, the net charge originally stored. Apparently, when $\int_o^1 P_s(x,o)dx$ is known from a TSD with shorted metallized electrets, we can subtract it from $q_r(\infty)$ to find the total excess charge density initially stored.

By substitution of the net electret charge $q(t)$ for $E_e(t)$, Eqs 7.11 and 7.13 become

$$dq(t)/dt + \beta_g(T)q(t) = -1^{-1} \frac{d}{dt} \int_o^1 P_s(x,t)dx \qquad (7.20)$$

$$\frac{d}{dt} \int_o^1 P_s(x,t)dx + \alpha(T) \int_o^1 P_s(x,t)dx = (\varepsilon_s - \varepsilon_\infty)\alpha(T)q(t)g(1 + \varepsilon_\infty g/1)^{-1} \qquad (7.21)$$

In this *final* set of ODE's for quantities, which are of direct practical interest, the initial values, $q(o)$ and $\int_o^1 P_s(x,o)dx$, are known. Note that the equations are similar to Eqs 6.19 and 6.20, in which, however, space charges were not considered. The isothermal solutions of Eqs 7.20 and 7.21 has been discussed in (Tu 70a), where we illustrated the unusual time behaviour of the combined decay of a polarization and an excess charge. For TSD, the equations have to be solved numerically, we took a 4th-order Runge-Kutta method with stepsize control.

Having indicated the formal solution of our problem, we refer to Fig. 10-60 for a released charge and current thermogram of homocharged PMMA electret. We decomposed the quantities into a depolarization and an excess charge decay by invoking the thermogram of a metallized electret. In accord with Fig. 7-2 the released current, j_r, shows two peaks, the first arising mainly from depolarization, and the second from ohmic conduction. It is interesting to note that the conduction or ρ_c peak exactly occurs at the ρ *peak* of the metallized electret. Most polymers showed such a behaviour. This confirms that this very ρ peak originates from SCL drift of stored excess charges, which during the formation were accumulated by the ohmic conduction of the polymer. Diffusion probably plays a minor role.

Eqs 7.18 and 7.21 suggest that besides the molecular parameters of the polymer, the gap width, or rather the ratio g/l, also affects the thermograms. This is so, because the reduced gap determines the field within the electrets. For high external currents, g/l should be low*. For foils a current measurement therefore becomes less attractive, and

*However, low g/l ratios may be unfavourable, because then the external field may become large, and so it may produce a disruptive discharge in the air gap, which will disturb the air-gap TSD measurement by neutralizing part of the electret charge.

measurement of the persistent charge by the field-cancelling principle is more appropriate; see Chap. 8.

Further examination of the equations shows that the net charge and the polarization are affected in different ways by the normalized air gap, especially as concerns their decay rates. Even in the absence of a polarization, the net charge decays with the *reduced* ohmic relaxation frequency β_g, rather than with the actual ohmic relaxation frequency β. In particular, at low g/l ratios, when the field in the electret is weak, the decay of the net charge is slowed down considerably. This is not so for the polarization, for which the resulting internal field in the first place determines the quasi-equilibrium value, which in the end always vanishes.

Looking at Eq. 7.18 again we clearly see that on the basis of current measurements no distinction can be made between surface charge and space charge. Neither can we find the internal distributions of $P_s(x,t)$ and $\rho(x,t)$. It is the total excess charge density $Q(t)$ and $\bar{P}_s(t)$, the average value of $P_s(x,t)$, that matters. With these quantities we may rewrite Eq. 7.16 as

$$q(t) = Q(t) - \bar{P}_s(t) \qquad (7.22)$$

where

$$Q(t) = \sigma(t) + \int_0^1 \rho(x,t)(1-x/1)dx \text{ and } \bar{P}_s(t) = 1^{-1} \int_0^1 P_s(x,t)dx$$

7:1.1 Model Thermograms of TSD with an Air Gap

To illustrate the foregoing theory, we compiled some typical model thermograms in Figs 7-3 to 7-6. Fig. 7-3 applies to a *highly heterocharged* electret, so we put the excess charge density zero, i.e. $Q(o)=0$. Contrary to practice we assumed the ohmic dissipation to occur at a lower temperature than the dipole relaxation: $T_m = 1.025\ T_c$. (Both characteristic temperatures are defined as in Eq. 2.20 so that e.g. $sT_c\beta(T_c) = C/kT_c$). To reveal the combined decay, we decomposed the polarization and excess charge contributions, by introducing the currents: $j_t = dq/dt$, $j_r = d\bar{P}_s/dt$ and $j_c = dQ/dt$; they all were reduced to $\alpha_m q_o$ in Fig. 7.3.

We see that first the decrease of $P_s(t)$ dominates, giving rise to a heteropolar discharge current, but that at high temperatures, when the conduction rises sharply, a *homocharge* is built up; mainly as a surface charge by MW charging at the insulating interface x = 0, but also, partly, as a space charge if the polarization is not uniform. This homocharge reaches a maximum at $t = \tau$, when the average internal field becomes zero, or what is the same when $Q(\tau) = P_s(\tau)$. Next the field in the polymer changes in sign, because the more stable $Q(t)$ exceeds $P_s(t)$. As a result, $\sigma(t)$ is destroyed and the discharge current *reverses* its sign. Without proper knowledge about the decay processes one would attribute this transient homocurrent to the presence of a small homocharge

at t = 0.

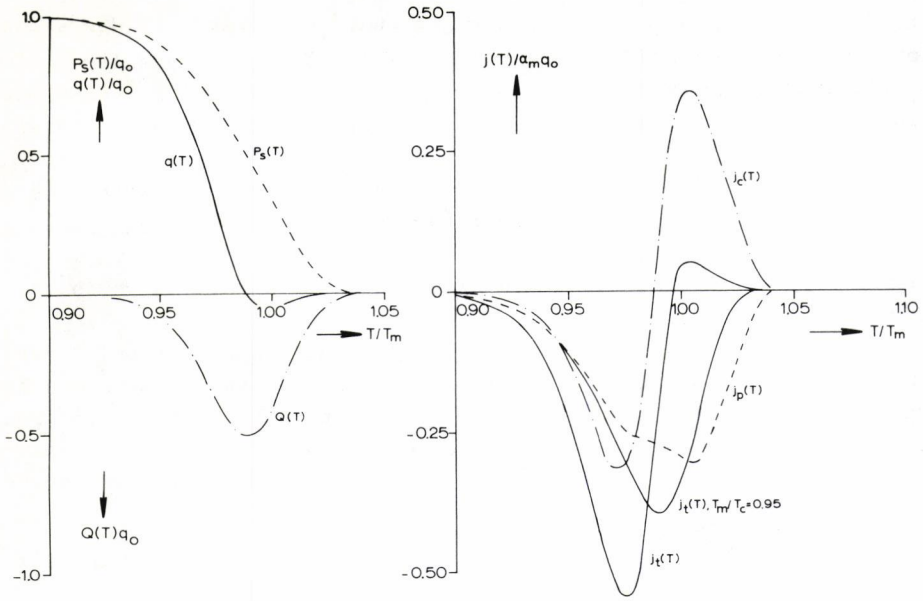


FIG.7-3 Calculated behaviour of a strong *hetero-electret* during TSD with an air gap. The observable quantities are plotted as full lines; the net charge q is mapped on the left and the total current j_t on the right. The temperature dependence of their components are also indicated; we chose the same type of line for related quantities. The field created in the polymer by the dominating polarization $P_s(T)$, gives rise to a temporary *homocharge* Q(T). As a result the total current eventually changes from a heterocurrent to a small transient homocurrent. We took Q(o) = 0, A/kT_m = 50, C/kT_c = 75, g/l = 1, T_m/T_c = 1.025 and ε_s = 2 ε_∞ = 6. The total current for T_m/T_c = 0.95 is also given; its homo part is hardly distinguishable.

In practice, however, ohmic conduction becomes operative later than the dipole reorientation i.e. $T_c > T_m$. Thus the fictitious homocurrent will hardly be observable when any homocharge is lacking initially, i.e. when Q(o) = 0. This can be seen from the total current for T_m/T_c = 0.95; the negative part of which can be neglected. The ohmic conduction now emerges when most dipoles are reoriented, so that the internal field is too small to create an appreciable homocharge. Thus, when in practice homocurrents are found, they are likely to arise from a true homocharge.

In Fig. 7-4 we considered the opposite case of a *strongly homocharged electret*. Here we took $P_s(t)$ = 0, which for a polar material will be true only at low formation temperatures. Now the decaying homocharge gradually creates a *polarization** which eventually, however, disappears

*The appearance of a polarization has not been visualized in older isothermal decay studies of charged polymers (Sh 58). This has led to a misinterpretation of the decay rate, which disobeys simple one exponential ohmic decay (Tu 70a).

when the internal field is destroyed. The total current, j_r, now shows two peaks of the same polarity, the first mainly due to the dipole orientation, and the second arising from the combined effects of ohmic conduction and dipole reorientation. (Note that the current thermograms are identical to those of MW charging in Fig. 6-6 except for a factor of 3 owing to a different choice of q_o. This is plausible, because the present thermograms correspond to those of MW discharging.)

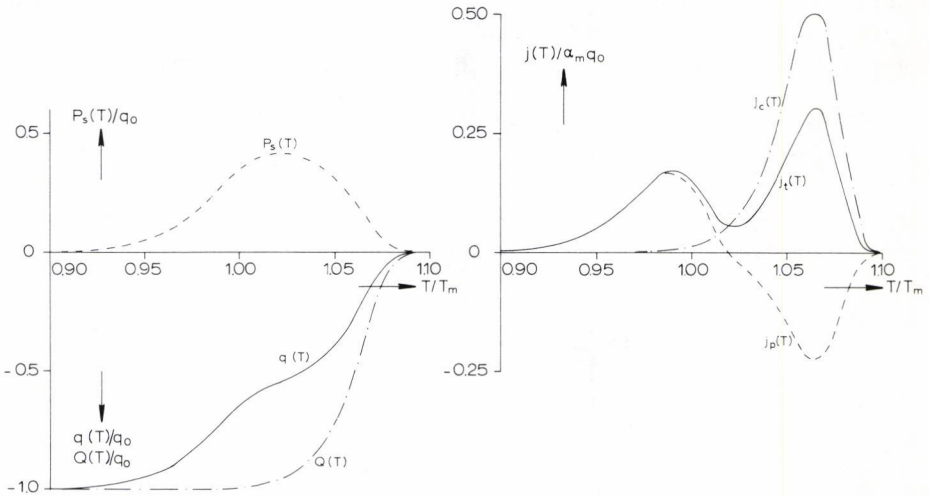


FIG.7-4 Theoretical behaviour of a strong *homo-electret* during TSD with an air gap. In this case, the large homocharge Q(T) creates the internal field, to which the permanent dipoles react with an evanescent *polarization* $P_s(T)$. The total current therefore shows a dipole peak ahead of its conduction peak. As in Fig. 7-3 we decomposed the net charge, q, and the total current, j_t, into their components. The same parameter values were chosen, i.e. $A/kT_m = 50$, $C/kT_c = 75$, $g/l = 1$, and $\varepsilon_s = 2\ \varepsilon_\infty = 6$, except that now $P_s(o) = 0$ and $T_m/T_c = 0.95$.

A similar behaviour may be expected for the TSD of polar polymers charged by friction or corona-discharge, which can also be studied with air-gap TSD. Experimental results for the current TSD of corona and friction charged PVC were given in Fig. 1-10. They indeed reveal the two peaks mentioned. On the other hand, if the polymer is *nonpolar*, we find an ohmic conduction peak. (This can be seen in Fig. 7-10, which gives the results for PE.)

The marked changes caused by the reduced *gap width* g/l on the thermogram of a homocharged polymer with dielectric absorption are shown in Fig. 7-5. (Note that the plots give the released current, $j_r = j_t(1 + \varepsilon_\infty g/l)^{-1}$. The current for $g/l = 1$ is therefore lower than that of Fig. 7-4 by the induction-loss factor of 4.) We see that the position of the maximum shifts to higher temperatures with decreasing g/l; the first peak or dipole peak gradually approaching T_m. Moreover, the reduced gap g/l affects the magnitude of the current not only because of

the induction loss to the lower electrode, but also by changes in the internal field, which in turn affects the ohmic conduction and the dipole alignment. The two current maxima do not vary in the same way. The conduction peak increases steadily with decreasing g/l, still tending to an optimum at g/l = 0.008, whereas the depolarization peak passes an optimum at g/l = 0.25. These optima are not shown in the figure, but can be calculated from Eqs 7.28 and 7.35 (below).

The upper part of the figure shows the course of the effective charge. For g/l = 0.01 this charge is retained up to very high temperatures; for larger gaps it drops much faster. This stabilization effect of a small

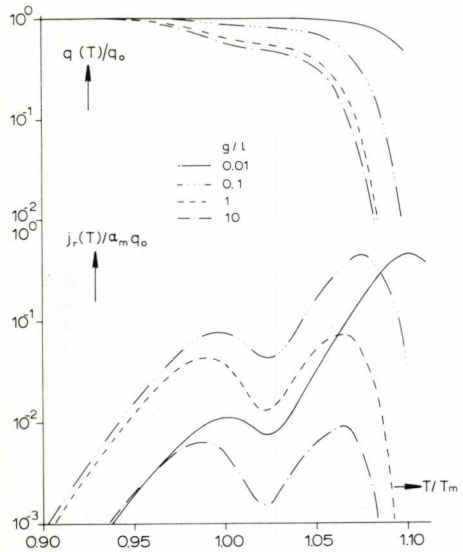


FIG.7-5 Effect of the reduced gap width g/l on the TSD of a strong homoelectret made of a polar polymer at *low* temperatures. The change in height of the the high-temperature conduction peak is wider than that of the low-temperature dipole peak (lower curves). The upper curves demonstrate that the net charge becomes more persistent, if the gap width is reduced, so that the internal field is weakened. The parameters were taken the same as in Fig. 7-4.

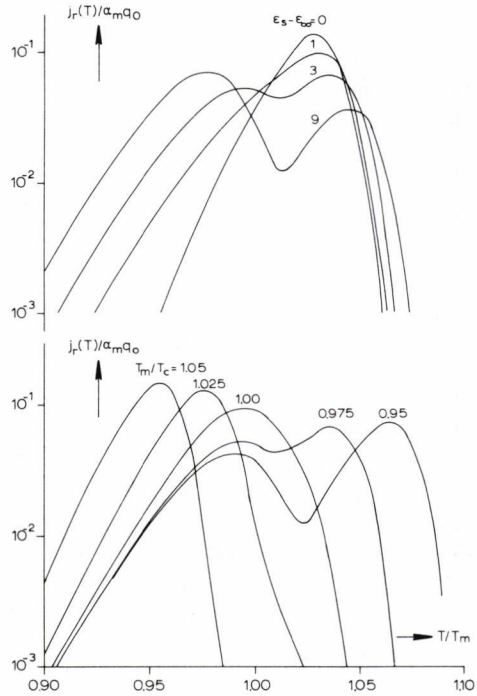


FIG.7-6 Above: Dependence of the air-gap thermograms of an absorptive homoelectret on the dipolar relaxation strength $\varepsilon_s - \varepsilon_\infty$. We put $T_m/T_c = 0.975$; the other parameters were as in Fig.7-4. For $\varepsilon_s - \varepsilon_\infty = 0$ (nonpolar polymer) there is only a conduction peak.
Below: The influence of the temperature dependence of the dipolar and ohmic relaxation frequencies as denoted by the temperature ratio T_m/T_c of their Debye maxima. If $T_m \gg T_c$ only the conduction peak emerges.

gap width has first been pointed out by Gubkin for an isothermal decay (Gu 57). On this is based the common practice of storing electrets between abutting short-circuited electrodes.

The upper plots in Fig. 7-6 demonstrate the effect of an increase in *dielectric absorption* of the homocharged polymer. For a nonpolar polymer, i.e. $\varepsilon_s - \varepsilon_\infty = 0$, only a conduction peak emerges, but when permanent dipoles are present a dipole peak arises in front of the conduction peak. It increases with $\varepsilon_s - \varepsilon_\infty$ and simultaneously shifts to a lower temperature.

The lower part of Fig. 7-6 illustrates the influence of the *temperature dependence* of the relaxation frequencies of the dipole reorientation and ohmic conduction. When $T_c > T_m$ two peaks appear, which gradually unite into one peak; for at low T_c values the homocharge is too rapidly dissipated by ohmic conduction to build up a noticeable polarization. The current for $T_m/T_c = 1.05$ therefore occurs at T_c, and is merely due to ohmic conduction.

7:1.2 Special Model Thermograms Calculated Analytically

Having considered some general aspects of the decay processes, we will now deal with some special cases for which an *analytical solution* is feasible. If the experimental thermogram is to be evaluated, such a solution is to be greatly preferred to a numerical one. Specific thermograms, which allow an analytical solution, are found, if the polymer has special properties. Typical examples are first, nonpolar polymers for which only conduction peaks are found, and, second, polar polymers having low ohmic conductivity, which show only dipole peaks. Obviously, for these single peaks, the set of two simultaneous ODE's (Eqs 7.20 and 7.21) reduces to one ODE, the solution of which is straight-forward. A similar line of attack can be followed if in an actual thermogram the two peaks are well resolved. These can also be analyzed separately, and this markedly simplifies the calculation of the relevant parameters.

7:1.2a Conduction Peak of Homocharged Nonpolar Polymers

For a *homocharged, nonpolar* electret we have $\varepsilon_s = \varepsilon_\infty$ and $P_s(t) = 0$. In this case, which applies to frictional or corona charged nonpolar polymers as well, Eqs 7.20 and 7.21 reduce to a single equation

$$dq(t)/dt + \beta_g(T)q(t) = 0 \tag{7.23}$$

the analytical solution of which reads

$$q(t) = q(o) \exp(- \int_0^t \beta_g(T)dt) \tag{7.24}$$

Although the charge decays solely by ohmic conduction, the rate constant is not $\beta(T)$, but $\beta_g(T)$, see Eq. 7.12. Hence, a small gap diminishes the decay considerably, since it weakens the internal field strongly*.

*In the limit $g \to 0$, $q(t)$ does not decrease at all, because the capacitance of the air gap becomes infinite, which results in an infinite decay time. However, a blocking electrode for intimate contact is unrealistic, and an open electrode is more likely; in this case excess charges do decay. In fact they do so at a rate $\beta(T)$, but we know from Chap. 5 that this decay cannot be observed.

On substituting Eq. 7.24 into Eq. 7.18 we get for the external current density

$$j_r(t) = \beta_g(T)q(t)(1 + \varepsilon_\infty g/l)^{-1} \qquad ...(7.25)$$

Apparently, in this technique a positive current is generated for a positive excess charging, as opposed to the negative current flow by SCL drift in shorted electrets. It is also clear, that the thermograms of ohmic charge decay are identical to those of a *Debye relaxation* (compare Eq. 2.11) with the exception that they depend on g/l. If the conduction increases according to an Arrhenius equation, with an activation energy C, we find from Eq. 2.21 that the current reaches a maximum when

$$sT_m\beta_g(T_m) = C/kT_m \qquad (7.26)$$

Note that T_m does not depend on polymeric constants only, but also on the gap width.

A family of thermograms of ohmic decay for various g/l values is shown in Fig. 7-7. They behave similar to the second peak of Fig. 7-5, which can now be

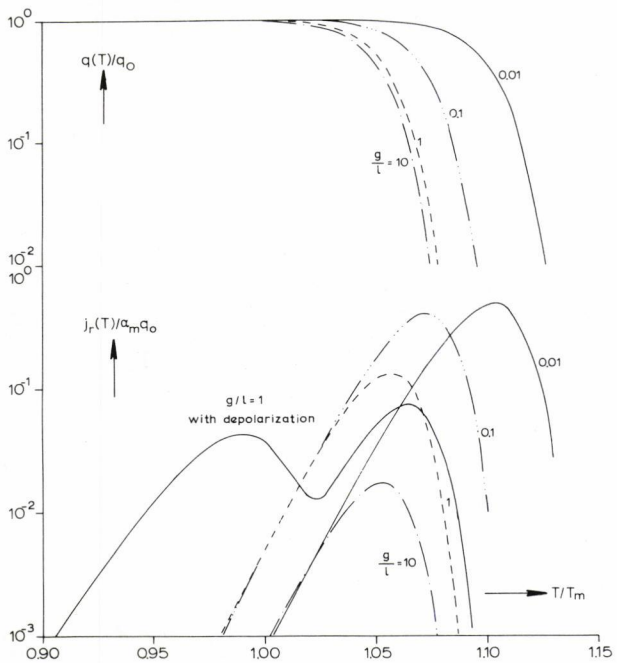


FIG.7-7 Computed thermograms representing the *pure-ohmic decay* of a homo-electret for various gap widths. The parameters are the same as in Fig. 7-4, and so we assumed the polymer to be nonpolar ($\varepsilon_s - \varepsilon_\infty = 0$). For comparison, a single curve of Fig. 7-5 belonging to a polar polymer with $\varepsilon_s - \varepsilon_\infty = 3$ and g/l = 1 is also shown. Its high-temperature conduction peak differs from that of the nonpolar polymer electret, because this is disturbed by the preceding dipole peak.

better interpreted. Obviously, for large gaps the external current is weak, and the temperature of fastest decay is low, because it is approximately determined by $\beta(T)$. If g/l is reduced, the induction loss to the lower electrode decreases, and the current density grows. Concurrently, its maximum shifts to higher temperatures, because the relaxation frequency $\beta_g(T)$ becomes smaller. When the gap is very narrow, however, the internal field becomes too weak to cause a perceptible charge decay and the current decreases again.

The gap for an optimum current maximum can be calculated from

$$dj_r(T_m)/d\kappa = \partial j_r(T_m)/\partial\kappa = 0 \qquad (7.27)$$

where $\kappa = g/l$ and $T_m = f(\kappa)$. Differentiation of Eq. 7.25 yields together with Eq. 7.12

$$1 - \varepsilon_\infty\kappa = s \int_{T_d}^{T_m} \beta_g(T)dT \simeq 1 - 2kT_m/C$$

where on the right-hand side the approximation for the exponential integral at T_m has been inserted. Hence, the optimum gap obeys

$$\varepsilon_\infty\kappa \simeq 2kT_m(\kappa)/C \qquad ...(7.28)$$

where the dependence of T_m on κ is implicitly given by Eq. 7.26. Since C/kT_m is large, low κ values result, e.g. $C/kT_m = 20$ gives $\varepsilon_\infty g/l = 0.1$. (The following, between the marks -***- can be skipped in a first reading.)

-***-

Some Aspects of the Internal Charge Decay

We have not yet specified the course of the retained excess charge, because it was of no interest with regard to $j_r(t)$. To illustrate the decay of space charges by ohmic conduction in air-gap system we assume a uniform penetration of positive carriers up to a depth r_o (see Fig. 7-8). In addition to putting $\varepsilon_s = \varepsilon_\infty$ and $P_s(o) = 0$, we take $\sigma(o) = 0$ so that the case applies to a homocharged electret, the spectacular features of which were discussed in Sect. 5:3. Here, however, the homocharges are supposed to be *immobile*. As a result the carrier front does not expand and the carriers are neutralized by ohmic conduction only. The decay rate of the net charge is given by Eq. 7.24, in which

$$q(o) = p_o r_o(1 - r_o/2l)$$

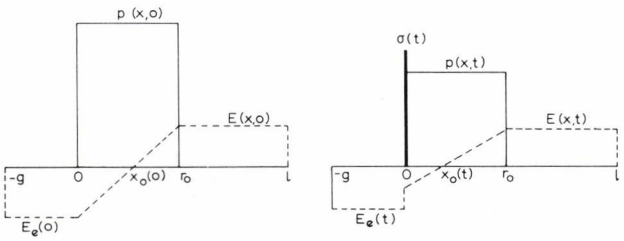


FIG.7-8 Decay of an immobile space-charge cloud p(x,t) in an air-gap TSD by pure ohmic conduction (schematic). Note that part of the space charges are converted into a surface charge $\sigma(t)$, which causes the zero-field point to move towards x = o. However, this surface charge does not persist.

The electric field within the electret has two opposite directions. Recalling Fig. 7-8 we see that $E(x,t)$ is negative for $x < x_o$ and positive for $x > x_o$, where x_o denotes the nonstationary zero-field point. As a result the conduction current is directed to the left for $x < x_o$, *creating a surface charge* due to charge-transfer blocking at the air-gap interface. Owing to the absence of $P_s(t)$ we have from Eqs 7.3 and 7.4

$$d\sigma(t)/dt + \beta(T)\sigma(t) = - \beta(T)q_i t$$

Upon inserting Eqs 7.17, 7,24 and using 7.12 we find as a solution of this equation

$$\sigma(t) = q(o)\{\exp(- \int_o^t \beta_g(T)dt) - \exp(- \int_o^t \beta(T)dt)\} \qquad (7.29)$$

According to which the surface charge first increases, next attains a maximum and finally drops to zero again. For small gaps we have $\beta_g(T) < \beta(T)$, and part of $\sigma(t)$ decays very slowly.

On the other hand the space charges decay much faster, according to

$$\rho(x,t) = \rho_o \exp(- \int_o^t \beta(T)dt) \qquad (7.30)$$

with the ohmic decay rate $\beta(T)$. Consequently, a long-living net charge density is solely due to a slowly decaying surface charge $\sigma(t)$.

As mentioned before, the surface charge reaches a maximum at $t = \tau$, when the field $E(o,\tau)$ becomes zero. During that time the zero-field point $x_o(t)$ has moved from its initial position towards the left side of the electret at $x = 0$. This motion, which is substantial for external current release, has been achieved by the increasing $\sigma(t)$; the immobile space charges contribute nothing to it. For times greater than τ, $x_o(t)$ remains zero, but $E(o,t)$ becomes positive, thus pointing to the contacting electrode on the right, as a result of which $\sigma(t)$ gradually vanishes.

-***-

7:1.2b Dipole Peak of Homocharged Polar Polymers

Let us next consider a homocharged *polar* electret. We assume, however, that the electret has been formed at low temperatures, so that $P_s(o) < q_r(o)$. This class of objects also includes polar polymers, charged by friction or corona discharge at room temperature.

We must now use the complete set of Eqs 7.20 and 7.21, the thermograms of which have been shown. However, if the conduction peak appears at a much higher temperature than does the dipole peak, we may put in the temperature range of the latter $\beta_g(T) = 0$. As a result the real charge $Q(t)$ will remain constant, and up to the temperature T_v in the valley between both peaks, we have

$$q(t) = Q(o) - P_s(t) \qquad (7.31)$$

where for convenience the bar of $\bar{P}_s(t)$ has been dropped.

On inserting Eq. 7.31 into 7.21 we find as the solution of the latter

$$P_s(t) = P_\infty + \{P_s(o) - P_\infty\} \exp(- \int_o^t \alpha^*(T)dt) \qquad (7.32)$$

where $P_\infty = (\varepsilon_s - \varepsilon_\infty)gQ(o)(1+\varepsilon_s g)^{-1}$ and $\alpha^*(T) = \alpha(T)(1+\varepsilon_s g)(1+\varepsilon_\infty g)^{-1}$
Such a $P_s(t)$ supplies the following discharge current

$$j_r(t) = \alpha^*(T)\{P_s(t) - P_\infty\}(1 + \varepsilon_\infty g/1)^{-1} \qquad ...(7.33)$$

The shape of the thermogram of $j_r(T)$ is again the *same* as that of a *Debye* curve. It shows a maximum at

$$sT_m\alpha^*(T_m) = A/kT_m \qquad (7.34)$$

A family of dipole orientation thermograms for various g/l ratios and $P_s(o) = 0$, is shown in Fig. 7-9; they have the same tendency as the first peak of Fig. 7-5. Since current increases with relaxation strength, according to Eq. 7.33 highly polar polymers will show the higher dipole peaks; this was already observed in Fig. 7-6. The figure also gives the temperature dependence of q(T) and $P_s(T)$. As before, q(T) remains most stable when g/l is small; for in that case the internal field is low and no strong heteropolarization is created.

The optimum gap giving the highest current maximum can be calculated from Eq. 7.27:

$$1 - q_\infty\kappa = \kappa(\varepsilon_s - \varepsilon_\infty)(1 + \varepsilon_s\kappa)^{-1}\, s \int_{T_d}^{T_m} \alpha^*(T)dt$$

when for the integral we substitute the approximate value $1 - 2kT_m/A$, we get

$$(\varepsilon_s\varepsilon_\infty\kappa^2 - 1)/\varepsilon_s - \varepsilon_\infty)\kappa = 2kT_m(\kappa)/A \quad \text{or} \quad \kappa \simeq (\varepsilon_s\varepsilon_\infty)^{-\frac{1}{2}} \qquad \ldots(7.35)$$

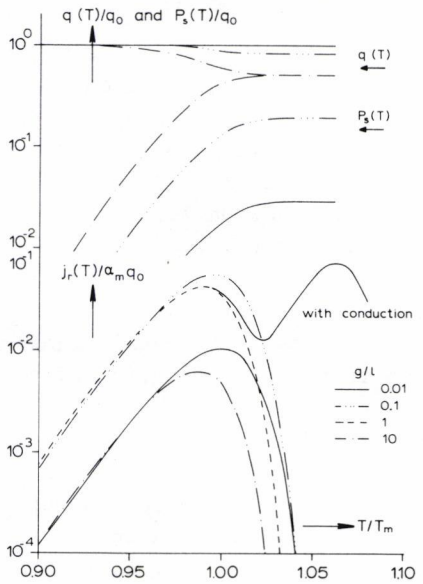


FIG.7-9 Air-gap thermograms representing *pure dipole orientation* in an absorptive homo-electret for various gap widths. We excluded ohmic conduction and took the parameter values of Fig. 7-4.
For comparison, the corresponding curve of a conductive polymer for g/l = 1 (cf. Fig.7-5) has been inserted; it has almost the same dipole peak. In the upper curves the net charge q and the persistent polarization P_s are plotted. For wide gaps, when the internal field is the strongest, the largest polarization is created. Neither q(T) nor $P_s(T)$ decrease at high temperatures, because we ignored homocharge decay by ohmic conduction.

For example, if $A/kT_m(\kappa) = 20$, and $\varepsilon_s = 2\varepsilon_\infty = 6$, the optimum gap amounts to g/l = 0.24, which is about eight times greater than the gap required for an optimum conduction peak. The dependence of T_m on κ follows from Eq. 7.34.

7:1.3 Experimental Results and Their Evaluation

Results on the air-gap TSD of PE* charged by corona or friction are plotted in Fig. 7-10. The charges deposited were about 2 nC/cm^2. The two current thermograms are much alike, despite the fact that the charging methods are quite different and that different carriers of opposite sign are deposited. This clearly indicates that ohmic conduction is the main decaying mode in this air-gap set-up: the contribution of SCL drift and diffusion being of minor importance, thus the two peaks are ρ_c peaks. There is no dipole peak because PE is a nonpolar polymer.

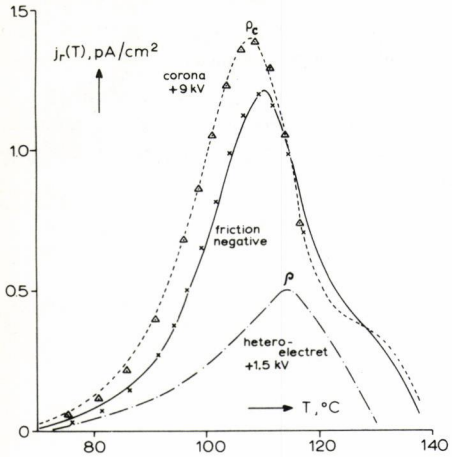


FIG.7-10 Experimental results of Ong on the current TSD with an air gap for a PE disc, charged by a positive corona and by friction (negative charge); g/l was 1.1 and s^{-1} was 1.3 °C/min. Least-squares fits to these curves, based on Eq. 7.25, are shown as triangles and crosses. The position of the ρ_c peak appearing in both thermograms corresponds reasonably well to that of the ρ peak found in the current thermogram of the shorted hetero-electret, formed at 125° - 3 kV/cm - 1.5 h.

The peaks neatly conform to the theoretical equation 7.25, since the two least-squares fits depicted, deviate only slightly from the experimental points. For the corresponding activation energies the fits yield 33 kcal/mol (corona) and 35 kcal/mol (friction). The latter value is just the same as that found from d.c. measurements on the ohmic conductivity. This close agreement once more confirms that ohmic conduction causes the decay of the implanted charges.

For comparison, the thermogram of a shorted PE hetero-electret is shown. Although this was also charged to about 2 nC/cm^2, the released current is much less than the air-gap currents, which themselves suffer from an induction loss. This discrepancy is plausible, because now only part of the excess-charge decay resulting from SCL drift (and diffusion) shows up. These processes are rather inefficient release processes, and moreover, they have to compete with the excess-charge dissipation by ohmic conduction, which for shorted electrets remains shrouded. Since the sample was partially crystalline, a portion of the ρ peak may be due to MW discharging, which also suffers from an inefficient release. The current peak found is shifted to a somewhat higher temperature than the ρ_c peak, occurring at 114 °C instead of at 109 °C. Nevertheless, the

*High density type, viz. Stamylan 9300.

overall resemblance is good, which shows that SCL drift, and obviously also MW discharging, have almost the same temperature dependence as ohmic conduction for similar carriers.

A less complicated way than the least-squares method, is to deduce the activation energy of the current thermograms from BFG plots. This is illustrated in Fig. 7-11 for the model thermograms of Fig. 7-4. The

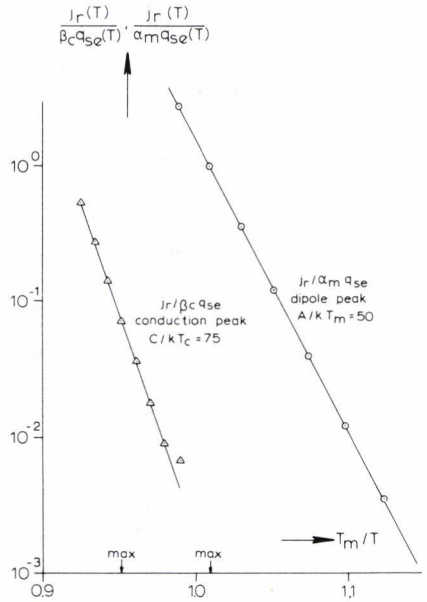


FIG.7-11 BFG plots of the conduction and dipole peaks of the model thermogram of Fig. 7-4, which pertains to the air-gap TSD of a homocharged electret without oriented dipoles. It appears that the straight lines have a slope that exactly yields the activation energies involved.

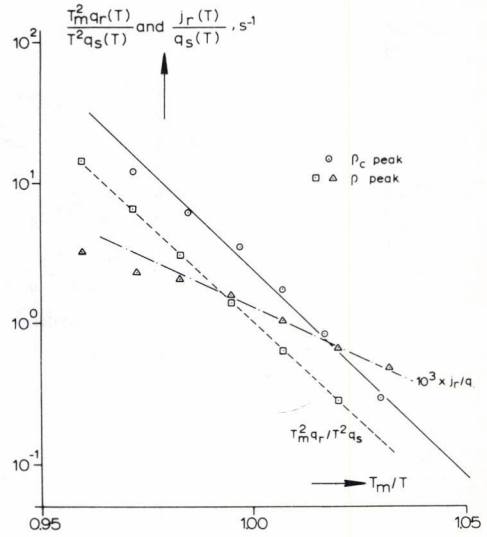


FIG.7-12 BFG plots and charge-ratio plot for the high-temperature peak of the heteroelectrets of PET-c film, depolarized with air gap (ρ_c peak), and without air gap (ρ peak). For data on the formation and TSD, see text of Fig. 10-61.

slope of the two straight lines gives the proper activation energy of the dipole and conduction peak concerned. Evidently, this method, which was also advocated for MW discharging in Sect. 6:2.3, can only be used if the peaks are well resolved. In practice, it can best be applied to the *conduction peak*, because actual dipole peaks very often involve a distribution of dipole relaxations. A final remark must be made about the stored charges needed in the calculation of the appropriate current-charge ratio $j_r(T)/q_{se}(T)$. For the conduction peak we took $q_{se}(T) = q_r(\infty) - q_r(T)$, and for the dipole peak $q_{se}(T) = q_r(T_v) - q_r(T)$, where T_v is the temperature of the valley between the two peaks. (Note that these charges correspond to the charge stored in the electret as it is experienced externally by the upper electrode.)

When we apply the BFG method to the ρ_c peaks of PE in Fig. 7-10 we find 31 kcal/mol (corona) and 33 kcal/mol (friction). These values are only slightly less than those found by the least-squares method.

The BFG plots for the ρ_c and ρ peak of a hetero-electret of PET-c film are shown in Fig. 7-12. Their thermograms are collected in Fig. 10-61.) The BFG plot of the ρ_c peak is much steeper than that of the ρ peak, their slopes give activation energies of 2.3 eV and 1.1 eV respectively. For former value agrees well, as it should, with that of the ohmic conductivity A = 2.2 eV. We also constructed the charge-ratio plot of the ρ peak; this also yields A = 2.3 eV. Apparently, the BFG plot of the ρ peak is not steep enough, because this is most affected by the proximate dipolar α peak.

7:2 Current TSD of Two-Sided Metallized Electrets

To study the heterocharging of polymers, we excluded homocharging by using metallized samples, the discharge current of which chiefly reflects the reorientation of dipoles in shorted electrets; at any rate the dissipation of excess charges by ohmic conduction does not show up. Only the excess-charge decay by SCL drift and diffusion may manifest itself. In order to learn more about the hidden ohmic decay of hetero space-charges, we found it attractive to introduce an air gap. This special technique may also disclose the penetration of homocharges. Since homocharges that are merely adsorbed at the surface, will be neutralized during the metallization, only the penetrated ones will remain. A difference in penetration has been observed for charge injection from a positive and negative corona, see Fig. 10-32.

Owing to the metallization, the effective charge density is no longer accessible, and current TSD is the only feasible technique. Now the *voltage* across the electret

$$V(t) = \int_0^l E(x,t)dx \tag{7.36}$$

becomes the most appropriate quantity for characterizing the stored charge. Moreover, this is the voltage which is exactly proportional to the charge released during TSD. We assume that the electret has been short-circuited before TSD begins so that V(o) = 0. Attributing the decay to depolarization and intrinsic ohmic conduction, the expressions for the discharge current are Eqs 7.7 and 7.8. Furthermore the short-circuit condition reads

$$E_e(t)g + V(t) = 0 \tag{7.37}$$

Upon eliminating $E_e(t)$ from Eq. 7.8 with Eq. 7.37 we get as the TSD current

$$j_r(t) = -(\varepsilon_o/g)dV(t)/dt \tag{7.38}$$

which yields for the released charge density

$$q_r(t) = -(\varepsilon_o/g)V(t) \qquad (7.39)$$

Since V(t) finally vanishes, $q_r(\infty) = 0$, as could be expected, because we started with a *neutral* electret.

From Eqs 7.38 and 7.10, in which we substitute Eq. 7.36, we can set up a differential equation for V(t)

$$dV(t)/dt + \beta_g(T)V(t) = -\{g/\varepsilon_o(1 + \varepsilon_\infty g)\} \frac{d}{dt} \int_o^1 P_s(x,t)dx \qquad (7.40)$$

while Debye's equation 7.1 can be rewritten as

$$\frac{d}{dt} \int_o^1 P_s(x,t)dx + \alpha(T) \int_o^1 P_s(x,t)dx = \varepsilon_o(\varepsilon_s - \varepsilon_\infty)\alpha(T)V(t) \qquad (7.41)$$

For TSD these ODE's must be solved numerically, from the initial conditions V(o) = 0 and $\int_o^1 P_s(x,o)dx$. Note that the set resembles Eqs 6.19 and 6.20, and also looks similar to Eqs 7.20 and 7.21; they can even be made identical to the latter by putting

$$\varepsilon_o\varepsilon_\infty V(t) = q(t)1(1 + 1/\varepsilon_\infty g)^{-1} \qquad (7.42)$$

Therefore, we did not write a new computer programme but simply replaced q(t) by V(t)* and took q(o) = 0. This unusual initial condition leads, however, to some pecularities.

Let $\int_o^1 P_s(x,o)dx = 0$. Now if the polarization is initially absent, it will remain so. As a result, Eq. 7.40 reduces to

$$dV(t)dt + \beta_g(T)V(t) = 0 \qquad (7.43)$$

with the trivial solution V(t) = 0, in view of the initial condition V(o) = 0. Thus we are led to the conclusion that *space charges alone* give *no* external current, for they induce image charges on the evaporated electrodes in such a way that the average field in the electret is zero. As a result there is no ohmic dissipation of the space charges during TSD, so that the initial condition of zero voltage is fulfilled throughout the experiment.

If, on the contrary, $\int_o^1 P_s(x,o)dx \neq 0$, a current is released, which will always change in polarity to make $q_r(\infty) = 0$. Obviously, the current passes through zero, when the dipolar current exactly cancels the conduction current, i.e. when the internal field vanishes. V(t) then reaches its maximum and decays to zero afterwards to restore the neutral state. Because $q_r(\infty)$ has to be zero, the area of the positive current *equals* that of the negative, as can also be seen from the calculated j_t thermogram shown in Fig. 7-13. Consequently, the conduction peak, i.e. the 2nd peak, is very *marked*, in spite of the fact that we started only with a polarization. This polarization, however, is compensated

*The resulting voltage may become quite large, e.g. for q(t) = 2 nC/cm^2, 1 = 2 mm, 1/g = 1, and ε_∞ = 3, we have V(t) = 1130 V.

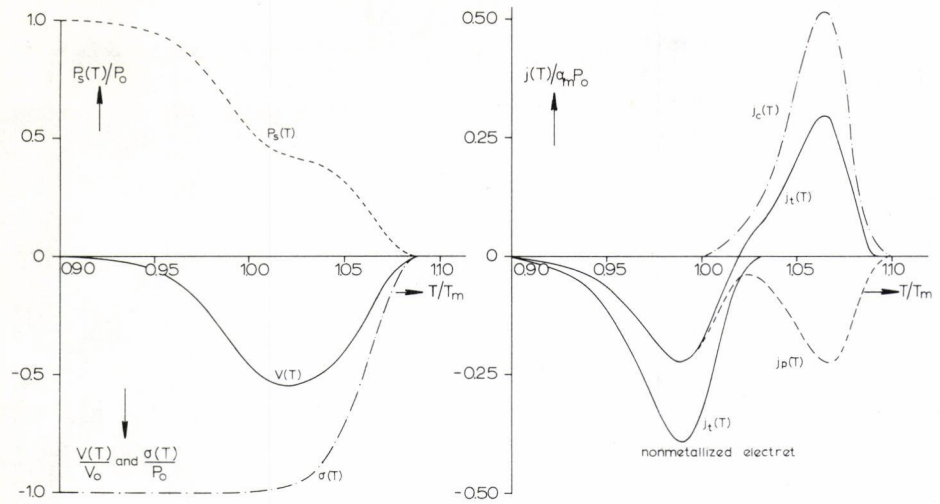


FIG.7-13 Air-gap TSD of a *two-sided metallized* electret after its short-circuit, i.e. V(o) = 0.We assumed the electret to contain a persistent polarization only. Yet there is a surface charge, $\sigma(T)$ on the evaporated electrodes, due to the image charges induced by $P_s(T)$. The other parameters are equal to those of Fig. 7-4. The relevant quantities are now the voltage across the electret, V, and the released current, j_t. The latter gives a pronounced conduction peak of the same area as the dipole peak in front of it. For comparison, the total current of a *nonmetallized* electret is shown; its conduction or homo-peak is extremely small.

by a surface charge $\sigma(T)$ of opposite polarity *induced* on the upper electrode as an image charge, in order to make V(o) = 0, (see Eq. 7.45). It is the ohmic dissipation of this very surface charge that causes the pronounced conduction peak. The reinforcement of the conduction peak by the two-sided metallization can clearly be seen from the corresponding thermogram of a one-sided metallized electret; this hardly shows a conduction peak at all.

In Fig. 10-62 we have compared a normal thermogram with an air-gap thermogram of a two-sided metallized electret of 80 S co 20 AN. We see that the ρ peak of the former corresponds quite well to the conduction peak of the latter. This proves unequivocally that the ρ peak is caused by the motion of excess charges and *not* by dipole relaxations.

To complete the discussion, we finally relate V(t) to the stored charge. By integrating Poisson's Eq. 7.5 twice we find

$$\varepsilon_o\varepsilon_\infty V(t) = \{\varepsilon_o\varepsilon_\infty E(o,t) + P_s(o,t)\}1 - \int_o^1 P_s(x,t)dx + \int_o^1 \rho(x,t)(1 - x)dx \qquad (7.44)$$

where $\varepsilon_o\varepsilon_\infty E(o,t) + P_s(o,t)$ equals the surface charge density $\sigma(t)$ *induced* on the upper metal layer of the electret as an image charge.The initial conduction V(o) = 0 requires that

$$\sigma(o) = \int_0^1 P_s(x,o)dx - \int_0^1 \rho(x,o)(1 - x)dx \qquad (7.45)$$

In other words to make V(o) zero, one needs a surface charge $\sigma(o)$ to cancel the electric field caused by the polarization and space charges stored in the electret. In Fig. 7-13 we used this charge to normalize V(t).

The activation energy of the resulting current peaks can again be calculated most conveniently from BFG plots. This is demonstrated in Fig. 7-14 for the two peaks of the model thermogram of Fig. 7-13. The application of this method to the ρ_c peak of the hetero-electret (80 S co 20 AN) just mentioned is illustrated in Fig. 7-15. From the straight part of the line we find an activation energy of 3.4 eV, which again is almost equal to that of 3.2 eV for the ohmic conductivity. The figure also shows the BFG plot for the ρ peak of the shorted electret, depolarized without an air gap; this has a slope that corresponds to A = 3.1 eV. The three values are in good accordance, this means that all three processes originate in similar molecular motions, viz. the field drift of carriers.

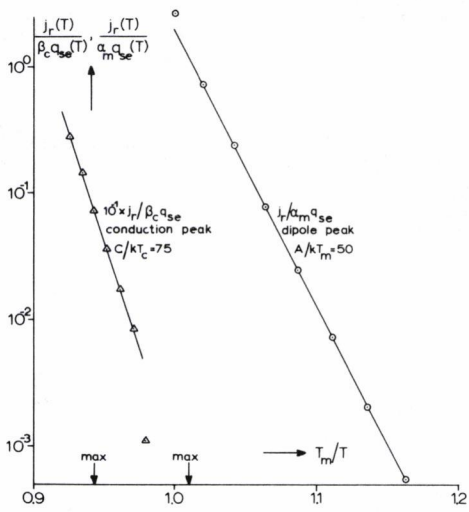


FIG.7-14 BFG plots for the conduction and dipole peaks of the model current thermogram of Fig. 7-10, which elucidates the air-gap TSD of a two-sided metallized electret. Both lines are straight and have a slope that gives the correct value of the specific activation energy involved.

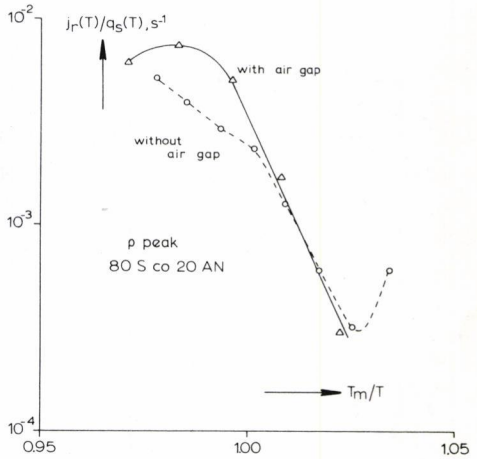


FIG.7-15 BFG plots for the ρ peak of a bilaterally metallized hetero-electret of 80 S co 20 AN, depolarized with and without an air gap. The electret was formed at 130° - 20 kV/cm - 1.5 h, and during TSD g/l was 0.3, and s was 1 min/°C, while T_m = 123 °C.

Chapter 8

CHARGE TSD OF FOIL ELECTRETS IN OPEN CIRCUIT

The TSD of foils is of paramount interest, because of their large-scale application in microphones. We mentioned, however, that the current TSD of homocharged nonpolar foils raises several problems. For instance, current TSD with shorted evaporated electrodes, discussed in Chap. 5, requires a significant penetration of the excess charges, and even then it reveals only a fraction of the charge stored. A significant penetration is only achieved by a thermal formation of several minutes or by electron bombardment; corona injection at room temperature usually does not penetrate deep enough. For low penetrations or mere surface charging, current TSD with an air gap outlined in Sect. 7:1 would be attractive. Unfortunately, the induction loss factor of $1 + \varepsilon g/l$ interferes prohibitively; for the ratio g/l cannot be made small, the more so because at high temperatures the foil is too easily deformed.

Charge measurements need not be hampered in these respects. Moreover, we should realize that for practical applications, information on the decay behaviour of the *persisting* charge is indeed of greater importance than information on current release. However, charge TSD cannot easily be performed continuously. Nevertheless, we succeeded in designing an apparatus to do this for foils (Tu 70a).

It is based on a continuous compensation of the external field of the electret by a backing voltage. The noncontacting electrode and the side of the electret facing it, therefore always have the same potential. As a result there is *no* external current, and so the equipment works in *open circuit*. The very fact that

$$E_e(t) = 0 \tag{8.1}$$

makes the backing or compensation voltage, $V_c(t)$, independent of the gap width. Since all the voltage is maintained across the electret, it is determined by the internal field only

$$V_c(t) = \int_0^l E(x,t)dx \tag{8.2}$$

or, rather, by the persisting electret charge, which according to Eq. 8.6 is now found *without* any induction loss. This is plausible, because the electret is constrained to induce all its image charges on the contacting electrode.

Fig. 8-1 shows the experimental set-up. The one-sided metallized electret foil is set into vibration by the sound impinging on it from a loudspeaker. As a result, the charged electret generates across its noncontacting back electrode an a.c. voltage, which is cancelled automatically by the backing voltage, $V_c(t)$. In recording this voltage continuous thermograms of the persisted charge are obtained. Further experimental details will be given in Sect. 9:2. It should be mentioned

here that nonautomated versions of this method were already known (RP 68, Ro 69, Tu 70a).

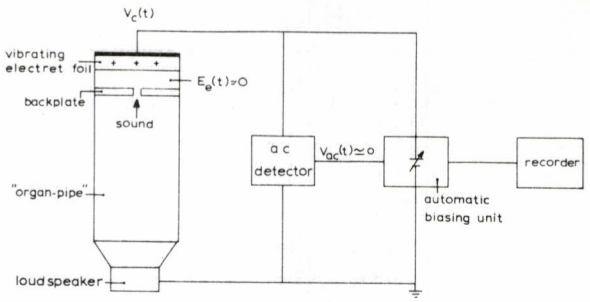


FIG.8-1 Diagram of automatic charge TSD on electret foils in open-circuit (cf. Fig. 9-4). The electret is stretched upside down, with its metallized side up. This side also receives the biasing voltage $V_c(t)$, whereas the noncontacting back plate is connected to ground. The upper part of the organ pipe is mounted in a thermostat (not shown).

In this chapter we shall consider three charge decaying modes: *reorientation of aligned dipoles, ohmic conduction, and SCL drift*. The two latter processes bring about the decay of the excess charges. The ohmic conduction of the polymer dissipates them by supplying intrinsic charges of opposite sign, and the SCL drift sweeps the excess charges themselves towards the (open) collecting electrode, where they finally recombine with their image charges. Evidently, the theory applies to charge TSD of polar foils and to that of the extensively used homocharged nonpolar foils. Trapping effects are not included, but in analogy with current TSD we might expect the theory to hold for severe retrapping as well. We shall prove that the relaxation transitions found by charge TSD and current TSD may differ. In particular, when SCL drift operates, large differences may appear. These have actually been observed for Teflon-FEP electrets (compare Fig. 10-34). Another interesting aspect of the decay by SCL drift is that the higher the electret is charged, the sooner it is discharged. Conversely, an electret can be stabilized by removing part of its (surplus) charge by preheating it (Fig. 1-7). These phenomena are of direct practical interest and will also be discussed.

8:1 Charge Decay by Dipole Reorientation and Ohmic Conduction

To give a general picture, we first attribute the decay processes to dipole reorientation and intrinsic ohmic conduction. Accordingly, this section applies to electret foils from polar polymers, such as PC and PET, which, owing to their inferior durability, are less suitable than nonpolar electret foils.

Since $E_e(t)$ is being continuously compensated there is no external

current (cf. Eq. 7.9). Integration of Eq. 7.8 between x = 0 and 1 therefore yields

$$\varepsilon_0\varepsilon_\infty dV_c(t)/dt + \gamma(T)V_c(t) = -\frac{d}{dt}\int_0^1 P_s(x,t)dx \qquad (8.3)$$

where the second term comes from ohmic conduction, and the right-hand side from dipole reorientation. Furthermore, we have for Debye's equation 7.1 after the same integration

$$\frac{d}{dt}\int_0^1 P_s(x,t)dx + \alpha(T)\int_0^1 P_s(x,t)dx = \varepsilon_0(\varepsilon_s - \varepsilon_\infty)\alpha(T)V_c(t) \qquad (8.4)$$

These equations are *similar* to the equations discussed in Sect. 7:1 for the effective electret charge q(t); they also resemble those for V(t) in Sect. 7:2. We can easily verify that they become equivalent if we put

$$\varepsilon_0\varepsilon_\infty V_c(t) = 1 \lim_{g\to\infty} q(t) \qquad (8.5)$$

In other words in current TSD the gap width g must go to infinity; otherwise the external field will not become zero.

This conversion formula enables us to *avoid* redeveloping the theory put forward in Chap. 7. For example, we can use Eq. 8.5 to indicate the relation between $V_c(t)$ and the stored charges; in view of Eq. 7.16 we find

$$\varepsilon_0\varepsilon_\infty V_c(t) = \sigma(t)1 - \int_0^1 P_s(x,t)dx + \int_0^1 p(x,t)(1-x)dx \qquad (8.6)$$

Clearly, $\varepsilon_0\varepsilon_\infty V_c(t)/1$ is exactly equal to the effective charge of the electret foil. Hence, the model thermograms previously calculated for q(t) are also *typical* for the trend of the TSD charge thermograms, $V_c(T)$ vs. T.

With reference to Sect. 7:1 some remarks should still be made. First of all, since $E_e(t) = 0$, no surface charge will ever be created in charge TSD in open circuit and any surface charge present will always disappear from the beginning. In fact, we have

$$d\sigma(t)/dt + \beta(T)\sigma(t) = 0 \qquad (8.7)$$

Moreover, the equivalence to $g \to \infty$ implies that pure ohmic decay is (in the absence of dipole reorientation) no longer delayed by the air gap, but is *speeded* up to the ohmic relaxation time, $\beta(T) = \gamma(T)/\varepsilon_0\varepsilon_\infty$, as can be seen from Eqs 8.3 and 8.7. The dipole reorientation itself is accelerated as well; to show this we take $\gamma(T) = 0$, and all excess charges zero initially. Eq. 8.4 then reduces to

$$\frac{d}{dt}\int_0^1 P_s(x,t)dx + \frac{\varepsilon_s}{\varepsilon_\infty}\alpha(T)\int_0^1 P_s(x,t)dx = 0 \qquad (8.8)$$

where the factor $\varepsilon_s/\varepsilon_\infty$ in front of the dipole relaxation frequency is greater than one.

Consequently, TSD transition temperatures due to dipole reorientation and ohmic conduction as measured by charge TSD, are essentially *lower* than those found in current TSD with an air gap, for which the rate constants are $\alpha(T)$ and $\beta_g(T)$ respectively. On the other hand, they have the advantage of being determined by polymeric constants only. In actual practice we found the transitions to be shifted negligibly, because the activation energies involved are large (see Fig. 8-2 below).

No doubt, the transitions appear less pronounced in charge measurements than in current measurements. To improve the situation, we might calculate the displacement current density, within the sample by differentiating $V_c(t)$ numerically. If $V_c(t)$ is printed digitally, this differentiation can readily be performed. The figures obtained are related to the TSD current, $j_r(t)$, of the previous chapter. By differentiating Eq. 8.5 we have, in view of Eq. 7.18

$$\varepsilon_0\varepsilon_\infty dV_c(t)/dt = - \lim_{g\to\infty}(1 + \varepsilon_\infty g)j_r(t) \qquad (8.9)$$

8:1.1 Some Experimental Results on PET Foil

Results of TSD charge measurements on electron-bombarded PET-c film are given in Fig. 8-2. The three charge thermograms (upper curves) have

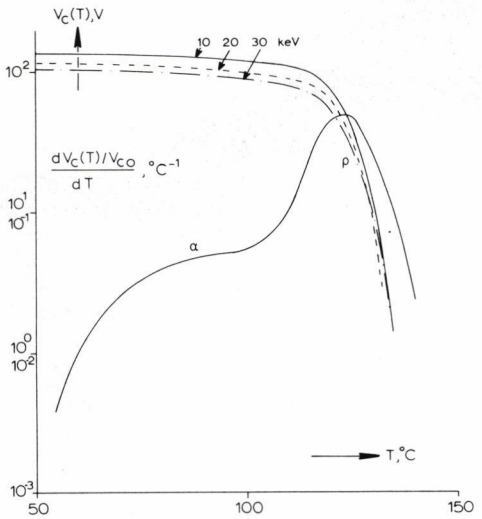


FIG.8-2 Charge TSD thermograms of electron-bombarded PET-c foil. The figure shows the actual charge diagrams and their averaged derivative, with respect to temperature. The latter diagram shows the α and ρ peak, known from TSD current measurements (cf. Fig. 10-38). The injection energies were 10, 20 and 30 keV, and the deposited electron charge density was 20 nC/cm^2.

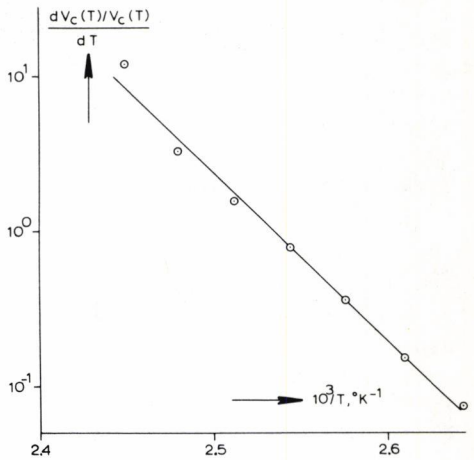


FIG.8-3 Calculation of the activation energy of the ρ peak in the $dV_c(T)/dt$ thermogram of electron-bombarded PET-c foil. The slope of the straight line corresponds to B = 2.2 eV.

the same trend, despite the fact that the electrons are injected to a different depth*. This close similarity indicates that SCL drift of the excess charges towards the collecting electrodes is less important than their dissipation by ohmic conduction. The derivative of the charge thermograms is also plotted; it clearly reveals two charge relaxation domains. The first peak derives from a transient dipole orientation, and the second from the ohmic dissipation of the injected electrons. They thus correspond to the well-known α and ρ peak of the TSD current thermograms and they appear at the same temperatures, viz. at 87 and 123 °C.

Since, in the temperature range of the second peak the vanishing dipole polarization is small, we have, from Eq. 8.3, that the charge decay of this peak satisfies

$$\frac{dV_c(T)/V_c(T)}{dT} \simeq -\beta(T) \tag{8.10}$$

Plotting the left-hand side on semilog paper against 1/T, we shall find a straight line, the slope of which is determined by the activation energy for ohmic conduction. The ρ peak of Fig. 8-2 shows indeed this behaviour. From the straight line of Fig. 8-3 we deduced an activation energy of 2.2 eV, which is precisely the value of the ohmic conductivity of PET-c.

8:2 Charge Decay by SCL Drift and Ohmic Conduction

We now pass on to the charge TSD resulting from the SCL drift of thermally mobilized excess carriers. The discussion will concern homocharged nonpolar films, such as the long lasting Teflon-FEP electrets. We thus neglect dipole (re)orientation, but we include excess-charge neutralization by ohmic conduction. Experimental evidence for SCL drift in the isothermal charge decay of polymers was first obtained by Davies (Da 67), and Ieda et al. (IS 67).

Let the homocharge be a positive space charge. If this is uniformly penetrated up to a depth r_o, we have the field configuration of Fig. 8-4. Obviously, the zero-field point appears at x = 0, and because of the automatic cancellation of the external field, it stays there during the decay. This implies that all excess carriers drift towards the collecting electrode at x = 1, where they are neutralized.

The equation that governs charge decay is the continuity equation, 5.14, which we have to solve in combination with Poisson's equation, 5.15. Some general solutions of these partly nonlinear PDE's were re-

*This is apparent from the different initial charges, which obey $\varepsilon_o\varepsilon_\infty V_c(o)/1 = p_o r_o(1 - r_o/21)$, in which $p_o r_o$ is about the same, since the deposited charge invariably was 20 nC/cm^2, while r_o increases with injection energy (cf. Fig. 5-7).

cently derived by Wintle (Wi 70) for the isothermal discharge. We worked on the problem independently, and we were able to reduce their solution to one in ODE's which seems to be more straightforward. Concurrently, Batra et al. (BK 70) followed a similar approach in studying the isothermal carrier flow on photoinsulators under a voltage stress; they neglected, however, ohmic conduction. The earlier work of Reiser et al. (RL 69) on corona-charged foils is also worthy of mention; these investigators also ignored ohmic conduction.

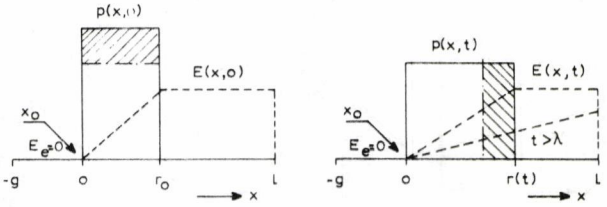


FIG.8-4 The retained space charge and electric field strength in an electret foil during charge TSD at times t = o and t ≠ o. If the electret is *nonconductive*, the charges spread only by their SCL drift towards the collecting electrode at x=1, and the hatched areas are equal. Then, up to the transit time λ of the leading front, the electric field E(1,t) remains the same. Thereafter it gradually diminishes, when the charges are neutralized by their image charges.

Upon integrating Eq.5.18 between x = 0 and 1, and recalling that $j_r(t) = 0$, we have

$$\varepsilon_o \varepsilon V_c(t)/dt + \gamma(T)V_c(t) = -\mu(T) \int_0^1 p(x,t)E(x,t)dx \qquad (8.11)$$

in which the 2nd term derives from ohmic conduction, and the right-hand side from SCL drift. From this equation p(x,t) can be eliminated by means of Poisson's equation. Since E(o,t) = 0, we obtain

$$\varepsilon_o \varepsilon dV_c(t)/dt + \gamma(T)V_c(t) = -\tfrac{1}{2}\mu(T)\varepsilon_o \varepsilon E^2(1,t) \qquad (8.12)$$

This ODE is the simplest in that only E(1,t) has to be specified.

As long as the carrier front has not reached the right electrode we have p(1,t) = 0, so by particularizing Eq.5.18 at x = 1, and integrating, we find for E(1,t)

$$E(1,t) = E(1,o) \exp(-\int_0^t \beta(T)dt) \quad , \quad t \leq \lambda \qquad (8.13)$$

where E(1,o) is given by the initial homocharge stored

$$\varepsilon_o \varepsilon E(1,o) = \int_0^1 p(x,o)dx \qquad (8.14)$$

Equation 8.12 expresses that up to the transit time of the leading front the space charge is neutralized only by ohmic conduction. Thus far, SCL drift merely causes the expansion of the charge cloud. This expansion does, however, diminish $V_c(t)$, because the carriers move away from the noncontacting electrode.

When we substitute Eq. 8.13 into 8.12, the resulting ODE can readily be solved on a computer by a Runge-Kutta method. However, for *nonconducting* polymers, in which $\gamma(T) = 0$, no space charge is lost for $t \leq \lambda$, and $E(1,t) = E(1,o)$, so that Eq. 8.12 possesses the simple solution

$$V_c(t) = V_c(o) - \tfrac{1}{2} E^2(1,o) \int_o^t \mu(T)dt, \quad t \leq \lambda \qquad \ldots(8.15)$$

If the carrier mobility $\mu(T)$ is thermally activated according to an Arrhenius equation, the integral can easily be evaluated (see Sect. 2:1.2). We recognize that the decay rate depends *quadratically* on the initially stored charge. Consequently, when SCL drift prevails, highly charged electrets will decay faster (cf. Fig. 8-7, below).

Up to now the spatial distribution of the excess charges has been immaterial. If we assume that for $t \geq \lambda$ the space charge has spread completely, which is true for a uniform distribution, and almost true for a non-uniform one, the right-hand side of Eq. 8.11 reduces to $-\mu(T)p(t)V_c(t)$, from which $p(t)$ can be eliminated by means of Eq. 8.6. As a result, Eq. 8.11 becomes

$$dV_c(t)/dt + \gamma(T)V_c(t) = -2\varepsilon_o\varepsilon\mu(T)V_c^2(t)/l^2 \ , \ t \geq \lambda \qquad (8.16)$$

This ODE can be integrated numerically, starting from $V_c(\lambda)$, which is the final value of the solution of Eq. 8.12. For a perfect insulator ($\gamma(T) = 0$), however, we easily arrive at the following analytical solution*

$$1/V_c(t) = 1/V_c(\lambda) + (2/l^2) \int_\lambda^t \mu(T)dt, \ t \geq \lambda \qquad \ldots(8.17)$$

If required, the value of $V_c(\lambda)$ can also be found analytically. From Eq. 8.6 we have

$$\varepsilon_o\varepsilon V_c(\lambda) = \tfrac{1}{2} p(\lambda)l^2$$

Furthermore, we have from Poisson's equation

$$\varepsilon_o\varepsilon E(1,\lambda) = p(\lambda)l$$

Combining these equations with Eq. 8.14 we find

$$V_c(\lambda) = \tfrac{1}{2}\{E(1,o)l\} \exp\{-\textstyle\int_o^\lambda \beta(T)dt\} \qquad (8.18)$$

which, for a shallow and uniform carrier injection into a nonconducting polymer simply yields $V_c(\lambda) = \tfrac{1}{2} V_c(o)$, so that the transit time is reached at a voltage of half the initial voltage.

*For the less severe restriction that $\gamma(T)$ and $\mu(T)$ have the same temperature dependence, the solution of Eq. 8.10 in the two time domains reads

$$V_c(t) = \{V_c(o) - ee(1 - e^{-\int_o^t \beta(T)dt})\}e^{-\int_o^t \beta(T)dt}, \quad t \leq \lambda$$

$$\frac{1}{V_c(t)} = -\frac{2\mu(T)}{\beta(T)l^2} + \left\{\frac{2\mu(T)}{\beta(T)l^2} + \frac{1}{V_c(\lambda)}\right\} e^{\int_\lambda^t \beta(T)dt}, \quad t \geq \lambda$$

where $ee = \tfrac{1}{2}\mu(T)E^2(1,0)/\beta(T)$.

The transit time, λ, which decides the choice between Eqs 8.11 and 8.15, follows from the path of the leading front, r(t). From Eq. 5.25

$$dr(t)/dt = \mu(T)E(1,t) = \mu(T)E(1,o)\ \exp\{-\int_o^t \beta(T)dt\} \qquad (8.19)$$

r(t) can readily be solved numerically, starting from the initial value r_o. The value of λ can then be calculated by inverse interpolation, using $r(\lambda) = 1$. Apart from $\mu(T)$ and $E(1,o)$, the latter of which is determined by the charge density stored, λ will depend on r_o; the larger r_o the smaller λ. However, for a strong ohmic conduction and low penetration, r(t) may never reach 1, because the carriers are neutralized too fast; compare the lower plots in Figs 8-5 and 8-6.

In retrospect, by working towards the relevant quantity, $V_c(t)$, the solution of the nonlinear PDE's has been avoided and reduced to that of ODE's.* Our description holds for $t \leq \lambda$ irrespective of the spatial charge distribution. The equations are also valid when only surface charges are present. We then put

$$\sigma(o) = \lim_{r_o \to o} \int_o^{r_o} p(x,o)dx$$

8:2.1 Model Thermograms of Charge TSD by SCL Drift and Ohmic Conduction

Charge thermograms of uniformly charged mono-electrets calculated for several penetration depths, and valid for $\gamma(T) = 0$, are shown in Fig. 8-5. For small depths the charge apparently becomes more stable, because the carrier front less soon reaches the collecting electrode at x = 1. The figures also show the corresponding $dV_c(t)/dt$ and r(T) thermograms. The former exhibit for low penetrations, $r_o \leq 0.5\ 1$, a remarkable cusp at the temperature, at which the space charges begin to be lost, through neutralization at the collecting electrode. However, the maximum of the curves of an almost completely filled electret, which all appear at T_D, are neatly rounded.

By virtue of Eq. 8.9 it is not astonishing that the dV_c/dt thermograms strongly resemble the j_r thermograms of the corresponding air gap TSD of Fig. 7-19 (App. II). Compared to the current maxima of a shorted, metallized electret (Fig. 5-8) there are large differences, however. A very striking one is the difference in the position of the maxima. In charge TSD they occur for *low* penetrations at a much *higher* temperature, e.g. for $r_o/1 = 0.1$, and $B/kT_D = 20$, at $1.12\ T_D$ instead of T_D. This can be understood because to get a significant change in V_c, the carriers have to cross the whole sample, whereas in current TSD (with short-circuited electrodes) they already become neutralized when they cross the penetration depth r_o.

The calculated thermograms for a combined decay by SCL drift and ohmic conduction in uniformly charged mono-electrets are given in Fig.

*In (Tu 72) we followed a different approach and emphasized the similarity between charge and current TSD.

8-6. As could be expected the charge now drops much faster and no cusp appears in the dV_c/dt thermograms. Moreover, their maxima shift much less; they gather around T_D. Obviously, the position of the dV_c/dt peak is now determined by the faster of the two discharge processes, i.e., for low penetrations, the ohmic conduction. The pronounced effect of the conduction can also be seen from the r(T) plots, the carrier cloud hardly expands for r_o = 0.1 1. Actual charge thermograms of Teflon-FEP behave like the curves in Fig. 8-5. This implies that ohmic conduction is negligible.

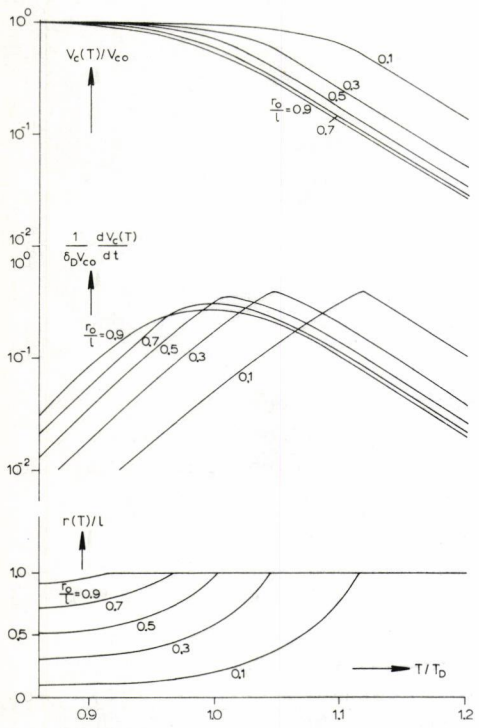


FIG.8-5 Calculated charge TSD due to SCL drift in a nonconducting electret foil for various charge penetration depths. The derivative of the retained charge and the position of the carrier front are also given.
We took B/kT_D = 20.

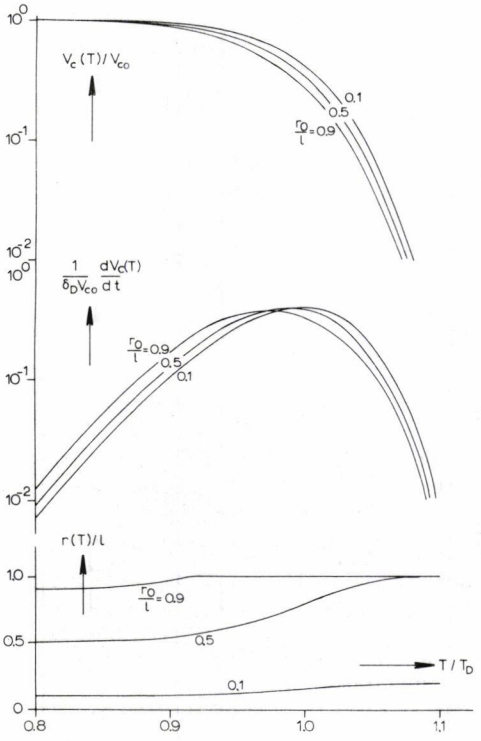


FIG.8-6 Charge TSD as in Fig. 8-5, but now for a conducting electret, so that the charge decays faster, and owing to the faster decrease of the driving field the carriers expand less rapidly. We assumed SCL drift and ohmic conduction to have the same temperature dependence, i.e. $B/kT_D = C/kT_c$ = 20, and $T_D = T_c$.

Although the internal decay of the space charge is not decisive for the $V_c(t)$ thermogram, it is interesting to study this decay. The solution of the space charge density from Eq. 5.14 is similar to that discussed in Sects 5:3 and 5:4. We there learned (see also (Wi 70)) that a uniform distribution will remain so. For other spatial charge distributions the PDE's 5.14 and 5.15 have to be solved numerically, in particular if we want to obtain exact results for $V_c(t)$ beyond the transit time. A great advantage is that the zero-field point remains constant, which makes the centred difference scheme of Wendroff-Thomée attractive. In addition, it is interesting to know the trend of the trajectories of the drifting carriers in the x-t plane. This is discussed in Sect. 5:6, App. II.

8:2.2 TSD Charge and Current Transitions in Mono-Electrets

The temperature at which $V_c(t)$ drops most rapidly has not yet been derived. We have just seen in Fig. 8-5 that for a nonconductive polymer and $r_o \leq 0.5\ 1$, a maximum in $dV_c(t)/dt$ is reached at the transit temperature, T_λ. For a uniform spatial charge distribution we find from Eq. 8.19 the implicit expression

$$1/r_o = 1 + (sp_o/\varepsilon_o\varepsilon) \int_0^{T_\lambda} \mu(T)dt \qquad (8.20)$$

By carrying out the integration for an Arrhenius shift, we obtain approximately

$$(1/r_o - 1)B/kT_m \simeq sT_m\delta_m \quad , \quad r_o \leq 0.5\ 1 \qquad (8.21)$$

where

$$\delta_m = (\mu_o p_o/\varepsilon_o\varepsilon)e^{-B/kT_m}$$

Comparing this equation with Eq. 5.37, which pertains to current TSD by SCL drift, and which in an approximate form reads

$$(1/r_o - 1)(1/r_o - 3/2 + 3r_o/4\ 1)^{-1}\ B/kT_m \simeq sT_m\delta_m \qquad (8.22)$$

we clearly see that for low penetrations the maximum of $dV_c(t)/dt$ will occur at a higher temperature than the corresponding current maximum of a metallized electret.

The same holds for higher penetrations. For $r_o \geq 0.5\ 1$ we find that the charge transition lies *above* T_λ, i.e. when Eq. 8.16 is valid. By differentiating this equation we find that the maximum now occurs when

$$B/skT_m^2 = 4\mu(T_m)V_c(T_m)1^{-2} \qquad (8.23)$$

Noting that in view of $T_m > T_\lambda$ the electret is completely filled, we have $V_c(T_m) = p(T_m)1^2/2\varepsilon_o\varepsilon$, and so we can rewrite Eq. 8.23 by means of the truncated expansion for the exponential integral as follows

$$sT_m\delta_m = B/kT_m \qquad (8.24)$$

which is exactly the condition for the maximum in current TSD at low penetration depths. Since it also is the definition chosen for the normalization temperature T_D, the maxima in the derivative of the charge all occur, for $r_o \geq 0.5\ 1$, at T_D in Fig. 8-5.

On the other hand, when *ohmic conduction* prevails, the condition for a maximum in dV_c/dt reads

$$sT_m\beta_m = C/kT_m$$

and charge as well as current TSD will exhibit almost the same transition. This is substantiated by the ρ peak of PET (cf. Fig. 8-2)

Hence, by *comparing* the transitions in a charge and current thermogram we can judge the contributions of SCL drift and ohmic conduction. We mentioned in Sect. 1:5 that for Teflon-FEP we found SCL drift to dominate; further experimental evidence is given in Fig. 10-34.

8:2.3 Additional Model Thermograms for Uniformly Charged Mono-Electrets

Since the excess charges create their own driving field, their transport rate towards the collecting electrode will be the higher, the higher the initial charge stored. This effect is illustrated in Fig. 8-7 for a threefold increase in charge density*. The higher charge decrease distinctly faster than the lower charge. Unless the initial charge penetrations are different, the curves therefore approach each other, and finally coincide. This situation is reached beyond the transit times or the half-value temperatures, when most of the excess charge of the higher charged mono-electret has disappeared at the collecting electrode, and the charge still remaining in the two electrets becomes the same. Such a trend can be expected for mono-electrets charged by corona or Townsend breakdown, where the penetrations will be practically the same.

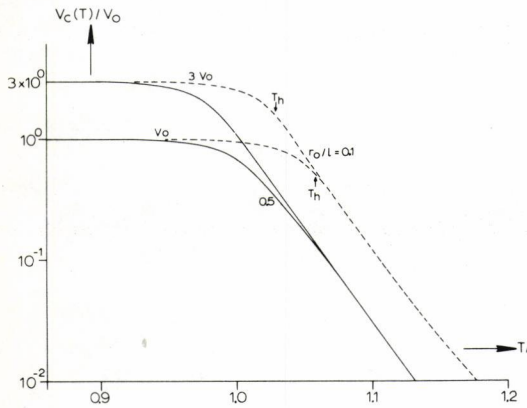


FIG. 8-7 Influence of the height of the stored charge on charge TSD by SCL drift. The curves for the higher initial charge drops faster. However, they only intersect those of the lower initial charge, if the inital penetrations are different. For similar penetrations the curves eventually join, viz. when the two charge densities retained have become the same. We took $B/kT_D = 40$ and $r_o/l = 0.1$ and 0.5.

*Note that for the normalization of $V_c(T)$ we used for all curves the initial charge of the curve of V_o.

For electron-bombarded foils, however, a cross-over effect may occur, if various injection energies are used. This is shown in the figure by the curves of $r_o/l = 0.1$, $3\ V_o$, and $r_o/l = 0.5$, V_o, which intersect each other.

Experimental results on the effect of the initial charge are given in Fig. 8-8. The two decay curves apply to Teflon-FEP foil charged by Townsend breakdown at two injection voltages. Since the two chargings were performed at room temperature, the penetrations will be low and about the same. The curves therefore resemble the theoretical ones of $r_o/l = 0.1$ in Fig. 8-7, the thermogram for 2 kV having the lower half-value temperature.

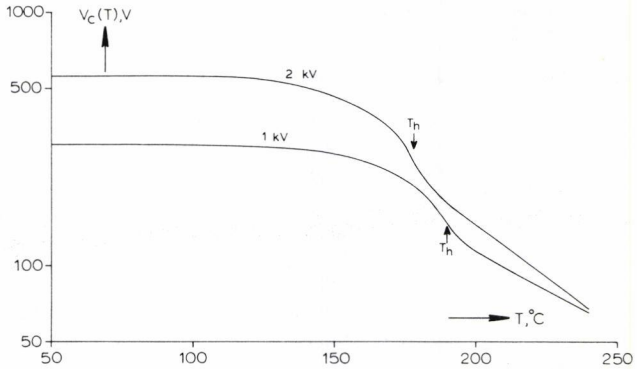


FIG.8-8 Effect of the height of the initial charge on the experimental thermograms of Teflon-FEP homo-electrets. Although the two curves approach each other at high temperatures, that for the lower initial charge has the higher half-value temperature and therefore corresponds to the most stable electret. These results neatly conform to the theoretical thermograms of Fig. 8-7. The electrets of 25 μm were charged by Townsend breakdown using 1 and 2 kV for 1 min at 25 °C.

If the charge thermograms of Fig. 8-7 are normalized to the actual initial charges, the curves of $r_o/l = 0.1$ take the form shown in Fig. 8-9. In this case the reduced charges differ at high temperature by a

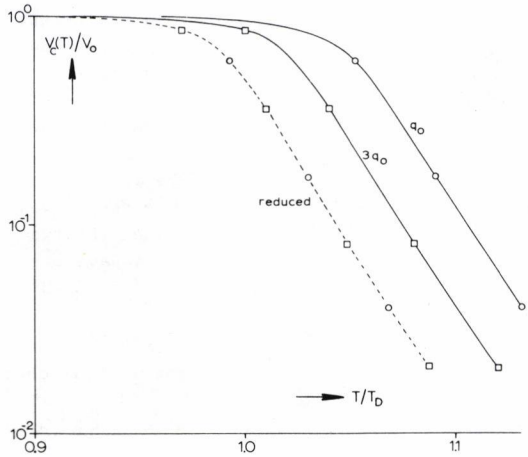


FIG.8-9 Another illustration of the effect of the initial charge on charge TSD by SCL drift. The charge scale is now normalized on the respective initial charges involved. The reduced curve shows that the effect of the initial charge can be eliminated by reducing the temperature scale of the thermograms to their respective half-value temperature instead of to T_D. As in Fig.8-7 we took $B/kT_D = 40$ and $r_o/l = 0.1$.

factor of three. If, furthermore, the normalization of the temperature scale is changed to the actual half-value temperature, a single curve (broken line) results, in which the effect of the initial charge is by no means visible. Obviously, in studying the influence of the initial charge, the normalization factors have to be chosen with care; this also applies to current TSD (cf. Fig. 5-11).

A *unique* aspect of the charge decay by SCL drift, closely connected with the initial-charge effect, is illustrated in the upper curves of Fig. 8-10. They show the behaviour of a nonconducting mono-electret during a multi-stage charge TSD. After some partial heatings, the decay rate is seen to decrease considerably, because the progressive depletion of the charges stored increasingly suppresses the transport rate of the remaining carriers. In other words, the charge becomes more persistent. This phenomenon can be utilized to increase the *thermal stability* of an electret. We refer to Fig. 1-7 and Sect. 10:7 for some experimental results. They strongly support the hypothesis that SCL drift is the main decaying mode in Teflon-FEP, since a high ohmic conduction would prevent any stabilization.

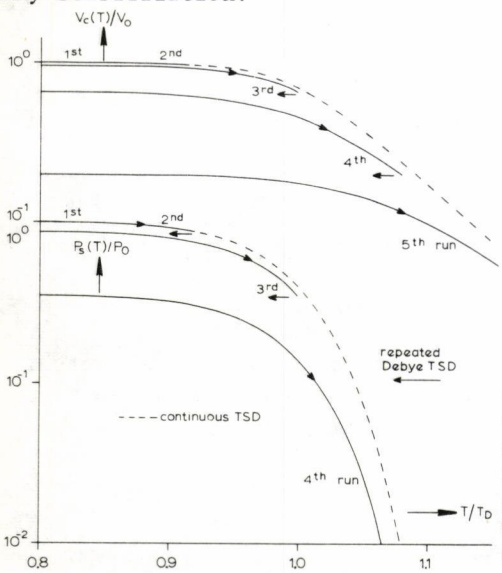


FIG.8-10. Multi-stage charge TSD of an electret foil (above). Interestingly, the charge decay rate of the SCL drift gradually decreases; the electret is stabilized. By contrast, a single Debye dipole polarization cannot be stabilized (below). We assumed $B/kT_D = A/kT_m = 20$ and $r_o/l = 0.5$.

The stabilization described was achieved for carriers of one and the same mobility, or correspondingly, for carriers trapped at a single energy level. If the carriers are trapped at various energy levels, the stabilization becomes even more pronounced. We call the reader's attention to Fig. 2-28, in which this stabilization was also noted for a distributed polarization. A nondistributed polarization, on the contrary, *cannot* be stabilized by a partial heating (lower curves in Fig. 8-10).

Fig. 8-11 exemplifies the effect of a twentyfold decrease in heating rate on the charge TSD by SCL drift in uniformly charged mono-electrets.

The lower heating rate causes the electret to be discharged at much lower temperatures. This happens because at the various temperatures scanned during TSD, the mobilized carriers are allowed more time to drift towards the collecting electrode. The shift of the half-value temperature, which changes from $T_h = 0.948\ T_D$ to $1.07\ T_D$ in Fig. 8-11 can be calculated approximately from Eqs 8.21 or 8.24 with $T_h = T_m$. Alternatively, if the shift is determined experimentally, these equations can be invoked to find the activation energy. For experimental results we refer to Fig. 10-71. This figure shows that the assumption of a heating-rate reduction by a factor of twenty is, in practice, justified, since in contrast to current TSD, the heating rate in charge TSD can be quite *low*. (We chose a uniform rate of 0.05°C/min as the lower limit.)

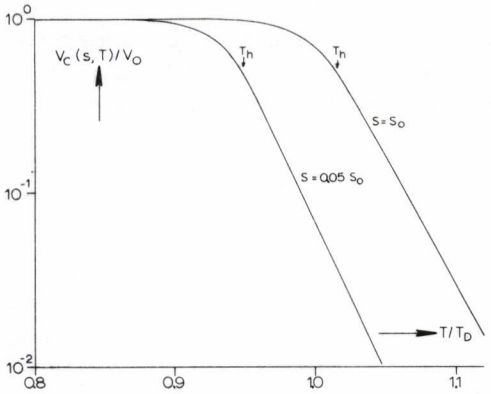


FIG.8-11 Effect of the heating rate on charge thermograms resulting from SCL drift. The charge is less persistent for the lower heating rate. We chose B/kT_D = 40 and r_o/l = 0.5.

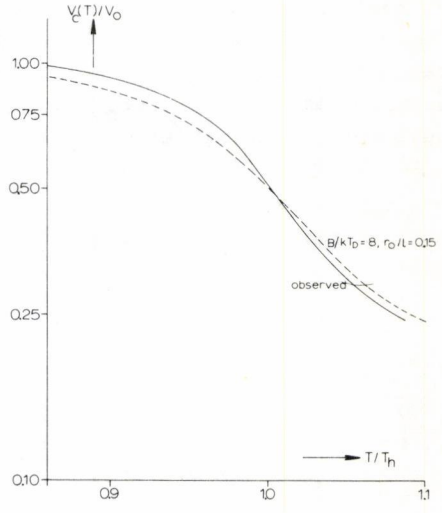


FIG.8-12 Trial fit, based on B/kT_D = 8 and r_o/l = 0.15, to the charge thermogram of electron-bombarded Teflon-FEP. The electron density deposited was 20 nC/cm^2, and the injection energy was 20 keV.

So far, we have not shown how to deduce the activation energy of the carrier mobility from charge thermograms for SCL drift. One way of doing this is by differentiating the charge thermogram, and to plot $dV_c(T)/dT$ for $t < \lambda$, and for $dV_c^{-1}(T)/dT$ for $t > \lambda$ versus 1/T on semi-log paper. Another way is presented in Fig. 8-12. This gives a trial fit to the charge thermogram of electron-bombarded Teflon-FEP. The fit is based on Eqs 8.15 and 8.17 and uses a reduced activation energy of $B/kT_D = 8$, and a penetration depth $r_o/l = 0.15$. The latter value was taken from the results on current TSD (see Fig. 5-7). The former value correspond to B = 0.47 eV, since T_h = 162 °C and $T_D = 1.58\ T_h$. The theoretical thermogram coincides only roughly with the experimental

results.

We attribute this to the fact that the electrons are trapped, and must first be released, after which they are quickly retrapped when drifting towards the collecting electrode. Moreover, the traps are not of a single energy level, but they are distributed over a broad range of energies. This also explains why we found a much higher value for the activation energy in current TSD (Figs 5-10 and 5-20). Hence, we come to the conclusion that it is incorrect to fit the charge TSD of Teflon-FEP to the theoretical curve for one carrier mobility, or what is the same, to that of a single trapping level. Further evidence for this was also obtained by the above-mentioned heating rate experiment, from which we found a change in half-value temperature of only 25 °C, whereas the reduced activation energy of $B/kT_D = 8$ would result in a change of 63 °C.

In view of the discrepancies pointed out, it seems of first importance to extend the above theory to include *trapping* and *retrapping* of carriers at *various* energy levels; preliminary work on this has been published by Reiser et al. (RL 69).

II - EXPERIMENTAL PART

CHAPTER 9 DESCRIPTION OF THE EXPERIMENTAL SET-UP

The first two sections of this chapter describe the automated equipment for current and charge TSD, the fundamentals of which were reviewed in Sect. 1:4, while Sect. 9:3 gives a brief account of the apparatuses used for conventional measurements. Next, in Sect. 9:4 measuring errors are estimated, and in Sect. 9:5 the choice of the polymers is outlined.

9:1 Automated Equipment for Current TSD

The essential parts of the equipment for current TSD are shown in Fig. 9-1. The electret is placed in a thermostat between two electrodes, which are connected to an electrometer E for measuring the liberated current. The electret is usually heated by circulating vaporized liquid nitrogen. This allows the temperature to be varied between - 180° and 280 °C, the low temperatures being necessary to study γ and β relaxations. When we were only interested in the α and ρ relaxations, however, the TSD was carried out above room temperature and warmed air was used for heating.

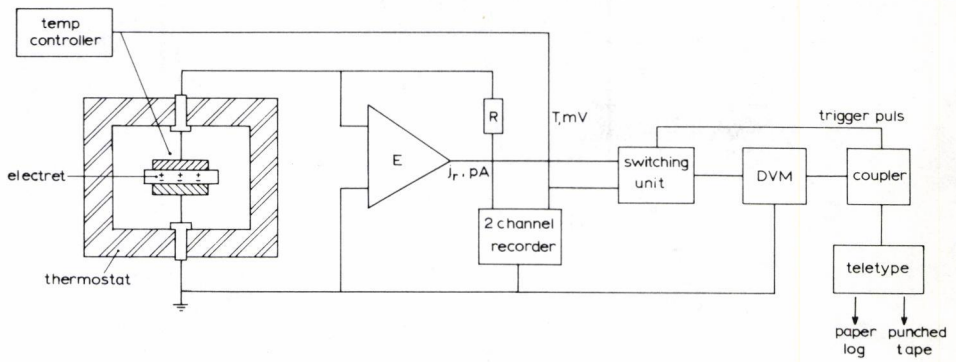


FIG.9-1 Main components of the fully automated equipment for current TSD. Most parts are also used for charge TSD on foils, except that the electrode system is different, and the electrometer E is replaced by an electronic integrator for nullifying the external electret field (cf. Fig. 9-4 and 5).

The temperature is raised linearly by a motor-driven potentiometer, and regulated by an electronic PID-controller to an accuracy of ± 0.2°C. As a rule, we chose a heating rate of 1 °C/min. We see that the output of the electrometer and the voltage of a thermocouple that measures the temperature are fed into a two-channel stripchart recorder for plotting purposes. Moreover, the results are typed on paper log and punched on tape. This acquisition of the data is made by a digital voltmeter, a coupler and a teletype. The rate of printing and punching is set by a switching unit. The tape is later on read and evaluated by the IBM-360 computer of the University of Technology at Delft.

The same equipment is used to form the electret. In this case, we put in series with the electrometer a high voltage supply and programmed the temperature in a way as illustrated in Fig. 1-1.

9:1.1 Thermostat and Electrode Systems

Several parts of the equipment will now be described in more detail. The thermostat was developed at our laboratory; a cross section of it is given in Fig. 9-2. The upper electrode is movable, and exerts a slight pressure on the electret. It is efficiently insulated from the metal parts with Teflon (Hüth, Germany) and connected by a coaxial cable to the electrometer. The fixed lower electrode is fed through with Fluorosint (Polypenco, U.S.A.), which is a ceramic-filled Teflon of excellent dimensional stability. It has a somewhat lower resistivity than

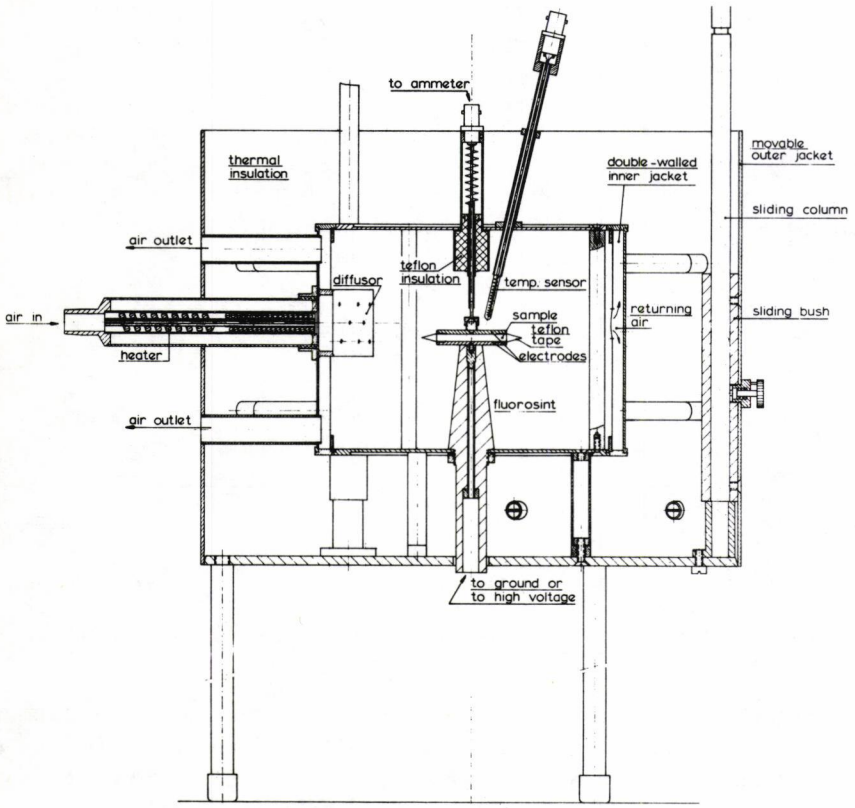


FIG.9-2 Cross section of the thermostat used for formation and TSD of electrets. The electrode system for current TSD is shown. For charge TSD on foils it is replaced by the organ-pipe unit of Fig. 9-4.

pure Teflon, but this is without harm, since any current leak of the lower feed-through does not affect the current measurement. Both electrodes are made of aluminium (51 ST). They are polished and chamfered to avoid sparking. As a result the thermostat will withstand voltages up to 30 kV. The electrodes have a diameter of 47.2 mm (area 17.50 cm^2) and to ensure better contact, gold was deposited on them by evaporation.

Two gold electrodes of the same diameter were evaporated onto the sample, except when homocharging was aimed at, then only one side was metallized. The samples were 1 to 5 mm thick and 56.2 mm in diameter, so that small insulating edges were provided for. However, at high forming voltages these edges were not wide enough to avoid arcing between the electrodes, and two rings of Teflon tape (Connecticut Hard Rubber Cy, U.S.A.) of 47/80 mm were stuck on the sample. Owing to this tape we were able to save considerable polymer material. Before starting TSD we removed the tape, except when the TSD was carried out down to -180 °C.

The electrodes are easily replaced by other electrode systems. For *air-gap* measurements on electret discs, two electrodes were used, of which the upper one was provided with a guard ring and mounted in a short aluminium cylinder of 54 mm outer diameter. The lower electrode, bearing the electret, could be screwed into this cylinder to obtain an air gap of the desired width. The air-gap system for current TSD on electret foils is of a different construction. This consists of a fixed lower electrode with a small rim on the outside, over which the foil is stretched.

In some cases we charged the polymer with *special electrodes*. For instance, we used tin-foil electrodes, which were pressed onto the polymer by soft silicone rubber. Occasionally, we have also utilized electrodes of liquid metal (Cerrolow 117, m.p. 47 °C, Mining Chem. Products, England). Moreover, we performed the formation in other environments, namely in a high vacuum and in a high frequency plasma. The plasma was ignited, at a pressure of 0.1 mm Hg, in Teflon caps that were pressed onto the sample with Viton O-rings. We also developed a cup-shaped electrode system for making electrets by polymerization in a strong electric field. In this case we started with a viscous solution of a prepolymer. The equipment for these special techniques is more fully described in (Tu 68). The homocharging of foils was often achieved by putting an insert of 0.1 mm thick glass cloth between the upper electrode and the one sided metallized foil. Some other methods for homocharging are indicated in Sect. 6:3; see also (Tu 68).

The thermal insulation of the thermostat consists of a one-inch layer of ceramic felt (Cerafelt CB 400, J.Manville, U.S.A.) covered on the outside with a one-inch layer of heat-resistant polyurethane foam (I.K.I., Breda). Cerafelt is also used to fill up the open spaces in the inner cell. The insulating jacket and the cylindrical part of the inner chamber can be tilted away, along three sliding columns, to facilitate insertion of the sample. The sample can be observed through two viewing windows. All metal parts of the cell are made of thin aluminium (51 ST),

which conducts heat rapidly, so that heating and cooling rates of up to 25 °C/min are possible. The feedthroughs, however, are of thin stainless steel, to reduce thermal losses.

For TSD experiments above *room* temperature, the sample is heated in hot air, flowing at a rate of 30 l/min, which is pneumatically controlled and can be read on a rotameter (controller-flowmeter, model 8800-50, Brooks Instr., Veenendaal). The air, which enters on the left side of the thermostat (Fig. 9-2), is heated in the space between two concentric stainless steel tubes, in which a doubly wrapped heating coil of Thermocoax (Philips, Eindhoven, type 1 Nc 10) is mounted. After having been heated, the air enters the inner chamber via a diffusor of perforated silver foil. Next, it flows back through the double-walled inner jacket, to achieve an optimal thermal efficiency. During the formation, the incoming air is precooled with solid carbon dioxide, so that a linear cooling to room temperature is obtained.

We mentioned already that the thermostat can be used from -180° to 280 °C. The low temperature range is meant to investigate dipolar side-chain relaxations. In this case the electret is cooled by circulating vaporized liquid nitrogen instead of air. The liquid nitrogen is vaporized from a 40 liter Dewar vessel, by a 100 watt heater. Provisions are made for level control and automatic refilling of the Dewar from a large storage Dewar of 160 liter.

An iron-constantan thermocouple and a platinum resistor are mounted close to the sample. The thermocouple measures the temperatures and feeds the digital voltmeter for digital temperature print-out; it is also connected to one of the channels of the strip-chart recorder. The tiny platinum resistor, of 1 mm diameter, which has a fast response (Hereaus, type GS 1218) is the sensor for the temperature controller.

9:1.2 PID Temperature Controller

A schematic diagram of this PID controller, which was built at this laboratory, is shown in Fig. 9-3. Part of its wiring is similar to that of a temperature controller developed by Van der Wal et al. (WN 69). It can be seen that the input circuit consists of a special Wheatstone bridge of which the platinum resistor, R(T), is put in the feedback loop of an operational amplifier (Analog Devices, U.S.A.). Such a feedback ensures a constant current flow through this arm of the bridge, irrespective of the resistance of the platinum resistor. In addition, the ten-turn potentiometer, R_p, for the temperature setting (Spectrol, U.S.A., type 860) is wired as a voltage divider, which is unloaded by the use of another operational amplifier. As a result, the *sensitivity* of the bridge is *in*dependent of the temperature setting. This is easily seen from the following expressions for its output voltage and its sensitivity:

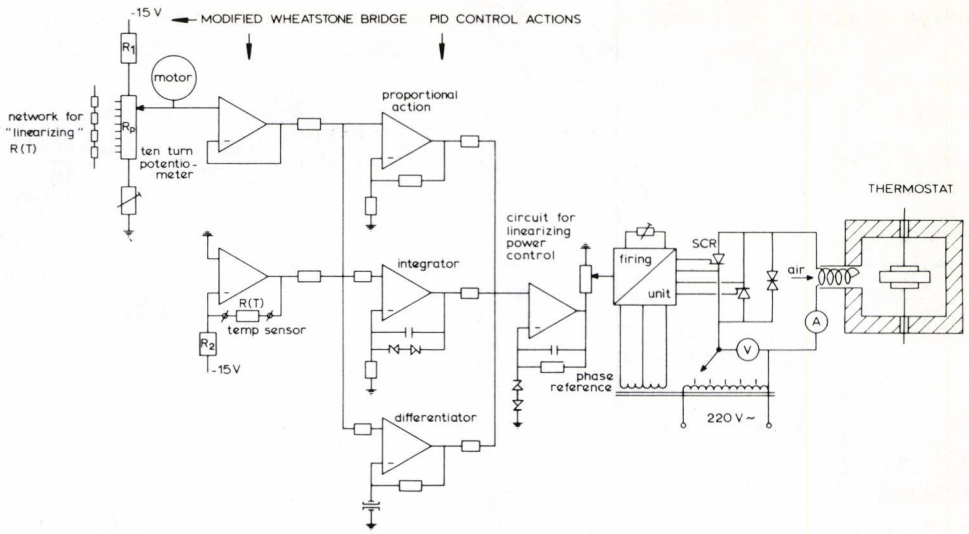


FIG.9-3 Block scheme of the PID temperature controller. Its input has a modified Wheatstone bridge for constant sensitivity. The power fed into the heater of the thermostat is controlled by SCR's.

$$V_u = [R_p(t)\{R_p(t) + R_1\}^{-1} - R(T)R_2^{-1}]V_i \qquad (9.1)$$

$$dV_u/dR(T) = - V_i/R_2 \qquad (9.2)$$

where $R_{1,2}$ are the constant resistances of the bridge and V_i is the input voltage.

Further we have corrected the bridge for the slight nonlinearity of the temperature dependence of the platinum resistor, which obeys

$$R(T) = R_o\{1 + AT + BT^2 + CT^3(T - 100)\} \qquad (9.3)$$

where $A = 3.92 \times 10^{-3}\ °C^{-1}$, $B = -5.86 \times 10^{-7}\ °C^{-2}$ and $C = -4.35 \times 10^{-12}\ °C^{-4}$. For TSD, the 3rd and 4th order terms manifest themselves especially in the low temperature range. The linearization was achieved by giving the setting potentiometer, R_p, a similar but opposite nonlinearity. To this end we used a polygon approximation by putting a shunt of ten resistors across the potentiometer*. This made the bridge linear to within ± 0.15 °C in the range of -200 to +300 °C.

The output of the bridge is fed into three operational amplifiers (Analog Devices, U.S.A.) which give the temperature controller a proportional, integral and differential action. The magnitude of these actions can be adjusted for optimal performance, which guarantees that the temperatures set are reached within the shortest possible time.

The power, P, supplied to the heating coil is regulated by silicon-controlled rectifiers (SCR). Unfortunately, these do not give a linear

*An interesting linearization method up to the 2nd-order term has been published by Van der Wal et al. (WS 69).

power control, because

$$P = \frac{V_m^2}{2R} \int_{\phi}^{\pi} \sin^2 \phi d\phi = \frac{V_m^2}{2R} \{1 - \frac{\phi}{\pi} (1 - \frac{\sin 2\phi}{2\phi})\}$$

where R is the resistance of the heating coil, V_m the maximum value of the rectified voltage that passes the SCR's, and ϕ is their control or firing angle. The latter depends linearly on the d.c. voltage fed to the firing unit of the SCR's, which in turn is directly proportional to the temperature offset.

At small and large fire angles, in particular, P vs. ϕ becomes strongly non-linear, which harms a proper action of the SCR's. The non-linearities can be removed by relating the firing voltage in an inverse non-linear way to the output voltage of the Wheatstone bridge. This was accomplished by modifying the gain of an operational amplifier by two Zener diodes. Finally, we infer from Fig. 9-3 that the voltage supplied to the heating coil of the thermostat, can be altered by a step-down transformer with secundary voltages from 10 to 220 volts.

The setting potentiometer for the temperature has a digital read-out knob, and it is driven by a synchronous motor with a changeable gearing unit (Halstrup, Germany, type 64.10). Ten heating and cooling rates are possible, but, as mentioned before we usually chose 1 °C/min. A slave potentiometer automatically stops the motor at a preset temperature.

9:1.3 Auxiliary Equipment

A few words may be added about the commercial apparatuses used. The high voltage for the formation of the electrets was obtained from a highly stable 10 kV supply unit (Fluke, U.S.A., model 410 B) having a digital read-out. For higher voltages, a source (Brandenburg, England, model 800) variable from 1.5 kV to 30 kV was employed. The electrometer was of a stable and accurate, vibrating capacitor type (Electronic Instrum., England, Vibron 62 A), which could measure currents down to 10^{-15} amp. The two-channel strip-chart recorder was a Moseley (U.S.A., model 9100 BM), and the digital voltmeter was a Hewlett Packard (U.S.A., type 3440 A). As shown in Fig. 9-1, the final results were typed on log paper and punched on tape by a teleprinter (Teletype, U.S.A.). The required conversion of the binary-coded-decimal output of the digital voltmeter to ASCII code was made by a data-acquisition interface or coupler (Hewlett Packard, U.S.A., type 2547 A).

The printing and punching of the Teletype are driven by a switching and counting unit developed at this laboratory. Its switching part consists of a rotating disc with an array of holes, which, via photodiodes, operates two relays. These relays connect the digital voltmeter and coupler to the thermocouple and electrometer, respectively. The cycling rate can be chosen at 0.2, 0.4, 1, 2 or 4 times/min. The counting circuit, which counts the temperature and current measurements, consists

of binary solid state counters (Motorola, U.S.A.). The unit can handle three TSD and/or formation experiments simultaneously.

9:2 Automated Equipment for Charge TSD on Foils

Next we turn to the equipment for charge TSD on foils (see Fig. 9-4). This system incorporates the same thermostat and temperature controller. However, the electrode system has been replaced by a stainless steel "organ pipe", on top of which a noncontacting back-electrode with a small hole is fitted, onto which the electret foil is stretched. The foil is set into vibration by the sound of a loudspeaker. To obtain maximum sensitivity the air in the organ pipe is excited at its fundamental tone. During the temperature rise the resonant frequency must be readjusted continuously, since $\nu_r \propto \sqrt{T}$. We therefore enlarged the excitation system of organ pipe and loudspeaker to a *self-adjusting* acoustical oscillator. To this end we mounted a crystal microphone at the pressure antinode just above the loudspeaker. The output of the microphone drives a positive feedback amplifier operating as an oscillator.

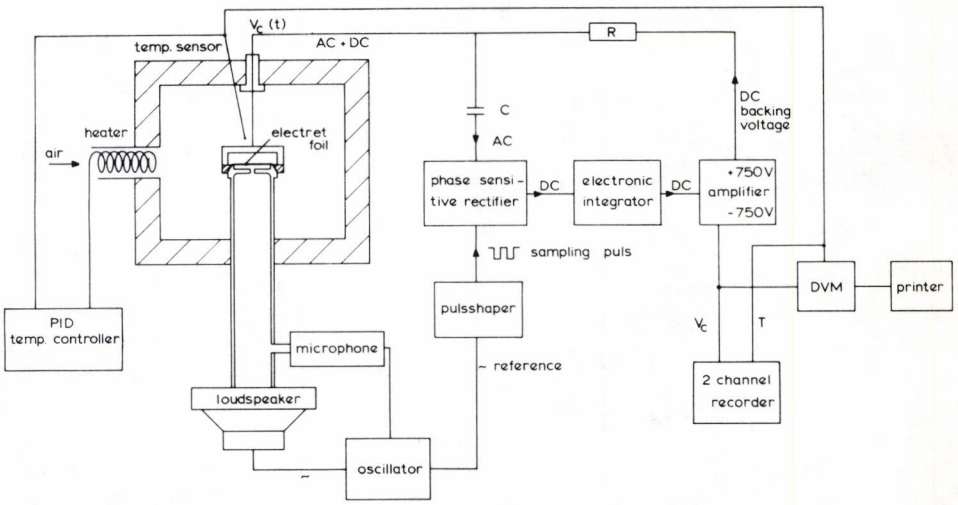


FIG. 9-4 Set-up, based on a field-cancelling principle, for fully automated charge TSD measurements on electret foils. The electronic circuit regulates the backing voltage V_c, in such a way that it always equals the equivalent voltage of the electret.

The essential parts of the compensating circuit, which automatically cancels the external field of the electret foil, are also depicted in Fig. 9-4. It can be seen that the a.c. signal generated by the vibrating electret is passed to a phase-sensitive rectifier. The resulting d.c. signal is fed to an operational amplifier (Intersil Inc., U.S.A., model 741 C), which is wired as an electronic integrator. The output of this integrator is amplified and fed back to the electret foil to compensate its external field. By continuously integrating, the offset signal be-

tween the compensation voltage, $V_c(t)$, and the equivalent voltage of the electret, $V_e(t)$, the integrator ensures that $V_c(t)$ is kept very close to $V_e(t)$.

Referring to Fig. 9-5 the integrator can readily be analyzed. Denoting the integrated voltage by $V_i(t)$, we have

$$V_i(t) = V_i(o) + (CR)^{-1} \int_0^t \{V_e(t) - V_c(t)\}dt \tag{9.4}$$

and

$$V_c(t) = GV_i(t) \tag{9.5}$$

where CR is the integration time and G the gain of the final amplifier stage. We want $V_c(t)$ to be as nearly as possible equal to $V_e(t)$, i.e.

$$V_c(t) \simeq V_e(t) \tag{9.6}$$

which can be achieved by choosing CR and G in the proper way. These quantities can be specified as follows. Differentiating Eq. 9.4 we find, in view of Eq. 9.5, that

$$dV_c(t)/dt + V_c(t)G/CR = V_e(t)G/CR \tag{9.7}$$

Obviously, for Eq. 9.6 to hold, we must have

$$dV_c(t)/dt << V_c(t)G/CR \tag{9.8}$$

As an example, we take $V_e(t) = at$, in this case

$$V_c(t) = a(t - CR/G) + \{V_c(o) + aCR/G\}e^{-Gt/CR}$$

which reduces to Eq. 9.6 for $t >> CR/G$. We chose G = 50 and CR = 1 sec.

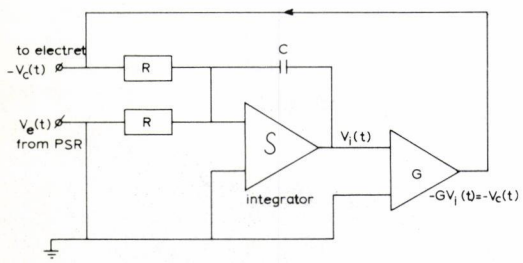


FIG.9-5 Diagram of the electronic integrator and amplifier which control the backing voltage $V_c(t)$ in charge TSD, The integration stops only when $V_c(t)$ exactly cancels the equivalent voltage of the electret $V_e(t)$.

The phase sensitive rectifier was developed by Ir G.A. Schwippert of our laboratory (SS 71), who also suggested the use of the electronic integrator instead of the servosystem we proposed earlier (Tu 70a). The reference signal that drives the phase-sensitive rectifier is obtained from the self-adjusting acoustical oscillator. The circuit can perform measurements on foils bearing charges equivalent to -750 to +750 V. For this wide range of voltages, special high-voltage transistors (Philips, Eindhoven, BU 105) were required in the final amplifier stage.

As can be seen from Fig. 9-4 the essential TSD parameters (i.e. temperature and compensation voltage), are recorded on a Moseley strip-chart recorder. After passing a digital voltmeter they are also printed out by a digital strip-printer (Hewlett Packard, U.S.A., model 5050 A).

9:3 Equipment for Conventional Measurements

In Chapt. 10 we shall often present, along with the TSD results, the corresponding results of conventional mechanical or dielectrical measurements. In this way we hope to aid the reader in acquiring a better understanding of the TSD results.

Results of mechanical measurements of 1 Hz were taken from Heijboer and coworkers of our laboratory. These measurements were carried out with the well-known torsional pendulum. The instrument in use has been described in detail by Nederveen et al. (NW 67), see also Heijboer (He 72). Occasionally, we shall refer to dielectric measurements of Heijboer at 60 and 110 Hz. These data were obtained by means of a commercial Schering bridge (Rohde & Schwarz, model VKB, Germany). This apparatus is widely used and has been described at several places in the literature, see e.g. (CR 67).

However, dielectric measurements at medium frequencies, in contrast with TSD, give no high resolution of the molecular processes. To improve this situation Ong, the author and their associates have designed a special apparatus working at *much lower* frequencies, viz. from 10^{-3} to 10 Hz. This apparatus applies a sinusoidal voltage from an ultra-low-frequency oscillator (Hewlett-Packard, model 203 A, U.S.A.) to the sample, and measures its current response with an electrometer (Vibron 62A, Electr. Instr., England). The magnitude and phase angle of this current determine the dielectric constant ε' and dielectric loss ε''. We have

$$\varepsilon' - i\varepsilon'' = j(t)/\varepsilon_o E(t) \qquad (9.9)$$

where $\varepsilon' - i\varepsilon''$ is the complex permittivity, while $j(t)$ and $E(t)$ are complex quantities, of which the real parts are the current density through the sample and the applied a.c. field. If the phase angle between these quantities is δ, we can put $j(t) = \exp(i\omega t - i\delta)$ and $E(t) = E_o \exp(i\omega t)$. By separating the real and imaginary parts in Eq. 9.9 we readily verify that

$$\varepsilon'(\omega) = (j_o/\varepsilon_o E_o)\cos\delta \quad \text{and} \quad \varepsilon''(\omega) = (j_o/\varepsilon_o E_o)\sin\delta \qquad (9.10)$$

The phase angle δ between the applied field, and the current measured by the electrometer, was found by a digital time-interval counter (Marconi Instrum., England, counter-frequency meter, TF 1417/5121).

Clearly, the apparatus is based on well-known principles. The key part of the assembly is the very-low-frequency oscillator, which previously was not available.*

*After we had completed this work we found that Schweitzer (Sc 69a) had built a similar instrument.

9:4 Measuring Errors of Current TSD

Apart from the small integration error, there are no fundamental errors in charge TSD. In current TSD, however, the development of a small voltage across the electrometer cannot be avoided. This causes a part of the released current to flow back through the sample (cf. Fig. 2-10 with S in position 2). Moreover, a minute part of the current is lost through the capacitance of the electrometer and the sample. This capacitive leak can virtually be neglected.

The fraction of the current lost through ohmic conduction, depends on the resistance ratio of the electrometer and the sample $R_e/R(T)$:

$$\Delta j_r = j_r R_e \{R_e + R(T)\}^{-1} \tag{9.11}$$

Obviously, for a correct measurement we must have $R_e << R(T)$. This condition was satisfied up to high temperatures, by putting R_e in the *feedback loop* of the electrometer, by which R_e was decreased a hundredfold.

In the theoretical part, we tacitly neglected this voltage drop, V(t). To see how it modifies the results, we consider the current TSD of a metallized electret. The short-circuit condition being violated changes to

$$\int_0^l E(x,t)dx = -V(t) \tag{9.12}$$

Representing the input of the electrometer as a capacitor C_e, shunted by a resistor R_e, we have the current voltage relation

$$Aj_r(t) = C_e dV(t)/dt + V(t)/R_e \tag{9.13}$$

where A is the area of the electret. Finally, the equations for the internal current and Debye's equation, i.e. Eqs 2.11 and 2.7, must be replaced by

$$j_r(t)1 = -\varepsilon_o\varepsilon_\infty dV(t)/dt + 1dP_s(t)/dt + \gamma(T)V(t) \tag{9.14}$$

and

$$dP_s(t)/dt + \alpha(T)P_s(t) = \varepsilon_o(\varepsilon_s - \varepsilon_\infty)\alpha(T)V(t)/1 \tag{9.15}$$

Introduction of the capacitance $C_\infty = \varepsilon_o\varepsilon_\infty A/1$, and the resistance $R(T) = 1/\gamma(T)A$ of the electret and elimination of $j_r(t)$ from Eqs 9.13 and 9.14 result in

$$(C_e + C_\infty)dV(t)/dt + \{1/R_e + 1/R(T)\}V(t) = AdP_s(t)/dt \tag{9.16}$$

Of the currents on the left-hand side of this equation only that through the electrometer resistance is observed; the other ones leak away unnoticed. *Our aim is that $V(t)/R_e$ approaches $AdP_s(t)/dt$ as closely as possible.* This requires the ohmic loss, V(t)/R(T), through the sample and the sum of the capacitive leakage currents, $(C_e + C_\infty)dV(t)/dt$ to be small, so that we must have

$$R_e << R(t) \tag{9.17}$$

and

$$(C_e + C_\infty)dV(t)/dt << V(t)/R_e \tag{9.18}$$

The latter is more easily fulfilled than the former, which was already known from Eq. 9.11. Noting that

$$V(t) \simeq AR_e(T)P_s(o) \exp\{-\int_0^t \alpha(T)dt\} \quad (9.19)$$

we can rewrite inequality 9.18 as

$$(C_e + C_\infty)R_e << 1/\alpha(T) \quad (9.20)$$

To avoid disturbing the depolarization rate, we furthermore aim at $\varepsilon_o(\varepsilon_s - \varepsilon_\infty)V(t)/1 << P_s(t)$ in Eq. 9.15. This requires, by virtue of Eq. 9.19, that

$$(C_s - C_\infty)R_e << 1/\alpha(T) \quad (9.21)$$

where $C_s = \varepsilon_o\varepsilon_s A/1$. This requirement is almost identical to that of criterion 9.20.

Summarizing, for the measurements to be accurate, the input resistor, R_e, and the input capacitor, C_e, of the electrometer should be *small*.* Since these quantities can be effectively reduced a hundredfold by using the feedback mode, the criteria 9.17, 9.20 and 9.21 can easily be met in the experiments. In our case, we had $C_\infty \simeq 15$ pF, $C_s \simeq 45$ pF, $C_e \simeq 15$ pF, $\alpha(T_g) \simeq 0.005$ Hz, $R(T_g) \simeq 3 \times 10^{12}\ \Omega$ and usually $R_e = 10^{10}\ \Omega$, and so all criteria are amply fulfilled.

Similar considerations apply to current TSD with an air gap.

Current TSD of metallized electrets is subject to a more serious error, however, which had not been foreseen. We found that at temperatures well above T_g many uncharged metallized polymers generate a *parasitic current*. This current is not caused by thermo-electric or photo-electric effects. We attribute it to a weak *electrochemical* potential, which arises in spite of the presence of identical electrodes. This explanation is supported by the fact that the temperature dependence of this current runs parallel to that of the conduction curve.

An example is given in Fig. 9-6 for uncharged PET film. Below 120 °C the parasitic current is virtually absent, because the ohmic conduction of the polymer is too low. Thereafter it clearly manifests itself, rising in the same way as a true ohmic conduction current. The onset of the parasitic current is probably accompanied by chemical changes such as oxidation, disproportionation, monomer, conversion, pyrolysis, etc. All our thermograms will be presented up to the onset of this current or are otherwise corrected for it. To this end we always performed a TSD without charging.

There is still another reason why such a preheating is necessary. From Fig. 9-6 it appears that a virgin sample may contain stray charges, which might disturb the thermogram of an electret. These so-called moulding charges are probably created during the production of the film. Although such charges are very persistent at room temperature, owing to

*We mentioned in Sect. 3:1 that we obtained the released charge by integrating the released current numerically. In the beginning, we performed this integration electronically (Tu 68), but this increased the voltage drop V(t), i.e. the current loss. We therefore abandoned electronic for numerical integration.

the extremely low conductivity of PET, they can easily be dissipated by preheating, when most of them disappear in the vicinity of the glass-rubber transition or α-peak. Note that the parasitic current is not altered by the preheating.

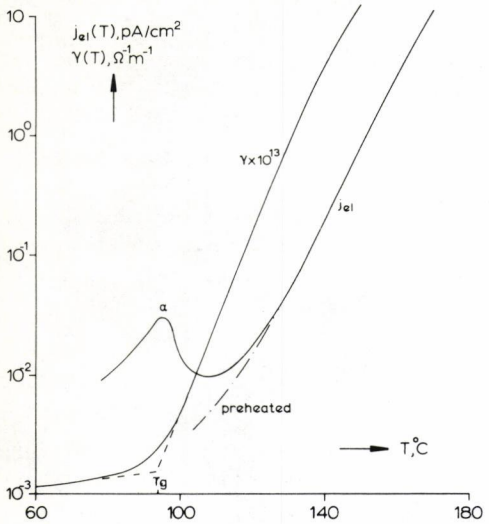


FIG.9-6 Parasitic current flow, j_{el}, in a noncharged PET-c foil at 0.5 °C/min. This current is observed only well above T_g, when the ohmic conduction becomes high.

9:5 Choice of the Polymers

The choice of polymers suitable for electrets in practical applications is governed by the requirement that they must support a high charge for prolonged periods. The nature of the polymer is not very critical if homocharging is aimed at; then only extrinsic carriers are injected and for this purpose even non-polar polymers are suitable. In practice they are even to be preferred, in view of their low ohmic conductivity, which ensures good charge stability. For heterocharging, however, we need polymers containing permanent dipoles preferably in or tightly bound to their main chains. The presence of dipoles will also promote space-charge polarization, because they facilitate dissociation of the impurities. A too high polarity is unwanted, however, because it results in a too low resistivity*. The Maxwell-Wagner effect is favoured by inhomogeneous structures such as are present in amorphous-crystalline polymers. We also tried composites of PMMA and ionic or semi-conductive compounds such as titanium dioxide, stannic oxide and anthracene.

The stability of the charge depends on the relaxation times of the dipoles, and on the ohmic relaxation time. Since these times decrease sharply at the onset of the conformational rearrangements of the main chains, stable electrets can usually be obtained only from polymers

*Compare the resistivity curves of PEMA and P2CEMA in Fig. 2-2. The substitution of an H atom by the strongly electronegative Cl atom is seen to lower the resistivity drastically.

having a sufficiently high T_g. The resistivity also depends on the amount of absorbed water, to ensure a low water absorption, the polymer should be hydrophobic. Non-polar polymers, in particular, have exceptionally low conductivities, as well as a negligible absorption of water. Teflon and Teflon-FEP e.g. are therefore excellent for forming very stable homocharged electrets.

These arguments prompted us to investigate several thermoplastic polymers, most of them methacrylic derivates. The facilities for these investigations having been available through Heijboer's work. The corresponding monomers were polymerized in bulk between two glass plates, by Miss M.P. van Duijkeren and Mr H.W. Bree, with careful control of their purity and chemical composition. Heijboer and coworkers were also able to modify the molecular structure of the polymers. This enabled us to determine the influence of specific modifications on the current thermograms of hetero-electrets. We also studied some methacrylic and other copolymers, not only because of their special properties, but also because their suitability as electret materials had not been studied before. The polymerizations were carried out with azo-bis-iso-butyronitrile (0.1 - 0.2 % w/w)or benzoyl peroxide (0.01 - 0.2 % w/w) as the radical initiator. For details of the procedure we refer to Heijboer's thesis (He 72).

Some commercial polymers were investigated as well. Most of them were partially crystalline and in the form of films. These were mainly used for homo-electrets. Special attention has been paid to the best homo-electret foil known to date, i.e. the non-polar Teflon-FEP (89 TFE co 11 HFP).

All samples were thoroughly dried in a high vacuum (10^{-5} mm Hg) at 70 °C for more than 48 hours, to remove most of the volatile impurities such as water and monomer residues.

CHAPTER 10

DISCUSSION OF EXPERIMENTAL RESULTS

10:1 Introduction

The first publications on current TSD of polymers have appeared only in the last two years. All these, except our own (Tu 70), concern commercial polymers. Lilly and co-workers (LH 70) studied homo- and hetero-charged PET-a film. Interestingly, they injected the homocharge not by means of Townsend breakdown, but rather by subjecting their *metallized* films to intense voltage pulses. The results for hetero- and homocharging were not consistent;there were, for instance, marked differences in the temperatures at which the current maxima appeared.

Takamatsu and Fukada (TF 70) investigated hetero-electrets of PE, PVF and PTFE. They observed complex thermograms with a great number of peaks; these have not been found by other workers in this field. As we have done in (Tu 70), Takamatsu et al. have tried to relate their TSD peaks to the transition regions known from conventional measurements.

Creswell and Perlman (CP 70) gave results on corona-charged PET. They showed that their data are consistent with four discrete trapping levels ranging from 0.55 to 2.2 eV. Their thermograms depended strongly on the storage time and were disastrously affected by high humidity (PC 71). Perlman and co-workers have also made an interesting study on a series of corona-charged substituted polyolefins (CP 71). They came to the conclusion that fluorine-substituted polyolefins are the most promising for making homo-electrets. Finally, Perlman (Pe 72) has recently given a comprehensive survey on the TSD work carried out in Canada. In this survey he has put forward some thought-provoking ideas about the molecular mechanisms that may be responsible for charge trapping in polymers.

Current thermograms of electron-bombarded PET and Teflon-FEP have first been published by Sessler and West (SW 70), working with pressed-on electrodes, they found marked deviations from the thermograms of thermo-electrets charged by Townsend breakdown.

We have mainly concentrated on a specific group of noncommercial polymers, viz. the *methacrylic* derivatives, the mechanical behaviour of which has been thoroughly studied in this laboratory by Heijboer and co-workers. Our first aim was to find out how the TSD thermograms of the polymers are related to their molecular structure. We have also included methacrylic *copolymers* in our research. This was not without success, because it turned out that copolymers can store a much higher charge than homopolymers. We reported part of this work in (Tu 70); in Sect. 10:2 it will be discussed more extensively.

The influence of the forming and storage conditions on the current thermograms of polymer electrets has hardly been investigated by other workers. Results on PET-c were given in (Tu 70); in Sects 10:3 and 10:4 the effects on PMMA and PC hetero-electrets will be described, and we shall show that the dipolar α peak of polar polymers might be deformed by an inaccurate formation, as was predicted by the theory of Sect. 2:2. On the other hand, a long storage was found to disturb mainly the ρ peak.

In Sect. 10:5 we shall give TSD current results on polymers that were made inhomogeneous by adding highly polar or semiconductive dopes. Especially after mixing with the organic semiconductor anthracene the released current increased strongly. Clear evidence that part of the heteropolarization of a polymer arises from excess charge accumulation will be given in Sect. 10:6, in which we shall discuss the TSD thermograms of *sectioned* electrets of PMMA and ChPEth (Penton). The sections adjacent to the electrodes were always found to be charged *highest*. The sectioning technique has previously been applied by Gross et al. (GM 62) to carnauba wax. By contrast, they observed a uniform distribution for the internal charge; however, they stored their electrets for a considerable time before starting TSD.

Further support for our view that the ρ peak found in the current TSD of shorted metallized hetero-electrets originates from space-charge motion, was provided by performing current TSD with an *air gap*. Results of this new technique will be given in Sect. 10:7; they show that the conduction peak observed with an air gap corresponds to the location of the ρ peak of shorted hetero-electrets.

Much less work has been done on charge TSD in open-circuit than on current TSD of shorted electrets. As far as we know, the former technique has only been explored by Perlman and co-workers (CP 71, Pe 72) and by the author. Since charge decay studies are of great importance for judging the application of electret foils, we have restricted the work described in Sect. 10:8 to commercially available polymer foils. Special attention has been given to the most promising electret foil known today, viz. Teflon-FEP-a. It has usually been charged homopolarly by Townsend breakdowns, but some charge thermograms of electron-bombarded FEP will also be given.

10:2 Relationship between Current TSD and Molecular Structure

In this section we shall confine ourselves to the *molecular* interpretation of the TSD data of methacrylic hetero-electrets. The measurements reported below were done with normal current TSD, using bilaterally metallized samples. Before the TSD, the electrets were stored overnight in short-circuit to allow the nonpersisting polarization to disappear. An attempt to interpret the TSD data will be made by invoking the corresponding results of conventional mechanical or dielectric mea-

surements. The theoretical basis for this comparison has been given in Chap. 4.

We have not tried to give a thorough quantitative analysis of all the data collected; this would have taken too much time. For we have shown that a proper evaluation of TSD data is rather complicated, even for the dipolar β and α peaks (cf. Chaps 2 and 3). The reason for this is that these peaks originate from a distributed polarization, which is difficult to analyze with one recorded curve at hand. Similarly, we may infer from Chap. 5 that the evaluation of the ρ peak is complex. So we have decided to emphasize here the general trend of the various thermograms and to relate their characteristic features to the molecular structures of the polymers. However, from the discussions in the theoretical part on the quantitative analysis of *some* of the observed thermograms, we may conclude that the theory presented there is compatible with most of the experimental results.

10:2.1 Thermograms of Hetero-Electrets of Methacrylic Homopolymers

Fig. 10-1 shows the current release of metallized PEMA and PMMA electrets. As depicted schematically in the figure, both polymers differ only in the alkyl substituent, R, of their ester side-groups, -COOR. The ester groups are polar, and so they form permanent dipoles which can be oriented during the formation.

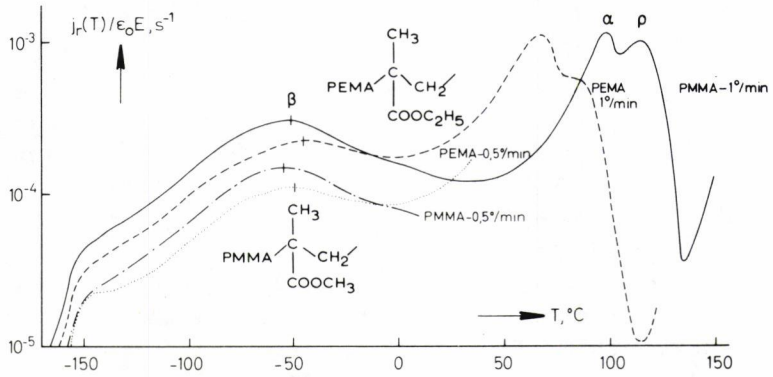


FIG.10-1 Reduced current thermograms of metallized PEMA and PMMA hetero-electrets showing three relaxation peaks. The electrets were formed at 100° - 27 kV/cm - 1.5 h and 140° - 75 kV/cm - 1.5 h, respectively. The effect of a twofold decrease in heating rate on the β peaks is also shown.

It is well-known that the ester groups can rotate singly or together with the main-chain segments $-\overset{|}{C} - CH_2-$. Evidently, their co-operative motion with the adjacent segments of the bulky main chain, which may contain all together at least 10,000 monomeric links, requires more energy, hence it occurs well above room temperature, when the polymers soften and become rubbery. The local motions of the polar ester groups

by rotations around their C-C links with the main chains, occur at much lower temperatures, when the polymers are in their glassy state. Heijboer (HS 62, He 65) has shown that these rotations are sterically hindered by the presence of the α-methyl groups on the main chains. To freeze in the segmental main-chain motions, as well as the local motions of the dipoles, we cooled our specimens to - 180 °C.

The thermograms give the reduced current, normalized to the forming field E, vs. the programmed temperature. For increasing temperature we found three maxima, designated β, α and ρ of which only the first and the second are due to the thermal release of the frozen polar ester groups. For the α and ρ peaks the current is higher than for the β peak, which is, however, much broader.

Following Heijboer's interpretation of conventional measurements, the β peaks, which occur in the glassy state at - 45 °C for PEMA and at - 51 °C for PMMA (when s = 1 min/°C), are ascribed to release of part of the polar ester side-groups by local motions. We observe that the ethyl β peak is a factor of 1.4 smaller than the methyl β peak. This is because the ethyl substituent is larger, so that the volume concentration of polar ester groups is lower, and in PEMA their motion is more impeded.

The α transitions at 66 and 103 °C are due to the release of the remaining part of the frozen ester groups by their co-operative motion with adjoining segments of the main chains, which at these temperatures start to rearrange their conformations. The larger ethyl substituents of PEMA which participate in this motion, will push the main chains in this polymer farther apart, thereby causing internal plastification. As a result, the α maximum of PEMA is observed at a lower temperature. As a matter of fact we have shown on p. 71 that the TSD α peaks correspond to the *glass-rubber transition*, T_g, as defined by Volkenshtein et al. (VP 57). Moreover, the TSD values will almost coincide with those found in dilatometric measurements, where a similar heating rate is used.

In Sect. 6:2 we proved for PVC and 80 S co 20 AN that the ρ peak of their electrets is not of a dipolar origin, but has the same temperature dependence as the artificially created ohmic-conduction peak in an air-gap system. On the basis of these findings, we attribute the two ρ peaks, appearing above T_g, viz. at 85 °C for PEMA and at 115 °C for PMMA, to the thermally stimulated *SCL drift and diffusion* of frozen-in excess charges, for it is only these processes that can be expected to have a temperature dependence similar to that of ohmic conduction.

Both ρ peaks in fact grow with the ohmic conductivity of the polymer and are less reproducible than the peaks of a dipolar nature, especially when different samples are considered*. They clearly originate from

*This irregular behaviour is not surprising, if one realizes that in the ρ peaks extremely low charge concentrations are involved. For instance for the ρ peak of PMMA we have estimated a storage of 1.2×10^{13} charges/cm^3 (see also Sect. 1:3).

those space charges that first took part in the conduction, and were accumulated in the polymer close to the electrodes during the formation. The peaks therefore depend on the nature of the electrodes and on the presence of impurities such as absorbed water (cf. Figs 10-38 and 10-39, below). It is now also clear why the ρ peaks always appear above the dipolar peaks, for the latter arise from local displacements of charges (dipoles), whereas the former arise from the gross motion of charges over macroscopical distances.

Beyond the ρ peaks the current rises again; this is due to the spurious current found in all *bilaterally metallized* polymers whether charged or uncharged (see p. 199). This current does not arise from stored charges, but probably from a weak conduction current generated by a small electrochemical potential difference between the two electrodes.

The dipolar β peaks are seen to shift slightly with heating rate, as was predicted by Fig. 2-8 and Eq. 3.8. When heating is slow, the polymer responds sooner, giving a current maximum at a lower temperature. Simultaneously, its intensity is lowered by about a factor of two which is the ratio of the inverse heating rates; this was again predicted theoretically (Eq. 3.9). The current is lowered, because the final *charge* released by the dipole reorientations should be the *same* in the two experiments. This invariance of the charge was actually proved; for both heating rates the β peak of PEMA, e.g., released a reduced charge of 1.3. Owing to their rather high activation energy of about 0.85 eV, the β peaks are shifted by a mere 4 °C. This matter has already been discussed on p. 70. The shift of the α peaks, with activation energies of some eV's is hardly detectable. The results exemplify the difficulties met in determining the activation energy by a change in heating rate, which in practice can only be varied by a factor of 5.

To compare our results with those of conventional measurements, dielectric data from Heijboer (HS 62) are given in Fig. 10-2. Only two peaks are present, α and β both located above room temperature now. Note that the shift of 5 °C of the β peaks for a twofold increase in frequency is comparable to that for TSD in Fig. 10-1. The ρ peak, associated with the motion of excess charges, is absent. Instead, gradually increasing conduction losses are found, because of the applied voltage. Due to the much higher measuring frequency of 60 Hz, the onset of these losses can only be noticed for PEMA; they begin at 120 °C. Moreover, particularly for PEMA, the α and β peaks are not well-resolved. Because its activation energy is 4.5 times less, the β peak is shifted so much that it almost overtakes the nearby α peak at the frequency given. This clearly indicates that TSD provides results at a much lower frequency. We recall from p. 93 that a current TSD at 1 °C/min should actually be compared to dielectric loss results at about 5×10^{-4} Hz.

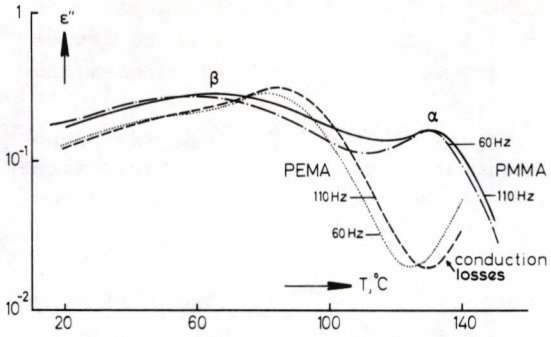


FIG.10-2 Appearance of the relaxation peaks of PEMA and PMMA in dielectrical measurements. The dielectric loss factor ε'', as found by Heijboer, is plotted for two frequencies. Note that the ρ peaks are missing.

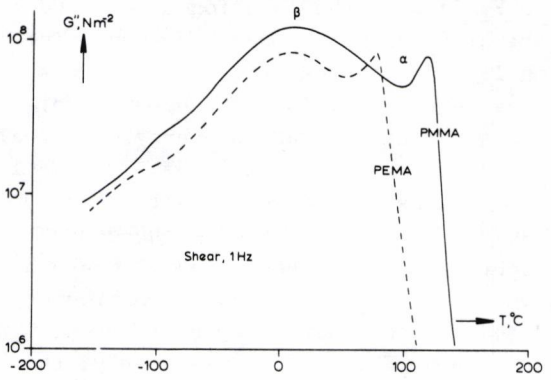


FIG.10-3 Appearance of the relaxation peaks of PEMA and PMMA in mechanical measurements. Data of the loss moduli in shear from Heijboer are given. As in Fig. 10-2 the ρ peaks are missing.

That the TSD thermograms also reflect the mechanical behaviour of both polymers can be seen from Fig. 10-3, in which we have plotted data from Heijboer for the loss modulus in shear vs. T at 1 Hz. Obviously, the resolution is still not so good as that for TSD and, as in the dielectric data, the ρ peaks are missing, which again shows that these peaks do not at all originate in relaxations of macromolecular groups.

Applying Eq. 4.31 to the β peaks of methacrylic polymers, we calculated on p. 93 for the equivalent frequency of TSD current measurements 3×10^{-4} Hz. This value is consistent with results from torsional creep measurements (WD 68). The low-frequency data presented in Fig. 10-4 were obtained by Heijboer and Struik of this laboratory. By a simple time frequency transformation based on

$$G''\{\omega(t_c)\} = \frac{\pi}{2}\, dJ(t_c)/d \ln t_c \quad , \quad \text{with } \omega(t_c) = 1/t_c \qquad (10.1)$$

the creep data were converted to loss shear moduli at 10^{-3} Hz. Since this frequency is still 3 times higher than that of TSD both β peaks are located at slightly higher temperatures, viz. at - 43 °C for PEMA and at - 45 °C for PMMA, than we found for a heating rate of 1 °C/min.

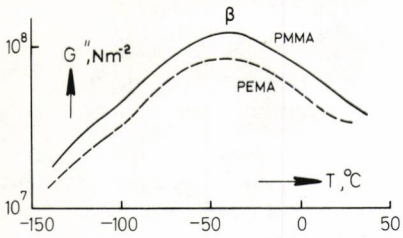


FIG.10-4 Loss modulus in shear at 10^{-3} Hz against temperature for the β peak of PEMA and PMMA. The temperature location of the peaks is still somewhat higher than in TSD.

The predicted equivalent frequency of TSD has been carefully checked by Ong of this laboratory. He has compared the TSD results of the α peak of KEL-F 5500 (i.e. PCTFE co PVDF) with the location of this peak in dielectric measurements at various frequencies; see Fig. 10-5. The TSD results appear at the extreme left, which confirms once more that their equivalent frequency falls below 10^{-3} Hz. In fact, by extrapolation, we find 0.4×10^{-3} Hz, whereas for an activation energy of 7.7 eV and a heating rate of 1.2 °C/min we calculate 2.5×10^{-3} Hz. The explanation for this discrepancy may lie in the *non*thermorheologically simple behaviour of this peak. As indicated in the figure the conventional measurements were carried out with three techniques. To obtain ε'' from the step-response data, Ong used the 1-point approximation of Hamon (Eq. 4.23). He further reduced his TSD current to $sj_r(T)/\varepsilon_o E$, whereas the proper conversion is given by Eq. 4.32. Consequently, the TSD values plotted are too low by a factor of 1.2.

Reconsidering Figs 10-1 and 10-2 we note that the dielectric β peak of PMMA is higher than its α peak, whereas in TSD we find the reverse. This disparity can be expected, in view of the higher activation energy of the α peak, by which the dipoles are forced to reorient in a narrow temperature range. On p. 94 we pointed out, however, that the difference between the activation energies of the α and β peaks can only account for part of the large increase in the TSD α peak. It seems to be further reinforced by the motion of excess charges. This view was later supported by sectioning experiments, which showed that the TSD α peak is not solely due to dipole reorientations.

In Fig. 10-6 we have compared the released charge with ε'(T) data at 0.1 Hz* and as we expected from theory, see Eq. 4.34, the agreement is good. Both quantities increase steadily with rising temperature, because of the increasing mobility of the dipoles. However, above 125 °C, the TSD curve, owing to the charge stored in the ρ peak, rises above that of ε'. The ε' values become even somewhat smaller in this temperature region. This means that the dipolar relaxation strength, $\varepsilon_s - \varepsilon_\infty$, is slightly temperature-dependent.

*The author is indebted to Ir H.J. van der Vossen for carrying out all the dielectric measurements at 0.1 Hz described in this chapter.

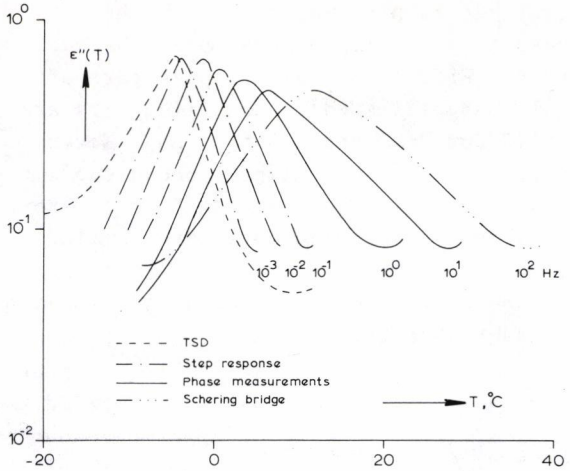


FIG.10-5 A TSD current thermogram, compared with the ε'' maxima at various frequencies for the α relaxation of Kel-F 5500, as measured by Ong. The results illustrate the extremely low equivalent frequency of TSD (the TSD current, dotted line, has been reduced to $sj_r(T)/\varepsilon_o E$).

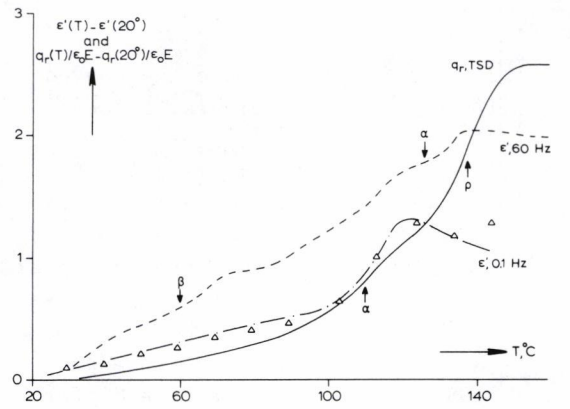


FIG.10-6 The charge released in the α and ρ peak of a PMMA heteroelectret, compared with the increase of the dielectric constant, ε', of PMMA with temperature (dotted-dashed line). Owing to the ρ peak the TSD curve (solid line) exceeds that of ε' at high temperature. The triangles represent theoretical q_r values, calculated from the ε' and ε'' data by Schwarzl's conversion formulae. These do not differ much from the ε' curve and therefore they also are too low at high temperatures.

To derive a better estimate for the released charge from ε' we have used the first conversion formula 4.27, which we have simplified to

$$q_r(T)/\varepsilon_o E \simeq \{\varepsilon'(T) - \varepsilon'_{20}\} + 0.403\{\varepsilon''(T) - \varepsilon''_{20}\}$$

by combining the first term of Eqs 4.27 and 4.28. Moreover, since we have plotted only the actual charge released above room temperature, we have substracted the values of ε' and ε'' at 20 °C on the right side. Again the $q_r/\varepsilon_o E$ calculated (triangles)do not match the actual charge released at high temperatures; obviously, because in this region the dielectric losses at 10^{-1} Hz are much lower than those at the equivalent frequency of TSD. Quite another aspect is, that it is hard to deduce the precise location of the relaxation peaks from the inflexion points of the actual q_r plot. The current thermogram is much more informative in this respect.

When the retained charge $\int_t^\infty j_r(t)dt$ is plotted instead of the released charge $\int_0^t j_r(t)dt$, the resulting thermogram resembles the curve of the storage modulus in shear (cf. Fig. 10-7 and the upper part of Fig. 10-8). Note that the initial charges stored in both electrets are nearly the same; they amount to 4.2 for PEMA and 4.8 for PMMA. Nevertheless, in practice PMMA electrets will be more stable, because of their higher α and ρ temperatures. It is also interesting to note from Fig. 10-8 that the mechanical loss tangent diagrams are more similar to the current plots of Fig. 10-1 than are the G'' = G' tan δ plots of Fig. 10-3; the α peaks now also exceed the β peaks, because the mechanical damping is larger in the glass-rubber transition.

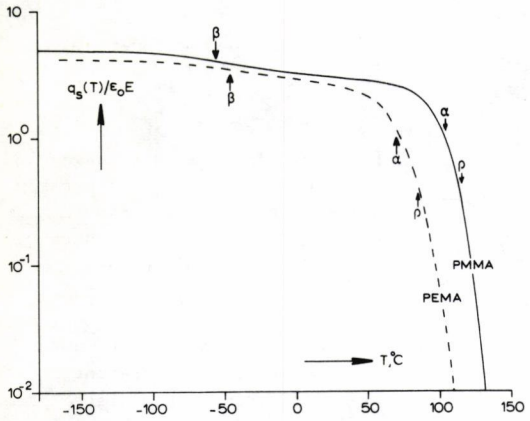


FIG.10-7 Reduced thermograms of the charge retained by PEMA and PMMA electrets. The curves were obtained by numerical integration of the currents shown in Fig. 10-1. The locations of the corresponding current maxima are indicated by arrows.

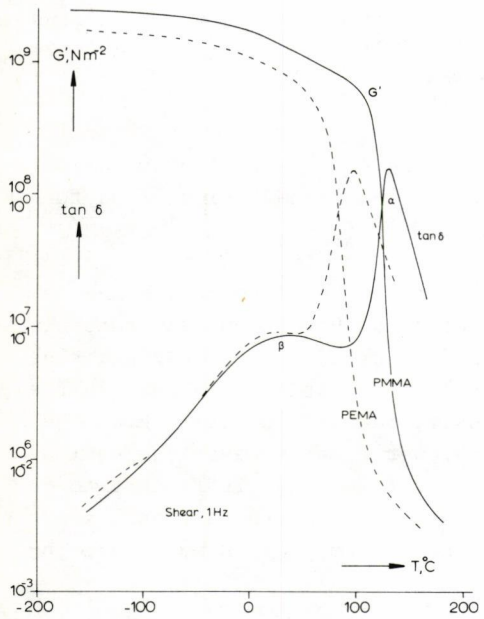


FIG.10-8 Temperature dependence of shear storage modulus, G', and loss tangent, tan δ, of PEMA and PMMA, according to Heijboer. The curves of G' strongly resemble those of the retained charge in Fig. 10-7 and the trend of tan δ is similar to that of the released current in Fig. 10-1, except that the ρ peaks are absent and the resolution is poorer, on account of the higher measuring frequency.

10:2.2 Thermograms of Hetero-Electrets of Methacrylic Copolymers

Fig. 10-9 shows results for methacrylic polymers with cyclic substituents, namely a flexible cyclohexyl group, and a stiff phenyl group. Furthermore, two copolymers with MMA were investigated. For PcHMA an interesting γ peak appears at - 120 °C. This peak was first interpreted by

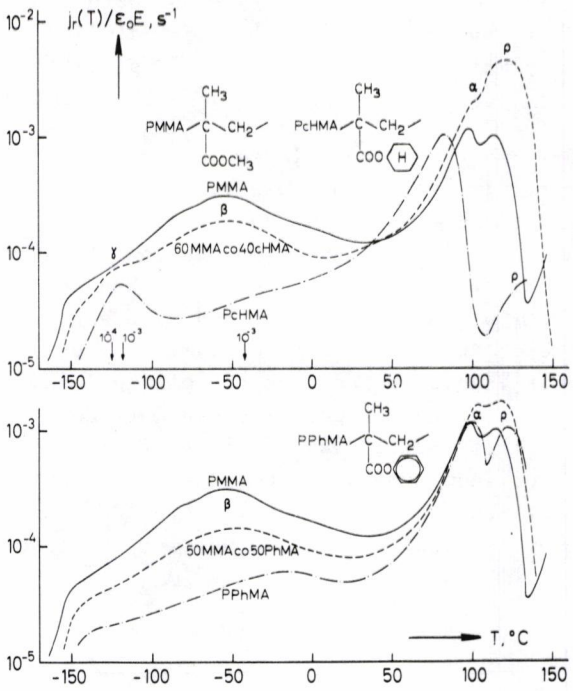


FIG.10-9 Current thermograms of methacrylic homo- and copolymers with a flexible hexyl group (upper curves) and a rigid phenyl group (lower curves). For comparison the thermogram of PMMA is also shown. The electrets were formed as follows: PcHMA 140° - 27 kV/cm - 1.5 h, 60 MMA co 40 cHMA 140° - 30 kV/cm - 1.5 h, 50 MMA co 50 PhMA 140° - 68 kV/cm - 1.5 h and PPhMA 140° - 68 kV/cm - 1.5 h.

Heijboer (He 56, He 60) as being due to a chair-chair transition of the six-ring, or, in other words, a local relaxation *within* the cycloalkyl group. A β peak is hardly observed, since any sweeping motion of the entire bulky side-group is prevented by steric hindrance. The phenyl group, being stiff, is incapable of a γ relaxation. It does give, however, a small β peak at -13 °C, which is partly due to its higher polarity. On the temperature axis of the upper plots we have indicated the positions of the γ and β peaks as observed in torsional creep measurements; they illustrate once more the extreme low frequency of TSD.

As in ordinary dielectric or mechanical measurements the copolymers exhibit a single TSD α peak. This indicates that the monomers are linked randomly, with their main-chain segments moving jointly. Identifying the α points with T_g, we see that the glass transitions for PMMA, PcHMA and 60 MMA co 40 cHMA are located at 106, 84 and 105 °C respectively. Hence the copolymer has about the same T_g as PMMA, so that it violates the empirical relation of Tobolsky

$$1/T_g = w_1/T_{g_1} + w_2/T_{g_2} \qquad (10.2)$$

where $w_{1,2}$ and $T_{g_{1,2}}$ are the weight fractions and glass transition of the components respectively. Unfortunately, our results do not permit a careful check of relations of this type, because the location of glass points is sensitive to the presence of monomer residues, which are difficult to avoid completely in bulk polymerizations (He 72).

Up to room temperature, the discharge current of the copolymers is equal to the sum of the weight fractions of their components

$$j = j_1 w_1 + j_2 w_2 \qquad (10.3)$$

This can be seen from Table 10-1, where the calculated and measured heights for the β peaks of the copolymers match closely. Such a result is consistent with the fact that γ and β peaks are due to dipoles, the polarizations of which add linearly. However, Eq. 10.3 does not hold for the space-charge peaks, which are found at 122 °C for 60 MMA co 40 cHMA, and at 118 °C for 50 MMA co 50 PhMA*. Nonlinear addition seems to be a general feature of space-charge peaks. For copolymers these peaks are therefore always larger than expected from the mixing rule. This behaviour agrees with the finding that copolymers are more conductive** than homopolymers (see Figs 2-2 to 2-4) and they often suffer higher dielectric losses. Moreover, copolymers may possess more *structural defects*, i.e. more trapping sites, then homopolymers. Nor do the α peaks satisfy the linear mixing rule, if they arise partly from space charge motions.

TABLE 10-1 Reduced Height, in s^{-1}, of the TSD β Peaks of Two Copolymers with Cyclic Substituents

polymer	$j_m/\varepsilon_o E$ measured	$j_m/\varepsilon_o E$ calculated
PcHMA	0.35 E-4	
60 MMA co 40 cHMA	0.19 E-3	0.19 E-3
PMMA	0.31 E-3	
50 MMA co 50 PhMA	0.15 E-3	0.17 E-3
PPhMA	0.46 E-4	

The TSD α peak of pure PcHMA, which is well separated from the attending weak ρ peak, has been analyzed on p. 55. We found that it fits to a Fuoss-Kirkwood distribution which indicates that to this peak the

*In Fig. 10-9 the ρ peak of PcHMA itself is hardly perceptible; for an undried specimen we later found a much higher ρ peak, which even exceeded the α peak and which had its maximum at 145 °C.

**Although a high ohmic conduction is advantageous in supplying more charges to accumulated during the formation, it has, on the other hand, the disadvantage of consuming more of the drifting charges during the subsequent TSD. Our results indicate that the first of these competitive processes dominates.

dipoles contribute most. In agreement with this its reduced charge of 2.2 is only slightly larger than the dipolar relaxation strength of 1.8 found by dielectric measurements.

Fig. 10-10 gives the dielectric relaxation plots of the cyclic methacrylic polymers. In the upper curves the γ peak of PcHMA does not yet emerge, because the measuring temperature was not low enough. As before the ρ peaks are missing. Although the trend of the TSD and ε'' curves is much the same, there are some interesting differences. We note, e.g. that the α peak of PcHMA now occurs at a higher temperature than that of PMMA. Obviously, the former shifts more with frequency than does the latter, and so its activation energy must be lower. In fact, we calculated from the frequency shift in conventional measurements 2.7 eV, which is about half the value for PMMA. On the other hand the activation energy of the α peak of 50 MMA co 50 PhMA must probably be higher than that of PMMA*. We further observe that the dielectric losses of

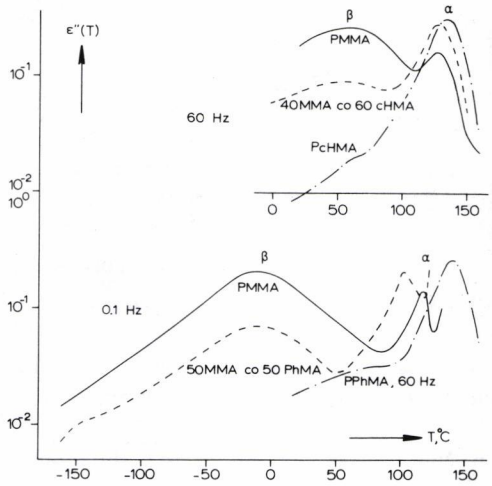


FIG.10-10 Dielectrical loss results at 60 Hz or 0.1 Hz for the same polymers as in Fig. 10-9.

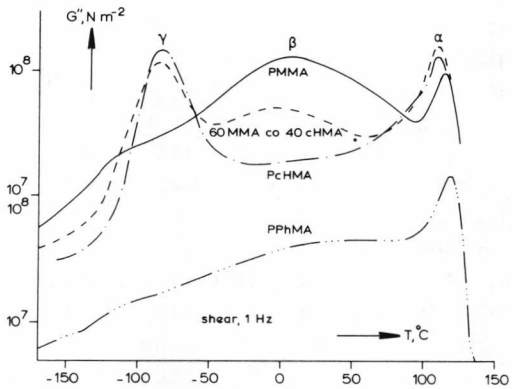


FIG.10-11 Mechanical analogue of the TSD results of Fig. 10-9, results from Heijboer. The upper curves show a marked γ peak, caused by the chair-chair transition of the cyclohexyl side group.

*It would not be justified to deduce values for the activation energy from the shifts found, because, as mentioned before, the location of a glass point depends on the monomer content, which sometimes may not be negligible.

the copolymers are not much higher than those of the homopolymers. This indicates that the strong TSD ρ peak of 60 MMA co 40 cHMA must arise from an enhanced space charge storage.

Fig. 10-11 shows the mechanical relaxation regions of the cyclic methacrylic derivatives. The γ peak of PcHMA is now very pronounced; even for the copolymer it is very marked. It is the weak polarity of the hexyl group that makes the γ peak in TSD less distinct. The further trends of the curves are similar to those of Figs 10-9 and 10-10.

Fig. 10-12 plots the released charge of the PMMA - PcHMA combination. These thermograms are less striking than the current diagrams in only having inflexion points corresponding to the ρ, α, β and γ transitions.

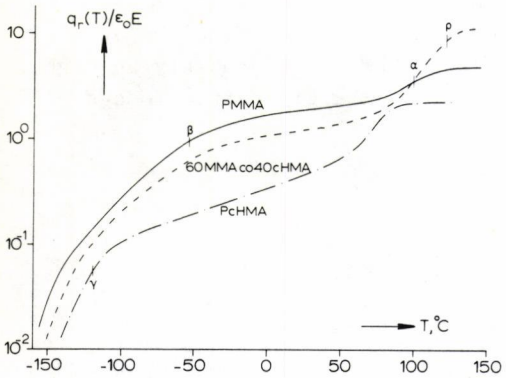


FIG.10-12 Charge thermograms of some methacrylic polymers. The copolymer is seen to release the highest charge.

The final value of the reduced charge yields, after subtraction of the charge resulting from the ρ peak, the dipolar relaxation strength, $\varepsilon_s - \varepsilon_0$ (see Eq. 3.10). Note that the final charge of the copolymer is distinctly higher, owing to its large ρ peak. Further details will be given in Table 10-4.

In Chap. 3 we have shown that even the narrow γ peak of PcHMA does not arise from a single dipole relaxation. We have further argued that the rotating polar groups are subject to various restoring forces of neighbouring groups, so the broadening of the peak is likely to originate from a distribution in activation energies. Heijboer (He 72) demonstrated this by mechanical measurements. Further evidence was obtained by performing a multi-stage TSD on this peak; the results are plotted in Fig. 10-13. We see that the activation energy derived from the initial slope gradually increases during such an interrupted TSD, owing to the increasing number of remaining subpolarizations which have a higher activation energy*. The value of the apparent activation energy just beneath the maximum of the noninterrupted thermogram lies between 9.7 and 12.5 kcal/mol. This agrees fairly well with the value of 11.3 kcal/mol derived by Heijboer from the frequency shift of the G'' maximum,

*Similar results were obtained for the β peak of PMMA, cf. Fig. 2-29.

which actually is the most probable value of the activation energy.

To deduce this activation energy from TSD experiments, we varied the heating rate. The position of the γ peak for four heating rates is listed in Table 10-2. As in the case of PEMA and PMMA the temperature shift is small, but, as they should,the results neatly fit to a straight line in an sT_m^2 vs. $1/T_m$ plot (Fig. 10-14). From the slope of this line we calculate an apparent activation energy of 10.9 kcal/mol, which is close to Heijboer's value.

TABLE 10-2 Position of the γ Maximum of PcHMA at Four Heating Rates

s^{-1} , °C/min	T_m , °C
2	- 115.0
1	- 119.1
0.5	- 121.4
0.2	- 125.0

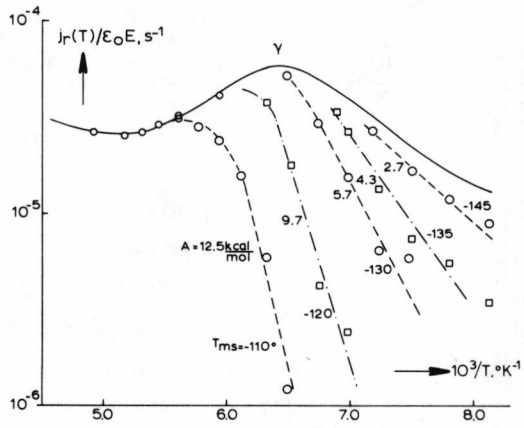


FIG.10-13 Multi-stage current TSD on the γ peak of PcHMA. The activation energy derived from the initial current slope increases gradually; this illustrates that the peak arises from a distribution in activation energies. For each run the previous final heating temperature T_{ms} is indicated. The electret was formed at 50° - 18 kV/cm - 1.5 h, and the heating rate was 1 °C/min.

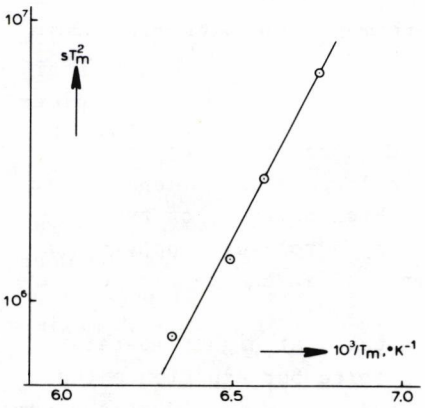


FIG.10-14 Plot for calculating the activation energy of the γ peak of PcHMA from the temperature shift with heating rate of its TSD current maximum.

In Fig. 10-15 we have summarized the TSD currents of other copolymers of PMMA. The curves are compared with that for pure PMMA. We first discuss the results of 60 MMA co 40 S. Since styrene has a nonpolar, bulky phenyl group, the intensity of the β peak of the copolymer is lower than that of PMMA. It also occurs at a lower temperature, viz. at - 76 °C, because part of the α-methyl groups protruding from the main chain, which sterically hinder the motion of the polar ester side-groups, are replaced by small H-atoms. However, the local motion of the ester groups seems to be blocked partly by the phenyl groups, for the intensity of the β peak is less than 60 % of that of PMMA. These ester groups, however, are liberated when the polymer becomes rubbery. This effect magnifies the α peak of the copolymer. Concurrently it shifts, in dielectric measurements, to a lower temperature, because the removal of part of the α-methyl groups enhances their mobility of the main chains; this agrees with the lower glass point of PS, which is 98 °C. The large

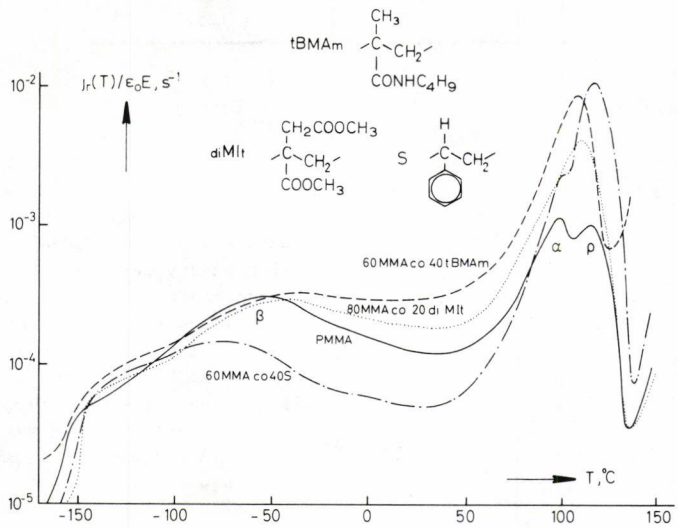


FIG.10-15 Current thermograms of PMMA copolymerized with the highly polar tBMAm, the polar diMIt and the nonpolar S. For all the copolymers the α and ρ peaks are remarkably high. They were all charged at 140 ° - 29 kV/cm - 1.5 h.

increase of the space charge peak at 118 °C is spectacular; it nearly drowns the α maximum. This indicates that a large storage capacity for space charges does not necessarily imply a high polarity of the molecular groups; structural defects may also play a role by supplying many trapping sites. In addition, during TSD only a few charge carriers are lost, because PS is a very good insulator.

For 80 MMA co 20 diMIt, only one peak appears at high temperatures. The α and ρ peaks are probably *combined*, despite our experience that such peaks are exceptional. The height of the β peak is almost the same

as that of PMMA, notwithstanding the replacement of α-CH_3 side-groups by the more polar-CH_2COOCH_3 side-groups. These groups, however, have their polar ester groups situated farther away from the main chain, so we may expect the low-temperature peak to be broader than that of pure PMMA. In line with this it seems resolvable into two peaks , located at - 132 °C and - 42 °C. By contrast, the height of the β peak need not necessarily increase and in fact it does not. From Fig. 10-16 we see that the α peak in dielectric measurements occurs at a lower temperature than for PMMA. Nevertheless, there is no indication for a lower glass point of the copolymer in the TSD results, but much difference could not be expected. An analysis of the high-temperature peak at 110 °C has been given on pp 129 and 130; this substantiates that it mainly arises from space-charge motions.

When considering the copolymer 60 MMA co 40 tBMAm, we note that in the latter polymer, one of the oxygen atoms in the -COOR side-group has been replaced by a more polar -NH- group. Moreover, the alkyl group has been enlarged from a methyl group to the stiff and bulky t-butyl group. As for diMIt, no separate α and ρ peaks appear, because in this conductive copolymer too many space charges are trapped (see however, Fig. 10-21, which shows that the joining of the peaks at 108 °C is a coincidence). Since the strong polarity of the -NH- group restricts the local motion of the side-group, the β peak is shifted to a higher temperature, viz. to - 36 °C, whereas its maximum remains the same as that of PMMA. There is a slight indication of a γ dispersion at - 136 °C, due to an intramolecular relaxation of the side-groups. This relaxation involves the motion of the t-butyl group around the polar -NH- link.

The dielectric measurements at 0.1 Hz also suggest this, see Fig. 10-16. It is clear from this figure that the α peak of the copolymer with the polar tBMAm has merged into the conduction losses. This shows that TSD, in addition to its higher resolution, has another advantage over dielectric measurements at 0.1 Hz, in enabling one to resolve the α relaxations of polymers having high conduction losses. We further observe that at high temperatures the dielectric losses of the copolymers are higher than those of PMMA, which agrees with their higher TSD α peaks. On comparing the location of the α peaks we may infer that the α peak of PMMA has a lower activation energy than those of 60 MMA co 40 S and 80 MMA co 20 diMIt.

Fig. 10-17 shows results of Heijboer and co-workers on the mechanical relaxations of some copolymers associated with those of Fig. 10-15. Data were available only for the β peaks, for which mechanical measurements often give more reliable results than for the α peaks. Since at its glass-rubber transition the polymer softens and has a high damping, so that the measurements can be carried out less easily and less accurately. In this respect TSD measurements are also superior to mechanical measurements.

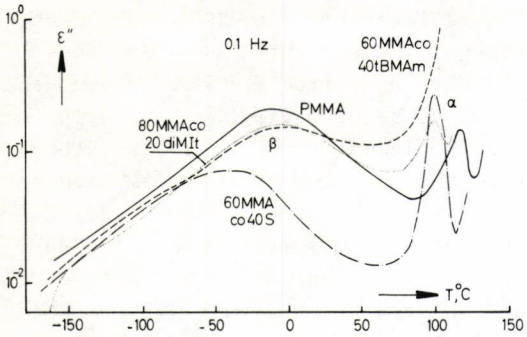


FIG. 10-16 Dielectric relaxation regions corresponding to the TSD peaks of Fig. 10-15. As before the ρ peaks are missing, while for MMA co tBMAm, even the α peak has merged with the conduction losses.

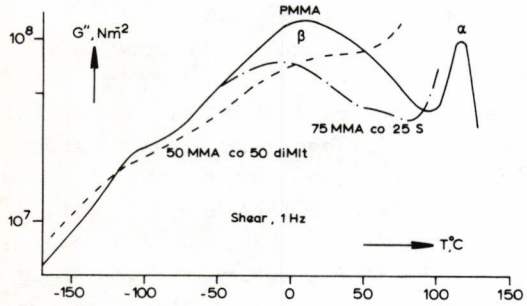


FIG.10-17 Mechanical low-temperature relaxations of some copolymers, similar to those of Fig. 10-15.

Fig. 10-18 gives results of copolymers of MMA and S with the highly polar PAN. For 80 S co 20 AN a low temperature maximum is virtually absent, because the highly polar -CN group has axial symmetry, and so its rotation around the C-C bond with the main chain does not give rise to polarization effects. Only at - 10 °C there is a slight indication of a

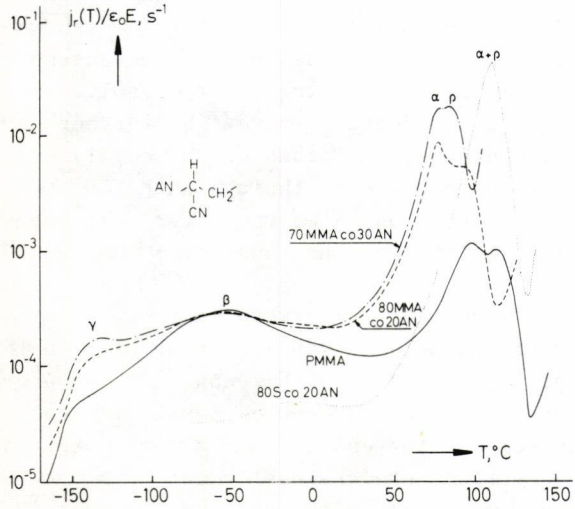


FIG.10-18 Current thermograms of PMMA and PS copolymerized with the highly polar PAN. The higher the PAN content the higher the α and ρ peaks. For 80 S co 20 AN these are combined into a single peak,* which is remarkably high. The electrets were formed at: 70 MMA co 30 AN 140° - 22 kV/cm - 1.5 h, 80 MMA co 20 AN 140° - 29 kV/cm - 1.5 h, 80 S co 20 AN 140° - 20 kV/cm - 1.5 h.

*In other recordings on this copolymer the high-temperature peak was often resolved in an α and ρ peak (cf. Fig. 10-62).

secondary relaxation, probably because of limited main-chain movements, which force some -CN groups to rotate as a whole. However, the bulk of the -CN groups start moving when the main chains begin their conformational rearrangements. This joint motion results in a strong α peak at 112 °C, notwithstanding the rather low concentration of -CN groups. A separate ρ peak was not found, and so the high-temperature peak is in fact generated by dipole reorientation as well as space-charge movement.

The copolymers of AN with MMA do show a β maximum, at - 59 °C, which has almost the same height as the β maximum of PMMA. This is not so in the mechanical results of Heijboer (He 56), who found a smaller β maximum for the copolymers; this is shown in Fig. 10-20. The same occurred in the dielectric measurements at 0.1 Hz (see Fig. 10-19). This lower-

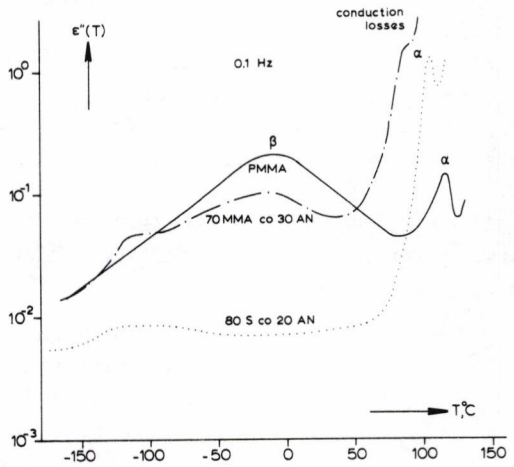


FIG.10-19 Dielectrical relaxation thermograms of the polymers given in Fig. 10-18. As in TSD, the α peaks are very pronounced.

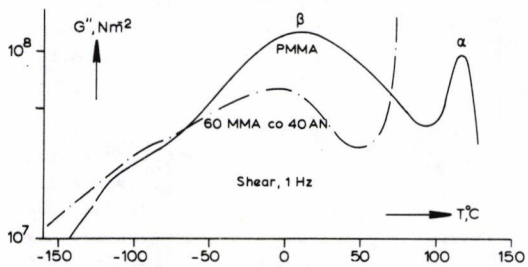


FIG.10-20 Mechanical low-temperature dispersions of the copolymer MMA co AN.

ing is plausible, because local motions of the symmetrical -CN groups do not contribute to the β peak. The slight differences between the TSD β peak of PMMA and those of the copolymers is therefore surprising. It is also conspicuous that, in TSD, the height of the β peaks of both copolymers is the same. Perhaps, on this particular copolymer, even at low temperatures, a contribution by space charge motions or rather electron or hole motions cannot be ruled out, since PAN is known to have

semiconductive properties. Differences only appear in the high-temperature α peaks to which the polar -CN groups do contribute and which therefore increase with the CN content. The same occurs for the ρ peaks at 90 °C which are not very distinct. The α and ρ peaks of the two copolymers are intense, being an order of magnitude larger than for PMMA. Their α points, i.e. the glass-rubber transitions, occur at 79 °C; this is below the T_g point of PAN, for which 85 °C has been cited. From Fig. 10-19 we recognize that the large TSD α peaks of *all* copolymers are compatible with their large dielectric losses.

Finally, at very low temperatures (- 132 °C) a γ peak seems to appear in the TSD thermogram and the ε" data of the copolymer with AN. Such a peak was also observed by Illers (Il 66), but not by Heijboer. This peak may therefore be due to traces of absorbed water, in spite of the fact that our specimens were carefully dried.

In Fig. 10-18 the α and ρ peaks of 70 MMA co 30 AN were hardly distinguishable, while for 60 MMA co 40 tBMAm they were found united in Fig. 10-15. However, in another experiment on different samples and restricted to the high-temperature region, we found the peaks for both copolymers well separated (see Fig. 10-21). This illustrates the poor reproducibility of ρ peaks, especially for TSD runs on samples of different batches. The figure also shows new results for 60 cHMA co 40 AN. It has a similar high storage capacity as 70 MMA co 30 AN.

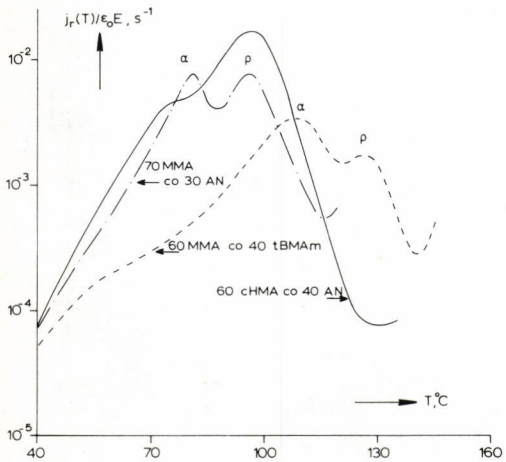


FIG.10-21 Illustration of the poor reproducibility of TSD ρ peaks when different samples are used. All the copolymers show distinct ρ peaks, whereas in Fig. 10-18 and 10-15 the ρ peak of MMA co AN and MMA co tBMAm were hardly discernible. The heating rate was 0.5 °C/min and the forming conditions were: 70 MMA co 30 AN 140° - 45 kV/cm - 1.5 h, 60 MMA co 40 tBMAm 135° - 42.5 kV/cm - 1.5 h and 60 cHMA co 40 AN 130° - 12 kV/cm - 1.5 h.

10:2.3 Current Thermograms of Hetero-Electrets of Halogen Homopolymers

Fig. 10-22 gives the current thermograms of vinyl polymers containing the highly polar C-Cl group. From these polymers PVC was "hot pressed" at the Plastics and Rubber Research Institute TNO. This PVC (Solvic 229, Solvay, Belgium) contained only a small amount of stabilizer (0.5 %); no other materials were added. As one can see at - 106 °C

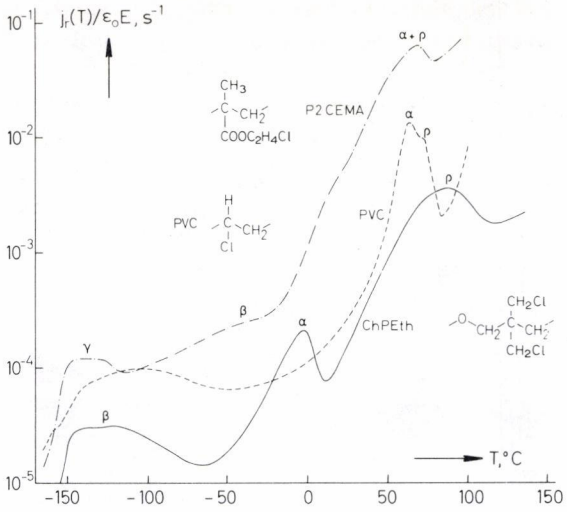


FIG.10-22 Current thermograms of polymers containing the highly polar C-Cl link. PVC and ChPEth were commercial makes, viz. Solvic 229 and Penton 9215. The electrets were formed at: P2CEMA 100° - 16 kV/cm - 1.5 h, PVC 120° - 23 kV/cm - 1.5 h and ChPEth 110° - 11 kV/cm - 1.5 h.

a small TSD β maximum and at 70 °C a high α and ρ maximum appear, of which the latter emerges as a small hump on the right shoulder of the α peak. (A better separated and more pronounced ρ peak has been shown in Fig. 1-10.) Since the high electronegative Cl atom is strongly bound to the main chain, Boyer (Bo 63) attributes the β maximum to a crankshaft motion of small parts of the main chain, which forces a few of the polar C-Cl bonds to move. The large α maximum originates from the normal segmental motion of the main chain, in which all the polar C-Cl bonds participate.

In the thermogram of P2CEMA, the β peak is partly submerged in the onset of the large α peak, and at low temperatures (- 130 °C) a γ peak appears. The latter is due to an intramolecular relaxation, within the 2-chloroethyl group. It is interesting to compare this thermogram with that of PMMA (Fig. 10-1), which differs from P2CEMA only in not having a Cl atom in its alkyl group. Apparently, this electronegative Cl atom gives rise to a much stronger space-charge trapping.

The thermogram of the partly crystalline ChPEth (Penton 9215, Hercules Powder, USA) exhibits three relaxation regions, the second of which is the α peak (- 3 °C), which is due to segmental motions of the main chain in the amorphous phase. The high temperature or ρ peak (86 °C) arises from molecular relaxations within the crystalline phase, since crystalline rearrangements will destroy the space charges trapped at the grain boundaries by the Maxwell-Wagner effect. The β peak at - 122 °C reflects the local mode dispersion of the two polar side-groups $-CH_2Cl$.

Figs 10-23 and 10-24 give the dielectric and mechanical relaxation regions of the chlorine containing vinyl polymers. Note that the dielectric measurements are severely hampered by the high conduction

losses, so that the α peaks of P2CEMA and PVC could not be revealed. The large TSD α peaks are consistent with the large value at the loss tangent of the α transition.

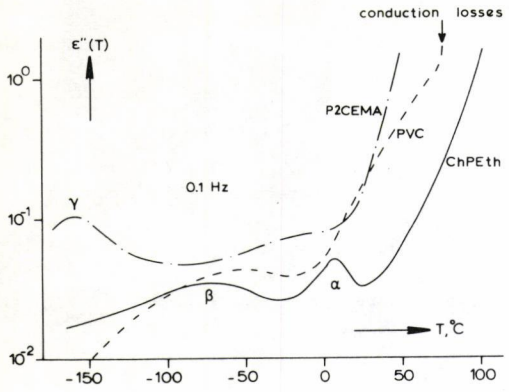


FIG.10-23 Dielectrical relaxation peaks corresponding to the TSD relaxation peaks of Fig. 10-22. Note that the α peaks of P2CEMA and PVC are drowned in the high conduction losses.

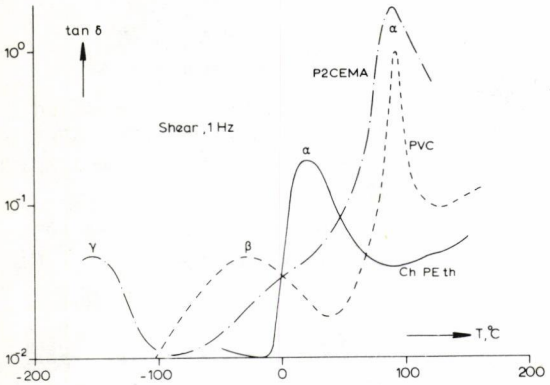


FIG.10-24 Mechanical relaxation peaks corresponding to the TSD peaks of Fig. 10-22; data taken from Heijboer and coworkers.

10:2.4 Current Thermograms of Hetero-Electrets of Commercial Polymers

In Fig. 10-25 TSD results are compiled of three commercial *foils*, all of which are partly crystalline. The thermogram of the polyester PET (Mylar-c film of 25 μm, DuPont de Nemours, USA) again shows three maxima, β, α and ρ. The β maximum, occurring at - 109 °C, is generally attributed to local relaxations of the polar carboxyl groups. This peak shows some structure and seemingly consists of two peaks. The molecular origin of these peaks is associated with the gauche and trans conformations of the polymer chain, which to some extent must partake in the local motions (IB 63). The α maximum at 88 °C is due to segmental motions of the main chain in the *amorphous* part of the polymer. It arises from the co-operative motion of the glycol residues, together with the -COO dipoles of the main chain. The ρ peak at 122 °C is due to space charges trapped at the crystal boundaries, because the amorphous phase

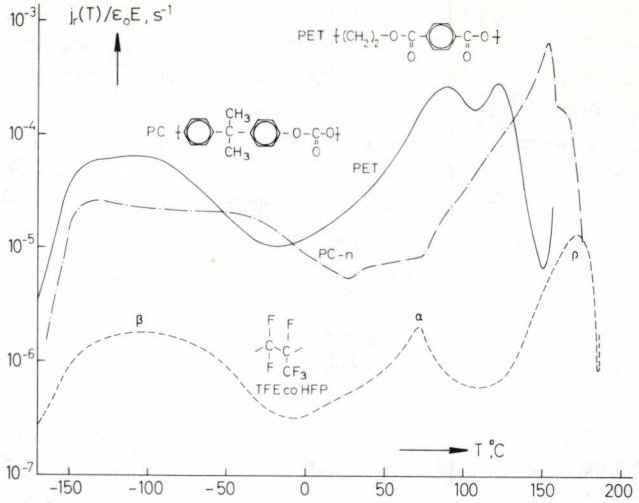


FIG.10-25 Current thermograms of some heterocharged commercial foils, viz. Mylar-c (PET), Makrofol-n (PC) and Teflon-FEP (89 TFE co 11 HFP) formed at 140° - 100 kV/cm - 1.5 h, 160° - 100 kV/cm - 1.5 h and 180° - 100 kV/cm - 1.5 h respectively. The nonpolar Teflon-FEP releases the lowest current.

is probably more conductive (MW charging). These charges are released when the crystal interfaces are changed, since this will destroy the trapping of the charges stored. The ρ peak therefore occurs at a temperature at which the crystallization rate is highest. This characteristic temperature is known from differential thermal analysis as the cold crystallization point (Ke 64). Here we meet another *advantage* of TSD over conventional measurements; for as is always the case with ρ peaks, they are not observed in dielectric or mechanical measurements, in which such crystallization effects pass unnoticed.

As an illustration of the reproducibility of TSD measurements, we have compared in Table 10-3 the results of two successive TSD experiments, on two PET samples which were charged at different field strengths; the heating rate was 0.45 °C/min. The agreement is gratifying especially for the dipolar α peaks; the values for the space charge or ρ peaks show more scatter, but the differences are not large.

TABLE 10-3 Reproducibility of the α and ρ Peaks of PET-c Film Electrets

experiment	peak	sample I, formed at 140° - 100 kV/cm - 1.5 h			sample II, formed at 140° - 200 kV/cm - 1.5 h		
		T_m, °C	$j_m/\varepsilon_o E$, s^{-1}	$\Delta q_r/\varepsilon_o E$	T_m, °C	$j_m/\varepsilon_o E$, s^{-1}	$\Delta q_r/\varepsilon_o E$
1	α	84	0.12 E-3	0.50	87	0.11 E-3	0.57
	ρ	118	0.15 E-3	0.48	119	0.73 E-4	0.28
2	α	86	0.12 E-3	0.53	88	0.11 E-3	0.59
	ρ	116	0.13 E-3	0.39	121	0.75 E-4	0.31

The polycarbonate PC-n (Makrofol-n film of 40 μm, Bayer, Germany) exhibits a very broad and flat β maximum, and in comparison with PET its α maximum is shifted to a much higher temperature, viz. 152 °C, because due to the two phenyl rings, its main chain is stiffer. As in the case of PET the β peak seems to consist of two peaks, the molecular origin of which is not yet clear. Furthermore, we see that the valley between the β and α peaks is rather irregular; this might be due to the "intermediate" peak discussed by McCrum et al. (CR 67). This relaxation is associated with frozen stresses, but the actual mechanism has not been established. As usual a ρ peak emerges to the right of the α peak at 164 °C, but is is not very pronounced.

The thermogram of the fluorocarbon film (Teflon-FEP of 25 μm, DuPont de Nemours, USA) lies more than one decade lower, because this polymer is hardly polar at all. Its second peak at 75 °C corresponds to the α relaxation or the glass-rubber transition T_g. The β peak at - 106 °C seems to be due to a crankshaft motion of short segments of the main chains (CR 67)*. As for the other films, the ρ peak located at 173 °C, which is absent in conventional measurements stems from molecular relaxations in the crystalline phase. In fact, its low polarity combined with its low electrical conduction and low water absorption, makes this polymer much more suitable for *homocharging*. It gives excellent homoelectrets of extreme longevity.

As can be seen in Fig. 10-26 we had only one ε" recording available, viz. that of PET-c. Its α peak is almost obscured by the increasing

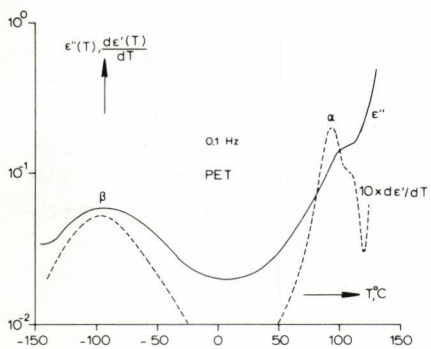


FIG.10-26 Dielectric loss factor of PET-c film versus temperature. The α peak is almost obscured by the high conduction losses. This is not the case in the plot of the derivative of the dielectric constant, dε'/dT.

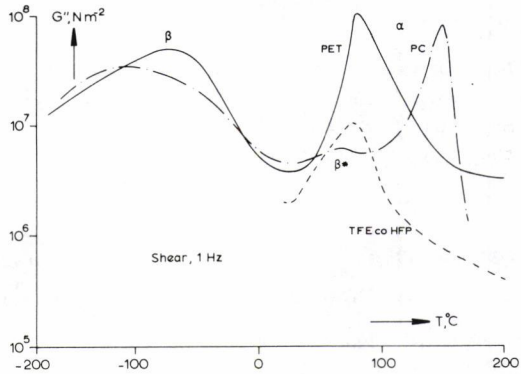


FIG.10-27 Mechanical relaxation thermogram of the polymers of Fig. 10-25. Results from Heijboer and co-workers on arnite (PET), makrolon (PC) and Teflon-FEP (in these torsional experiments rectangular bars were used instead of films).

*According to this reference the β peak may also be a combined β and γ peak.

conduction losses. The figure also shows a plot of $d\varepsilon'/dT$, which exhibits the α maximum much more clearly. This is understandable, because the quantity ε', which represents the charge storage capacity, is not affected by the conduction losses of the dielectric*. The mechanical spectra shown in Fig. 10-27 are more complete. They have a similar trend as the TSD curves, and for PC we can observe quite clearly the above-mentioned intermediate peak β*.

The current thermogram of a hetero-electret of a PP disc† is shown in Fig. 10-28. Since PP is nonpolar, its thermogram falls an order of magnitude lower than that of PMMA. We see from the accompanying mechanical spectrum (Fig. 10-29) that the high-temperature TSD peak shown at 118 °C is, in fact, a ρ peak, associated with the dissipation of space charges by molecular rearrangements of the crystalline phase.

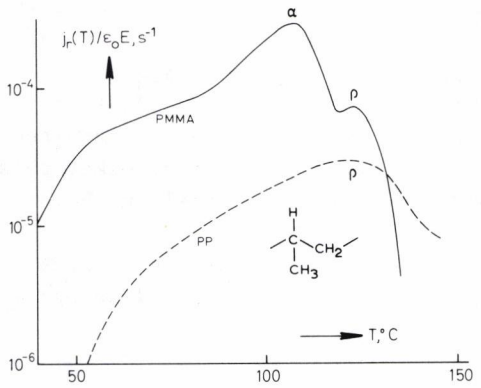


FIG 10-28 Current thermogram of a PP hetero-electret. This falls an order of magnitude lower than the thermogram of the much more polar PMMA. The electrets were formed at 120° - 100 kV/cm - 1.5 h.

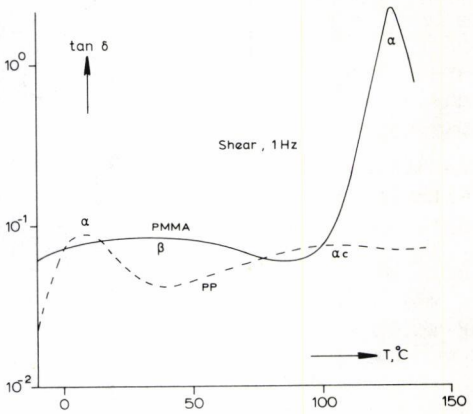


FIG.10-29 Mechanical relaxation thermogram corresponding to the TSD results shown in Fig. 10-26; data of Heijboer.

10:2.5 Heterocharge Storage Capacity of Various Polymers

To limit the number of graphs, we have given only two charge plots (Figs 10-7 and 10-8). The charges displayed were obtained by numerical integration of the released currents, since the charge of metallized electrets cannot be measured directly. An overall impression of the charge storage in the TSD relaxations of the various polymers can be gained from Table 10-4. It gives the reduced charge density $\Delta q_r/\varepsilon_o E$ released by the distinct peaks. For dipole relaxations, this charge density should equal, according to Eq. 3.10, the dipolar strength

*The author is indebted to Dr P.H. Ong for suggesting the use of $d\varepsilon'/dT$.

†Carlona P, Shell Plastics Laboratory, Delft.

$\varepsilon_s - \varepsilon_\infty$*. This equality is seen to be satisfied for most γ and β relaxations. For most α peaks, however, the dipole strength is lower than the reduced heterocharge. In these cases the dipolar α peak must have been enlarged by the motion of space charges.

TABLE 10-4 Reduced Released TSD Heterocharge and Dipolar Relaxation Strength (at 0.1 Hz) for the Relaxations of Various Metallized Polymers

polymer	γ		β		α		ρ	$\alpha+\rho$
	$\Delta q_r/\varepsilon_o E$	$\Delta\varepsilon$	$\Delta q_r/\varepsilon_o E$	$\Delta\varepsilon$	$\Delta q_r/\varepsilon_o E$	$\Delta\varepsilon$	$\Delta q_r/\varepsilon_o E$	$\Delta q_r/\varepsilon_o E$
P2CEMA	0.3	0.6					120	120
PcHMA	0.13				2.2*	1.8		2.2
PEMA			1.3	1.2	2.2		0.7	2.9
PMMA			1.9	1.9	1.7	0.8	1.2	2.9
PPhMA			0.4		3.0			3.0
ChPEth			0.13	0.2	0.37	0.2	11	11.4
PC-n			0.2					0.8
PET-c			0.33	0.37	0.5	0.36	0.55	1.1
PVC			0.5	0.45		$\sim$7		16.5
80 MMA co 20 AN			2.1					14.6
70 MMA co 30 AN	0.35	0.2	1.7	1.0		$\sim$9	25.5	25.5
60 MMA co 40 tBMAm			2.0	1.5		$\sim$4	12.7	12.7
60 MMA co 40 cHMA			1.1†				10	10
80 MMA co 20 diMIt			4.0	1.8		1.1		14
50 MMA co 50 PhMA			0.9	0.7	2.3	1.3	2.1	4.4
60 MMA co 40 S			1.0	0.8		1.2		14
80 S co 20 AN			0.8			5.3		82
89 TFE co 11 HFP			0.011		0.004		0.022	0.02
100 PMMA + 1.7 Anth			2.0			$\sim$1		20
100 PMMA + 7 DBP + 10 SnO_2			2.3	2.5		1.5	2.5	5

† means γ + β peak and * means β + α peak

In the last column we have listed the sums of the charges stored in the α and ρ peaks; these values are important for practical purposes, since it is these charges which can be frozen-in after cooling to room temperature. Inspection of the table shows that the more polar polymers acquire higher heterocharges. The total charges of the copolymers are also strikingly high, most of them reaching a value well above 10; this large value is mainly due to the presence of a strong ρ peak. For the copolymers of MMA with AN we see that the charge storage grows with increasing AN content.

However, it is not only the initial charge stored that decides the

*In Table 10-4 this quantity has been approximated by taking the difference in ε' at the successive minima of the corresponding ε'' curve.

quality of an electret in practice. It should also possess good stability, for which a high T_g and a low ohmic conductivity are prerequisites. In these respects copolymers are also promising, in particular MMA co cHMA and MMA co S (cf. Figs 2-2 to 2-4). The outstanding behaviour of these electrets becomes clear from Table 10-5, in which are compiled results of charge decay measurements at room temperature on *non*metallized disc electrets with a net homocharge (results of homocharged electret foils are given in Fig. 10-65). We see that, in addition to MMA co cHMA and MMA co S, which retain a high charge for more than a year, MMA co An is also promising, while of the homopolymers PMMA and ChPEth are satisfactory. PtBMAm, PA 6-10 and PVC, on the other hand, are poor electret materials; they decay too fast. We have also indicated the forming conditions. Most formations were performed in two steps. By choosing a

TABLE 10-5 Charge Decay of Several Nonmetallized Polymer Homo-Electrets at Room Temperature

polymer	surface charge in nC/cm^2 after				formation
	50 d	150 d	250 d	350 d	°C - kV/cm - h
PtBMAm	0.6	0.65	0.5	0.3	130/100 - 25/30 - 3/2
PMMA	0.85	0.65	1.0	0.9	170/100 - 35/90 - 2/3
60 cHMA co 40 AN	0.8	0.3	0.6		130/100 - 30/50 - 3/2
60 MMA co 40 AN	2.7	1.8	1.6	1.6	130/120 - 60/20 - 1/1
60 MMA co 40 cHMA	3.0	1.4	1.8	2.1	150/130 - 60 - 3/2
60 MMA co 40 S	2.5	1.6	1.65	1.7	130 - 50 - 6
80 S co 20 AN	0.4	0.5	0.4	0.35	130 - 75 - 5
60 S co 40 AN	1.7		0.95		105/100 - 30/35 - 1/2
60 S co 40 tBMAm	1.3	1.0		0.65	125 - 45 - 5
100 PMMA + 10 SnO_2 + 7 DBP	0.9	1.0	0.6		160/110 - 40/80 - 3/2
100 PMMA + 10 TiO_2 + 7 DBP	0.8	0.8	0.7	0.6	170/100 - 42 - 6
PA 6-10	0.7			0.35	90 - 20 - 5
ChPEth	1.2		0.8	1.2	140/110 - 20/40 - 2/2
PVC	0.3	0.35	0.05		120 - 30/40 - 1/2

lower temperature in the second step, we could often increase the forming field, and so intensify the homocharging.

Note that the charges tabulated here are often considerably less than those corresponding to the reduced values of Table 10-4, for they represent the *effective* surface charge measured by an inductive method, which determines the differences between the actual hetero- and homocharge of the bare electret (Tu 70a). Since most electrets were wrapped in tin or lead foil during their storage, the charges show some scatter. This handling was avoided in our measurements on foils, the decay curves of which do not fluctuate (see Figs 10-65 and 10-66).

Finally, in Table 10-6 the locations of some TSD α points, which are decisive for the temperature stability of the electrets, are compared with dilatometric T_g values, cited in (BI 66). There is close agreement

between these results, which suggests that current TSD is very suitable for determining the glass-rubber transition of a polymer.

TABLE 10-6 Glass-Rubber Transition, T_g, as Found by Current TSD

polymer	TSD value	literature value
P2CMEA	69	103*
PcHMA	85	90**
PEMA	66	65
PMMA	105	105
PPhMA	106	105
ChPEth	- 3	
PC-n	152	149
PET	88	81
89 TFE co 11 HFP	75	77
PVC	75	74

* This value from Brandup et al. (BI 66) must be definitely wrong.
** We have taken the value cited by Heijboer (He 65), the value given in (BI 66) is too low.

10:2.6 Current Thermograms of Homo-Electrets

So far we have dealt with current thermograms of hetero-electrets, of which the charging is closely related to the intrinsic properties of the polymer. This need not be the case for homo-electrets in which most carriers are injected from the outside, e.g. by corona injection or electron bombardment. These injected charges are trapped in the polymer at different energy levels, since the various trapping sites often are of a different nature.

10:2.6a Possible Trapping Sites in Homocharged Polymers

Perlman and associates (CG 71, Pe 72) have recently suggested some possible trapping sites in corona-charged polyolefins (see Fig 10-30).

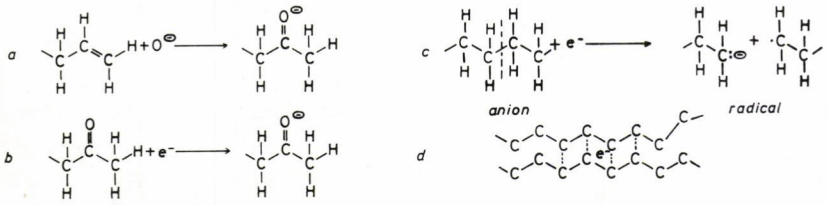


FIG.10-30 Electron trapping schemes in corona-charged polyethylene.

As shown by the reaction schemes a and b the trapping might occur at the double bonds $\rangle C=C\langle$ and carbonyl groups $\rangle C=O$ formed by the (negative) corona exposure in air. This trapping will take place near the surface of the polymer, because the necessary oxygen atoms will not penetrate far. Reaction c, which can take place farther inside the polymer, il-

lustrates the forming of a rather stable anion and a neutral radical, due to main-chain scission by the impact of a high energy electron. The radical fragment is likely to react further to cause crosslinking and branching.

Since all these traps are on the main chain with the charges captured at atomic sites Perlman calls this a trapping at the *primary* level. He also advocates trapping at a *secondary* level. This involves caging of the decelerated electrons between adjacent main chains, due to the electron affinity of the neighbouring molecular groups; this trapping is sketched in Fig. 10-30d. He finally suggests trapping at a *tertiary* level, which accommodates trapping of the slowed electrons in cavities (structural defects) within the crystalline or amorphous regions, or at the crystalline-amorphous interfaces.

As Perlman et al. have pointed out, the different categories of traps will have different temperature stabilities, for untrapping is a *dual* process that arises from both a lowering of the trap with molecular motion plus thermal excitation of the charges out of the trap. Obviously, charge release from primary sites can be initiated by limited chain motions occurring below T_g, whereas charges trapped at the secondary level require gross main-chain rearrangements, which start at T_g, and the trap barriers at the tertiary level are only lowered when the crystalline structure is destroyed, i.e. at temperatures above T_g.

Following Sessler and West (SW 70) we have concentrated on homo-electrets made by electron bombardment in a vacuum. In this way we were sure of the nature of the injected carrier and of the injection energy. To limit the radiation damage we bombarded with low electron densities at moderate energies, so that the dose rates were less than 10^5 rads. The polymer we used was Teflon-FEP, which is the most interesting for electret applications. This polymer has strongly electronegative F-atoms instead of H-atoms in its backbone. In some aspects, trapping in homo-electrets obtained by electron bombardment, differs from the above mechanisms. In particular, the processes 30a and b are missing.

Perlman and Unger (PU 72) have suggested that in this case the electrons are accommodated on unsaturated groups intrinsically available in polymers. In Teflon these are the trifluoro-vinyl endgroups $-CF=CF_2$, and the difluorovinylene groups -CF=CF- occasionally present in the main chains; which groups have a strong electron affinity. The concentration of these groups is roughly 1 per 1000 C-atoms of the main chain. Their capture of an electron is illustrated in Fig. 10-31a and b, this shows that in both anion radicals the excess negative charge can be distributed over the two carbon atoms. The radicals formed are apt to react further, but their electron charge will be conserved.Fig.10-31c shows a different trapping mechanism; it involves an F-atom stripped from the main chain by the electron impact, which carries the electron with it, forming a stable F^-ion.

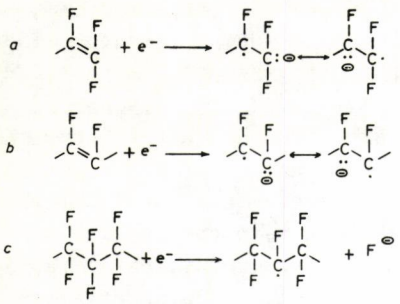


FIG.10-31 Electron trapping schemes in electron-bombarded Teflon.

Electron trapping on a primary level may also take place on electron acceptors of *low* molecular weight. These may have been added in the manufacturing of the polymer, but they may also be O_2, CO_2 and H_2O molecules, which have diffused in from the atmosphere. On the other hand, trapping on the secondary and tertiary levels will not differ from that for corona-charged polyolefins, except that process d is more favoured, because the F-atoms have a stronger electron affinity.

After this tentative classification of electron traps in Teflon, we can be brief about traps for positive carriers. Apparently, these will be captured much less efficiently, because of the electronegative F-atoms present. In fact, only the unsaturated groups will show some hole affinity. It is therefore understandable that Teflon electrets are most stable when they are charged negatively (cf. Fig. 10-69).

10:2.6b Experimental Results on Corona-Charged and Electron-Bombarded Foils

We first studied corona-charged PET-c. We used the charging procedure described by Creswell and Perlman (CP 71), with a razor blade mounted 2 mm above a rotating one-sided metallized sample. The charging voltage was - 6 kV and the charging time was 2-3 sec. After the charging, which was carried out in the ambient air, another electrode was evaporated onto the sample. This was done rapidly to minimize loss of charge. We performed the current TSD on a freshly prepared sample and after 24 hrs of short-circuiting.

These results are indicated in the lower curves of Fig. 10-32. The upper curves give results on PET film charged with a positive corona of 6 kV, in which only ions are deposited, while in a negative corona electrons are injected as well. We see that this negatively charged film releases a much larger current. Evidently, the electrons have penetrated deeper into the polymer than the much larger positive ions, which as a consequence are more quickly neutralized generating a lower current (compare Figs 5-8 and 11-6). We further recognize that the relatively short storage diminishes significantly the currents at low temperatures. This is probably due to a loss of charge from the primary traps, which are emptied most easily.

Although the mono-electrets contain only excess charges, the thermograms exhibit not only a ρ peak, but also an α peak. The temperatures of these peaks are the same as found for hetero-electrets of PET. This corroborates the fact that the onset of the macromolecular motions facilitate the escape of the charges from their traps, probably by lowering the energy barrier. From the deposited effective surface charge of about 100 nC/cm^2 , and from the released charges, which are 6.2 and 4.4 nC/cm^2 for the thermograms of the negative corona, and 1.9 and 1.4 nC/cm^2 for those of the positive corona, we calculated by means of Eq.5.35 a relative penetration depth of 0.10 and 0.03 respectively. The former value is twice as large as that determined by Creswell et al., who used a capacitive method. They also recorded more structured thermograms composed of four peaks, viz. at 60°, 83°, 104° and 118 °C of which the first and third peak have not been found by us. However, their experimental conditions were slightly different; they charged at a distance of 0.5 mm for 1 min, and used silver-painted electrodes and perhaps another type of Mylar. Moreover, they only studied the negative corona.

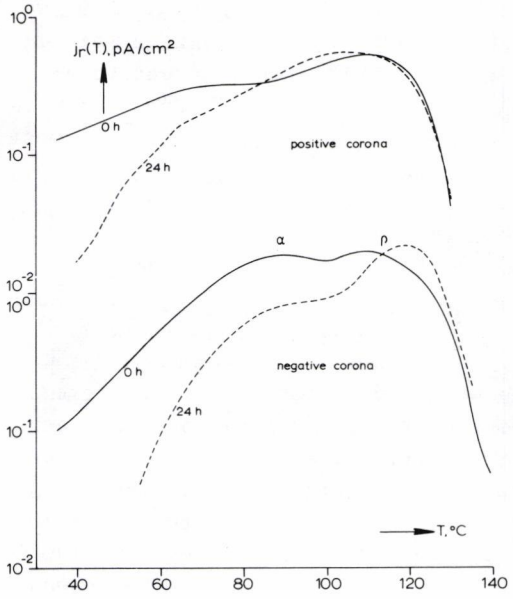


FIG.10-32 Current thermograms of positive and negative corona-charged PET-c films. The recordings were made just after the charging, and 24 hrs later. Before TSD the samples were metallized.

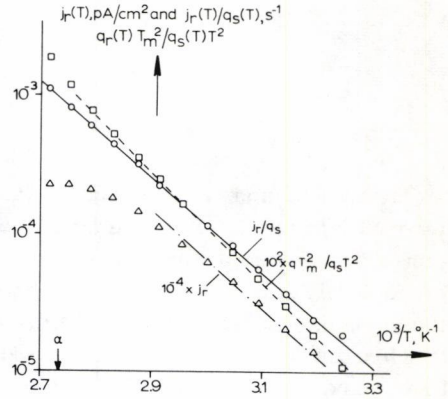


FIG.10-33 Calculation of the activation energy of the α peak of corona-charged PET-c (lower curve for 0 hrs, of Fig. 10-32). The initial rise and BFG plots give an activation energy of 0.7 eV, and the charge-ratio plot gives 0.8 eV.

Creswell et al. attributed thermograms such as these to charge release from traps in which retrapping is *slow*. On pp 121 and 122 we advocated the use of the charge-ratio plot and the BFG plot to differentiate between this trapping behaviour and the opposite behaviour involving fast retrapping. The calculated graphs of Fig. 10-33 for the α peak of the negative corona at 0 hrs substantiate Creswell's view. We see that the BFG plot is perfectly straight, whereas the charge-ratio plot begins to deviate already below the α point. From the initial rise and BFG plot we deduced an activation energy of 0.7 eV; similar plots for the α peak after 24 hrs storage yield 0.95 eV. Thus, on the average, we find 0.87 eV, which agrees neatly with Creswell's value of 0.85 eV.

Fig. 10-34 gives the results of Teflon-FEP charged by Townsend breakdown and by electron bombardment*. The homocharging by air breakdown was carried out on one-sided metallized samples at 180 °C, with a glass

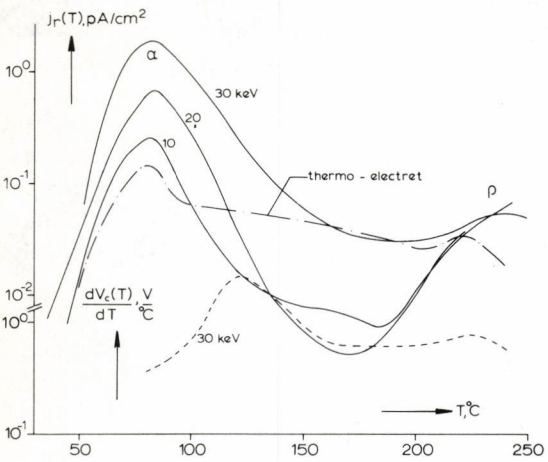


FIG. 10-34 Current thermograms of Teflon-FEP charged by electron bombardment (full lines) and by homocharging (dotted and dashed lines). The bombardment was done at three energies, and the homocharging was achieved at 180° - 1 kV/25 μm - 5 min. On the nonmetallized side of samples electrodes of 47 mm were evaporated before TSD. The derivative of a TSD charge thermogram, $dV_c(T)/dT$, of a bombarded foil is also shown. Its first peak is shifted to a much higher temperature.

cloth insert and a negative voltage of - 1.5 kV for 5 min. As for the homo-electrets of PET, we again observed the α and ρ peaks. The thermogram of the homopolar thermo-electret (dotted-dashed line) therefore looks similar to that of the hetero-electret (Fig. 10-25), although the ρ peak now appears at a higher temperature. However, the position of this peak is not well-defined. We have also found it, e.g. at 190°C. This peak might be sensitive to the crystalline structure. The released charge amounted to about 10 % of the homopolar surface charge initially present. According to Eq. 5.35 this implies a penetration depth of $r_o/l = 0.2$. This value is higher than that found for PET which was, however, charged at room temperature for a much shorter time.

*Thanks are due to Ir W.H. Iding (N.V. Philips' Gloeilampenfabrieken, Dept. ELA, Breda), and to Dr Ir L.A. Fontijn (Institute of Applied Physics TNO-TH, Delft), for carrying out the bombarding experiments.

We see that the three current thermograms obtained after electron-bombardment for one-sided metallized FEP are similar to that of the thermo-electret. The occurrence of two current peaks for one type of carrier indicates that this polymer contains electron traps of at least two different depths. Again, the thermal release of the injected electrons from these traps is strongly related to the molecular motion of the host polymer. The α peak, for instance, occurs at 81 °C, which is close to the T_g point. As before the location of the 2nd peak is ill-defined; in another series of experiments with injection into two-sided metallized FEP, we observed it at 188 °C (cf. Fig. 10-35).

For increasing injection energy, E_i, the first current peak is seen to rise, owing to the deeper penetration of high-energy electrons. This matter has been discussed on p. 110, where we deduced from our thermograms that $r_o \propto E_i^{1.8}$, whereas according to the theoretical calculations of Berger et al. (BS 64) the exponent should be 1.75.

Anticipating the results of charge TSD in Sect. 10:8, we have also inserted the derivative of a TSD charge thermogram of one of the bombarded foils (dashed line). As has been pointed out in Sect. 8:2.2, its first peak is shifted to a much higher temperature than that of the current thermogram, because the electrons have to travel a much larger distance in charge TSD to become neutralized. As a result this maximum does *not* occur at the glass-rubber transition, but at 122 °C. The striking temperature difference favours in contrast to the outcome for PET, fast retrapping over slow, for which the difference would be much less. This contrasting behaviour of Teflon-FEP has been confirmed by comparing the charge ratio and BFG plot in Fig. 5-20. Nevertheless, the difference is larger than expected for a single trap (cf. Eqs 5.39 and 8.21, in which $A/kT_m \simeq 70$ and $r_o/l \simeq 0.25$). This implies that the α peak results from electrons being captured in a broad distribution of traps.

Later we have repeated the experiments on samples *metallized bilaterally before* the bombardment. The results, represented in Fig. 10-35, are more consistent as far as the ρ peak is concerned. This now appears

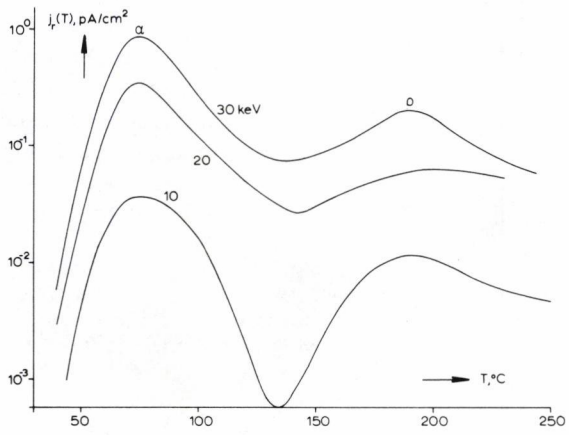


FIG.10-35 Current thermograms of *two*-sided metallized Teflon-FEP, bombarded with electrons of three different energies. The deposited charge was 20 nC/cm².

at 188 °C, not very far from the 183 °C found for hetero-electrets. The released currents are less than in the Fig. 10-34, because the evaporated metal layer intercepts part of the injected electrons. Table 10-7 gives the released charges and mean penetration depths calculated for the two experiments. In experiment I we bombarded unilaterally metallized samples, and in experiment II bilaterally metallized samples.

TABLE 10-7 Released Charges and Relative Penetration Depths for Electron Bombarding in Teflon-FEP

energy keV	q_r , nC/cm^2		r_o/l		R/l lit.values
	exp. I	exp. II	exp. I	exp. II	
10	0.5	0.2	0.06	0.03	0.05
20	1.3	1.3	0.14	0.14	0.18
30	4.4	2.6	0.37	0.26	0.35

Before TSD we measured on the electrets of experiment I an effective surface charge of 19 nC/cm^2. This surface charge was also used in calculating r_o/l for experiment II, even though the true charge trapped in the polymer is then overestimated. The relative penetration depths calculated, by means of Eq. 5.35, for experiment I therefore agree better with the values of the electron range R/l than do those of experiment II. (Note that for our foils l = 25 μm.)

The effect of the magnitude of the injected charge on the current thermogram is displayed in Fig. 10-36. The results conform to the theoretical thermogram of Fig. 5-11. After multiplying the curve for 12 nC/cm^2 by a factor of 2.5, the thermograms almost coincide. This is plausible, because the total area below the original thermograms for 12 and 30 nC/cm^2 should differ only by a factor of 2.5. We thus see that current release by SCL drift behaves *almost linearly*. Moreover, the peak temperatures of the higher charged mono-electret scarcely differ from

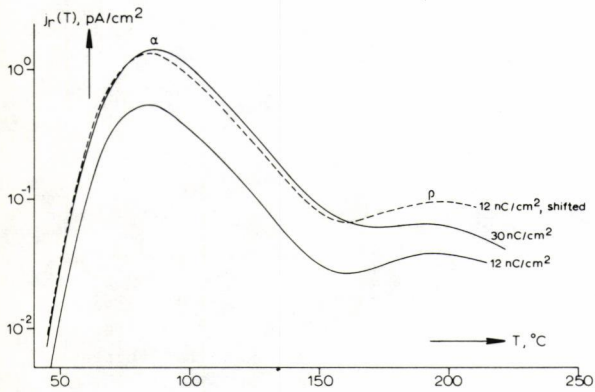


FIG.10-36 The effect of the height of the inital charge on the current TSD of electron-bombarded Teflon-FEP. The bombarding energy was 20 keV. For the shifted curve (dashed line) the current values have been multiplied by the ratio of the initial charges, i.e. 2.5.

those of the lower charged mono-electret; this is due to the large activation energies, which outweigh the effect of a larger drift velocity in the higher charge sample.

Finally, we recall the experimental results presented earlier in Figs 5-10 and 5-14, which give further support to the view that retrapping is fast in Teflon-FEP and involves traps with a distribution in energy levels.

10:3 Influence of Forming Conditions on Current TSD

In the previous section we have dealt with current thermograms that were typical of the dipolar and space charge relaxations of the polymer; this was achieved by charging the polymer completely. However, we have shown in Sect. 2:2 that, if the forming conditions are chosen *inaccurately*, the height and shape of the thermogram of a polymer that contains a distributed dipole relaxation, will not only depend on the molecular structure of that polymer, but also on the forming conditions. Similarly, we may infer from Sects 6:1, 5:5 and 5:6, that the current peaks resulting from Maxwell-Wagner charging and the space charge polarization will be affected by the forming conditions.

This section discusses the influence of the forming conditions on the current TSD of hetero-electrets; the effects on the charge TSD of homo-electrets will be given in Sect. 10:8. First, the effects of trivial parameters, such as temperature, field, time and electrode material will be illustrated. Next, the effects of nonconventional forming techniques will be described. For this purpose we have studied the special forming techniques that were briefly outlined on p. 191.

The dependence of electret properties on the temperature, field and time during the formation has been investigated for PMMA, PET and PC. The amorphous PMMA was machined in discs of 1 mm thick, the partially crystalline polyesters PET and PC were commercially available as foils. Only TSD relaxations *above* room temperature were investigated and, unless stated otherwise, evaporated electrodes of silver were used.

The results for PMMA are shown in Fig. 10-37. The figures show from the top downwards, the effects of temperature, field and time. As a reference we chose the conditions 130° - 100 kV/cm - 1.5 h. The forming temperature has the greatest effect. A temperature of 100 °C is too low to fill both the space charge peak and the high-temperature part of the dipolar α peak. For both peaks the field dependence between 10 to 100 kV/cm is almost linear. The lower curves illustrate that the 130 - 1/6 h combination is somewhat too critical for the space charge peak to emerge completely.

Later the temperature dependence of PMMA was investigated in more detail. The results then obtained were given in Fig. 1-11; they convinced us that the dipole polarization of PMMA is distributed, since at too low forming temperatures the α peak is not only weakened, but also

cut off on the high-temperature side. As a result the first current maximum no longer appears at the characteristic temperature T_g, but just beyond the forming temperature*. By contrast, the space charge

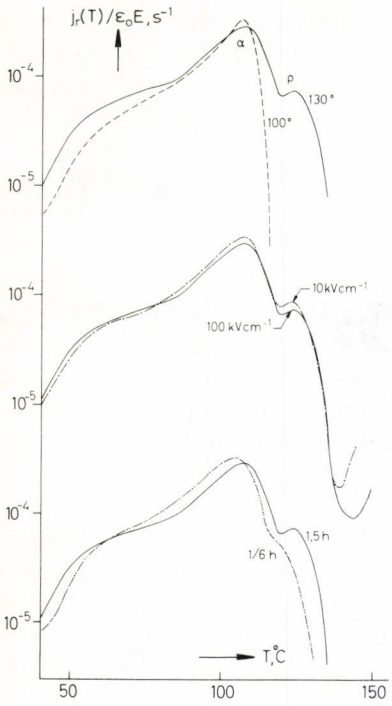


FIG.10-37 Effect of the forming conditions on the TSD α and ρ peaks of metallized PMMA electrets. As a reference we chose 130° - 100 kV/cm - 1.5 h. The heating rate was 0.45 °C/min.

or ρ peak is still there, though not prominent, because at low temperatures the ohmic conduction is too low to supply enough charge carriers. As has been shown in Sect. 2:2, the truncation of the dipolar α peak is due to incomplete filling of the slow subpolarizations of the distributed polarization.

As Figs 10-38 and 10-39 show, the behaviour of PET (Mylar-c of 25 μm, DuPont, USA) and PC (Makrofol-n of 40 μm, Bayer, Western Germany) is similar to that of PMMA. Again, the peaks are cut off at low forming temperatures because of incomplete filling of part of the subpolarizations. Note, however, that at too high forming temperatures, viz. 160°C for PET and 190 °C for PC, the ρ peak becomes smaller again. At these high temperatures chemical decomposition may have set in. This would

*Note that in conventional dielectric measurements, a distributed polarization is recognized by its width on the frequency scale, whereas in TSD it is the dependence on the forming conditions which enables one to distinguish between a distributed and a nondistributed polarization. For the latter, namely,the shape of the current thermogram is *not* deformed by an incomplete formation, the current is merely lowered by a constant factor over the whole temperature range.

lead to a higher ohmic conduction, so that a greater part of the stored space charges are dissipated unnoticed. Another cause could be that the Maxwell-Wagner charging has been lowered by changes in the crystalline structure. We have noted such changes from microscopical studies using

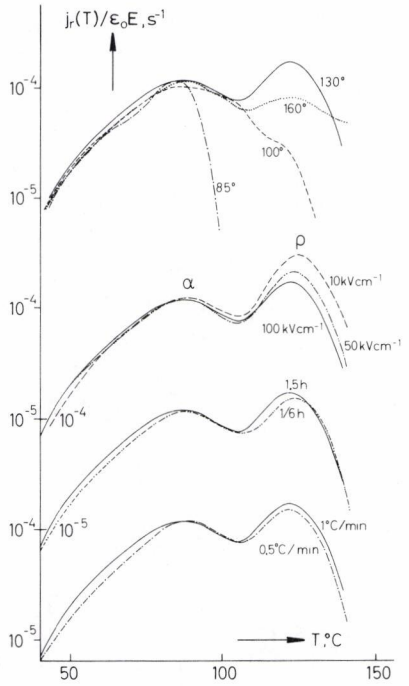


FIG.10-38 The same as in Fig. 10-37, but now for hetero-electrets of PET-c foil. As a reference we chose 130° -100 kV/cm - 1.5 h - 1 °C/min; the heating rate was 0.5 °C/min.

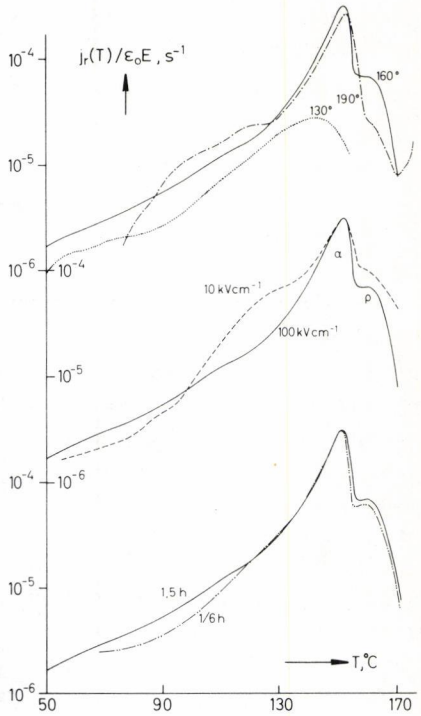


FIG.10-39 The same as in Figs 10-37 and 10-38, but now for hetero-electrets of PC-n foil. As a reference we chose 160° - 100 kV/cm - 1.5 h; the heating rate was 0.5 °C/min.

polarized light. It is also probable that the thickness of the space charge layers near the electrodes has been decreased owing to the higher mobility of the carriers; this also lowers the external current release, cf. Fig. 5-6. Examination of the field dependence shows that the ρ peaks of both foils behave slightly nonlinearly, being the lower the higher the forming field. Conversely, the thermograms show *no* variations with forming time and cooling rate in the ranges investigated. In the thermograms of PC we observe some irregularities below the α peak as discussed on p. 224; these may arise from the obscure intermediate relaxation of this polymer.

More quantitative data on the field dependence are given in Table 10-8. The currents and charges are on the average lowered by a factor of 0.65 for a tenfold increase in field strength. This decrease is prob-

ably to be attributed to a decrease in the thickness of the charge layers, for the higher field will sweep the carriers nearer to the electrodes, and this will lower the current release by SCL drift. The current release by diffusion would be lowered in a similar way, though, according to the simplified theory of Sect. 5:5.4, this drop should be larger. Hence, diffusion is of less importance, probably because the electrodes are open.

TABLE 10-8 Field-Dependence of the ρ Peaks of PET-c and PC-n

polymer	10 kV/cm		100 kV/cm	
	$j_m/\varepsilon_o E$, s^{-1}	$\Delta q_r/\varepsilon_o E$	$j_m/\varepsilon_o E$, s^{-1}	$\Delta q_r/\varepsilon_o E$
PET-c	3.1 E-4	0.82	1.8 E-4	0.48
PC-n	1 E-4	0.06	0.7 E-4	0.04

We also varied the thickness of the PET-c film by a factor of 4, keeping the field strength *constant*. We see from Fig. 10-40 that the α peak remains almost the same, whereas for the thinner foil the ρ peak increases by a factor of 1.8. This illustrates once more that this peak arises from the motion of space charges, which is likely to depend on the thickness of the sample.For the thinner foil, the reduced charge-layer thickness r_o/l will be larger, and this has a marked effect on the current release (cf. Fig. 5-6). By contrast, a volume polarization does not depend on the sample thickness; this is consistent with the constancy of the α peak, which is mainly due to dipole reorientation. Note that for the thinner sample the ρ peak also shifts to a lower temperature, because the excess charges have to move a shorter distance to become neutralized at the electrodes.

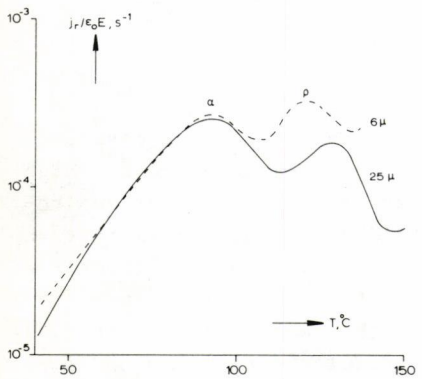


FIG.10-40 Current thermograms of hetero-charged PET-c for two film thicknesses. The forming conditions were: 140°-100 kV/cm - 1.5 h.

For PMMA we varied the electrode material; we tried three metals, viz. silver, gold and aluminium, which were evaporated onto three different samples. As shown in Fig. 10-41 the choice of the metal somewhat modifies the space charge peak, probably because the various metal-poly-

mer interfaces possess different charge exchange rates and so alter the space charge storage, and also the current release by diffusion. When aluminium is used the lowest space charge peak is found; the difference between silver and gold is less marked. As before, the α peak remains perfectly the same.

The effect of absorbed water on the α and ρ peak of PMMA was also examined (see Fig. 10-42). After absorption of an amount of water up to about 0.7 wt % in a humid atmosphere prior to formation, the peaks are changed. In particular, the space charge peak is enlarged, because the water raises the number of charge carriers that can be frozen-in. Other impurities also increase the space-charge peak perceptibly. (For this reason we abandoned, whenever possible, the use of painted electrodes, since most conductive paints contain ethyl acetate as a solvent.) Thermal degradation of the polymer from annealing at too *high* temperatures also causes deviations of the ρ peak.

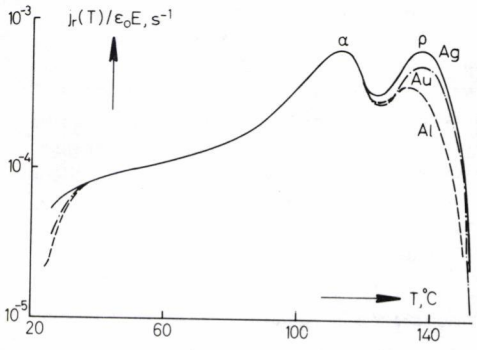


FIG. 10-41 Effect of three electrode materials on the current thermograms of metallized PMMA hetero-electrets, formed at 140° - 100 kV/cm - 1.5 h.

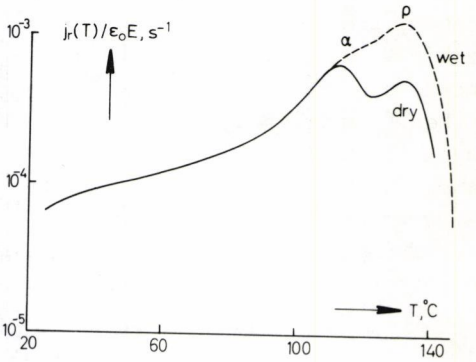


FIG. 10-42 Influence of adsorbed water on the current thermogram of PMMA. Before the formation at 130° - 40 kV/cm - 1.5 h, the "wet" sample was held at 70 °C and 100 % relative humidity for 16 hrs.

10:3.1 Thermograms of Electrets Formed by Special Techniques

In Fig. 10-43 we have compiled the TSD results of different PMMA electrets formed by special techniques*. We discussed these methods briefly on p. 191; they are described more fully in (Tu 68). Polymerization in an electric field was carried out by heating a viscous prepolymer containing 82 wt % of monomer for 14 hrs at 45 °C in a special electrode system under a high field of 12 kV/cm. Thereafter, the temperature was raised to 110 °C to complete the polymerization, after 4 hours the sample was cooled and the field switched off. Strikingly, the resulting electret gives a thermogram with an α peak located at a 5 °C higher tem-

*In this case the electrets could not be vapour-coated in advance, so to study their TSD we had to coat them with a fast-drying silver paint.

perature than usual. This is probably due to changes in inter- and intramolecular interactions resulting in a higher tacticity due to a better alignment of the dipoles in the liquid state. Moreover, low molecular impurities, which work as a plasticizer, might have been effectively removed by the electrophoresis that takes place during the formation.

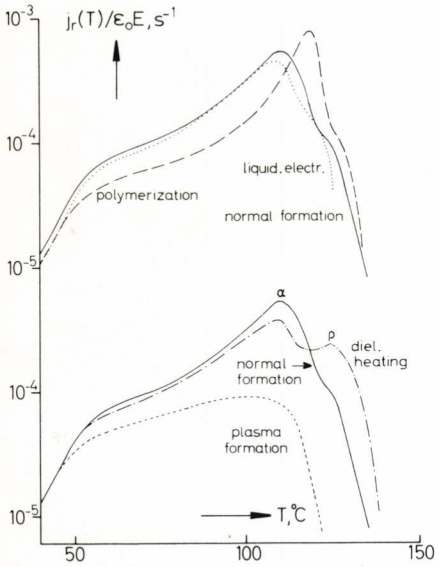


FIG.10-43 Current thermogram at 0.5 C/min of PMMA electrets, formed by different techniques. In most thermograms the α and ρ peaks appear, although the latter often are not very pronounced. The forming conditions were for the normal electret and the liquid electrodes: 130° - 28 kV/cm - 1.5 h, for the polymerization 45°/110° - 12 kV/cm - 14/4 h, for the dielectric heating 130° - 40 kV/cm - 1/6 h, and the plasma formation 130° - 50 kV/cm - 1/6 h.

Use of liquid metal electrodes (Cerrolow 117) gives no significant change in the thermograms, which is not surprising. Similarly, the formation with dielectric heating gives no distinct changes; the space charge peak is more pronounced, but this may be due to differences in the specimens. In this formation, the polymer is exposed to an alternating field at radiofrequency (30 MHz) of about 2.6 kV/cm which is superimposed on the high d.c. forming field of 40 kV/cm. Apart from the fact that the a.c. field will heat the sample dielectrically to a temperature above that of the ambient air*, Polovikov (Po 59) suggests that it will increase the charging, but obviously this does not occur. Theoretically it is hard to understand why a small superimposed high frequency field should increase significantly either the orientation of dipoles or the space charge accumulation. The main effect of this field would be to orient *part* of the *fast* reacting charge species parallel or antiparallel to the static forming field. However, it must be realized that only the *slow* reacting species are relevant to the electret effect. Polovi-

*In the thermogram, the actual temperature of the sample was given, so the forming temperature was corrected for the dielectric heating by measuring the temperature inside a dummy sample.

kov's conclusion that such an additional a.c. field would improve charge stability at room temperature could not be confirmed either. (It should be mentioned that Polovikov did not actually apply the a.c.field and the d.c. field simultaneously. In fact, he first applied the a.c. field and then the d.c. field. This makes his conclusion even more doubtful.)

By contrast, the plasma formation, in which the homocharging is optimalized by using two "plasma electrodes" gives a much *lower* current than the other formations. At the high forming temperature used, the injected homocharges will penetrate deep into the sample, thus compensating or even overcompensating the internal heteropolar space charges. Clearly, a net homopolar space charge will generate a current opposite to that of the reorienting dipoles. This homocurrent, however, will be rather weak, because the injected homocharges will readily recombine with the nearby heteropolar space charges of opposite polarity. As a result the TSD current is mainly generated by dipole reorientations. The reduced charge released, which amounts to 0.6, is therefore only slightly lower than the value of $\varepsilon_s - \varepsilon_\infty = 0.8$, found from dielectric measurements.

Summarizing: The thermograms mainly reflect polymeric properties; they are to a large extent independent of the charging process, provided that the forming temperature is chosen above T_g. This insensitivity applies particularly to the α peak, whereas the ρ peak by its very nature is more sensitive to changes in the forming conditions and to the presence of impurities. The special forming processes explored yielded neither a higher, nor a more stable heterocharge than the well-established thermal method already applied by the discoverer of electrets, Eguchi. This simple method still works satisfactorily, and is therefore to be preferred for forming hetero-electrets.

10:4 Influence of Storage Conditions on Current TSD

Fig. 10-44 shows the influence of a storage of two months in ambient air on the current release of metallized PET hetero-electrets. We see that the α peak has mainly been diminished in the low temperature range; this is caused by the reorientation of the faster reacting dipoles as has been discussed on pp 46 and 52. The ρ or space charge peak as a whole has become smaller. The 2nd and 3rd row in Table 10-9 show that the charge released by this peak is four times less than before the storage. During the storage the total charge has decayed by about 45 %. This is exactly the percentage we have found from charge decay measurements on one-sided metallized PET foil electrets (compare Fig. 10-65). The two measurements are thus consistent.

Interestingly, the current measurements reveal that the charge decay is mainly due to a neutralization of the space charges and *not* to the reorientation of dipoles. This contradicts expectation, since as a

function of *temperature* the dipole polarization is less stable. An explanation for this controversy may be that the number of space charges stored in an electret is about 3000 times less than the number of dipoles. Consequently, the loss of a few space charges is more disastrous than the loss of thousands of dipoles. Moreover, we must realize that although at high temperatures the relaxation time of ohmic conduction is greater, this need not be so at room temperature. Actually, for the reorientation of the dipoles, segments of the main chains have to move, and it is generally accepted that these are immobile at room temperature. On the other hand, we see from Figs 2-2 to 2-4 that the ohmic conduction, though it is low, is still there at room temperature.

TABLE 10-9 Reduced Released Charge by α and ρ Peak of PET-c after a Storage in Air and in Vapours

storage	α peak	ρ peak	total charge
air, 1 d, shorted	0.58	0.47	1.05
air, 60 d, nonshorted	0.49	0.14	0.63
air, 60 d, shorted	0.44	0.12	0.56
water vapour, 60 d, shorted	0.37	0.09	0.46
benzene vapour, 60 d, shorted	0.49	0.12	0.61

As outlined in Chap. 5, the space charges are not only destroyed by ohmic conduction, but they may also disappear by their motion towards the electrodes. These processes seem to operate simultaneously, because the space charge peaks for shorted and nonshorted electrodes are slightly different. For the latter, a return voltage is built up which slows down the space charge motion by SCL drift, so that the current decreases less. At low temperatures we similarly find that the α peak decreases less for nonshorted electrodes. This is plausible, because the return voltage induces a new dipole orientation of the same sign as the decaying one*, thus virtually stabilizing the dipole decay.

Shorted, metallized, heterocharged PET electrets have also been stored for two months in saturated water and benzene vapour at room temperature. The TSD results which were obtained after thorough drying of the specimens are given in Fig. 10-45. The values for the dummy sample were taken from the corresponding curve of the previous figure.

*Putting $\beta_g = 0$ and $g \to \infty$ in Eqs 7.40 and 7.41, we readily verify that, in a nonconducting dielectric with nonshorted electrodes, a single Debye polarization decays according to

$$(2 - \varepsilon_s/\varepsilon_\infty)P(t) = P_0 \exp\{-(2 - \varepsilon_s/\varepsilon_\infty)\alpha t\} + (1 - \varepsilon_s/\varepsilon_\infty)1_0$$

Apparently, the polarization does *not* drop eventually to zero, but it reaches a stable value of $P(\infty) = (1 - \varepsilon_s/\varepsilon_\infty)P_0$. This is quite different from the decay in shorted electrodes, for which $P(t) = P_0 \exp(-\alpha t)$ and $P(\infty) = 0$.

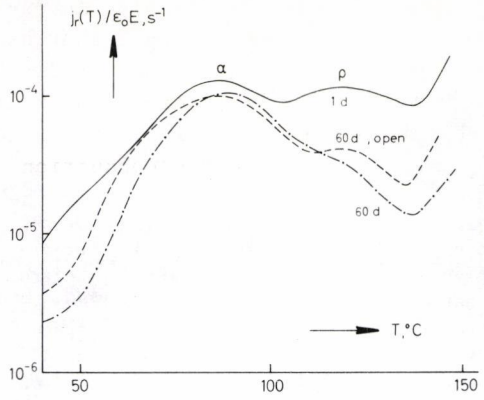


FIG.10-44 Effect of storage time on the current thermograms of heterocharged PET-c film. A prolonged storage lowers the ρ peak in particular. The electrets were formed at 140° - 100 kV/cm - 1.5 h, and the TSD was carried out at 0.45 °C/min.

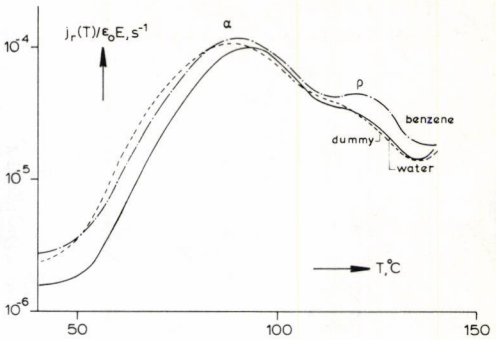


FIG.10-45 Changes in the current thermogram of heterocharged PET film by a two-months storage in saturated vapour of benzene and water. The dummy electret was stored in ambient air. The electrets were formed at 140° - 100 kV/cm - 1.5 h, and the TSD was carried out at 0.45 °C/min.

All thermograms are much the same, although the curve for the water vapour lies somewhat lower. At first sight one would have expected larger differences, because the adsorbed substances are likely to act as plasticizer in the amorphous phase of the polymer, where they will increase both the reorientation of dipoles and the ohmic conductivity. It must be borne in mind, however, that the dummy sample has likewise adsorbed water from the atmosphere during its storage. This adsorption is only half that at 100 % RH, which amounts to about 0.5 %. The quantity of adsorbed benzene will be of the same magnitude. Nevertheless, the benzene is seen to decrease the electret charge somewhat less than water; this is also apparent from Table 10-9 Our results are less dramatic than those reported by Perlman and Creswell (PC 71), who studied the influence of water on *mono-electrets* of corona charged PET. (These mono-electrets are near-surface charged and do *not* contain dipoles.) They found that such electrets release only a fraction of their original current after 10 days' exposure to 100 % RH at 50 °C.

In view of the possible application of the current TSD of electrets in radiation dosimetry, Ong of our laboratory (OV 68) has studied the effect of γ rays of 0.2 Mrad and 1.6 Mrad on heterocharged PET-c film electrets. The electrets were irradiated by a strong Co^{60} source emitting 0.1 Mrad/h. His results are shown in Fig. 10-46. Once again it is mainly the space charge peak that is affected, although at a high irradiation the α peak also becomes smaller. Both effects are attributed to radiation damage, which causes a temporary increase in ohmic conduction, by which most of the stored space charges are dissipated.

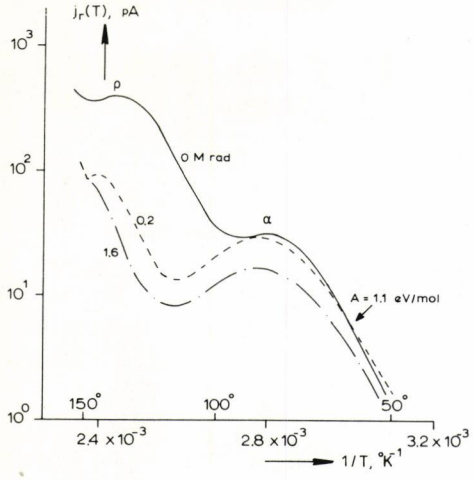


FIG. 10-46 Effect of a strong γ irradiation on the TSD α and ρ peaks of a heterocharged PET-c capacitor of 10 nF. The ρ peak is most affected, because the space charges are dissipated by the increased ohmic conduction resulting from radiation damage. The capacitor had an area of 45 cm^2 and was charged at 145° - 95 V/12 μm - 1 h; the heating rate was 0.4 °C/min.

10:5 Current TSD of Polymers that Contain Additives

We have studied the increase in the heterocharge of PMMA upon adding highly polar materials such as TiO_2 and SnO_2. These oxides have dielectric constants of 80 and 30, respectively. We added 1 wt % TiO_2 and 10 wt % SnO_2. Unfortunately, they could not be dispersed in the polymers without using a plasticizer, for which we took dibutylphthalate (DBP); this has a dielectric constant of 6.4. The DBP was added in weight percentages of 7 to 8 %. Nevertheless, it occupies more volume than 10 wt % SnO_2, because of its low specific gravity, which is 1.04 for DBP, 6.95 for SnO_2, 4.26 for TiO_2 and 1.18 for PMMA.

Fig. 10-47 shows the TSD current results. Since the plasticizer facilitates the segmental motion of the main chain, the α and ρ peaks are shifted to lower temperatures. At the same time, the peaks become much higher than for pure PMMA, because the plasticizer and the dopes are highly polar and also *semiconductive*. The latter property is exemplified in Fig. 2-3, where we see that the resistivity of doped PMMA is an order of magnitude less than that of pure PMMA. The resistivity of PMMA with 10 % SnO_2 being the lower, it will accumulate more space charges during the formation. As a result, this mixture releases a higher TSD current than PMMA doped with 1 % TiO_2, especially the ρ peak is larger. The difference between the two α peaks is less pronounced, because to these peaks the dipoles still contribute to a large extent. But although we see that the SnO_2 mixture, which contains more polar material, exhibits a higher α peak, the role of the permittivity of the dopes is not clear. For this we should have performed additional experiments on PMMA with the same volume fraction of SnO_2 and TiO_2. We finally observe that the two α peaks do not occur at the same temperature, for the large amount of SnO_2 lessens the temperature shift due to

the plasticizer.

The figure also shows a thermogram of PMMA mixed with 1.7 wt % of anthracene. This has a dielectric constant of 3.2 and a specific gravity of 1.25. The addition of anthracene produces an enormous charge; the current is magnified by a factor of no less than twenty. Moreover, the α and ρ peaks degenerate into one peak. It is known that anthracene is an organic semiconductor, in which the majority of charge carriers are holes and even at this low concentration it raises the conductivity of the polymer considerably (see Fig. 2-3). The carriers supplied by the anthracene are likely to be trapped in the polymer matrix during electret formation, giving rise to a marked space charge polarization.

Fig. 10-48 gives the dielectric spectra analogous to the TSD spectra of Fig. 10-47. Although we are mainly interested in the α peak, the β peak has also been included. The small increase of this pure dipole peak by the additives are in accordance with existing theories on heterogeneous mixtures (Be 67, Bö 52, Lo 65). In both spectra the α peak of PMMA containing SnO_2 increases and shift in a similar way, whereas

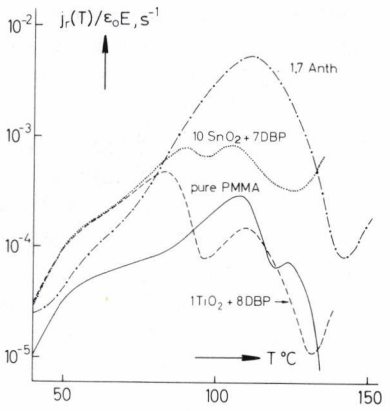


FIG.10-47 Effect of organic and inorganic additives on the TSD α and ρ peaks of PMMA hetero-electrets. Anthracene, in particular, increases the released current considerably. The forming conditions were PMMA + Anth. 140° - 30 kV/cm - 1.5 h, PMMA + SnO_2 140° - 23 kV/cm - 1.5 h and PMMA + TiO_2 140° - 16 kV/cm - 1.5 h; the heating rate was 0.45 °C/min.

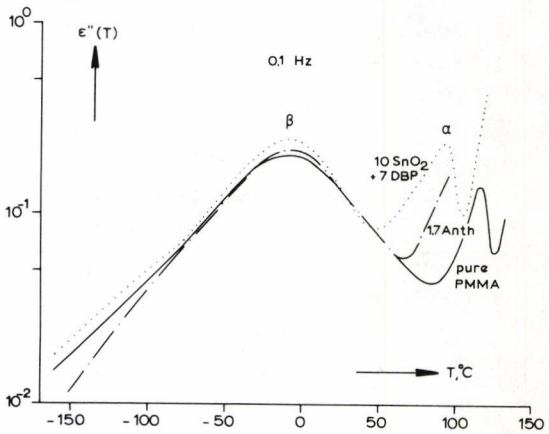


FIG.10-48 Dielectrical relaxation diagram of PMMA containing additives. It includes the low-temperature region, so that the β and α peaks are shown, although for anthracene the α peak is hidden by the conduction losses.

for PMMA containing anthracene the dielectric α dispersion is overshadowed by the large conduction losses. Such a behaviour is consistent with the large TSD peak of this mixture.

The large TSD currents found cannot be explained by the simple two-layer model for heterogeneous systems presented in Chap. 6. This can

easily be shown for the mixture of PMMA with SnO_2. Visualizing this mixture as one layer of SnO_2 and DBP and another of PMMA we expect the applied voltage to fall across the more insulating PMMA layer. From the weight percentages and the specified gravities of the constituents we find the effective thickness of this layer to be 9 % less than that of the sample. This would imply a relative current increase of about 11 % with respect to pure PMMA.

Such an increase is much like the one we have found for the dielectric β peak of the SnO_2 mixture. By contrast, we observed much higher increase factors for the TSD α and ρ peaks, viz. 2.6 and 11.3. Similarly, the stored charges are much higher than expected; this can be seen from Table 10-10. We believe that the failure of the theory to describe these TSD peaks is not primarily due to the simplicity of the MW model used, but rather to the fact that the theory ignores space-charge storage*. If this had been taken into account, the larger storage capacity of doped PMMA would be less surprising. For anthracene, e.g., the doping concentration is about 6×10^{19} anthracene molecules/cm^3, which is much larger than the number of charges needed to produce the observed effects. From the arguments given on p. 5 we readily verify that only one charge has to be supplied by 5×10^5 anthracene molecules. Doping therefore seems an interesting tool to improve the electret effect of polymers.

TABLE 10-10 Effect of Additives on the Reduced Heterocharge of PMMA

polymer	α peak	ρ peak	total charge
PMMA	1.1	0.3	1.4
100 PMMA + 1 TiO_2 + 8 DBP	1.7	0.6	2.3
100 PMMA + 10 SnO_2 + 7 DBP	2.5	2.5	5.0
100 PMMA + 1.7 Anthracene			20

10:6 Sectioning of Electrets to Reveal Internal Charge Distributions

We mentioned several times that the high-temperature TSD ρ peak of hetero-electrets originates from the motion of space charges. In homogeneous polymers, space charges will pile up in the vicinity of the electrodes. Since we assume the charge carriers to be intrinsic, negative charges will be drawn to the positive electrode and the positive charges to the negative electrode. We thus neglect emission of charges from the electrodes, which is justified by the results of Antenen who in carnauba wax electrets invariably found heterocharges rather than homocharges. To study the spatial distribution of the internal charge

*In view of our findings, the practice of neglecting space charges in describing the dielectric a.c. behaviour of heterogeneous systems also seems questionable.

we used the sectioning technique elaborated by Gross* and co-workers (GM 62) in their study of carnauba wax electrets.

The method consists in first taking a TSD thermogram of the unsectioned sample. Next, the sample is recharged and then perpendicular to its axis, sectioned into three equal parts. This was done with a thin circular saw (0.5 mm). Care was taken not to heat the sample, by choosing a low sawing speed and air cooling. After sectioning, gold electrodes were applied by fast evaporation in vacuum. During the formation the upper and lower section to which we refer below, faced the negative and positive forming electrodes respectively.

First we checked, on uncharged samples, whether tribo-electric charging generated during sawing, would release spurious currents. No significant currents were found; obviously, any superficial applied frictional charge had either been neutralized during metallization or had a too low penetration to release a perceptible current. We studied the TSD of two polymers: PMMA and ChPEth (Penton 9215, Hercules Powder Cy, USA), the first of which is amorphous, while the second is partially crystalline.

Results of the sections of a PMMA electret are shown in Fig. 10-49.

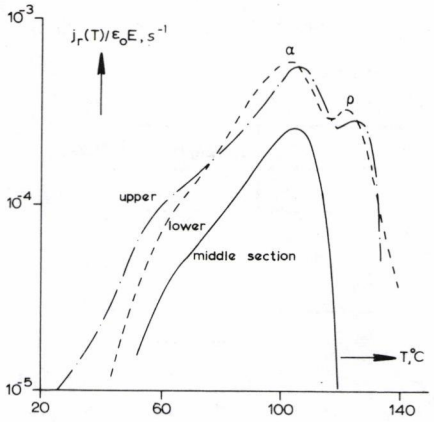


FIG.10-49 Current thermograms of the three sections of a PMMA electret, showing that the outer sections are charged higher than the middle section. The electret was formed at 140°-20 kV/cm - 1.5 h; the original thickness was 4.8 mm and the heating rate 0.5 °C/min.

Remarkably, the middle section releases much less current than do the top and bottom sections. Its thermogram does not even contain the ρ peak. Apparently, this section contains fewer space charges. The thermograms of the outer sections do not differ appreciably, which implies that the number and mobility of the positive and negative carriers stored in them, are almost equal. From the first row in Table 10-11 we see that, on the average, the outer sections release a charge 2.5 times larger than that of the middle section. Part of the reduced charge of these sections results from the ρ peak, which supplies 0.4 - 0.5. This value is about 3

*We are grateful to Professor Gross, who, in a personal communication, pointed out the potentialities of the section technique.

times lower than the charge of the ρ peak of an unsectioned PMMA electret (see Table 10-4). Whether this difference is significant is doubtful, in view of the limited reproducibility of the ρ peak. Even more interesting, therefore, is the fact that the ultimate charge released by the middle section is compatible with the dipolar relaxation strength of the α peak, which is 0.8. Apparently, it is in this section that we measure the true dipolar relaxation of the polymer, caused by the segmental motions of the main chains.

Similar results were obtained for the three sections of ChPEth (see Fig. 10-50); again the current of the middle section is about two times lower. The figure also shows the charge released by the sections, and moreover, the thermograms of the unimpaired electret have been included. Its thermograms approximate the average values over the three sections, and so these thermograms lie somewhat below those of the two outer sections. These trends are also apparent from Table 10-11, which gives the reduced charges of the sectioned and unsectioned ChPEth electret. The latter releases 10.8, whereas the average value over the sections is 11.8. We further note that the charges of the outer sections exceed the charge of the unsectioned electret by a factor of 1.4, and that of the middle section by 2.9.

TABLE 10-11 Reduced Charges Released by Sectioned Hetero-Electrets of PMMA and ChPEth

polymer	sections				unsectioned
	upper	middle	lower	mean value	electret
PMMA (pure)	2.3	1.0	2.7		
ChPEth	15.6	5.2	14.5	11.8	10.8
PMMA (impure)	19.1	0.25	30.1	18.5	35.5

The occurrence of a nonuniform internal charge distribution has far-reaching consequences; for it implies that *space charges* play a *significant* role in the current release of hetero-electrets. They determine not only the ρ peak, but to some extent also the α peak in the polymers investigated. Our findings are in agreement with the results of Antenen (An 56), who, by probe measurements, obtained clear indications of a space charge polarization in carnauba wax.

By contrast, Gross and de Moraes (GM 62) found, for carnauba wax electrets, virtually the same charge release for all sections.It should be mentioned, however, that they had stored their electrets up to *seven* weeks prior to TSD. We have shown in Fig. 10-44 that such a prolonged storage, reduces in particular the space charge storage. We therefore always used freshly prepared electrets. There may be still other reasons for the discrepancy. Gross et al. chose a high forming temperature near the melting point of the wax; this procedure gives thin space-

charge layers, which are unfavourable for releasing a high current. Moreover, they painted their electrets with a solution of "Aquadag", which may have neutralized part of the near-surface charges. Finally, our evaporated electrodes may have been partly blocking, whilst the painted electrodes of Gross may have been open, preventing any contribution of diffusion to the current release.

Before presenting a tentative explanation of our results, we shall first give data on another sectioned PMMA electret. In the thermograms shown in Fig. 10-51, we have included the thermogram of the unsectioned electret. The new data differ markedly from the data in Fig. 10-49, because we used PMMA from another batch, which contained about 4 % of monomer. Since the monomer promotes the ohmic conduction, it leads to a much higher space charge storage by supplying more charge carriers during the formation. As a result, the current of the outer sections is an order of magnitude larger than before, and concurrently, the difference with the current of the middle section has increased by two orders of

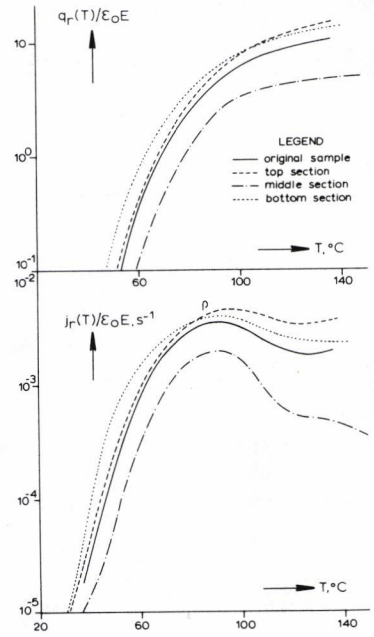


FIG.10-50 Released charge and current of the three sections of a ChPEth electret. As for PMMA in Fig. 10-49, the internal charge distribution is found to be nonuniform. For comparison, the thermogram of the unsectioned electret is also given. The electret was formed at 115°-14.5 kV/cm - 1.5 h and its thickness was 6.9 mm.

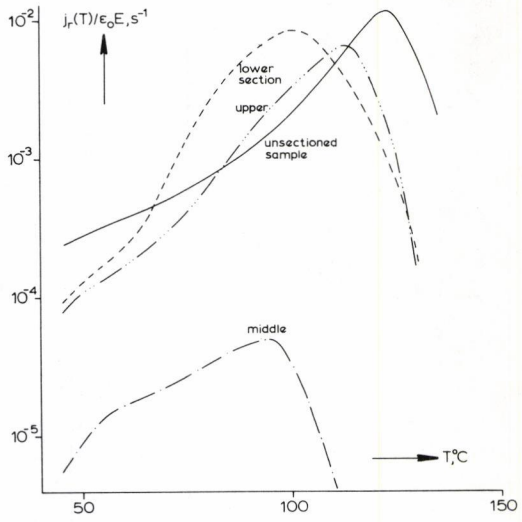


FIG.10-51 Current thermogram at 0.5 °C/min of an *impure* PMMA electret containing 4 % of monomer, plotted together with the thermograms of its three sections. The internal charge is less uniform than that of pure PMMA, cf. Fig. 10-49; only the thermogram of the middle section is very much the same as that of pure PMMA. The electret was formed at 140° - 21 kV/cm - 1.5 h and its thickness was 4.8 mm.

magnitude. We also note that for this new specimen the intense ρ peak conceals the α peak. The thermogram of the middle section is, however, much the same as that for pure PMMA. The values of the charges released by the various specimens are given in the last row of Table 10-11. The reduced charge of the middle section is remarkably low, being three times lower than the dipolar relaxation strength of the α peak. It is also surprising that the currents of the two outer sections are not similar, and that they are lower than the current of the unsectioned electret, and their peaks appear at a lower temperature.

Let us now try to account for our results. We shall first discuss the data on PMMA, in which no MW charging takes place. The space charge polarization stored in the electret will be divided over three sections, as illustrated in Fig. 10-52. The section adjacent to the negative forming electrode on the right, will bear a predominantly positive space charge, the middle section will be bipolarly charged and approximately neutral, and the section next to the positive forming electrode on the left, will carry a net negative space charge. In the figure we have al-

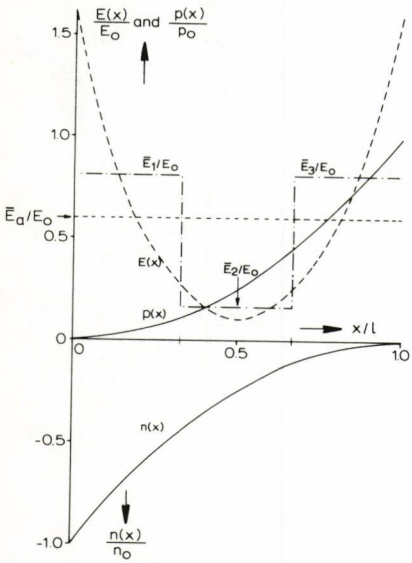


FIG.10-52 Spatial distribution of positive and negative excess charges in a hetero-electret just before the forming field E_a is switched off (schematic). Most excess charges are driven to the electrodes i.e. to the outer sections 1 and 3, where, as a consequence, the internal field is highest. Hence, the dipole polarization will also be highest in the outer sections. (Note that when the electret is shorted, the fields at the electrodes become equal to the field used for normalizing, E_o.)

so sketched the internal electric field at the end of the formation. This field is *nonuniform*, being highest in the sections near the electrodes, where the average field *exceeds* the applied field $E_a = V_a/l$. By contrast, the average field in the middle section is much *lower* than the applied field.

The large differences in the internal fields will result in unequal values for the average dipole polarizations. We have

$$\int_0^1 P_s(x,t)dx < \int_0^{1/3} P_s(x,t)dx \simeq \int_{2\,1/3}^{1} P_s(x,t)dx$$

and

$$\int_0^1 P_s(x,t)dx >> \int_{1/3}^{2\,1/3} P_s(x,t)dx$$

Apparently, the outer sections generate a higher dipole reorientation current than the original electret, the dipole current of which in turn exceeds that of the middle section. It is now clear why the charge of the middle section, when reduced to the applied field, may be lower than the dipolar relaxation strength, for we should actually have normalized this charge to $\bar{E}_2$.

The currents resulting from the motion of the charges themselves will also be different. As pointed out in Sect. 5:2.2 the SCL drift of the unipolar space charges in the outer sections will generate a current *opposite* to the dipole reorientation current, while the SCL drift of the relatively small bipolar space charge in the middle section wil slightly increase the dipole current. In the various sections, the SCI drift thus tends to weaken the differences between the dipole reorienta tion currents. The experimental results indicate that this happens only to some extent. The differences in the dipole current still dominate, and so the overall current of the middle section is far exceeded by those of the outer sections.

It is now also clear why the TSD current of the outer sections of the PMMA electret is lower than that of the unsectioned electret; for in the latter the space charges are bipolar and the dipole current is strengthened by the SCL drift, whereas in the outer sections the space charges are almost unipolar and the dipole current is attenuated. This attenuation manifests itself especially at high temperatures, and it is for this reason that in Fig. 10-51 the currents of the outer sections are displaced to the left of the peak for the unsectioned electret. The deviations between these outer currents probably arise from differences in the concentration and mobility of the negative and positive charge carriers.

If the electrodes are blocking or partly blocking, the motion of the space charges may also be initiated by diffusion. This process will intensify the dipole current in all cases. Simplifying the actual charge distribution to a uniform one, we have from Eq. 5.60, for the ultimate charge released by symmetrically and bipolarly charged samples:

$$q_r(\lambda)/q_o = (1 - r_o/1)$$

and

$$q_r(\lambda)/q_o = \tfrac{1}{2}(1 - r_o/1)$$

for unipolarly charged samples, where r_o is the thickness of the charge

layers and $q_o = p_o r_o = n_o r_o$. Apparently, the diffusion current is largest in bipolarly charged samples. If, for instance, $r_o/l = 0.1$, these equations predict for the outer sections a charge release of only $0.35\ q_o$, as compared to $0.9\ q_o$ for the original electret. These large differences would completely cancel the increase due to the nonuniform dipole reorientation. Thus, if diffusion were strong, the current of the outer sections would be considerably less than that of the unsectioned sample, and, moreover, there would be no explanation for a shift of their peaks to a lower temperature. Since these facts conflict with the observations, diffusion does not seem to be significant. However, we do believe that it is responsible for the small ρ peaks shown in Fig. 10-49 for pure PMMA.

After this discussion on homogeneous electrets, we can be short about the effects observed in the partially crystalline polymer ChPEth. In this heterogeneous polymer, the charging will mainly be a MW polarization at the crystal boundaries. Obviously, this polarization will be largest in the outer sections, which explains the appearence of large currents from these sections, and also the fact that the current from the central section is low. The outer currents were found to exceed the current from the unsectioned electret, which apparently is less intensified by SCL drift and by the diffusion of the space charges themselves. The reason for this may be that in this polymer the gross motion of space charges is hindered by the heterogeneous structure, so that the TSD currents recorded are largely MW discharge currents arising from the dissipation of the nonuniformly distributed interfacial charges.

We have just shown that the charge inside the electret is unequally distributed, and it would be interesting to know how far the space charge layers extend into the bulk of the polymer. This can be estimated from Table 10-12, which lists the released charge of (undried) PMMA

TABLE 10-12 Reduced Charge Released by Planed Hetero-Electrets of (Undried) PMMA

thickness, mm	$\Delta q_r/\varepsilon_o E$
2.6	15.2
2.6 - 2 × 0.2 †	1.2
2.2	13.6
2.2 - 2 × 0.1 †	8.2
2.0	11.1
2.0 - 2 × 0.25†	1.8
1.5	12.7

†Results labelled with a dagger refer to the planed electrets, from which the two outer layers were removed after the formation.

hetero-electrets, from which the outer layers have been removed by planing on a lathe. To avoid the use of different samples, we used the same sample over and over. In other words, we charged it, measured its TSD, recharged it, planed it, measured its TSD again, and so on. We see that the charges released by the three planed electrets is lower, in particular after the removal of 0.2 and 0.25 mm. After the removal of 0.1 mm the difference with the unplaned electret is less. This suggests that for this PMMA electret the charge layer thickness lies between 0.1 and 0.2 mm.

Fig. 10-53 shows some typical thermograms of these experiments on planed electrets. We notice that the current is lowered by more than a factor of 10 after planing, and that the sample regains most of its original current when it is recharged. Obviously, the planing removes most of the space charges, which are restored when the sample is recharged. As a consequence, the planed electret exhibits the pure dipolar α peak. In accordance with this, it has its current maximum at T_g, while it releases a charge that almost equals the dipolar relaxation strength, $\varepsilon_s - \varepsilon_\infty$.

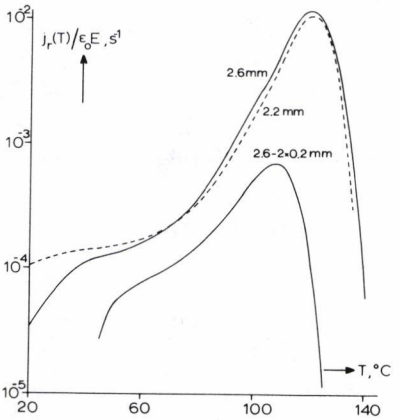


FIG.10-53 Current thermograms of a hetero-electret of undried PMMA before and after removing 0.2 mm from its plane surfaces. The planed electret gives a much lower current release and has its maximum at the proper α transition temperature. However, if the thinner sample is recharged, it gives a thermogram which almost coincides with that of the original sample. The electrets were formed at 140° - 38 kV/cm - 1 h.

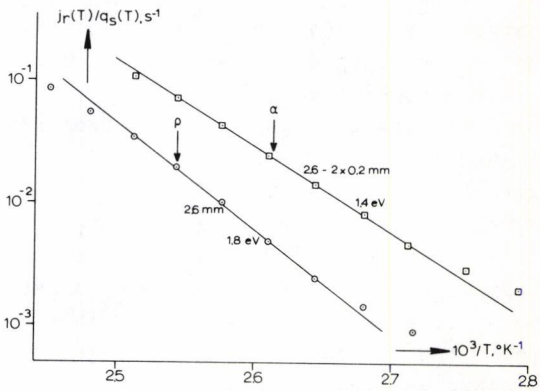


FIG.10-54 Two BFG plots of the current thermograms belonging to the planed and unplaned PMMA electret of Fig. 10-53. Interestingly, the latter has an activation energy exactly equal to that for ohmic conduction.

To improve the space charge accumulation, we deliberately used undried PMMA. As a result we find for the unplaned electret an intense ρ peak, which masks the dipolar α peak. Since the space charges stored previously took part in the ohmic conduction of the polymer, we may expect that the ρ peak will have a similar activation energy as the ohmic conductivity, which has a value of 1.9 eV. In agreement with this the BFG plots of Fig. 10-54 yield an activation energy of 1.8 eV for the ρ peak. (On p. 62 such a satisfactory agreement was also reported for the PMMA ρ peak cleaned by a two-stage TSD.) We further observe that the activation energy of the dipolar α peak of the unplaned electret is 1.4 eV, whereas from the G" shift in mechanical measurements, a value of 4.2 eV is qbtained. We discussed the reason for this discrepancy on pp 54 and 72; it results from the distribution of the dipole polarization. The width of the distribution m can readily be derived from Eq. 2.45; for a Fuoss-Kirkwood distribution m would be 0.3.

Fig. 10-55 illustrates the temperature dependence of the internal charge distribution of a ChPEth hetero-electret. At 75 °C, when ohmic conduction is low, fewer space charges are supplied and accumulated than at 115 °C, and as a result the current release of the upper and lower sections differ less. Because of incomplete filling of the inherent polarization available, the peaks at T_f = 75 °C are cut off so that they are located just beyond T_f. However, they are of the same height as the thermogram of the middle section at 115 °C. Obviously, for forming temperatures higher than 75 °C, it is mainly the space charge storage that increases, the uniform part of the polarization due to microscopic charge displacements remaining almost the same.

Further evidence of a nonuniform charge distribution in ChPEth hetero-electrets was also obtained from air-gap measurements (Fig. 10-56). Since *metallized* samples were used, which were initially *neutral*, a current reversal occurred in order to make the total current-time integral zero. First we obtain a heterocurrent due to the normal MW discharge, followed by an opposing peak which is mainly due to the ohmic dissipation of the image charges induced by the electret charges on the electrodes. (More details on this current reversal and on the origin of the current peaks have been given in Sect. 7:2.)

Again we find the middle section to be charged 2.5 times less than the outer sections. The results of the unsectioned sample, depolarized with an air gap suggest that this sample releases a higher current than the outer sections; this is not likely in view of Fig. 10-50. However, the difference is only an apparent one, because we have not corrected the thermograms for the induction loss, $1 + \varepsilon g/l$, caused by the air gap. If for ε we take the reasonable value of 8, the results become almost the same.

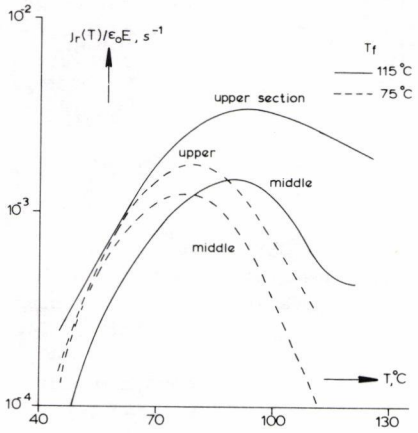


FIG.10-55 Effect of the forming temperature on the charge distribution within a ChPEth hetero-electret. At low forming temperatures fewer space charges are formed and the current release of the upper and middle sections differs less. The forming field and time were 14.5 kV/cm and 1.5 h, respectively, and the heating rate was 0.5 °C/min.

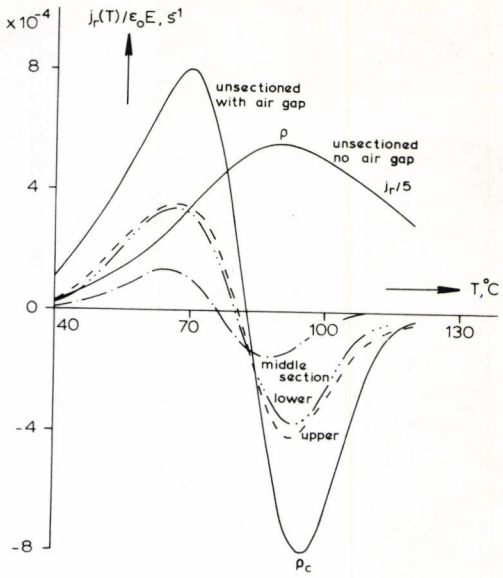


FIG.10-56 Air-gap current thermograms at 0.5 °C/min of the three sections of a ChPEth hetero-electret. Results for the unsectioned electret, depolarized with and without an air-gap, are also shown. The electret was formed at 115° - 14.5 kV/cm - 1.5 h, the air gap was 0.6 mm and the thickness of the unsectioned electret and the sections were 6.8 and 2.1 mm. Note that all samples were *bilaterally metallized*.

In order to find out whether the TSD peaks are related to the ohmic conduction of ChPEth, we compare in Fig. 10-57 the BFG plots for the ρ and ρ_c peaks of the unsectioned sample. Of the activation energies found, only that of the ρ_c peak comes close to the activation energy for the ohmic conductivity, which is 1.5 eV. This confirms that this peak is generated by the ohmic dissipation of the image charges. The ρ peak of the shorted electret, which probably arises from Maxwell-Wagner discharging, has only half this activation energy. This is somewhat surprising, because we have shown in Chap. 6 that ohmic conduction is the basis of MW discharging. However, our theory does not take into account the fact that the charges gathered at the grain boundaries may be trapped at different energy levels; this may be one reason for the broadening of the peak and the concomitant lowering of its apparent activation energy.

Our finding that *space charges* may play an *important* role in the TSD of heterocharged electrets will be checked in due course for other sectioned polymers. More experimental evidence seems to be needed, because in the current literature, space charges are considered to play only a minor role, whereas they clearly do not, in particular not in polymers

that contain impurities.

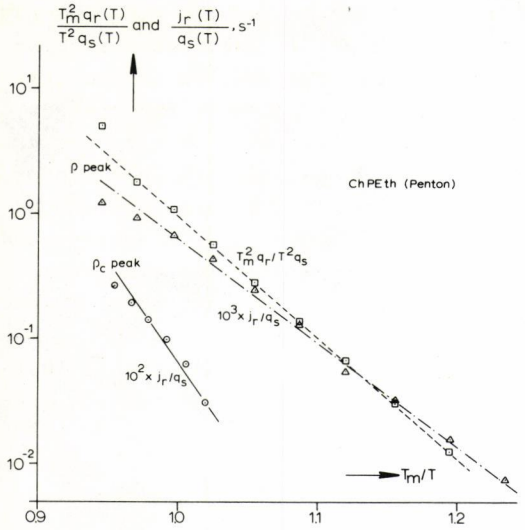


FIG.10-57 Calculation of the activation energies of the TSD ρ and ρ_c current peaks of two-sided metallized hetero-electrets of ChPEth. For the former we find A = 0.6 eV (BFG plot) and 0.7 eV (charge-ratio plot) and for the latter A = 1.2 eV.

10:7 Results of Current TSD with an Air Gap

The data that have been presented so far pertain to short-circuited electrets. When an air gap is introduced, e.g. adjacent to the upper live electrode, the electret itself is no longer shorted. Consequently, an appreciable electric field appears in the electret, which generates an ohmic conduction current that neutralizes the excess charges stored. Hence, this set-up reveals the *ohmic charge decay*, which cannot be observed in normal current TSD.

Some air-gap thermograms of partially crystalline ChPEth have just been described. They pertained to metallized hetero-electrets and, being neutral at the beginning of the TSD, they gave two opposed current peaks, and a total current-time integral of about zero. We also recall Figs 6-8 and 6-9, in which for PVC and 80 S co 20 AN, results are shown on the Maxwell-Wagner charging and discharging with an air gap. Then two current peaks were found, the temperatures of which almost coincided with those of the normal TSD α and ρ peaks of shorted metallized hetero-electrets. Moreover, we could prove that the 2nd MW peak arises from (dis)charging by ohmic conduction. We thus obtained clear evidence for our view that the formerly unknown ρ peak of shorted electrets is due to the motion of space charges, whereas the α peak is mainly due to dipole orientation.

Most of the air-gap thermograms in this section will be concerned with *bare* electrets carrying a net homocharge. They invariably give two opposed current peaks, and we shall show that they are again closely related to the α and ρ peaks found in normal current TSD of shorted hetero-electrets.

10:7.1 Air-Gap Thermograms of Nonmetallized Electrets

Most of the polymers, of which the heterocharge results were described in Sect. 10:2, were also depolarized with an air gap. These experiments were done at the beginning of this research, when we had no evaporation unit at our disposal; we then used bare polymers and charged these homopolarly with laid-on electrodes. At that time we made the desired air gaps by sticking Teflon spacers of 0.15 mm on the electrodes. Prior to their TSD, the electrets had been stored for more than one or two years in ambient air, during which period some of their hetero- and homocharge was lost. Apparently, this loss is low, for the electrets still generate an appreciable hetero- and homocurrent, as can be seen from Figs 10-58 and 10-59.

The curves constitute experimental proof of Gross's hypothesis that two *opposed charges* (viz. a hetero- and a homocharge) are created, when electrets are formed with contiguous electrodes. For all polymers we first find the heterocurrent, which only reverses to a homocurrent above their T_g's. (Note that PPO shows no current reversal, because it was mainly heterocharged.) This implies that the *homocharge* is more *stable* than the heterocharge; in other words, dipolar reorientations set in at a lower temperature than does homocharge dissipation by ohmic conduction. This seems to be a general feature of all kinds of electrets, apparently because the ohmic decay involves a gross motion of charges, whereas the dipole reorientation only involves rotational movements. It explains why homocharging is so interesting for electrets intended for practical applications.

Apart from these general trends the thermograms seem to be typical of the polymer in question. This becomes clear from comparison of the air-gap thermograms of the noncommercial polymer (Fig. 10-59) with those of the corresponding shorted hetero-electrets depolarized without an air gap (see Sect. 10:2). We then notice that the temperatures of the α and ρ peaks of the shorted hetero-electrets are about the same as those of the hetero- and homocurrent maxima of the homo-electrets. This means that in the air-gap technique the heteropeak also appears at about T_g. For PEMA and PC, for instance, the α peaks appear at 66° and 144 °C, whereas the glass transitions of these polymers are 65° and 149 °C. We thus find once more that polymers with a low T_g, such as PVB and PEMA, are rapidly discharged. Therefore, we cannot expect electrets made of these to be very stable at room temperature. Electrets made of MMA co S and MMA co cHMA seem to be much better in this respect; that this is so, in fact, was already illustrated in Table 10-5.

When in Figs 10-58 and 10-59 we consider the area below the hetero- and homocurrent, the latter area does not seem to prevail, notwithstanding the fact that the net charge of the electrets was homopolar. This unexpected loss of homocharge may be due to an instrumental error, for the homocurrent is probably lowered at high temperatures by changes in

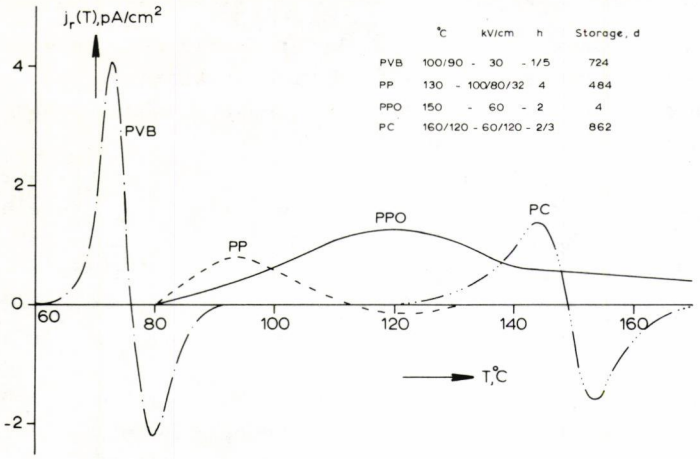


FIG.10-58 Current thermograms of non-metallized electrets of four commercial polymers, depolarized with *two* air gaps. Except PPO, they were all homo-electrets and therefore gave a current reversal. Note that the heterocharge is always released first, and that three of the electrets were stored for a long time.

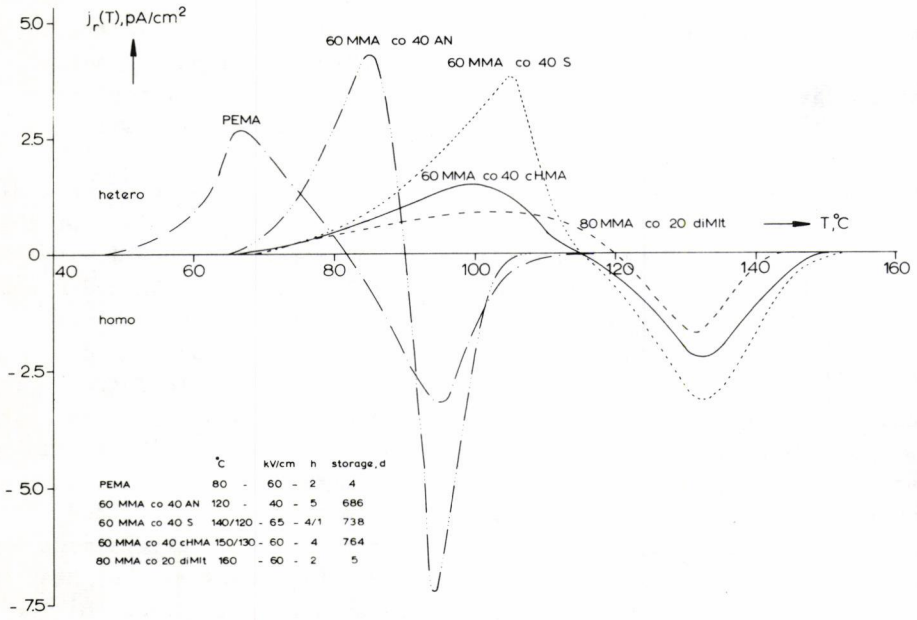


FIG.10-59 Current thermograms of non-metallized electrets of methacrylic homo- and copolymers, depolarized with *two* air gaps. For all polymers we get a current reversal. As in Fig. 10-58 most of the electrets had been stored for a long time.

the air gaps. In fact, in the twin air-gap system used it is likely that when the polymer softens, the sample will sag; moreover the Teflon stick-

ers will sink into it. Eventually, the electret may even touch the lower electrode*.

10:7.2 Air-Gap Thermograms of One-Sided Metallized Electrets

To eliminate the measuring errors resulting from the variations in the air-gap width, we changed to an assembly with a single air gap, in which we studied one-sided metallized electrets, with their metallized side on the lower electrode. Moreover, we abandoned the Teflon stickers and employed in our latest experiments the air-gap system briefly described on p. 191. In this way we obtained pronounced homopeaks, as can be seen in Figs 10-60 and 10-61.

Fig. 10-60 shows the air-gap thermograms of a homo-electret of PMMA, formed with a laid-on electrode of aluminium. The charge and current released are plotted as solid lines on the left and right of the figure.

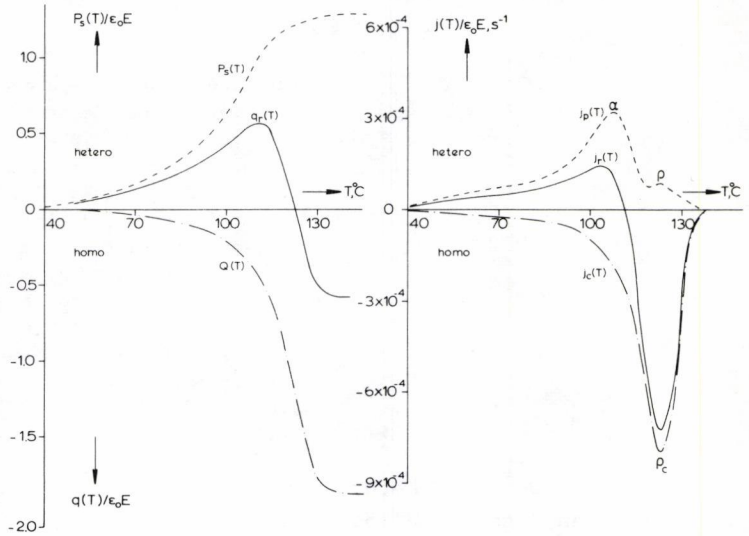


FIG.10-60 Air-gap thermograms of a homo-electret of PMMA, formed at 130° - 100 kV/cm - 1.5 h. By invoking the corresponding thermograms of the hetero-electret (dashed lines), we have resolved the released charge q_r and released current j_r of the homo-electret into a dipolar part j_p and a part j_c which describes the excess-charge decay by ohmic conduction. Note that the negative homopeak occurs at the *same* temperature as the ρ peak of the hetero-electret. The reduced air gap g/l was 0.06 and s^{-1} = 0.5 °C/min.

We observe a rather small heterocurrent, which reverses to a large homocurrent. As a result , the final charge released becomes homopolar, as expected. We divided the released current into a heteropolar part,

*Another, less probable, source of error, which is more difficult to avoid, is that in the course of the TSD the external fields are intensified to above the breakdown field of the air. In this case part of the electret charge is neutralized by a back discharge.

$dP_s(T)/dt$, and a homopolar part, $dQ(T)/dt$, representing excess charge decay by ohmic conduction. The former quantity was obtained from the released current of the corresponding shorted hetero-electret (taking into account the induction loss by the air gap), and we note that the temperatures of its α and ρ peaks neatly coincide with those of the respective hetero- and homopolar current maxima of the air-gap thermogram. This constitutes further evidence to the proposed origin of the ρ peak.

Fig. 10-61 gives the air-gap current and charge thermograms of a homo-electret of PET-c foil. It shows similar trends as the previous thermogram. Again its homo- or ρ_c peak dominates and occurs at the same temperature as the ρ peak of the accompanying thermogram of the shorted

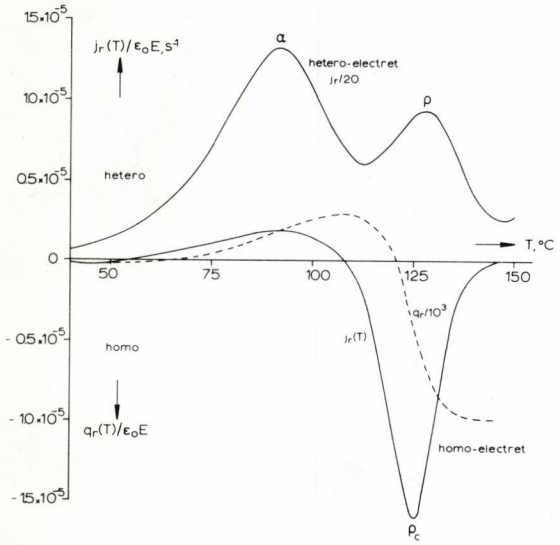


FIG. 10-61 Current and charge thermograms of a homo-electret of PET-c discharged with an air gap. Its opposed current peaks are compared with the α and ρ peaks of a hetero-electret (upper solid line). Interestingly, the negative homocurrent peak occurs at the *same* temperature as the ρ peak. The homo-electret was formed at 140° - 1 kV/25 µm - 5 min, with glass-cloth insert, and the hetero-electret at 140° - 100 kV/cm - 1.5 h. We chose an air gap of 0.15 mm and s = 1 min/°C.

hetero-electret. (As shown, this heterocurrent is much higher, because it is not subject to any induction loss caused by an air gap.) On p.170 we discussed the calculation of the activation energy for the ρ and ρ_c peaks of PET. We then indicated that the activation energy of the ρ_c peak, as found by a BFG plot, agrees perfectly with that of the ohmic conductivity. This corroborates that in this polymer the decay of the deposited homocharges is mainly due to ohmic conduction.

Fig. 10-62 shows the air-gap thermogram of a *two-sided metallized* hetero-electret of 80 S co 20 AN. The area of the positive and that of the negative current are now equal, since we started with a sample that was neutral owing to the metallization. As was discussed in Sect. 7:2, the first peak is mainly due to the reorientation of dipoles, while the second peak now originates from the dissipation of the *image charges* induced on the electrodes by ohmic conduction. For comparison, the thermogram of a hetero-electret depolarized without air gap is also given. It is interesting to note that its α and ρ peaks are again located at

almost the same temperature as the two air-gap peaks. The ρ and ρ_c peaks of these thermograms were also analyzed in Chap. 7. Their activation energies agreed well with that for ohmic conduction; for further details we refer to p. 173.

In our early investigations we performed TSD experiments on electreted PC capacitors. These are composed of *one*-sided metallized PC-kg film*, in which the other electrode is pressed onto the PC and virtually makes contact with it. We then found (Tu 68) a clear indication of a relaxation peak at about 85 °C; see Fig. 10-63. Strikingly, this peak is virtually absent in the normal TSD thermogram of a *two*-sided metallized foil (dashed line) and in the air-gap thermogram of the amorphous PC disc (Fig. 10-58).

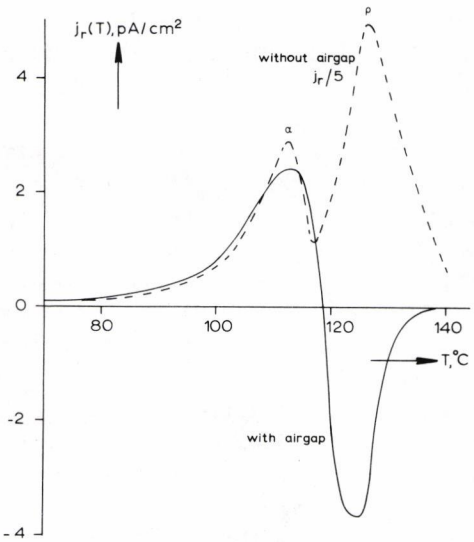


FIG.10-62 Current thermograms of a bilaterally metallized hetero-electret of 80 S co 20 AN depolarized with and without an air gap. For the former the areas of the positive and negative parts of the current are equal, owing to the metallization. In both thermograms the position of the peaks nearly coincide; this indicates that the ρ peak found without air gap originates from the motion of space charges. The forming conditions were: 130° - 20 kV/cm - 1.5 h and the reduced air gap g/l = 0.3.

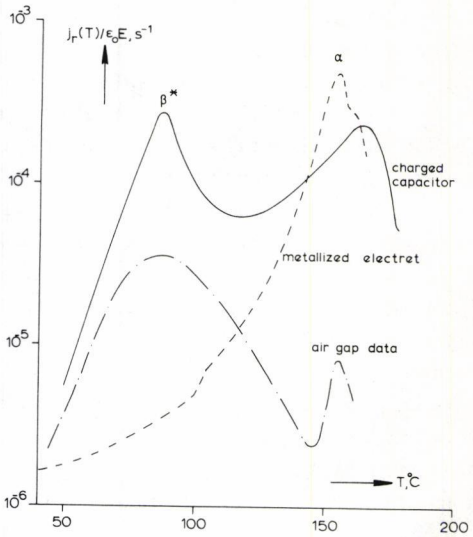


FIG.10-63 Air-gap current thermogram (dotted-dashed line) of a PC-kg heteroelectret showing its intermediate relaxation peak, β*, which was already known from ordinary dielectric measurements, although we see that it does not occur in the normal TSD of a bilaterally metallized electret (dashed line). We observed this peak for the first time during a TSD of a charged PC-capacitor; this thermogram is also shown. The charging conditions were 160° - 100 kV/cm - 1.5 h for the metallized electret and the capacitor, and 140° - 100 kV/cm - 1.5 h for the air-gap sample.

*kg stands for the German "kristallisiert gegossen gestreckt", i.e. crystalline casted and drawn.

This led us to conclude that this peak originates from space charges trapped at the crystal boundaries, which are mainly neutralized by ohmic conduction. To enhance the ohmic dissipation we decided to perform a well-defined air-gap experiment by stretching a heterocharged foil, metallized on one side, around a Teflon rim 0.15 mm above a metal electrode. The resulting thermogram is shown in Fig. 10-63, it indeed gives the desired peak. Although this so-called intermediate peak is also known from mechanical and dielectrical measurements (see Fig. 10-27), its molecular origin is still obscure. But it seems to arise from frozen-in stresses (CR 67) and therefore it is more pronounced in stretched films.

The results given so far suggest that air-gap TSD is an interesting technique which should be exploited more fully. For instance in the way illustrated in Fig. 10-60 the homocharge can be resolved and related to the forming conditions. Up to now, the effect of the forming field, temperature and time on homocharging of disc electrets are not known. We did such experiments in the beginning of our work, but unfortunately we used contiguous electrodes during TSD, and so the results are not very conclusive. Therefore, they will not be discussed here (see (Tu 68)). But some recent work on the homocharging of foils, which are more important than discs, will be discussed in the section on charge TSD. Furthermore, we shall describe in Sect. 7:4, App. II) the air-gap thermograms obtained for metallized hetero-electrets of PVC charged at various temperatures.

Finally, TSD with air gap is not restricted to electrets; it also enables one to study the TSD behaviour of excess charges deposited on polymers by friction or corona discharge. Here, too, it turns out to be a useful technique for gaining insight into the relevant decay processes (OT 73). This is illustrated in Figs 1-10 and 7-10. This seems an important development, since triboelectricity occurs in several applications of polymers, and is still a phenomenon that is not well understood.

10:8 Charge TSD of Electret Foils in Open Circuit

Charge thermograms are less spectacular than current thermograms, but they elucidate all possible decay processes, including the charge decay by ohmic conduction, which in normal current TSD is obscured by the short-circuiting. Moreover, they are very important for practical purposes, because they directly reveal the highest permissible working temperature of the electret foil.

Fig. 10-64 gives charge decay thermograms of several commercially available polymer foils; all were unilaterally metallized and charged homopolarly by Townsend breakdown, using glass cloth as an insert. The forming conditions are indicated in the text of the figure. The electrets were formed well above room temperature, so that some hetero-

charging is likely to have occurred in the more polar foils. Nevertheless, the homocharge dominates. Prior to their homocharging, the foils were in general thermally discharged in order to remove frictional and moulding charges.

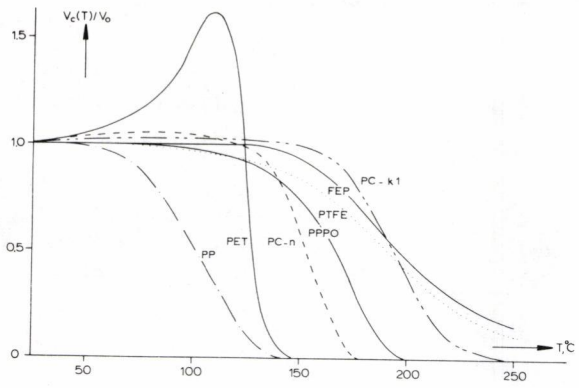


FIG.10-64 Charge thermograms of several homocharged commercial foils. The most stable are Teflon-FEP, Teflon (PTFE) and PC-k1. The temporary charge increase shown by PET is due to the disappearance of its heterocharge. The heating rate was 1.3 °C/min. After applying the forming voltage of + 1 kV for 5 sec, all foils were cooled at 5 °C/min. The forming temperatures were 200 °C for PC-k1 (25 μ), FEP (25 μ), PTFE (50 μ) and PPPO (25 μ); 160° for PC-n (40 μ); 145° for PET (25 μ) and 140° for PP (20 μ).

At their beginning the TSD curves of the more polar foils show a slight increase in charge. This effect is particularly pronounced with PET. We attribute it to the disappearance of an opposed heterocharge, of which we know that it is less stable than the dominating homocharge. We further recognize that the most stable foils are 89 TFE co 11 HFP (Teflon-FEP, DuPont de Nemours, USA), PTFE (Teflon, DuPont), and PC-k1 (Eastman Kodak, USA); their half-value temperatures are about 195 °C. Like the current thermograms the charge thermograms are characteristic of the polymers.

We note that the half-value temperatures are lower than the temperatures at which the electrets are formed. We may therefore expect that after the forming the front of the injected carriers will extend towards the back electrode. Since the injection is probably space-charge limited (cf. Sect 5:6.2, App. II), the spatial distribution sketched in Fig. 5-32 is the most probable one. As has been discussed in Chap. 8, in the more conductive polymers this charge distribution disappears by ohmic conduction, and in the highly insulating fluorocarbon foils mainly by SCL drift of the injected carriers. This implies that the inflexion points in the charge thermograms will lie close to the ρ peaks of the corresponding current thermograms. For example we find for PET, PC-n and Teflon-FEP 124°, 150° and 190 °C as the charge transition temperatures, which agree with the values 122°, 164° and 188° for their ρ peaks in current TSD.

From Figs 10-65 and 10-66 it is clear that TSD is valuable for predicting charge decay at room temperature. As might have been expected, Teflon and Teflon-FEP again yield excellent results; they are the best

electret foils known today. During a storage of three years at room temperature Teflon-FEP is seen to decay by 8 % only. The next best choice is PC-k1 film. The Teflon films, however, have the great advantage of being highly hydrophobic, so that they also perform well in a very humid atmosphere. This is illustrated in the lower curves of Fig. 10-66. After a storage of 500 days at 70 °C and 100 % RH, the charges of the thermo-electrets drop by no more than ca 50 %.

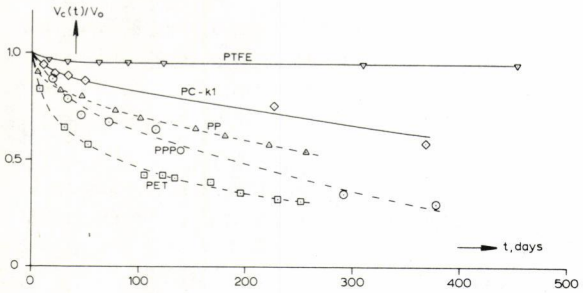


FIG.10-65 Decay curves of various homocharged foils at room temperature. Note the excellent stability of the PTFE electret. The forming conditions are: PTFE 160° - 1 kV/50μ - 1 min, PC-k1 200° - 1 kV/25 μ - 1 min, PP 120° - 5 kV/20 μ- 1.5 h, PPPO 200° - 1 kV/25 μ- 1 min and PET-c 120° - 5 kV/25 μ - 1.5 h.

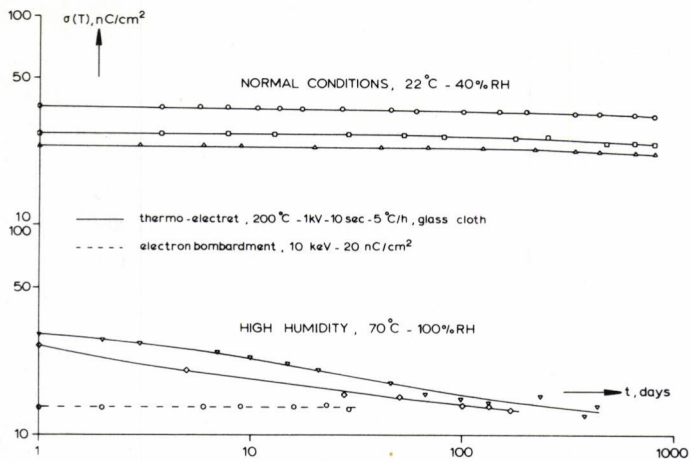


FIG.10-66 Remarkable stability of Teflon-FEP homo-electrets at room temperature (upper curves). Even under extremely humid conditions they remain quite stable (lower curves); this is especially so for the electron-bombarded foil.

Our further experiments have been concentrated on Teflon-FEP. We shall show in a moment that its charge decays in two steps, because at high temperatures the decay rate levels off; this is consistent with the occurrence of two current peaks in Figs 10-34 and 10-35. Such a two-step charge decay was not only found for thermo-electrets, but also for electron-bombarded foil (cf. Fig. 1-7). In the latter case we are sure that only one type of carrier is involved. We are therefore inclined to attribute the finding of two dispersion regions to the release

from *traps*, rather than to carriers of two different thermally activated mobilities. The traps are not discrete, but they are distributed around two different values, that depend on the relaxation properties of the polymer. The occurrence of a distribution in traps has been made plausible in Sect. 10:2.6a on p. 228, where we discussed some possible trapping sites. A more direct proof was given on p. 187, where we showed that the actual charge thermogram could not be fitted to a thermogram based on a single trap*.

The second step in the charge thermograms does not appear clearly; it can be shown more clearly by differentiating the retained charge. The results obtained for $dV_c(T)/dt$ of an electron-bombarded foil have already been given in Fig. 10-34. In accordance with the theoretical predictions on charge decay by SCL drift (Sect. 8:2) we find the first charge transition at a higher temperature (122 °C) than the maximum in the current thermogram (82 °C). As discussed on p. 233 this deviating behaviour is plausible because in charge TSD the carriers have to cross the whole sample to become neutralized, whereas in current TSD they become neutralized as soon as they pass the penetration depth. The shift of the maximum at higher temperatures could be established less satisfactorily, because this peak reproduces less beautifully.

Fig. 10-67 shows the charge thermograms of Teflon-FEP, charged neg-

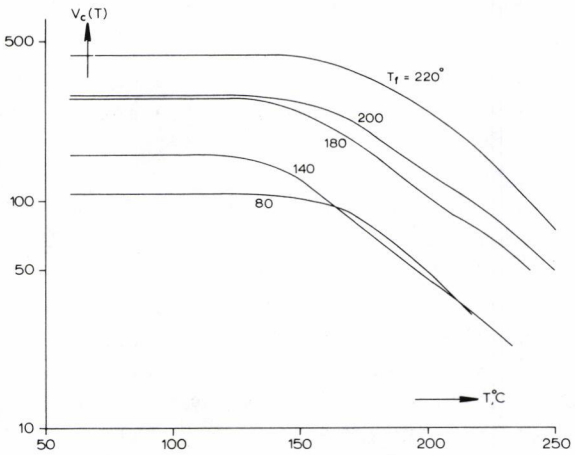


FIG.10-67 Charge thermograms of Teflon-FEP homo-electrets formed in 5 min at various temperatures. The forming field was 1 kV/25 μm, and the cooling rate was 5 °C/min. Note that a compensating voltage V_c of 100 V is equivalent to a surface charge of 7 nC/cm^2.

*A charge thermogram for bombarded PET-c film is presented in Fig. 8-2. It also exhibit two distinct steps, but these are of a different origin, for in this polar and more conductive polymer, SCL drift is less important. By differentiating the charge we could show that the charge transitions coincided with the α and ρ current peaks, which means that they arise from charge decay by dipole (re)orientation and ohmic conduction.

atively by Townsend breakdown at various temperatures, but at one and the same voltage*. We see that at lower forming temperatures less homocharge is acquired. This may be due to three effects: a) a less efficient homocharging due to a higher voltage drop across the sample at low forming temperatures, when the resistivity is high, b) a smaller penetration resulting in a lower charge accommodation at low forming temperatures and c) such differences in the discharge characteristics of the air that the breakdown is facilitated at higher temperatures. (In fact we observed that at higher temperatures the threshold voltage needed to induce breakdown is lower.)

The shape of the charge decay curves is very similar; nevertheless we expected from the theory on SCL drift that the curves of the lower initial charge would have remained more stable up to higher temperatures. The failure of the theoretical predictions may be due to several causes: i) the higher initial homocharges may be accompanied by higher heterocharges, which virtually stabilize the opposed homocharge decay, ii) the theory of Sect. 8:2 was derived for a single trap, whereas here we are dealing with a distribution of traps, of which the deep traps are preferentially filled at high temperatures, iii) the spatial charge distribution may be different for the various forming temperatures and iv) the actual decay may have been distorted owing to back discharges by which opposed charges are sprayed into the electret. (However, such back discharges take place only on highly charged foils, and they usually occur when the forming field is switched off, cf. p. 303.)

Obviously, the influence of the initial charge can be better studied when the polymer is charged at the *same* temperature at different (moderate) charging voltages, for then we exclude all these disturbances. The results, already given in Fig. 8-8, are compatible with our theory on charge decay by SCL drift; they actually showed that higher charged Teflon electrets are less stable. Similar results were obtained in Fig. 1-7 for electron-bombarded Teflon-FEP.

Fig. 10-68 gives the charge decay curves of electron-bombarded foils for four injection energies. We see that the foils bombarded at higher energies decay faster, for the half-value temperatures decrease from 170° to 140 °C. This is plausible, because at these energies the electrons penetrate deeper into the polymer (cf. Table 10-7), so that in the subsequent TSD they reach the neutralizing back electrode more quickly. Owing to the differences in the penetration depth, and probably also to the causes mentioned under ii) and iv), the figure does not reveal the effect of the initial charge. This can be studied better by varying the (moderate) electron density and keeping the bombarding ener-

*The charges attained on foils are considerably higher than those on discs; cf. Table 10-5. An explanation for this has been given by Roos (Ro 69), who states that foils are less easily discharged by air breakdown; see also Sect. 6:3 (App. II).

gy constant, as we did for the charge thermograms plotted in Fig. 1-7.

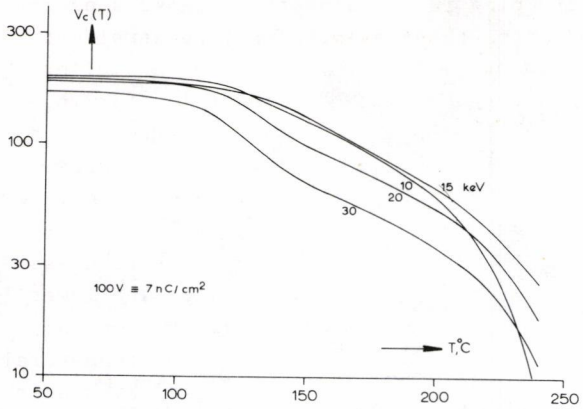


FIG. 10-68 Charge thermograms of electron-bombarded Teflon-FEP foil (25 μm) for four bombarding energies. The bombarded foils are somewhat less stable than the thermo-electrets of Fig. 10-57.

From a comparison of Fig. 10-67 with Fig. 10-68 we note that the half-value temperatures of the thermo-electrets are about 30 °C higher than those of electron-bombarded foils of Teflon-FEP. Presumably, because in the thermo-electrets the bulk of the charges have penetrated *less* far. Moreover, thermo-electrets may contain a weak dipole polarization, the decay of which partly compensates the homocharge decay. The more rapid discharge of electron-bombarded foils may also be caused by an enhanced ohmic conduction due to radiation damage. For these reasons we expect the long-term stability of electron-bombarded Teflon-FEP at room temperature to be less than that of thermo-electrets.

Yet electron-bombarded Teflon-FEP foils were found to be less sensitive to moisture (see Fig. 10-66). We attribute this to their typical spatial charge distribution in which the near-surface region is *deprived* of electrons. This means that electron-bombarded foils are not easily discharged by moisture, which first penetrates the outer layers. By contrast, in thermo-electrets part of the charges may arise from loosely bonded negative ions and from electrons trapped in surface states, and so these electrets are more sensitive to moisture.

From Fig. 10-69 it is apparent that in some *nonpolar* foils the SCL drift and trapping of the injected carriers dominate over ohmic dissipation. The figure shows the charge decay of positively and negatively charged thermo-electrets. While the more polar and more conductive PC-n foil exhibits no significant difference in decay rate, that of Teflon-FEP, and to a lesser extent that of PP*, is distinctly higher for positive carriers. Clearly, such differences would not occur if ohmic conduction were the main decay mode in these two polymers. This marked polarity dependence of Teflon-FEP has also been noted by Perlman et al. (CP 71). The obvious reason for it is that the negative carriers are more stably trapped in Teflon-FEP, because its fluorine atoms are highly

*Moplefan OKT, Montecatini Edison, Italy.

electronegative. On the other hand, the positive acceptor sites are shallow and easily discharged (cf. Sect. 10:2.6a). The positive carriers are further subject to trapping in surface states only, since they hardly penetrate at all, and so they may be quickly neutralized by surface recombination.

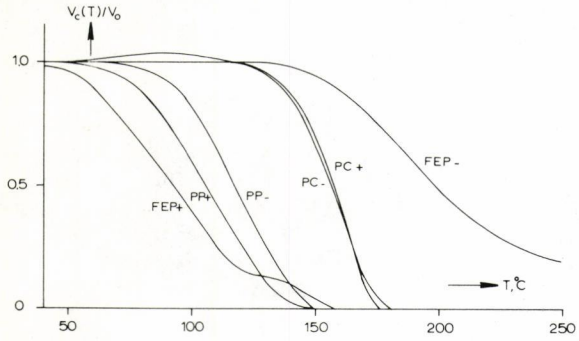


FIG.10-69 Thermograms of positively and negatively charged homo-electret foils. Negative foils are the most stable. Especially for Teflon-FEP the difference is strikingly large. Forming conditions were as follows: FEP 200° - 1 kV/25 μ - 1 min, PC-n 160° - 1 kV/25 μ - 1 min and PP-okt 140° - 1 kV/20 μ - 1 min.

Further evidence of charge-trapping in Teflon-FEP has been obtained from a two-stage TSD of two thermo-electrets. Fig. 10-70 shows the results; after the first runs, up to 170 °C and 200 °C, a second run was started. It is interesting to see that the onset of the decay is shifted to a higher temperature; this is particularly true for a preheating to 200 °C. This can readily be explained by supposing that the traps are distributed, the shallow traps being discharged first. The results also indicate that ohmic conduction is almost negligible, for otherwise the charge curves would have bent downwards at the same temperature as in the first run and no thermal stabilization would have taken place.

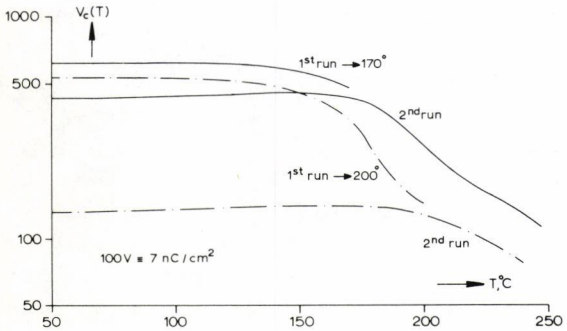


FIG.10-70 Increase in thermal stability of two homocharged Teflon-FEP foils after a preheating. In particular after a preheating to 200 °C the charge remains remarkably stable. The electrets were formed at 25° - 4 kV/25 μm - 1 sec.

We already mentioned that charge TSD has the advantage over current TSD of revealing all decay processes. It has another advantage in enabling one to use extreme low heating rates, since in contrast with current TSD, its output is not reduced by low heating rates. This provides a means of finding the activation energy of the change decay process. Fig. 10-71 demonstrates the results for a twentyfold charge in heating

rate on electron-bombarded Teflon-FEP. The charge transition is displaced to a lower temperature, because the electret has more time to respond at the temperatures scanned. The actual shift amounts to 25 °C, which corresponds to an apparent activation energy of 1.8 eV. On pp 117 and 122 a similar value was derived from the current thermograms. From the G" shift in mechanical measurements, however, we derived an apparent activation energy of 6 eV for the α transition. This discrepancy also indicates that in TSD we are dealing with charge release from a distribution of traps. So, in retrospect, we see that there is a need to extend the theory of Chap. 8 to trapped charges; this can be accomplished along the lines outlined for current TSD in Chap. 11.

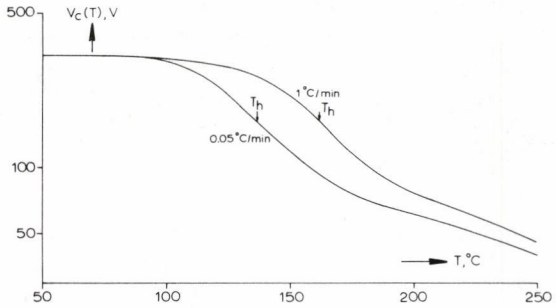


FIG 10-71 Effect of a twentyfold change in heating rate on the TSD charge thermogram of electron-bombarded Teflon-FEP foil (20 keV, 20 nC/cm^2). The half-value temperature shifts from 162 °C to 137 °C.

10:9 Conclusions

In discussing the experimental results on the current TSD of bilaterally metallized hetero-electrets we have stressed the molecular interpretation of the TSD peaks by invoking, in line with the theory of Chap.4, the relationship between TSD and well-established conventional measurements. We have shown that all relaxations from conventional dielectric measurements can be traced back in TSD. However, we have observed a *new* kind of relaxation that we propose to call ρ peak, because it is due to the *motion of space charges*.

It was found that the β and α peaks of the TSD thermograms hardly depend on the forming conditions and the forming technique, provided the polarization is completely filled by choosing the forming temperature above T_g. The ρ peak on the other hand, is more affected by the kind of forming. Reproducibility is good, although again the ρ peak may vary from sample to sample, because it is sensitive to impurities or additives.

From experiments on sectioned hetero-electrets it was found that the outer sections release the highest current. This is an interesting aspect; it means that *space charges* may play a significant role in current TSD of polymers; they even determine the α peak, i.e. the dispersion at T_g, to some extent.

In air-gap current measurements on unilaterally metallized samples appreciable homocharges were released; these findings support Gross's

ideas about the *bipolar* charging of *nonmetallized* electrets by internal and external mechanisms. Interestingly, the homopeak caused by ohmic conduction, was found at the same temperature as the ρ peak of the corresponding hetero-electret in normal current TSD. This is consistent with our idea that in this measurement the latter peak originates from the motion of the excess charges to the shorted electrodes under their own field (SCL drift) or from diffusion, both of which will have about the same temperature dependence as the ohmic conduction.

The molecular interpretation of the TSD of homocharged foils is much less advanced. However, we obtained strong evidence that in *non*polar foils their TSD must be attributed mainly to the thermal release of charge carriers from traps. Some possible trapping sites, which are likely to occur in Teflon-FEP, have recently been suggested by Perlman and co-workers (Pe 72, PU 72). Further work should therefore aim especially at this important topic. We believe that some relevant molecular mechanisms may be revealed by studying the TSD of foils bombarded with specific *ions*. Work on this subject is in progress at our laboratory. In this work a modified mass spectrograph is used to select the desired ions.

APPENDIX I

Chapter 11

CURRENT TSD BY RELEASE OF TRAPPED EXCESS CHARGES IN SHORTED ELECTRETS

In Chap. 5 we described the current TSD due to SCL drift of carriers with a thermally activated mobility. As is usually done, we assumed that all carriers had to surmount the same potential barrier and thus had the same mobility. In Chaps 1 and 5, and more extensively in Chap. 10, we showed, however, that the current TSD of electron-charged mono-electrets of Teflon-FEP always exhibit at least two current peaks rather than one. Moreover, these peaks are broad despite the fact that the effective activation energy is large. Obviously, these findings are incompatible with the assumption that the electrons have a single mobility; we are therefore led to the conclusion that the injected electrons are captured at *various* localized energy levels, from which they have to be released before they can drift towards the shorted electrodes, along a series of higher energy levels, which constitute a conduction band.

The localized trapping levels, at which the electrons are not free to move through the polymer, can arise from various sources. Some of them are:

- impurities (catalyst, monomeric residues, antioxidants)
- structural defects in the monomeric units (branching, crosslinking, double bonds)
- irregularities in the conformation of the molecular chains (kinks, chain folding, chain ends)
- imperfections in the crystallites (dislocations), especially at the boundaries with the disordered amorphous parts

In Teflon-FEP the localized trapping states are centred around two well-separated mean values, of which the first gives a current peak at the glass-rubber transition of the polymer. The trapping depths of some structural defects and impurities in PE have recently been listed by Bauser (Ba 72); see Table 11-1. It appears that in particular the antioxidants give deep hole-traps, and that the defects within the main chains only give shallow traps. Earlier we have indicated (Fig. 10-30) possible trapping sites in corona-charged polyolefins, as suggested by Perlman and associates (Pe 72).

TABLE 11-1 Some Trapping Sites in PE

source	hole (eV)	electron (eV)
carbonyl group	0.5 to 1	1.0
vinyl double bond (end group)	0.5	
vinylene double bond	0.9	
two conjugated vinylene double bonds	$\simeq$ 1	
p-benzoquinone (stabiliser)	0.3	$>$ 1.4
oxygen		0.4
antioxidants:		
α-naphthylamine	2.6	
p-phenylenediamine	2.9	
N,N'-dimethyl-p-phenylene diamine	3.1	

Summarizing, there seems no doubt that in polymers many trapping sites are available, but the question is whether we are allowed to describe the thermal release of the trapped electrons by the energy band model, which is successfully applied to the carrier transport in inorganic semiconductors such as Ge and Si. These materials, however, are crystalline and have a periodic structure (long-range order), whereas polymers are at best partially crystalline, and thus have a non-periodic structure (short-range order). In such structures then it is difficult for electrons to have wave functions that would permit them to move over considerable distances through the lattice without being captured or scattered. As a result the permissible conduction bands become narrow, and the electron mobility low.

The band may even split into individual energy levels spaced closely with respect to location (intermolecular distance) and energy (see Fig. 11-1). Each level represents a whole molecular unit (e.g. hydrocarbon chain or benzene ring). The energy differences are due to local differences in the overlap integrals,

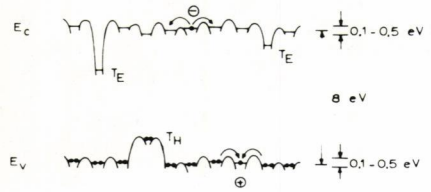


FIG.11-1 Energy diagram for polymers as advocated by Bauser (Ba 72). Excess electrons move along the structured conduction band and excess holes (missing electrons) along the valence band. Electron and hole traps are also indicated.

which, in turn, result from differences in the local environment of each molecular unit.

Under such conditions wavelike motion of the electrons is no longer likely, and conduction is assumed to be of a hopping nature, the electrons jumping from molecule to molecule. This transport generally takes place along the energy levels of the weakest bound electrons. For PE these are, e.g., the σ-electrons of the carbon chains. Besides this intramolecular transport, the electrons can also make intermolecular jumps to molecules on neighbouring chains; this has lately been pointed out by Martin and Hirsch (MH 72) in their interesting studies on electron-induced conduction in plastics.

Examination of Fig. 11-1 shows that the spread in the conduction and valence levels is small compared with the forbidden gap width. In view of this, it seems justified to describe the trap emptying in polymers with a conventional energy band scheme. The actual carrier transport, however, is likely to be a hopping transport rather than a normal band conduction. Nevertheless, for the sake of convenience, we shall in the following consider the latter process to be active. This does not imply a limitation, because for both mechanisms the final outcome is that the emptying of the traps is a thermally activated process.

The energy-band model was first applied by Creswell and Perlman (CP 70) to the current TSD of plastic foils charged negatively by corona injection. Their analytical solution holds only for mono-electrets uniformly charged to small penetration depths; we shall develop their ideas further by drawing upon the theory of Chap. 5. We shall also discuss results of a more general numerical solution, which includes nonuniformly charged mono-electrets having a continuous range of trapping levels. This numerical solution was taken from Monteith and Hauser (MH 67). They considered, however, the isothermal current discharge and we first had to adapt their theory to TSD.

11:1 Short Outline of the Energy-Band Model

Fig. 11-2 illustrates the band-structure model for a uniform cloud of electrons trapped in a shorted mono-electret. The figure is an energy scheme for electrons, in which the x-axis runs in the lateral extension of the electret. The upper band is the conduction band, in which electrons escaped from their traps may drift freely towards the shorted electrodes. Some electronvolts lower runs the valence band, in which the electrons of the polymer molecules are bound to their atoms. Valence electrons that pick up enough energy can cross the forbidden energy gap to the conduction band, leaving a positive hole behind. This hole can also move gradually towards the electrodes.

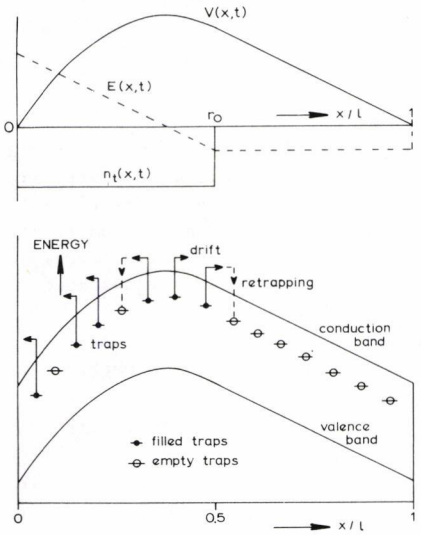


FIG.11-2 Energy band diagram (below) for excess electrons trapped uniformly up to a depth r_o at a single trap level in a shorted electret. Above, the profiles of the corresponding field and voltage are shown. The conduction and valence band are referred to the voltage, and therefore they are also concave. Accordingly, the freed electrons fall from a potential hill in their drift to the electrodes.

Due to impurities or structural defects, the forbidden gap contains localized energy levels, in which the electrons injected are captured or trapped during the electret formation. From these localized levels the trapped electrons are released thermally during TSD. On the other hand, freed electrons, which move along the conduction band to the shorted electrodes, may be *retrapped* in empty traps. Moreover, some of the localized levels may act as centres for *recombination* between electrons and holes. The distribution of electrons over the various trapping energies is governed by the Fermi-level*, which has the same value at the shorted electrodes and lies somewhat below the conduction band. Generally, the trapping distribution degenerates into Boltzmann statistics. The energy of the local trap levels may be distributed discretely or continuously.

11:2 General Equations for a Single Trapping Level

In discussing the pertinent equations, free and trapped charges are distin-

*In the present problem, which corresponds to a nonequilibrium state, in which there are carriers in excess of those in thermal equilibrium, the Fermi level in fact is a so-called quasi-Fermi level, the position of which depends not only on temperature, but also on the filling state of the traps.

guished by a subscript t for trapped. Focusing our discussion on current TSD of electron-charged foils we assume the injected excess charges to be negative. Let n_e and n_{te} denote the equilibrium negative charge densities in the neutral state, which are independent of x and t. We then have the Poisson equation

$$\varepsilon_o \varepsilon \partial E(x,t)/\partial x = -n(x,t) + n_e - n_t(x,t) + n_{te} \qquad (11.1)$$

The differences $n(x,t) - n_e$ and $n_t(x,t) - n_{te}$ are the free and trapped charge densities respectively. The continuity equation is

$$\partial n(x,t)/\partial t = \mu(T)\partial n(x,t)E(x,t)/\partial x - \partial n_t(x,t)/\partial t - \{n(x,t) - n_e\}/\tau_r \qquad (11.2)$$

where τ_r is the recombination life time of the freed excess carriers.

For one trap level of depth E_t, the trap kinetics, which involve the retrapping and recombination processes and therefore determines $\partial n_t/\partial t$, can be described by

$$\partial n_t(x,t)/\partial t = c_n n(x,t)\{N_t - n_t(x,t)\} - \nu(T) n_t(x,t) \qquad (11.3)$$

where c_n is the capture coefficient, N_t the total available trap density, and $\nu(T)$ the stimulated escape frequency, $\nu(T) = \nu_o \exp(-E_t/kT)$.* Since the capture coefficient will barely change with temperature, it is taken constant. Clearly, the first term on the right-hand side of Eq. 11.3 represents the retrapping of the freed carriers, and the second term the thermal release of the trapped carriers. For n discrete trapping levels, we get n simultaneous differential equations like Eq. 11.3; continuous distributions of trapping levels will be discussed in Sect. 11:3. (The following between -***- can be skipped in a first reading.)

-***-

The equations given are similar to the ones for thermally activated SCL drift in the absence of trapping in Chap. 5, cf. Eqs 5.14 and 5.15; only $n_t(x,t)$ has entered as an additional variable, while recombination replaces ohmic conduction as the neutralization process. Yet there is a marked difference in *rate constants*. In band theory, $\mu(T)$ and τ_r *hardly* vary with temperature, because they relate to drifting electrons, which do not have to surmount potential barriers. The number that enters the conduction band is only thermally activated. To calculate the occupancy of the conduction band, we consider the steady-state. Eq. 11.3 then yields

$$n(T) = \nu_o n_t e^{-E_t/kT}/c_n(N_t - n_t)$$

On the contrary in the charge-motion model discussed in Chap. 5 the number of carriers is approximately constant, and their mobility $\mu(T)$ is considered to be thermally activated. These differences, however, do not influence the final temperature dependence of the corresponding terms; in both cases they will decrease exponentially with 1/T.

-***-

* As done before n and also n_t are considered as charge densities and therefore N_t should also have the dimension of a charge density.

Now Monteith and Hauser (MH 67) have pointed out that, generally, $n_t(x,t) >> n(x,t)$**, and therefore they postulate

$$\partial n_t(x,t)/\partial t >> \partial n(x,t)/\partial t \tag{11.4}$$

Consequently, the continuity equation 11.2 then simplifies to

$$\mu \partial n(x,t)E(x,t)/\partial x = \partial n_t(x,t)/\partial t \tag{11.5}$$

and Eq. 11.1 reduces to

$$\varepsilon_o \varepsilon \partial E(x,t)/\partial x = -n_t(x,t) \tag{11.6}$$

For the discharge current density we again have Eq. 5.18

$$j_r(t) = \varepsilon_o \varepsilon \partial E(x,t)/\partial t + \mu n(x,t)E(x,t) \tag{11.7}$$

where μ is taken constant, since it is not thermally activated. Note that n is the total negative charge density and so the second term also accounts for intrinsic ohmic conduction arising from the equilibrium density, n_e. However, we have not included the contribution of the positive carriers (of which there are no excess charges), assuming that either their mobility is negligible, or that they are strongly trapped in recombination centres. Integrating Eq. 11.7 we obtain, in view of the short-circuit

$$j_r(t)l = \mu \int_o^l n(x,t)E(x,t)dx \tag{11.8}$$

Prerequisites for an analytical solution of the general PDE's 11.1 to 11.3 are a uniform carrier distribution in combination with simple trap kinetics.

11:2.1 Analytical Solution for Fast Recombination and Fast Retrapping

If the trapped carriers are released and none of them is retrapped or lost by recombination, there is no external current. This can easily be verified. In this case we have that $\tau_r = \infty$ (no recombination), $n_e = n_{te} = 0$ (perfect insulator) and $c_n = 0$ (no retrapping). Moreover, let the implanted carriers be uniformly trapped up to r_o at t = 0. Then Eq. 11.3 can be integrated to give

$$n_t(x,t) = n_t(x,o) \exp\{- \int^t \nu(T)dt\} \tag{11.9}$$

which implies that n_t remains uniform, and decreases without spreading.

Considering Eq. 11.5 at the zero-field point x_o, we have, by virtue of Eq. 11.9

$$n(x_o,t) = (\varepsilon_o \varepsilon \nu_o/\mu) \exp(-E_t/kT) \tag{11.10}$$

Due to the absence of retrapping this free charge density n(x,t) occurs for every value of x, and the released carriers spread instantly over the entire specimen. Accordingly, Eq. 11.8 yields a vanishing current density for shorted electrets. This proves that a single trap level which does *not* show *retrapping*, cannot generate an external current. Lindmayer (Li 65) came to the same conclusion, by considering the zero-field point movement. At x_o we have, instead of Eq. 5.28

**This may not be true at the end of a TSD experiment, when most of the electrons have been released and n becomes comparable to n_t. For this reason our computer calculations, discussed in Sect. 11:3, sometimes give diverging results for high release temperatures.

$$j_r(t) = \{n(x_o,t) + n_t(x_o,t)\}dx_o(t)/dt \qquad (11.11)$$

but because $n_t(x,t)$ does not expand, x_o remains constant and $j_r(t)$ is zero.

Thus, for little retrapping, the external current becomes significant only if recombination prevails, or if the traps are distributed over various energy levels.

11:2.2 Fast Recombination in Uniformly Charged Mono-Electrets

Recombination will dominate retrapping if

$$1/\tau_r >> c_n\{N_t - n_t(x,t)\} \qquad (11.12)$$

We shall briefly discuss Creswell and Perlman's solution (CP 70) for this case. In view of Eq. 11.12 substitution of Eq. 11.3 into Eq. 11.2 leads to

$$\partial n(x,t)/\partial t = \mu\partial n(x,t)E(x,t)/\partial x + \nu(T)n_t(x,t) - n(x,t)/\tau_r \qquad (11.13)$$

where we have put $n_e = n_{te} = 0$ (nonconducting polymer). Creswell et al. argued that in the present case each released electron, is almost immediately lost by the predominant recombination, so that*

$$\nu(T)n_t(x,t) \simeq n(x,t)/\tau_r \qquad (11.14)$$

Integrating Eq. 11.3 and remembering Eq. 11.12, we further have

$$n_t(x,t) = n_t(x,o)\ \exp\{-\int_o^t \nu(T)dt\} \qquad (11.15)$$

Again the trapped charges, $n_t(x,t)$ will not spread. This is not true for the free charge density $n(x,t)$, which is extended beyond the original depth r_o by those released charges that escape recombination. This expansion will be uniform, and will obey equations similar to those of SCL drift in the presence of ohmic conduction (Sect. 5:3) from which we know (compare Fig. 5-9) that the expansion can virtually be neglected for $r_o \leq 0.25\ 1$. Eq. 11.8 therefore yields for *low* penetration depths

$$j_r(t)1 \simeq \mu n(x_o,t) \int_o^{r_o} E(x,t)dx$$

The integral of this equation can be evaluated with Poisson's equation, on assuming that $n_t(x_o,t) >> n(x_o,t)$, we find

$$j_r(t) \simeq \mu n(x_o,t)n_t(x_o,t)r_o^2\ (1-r_o/1)/2\varepsilon_o\varepsilon 1 \qquad (11.16)$$

Substitution of Eqs 11.14 and 11.15 finally gives

$$j_r(t) \simeq (\mu\tau_r/2\varepsilon_o\varepsilon 1)n_{to}^2 r_o^2(1-r_o/1)\nu(T)e^{-2\int_o^t \nu(T)dt} \qquad ...(11.17)$$

where $n_{to} = n_t(x_o,o)$. This current shows a similar temperature dependence as a dipolar *Debye relaxation*, but its peak will be somewhat more pronounced because of the factor of 2. Furthermore, it has the *same* polarity as the TSD current released by SCL drift of negative carriers with a thermally activated mobility (Eq. 5.24).

The released charge can be found from the time-integral of Eq. 11.16; this gives for the ultimate charge density at time $t = \infty$

$$q_r(\infty)/n_{to}r_o \simeq (\mu\tau_r n_{to}r_o/4\varepsilon_o\varepsilon 1)(1-r_o/1) \qquad (11.18)$$

*By particularizing Eq. 11.13 at the zero-field point, we readily verify that Eq. 11.14 holds only for $\nu(T) > \mu n(x,t)/\varepsilon_o\varepsilon$.

Actually, the ultimate charge is reached as soon as the charges have spread all over the specimen, i.e. at time $t = \lambda$, but since λ is large, Eq. 11.18 is a fair approximation. We see that $q_r(\lambda)$ is not a function of $r_o/1$ only; the *recombination time* and *carrier mobility* are also decisive. However, as we did for the SCL drift studied in Sect. 5:3 we may equally well for the release by the present mono-electret invoke Eq. 5.31, in which for small penetrations we can put $E(1,\lambda) = 0$.

Accordingly, we have, in addition,

$$q_r(\lambda)/n_{to}r_o \simeq r_o/21 \qquad \ldots(11.19)$$

This equation and that for the initial effective charge density, Eq. 5.34, enable one to calculate the trapped charge density n_{to}, and the maximum trapping depth r_o, while by combining Eqs 11.19 and 11.18 we can deduce the mobility-lifetime product $\mu\tau_r$

$$\mu\tau_r \simeq \varepsilon_o\varepsilon r_o^2/q_r(\lambda)1 \qquad \ldots(11.20)$$

Evidently, it is again advisable to measure the effective electret charge density q(o) before TSD, for otherwise the first calculation cannot be made. For corona-charged polymers Creswell and Perlman advocated an independent dielectric measurement to find r_o; however, we found the reproducibility of this method to be disappointing.

In Sect. 10:1 we used Eqs 11.19 and 11.20 to evaluate experimental results on PET film charged by a negative corona. We also indicated the calculation of the activation energy by constructing the appropriate BFG plot (Fig. 10-33). This fitted the results slightly better than the charge-ratio plot, which in fact only holds for fast retrapping (cf. Fig. 5-18 in Sect. 5:3.4) and therefore already deviated from a straight line below the maximum. We thus substantiated Creswell and Perlman's view that retrapping is slow in corona charged PET-c, so that *recombination* is the prevailing loss mechanism.

11:2.3 Fast Retrapping in Uniformly Charged Mono-Electrets

Next we will discuss the analytical solution for fast *retrapping*, $N_t >> n_t(x,t)$; the isothermal discharge of which has been studied by Monteith et al. (MH 67) for electron-bombarded mylar, and by Many and Rakavy (MR 62) for transient SCL currents in crystals. Experimental evidence for fast retrapping was given in Chaps 1 and 10 for electron-bombarded Teflon-FEP. In this case, $n_t(x,t)$ and $n(x,t)$ do spread considerably, because electrons drifting to the right will be retrapped, building up a space charge to the right of the previous front. Creswell et al. (CP 70) neglected such an expansion, in treating current TSD of trapped *near*-surface carriers that show fast retrapping.

The fact that each released electron will soon be retrapped implies that $\partial n_t(x,t)/\partial t$ attains its minimum value, so that

$$\partial n_t^2(x,t)/\partial t^2 = 0$$

A minimum in $\partial n_t(x,t)/\partial t$ and $N_t >> n_t(x,t)$ reduces Eq. 11.3 to

$$c_n N_t n(x,t) \simeq \nu(T) n_t(x,t) \qquad (11.21)$$

This equation enables us to eliminate either $n(x,t)$ or $n_t(x,t)$ from Eqs 11.1 and 11.2.

When we introduce the new variables

$$n^*(x,t) = n(x,t) + n_t(x,t) = a(T)n(x,t)$$
$$\mu^*(T) = \mu/a(T) \quad \text{and} \quad \tau_r^*(T) = \tau_r a(T) \tag{11.22}$$

where $a(T) = 1 + c_n N_t/\nu(T) \simeq c_n N_t/\nu(T)$, the continuity equation and Poisson's equation can, for zero ohmic conduction ($n_e = n_{te} = 0$), be written

$$\partial n^*(x,t)/\partial t = \mu^*(T)\partial n^*(x,t)E(x,t)/\partial x + n^*(x,t)/\tau_r^*(T) \tag{11.23}$$

$$\varepsilon_o \varepsilon \partial E(x,t)/\partial x = -n^*(x,t) \tag{11.24}$$

These quantities have the *same* form as those discussed in Sect. 5:3 for SCL drift of thermally mobilized carriers in the presence of ohmic conduction. This emphasizes that the results previously obtained are directly applicable to *fast retrapping*. Note, however, that recombination takes over the role of intrinsic conduction as the neutralization process. In other words, we can simply apply the equations for the current and charge release derived in Chap. 5. There we also discussed the evaluation of the molecular parameters, and in particular we illustrated the calculation of the activation energy. This can most conveniently be deduced from a charge-ratio plot (cf. Fig. 5-18).

An approximate solution for fast retrapping was indicated earlier by Monteith et al. (MH 67); they started from their postulate 11.4, $n_t(x,t) >> n(x,t)$ and neglected recombination ($\tau_r = \infty$). Their approximate solution, which corresponds to $a(T) = c_n N_t/\nu(T)$, is almost identical to our exact solution.

No such fair agreement could be obtained for Creswell and Perlman's solution for fast retrapping; they included recombination putting $c_n\{N_t - n_t(x,t)\} >> \tau_r^{-1}$ in Eq. 11.3. As was done for slow retrapping, they neglected $\partial n(x,t)/\partial t$ and $\mu\partial n(x,t)E(x,t)/\partial x^*$ in Eq. 11.2, and took

$$\partial n_t(x,t)/\partial t \simeq -n(x,t)/\tau_r \tag{11.25}$$

Integrating this equation, after having eliminated $n(x,t)$ with the condition for fast retrapping (Eq. 11.21), they got on writing $N_c c_n$ for ν_o:

$$n_t(x,t) \simeq n_t(x,o)\, \exp\left(-\frac{s}{\tau_r} \int_{T_d}^{T} \frac{N_c}{N_t} e^{-E_t/kT}\, dT\right) \tag{11.26}$$

By virtue of Eq. 11.21, a similar equation applies to $n(x,t)$. Disregarding any carrier expansion, they finally substituted the resulting $n(x,t)$ and $n_t(x,t)$ in the current equation 11.16.

Upon comparing Eq. 11.25 with our Eq. 11.23, which is exact, it is obvious that their solution holds only for high recombination rates. It is also in view of footnote * that the solution of Eq. 11.23 as described in Sect. 5:3 is expected to give a better description of the current TSD of homocharged foils in which fast retrapping predominates.

11:3 General Numerical Solutions

The analytical solutions just described, though attractive for evaluating experimental results, put severe restrictions on the spatial distributions and the trapping kinetics. Solutions could be found only for uniform initial dis-

*Neglect of this term does not seem justified for carriers drifting under their own field. However, it can be neglected, if the discharge is studied with an applied field, as is done in recording photoconductive glow curves.

tributions showing fast recombination or fast retrapping. The general problem can be solved only by numerical computation, which, however, is intricate and less suitable for evaluating experimental results. Nevertheless, these computations are of prime importance for gaining insight into practical charge decay events.

Neglecting n_e and n_{te} (perfect insulator), and writing again $n^*(x,t)$ for $n(x,t) + n_t(x,t)$, we have for a single trap level the following PDE's

$$\partial n^*(x,t)/\partial t = \mu \partial n(x,t) E(x,t)/\partial x - n(x,t)/\tau_r \qquad (11.27)$$

$$\partial n_t(x,t)/\partial t = c_n n(x,t)\{N_t - n_t(x,t)\} - \nu(T) n_t(x,t) \qquad (11.28)$$

$$\varepsilon_o \varepsilon \partial E(x,t)/\partial x = -n^*(x,t) \qquad (11.29)$$

Moreover, we have the short-circuit condition (Eq. 5.6).

Of this set of equations, Eq. 11.27 can be solved by the LWR or WT scheme. At each time level the appropriate E-values are calculated by integrating Eq. 11.29 with the trapezoidal rule. Simultaneously Eq. 11.28 is integrated, which is an ODE at a particular x. It is useless to solve this equation more accurately than Eq. 11.27. Of the 2nd order Runge-Kutta methods, the modified Euler method (Eq.5.108) combines best with the LWR scheme, while Heun's method (Eq. 5.109) fits the WT scheme. The required "boundary" values, $n(x_o,t)$ and $n_t(x_o,t)$, follow from Eqs 11.27 and 11.28 taken at the zero-field point. For uniform distributions Eq. 11.27 reduces to an ODE at $x = x_o$, which, together with Eq. 11.28 can readily be solved starting from the initial values $n(x_o,o)$ and $n_t(x_o,o)$.

This general numerical solution has not yet been programmed. Instead, we have studied an *approximation* due to Monteith and Hauser (MH 67), who reduced the problem to the solution of ODE's. As mentioned before, Monteith et al. *neglected recombination* and took $n_t(x,t) >> n(x,t)$ together with Eq. 11.4. These assumptions reduce Eqs 11.27 and 11.29 to Eqs 11.5 and 11.6, respectively. Substitution of Eqs 11.28 and 11.6 into Eq. 11.5 leads to

$$\mu E(x,t)\partial n(x,t)/\partial x = \mu n(x,t) n_t(x,t)/\varepsilon_o\varepsilon + c_n n(x,t)\{N_t - n_t(x,t\} - \nu(T) n_t(x,t) \qquad (11.30)$$

which, for a given time t, can be considered as an ODE with respect to x. Monteith et al. suggest to solve it starting from the zero-field point. However, at $x_o(t)$ we have $E(x_o,t) = 0$ and for $\partial n(x_o,t)/\partial x$ to remain finite, $n(x_o,t)$ has to obey

$$n(x_o,t) = \nu(T) n_t(x_o,t)[c_n\{N_t - n_t(x_o,t)\} + \mu n_t(x_o,t)/\varepsilon_o\varepsilon\}]^{-1} \qquad (11.31)$$

Taking $n(x_o,t)$ as initial value, we integrated Eq. 11.30 to the left and right of x_o, using the modified Euler method, and we calculated the appropriate E-values with the trapezoidal rule. Similarly, Eq. 11.28 was solved with the modified Euler method. To find the appropriate $x_o(t)$ and $n_t(x_o,t)$ we used a 3rd-order interpolation of Aitken*. We worked with fixed mesh points and at each time level we made the first step from x_o to the nearest mesh point, x_k, with a simple Euler integration, according to

$$n(x_k,t) = n(x_o,t) + (x_k - x_o)\partial n(x_o,t)/\partial t \qquad (11.32)$$

*C.J. Mifsud, "Interpolation by Aitken", Algorithm 70, Collected Algorithms Comm. Ass. Comp. Mach.

where $\partial n(x_o,t)/\partial t$ follows from application of l'Hôpital's rule by differentiating Eq. 11.30 with respect to x_o

$$\frac{\partial n(x_o,t)}{\partial t} = \frac{\{n(x_o,t)(c_n - \mu/\varepsilon_o\varepsilon) + \nu(T)\}\partial n_t(x_o,t)/\partial x}{2\mu n_t(x_o,t)/\varepsilon_o\varepsilon + c_n\{N_t - n_t(x_o,t)\}} \qquad (11.33)$$

For initially *uniform spatial* distributions of trapped charges the number of calculations can be reduced considerably by argueing that such distributions persist in their uniformity between $x = 0$ and r_o. This is not only so for $n_t(x,t)$, but it also holds for $n(x,t)$. Consequently, $n(x_o,t)$ appears for every x between $x = 0$ and r_o. Moreover, Eq. 11.28 simplifies in this range to the following ODE

$$dn_t(x,t)/dt = -\mu n_t n(x_o,t)/\varepsilon_o\varepsilon \qquad (11.34)$$

11:3.1 Model Calculations for a Single Trap Level Based on Monteith's Approximation

The spatial expansions, calculated for various temperatures during current TSD, of electrons trapped at a single level that shows weak retrapping, are shown in Figs 11-3 and 11-4. We considered two degrees of retrapping and omitted

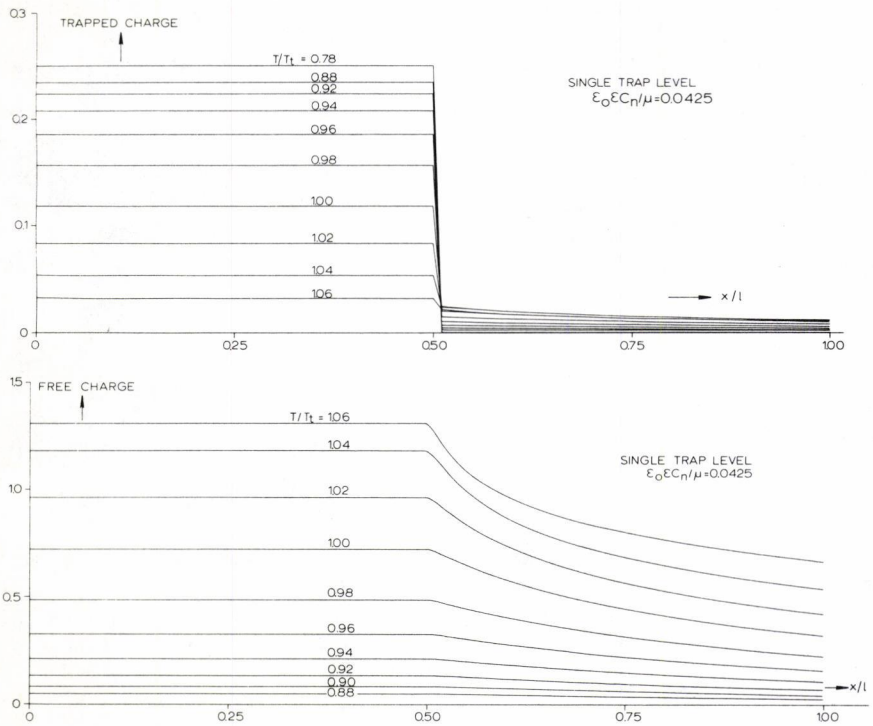


FIG.11-3 Spatial distribution of the reduced trapped and the reduced free excess charge densities at various release temperatures during TSD of a mono-electret having a single trapping site and no recombination centres. The calculations were carried out with 93 spatial grid points, for the indicated retrapping ratio $\varepsilon_o\varepsilon c_n/\mu$, and $E_t/kT_t = 20$.

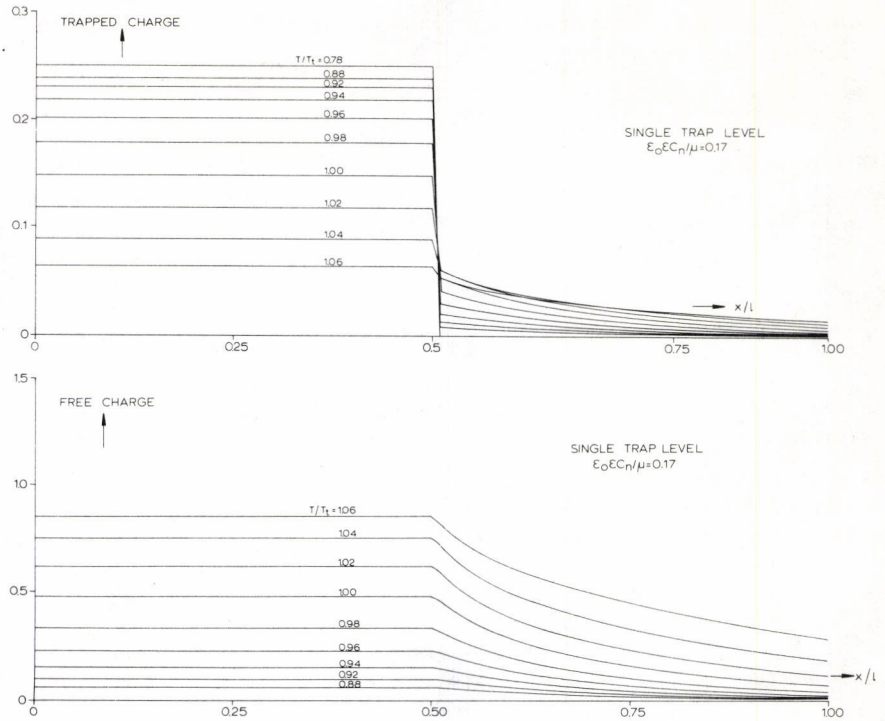


FIG.11-4 Like Fig. 11-3 but for a four times higher retrapping ratio.

carrier recombination. The trapped and free charge densities given are reduced to $n_t(x,T)/N_t$ and $\mu_n n(x,T)/N_t$ respectively, where the dimensionless parameter $\mu_n = \mu N_t/\varepsilon_o \varepsilon \nu(T_o)$. The temperatures are reduced to T_t, which is defined by the Debye maximum

$$sT_t \nu(T_t) = E_t/kT_t \qquad (11.35)$$

We assumed $E_t/kT_t = 20$.

A salient feature of the expansions is that they only remain partly uniform. Owing to retrapping, electrons also appear to the right of the original front. We see that for a higher retrapping, the trapped charges persist longer and more of them appear to the right of r_o. The free charge densities behave in the opposite way; they are lower for more retrapping. The largest changes in the densities occur at $T \simeq T_t$, when the corresponding current thermograms show their maximum, see Fig. 11-5. Eventually, all distributions will collapse uniformly, and current release will cease. The figures also indicate the trend for the two extremities: no retrapping and severe retrapping*. For the former no trapped charges would emerge beyond r_o and the freed charges would instantly spread over the entire sample, whereas for severe retrapping, the distributions of the trapped and free charge density would reduce to those shown in Fig. 5-3.

The upper curves of Fig. 11-5 show that the current density for a single trap level increases, when retrapping increases. In an absolute sense the currents are rather low, releasing a charge that is only a fraction of the elec-

* This would correspond to $\varepsilon_o \varepsilon c_n/\mu = n_{to}/N_t$.

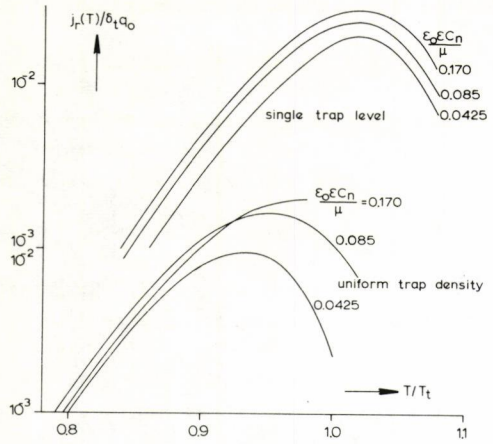


FIG.11-5 Computed current thermograms of a uniformly charged monoelectret for different degrees of retrapping. The upper curves refer to a single trap level with $n_{to}/N_t = 0.25$ and the lower curves to a uniform trap with $n_{to}T_u/N_uT_t = 2$. We further assumed that there was no recombination, and we took $r_o/l = 0.5$, $E_t/kT_t = 20$ and $E_{fo}/kT_t = 20$.

trons originally trapped (cf. Fig. 11-8). Note that the shape and location of the current peak does not alter with the retrapping ratio $\varepsilon_o \varepsilon c_n/\mu$. The current scale was normalized to $\delta_t q_o = \nu(T_t) n_{to} r_o$.

Fig. 11-6 gives the dependence of the current thermograms on the penetration depth. Their trend is broadly similar to that in Fig. 5-8, the curves changing in height with r_o/l. Yet, there are marked differences, for the current does not cease abruptly above T_t, because the charges spread *without* a sharp front

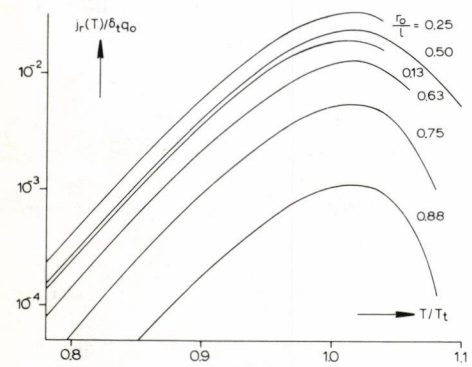


FIG.11-6 Current thermograms for various penetration depths, of a monoelectret free of recombination centres and accommodating a single trap level with $\varepsilon_o \varepsilon c_n/\mu = 0.085$. We took $n_{to}/N_t = 0.25$ and $E_t/kT_t = 20$.

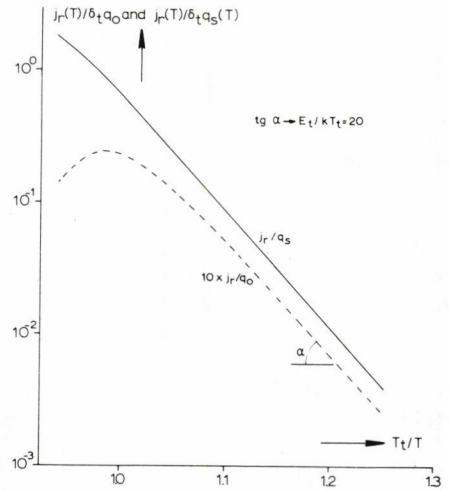


FIG.11-7 Calculation of the activation energy for current TSD from a single trap level that shows weak retrapping. The presented initial rise and BFG plots refer to one of the model thermograms of Fig. 11-6, for which $r_o/l = 0.5$; they both give the correct activation energy of $E_t/kT_t = 20$.

over the sample. It is also interesting to observe that the current maximum hardly shifts with r_o/l.

Another striking aspect of the thermograms is that the initial current-rise does not depend on r_o/l either, being solely determined by the activation energy. This becomes apparent from Fig. 11-7, which shows the initial current and the BFG plot of the model-thermogram for $r_o/l = 0.5$. Both curves give a slope which corresponds exactly to $E_t/kT_t = 20$. The BFG plot is remarkably straight, and so it is to be preferred for calculating the activation energy of actual data.

The ultimate charge released for the various penetration depths is shown in Fig. 11-8**. The curve resembles that of Fig. 5-6 (which holds for strong retrapping), but its height is less, the maximum now amounting to 9 % of $n_{to}r_o$. Notice that less charge is released for high penetrations when the charge distributions quickly become uniform. Likewise, for low penetrations the release is less efficient, because the freed charges then quickly leave the electret at the nearby electrode. The maximum occurs at $r_o = 0.33\ 1$.

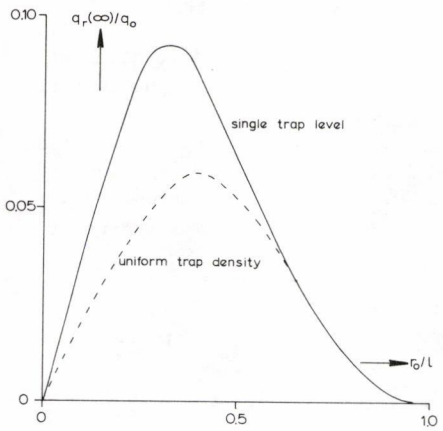


FIG. 11-8 Ultimate charge released by a mono-electret as a function of penetration depth, for a single trap level, and for a uniform trap density. We took $\varepsilon_o \varepsilon c_n/\mu = 0.085$ and neglected recombination.

11:3.2 Model Calculations for a Continuous Distribution of Traps

So far we have outlined the theory of one trapping level. Several polymers, however, possess traps varying in depth. This can be seen from the current thermogram of electron-bombarded Teflon FEP, Fig. 10-35, in which two broad current peaks appear, centred at 75° and at 190 °C.

For a discrete trap distribution of, say, m levels we get m differential equations similar to Eq. 11.28, each with a particular c_n, N_t and $\nu(T)$. For a *continuous* distribution, Monteith et al. derived, instead of Eq. 11.28

$$\partial n_t(x,t)/\partial t = n(x,t) \ \langle c_n \rangle \int_0^{E_{fn}} g(E)dE - \langle \nu_o \rangle \int_{E_{fn}}^{\infty} g(E) \exp(-E/kT)dE \qquad (11.36)$$

where $g(E)=\partial N_t/\partial E$ is the distribution function of the traps (i.e. the density of traps per unit of energy), where E_{fn} is the quasi-Fermi level, and < > indicates mean values.

**Part of this graph had to be obtained by extrapolation because of the difficulties encountered in using approximation 11.4 at high temperatures.

The energy distributions of traps may be, for instance, uniform or exponential. Monteith et al. showed that for electron-bombarded PET the former is more likely. For this distribution they put

$$g(E) = N_u/kT_u \tag{11.37}$$

and for the exponential one

$$g(E) = N_t/kT_e e^{-E/kT_e} \tag{11.38}$$

where N_u, T_u and T_e are constants characterizing the two trap distributions.

Substitution of Eq. 11.37 into Eq. 11.36 results in the following continuity equation for electrons trapped in uniformly distributed traps

$$\partial N_t(x,t)/\partial t = \langle c_n \rangle\, n(x,t)\{N_t - n_t(x,t)\} - \langle \nu_o \rangle (N_u T/T_u) \exp[-(T_u/N_u T)\{N_t - n_t(x,t)\}] \tag{11.39}$$

This equation must be solved in combination with the Poisson equation 11.29 (or Eq. 11.6) and the continuity equation for the free charge, Eq. 11.27 (or Eq. 11.5) which both remain valid.

A simple analytical solution for severe retrapping, for which $\varepsilon_o \varepsilon \langle c_n \rangle/\mu >> n_{to}/N_t$, has been indicated by Monteith and Hauser. The model thermograms given below apply to moderate retrapping and were computed numerically along the same lines as described above for a single level. Following Monteith and Hauser we chose $N_t T_u/N_u T_t = E_{fo}/kT_t$.

Some calculated results for the uniform trap distribution have already been displayed in Figs 11-5 and 11-8. In Fig. 11-5 its current thermograms (lower curves) are somewhat broader than those for a single level and the maxima of these curves occur at a lower temperature due to the presence of shallow traps. However, it should be mentioned that the temperature scale of the thermograms is normalized slightly differently. Instead of Eq. 11.35 we took

$$sT_t \langle \nu(T_t) \rangle = E_{fo}/kT_t \tag{11.40}$$

where $\langle \nu(T_t) \rangle = \langle \nu_o \rangle \exp(-E_{fo}/kT_t)$. Similarly, the current values were reduced to $\delta_t q_o = \langle \nu(T_t) \rangle n_{to} r_o$. We recognize that in contrast to the current for a single trap level, the width and location of the peaks increase with the retrapping ratio, presumably because the electrons in shallow traps are lost less quickly to the electrodes when retrapping is higher.

From Fig. 11-8 we observe that the uniform trap density releases less charge than a single trap level owing to the presence of shallow traps, the maximum now amounting to 6 % of $n_{to} r_o$. Such a figure of "merit" was also calculated by Monteith and Hauser (MH 67) for isothermal discharges.

Fig. 11-9 illustrates the spatial expansion of carriers trapped in sites uniformly distributed in energy; as before the normalized trapped and free charge densities are presented. However, we chose a different normalization, viz. $n_t(x,t)T_u/N_u T_t$ (trapped charges) and $\mu_n N(x,t) T_u/N_u T_t$ (free charges), where μ_n is now $\mu N_u T_t/\varepsilon_o \varepsilon \nu(T_t) T_u$. There are no significant differences between Fig. 11-9 and Figs 11-3 and 11-4, although the trapped charge density drops more

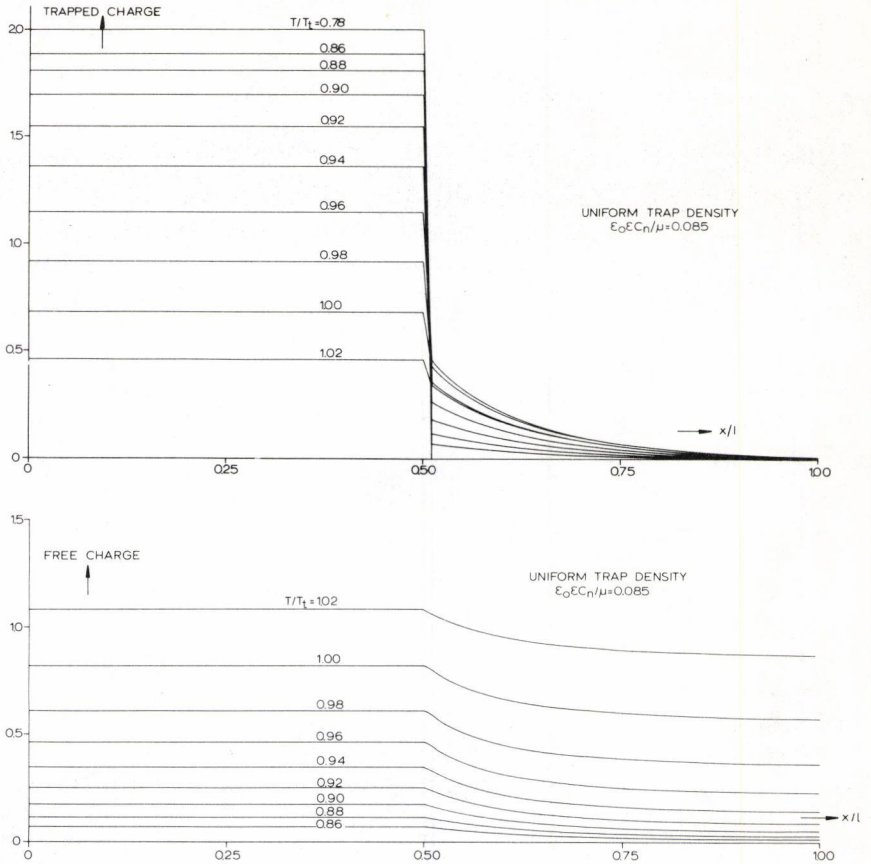


FIG.11-9 Spatial distribution of trapped and freed excess charges at various release temperatures during current TSD of a mono-electret, devoid of recombination centres and having a continuous set of trapping sites uniformly distributed in energy with $E_{fo}/kT_t = 20$.

rapidly beyond r_o. Fig. 11-10, finally, shows the effect of the penetration depth on the current thermograms for a uniform trap density. The curves behave similarly to those of Fig. 11-6.

So far we have not applied the numerical solution to experimental results, because it requires much computer time. After all, it would have been worthwhile to evaluate the experimental results of electron-bombarded Teflon-FEP with Monteith and Hauser's analytical solution for a uniform trap distribution that shows fast retrapping.

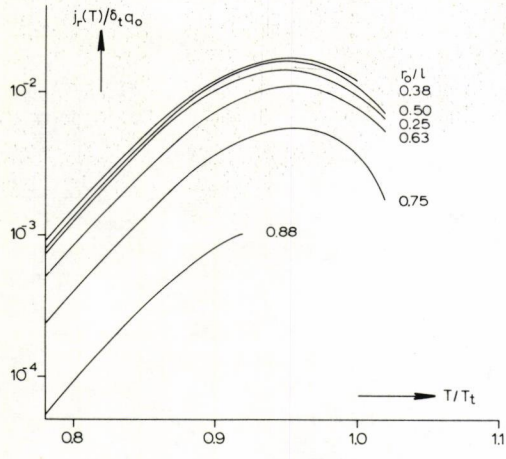


FIG.11-10 Computed current thermograms of an uniformly charged monoelectret without recombination centres and having a uniform trap density with $\varepsilon_o \varepsilon c_n/\mu = 0.085$. The thermograms are shown for various penetration depths, $E_{fo}/kT = 20$, and $n_{to}T_u/N_uT_t = 2$.

APPENDIX II

2:4 Current TSD of Shorted Electrets with a Spatial Nonuniform Dipole Relaxation

In most hetero-electrets the dipole polarization will be nonuniform because they accumulate excess charges near their electrodes. In such electrets the *local* internal field will be *nonzero* during current TSD, despite the short-circuit. This may have two major effects: a renewed orientation of dipoles and a local charge neutralization by the ohmic conduction of the polymer. It seems interesting to study what the effects on this are in the final current release. We shall also give an outline of the internal charge decay, for this may provide a deeper insight, although it is immaterial to the derivation of the external current release.

In this extension of the theory on dipole relaxations in Chap. 2 where excess charges were neglected, the discharge is ascribed to dipole reorientation and intrinsic ohmic conduction. SCL drift, diffusion and recombination of space charges are neglected, and also trapping effects are excluded. The theory therefore applies particularly to thick polar polymers.

We first consider *open electrodes*. For the reorientation of the permanent dipoles we now have to apply the Debye equation 2.1 locally as has been done before in Eq. 7.1, while the decay of the space charges follows the continuity equation which, by virtue of our assumption of immobile excess charges, becomes identical to Eq. 7.2. As in Chap. 7 we assume P_s to be space-dependent, in view of the presence of excess charges. The local electric field $E(x,t)$ follows from Poisson's equation, which again takes the form of Eq. 7.5, since $E(x,t)$ also depends on $P_s(x,t)$.

During the heating the excess-charge density $\rho(x,t)$ and the dipole polarization $P_s(x,t)$ will decrease, generating an external current density given by Eq. 7.7. Since the total quantities $\int_0^1 P_s(x,t)dx$ and $\int_0^1 \rho(x,t)dx$ are more deciding for the external current, than the local quantities $P_s(x,t)$ and $\rho(x,t)$ are, we integrate Eq. 7.1 between $x = 0$ and 1. By virtue of the short-circuit condition $\int_0^1 E(x,t)dx = 0$, we obtain

$$\frac{d}{dt}\int_0^1 P_s(x,t)dx + \alpha(T)\int_0^1 P_s(x,t)dx = 0$$

which upon integration from 0 to t gives

$$\int_0^1 P_s(x,t)dx / \int_0^1 P_s(x,o)dx = \exp(-\int_0^t \alpha(T)dt) \qquad (2.63)$$

where $\int_0^1 P_s(x,o)dx$ is the value at the beginning of the TSD experiment. It is interesting to note that the decrease of a *space-dependent* polarization shows the *same* temperature dependence as a *uniform* polarization (cf. Eq. 2.14), provided that we take its mean value. This is simply so because of the short-circuit, which makes the average field zero, so that the excess charges do not affect the decay rate of the average polarization, although, according to Eq. 7.1 they do change the dipole strength locally.

By integrating Eq. 7.7 in the same way as Eq. 7.1 we obtain

$$j_r(t) = \frac{d}{dt}\int_0^1 P_s(x,t)dx \qquad (2.64)$$

Apparently, only the decrease in $P_s(x,t)$ is revealed in the external current. The dissipation of the excess charges by ohmic conduction escapes our attention, because the mean value of its internal current is zero. Therefore, when *intrinsic*

conduction prevails over SCL drift and diffusion, the decay of the excess charges is *not* detected, and only the dipolar part of the heterocharge shows up. This is a great advantage in the current TSD of shorted electrets, for it is exactly this dipolar part that is most closely related to molecular relaxation processes. (The following between *** can be skipped in a first reading.)

- *** -

The externally measurable quantity j_r having been derived, we are still interested in the decay of the internal variable $\rho(x,t)$. Substitution of Eq. 7.2 into Eq. 7.5 yields upon integration

$$\frac{d}{dt}\int_0^1 \rho(x,t)dx = -\beta(T)\{\int_0^1 \rho(x,t)dx + P_s(o,t) - P_s(1,t)\} \tag{2.65}$$

which, for a symmetrical polarization, i.e. $P_s(o,t) = P_s(1,t)$ leads to

$$\int_0^1 \rho(x,t)dx / \int_0^1 \rho(x,o)dx = \exp(-\int_0^t \beta(T)dt) \tag{2.66}$$

In this case $\int_0^1 \rho(x,t)dx$ decays simply with the ohmic relaxation time as rate constant. Hence, the excess charges actually disappear, but we cannot notice it.

We emphasize that, if excess charges are initially missing, which is unlikely, they can be created by a decaying nonuniform polarization, in view of Eq. 2.65. The appearing excess charges originate from the nonuniform ohmic conduction current, and will be homopolar in order to compensate part of the heterocharge $P_s(x,t)$.

- *** -

Let us next consider the unusual case of *blocking evaporated electrodes*. The passage of ohmic currents being prevented at the electrodes x = 0 and x = 1, surface charges will be built up according to

$$\begin{aligned} d\sigma_1(t)/dt &= -\gamma(T)E(0^+,t) \\ d\sigma_2(t)/dt &= \gamma(T)E(1^-,t) \end{aligned} \tag{2.67}$$

The initial values of these surface charges are zero, if the electret has been metallized just before TSD. Eqs 2.67 complete the preceding ones, which all remain valid. The released current therefore again obeys Eq. 2.64, and only the dipole reorientation current is observed.

In summary, we can state that the current release by a nonuniform dipole polarization is just the *same* as that for a uniform one, provided that *mean values* are taken. With this restriction, all equations previously derived in Chap. 2 for a uniform dipole polarization remain valid.

Moreover, if current TSD is caused by the combined effects of *dipole reorientation* and ohmic conduction, only the former process is observed in *shorted* electrets containing dipoles and excess charges. This holds regardless of whether the electrodes are open or blocking. This behaviour benefits fundamental studies on dipolar relaxations of polymers. We have seen in Chaps 1 and 10 that the main part of the thermograms of heterocharged polymers viz. that from cryogenic temperatures up to T_g, exhibits dipolar features. However, *above* T_g another current peak often emerges, that is not due to dipole reorientations, but which arises from SCL drift and diffusion of the excess charges themselves. These motions were considered in Chap. 5.

5:6 Estimates for Hetero- and Homocharging by Space Charges

In Sect 5:1 we reviewed the general transport equations and boundary conditions for excess charge motion in dielectrics. The transport equations are nonlinear PDE's for which no general solution is known, not even for the isothermal steady state. Nevertheless, there are two interesting approximate solutions, derived long ago, which allow one to estimate the heterocharging of electrets by the accumulation of space charges near the forming electrodes.

5:6.1 Estimates for Heterocharging

The calculation of this estimate is based on the following method. We have seen from the nonisothermal charging of polymers by the orientation of dipoles that most of the polarization arises during the isothermal part of the charging period at the forming temperature T_f (cf. Fig. 2-1). The same will be true for excess charge polarizations. Moreover, we are not so much concerned with the transient behaviour, when the applied voltage is switched on, as with the final charge reached at time t_f (Fig. 2-1) where the *steady state* prevails.

Of the two approximate solutions known for this case, the first is due to Jaffé (Ja 33) and the second to Thomson, Mie and Herzfeld (He 29); see also Croitoru (Cr 65). Jaffé's solution is based on *blocking* electrodes (which present the outflow of particle currents at the electrodes), and neglects dissociation and recombination. Hence, Jaffé's theory accounts only for *field drift* and *diffusion* in the charge transport equations 5.1 and 5.2. A simplified version of this solution, in which the forming field is taken uniform, has been outlined in Sect. 5:5. The TMH theory, on the other hand, disregards diffusion, and is valid for *open* electrodes. This theory thus considers the charge transport to be governed by *dissociation, recombination* and *field drift*. Antenen (An 56) studied the application of both theories on carnauba wax electrets; his results agreed best with TMH theory. This is not surprising, since in electret charging field drift dominates over diffusion owing to the high field applied.

Assuming equal carrier mobilities $\mu_p = \mu_n = \mu$, the TMH theory gives the following approximate relations for the internal field after the isothermal formation period at T_f and t_f

$$
\begin{aligned}
E(x) &\simeq E(o)\sqrt{\ell^{-1}(T_f) + \exp\{-2x/\bar{r}(T_f)\}} && 0 < x < x_k \\
E(x) &\simeq E(o)\sqrt{\ell^{-1}(T_f)} && x_k < x < 1-x_k \\
E(x) &\simeq E(o)\sqrt{\ell^{-1}(T_f) + \exp\{-2(1-x)/\bar{r}(T_f)\}}, && 1-x_k < x < 1
\end{aligned}
\qquad (5.82)
$$

where $\ell(T_f)$ is Langevin's constant, $\ell(T_f) = 2\mu(T_f)/\varepsilon_o\varepsilon R$, with R being the recombination constant, and $\bar{r}(T_f)$ is the mean spatial width of the space charge layers. If $\ell(T_f) >> 1$, $\bar{r}$ is given by

$$\bar{r}(T_f) = x_k(1 + x/4x_k)\sqrt{2\ell^{-1}(T_f)}$$

Note that x_k demarcates the validity regions of the three approximations of E(x). Obviously, for $x_k < x < 1-x_k$ the sample is free of excess charges. Generally, x_k takes its ultimate value, so $x_k \simeq 1/2$, resulting in $\bar{r}(T_f) \simeq 1/\sqrt{2\ell(T_f)}$.

By inserting E(x) from Eq. 5.82 into Poisson's Eq. 5.5 the charge density stored at T_f can readily be calculated. Results for $\ell(T_f) = 50$ are shown in Fig. 5-31. The field E(x) is symmetrical, and it falls off sharply near the electrodes, where most of the positive and negative excess charges are accumulated.

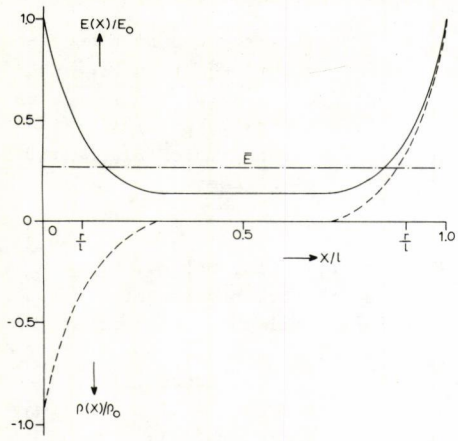


FIG.5-31 Local field (full line) and excess-charge density (broken line) after an isothermal heteropolar formation, according to the TMH theory, for $\ell(T_f) = 50$. The dotted and dashed line indicates the average field, $\bar{E}$.

The excess charge density also is symmetrical, by virtue of our assumption that the positive and negative carrier mobilities are the same. We recognized that the excess charge density hardly extends beyond $\bar{r}(T_f) = 0.1\ 1$, where it has dropped by a factor of e.

The mean value of the electric field $\bar{E}$, which is equal to $V_a/1$, is also indicated; it is much lower than the field near the electrodes E(o). This implies that excess charges may raise the charge storage capacity well above the value corresponding to its capacitance $\varepsilon_o\varepsilon V_a/1$. For large $\ell(T_f)$ we find by substituting Eq. 5.82 in the line integral for the electric field $\int_0^1 E(x,t)dx = V_a$:

$$V_a \simeq 2E(o)\bar{r}(T_f)$$

This equation indicates that most of the forming voltage is needed in the regions where the excess charges are stored, whereas without excess charge polarization we should have

$$V_a = E(o)1$$

because then the field is uniform. Now the induced charge on the electrodes by the excess charges is given by

$$\sigma(o) = -\varepsilon_o\varepsilon E(o)$$

Obviously, this charge is equal to $\varepsilon_o\varepsilon V_a/2\bar{r}$ rather than the normal value of $\varepsilon_o\varepsilon V_a/1$. Hence, the excess charge polarization *enhances* charge storage with the factor

$$1/2\bar{r}(T_f) = \sqrt{\ell(T_f)/2} \qquad \ldots(5.83)$$

Moreover, we see that for $\ell(T_f) >> 1$ the induced charge increases linearly with the applied voltage.

Antenen found e.g. for carnauba wax $\ell(70^o) = 900$, resulting in a charging 21 times higher than the normal value of $\varepsilon_o\varepsilon V_a/1$. In Chap. 10 we reported similar increases for strongly polar polymers. Compare Tabel 10:2 which lists values of $q_r(\infty)/\varepsilon_o\bar{E}$ up to 103, i.e. 34 times ε, when $\varepsilon = 3$.

5:6.2 Estimates for Homocharging

Likewise, space charges may be created during homocharging. In particular, at high forming temperatures the injected carriers may penetrate into the poly-

mer. Recently, Schneider and Watson (SW 71) pointed out that this carrier injection may be regarded as being space-charge limited, and they argued that it can be described as a steady-state phenomenon.

Since diffusion is normally small, we have for the steady state current density of a positive carrier injection at x = 0

$$j = \mu(T)p(x)E(x) \tag{5.84}$$

in which p(x) and E(x) are related by Poisson's equation

$$\varepsilon_o \varepsilon dE(x)/dx = p(x) \tag{5.85}$$

Substitution of Eq. 5.85 in 5.84, followed by integration, gives

$$2jx = \varepsilon_o \varepsilon \mu(T)\{E^2(x) - E^2(o)\}$$

On eliminating E(x) and E(o) by 5.84 it is easily verified that the injected charge density obeys

$$1/p^2(x) = 1/p^2(o) + 2x\mu(T)/\varepsilon_o \varepsilon j \qquad \ldots(5.86)$$

Thus, to calculate p(x), the charging current density j should be measured. Note that the charge density on the injection side p(o) follows from Eq. 5.84 at x = 0. At this position we have E(o) ≈ 0, since the field in the adjacent ionized air will be low. As a result p(o) is large, so that the injected homocharge density drops sharply with increasing x. This is plausible, because most of the homocharges have been implanted on the injection side. Compare Fig. 5-32, which represents the calculated injection pattern of a one-sided metallized foil at high forming temperatures. We took E(o) = 0 by which the variables μ(T) and j are dropped when the charge-density ratio p(x)/p(1) is calculated from Eq. 5.86. As in Fig. 5-31 the mean depth of the space charge layer

$$\bar{r} = \int_0^1 xp(x)dx / \int_0^1 p(x)dx$$

is indicated; it amounts to $\bar{r}$ = 0.33 1.

Finally, it is instructive to introduce the applied voltage into the equations. Noting that $V_a = \int_0^1 E(x)dx$, we readily verify that

$$j = 9\varepsilon_o \varepsilon \mu(T) V_a^2 / 8\ 1^3 \tag{5.87}$$

and

$$\int_0^1 p(x)dx = 3\varepsilon_o \varepsilon V_a / 2\ 1 \qquad \ldots(5.88)$$

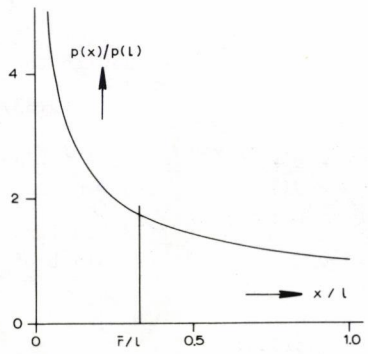


FIG.5-32 Spatial distribution of unipolar homocharges injected at x = 0 from breakdown in the air gap between the electrode-polymer interface, according to Schneider et al.

if $E(o) \simeq 0$, i.e. if the voltage across the ionized air gap can be neglected. Equation 5.87 shows that the current increases with the carrier mobility. Such a behaviour was indeed observed for homocharge injection into Teflon-FEP, where the positive ions have a higher mobility than the electrons (presumably because they are less frequently trapped). At T_f = 200 °C, and $V_a = \pm$ 1 kV, we found j_{pos} = +2.5 pA/cm^2 and j_{neg} = -0.4 pA/cm^2.

Equation 5.88 shows that the net charge is only 1.5 times greater than $\varepsilon_o \varepsilon V_a/l$, and that it grows linearly with the applied forming field. However, it should be remembered that the charge on the uncovered side of an electret is limited by air breakdown, since when the charge density is too high, the electret induces a back discharge, which partly neutralizes it. Calculations on the ultimate permissible charge have been published by Roos (Ro 69) and Schäffert (Sc 65).

5:7 Particle Flow Lines for Uniform Charge Profiles in Current and Charge TSD

In the theory given in Sect. 5:3, on the SCL drift of excess charges in shorted electrets, we supposed that any uniform charge distribution will retain its form during TSD. This will now be proved by considering the course of the relevant quantities along the characteristics of the PDE's involved. These characteristic curves, in fact, correspond to the particle flow lines in the x-t plane. In particular, we shall illustrate in greater detail the spatial-expansion for the uniform charge within a nonconducting polymer (cf. Fig. 5-1). This will enable us to indicate which part of the excess carriers will travel to the left electrode, and which part will remain in the electret when the current flow stops. First we shall consider current TSD.

5:7.1 Flow Lines for SCL Drift in Current TSD of Shorted Mono-Electrets

We shall broadly follow the approach advocated by Many et al. (MR 62) in their discussion on transient SCL currents in solids under an applied voltage stress.

Upon neglecting, in Eq. 5.14 the intrinsic ohmic conduction of the polymer and eliminating $\partial E(x,t)/\partial x$ with Poisson's equation, the continuity equation becomes

$$\partial p(x,t)/\partial t + \mu(T)E\partial p(x,t)/\partial x = -\mu(T)p^2(x,t)/\varepsilon_o\varepsilon$$

of which the ordinary differential equations for the characteristics are

$$dt = dx(t)/\mu(T)E(x_t,t) = -\varepsilon_o\varepsilon dp(x_t,t)/\mu(T)p^2(x_t,t) \qquad (5.89)$$

Since $x = f(t)$, we have attached the subscript t to the x-values. The first of these equations, viz.

$$dx_t/dt = \mu(T)E(x_t,t) \qquad (5.90)$$

describes the trajectories or flow lines of the carriers in the x-t plane. Along these flow lines, p and E take particular values. According to Eq. 5.89 we have for p

$$dp(x_t,t)/dt = -\mu(T)p^2(x_t,t)/\varepsilon_o\varepsilon \qquad (5.91)$$

while for E we have

$$dE(x_t,t)/dt = \partial E/\partial t + \partial E/\partial x_t dx_t/dt = \partial E(x_t,t)/\partial t + \mu(T)p(x_t,t)E(x_t,t) = j_r(t)/\varepsilon_o\varepsilon \qquad (5.92)$$

Apparently, along the flow lines the displacement current *equals* the discharge current.

Restricting ourselves to the *isothermal* case, we obtain by integrating Eq. 5.91 for the space-charge density along the flowlines

$$p(x_t,t) = p(x_{to},t)\{1 + \mu(T)p(x_{to},t)t/\varepsilon_o\varepsilon\}^{-1} \qquad (5.93)$$

We recognize that if the initial value $p(x_{to},o)$ is the same for every x_{to}, the later values $p(x_t,t)$ will likewise be the same for every x_t. This justifies our assumption of Sect. 5:3, that any uniform distribution will *continue* to be uniform.

In order to indicate the shape of the flow lines, we substitute the appropriate $E(x,t)$ (see below Eq. 5.20) into Eq. 5.90; this yields for $0 \leq t \leq \lambda$

$$dx_t/dt - \mu(T)p(x_t,t)x(t)/\varepsilon_o\varepsilon = -r(t)\{1-r(t)/2\ 1\}\mu(T)p(x_t,t)/\varepsilon_o\varepsilon \qquad ...(5.94)$$

where $r(t)$ is the flow line of the carriers at the leading front; its equation has been given before (see Eq. 5.26; note, however, that for the isothermal case $\mu(T)t$ replaces $\mu_o\xi(T)$). To the right of $r(t)$ no other flow line exists. As indicated, Eq. 5.94 holds for $t \leq \lambda$. The value of the transit time, λ, follows from Eq. 5.27, writing $\mu(T)\lambda$ for $\mu_o\xi(T_\lambda)$.

At $t \geq \lambda$ the space charge has spread completely, and $r(t) = 1$. Eq. 5.94 then yields upon integration with respect to time

$$(x_t - 0.5\ 1)\{x_\lambda - 0.5\ 1\}^{-1} = (1 + \mu(T)p_o t/\varepsilon_o\varepsilon)(1 + \mu(T)p_o\lambda/\varepsilon_o\varepsilon)^{-1} \qquad ...(5.95)$$

Obviously, for $t \geq \lambda$ all flow lines become straight. This implies, according to Eq. 5.90, that all the carriers experience a constant driving field, $E(x_t,t)$, which causes the discharge current $j_r(t)$ to vanish.

A family of flowlines in a half-filled mono-electret is shown in Fig. 5-33. They were calculated from Eq. 5.94 with a 4th order Runge-Kutta method (Bull-Honeywell subroutine package). We see that during $t \leq \lambda$ most of the flow lines,

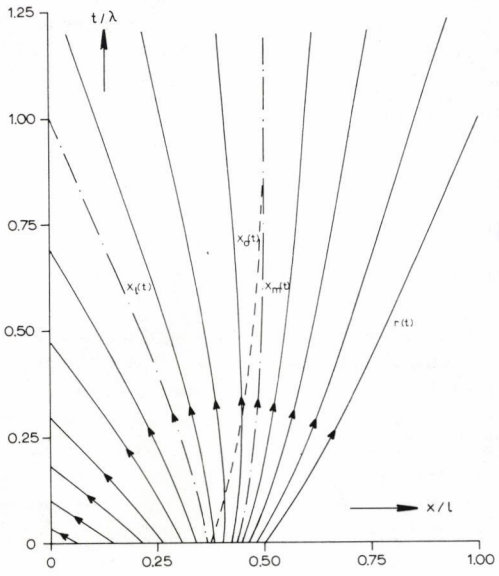


FIG.5-33 Trajectories or flow lines of carriers drifting, during an isothermal *current* discharge, in their own electric field towards their image charges at the two shorted electrodes. The particular flow lines $x_1(t)$, $x_m(t)$ and $r(t)$ are discussed in the text. The motion of the zero-field point, $x_o(t)$, is also shown (dashed line). It intersects all the flow lines between $x_1(t)$ and $x_m(t)$, which therefore show a turning point.

viz. those between $0 \leq x \leq x_1$, end at the left electrode, whereas only one flow line, r(t), reaches the right electrode. It is due to this asymmetry in charge motion that an external current arises. There exists one flow line $x_m(t)$ along which a carrier never reaches an electrode. This flow line terminates for $t = \lambda$ at 1/2, being the zero-field point from then on. Note, that the carriers starting between $x_o(o)$ and $x_m(o)$ first move to the right, but when they are passed by $x_o(t)$, they return to the left. If $t > \lambda$, the charges flow away symmetrically to both collecting electrodes, making $j_r(t) = 0$. The values of the most interesting carrier-starting points $x_1(o)$ and $x_m(o)$ are interrelated. From Fig. 5-33 we see that all charges stored between $x_1(o)$ and $x_m(o)$ drift during the transit time λ to the region $0 \leq x \leq 1/2$, whereas those between $x_m(o)$ and r_o drift towards the region $1/2 \leq x \leq 1$. Since the polymer is nonconductive, we have, by virtue of the conservation of the charge of the carriers

$$p_o\{x_m(o) - x_1(o)\} = p_o\{r_o - x_m(o)\} = p(x_o,\lambda)1/2$$

Combination of these equations gives the relationship

$$2\, x_m(o) = x_1(o) + r_o \tag{5.96}$$

Substitution of $p(x_o,\lambda)$ into Eq. 5.94 yields

$$x_m(o) = r_o - 0.5\ 1\ \exp\{-2(1-1/r_o)\} \tag{5.97}$$

For $r_o/1 = 0.5$, we find respectively $x_1(o) = 0.365\ 1$, $x_m(o) = 0.432\ 1$, while $x_o(o) = 0.375\ 1$. Hence, in this case, 73% of the charge carriers has moved towards the left electrode, when the current flow ceases; the remaining 27% still reside in the electret at $t = \lambda$. Note that $x_1(o)$ lies near the zero-field point at time $t = 0$; this is simple, because up to the zero-field point the field is directed to the left.

5:7.2 Flow Lines for SCL Drift in Charge TSD of Mono-Electrets

The derivation of the particle flow lines in open-circuit charge TSD follows the same lines. Because $j_r(t) = 0$, all flow lines are straight and their equations can be deduced from Eq. 5.90 in which we have for the field intensity, if the ohmic conductivity $\gamma(T) = 0$,

$$\begin{aligned} E(x,t) &= (p_o x/\varepsilon_o\varepsilon)\{1 + (p_o/\varepsilon_o\varepsilon)\textstyle\int_o^t \mu(T)dt\}^{-1} && x \leq r(t) \\ E(x,t) &= p_o r_o/\varepsilon_o\varepsilon && x \geq r(t) \end{aligned} \tag{5.98}$$

As a result we obtain

$$x_t/1 = (x_{t_o}/1)\{1 + (p_o/\varepsilon_o\varepsilon)\textstyle\int_o^t \mu(T)dt \tag{5.99}$$

This equation also holds for the leading front, which demarcates the flow line region.

A family of isothermal flow lines is shown in Fig. 5-34, they all point to the collecting electrode, to which the driving field is directed. Going to the left the carriers move more slowly, because they experience a lower accelerating field; the carriers at x = 0 even never arrive at the collecting electrode at x = 1, because E(o,t) = 0. The first carriers starting from r_o reach the collecting electrode at $t = \lambda$. At $t = 2\lambda$ the carriers between $0.33 \leq x(o)/1 \leq 0.5$ have reached the back electrode, and so on. Note that the diagram also applies to TSD, when the normalized time t/λ is replaced by $\int_o^t \mu(T)dt / \int_o^\lambda \mu(T)dt$.

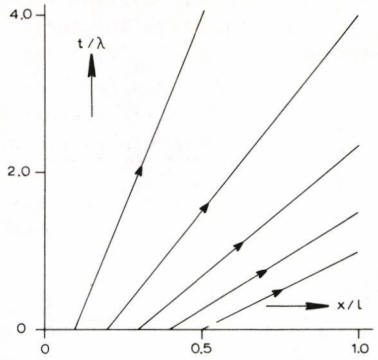


FIG.5-34 Particle flow lines in a nonconducting mono-electret foil during isothermal *charge* decay, by SCL drift towards the collecting electrode at x = 1.

5:8 SCL Drift of Uniform Excess Charges in Shorted Electrets with Blocking Electrodes

In treating the SCL drift of excess charges in Sects 5:3 and 5:4, we assumed the electret to be open, so that they do not hinder the outflow and neutralization of the particle conduction currents. It would be interesting to know whether the current and charge releases are modified if the electrodes are *blocking*. If they are, *surface charges* are built up at the polymer-electrode interfaces. In the following the blocking electrodes are considered to be in intimate contact with the electret, which is the case for evaporated electrodes. Nevertheless, the contact is poor in that it constitutes an energy barrier to charge exchange.

Let the mobile space charges be unipolar, and be uniformly distributed (cf. Fig. 5-1) to make an analytical solution feasible. In view of the blocking contacts we are left with displacement currents at x = 0 and 1, hence

$$j_r(t) = \varepsilon_o \varepsilon dE(o,t)/dt = \varepsilon_o \varepsilon dE(1,t)/dt \qquad (5.100)$$

Concurrently the particle currents at these boundaries will build up mere surface charges $\sigma_{1,2}$, because diffusion is absent. This charge conversion satisfies

$$d\sigma_1(t)/dt = -\{\mu(T)p(o^+,t) + \gamma(T)\}E(o^+,t) \qquad (5.101)$$

$$d\sigma_2(t)/dt = \{\mu(T)p(1^-,t) + \gamma(T)\}E(1^-,t) \qquad (5.102)$$

Initially we take both surface charges to be zero. Note that as long as the excess carriers have not reached the far electrode, i.e. for $t \leq \lambda$, the carrier density $p(1^-,t)$ in Eq. 5.102 will be zero as well.

Eq. 5.100 indicates that the space charge originally stored is conserved

$$\int_o^1 p(x,o)dx = \int_{o^+}^{1^-} p(x,o)dx + \sigma_1(t) + \sigma_2(t)$$

This equation relates the decaying space charge with the two surface charges which it creates. As for open electrodes, the space charge distribution will, again, remain uniform. The decrease in p(x,t) can therefore be described by Eq. 5.23.

For the released current, $j_r(t)$, we have, apart from Eq. 5.100, the simple Eq. 5.19, which now applies to $E(o^+,t)$ and $E(1^-,t)$. Hence

$$j_r(t) = (\varepsilon_o \varepsilon \mu(T)/2)1\{E^2(1^-,t) - E^2(o^+,t)\} \qquad ...(5.103)$$

The released charge follows from integrating Eq. 5.100 with respect to t

$$q_r(t) = \varepsilon_o \varepsilon\{E(1,t) - E(o,t)\} \qquad (5.104)$$

To derive the fields E(o,t) and E(1,t) we apply Gauss's law to the imaginary boundaries at o^+ and 1^-

$$E(o^+,t) - E(o,t) = \sigma_1(t)/\varepsilon_o\varepsilon$$

$$E(1,t) - E(1^-,t) = \sigma_2(t)/\varepsilon_o\varepsilon$$

where $E(o^+,t)$ and $E(1^-,t)$ can be found from Poisson's equation and the short-circuit condition. These in fact obey Eqs 5.15 and 5.16 and consequently

$$\varepsilon_o\varepsilon E(1,t) = \sigma_2(t) + p(x_o,t)r^2(t)/2\ 1 \qquad (5.105)$$

where the position of the leading front, r(t), satisfies Eq. 5.25.

According to Eq. 5.103 current flow ceases at $t = \lambda$, when the space charge cloud has spread completely over the specimen, and $E(o^+,t) = |E(1^-,t)|$. Then the ultimate charge is reached, for which we find, after substituting Eq. 5.105 into 5.104

$$q_r(\lambda) = \sigma_2(\lambda) + p(x_o,\lambda)1/2 - p_o r_o^2/2\ 1 \qquad (5.106)$$

Now, when intrinsic ohmic conduction is absent, i.e. $\gamma(T) = 0$, this equation reduces to the expression for shorted open electrodes, Eq. 5.32; since $\sigma_2(\lambda) = 0$, in virtue of Eq. 5.102, where $p(1^-,t) = 0$ up to $t = \lambda$.

When current flow stops, the conversion of space charges into surface charges continues at such a rate, that E(o,t) and E(1,t) remain constant. Reconsidering the space charge motion discussed in Sect. 5:7, see Fig. 5-33, the final values of $\sigma_{1,2}(\infty)$ can readily be deduced from $x_m(o)$. Obviously

$$\sigma_1(\infty) = p_o x_m(o) \quad \text{and} \quad \sigma_2(\infty) = p_o\{r_o - x_m(o)\} \qquad (5.107)$$

where $x_m(o)$ follows from Eq. 5.97.

Summarizing, we may conclude that with regard to SCL drift, there is *no difference* in current flow and charge release between shorted *open* and *blocking* electrodes, except that for the latter, surface charges are built up, which, however, do not alter the release. Consequently, if SCL drift dominates in current TSD of shorted electrets we cannot decide experimentally whether the electrodes are open or blocking. Our conclusion disagrees with that of Gross, who stated in (Gr 71) that for blocking electrodes $q_r(\lambda)$ would not satisfy Eq. 5.32 but would be equal to $-p_o r_o^2/2\ 1$, because he tacitly assumed that $E(1,\infty) = 0$, which we believe to be incorrect. However, for $r_o << 1$, Gross's result is a suitable approximation.

In practice, open and blocking electrodes may nevertheless behave differently, for when surface charges are created the diffusion will be intensified, which will generate a discharge current in the *normal* heteropolar sense, thus opposing to SCL drift current in one-sided homocharged foils (cf. Sect. 5:5).

5:9 Finite-Difference Schemes for the Solution of the PDE's for SCL Drift and Ohmic Conduction

This section discusses the finite-difference schemes for solving the PDE's describing the excess-charge decay by SCL drift and ohmic conduction during current TSD of shorted electrets. We mentioned in the introduction to Sect. 5:4 that most computations were carried out with the two-step Lax-Wendroff-Richtmeyer (LWR) scheme (RM 67), and with the central Wendroff-Thomée (WT) scheme (Th 62),

on the IBM-360 computer of the University of Technology in Delft. The modified LWR scheme proposed by Gourlay and Morris (GM 68) also functioned rather well, but the leap-frog scheme (Am 69) turned out to be inadequate for solving the present problem.

The three schemes applied have second-order accuracy, and are essentially predictor-corrector techniques. We shall discuss them briefly; for more details we refer to the pertinent literature (RM 67, Th 62, GM 68, Am 69, Mi 69, Ro 70). First we recall the principles of the 2nd order Runge-Kutta methods for ordinary differential equations, to which the LWR-schemes are similar.

Let us consider the differential equation

$$dy/dx = F(x,y)$$

In the modified Euler or polygon method, this equation is solved in two steps

$$\begin{aligned} y_{k+\frac{1}{2}} &= y_k + F_k \Delta x/2 \\ y_{k+1} &= y_k + F_{k+\frac{1}{2}} \Delta x \end{aligned} \tag{5.108}$$

where F_k stands for $F(x_k,y_k)$ and Δx is the x-interval used. Apparently, the first step is taken halfway. The improved Euler method or Heun's method, however, employs two full steps

$$\begin{aligned} y^*_{k+1} &= y_k + F_k \Delta x \\ y_{k+1} &= y_k + (F_k + F^*_{k+1})\, \Delta x/2 \end{aligned} \tag{5.109}$$

In both methods, the first step, being a predictor, has first-order accuracy; second-order accuracy is achieved in the second step, which is a corrector. Starting from a given initial value $y = y_1$ at $x = x_1$ one proceeds step by step to the next x-levels. The error of Eq. 5.108 is somewhat less than that of Eq. 5.109, but the latter has the advantage that its corrector can be used iteratively as follows

$$y_{k+1}{}^j = y_k + (F_k + F_{k+1}{}^{j-1})\Delta x/2 \tag{5.110}$$

5:9.1 LWR Scheme for Solving Hyperbolic PDE's

The LWR scheme corresponds to the polygon method and has been developed for conservative hyperbolic PDE's. Thus, it can be applied to PDE's of the type

$$\partial u(x,t)/\partial t = \partial F(u,x,t)/\partial x \tag{5.111}$$

in which $u(x,t)$ may be a vector with components $u_i(x,t)$. As pointed out by Wendroff (We 67), the scheme can be generalized to integrate

$$\partial u(x,t)/\partial t = \partial F(u,x,t)/\partial x + G(u,x,t) \tag{5.112}$$

This equation has the same structure as the continuity equation for SCL drift in conductive polymers (see Eq. 5.14) which, by virtue of Poisson's equation, may be converted into

$$\partial p(x,t)/\partial t = -\mu(T)\partial p(x,t)E(x,t)/\partial x + \beta(T)p(x,t) \tag{5.113}$$

For nonconductive polymers, $\beta(T) = 0$, and Eq. 5.113 becomes identical to Eq. 5.111

$$\partial p(x,t)/\partial t = -\mu(T)\partial p(x,t)E(x,t)/\partial x \tag{5.114}$$

Simultaneously with the local excess-charge density $p(x,t)$ we also have to find the local electric field $E(x,t)$; this is done by integration of Poisson's equation 5.15 with the trapezoidal rule

$$E_{i+1,k} = E_{i,k} + (p_{i+1,k} + p_{i,k})\Delta x/2\varepsilon_o\varepsilon \tag{5.115}$$

in which the first value $E_{1,k}$ is found from Eq. 5.16, using the extended trapezoidal rule

$$E_{1,k} = -\{p_{1,k}/2 + (n-1)^{-1} \sum_{i=2}^{n-1} p_{i,k}(n-i)\}\Delta x/\varepsilon_o\varepsilon \tag{5.116}$$

which comprises the sum over the entire specimen.

The LWR scheme to solve Eq. 5.111 is illustrated in Fig. 5-35 and reads

$$u_{i+\frac{1}{2},k+\frac{1}{2}} = (u_{i+1,k} + u_{i,k})/2 + (F_{i+1,k} - F_{i,k})\Delta t/2\Delta x \tag{5.117}$$

$$u_{i,k+1} = u_{i,k} + (F_{i+\frac{1}{2},k+\frac{1}{2}} - F_{i-\frac{1}{2},k+\frac{1}{2}})\Delta t/\Delta x \tag{5.118}$$

where $F_{i,k} = F(u_{i,k},x_i,t_k)$, $x_i = (i-1)\Delta x$ and $t_k = (k-1)\Delta t$.

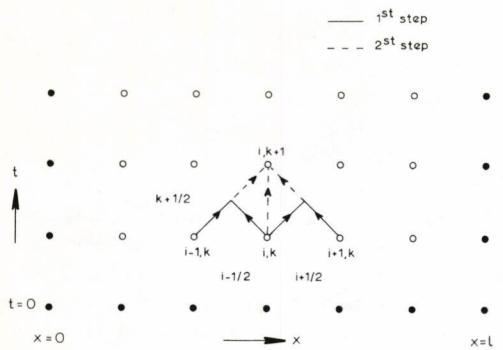


FIG.5-35 Triplet of mesh points used in the LWR scheme. The filled circles denote the necessary boundary and initial values.

For n-lattice points in the x-direction, i runs from 1 to n-1 in Eq. 5.117, and in Eq. 5.118 from 2 to n-1. Thus, with these finite-difference analogues applied to the local charge density $p(x,t)$ in Eq. 5.114 and the given boundary conditions $p_{1,k}$ and $p_{n,k}$ we can calculate the local charge density $p(x,t)$ successively at all k-time levels starting from a triplet of initial values, $p_{i,1}$. In order to apply Eqs 5.117 and 5.118 correctly, we also calculated the local field $E(x,t)$ in two steps. The E-values at a $k+\frac{1}{2}$-level were found from $p_{i+\frac{1}{2},k+\frac{1}{2}}$, and those at k+1 from $p_{i,k+1}$.*

*Gourlay and Morris's modification of the LWR scheme (GM 68) is equivalent to Heun's method. Applied to Eq. 5.111, it reads

$$u^*_{i,k+1} = (u_{i+1,k} - u_{i-1,k})/2 + (F_{i+1,k} - F_{i-1,k})\Delta t/2\Delta x$$

$$u_{i,k+1} = u_{i,k} + (F_{i+1,k} - F_{i-1,k} + F^*_{i+1,k+1} - F_{i-1,k+1})\Delta t/\mu\Delta x$$

The 2nd step is identical to an implicit scheme proposed earlier by Gary (RM 67). As in Heun's method, the corrector can be used iteratively; two iterations were found to be sufficient. The results agreed with those of the LWR scheme. For a uniform distribution, however, its results were less reliable; it moreover required more computer time, so that we abandoned this scheme.

The generalized LWR scheme for the continuity equation involving intrinsic ohmic conduction, Eqs 5.112 and 5.113, has the following structure

$$u_{i+\frac{1}{2},k+\frac{1}{2}} = (u_{i+1,1} + u_{i,1})/2 + (F_{i+1,k} - F_{i,k})\Delta t/2\Delta x + G_{i+\frac{1}{2},k}\Delta t/2 \qquad (5.119)$$

$$u_{i,k+\frac{1}{2}} = u_{i,k} + (F_{i+\frac{1}{2},k} - F_{i-\frac{1}{2},k})\Delta t/2\Delta x + G_{i,k}\Delta t/2$$

$$u_{i,k+1} = u_{i,k} + (F_{i+\frac{1}{2},k+\frac{1}{2}} - F_{i-\frac{1}{2},k+\frac{1}{2}})\Delta t/\Delta x + G_{i,k+\frac{1}{2}}\Delta t \qquad (5.120)$$

We see that u is now predicted twice, viz. at the grid points and halfway in between in order to find the functions $F_{i+\frac{1}{2},k+\frac{1}{2}}$ and $G_{i,k+\frac{1}{2}}$ of the corrector Eq. 5.120.

5:9.2 WT Scheme for Solving Hyperbolic PDE's

In the WT-scheme (Th 62), see Fig. 5-36, the derivatives are replaced by central differences in space and time. We thus take for the time and space derivatives of the local charge density p(x,t)

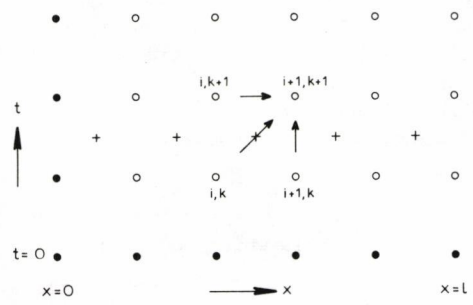


FIG.5-36 Triplet of grid points used in the WT scheme, which requires only one boundary condition (on the left).

$$(\partial p/\partial t)_{i+\frac{1}{2},k+\frac{1}{2}} = (p_{i+1,k+1} - p_{i+1,k} + p_{i,k+1} - p_{i,k})/2\Delta t$$
$$(\partial p/\partial x)_{i+\frac{1}{2},k+\frac{1}{2}} = (p_{i+1,k+1} - p_{i,k+1} + p_{i+1,k} - p_{i,k})/2\Delta x \qquad (5.121)$$

Similarly, the values of the local charge density p(x,t) and the local field strength E(x,t) are centred at the midpoint $i+\frac{1}{2},k+\frac{1}{2}$

$$p_{i+\frac{1}{2},k+\frac{1}{2}} = (p_{i,k+1} + p_{i+1,k+1} + p_{i,k} + p_{i+1,k})/4$$
$$E_{i+\frac{1}{2},k+\frac{1}{2}} = (E_{i,k+1} + E_{i+1,k+1} + E_{i,k} + E_{i+1,k})/4 \qquad (5.122)$$

In these central difference analogues, the quantities $E_{i,k}$, $p_{i,k}$, $p_{i+1,k}$ and $p_{i+1,k+1}$ are known. Substitution of Eqs 5.121 and 5.122 into the PDE 5.114 leads to a nonlinear equation for the unknown $p_{i+1,k+1}$. To linearize this equation, we solve it iteratively. For this purpose, we convert Eq. 5.114 with Poisson's equation into

$$\partial p(x,t)/\partial t = -\mu(T)E(x,t)\partial p(x,t)/\partial x - \mu(T)p^2(x,t)/\varepsilon_o\varepsilon \qquad (5.123)$$

Writing p_h for $p_{i+\frac{1}{2},k+\frac{1}{2}}$, e_h for $E_{i+\frac{1}{2},k+\frac{1}{2}}$, and introducing $ep = (e_h + p_h/2\varepsilon_o\varepsilon)\mu(T)\Delta t/\Delta x$ and $pe = (e_h - p_h/2\varepsilon_o\varepsilon)\mu(T)\Delta t/\Delta x$, we then obtain the following linearized equation for the space charge density at i+1,k+1

$$(1+ep)p_{i+1,k+1} = (pe-1)p_{i,k+1} + (1-ep)p_{i+1,k} + (pe+1)p_{i,k} \qquad (5.124)$$

We used for $p_{i+1,k+1}$ in p_h and e_h the values of the previous iteration and calculated $E_{i,k+1}$ from the $p_{i,k+1}$ values latterly obtained by Eq. 3.112. However, for the 1st iteration we put $p_{i+1,k+1} = p_{i+1,k}$, and $E_{i,k+1} = E_{i,k}$. In our computer programme two iterations were generally sufficient to attain a prescribed accuracy.

The solution of Wendroff-Thomée needs only *one* boundary condition, as can be seen from Fig. 5-36. We started the scheme at each k-level from the zero field point, at which the charge density $p(x_o,t)$ is known from Eq. 5.23. In doing so, we were able to disregard the ambiguity of the boundary conditions, see Eqs 5.128 and 5.129 below. Moreover, we integrate in the direction of the characteristic.

The WT scheme can easily be extended to include intrinsic conduction. We then linearize the continuity equation as follows

$$\partial p(x,t)/\partial t = -\mu(T)e_h\partial p(x,t)/\partial x - \{\mu(T)p_h + \gamma(T)\}p(x,t)/\varepsilon_o\varepsilon \qquad (5.125)$$

and solve Eq. 5.21 to obtain the charge density at the zero field point $p(x_o,t)$. The latter was again converted into an ordinary differential equation, by putting $\partial p(x_o,t)/\partial t \simeq dp(x_o,t)/dt$, which is approximately correct to 2nd order accuracy.

Later Thomée suggested a predictor for his scheme, to limit the number of iterations (Th 63). As had been found earlier by Von Rosenberg (Ro 70), this predictor-corrector scheme does not work faster than the normal scheme.

When the internal variables $p(x,t)$ and $E(x,t)$ are solved by one of the above-mentioned schemes, one can proceed to find the measurable quantities, $j_r(t)$ and $q_r(t)$. The released current is simply found from Eq. 5.19 which now reads

$$j_k = (\mu(T)\varepsilon_o\varepsilon/2\ 1)(E^2_{n,k} - E^2_{1,k}) \qquad (5.126)$$

while the released charge density was evaluated step by step on integrating the current by the trapezoidal rule

$$q_k = q_{k-1} + (j_k + j_{k-1})\Delta t/2 \qquad (5.127)$$

where the initial value $q_1 = 0$

Often the path of the zero field point was followed; this was done by applying inverse Lagrange interpolation in four nearby $E_{i,k}$ values*.

5:9.3 Programming of the Boundary Conditions

Up to now we have not discussed the insertion of the boundary conditions for open electrodes into the computer programme. We know from Sect. 5:1 that for open electrodes, which allow free neutralization of the excess charges by their image charges, the excess-charge density becomes zero at the electrodes (Eq. 5.8). However, for the application of finite differences this equation had to be replaced by

$$p(o^-,t) = p(1^+,t) = 0 \qquad (5.128)$$

which is valid for the region just *outside* the open interface, whereas just *inside* the open interface we take

$$p(o^+,t) = 0 \quad \text{and} \quad p(1^-,t) = 0 \qquad (5.129)$$

*C.J. Mifsud, "Interpolation by Aitken", Algorithm 70, Collected Algorithms Comm. Ass. Comp. Mach.

The latter conditions are evident from the figures given, in Sect. 5:3 for the charge distributions, of which the charges redistribute in such a way that $p(o^+,t)$ and $p(1^-,t)$ become nonzero. Thus in harmony with Eq. 5.129 we do not get depletion just inside an open interface, despite the fast discharge rate. Apparently, because the excess charges are supplied at too high a rate.

Consequently, the boundary values for which we should take $p(o^+,t)$ and $p(1^-,t)$ can no longer be prescribed, which handicaps the use of the fast LWR scheme. To overcome this difficulty, we calculated the boundary values by extrapolation, using the adjacent values obtained by the scheme. We applied Newton's 4th order forward and backward formula, according to which

$$p_{1,k} = 5\,p_{2,k} - 10\,p_{3,k} + 10\,p_{4,k} - 5\,p_{5,k} + p_{6,k}$$

$$p_{n,k} = 5\,p_{n-1,k} - 10\,p_{n-2,k} + 10\,p_{n-3,k} - 5\,p_{n-4,k} + p_{n-5,k}$$

However, for $r(t) < 1$ we simply took $p_{n,k} = 0$.

This extrapolation worked well. Seemingly, the LWR scheme is quite stable and needs no reference for $p(x,t)$ at each time level. We also found that it did not pay to correct the extrapolated values by means of the current equation.

A great advantage of the slower WT scheme is that it only requires one boundary condition, for which we took the charge density at the zero-field point $p(x_o,t)$. In this way the values at the electrodes follow unambiguously from the scheme. However, it should be realized that $x_o = f(t)$, so we must start on a different x-value at each time level. Though x_o is not known in advance, it can be predicted accurately. For this we used a 4th order forward Newton extrapolation.

$$x_o(t+\Delta t) = 4x_o(t) - 6x_o(t-\Delta t) + 4x_o(t-2\Delta t) - x_o(t-3\Delta t)$$

which gives more reliable values of $x_o(t)$ than the integral of Eq. 5.28.

In order to preserve the original difference mesh, we extrapolated from $p(x_o,t)$ to p at the nearest mesh point, say at $i_o = k+1$. For this purpose we applied a local WT scheme to the points (x_o,k), $(x_o, k+1)$, (i_o,k), $(i_o,k+1)$. The required value of $E(i_o,k+1)$ was found by forward extrapolation. Finally, all other $p(i,k+1)$ values are obtained from $p(i_o,k+1)$ by the normal scheme.

The WT scheme requires twice as much computer time as the LWR scheme, but it performs much better. For uniform distributions, in particular, the LWR scheme showed oscillations at large $p(x,t)$ gradients. These oscillations sometimes lead to negative $p(x,t)$ values, which were eliminated by putting $p(x,t) = 0$. Fortunately, such oscillations barely disturb the calculations of $j_r(t)$, for which the mean value of $p(x,t)$ over all x values is determinant.

6:3 Injection of Homocharges by Townsend Breakdown, Treated as a MW Charging

At present homocharging is preferred to heterocharging because it is fast and easily applicable to films. It has the further advantage of not being restricted to polar polymers. It is even better to inject the extrinsic charges into nonpolar polymers, which have a much higher resistivity (Fig. 2-4) and are less sensitive to water, and so from them electrets of an extreme longevity can be made.

In Sect. 5:6.2 we discussed the homocharging of foils and we described it as an SCL steady-state process, in which the reaction of the homocharges to the breakdown conditions in the air gap was neglected. Here this reaction will be taken into account. However, the injected charges will now be visualized simply as *surface charges;* this was also done in our treatment on MW effects in Chap. 6.

6:3.1 Homocharging of Nonpolar Polymers

We suppose the polymer to be metallized on the lower side, so let (in Fig. 6-1) layer 1 represent the effective air gap, i.e. the average height of the air inclusions between the adjoining upper electrode and the polymer. Without air breakdown the air gap is perfectly insulating, $\gamma_1(T) = 0$, and so the voltage across it, $V_1(t)$, tends to approach the applied voltage, V_a, compare Eq. 6.9. However, if V_a exceeds the breakdown voltage V_b of the air gap*, a discharge will be ignited. This will raise $\gamma_1(T)$ from zero to a very low value of, say, $\gamma_e(T)$* and the increase in $V_1(t)$ will be stopped. Instead, $V_1(t)$ will decrease towards a minimum value, which equals

$$V_1(\infty)/V_a \simeq \gamma(T)1_1/\gamma_e(T)1 \qquad (6.26)$$

(provided that the conductivity of the air $\gamma_e(T)$, is much smaller than that of the polymer $\gamma(T)$, as is usual the case). This decrease will be cut off as well, when $V_1(t)$ reaches the extinction voltage, V_e, of the air gap. Then the cycle starts again, with $\gamma_1(T)$ being zero, etc. Apparently, we have a special MW charging, with $V_1(t)$ the air-gap voltage $V_1(t)$ varying periodically.

Nevertheless, the ODE for $V_1(t)$, Eq. 6.5, remains valid, when $\gamma_1(T)$ is taken properly zero or $\gamma_e(T)$. In addition, the initial values of $V_1(t)$, which vary cyclically between V_b and V_e, must be adapted. Calculated curves for the isothermal period of the homocharging at the forming temperature T_f are shown in Fig. 6-11. The calculations were done for $V_b = 0.15\ V_a$, $V_e = 0.1\ V_a$, $\varepsilon/1 = 0.25\ \varepsilon_1/1_1$, and $\gamma(T)/1 = 0.1\ \gamma_e(T)/1_1$. For these parameter values (which apply

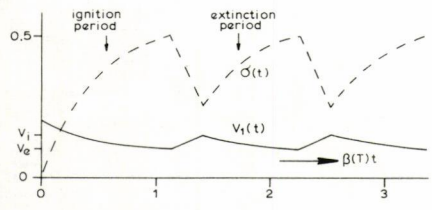


FIG.6-11 Calculated time dependence of the reduced voltage across the air gap, $V_1(t)/V_a$, and the reduced injected surface charge, $\sigma(t)1/\varepsilon_o\varepsilon V_a$, during homocharging of polymers *without* dielectric absorption. In the rising parts of $\sigma(t)$ the air gap is ignited, while in the declining parts it is extinguished. The parameter values are given in the text.

*Note that the breakdown voltage is a function of the gap width (Paschen curve); the minimum value for air amounting to 360 V (see (Ro 69)).

to relatively thick samples at high forming temperatures) we have $V_1(o) > V_b$, which results in immediate breakdown. Reduced units are used: $V_1(t)$ is divided by V_a and $\sigma(t)$ by $\varepsilon_o \varepsilon V_a/l$, while t is multiplied by the ohmic relaxation frequency of the polymer $\beta(T) = \gamma(T)/\varepsilon_o\varepsilon$. The resulting voltage waveform, $V_1(t)/V_a$, resembles that of a *relaxation oscillator*. Its sections are composed of two different exponentials. As can be seen, the injected homocharge, $\sigma(t)$, which acquires a maximum of $0.5\ \varepsilon_o \varepsilon V_a/l$, exhibits an inverted similar waveform. Likewise the homocharging current varies, which makes it noisy; this is well-known experimentally. Measurements are under way to verify the calculated voltage waveforms by means of an oscilloscope.

In contrast to a heterocharging, the homocharging is created almost *at once*, which offers a great advantage in practice. We see from Fig. 6-11 that the homocharge already reaches its maximum after the first breakdown surge. From Eq. 6.8 we easily verify that the maximum amounts to

$$\sigma_{max} = \varepsilon_o \varepsilon (V_a - V_e)/l - \varepsilon_o \varepsilon_1 V_e/l_1 \qquad ...(6.27)$$

after which the charge decreases (owing to charge neutralization by internal ohmic conduction of the polymer) to a minimum value

$$\sigma_{min} = \varepsilon_o \varepsilon (V_a - V_b)/l - \varepsilon_o \varepsilon_1 V_b/l_1 \qquad ...(6.28)$$

during the extinction period. Since $V_b \simeq V_e$, we have $\sigma_{max} \simeq \sigma_{min}$. Note that the injected homocharge can never exceed the charge density, $\varepsilon_o \varepsilon V_a/l$, corresponding to the capacity of the polymer.

For Teflon-FEP foil of 25 μm, we obtained a homocharge of 50 nC/cm^2 at V_a = 1.7 kV, whereas Eq. 6.27 predicts σ_{max} = 95 nC/cm^2 (ε = 2, V_e = 360 V), which is substantially higher. This inconsistency is due to the fact that when the applied voltage is switched off, Eq. 6.8 gives for the air-gap voltage

$$V_1(t_s) = \sigma(t_s)/\varepsilon_o(\varepsilon_1/l_1 + \varepsilon/l)$$

This voltage might well be above the breakdown voltage. As a result the homocharge created is unstable and is partly neutralized by a back discharge, which reduces it to about 50 nC/cm^2. This value agrees well with Roos's calculations of the maximum charge density attainable on foils in ambient air (Ro 69).

6:3.2 Homocharging of Polar Polymers

Measurements on the homocharging of PMMA electrets during the isothermal formation, and the cooling period are shown in Fig. 6-12. The results were obtained with an inductive charge meter of the elevating type (Tu 66, Tu 70a), which was operated by a solenoid. As can be seen, the charge barely changes during the isothermal part of the formation at T_f, and also it hardly changes during the cooling period. The drop at the removal of the forming field is due to the disappearance of the instantaneous polarization $\varepsilon_o \varepsilon_\infty V_a/l$, which also contributed to the charge measured. At high field strengths (50 kV/cm) the final net charge is homopolar, whereas at low field strengths (10 kV/cm), when no breakdown takes place, it is heteropolar. The remaining heterocharge at 10 kV/cm originates from the oriented frozen-in dipoles.

To account for dielectric absorption during homocharging of polymers, we introduce the persistent polarization $P_s(t)$ in the equations containing E(t). Taking from now on the dielectric constant of the air ε_1 = 1, Eq. 6.1 changes

to

$$j(t) = \varepsilon_0 dE_1(t)/dt + \gamma_1(T)E_1(t) = \varepsilon_0\varepsilon_\infty dE(t)/dt + \\ + dP_s(t)/dt + \gamma(T)E(t) \qquad (6.29)$$

while Eq. 6.8 becomes

$$\sigma(t) - P_s(t) = \varepsilon_0\varepsilon_\infty V_a/l - \varepsilon_0(1/g + \varepsilon_\infty/l)V_1(t) \qquad (6.30)$$

where the charge $\sigma(t) - P_s(t)$, being the difference between the injected homocharge and the persistent polarization, is termed the *effective charge density* of the polymer, q(t).

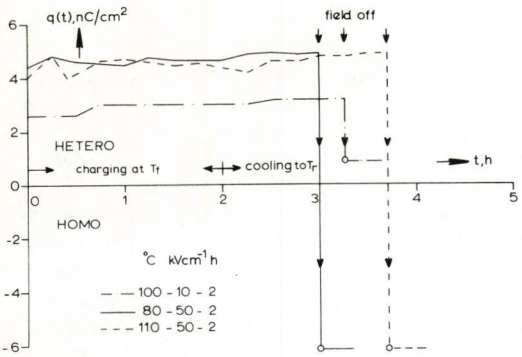


FIG.6-12 Measured time dependence of the surface charge density during the formation of PMMA electrets. The isothermal charging period at T_f lasts for 2 hrs, then the cooling is started which takes different times. When at room temperature the forming field is switched off, the charge drops sharply due to the disappearance of the instantaneous polarization. The net charge remaining is semipermanent: this is homopolar at high field strengths (50 $kVcm^{-1}$), and heteropolar at low field strengths (10 $kVcm^{-1}$).

On eliminating E(t) from Eq. 6.29 by means of Eq. 6.2 and writing g (*g*ap) for l_1, we find as new differential equation for the air-gap voltage $V_1(t)$

$$dV_1(t)/dt + \beta_g(T)V_1(t) = \frac{dP_s(t)/dt + \gamma(T)V_a/l}{\varepsilon_0(1/g + \varepsilon_\infty/l)} \qquad (6.31)$$

in which the rate constant $\beta_g(T)$ has been defined in Eq. 6.5.

Furthermore, if the dipoles react with a single Debye relaxation we have

$$dP_s(t)/dt + \alpha(T)P_s(t) = \varepsilon_0(\varepsilon_s - \varepsilon_\infty)\alpha(T)\{V_a - V_1(t)\}/l \qquad (6.32)$$

As outlined in Sect. 6:2.1, the Eqs 6.31 and 6.32 can be solved numerically to give the unknowns $V_1(t)$, and $P_s(t)$ or rather q(t). The initial values are $P_s(o) = \sigma(o) = 0$, while $V_1(o)$ again obeys Eq. 6.6. Results for the isothermal formation period obtained by an integration with a 4th order Runge-Kutta method are shown in Fig. 6-13. The calculations were carried out for $V_b = 0.15\ V_a$, $V_e = 0.1\ V_a$, $\varepsilon/l = 0.25\ \varepsilon_1/l_1$, $\gamma(T)/l = 0.1\ \gamma_1(T)/l_1$, $\alpha(T) = 5\ \beta(T)$ and $\varepsilon_s = 2\ \varepsilon_\infty$. We observe a similar trend as in Fig.6-11, the main difference being that now each section of the curves is determined by two exponentials, so that the recovery sections are slightly enlarged. Apart from its very beginning, when $P_s(t)$ dominates, the effective charge density q(t) varies between the same values as previously did $\sigma(t)$. Note that the changes in $V_1(t)$, which are relatively small compared to V_a, hardly affect $P_s(t)$.

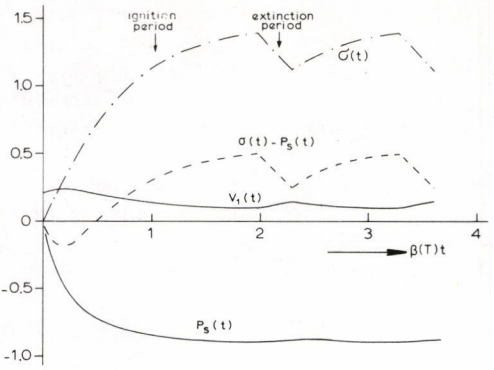


FIG.6-13 Time dependence of the relevant quantities during homocharging of polymers *with* dielectric absorption. The injected charge density $\sigma(t)$, the net charge density $\sigma(t)-P_s(t)$ and the persistent polarization $P_s(t)$ are normalized to $\varepsilon_o\varepsilon V_a/l$, while the air-gap voltage $V_l(t)$ is normalized to V_a. The net charge density varies between the same limits as $\sigma(t)$ in Fig. 6.2 (see text for parameter values).

We are now in a position to explain Fig. 6-12 further. If we disregard the last term in Eq. 6.30 we obtain for the final homocharge $q_{max} \simeq \varepsilon_o\varepsilon_\infty V_a/l$, which would amount to 11 nC/cm^2 at 50 kV/cm. However, such a large charge creates after the short-circuit an external field that again exceeds the breakdown field. This charge is therefore partly neutralized by a back discharge, so that experimentally we have only found a homocharge of q_{max} = 6.1 nC/cm^2. This value is eight times lower than the permissible charge for foils, from which back discharge takes place less easily, because the external field of the foil drops more sharply with distance (see further (Ro 69)).

For laid-on forming electrodes our description of homocharging is an oversimplification. In that case, the width of the air gap is not uniform and the theory merely holds for local breakdown in the air inclusions; for at points of intimate contact breakdown does not occur. As a result, the homocharge is not evenly distributed.

To improve its uniformity we have developed a special formation (Tu 68), which uses a gap of about 5 mm, wherein a stationary plasma is formed by a capacitive gas discharge at radiofrequency. Alternatively, a scanning corona discharge may be used as advocated by Creswell and Perlman (CP 70). Another promising technique is charge injection in a vacuum by electron bombardment (SW 70), the electrons being subjected to acceleration energies of 25 keV. This method, however, is only feasible for foils, as thick samples would be largely neutralized by back discharges when air is let in, and the breakdown voltage passes through its minimum value of 360 V.

Another charging arrangement commonly used for one-sided metallized foils consists of a three layer system and embodies a relatively thick semiconductive insert between the upper electrode and the foil (PR 68)*. This insert avoids, even at high forming voltages, breakdown punctures in thin foils and therefore allows the attainment of higher homocharge densities. This sandwich system can be analyzed in the same way. Instead of Eq. 6.27 or 6.30, one finds for the ultimate charge density

$$\sigma(t) - P_s(t) = \varepsilon_o\varepsilon(V_a - V_i - V_e)/l - \varepsilon_o V_e/g$$

* "Unilaterally Metallized Electret Foil", Canad. Patent 878178, granted to TNO, Delft, Aug. 10, 1971.

"Electrets and Methods of Making Them", English Patent Application, a 53688/70, filed by TNO, Delft, Nov. 11, 1970.

where V_i denotes the voltage drop across the insert. Obviously, to get a gain in homocharge, the voltage difference $V_a - V_i$ should exceed V_a without insert. We also applied this sandwich structure for obtaining electret fibres**.

It is well-known that the breakdown strength of air depends on the gap width (Paschen curve). With electrodes that touch the polymer, i.e. when the effective air gap is extremely narrow, relatively high forming voltages are needed to achieve homocharging. To facilitate the breakdown, we have introduced an insert with an *open* structure, viz. glass cloth of 0.12 mm thickness. The polymer can then be homocharged at quite low forming voltages (for 25 μm foils from 600 V onwards). Consequently, this is another method to avoid disruptive breakdown through the foil.

** "Device for Forming Electrets", Canad. Patent 858140, granted to TNO, Delft, Dec. 8, 1970.

7:3 Current TSD of Nonmetallized Electrets Sandwiched Between Two Air Gaps

In the beginning of our TSD research we unfortunately used two air gaps (Tu 68) and applied nonmetallized samples, not only during the formation, but also during TSD. Then, when the electret is made, two surface charges $\sigma_{1,2}(t)$ may be created, besides a dipole polarization $P_s(x,t)$ and a space charge $\rho(x,t)$. Both surface charges will decay in the course of the subsequent current TSD. As a result we have two continuity equations like Eq. 7.3, one for the interface near the upper gap, and the other for that near the lower gap. Similarly, the number of boundary equations (7.4) and current equations in the air gap is doubled. Indexing the quantities pertaining to the two air gaps with 1 and 2 we have

$$d\sigma_1(t)/dt = -\gamma(T)E(o,t) \; ; \; d\sigma_2(t)/dt = \gamma(T)E(1,t) \tag{7.46}$$

$$\varepsilon_o\varepsilon_\infty E(o,t) + P_s(o,t) - \varepsilon_o E_1(t) = \sigma_1(t)$$

$$\varepsilon_o E_2(t) - \varepsilon_o\varepsilon_\infty E(1,t) - P_s(1,t) = \sigma_2(t) \tag{7.47}$$

and

$$j_r(t) = \varepsilon_o dE_1(t)/dt = \varepsilon_o dE_2(t)/dt \tag{7.48}$$

Moreover, we have as the short-circuit condition instead of Eq. 7.6

$$E_1(t)g_1 + \int_o^1 E(x,t)dx + E_2(t)g_2 = 0 \tag{7.49}$$

According to Gauss's law, the difference between the two external fields $E_{1,2}(t)$ is determined by the total excess-charge density stored in the electret

$$\varepsilon_o\{E_2(t) - E_1(t)\} = \sigma_t(t) \tag{7.50}$$

where

$$\sigma_t(t) = \sigma_1(t) + \sigma_2(t) + \int_o^1 \rho(x,t)dx \tag{7.51}$$

Note that for a neutral electret, for which the positive and negative excess charges are equal, $\sigma_t(t) = 0$. From Eq. 7.48 it follows that

$$d\sigma(t)/dt = 0, \text{ and therefore, } \sigma_t(t) = \sigma_t(o)$$

This means that the total charge remains *constant*, simply because the two perfectly insulating air gaps prevent the total electret charge to drain away.

The external field in the upper gap depends on the charges present in the electret, by invoking Poisson's equation we can derive, similarly to the situation for one air gap

$$\varepsilon_o E_1(t)(1+\varepsilon_\infty g^*) = -\sigma_1(t)1 + \int_o^1 P_s(x,t)dx - \int_o^1 \rho(x,t)(1-x)dx - \varepsilon_\infty g_2\sigma(o) \tag{7.52}$$

where $g^* = g_1 + g_2$. This equation differs from Eq. 7.14 only in the last term. Correspondingly, the decay equation 7.11 and the Debye equation 7.13 are altered, these now take the form

$$dE_1(t)dt + \beta g^*(T)E_1(t) = \{\frac{d}{dt}\int_o^1 P_s(x,t)dx - \sigma_t(o)\gamma(T)g_2/\varepsilon_o)\}/\varepsilon_o(1+\varepsilon_\infty g^*) \tag{7.53}$$

and

$$\frac{d}{dt}\int_o^1 P_s(x,t)dx + \alpha(T)\int_o^1 P_s(x,t)dx = -\varepsilon_o(\varepsilon_s-\varepsilon_\infty)\alpha(T)\{g^*E_1(t) + g_2\sigma_t(o)/\varepsilon_o\} \tag{7.54}$$

Obviously, if the lower air gap is zero, i.e. $g_2 = 0$, the last term in each of the three equations disappears and they reduce to Eqs 7.14, 7.11 and 7.13 as

they should.

Because the sum of the excess charges, σ_t, remains constant*, the external fields and in particular $E_1(t)$ will not fall to zero when t becomes infinite. Hence, at the end of the TSD experiment the electret still induces an image charge on the upper electrode. Nevertheless, in that time the steady state must have been reached, so that $dE_1(\infty)/dt$ and $\frac{d}{dt}\int_0^1 P_s(x,\infty)dx$ will be zero, and Eq. 7.53 gives

$$\varepsilon_0 E_1(\infty) = -\sigma_t(o)g_2/g^* \qquad (7.55)$$

We easily verify, via Eqs 7.51 and 7.50 that Eq. 7.55 implies the total excess charge to be finally spread in such a way that the average field within the sample becomes zero: $\int_0^1 E(x,\infty)dx = 0$. This is plausible, because otherwise the average ohmic conduction current would not become zero, so that the ohmic dissipation of the excess charges would not stop.

Integrating Eq. 7.48, we again find for the released charge density the expression 7.9 which, in view of Eqs 7.52 and 7.55, for the ultimate charge density yields

$$q_r(\infty) = (1+\varepsilon_\infty g^*)^{-1}\{\sigma_1(o)1 - \int_0^1 P_s(x,o)dx + \int_0^1 \rho(x,o)(1-x)dx - 1\sigma_t(o)g_2/g^*\} \qquad \ldots(7.56)$$

Comparison of this equation with Eqs 7.16 and 7.19 shows that, owing to the 4th term in Eq. 7.56, the TSD results for one air gap and two air gaps will differ, unless the electret as a whole is electrically neutral, which is rather exceptional.

In particular, if there are no space charges and no dipole polarization we find

$$q_r(\infty) = \{\sigma_1(o) - \sigma_2(o)\}/2(1 + \varepsilon_\infty g^*/1)$$

where we have taken into account that, experimentally, $g_{1,2} = g^*/2$. Consequently, for a unipolar electret with equal surface charges $\sigma_1(o) = \sigma_2(o)$, we obtain $q_r(\infty) = 0$, and no charge is released at all. This is so because the electric field in the sample is now zero from the beginning, so that there is neither an internal nor an external conduction current.

There is still another difference in that the induction loss, manifested in the term $1 + \varepsilon_\infty g^*/1$, is greater for two gaps, because $g^* > g_1$. Consequently, the ultimate released charge will always be lower than for one air gap.

Summarizing we have found that two air gaps release less charge, in addition their mathematics is more complex than for a single one. Moreover, when suspended between two air gaps, e.g. by means of Teflon stickers, the electret may sag during TSD. Use of a single air gap is therefore recommended.

7:4 Air-Gap Current TSD of Electrets with Multiple Dipole Relaxations

In discussing the air-gap current TSD in Chap. 7, we have assumed the dipoles to respond according to a single Debye equation. However, we know that for most polymers a distributed polarization is more likely. Before discussing the formal solution of a continuous distribution we consider the behaviour of a

*The different terms that represent the total excess charge do change, however, for the space charges will, in general, be converted into surface charges, and so the field in the electret becomes zero.

discrete distribution of two polarizations.

Denoting the space averages of both polarizations by $P_1(t)$ and $P_2(t)$, we have instead of Eq. 7.1

$$dP_{1,2}(t)/dt + \alpha_{1,2}(T)P_{1,2}(t) = \varepsilon_0(\varepsilon_s - \varepsilon_\infty)_{1,2}\alpha_{1,2}(T)E(t) \qquad (7.57)$$

while Eq. 7.20, which describes the excess charge decay, becomes

$$dq(t)/dt + \gamma(T)E(t) = -dP_1(t)/dt - dP_2(t)/dt \qquad (7.58)$$

where the internal field depends on the effective electret charge according to

$$E(t) = gq(t)/\varepsilon_0(1 + \varepsilon_\infty g) \qquad (7.59)$$

We have solved this set of ODE's numerically by a Runge-Kutta method, for the initial values $P_{1,2}(o)$ and $q(o) = Q(o) - P_1(o) - P_2(o)$.

As an example we envisaged a two-sided metallized electret formed at low temperature, so that its polarization was incompletely filled. We took $P_1(o) \neq 0$, and $P_2(o) = 0$, and in addition, we put $Q(o) = -P_1(o)$; this yields $V(o) = 0$, in accordance with the shorting before TSD. Although the third current maximum does not show up clearly, three current maxima are seen to emerge in the j_t-thermogram of Fig. 7-16. We recognize from the temperature dependence of the various components of the electret charge that the first peak originates from the emptying of $P_1(t)$, the second from the filling of $P_2(t)$, and the third from

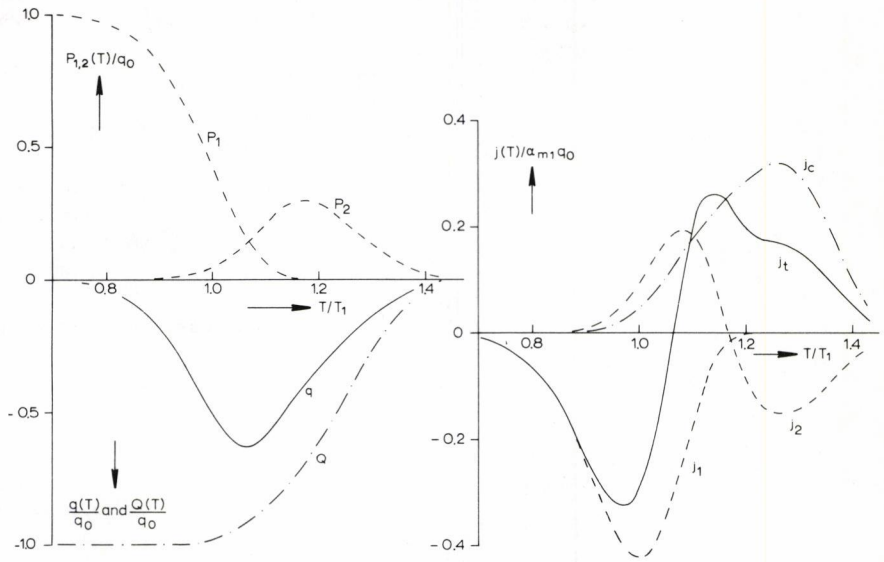


FIG.7-16 Combined response of two dipole polarizations $P_{1,2}$ and ohmic conduction in a current TSD with air gap. We assumed the electret to be metallized on both sides and took $P_2(o) = V(o) = 0$; moreover, we put $A_1/kT_1 = 11$, $A_2/kT_2 = 11.5$, $C/kT_c = 12$, $T_1/T_2 = 0.9$, $T_1/T_c = 0.85$, $\varepsilon_\infty = \varepsilon_{s1} = 3$, $\varepsilon_{s2} = 6$ and $g/l = 1$. The released current, j_t, exhibits two positive peaks, the first of which is principally due to the filling of the dipole polarization P_2 , while the second is mainly due to the ohmic dissipation of the induced image charge Q.

two opposed actions: the destruction of $P_2(t)$ and the dissipation of the image charge $Q(t)$ by the ohmic conduction $\gamma(T)$. This image charge was originally induced by the dipole polarization P_1 on the evaporated electrodes of the electret. We recall from Sect. 7:2 that on the average the released current is zero. This is so because the ultimate released charge must be zero, for we started with a neutral (metallized) sample.

Such a behaviour has actually been observed by Ong and the author (to be published), in a study of the TSD of two-sided metallized PVC electrets formed at various temperatures, T_f. The results are shown in Fig. 7-17. For forming temperatures below the glass-rubber transition at 80 °C, two positive maxima appear in the current thermograms. They indicate that the distributed dipole polarization is incompletely filled during the low-temperature formation, so that the remaining part is filled during TSD. At high forming temperatures, the positive dipole peak, which arises from incomplete formation, fades away and besides the usual negative dipole peak, only one positive peak remains. This peak is the normal conduction peak ensuing from the ohmic dissipation of the image charges induced on the evaporated electrodes by the aligned dipoles of the PVC electret.

The generalization to m discrete dipole relaxations is straightforward. We then obtain a set of m + 1 differential equations, the numerical solution of which causes no trouble, unless m becomes large.

Next, we proceed to a continuous distribution; this poses a complex problem that *cannot* be solved in closed form not even for isothermal discharges with an air gap. We shall therefore put nonisothermal decay aside for a moment.

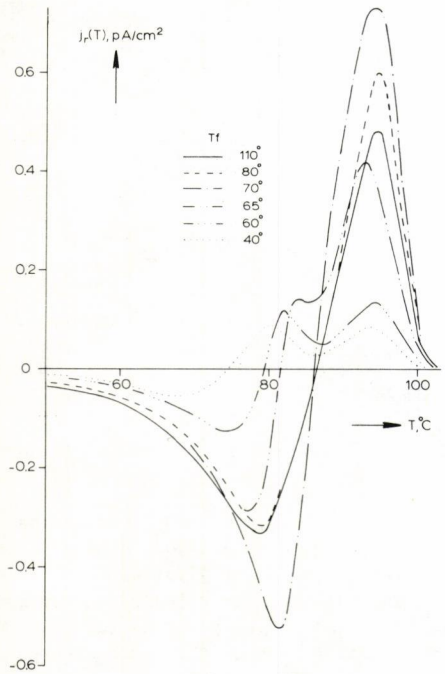


FIG.7-17 Air-gap current thermograms of a two-sided metallized PVC electret formed at various temperatures. The forming conditions were 2.5 kV/cm - 1 h, the reduced air gap g/l was 1 (measurements by Ong). At low forming temperatures, when not all subpolarizations are filled, the thermograms exhibit the two positive current peaks predicted by the model thermogram of Fig. 6-11.

For a continuous distribution, the polarization response can elegantly be described by the integral transform

$$P_s(t) = \varepsilon_o(\varepsilon_s - \varepsilon_\infty) \int_{-\infty}^{t} \frac{dE(t)}{d\theta} \psi(t - \theta)d\theta \qquad (7.60)$$

which replaces the appropriate infinite set of Debye equations (see Eq. 2.27) and forms the basis of Boltzmann's famous superposition principle. In Eq. 7.60, $\psi(t)$ represents the dielectric after-effect function, for which we have

$$\psi(t) = \int_{o}^{\infty} f(\alpha)(1 - e^{-\alpha t})d\alpha \qquad (7.61)$$

where $f(\alpha)$ is known to be the distribution function of relaxation frequencies. In Sect. 2:2 we avoided the explicit use of Eq. 7.60, but we have applied it before (Tu 70). Formally, both descriptions, cf. Eqs 2.27 and 7.60, are equivalent. Putting, e.g. $\psi(t) = 1 - e^{-\alpha t}$, Eq. 7.60 also includes the response of a single Debye relaxation.

Starting the discharge experiment at $t = 0$, we have from Eq. 7.60

$$P_s(t) = \varepsilon_o(\varepsilon_s - \varepsilon_\infty)\{\psi(t)E(o) + \int_{o}^{t} \frac{dE}{d\theta} \psi(t - \theta)d\theta\} \qquad (7.62)$$

Replacing $E(t)$ by $q(t)$ by means of Eq. 7.59 we get

$$P_s(t) = \kappa_g\{\psi(t)q(o) + \int_{o}^{t} \frac{dt}{d\theta} \psi(t - \theta)d\theta\} \qquad (7.63)$$

where $\kappa_g = (\varepsilon_s - \varepsilon_\infty)g(1 + \varepsilon_\infty g)^{-1}$. The solution of the integro-differential system Eqs 7.63 and 7.20 constitutes our problem.

As was done by Feaster (Fe 53) and Perlman (Pe 68), we use the powerful method of the Laplace transform. Denoting the one-sided Laplace integral transform by £

$$£\ F(t) = \int_{o}^{\infty} e^{-ut} F(t)dt \qquad (7.64)$$

where u is the transform variable, we may write Eq. 7.20 in the form

$$u\ £\ q(t) - q(o) + \beta_g(T)\ £\ q(t) = u\ £\ P_s(t) - P_s(o)$$

Similarly, Eq. 7.63 becomes

$$£\ P_s(t) = \kappa_g\ u\ £\ q(t)\ £\ \psi(t)$$

Elimination of £ $P_s(t)$ from this set of equations yields

$$£\ q(t) = \{q(o) - P_s(o)\}\{\kappa_g u^2\ £\ \psi(t) + u + \beta_g(T)\}^{-1} \qquad (7.65)$$

In order to calculate $q(t)$, we must invert this equation, for which we require the value of £ $\psi(t)$. By virtue of Eqs 7.61 and 7.64 we have

$$£\ \psi(t) = \frac{1}{u} \int_{o}^{\infty} \frac{f(\alpha)d\alpha}{1 + u/\alpha}$$

For most distribution functions so far known, this equation has to be integrated numerically. An exception can be made for Gevers' distribution in natural frequencies (Table 2-2) for which we readily verify that

$$£\ \psi(t) = \frac{\ln(u + \alpha_2)/(u + \alpha_1)}{u \ln(\alpha_2/\alpha_1)}$$

Therefore, for a Gevers distribution Eq. 7.65 becomes

$$\mathcal{L}\,\psi(t) = \{q(o) - P_s(o)\}\{\kappa_g \frac{\ln(u + \alpha_2)/(u + \alpha_1)}{\ln \alpha_2/\alpha_1} + u + \beta_g(T)\}^{-1} \quad ...(7.66)$$

To obtain q in the time domain we must invert this equation numerically. Several inversion techniques have recently been reviewed by Piessens (Pi 69).

Summarizing, for a continuous dipole distribution the evaluation of the discharge using an air gap is very complicated, even for the isothermal case. Feaster (Fe 53) and Perlman (Pe 68) do not mention this fact, because they restrict their final discussion to a few discrete relaxations.

7:5 Air-Gap Current TSD by SCL Drift of Excess Charges

In Chap. 7 we assumed the frozen-in excess charges to decay by ohmic conduction only. Generally, however, these charges become mobile upon heating, and our previous assumption that they are immobile is merely an approximation, in particular for highly insulating electret foils. Though excess charges will migrate under the influence of electric fields (SCL drift) as well as concentration gradients (diffusion), we shall only consider the first migration and we shall confine ourselves to those electrets most commonly used nowadays, viz. *nonpolar* homocharged electret foils. Thus, we shall neglect dielectric absorption, although this could easily be included in the description. The present theory is an extension of that of Chap. 5, which was devoted to current TSD by SCL drift with shorted electrets.

We suppose that the electrets are charged unipolarly and uniformly up to a depth r_o. The field configuration corresponding to this situation is shown in Fig. 7-18. We have a spatially varying internal field E(x,t) and a uniform external field $E_e(t)$. The internal field intersects the zero-field point close to

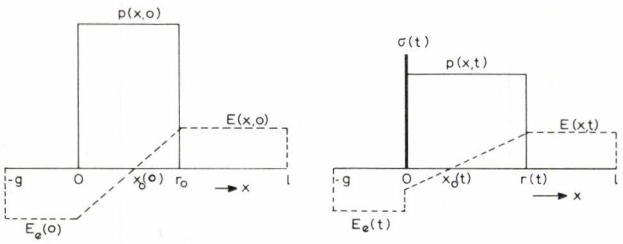


FIG.7-18 Decay and expansion of a mobile space charge cloud by its own SCL drift in a mono-electret during air-gap TSD (schematic). As in Fig. 7-8, a temporary surface charge is created at the air-gap interface, by which the zero-field point, x_o, moves to x = 0.

the left electrode. Between $0 < x < x_o$ the negative field attracts part of the mobilized frozen excess charges, as well as positive carriers supplied by ohmic conduction to x = 0, so that at this blocking electrode a surface charge σ(t) is built up. In other words, the excess-charge cloud is partly converted into a surface charge. The field on the right of the cloud, E(1,t), on the contrary, pushes the positive carriers to the right electrode. As a result, the excess charges also spread out, part of them finally reaching the right electrode, where they are neutralized.

The theory runs parallel to that of Sects 5:3 and 7:1. Evidently, the short-circuit condition, Eq. 7.6, remains the same, and for the current density in the polymer and the air gap we have the expressions 5.40 and 7.3, respectively. By integrating Eq. 5.40 between x = 0 and 1, and taking into account Eqs 7.6 and 7.8, we obtain the integral form of $j_r(t)$

$$j_r(t) = (1 + \varepsilon g)^{-1}\{\mu(T)\int_0^1 p(x,t)E(x,t)dx + \gamma(T)\int_0^1 E(x,t)dx\} \qquad (7.67)$$

The terms on the right side are easily recognized as being due to SCL drift and intrinsic ohmic conduction. We may rewrite the drift term in the form of 5.19 by invoking Poisson's equation. Moreover, we can express the conduction term in the form of 7.25, this gives

$$j_r(t) = (1 + \varepsilon g/1)^{-1}[(\varepsilon_o\varepsilon\mu(T)/21)\{E^2(1,t) - E^2(o,t)\} + \beta_g(T)q(t)] \quad ...(7.68)$$

where the effective charge density q(t) follows from Eq. 7.16 from which the polarization should be left out, because the electret is nonpolar. The quadratic field dependence makes this current TSD *non-linear* with respect to the stored charge. Moreover, most of the excess charges move towards the right and the resulting current is always *positive* for a positive excess charge. Its polarity is therefore *opposite* to that released by SCL drift in shorted electrets.

The fields appearing in Eq. 7.68 are related to the stored charge. From Poisson's equation and Eq. 7.6 we have

$$E(o,t) = -(1/\varepsilon_o\varepsilon)\int_0^1 p(x,t)(1-x/1)dx + gq(t)/\varepsilon_o(1+\varepsilon g)$$

$$E(1,t) = (1/\varepsilon_o\varepsilon)\int_0^1 p(x,t)(x/1)dx + gq(t)/\varepsilon_o(1+\varepsilon g)$$

To evaluate the integrals, we note that apart from the production of a surface charge, the excess charge distribution remains uniform; it only decreases in time and expands towards r(t). This reduces the expression for E(1,t) to

$$E(1,t) = p(x,t)r^2(t)/2\varepsilon_o\varepsilon 1 + gq(t)/\varepsilon_o(1+\varepsilon g)$$

When we use this equation, and the corresponding one for E(o,t), Eq. 7.68 gives after eliminating $j_r(t)$, the following ODE for the decay of the effective electret charge q(t)

$$dq(t)/dt + \{\beta_g(T) + \delta_g(T)\}q(t) = \mu(T)p^2(x_o,t)r^2(t)\{1-r(t)/1\}/2\varepsilon_o\varepsilon 1 \quad ...(7.69)$$

where $\delta_g(T)$ is the equivalent ohmic relaxation time of the mobile carriers, it equals $\delta_g(T) = \mu(T)p(x_o,t)r(t)/\varepsilon_o\varepsilon 1(1+1/\varepsilon g)$. The decay equation 7.69, being a hybrid of Eqs 5.24 and 7.23, has to be completed with the proper equations for $p(x_o,t)$ and r(t), for which we can take resource to Eq. 5.21 and the first identity of 5.25, where $E\{r(t),t\} = E(1,t)$.

Actually, Eq. 7.69 is valid up to the transit time, $t = \lambda$, for when the carrier front reaches the collecting electrode on the right, r(t) remains equal to 1, and Eq. 7.69 reduces to

$$dq(t)/dt + \{\beta_g(T) + \delta_g^{\dagger}(T)\}q(t) = 0 \qquad (7.70)$$

where $\delta_g^{\dagger}(T) = \mu(T)p(x_o,T)/\varepsilon_o\varepsilon(1 + 1/\varepsilon g)$. In contrast with the TSD of shorted electrets, external current flow does *not* cease when $t \geq \lambda$. In passing, we note that λ depends on g/1.

Having our set of differential equations completed, our problem is formally

solved, since from q(t) we can find the measurable quantity $j_r(t)$, by using Eq. 7.18. It goes without saying that we solved Eqs 5.24, 5.25, 7.69 or 7.70 numerically by Runge-Kutta method, starting from the initial values, $\sigma(o) = 0$, $p(x_o,0) = p_o$, $r(o) = r_o$ and $q(o) = p_o r_o(1 - r_o/21)$.

The ultimate released charge density satisfies again Eq. 7.19. Hence, we measure apart from the induction-loss factor $1 + \varepsilon g/l$ the excess charge initially stored. Thus compared to current TSD with shorted contacting electrodes, for which the ultimate charge density is given by Eq. 5.32, the air-gap method is more efficient. This is understandable, because in this set-up all excess charges finally travel away in *one* direction, i.e. towards the collecting back-electrode, whereas in current TSD with shorted electrodes, they travel away in *two* directions to both electrodes, and part of the charge decay remains unobservable. Yet the overall efficiency need not necessarily be greater for thin foils, because for these the term $\varepsilon g/l$ in the induction-loss factor cannot easily be made small. For such foils the charge TSD method described in Chap. 8 is to be preferred.

Some calculated thermograms are shown in Fig. 7-19 for various penetration depths; we neglected charge decay by ohmic conduction and considered only SCL drift. It can be seen that the penetration depth has a marked effect, especially on the location of the maximum of the released current, $j_r(T)$. The height of the current, however, varies less drastically than for shorted electrets (cf. Fig. 5-8). For penetration up to $r_o = 0.5\ l$ the maximum is reached at the transit

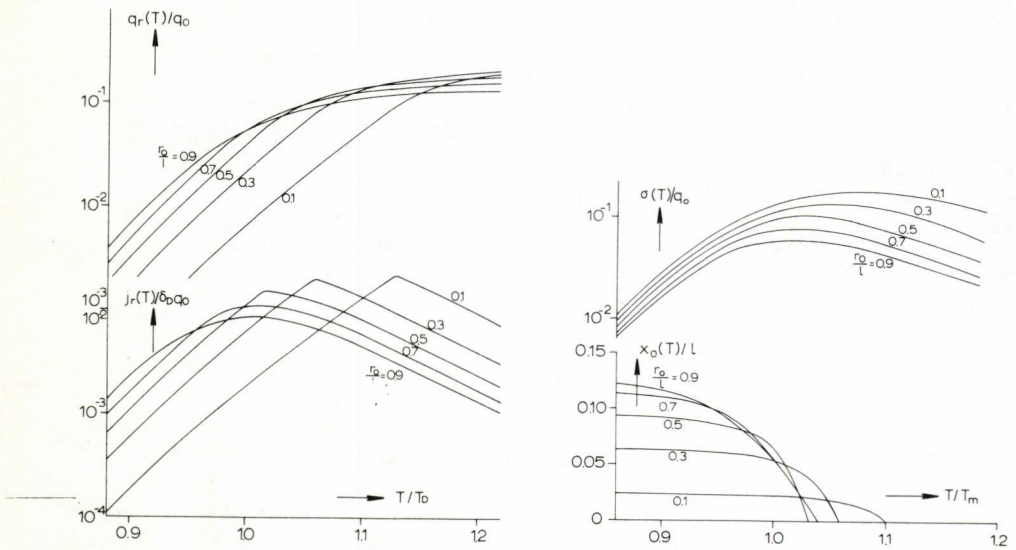


FIG.7-19 Charge and current thermograms arising from the SCL drift of the excess charge cloud in a mono-electret during air-gap TSD. The observable quantities are plotted on the left for various penetration depths. The course of the interfacial charge created and that of the zero-field point are given on the right. We used the same normalization as in Fig. 5-8 and we assumed $B/kT_D = 20$, $g/l = 1$ and $\varepsilon_\infty = 3$.

time, so that for low penetration depths the release temperature is highest. For high penetrations $r_0 \geq 0.5$ 1, on the other hand, the position of the maximum does not change, all maxima now appearing at the usual normalization temperature T_D. It is noteworthy that the current maxima form a kind of cusp, except when the electret becomes more and more filled. The cusp would also be rounded if $\gamma \neq 0$.

Surprisingly, the thermograms are much *broader* than those in which ohmic conduction dominates (cf. Fig. 7-7). To explain this, we take $r_0 = 1$; since in the present case $\beta_g(T) = 0$, Eq. 7.70 now reduces to

$$dq(t)/dt + \delta_g^{\dagger}(T)q(t) = 0$$

Comparing this equation with Eq. 7.23, which holds for pure conduction, we cannot fail to note that the temperature dependence of $\delta_g^{\dagger}(T)$ differs markedly from that of $\beta_g(T)$. In fact we have $\mu(T)p(x_0,T)$ against $\gamma(T)$. In the former the exponential increase in the carrier mobility $\mu(T)$ is partly nullified by the decrease in the carrier density $p(x_0,t)$, whereas the ohmic conductivity $\gamma(T)$ increases truely exponentially.

Fig. 7-19 also illustrates the course of $q_r(T)$, $x_0(T)$ and $\sigma(T)$. The first increases monotonously, whereas x_0 gradually falls to zero in accordance with the positive current flow. When $x_0(t)$ has become zero, the surface charge created, σ, reaches its maximum; thereafter it also decreases to zero, because $E(o,t)$ has reversed in polarity, and is pointing to the contacting electrode. Note that $q_r(T)$ is normalized to $q_0 = p_0 r_0$. The final value of this reduced quantity is not unity; it rather is equal to $(1 - r_0)(1 - \varepsilon g/l)^{-1}$ the last term of which represents the loss of induction to the contacting electrode. Nevertheless, it is definitely larger than the ultimate charges given for shorted electrodes in Fig. 5-8.

As we have found for all current thermograms resulting from SCL drift, we see in Fig. 7-19 that the initial current rise does not depend on the penetration depth. This enables us to find the activation energy from the initial current. This is exemplified in Fig. 7-20 for the model thermogram for $r_0/l = 0.3$ in Fig. 7-19. The initial slope corresponds exactly to the reduced activation

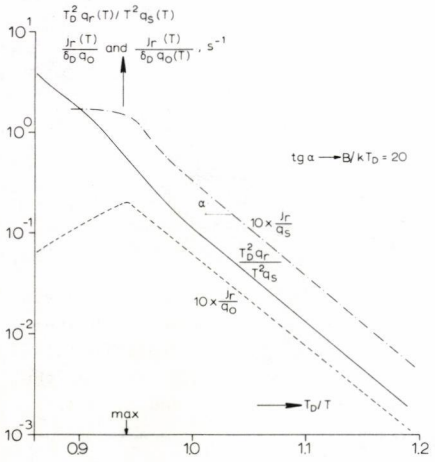


FIG.7-20 Calculation of the activation energy for current release by SCL drift in an air-gap TSD. The three plots shown all give the correct activation energy. However, neither the BFG plot nor the charge-ratio plot are straight up to higher temperatures than the simple current plot. The latter is therefore to be preferred.

energy, $B/kT_D = 20$. As usual the BFG plot and charge-ratio plot are also given. It hardly pays to construct these, however, because they do not remain straight to higher temperatures than the simple current plot.

Actually, SCL drift is difficult to observe in an air-gap system, because in most polymers it is overwhelmed by ohmic conduction. Even for a good insulator, such as PE, we found in Sect. 7:1 that ohmic conduction, rather than SCL drift, is the dominating charge decay mechanism in current TSD with an air gap (cf.Fig. 7-10). So far, we know one polymer in which SCL drift predominates, viz. Teflon-FEP. Unfortunately, air-gap measurements on this material are impossible, since Teflon itself is used as the insulator for the floating upper electrode and spurious leakage current prevent measurements from being made.

REFERENCES*

Ad 71 V. Adamec, Electric Polarization and Conduction in PMMA and PVC in Unidirectional Electric Field, *Kolloid Z. und Z. Polymere 249*, 1085-1095 (1971).

Al 37 O.G. von Altheim, Das Verhalten von amorphen und kristallisierten Quarz in elektrostatischen Feld, *Ann. d. Phys. 35*, 417-430 (1939).

Ad 45 T. Alfrey and P. Doty, The Methods of Specifying the Properties of Viscoelastic Materials, *J. Appl. Phys. 16*, 700-712 (1945).

Am 69 W.F. Ames, *"Numerical Methods for Partial Differential Equations"*, Acad. Press, New York 1969, Ch. 4.

An 56 K. Antenen, *Untersuchungen über den Mechanismus der Elektrete*, Ph.D. Thesis-Zürich, 1956.

AS 65 M. Abrowitz and J.A. Stegun, *"Handbook of Mathematical Functions"*, Dover, New York 1965.

Ba 72 H. Bauser, Ladungsspeicherung in Elektronenhaftstellen in organischen Isolatoren, *Kunststoffe 62*, 192-196 (1972).

Be 67 L.H.K. van Beek, Dielectric Behaviour of Heterogeneous Systems in *"Progress in Dielectrics"*, *Vol. 7*, J.B. Birks Ed., Heywood, London 1967, pp 69-114.

BF 66 C. Bucci, R. Fieshi and G. Guidi, Ionic Thermocurrents in Dielectrics, *Phys. Rev. 148*, 816-823 (1966).

BK 70 J.P. Batra, K.K. Kanazawa, H. Seki, Discharge Characteristics of Photoconducting Insulators, *J. Appl. Phys. 41*, 3416-3422 (1970).

Bö 52 C.J.F. Böttcher, *"Theory of Electric Polarization"*, Elsevier Publ., Amsterdam 1952.

Bo 63 R.F. Boyer, The Relation of Transition Temperatures to Chemical Structure in High Polymers, *Rubb. Chem. Technol. 36*, 1303-1421 (1963).

BP 68 L.M. Baxt and M.M. Perlman Eds, *"Electrets and Related Electrostatic Charge Phenomena"*, Symposium Series, Electrochem. Society, New York 1968.

Br 63 P. Bräunlich, Zur Elektronenkinetik photoleitender anorganischer Leuchtstoffe, *Ann. Physik 12*, 262-274 (1963).

Br 69 A. Broida, A Simple, Sensitive Graphical Method of Treating Thermogravimetric Analysis Data, *J. Polymer Sci. (A-2) 7*, 1761-1773 (1969).

BS 64 M.J. Berger and S.M. Seltzer, *Tables of Energy Losses and Ranges of Electrons and Positrons*, NASA SP-3012, Washington D.C. 1964.

BS 70 J.P. Batra and H. Seki, Photocurrents Due to Pulse Illumination in the Presence of Trapping, *J. Appl. Phys. 41*, 3409-3415 (1970).

BW 34 W.L. Bragg and E.J. Williams, The Effect of Thermal Agitation on Atomic Arrangement in Alloys, *Proc. Roy. Soc. (London) 145 A*, 699-730 (1934).

CC 42 K.S. Cole and R.H. Cole, Dispersion and Absorption in Dielectrics II: Direct Current Characteristics, *J. Chem. Phys. 10*, 98-105 (1942).

CP 70 R.A. Creswell and M.M. Perlman, Thermal Currents from Corona Charged Mylar, *J. Appl. Phys. 41*, 2365-2375 (1970).

CP 71 R.A. Creswell, M.M. Perlman and M. Kabayama, The Electret Properties of a Series of Corona-Charged Substituted Polyolefins (Paper Los Angelos Meeting, Am. Chem. Soc. 1971) in *"Dielectric Properties of Polymers"*, F.E. Karasz Ed., Plenum Publ. Corp., New York 1972, pp 215-312.

Cr 65 Z. Croitoru, Space Charges in Dielectrics, in *"Progress in Dielectrics"*, *Vol. 6*, J.B. Birks Ed., Heywood, London 1965, pp 105-146.

*Papers presented at conferences are referred to by the date of the conference in question, and not by the date of publication of the conference proceedings.

CR 67 N.G. McCrum, B.E. Read and G. Williams, *"Anelastic and Dielectric Effects in Polymeric Solids"*, Wiley & Sons, New York 1967.

CS 70 J.H. Calderwood and B.K. Scaife, On the Motion of Space Charge in a Dielectric Medium, *Phil. Trans. Royal Soc. 269*, 217-232 (1970).

Cu 60 A.J. Curtis, Dielectric Properties of Polymeric Systems, in *"Progress in Dielectrics", Vol. 2*, J.B. Birks and J.H. Schulman Eds, Heywood, London 1960, pp 29-76.

CW 67 T.A.T. Cowell and J. Woods, The Evaluation of Thermally Stimulated Current Curves, *Brit. J. Appl. Phys. 18*, 1045-1051 (1967).

Da 67 D.K. Davies, The Generation and Dissipation of Static Charge on Dielectrics in a Vacuum, *Proc. 2nd Conf. on Static Electricity*, London 1967 (Inst. of Physics and Phys. Society), pp 29-36.

DB 67 G.A. Dussell and R.H. Bube, Theory of Thermally Stimulated Conductivity in a Previously Photoexcited Crystal, *Phys. Rev. 155*, 746-779 (1967).

Eu 64 J. Euler, *"Neue Wege zur Stromerzeugung"*, Akad. Verlag, Frankfurt 1964, Ch. 4.

Fe 53 G.R. Feaster, *A Formal Theory of Electret Behaviour*, Ph.D. Thesis, Univ. Kansas, 1953.

FG 36 H. Frei and G. Groetzinger, Über das Freiwerden elektrischer Energie beim Aufschmelzen des Elektreten, *Physik. Z. 37*, 720-724 (1936).

Fo 72 L.A. Fontijn, *An Electron Exposure System for Recording and Printing*, Ph.D. Thesis, Techn. Univ.-Delft, 1972.

FZ 61 V.M. Fridkin and I.S. Zheludev, *"Photoelectrets and the Electrographic Process"*, Consult. Bureau, New York 1961, Ch. 1.

GL 67 F. Gutmann and L.E. Lyons, *"Organic Semiconductors"*, Wiley & Sons, New York 1967.

GM 62 B. Gross and R.J. de Moraes, Polarization of the Electret, *J. Chem. Phys. 37*, 710-713 (1962).

GM 62a A.N. Gubkin and B.N. Matsonashvili, The Physical Nature of the Electret Effect in Carnauba Wax, *Soviet Phys. Solid State 4*, 878-884 (1962).

GM 68 A.R. Gourlay and J.L. Morris, Finite-Difference Methods for Nonlinear Hyperbolic Systems, *Math. Comp. 22*, 28-39 (1968).

Gr 48 B. Gross, On Creep and Relaxation II, *J. Appl. Phys. 19*, 257-264 (1948).

Gr 49 B. Gross, On Permanent Charges in Solid Dielectrics II: Surface Charges and Transient Currents in Carnauba Wax, *J. Chem. Phys. 17*, 866-872 (1949).

Gr 50 B. Gross, Static Charges on Dielectrics, *Brit. Journ. Appl. Phys. 1*, 259-267 (1950).

Gr 53 B. Gross, *"Mathematical Structure of the Theories of Viscoelasticity"*, Herman & Cie, Paris 1953.

Gr 64 B. Gross, *"Charge Storage in Solid Dielectrics"*, Elsevier Publ., Amsterdam 1964.

Gr 68 B. Gross, Time-Temperature Superposition Theory for Electrets, *J. Electrochem. Soc. 115*, 376-381 (1968); in (BP 68), pp 8-13.

Gr 69 B. Gross, Persistent Internal Polarization and Distribution of Activation Energy, in *"Electrophotography", Applied Optics Suppl. 3*, J.H. Howard Ed. (American Inst. of Physics), New York 1969, pp 176-179.

Gr 70 B. Gross, *Models and the Kinetics of Thermally Activated Processes*, Lectures at Northern Electric, Canada, Report T0145 (1970). Later publ. as Linear Models and the Kinetics of Thermally Activated Currents and Voltages in: *J. Electrochem. Soc. 119*, 855-860 (1972).

Gr 70-ET J. van den Eijkhoff and J. van Turnhout, *Non-Isothermal Relaxation Theory*, Lectures given by B. Gross, Delft, TNO-Report CL 235 (1970).

Gr 70a B. Gross, *Persistent Polarization and Space Charge Layers in Dielectrics*, Lecture at Northern Electric, Canada, Report T0144 (1970).

Gr 71 B. Gross, The Sectioning Technique for the Determination of the Volume Polarization of the Thermoelectret, in *Proc. 3rd Conf. on Static Electricity*, D.K. Davies Ed. (Inst. of Physics & Phys. Society) London 1971, pp 33-43.

GS 58 A.N. Gubkin and G.I. Skavani, Preparation and Properties of New Electrets of Inorganic Dielectrics, *Izv. Akad. Nauk. SSSR (Bull. Acad. Sciences SSSR) 22*, 327-339 (1958).

Gu 57 A.N. Gubkin, The Phenomenological Theory of Electrets, *Soviet Phys.-Tech. Phys. 2*, 1813-1824 (1957).

Ha 55 E. Hastings, *"Approximation for Digital Computers"*, Princeton Univ.Press, Princeton 1955, p. 188.

He 29 K.F. Herzfeld, The Influence of Surface Conditions and Space Charges on the Conductivity of Poor Conductors, *Phys. Rev. 34*, 791-807 (1929).

He 56 J. Heijboer, Molekulare Deutung sekundärer Dämpfungsmaxima, *Kolloid Z. 148*, 36-47 (1956).

He 60 J. Heijboer, The Movement of the Cyclohexyl Group in Glassy Polymers, *Kolloid Z. 171*, 7-15 (1960).

He 65 J. Heijboer, Mechanical Properties and Molecular Structure of Organic Polymers, in *Physics of Non-Crystalline Solids*, J.A. Prins Ed., North-Holland Publ., Amsterdam 1965, pp 231-254.

He 69 J. Heijboer, Modulus and Damping of Polymers in Relation to their Structure, *Brit. Polymer 1*, 3-14 (1969).

He 70 A. Hersping, Polarisations- und Depolarisationseffekte bei Isolierstoffen mit geringer elektrischer Leitfähigkeit, *ETZ - A 91*, 265-269 (1970).

He 72 J. Heijboer, *Mechanical Properties of Glassy Polymers Containing Saturated Rings*, Ph.D. Thesis - Leiden, 1972.

HP 67 A.N. Hayhurst and P.J. Padley, Mass Spectrometric Observations of Ions in Flow Discharges, *Trans.Faraday Soc. 63*, 1620-1630 (1967).

HP 69 S.A. Hovanessian and L.A. Pipes, *"Digital Computer Methods in Engineering"*, McGraw Hill, New York 1969, Ch. 4.

HS 62 J. Heijboer, F.R. Schwarzl and H. Thurn, Verhalten in schwachen mechanischen Wechselfeldern, in *"Struktur und physikalisches Verhalten der Kunststoffe"*, K.A. Wolf Ed., Springer Verlag, Berlin 1962, pp 363-404.

IB 63 K.H. Illers and H. Breuer, Molecular Motion in PET, *J. Coll. Sci. 18*, 1-31 (1963).

Il 66 K.H. Illers, Glasige Erstarrung und Relaxationsverhalten von amorphen Copolymeren im festen Zustand, *Ber. Bunsenges. physik. Chemie 70*, 353-375 (1966).

Io 60 A.F. Ioffé, *"Physics of Semiconductors"*, Infosearch, London 1960.

IS 67 M. Ieda, G. Sawa, U. Shinohara, A Decay Process of Surface Electric Charges across PE Film, *Japan. J. Appl. Phys. 6*, 793-794 (1967).

Is 69 Y. Ishida, Dielectric Relaxation of High Polymers in the Solid State, *J. Polymer Sci. A-2, 7*, 1835-1861 (1969).

Ja 33 G. Jaffé, Theorie der Leitfähigkeit polarisierbarer Medien, *Ann. Physik. 16*, 217-284 (1933).

JE 45 Wagner's After-Effect Function in: E. Jahnke and F. Emde, *"Tables of Functions"*, Dover, New York 1945, pp 38-39.

JL 53 G. Jaffé and C.Z. LeMay, On Polarization in Liquid Dielectrics, *J. Chem. Phys. 21*, 920-929 (1953).

Jo 62 V.A. Johnson, *"Electrets" Pt 1-A State of the Art Survey, Pt 2-A Bibliography*, U.S. Governm. Research Reports TR-1045 and TR-1074, Harry Diamond Laboratories, Washington 1962.

Ke 62 W.M. McKeeman, Adaptive Numerical Integration by Simpson's Rule, *Algorithm 145*, Collected Algorithms Comm., Ass. Comp. Mach.

Ke 64 B. Ke, *"Newer Methods of Polymer Characterization"*, Interscience, New York 1964.

KK 70 M. Kryszewski, H. Kasica, J. Patora and J. Pirtrowski, Relationship between Electric Conductivity, Thermally Stimulated Current Thermoluminescence and Polymer Structure, *J. Polymer Sci. C 30*, 243-260 (1970).

La 67 D.R. Lamb, *"Electrical Conduction Mechanisms in Thin Insulating Films"*, Methuen & Co., London 1967.

La 70 C. Laj, The Thermocurrents Technique: A Method for the Study of Dielectric and Electronic Properties of Solids and Liquids, *Radiat. Effects 4*, 77-83 (1970).

LH 70 A.C. Lilly, R.H. Henderson, P.S. Sharp and L.L. Stewart, Thermally Stimulated Currents in Mylar, *J. Appl. Phys. 41*, 2002-2014 (1970).

Li 65 J. Lindmayer, Current Transients in Insulators, *J. Appl. Phys. 36*, 196-201 (1965).

Ma 61 J.R. Macdonald, Theory and Application of a Superposition Model of Internal Friction and Creep, *J. Appl. Phys. 32*, 2385-2398 (1961).

Ma 62 J.R. Macdonald, Restriction on the Form of Relaxation-Time Distribution Functions for a Thermally Activated Process, *J. Chem. Phys. 36*, 345-349 (1962).

Ma 63 J.R. Macdonald, Transient and Temperature Response of a Distributed, Thermally Activated System, *J. Appl. Phys. 34*, 538-552 (1963).

Ma 70 S. Mascarenhas, Charge and Polarization Storage in Solids, *Radiat Effects 4*, 263-270 (1970).

MC 63 P.V. Murphy and S. Costa Ribeiro, Polarization of Dielectrics by Nuclear Radiation I: Release of Space Charge in Electron Irradiated Dielectrics, *J. Appl. Phys. 34*, 2061-2063 (1963).

MH 67 L.K. Monteith and J.R. Hauser, Space-Charge Effects in Insulators Resulting from Electron Irradiation, *J. Appl. Phys. 38*, 5355-5365 (1967).

MH 72 E.H. Martin and J. Hirsch, Electron-Induced Conduction in Plastics, *J. Appl. Phys. 43*, 1001-1015 (1972).

Mi 69 A.R. Mitchell, *"Computional Methods for Partial Differential Equations"*, Wiley, New York 1969, Ch. 4.

ML 65 P.B. Macedo and T.A. Litovitz, On the Relative Roles of Free Volume and Activation Energy in the Viscosity of Liquids, *J. Chem. Phys. 42*, 245-256 (1965).

MR 62 A. Many and G. Rakavy, Theory of Transient Space-Charge-Limited Currents in Solids in the Presence of Trapping, *Phys. Rev. 126*, 1980-1988 (1962).

NB 61 P.S. Nowick and B.S. Berry, Lognormal Distribution Function for Describing Anelastic and Other Relaxation Processes, *I.B.M. Journal 5*, 297-320 (1961).

NF 59 K. Ninomiya and J.D. Ferry, Some Approximate Equations Useful in the Phenomenological Treatment of Linear Viscoelastic Data, *J. Colloid Sci. 14*, 36-48 (1959).

NT 66 P.J. Nederveen and J. van Turnhout, *An Electret Microphone - its Working, its Properties and its Making*, TNO-Report CL 98 (1966), in Dutch.

NW 67 C.J. Nederveen and C.W. van der Wal, A Torsion Pendulum for the Determination of Shear Modulus and Damping around 1 Hz, *Rheol. Acta 6*, 316-323 (1967).

On 72 P.H. Ong, *Thermo-Stimulated Discharge of Polymers Charged by Friction, Corona-Injection and Maxwell-Wagner Effect*, TNO-Report CL 98 (1972).

OT 72 P.H. Ong and J. van Turnhout, TSD of Polymer Electrets Having a Distributed Dipole Polarization, Paper *Intern. Conf. on Electrets, Charge Storage and Transport in Dielectrics*, Fall Meeting ECS, Miami Beach, Oct. 1972.

OT 73 P.H. Ong and J. van Turnhout, Air-Gap Current TSD of Polymers Charged by Friction or Corona Injection, Paper to be presented on *2nd Intern. Conf. on Static Electricity*, Frankfurt, April 1973.

OV 68 P.H. Ong and H.J. van der Vossen, *The Electrical Properties of Mylar Capacitors*, TNO-Report CL 17 (1968), in Dutch.

PC 70 F.L. Palaia and A. Catlin, Electret Behaviour at Low Pressure, *J. Chem. Phys. 52*, 3651-3654 (1970).

PC 71 M.M. Perlman and R.A. Creswell, Thermal Current Study of the Effect of Humidity on Charge Storage in Mylar, *J. Appl. Phys. 42*, 531-533 (1971).

Pe 68 M.M. Perlman, A Non-Isothermal Electret Charge Decay Theory, *Am. Acad. Brasil Cienc. 40*, 437-446 (1968).

Pe 70 J. Perret, Les charges d'espace dans les isolants solides II: Étude des polymères par l'effet électret, *Bull. Direct. Étud. et Rech. B (France) no. 3*, 55-104 (1970).

Pe 71 M.M. Perlman, Thermal Currents and the Internal Polarization in Carnauba Wax Electrets, *J. Appl. Phys. 42*, 2645-2652 (1971).

Pe 72 M.M. Perlman, Thermally Stimulated Currents and Voltages and Dielectric Properties, *J. Electrochem. Soc. 119*, 892-398 (1972).

Pet71 V.P. Petrosyan, Dielectric Relaxation in Polymers, *Polymer Sci. USSR 13*, 857-866 (1971).

Pi 69 R. Piessens, Numerical Inversion of the Laplace Transform, *Ing. blad (Antwerp) 38*, 266-280 (1969), in Dutch.

Po 59 P.I. Plovikov, Concerning the Effect of an Alternating Electrical Field on the Forming of Electrets, *Soviet Phys. Solid State 1*, 711-715 (1959).

Po 67 M.J.D. Powell, Curve Fitting by Cubic Splines, *Conf. on Numerical Approximation to Functions and Data*, Univ. of Kent, England, Sept. 1967, AERE Report TP 307.

Pr 60 W. Primak, Large Temperature Annealing, *J. Appl. Phys. 31*, 1524-1533 (1960).

PR 68 M.M. Perlman and C.W. Reedijk, Production and Charge Decay of Film Electrets, *J. Electrochem. Soc. 115*, 45-49 (1968); in (BP 68), pp 86-89.

PU 72 M.M. Perlman and S. Unger, TSC Study of Traps in Electron-Irradiated Teflon and PE, *Paper Intern. Conf. on Electrets, Charge Storage and Transport in Dielectrics*, Fall Meeting ECS, Miami Beach, Oct. 1972.

Ra 66 P. Rabinowitz, Automatic Integration of a Function with a Parameter, *Comm. Ass. Comp. Mach. 9*, 804-806 (1966).

Re 58 W. Reddish, Chemical Structure and Dielectric Properties of High Polymers, *Pure Appl. Chem. 5*, 723-742 (1962).

Re 67 C.H. Reinsch, Smooting by Spline Functions, *Num. Math. 10*, 177-183 (1967).

RL 69 A. Reiser, M.W.B. Lock, J. Knight, Migration and Trapping of Extrinsic Charge Carriers in Polymer Films, *Trans. Faraday Soc. 65*, 2168-2185 (1969).

RM 67 R.D. Richtmyer and K.W. Morton, *"Difference Methods for Initial Value Problems*, Interscience, New York 1967, pp 300-306.

Ro 69 J. Roos, Electrets, Semipermanently Charged Capacitors, *J. Appl. Phys. 40*, 3135-3139 (1969).

Ro 70 D.U. von Rosenberg, *"Methods for the Numerical Solution of Partial Differential Equations"*, Elsevier Publ., Amsterdam 1970, Chs 3 and 6.

RP 68 C.W. Reedijk and M.M. Perlman, The Measurement of Surface Charge, *J. Electrochem. Soc. 115*, 49-51 (1968), in (BP 68), pp 97-99.

Ru 68 K.C. Rush, Time-Temperature Superposition and the Relaxation Behaviour in Polymeric Glasses, *J. Macromol. Sci. Phys. B 2*, 179-204 (1968).

Sc 33 W.O. Schumann, Strom- und Feldverlauf in Isolierstoffen mit beweglichen dünnen geladenen Schichten, *Arch. f. Elektrotechn. 27*, 241-253 (1933).

Sc 61 R.A. Schapery, Approximate Methods of Transform Inversion for Viscoelastic Stress Analysis, *Proc. 4th U.S. National Congress of Appl. Mechanics, 1961*, pp 1075-1085.

Sc 63 F.R. Schwarzl, *"Das mechanische und thermische Verhalten von Polymeren"*, in *"Chemie und Technologie der Kunststoffe", Vol. 1*, R. Houwink and A.J. Staverman Eds, Springer Verlag, Berlin 1962, pp 633-712.

Sc 65 R.M. Schäffert, *"Electrophotography"*, Focal Press, London 1965.

Sc 69 F.R. Schwarzl, The Numerical Calculation of Storage and Loss Compliance from Creep Data for Linear Viscoelastic Materials, *Rheol. Acta 8*, 6-17 (1969).

Sc 69a G. Schweitzer, *"Untersuchungen zur Raumladungspolarisation in Ionenleitern*, Ph.D. Thesis - Aachen, 1969.

Sc 71 F.R. Schwarzl, Numerical Calculation of Storage and Loss Modulus from Stress Relaxation Data for Linear Viscoelastic Materials, *Rheol. Acta 10*, 166-173 (1971).

Se 72 G.M. Sessler, Spatial Depth and Density of Charge in Electrets, *J. Appl. Phys. 43*, 408-411 (1972).

Sh 58 V.E. Shashoua, Static Electricity in Polymers I: Theory and Measurement, *J. Polymer Sci 33*, 65-85 (1958).

Sh 69 M.M. Shahin, *"Nature of Charge Carriers in Negative Coronas, in Electrophotography"*, Applied Optics Supplement 3, J.N. Howard Ed., Amer. Institute of Phys., New York 1969, pp 106-110.

SO 63 N. Saito, K. Okano, S. Iwayanagi and T. Hideshima, *"Molecular Motion in Solid State Polymers"*, in *"Solid State Physics", Vol. 14*, F. Seitz and D. Turnbull Eds, Academic Press, New York 1963, pp 343-502.

Sp 67 H. Späth, The Damped Taylor's Series Method for Minimizing a Sum of Squares and for Solving Systems of Nonlinear Equations, *Algorithm 315*, Collected Algorithms Comm. Ass. Comp. Mach.

SS 52 F.R. Schwarzl and A.J. Staverman, Time-Temperature Dependence of Linear Viscoelastic Behavior, *J. Appl. Phys. 23*, 838-843 (1952).

SS 52a F.R. Schwarzl and A.J. Staverman, Higher Approximations of Relaxation Spectra, *Physica 18*, 791-798 (1952).

SS 56 A.J. Staverman and F.R. Schwarzl, *"Linear Deformation Behaviour of High Polymers"* in *"Die Physik der Hochpolymeren", Vol. 4*, H.A. Stuart Ed.,

Springer Verlag, Berlin 1956, pp 1-125.

SS 67 F.R. Schwarzl and L.C.E. Struik, Analysis of Relaxation Measurements, *Advan. Mol. Relaxation Processes 1*, 201-255 (1967-1968).

SS 67a R.B. Schilling and H. Schachter, Neglecting Diffusion in Space-Charge-Limited Currents, *J. Appl. Phys. 38*, 841-844 (1967).

SS 71 G.A. Schwippert and W. Smits, *A Phase Sensitive Detector for Measuring Amplitude Modulated*, TNO-Report CL 47 (1971), in Dutch.

St 59 A.J. Staverman, *"Quantitative Relations Concerning the Glass Transactions Point"*, Symposium on Macromolecules Wiesbaden, W. Kern Ed., Verlag Chemie, Weinheim 1959.

Sw 50 W.P.G. Swann, On Certain Matters Pertaining to Electrets, *J. Franklin Institute 250*, 219-248 (1950).

SW 66 G.M. Sessler and J.E. West, Foil-Electret Microphones, *J. Acoust. Soc. Am. 40*, 1433-1440 (1966).

SW 70 G.M. Sessler and J.E. West, Charging of Polymer Foils with Monoenergetic Low-Energy Electron Beams, *Appl. Phys. Letters 17*, 507-509 (1970).

SW 71 J.M. Schneider and P.K. Watson, Transient Space-Charge-Limited Conduction in Liquid Dielectrics II, *1970 Annual Report Conf. on Electr. Insulation and Diel. Phenomena*, Nat. Acad. Sciences, Washington 1971, pp 125-132.

SW 72 G.M. Sessler and J.E. West, Production of High Quasipermanent Charge Densities on Polymer Foils by Application of Breakdown Fields, *J. Appl. Phys. 43*, 922-926 (1972).

TF 70 T. Takamatsu and E. Fukada, Thermal Change of Depolarization Current in Polymer Electrets, *Polymer J. 1*, 101-106 (1970).

Th 62 V. Thomée, A Stable Difference Scheme for the Mixed Boundary Problem for a Hyperbolic, First-Order System in Two Dimensions, *J. Soc. Indust. Appl. Math. 10*, 229-245 (1962).

Th 63 V. Thomée, A Predictor-Corrector Type Scheme for the Mixed Boundary Problem for a First-Order System in Two Dimensions, *J. Soc. Indust. Appl. Math. 11*, 964-975 (1963).

To 46 A.Q. Tool, Relation Between Inelastic Deformability and Thermal Expansion of Glass in its Annealing Range, *J. Am. Ceram. Soc. 29*, 240-253 (1946).

Tu 66 J. van Turnhout, The Measurement of Static Charges, *TNO-Nieuws 21*, 252-260 (1966), in Dutch.

Tu 67 J. van Turnhout, *Practical Applications of Electrets*, TNO-Report CL 85 (1967), in Dutch.

Tu 68 J. van Turnhout, *The Formation of Electrets*, TNO-Report CL 4 (1968), in Dutch.

J. van Turnhout, *The Thermal Depolarization of Electrets*, TNO-Report CL 18 (1968), in Dutch.

Tu 70 J. van Turnhout, Thermally Stimulated Discharge of Electrets, Paper 1st Intern. Conf. on Static Electricity, Vienna, May 1970, in *"Advances in Static Electricity", Vol. 1*, W.F. de Geest Ed., Auxilia, Brussels 1971, pp 164-194.

Tu 70a J. van Turnhout, Methods for Measuring Static Charges, Paper 1st Intern. Conf. on Static Electricity, Vienna, May 1970, in *"Advances in Static Electricity", Vol. 1*, W.F. de Geest Ed., Auxilia, Brussels 1971, pp 56-81.

Tu 72 J. van Turnhout, Current and Charge TSD of Polymer Electrets Resulting from the Motion of Excess Charges, Paper *Intern. Conf. on Electrets, Charge Storage and Transport in Dielectrics*, Fall Meeting ECS, Miami Beach, Oct. 1972.

Va 43 V. Vand, A Theory of the Irreversible Electrical Resistance Changes of Metallic Films Evaporated in Vacuum, *Proc.Phys.Soc.(London) 55A*,222-245 (1943).

VP 57 M.V. Volkenshtein and O.B. Ptitsyn, The Relaxation Theory of Vitrification, *Soviet Phys. Techn. Phys. 1*, 2138-2156 (1957).

WB 65 B. Wunderlich, D.M. Bodily and M.H. Kaplan, Theory and Measurement of the Glass-Transformation Interval of PS, *J. Appl. Phys. 35*, 95-102 (1965).

WD 68 C.W. van der Wal and R.H.J.W.A. Drent, A Torsional Creep Apparatus, *Rheol. Acta 7*, 265-271 (1968).

We 60 J. Wegstein (H.C. Tacher and J.G. Herriot), Rootfinder, *Algorithms 2, 15 and 26*, Collected Algorithms Comm. Ass. Comp. Mach.

We 67 B. Wendroff, *"Theoretical Numerical Analysis"*, Academic Press, New York 1967, p. 183.

Wi 55 G.G. Wiseman and co-workers, *"Research Studies on Electrets"*, Final Report 1951-1954, and *"Research and Development Studies of Electrets"*, Final Report 1954-1955, Univ. Kansas.

Wi 62 G. Williams, Evaluation of Dielectric Loss Data from Dc Measurements, *Trans. Faraday Soc. 58*, 1041-1044 (1962).

Wi 70 H.J. Wintle, Decay of Static Electrification by Conduction Processes in PE, *J. Appl. Phys. 41*, 4004-4007 (1970).

Wi 71 H.J. Wintle, Decay of Excess Charge in Dielectrics Having Shorted Electrodes, *J. Appl. Phys. 42*, 4724-4730 (1971).

WN 69 C.W. van der Wal, C.J. Nederveen and G.A. Schwippert, A Torsional Creep Instrument and a Torsional Pendulum, Both with Accurate Temperature Control, *Rheol. Acta 8*, 130-133 (1969).

WS 65 A.E. Woodward and J.A. Sauer, *"Mechanical Relaxation Phenomena"* in *"Physics and Chemistry of the Organic Solid State" Vol. 2*, D. Fox, M.M. Labes and A. Weisberger Eds, Interscience Publ., New York 1965, pp 638-723.

WS 69 C.W. van der Wal and L.C.E. Struik, A Direct-Reading Bridge for a Platinum Resistance Thermometer, *J. Sci. Inst. (Journ. Phys. E) 2*, 143-145 (1969).

YI 67 K. Yamafuji and Y. Ishida, An Interpretation on the Broadness of Low Temperature Dielectric Absorption Curve in High Polymers, *Kolloid-Z. u. Z. Polymere 221*, 63 (1967).

SUMMARY

The thermally stimulated discharge (TSD) of polymer electrets was studied theoretically and experimentally, with the aim of gaining a better insight into the molecular processes underlying the electret effect, and also to elucidate the nonisothermal, low-frequency, dielectric behaviour of polymers.

The introductory Chapter 1 outlines the tenor of this work. It surveys the experimental techniques used, describes the possible decay mechanisms, and summarizes the methods elaborated to unravel them. Our investigations have been concentrated on three experimental techniques:

1. The well-known current release of two-sided metallized electrets in *short*-circuit (normal current TSD), and two new techniques,
2. Current release of one and two-sided metallized electret *shorted together* with an adjacent *air gap* (current TSD with an air gap).
3. Continuous measurement of the retained charge on one-sided metallized electret foils in *open* circuit (charge TSD).

The two-sided metallized electrets were as a rule hetero-electrets, and contained aligned dipoles and intrinsic excess charges stored near the electrodes. The one-sided metallized electrets were homo-electrets, in which the excess charges are dominant, and extrinsic because they are injected by Townsend breakdown. These electrets are the most interesting for applications. In this work most hetero-electrets were formed from methacrylic homo- and copolymers polymerized at this laboratory, whereas most homo-electrets were made from commercial foils, such as Mylar, Makrofol and Teflon-FEP. These are partially crystalline and so are nonhomogeneous. We also doped polymers with additives to obtain nonhomogeneous structures.

For the shorted hetero-electrets of polar polymers we found three TSD current peaks, designated β, α and ρ. The first two peaks were already known from ordinary dielectric measurements; they are caused by the reorientation of the aligned *dipoles* by relaxations of the side-groups and main chain segments. The ρ peak which appears above the glass-rubber transition was formerly unknown. By performing current TSD with an air gap, in which the dissipation of the excess charges by ohmic conduction of the polymer is revealed, we could prove that this peak is due to the *motion of the excess charges*. The ρ peak was likewise observed for shorted metallized homo-electrets. Interestingly, these also exhibited the α peak, although they were obtained from *non-polar* polymers. The motions of the extrinsic carriers thus seem to be triggered by the macromolecular motions of the host polymer.

The charge thermograms were less structured, the charge decreasing steadily. Nevertheless, the *two-stage* charge TSD of Teflon-FEP turned out to be remarkable, since during the second heating run the charge remained almost constant up to the final heating temperature of the

first run. This indicates that the motion of the electrons injected, is accompanied by *trapping and retrapping* at various energy levels. Obviously, electrons in shallow traps are released first, so we are left with persistent electrons captured in deep traps after the first run.

To account for the phenomena just mentioned we give in the theoretical part a detailed phenomenological theory of TSD current and charge measurements. Attention is paid to the following decay processes:

1. reorientation of aligned dipoles;
2. motion of the excess charges towards the opposed image charges of the electrodes or towards opposed charges within the polymer;
3. neutralization of the excess charges by carriers supplied by the ohmic conduction of the polymer. (This decay passes unnoticed in shorted electrets.)

The motion of the excess charges is considered to arise from:

a. drift of the excess charges under their own electric field; this motion is space-charge limited and therefore called SCL drift. We have just seen that it may be accompanied by trapping.
b. diffusion, which has the concentration gradients as the driving force.

In heterogeneous polymers an additional discharge process may contribute to the ρ peak, viz.

4. the Maxwell-Wagner (MW) effect.

In such polymers most of the excess charges will not be stored at the electrodes, but rather at the interfaces of the two components, provided that these have a different ohmic conductivity. During TSD, these interfacial charges cause unequal ohmic conduction currents to flow in the two phases, which supply to the interfaces new carriers that neutralize the existing ones. Clearly, the decay of excess charges by the MW effect is the extension of process 3. to composites. However, the MW effect can be observed in shorted nonhomogeneous electrets, whereas ohmic dissipation in shorted homogeneous electrets cannot, because their conductivity is space-independent.

All the processes are accelerated during TSD, for they are thermally activated. In general, we have supposed this activation to obey an Arrhenius equation.

Let us now review the contents of the individual chapters. Current release by the reorientation of aligned dipoles is treated in Chap. 2. As was done by Gross, we extended the scope of the theory of Bucci et al. for a single Debye relaxation to include a distributed polarization having a continuous set of relaxation times. This seemed worthwhile because the recorded dipolar β and α peaks were broad. By solving on a computer the pertinent Laplace transforms for five distribution func-

tions, viz. those of Gevers, Gross, Cole-Cole, Fuoss-Kirkwood and Wagner, we have shown that the current release of a distributed polarization may be deformed by an incomplete formation. For example, at low formation temperatures, T_f, the high-temperature tail of the thermograms will be cut off, because the slow polarizations have not been activated. In that case the high-temperature current maximum is no longer characteristic of the polymer, appearing just above T_f. Similarly, if the electret is stored too long before a TSD, the fast polarizations will have relaxed, hence they are missing from the low-temperature tail of the thermograms. Thus, unless the polymer is fully charged, the current thermograms recorded will not be specific for the polymer in question.

Model calculations on completely charged polymers revealed that the distributions of Cole-Cole and Fuoss-Kirkwood are the most appropriate for fitting experimental TSD data. The distribution of Wagner is the next best choice, although this yields a too high initial current rise. The distributions of Gevers and Gross, which are very similar, exhibit unreal broad peaks and they also lead to a too high initial slope. Chap. 2 also discusses the resolving power of TSD for proximate dipole relaxations and it advocates in Sect. 2:3.1 the use of multi-stage TSD for differentiating between a distribution in natural frequencies and activation energies of the dipole groups.

In discussing the evaluation of TSD data on dipole relaxations we derive in Chap. 3 a simple formula from which the activation energy of a distributed polarization can be deduced from the initial slope and the half-value temperature of the current thermograms. We also present a method, based on a Laplace transform inversion and first suggested by Schwarzl and Staverman, to calculate the distribution function from TSD data. The evaluation of the γ peak of PcHMA, which is due to a chair-chair transition of its flexible cyclohexyl ring, is discussed in more detail. We found that this peak can be described by a Fuoss-Kirkwood distribution of width $m = 0.44$ and having an activation energy of 9 kcal/mol. These results agree well with those of Heijboer on torsional creep measurements.

In Chap. 4 we compare current TSD by dipole reorientation with conventional dielectric and mechanical measurements. Modifying conversion formulas due to Schwarzl and Struik we were able to convert TSD data into dielectric loss results. We show that TSD works nearly isochronously and is centred at a very low frequency, equivalent to about 10^{-3} Hz. Converting the β and α peaks of PMMA we found that the latter was too high, as compared with the dielectric results, presumably because it is increased by the motion of excess charges; this was later confirmed by sectioning experiments. We already mentioned that only TSD peaks of a dipolar origin appear in sinusoidal dielectric measurements; the ρ peak was unknown. However, we proved that this peak can be revealed by isothermal DC step-response measurements. This has recently also been shown

by Adamec.

In Chap. 5 we discuss new work on the current TSD by the motion of excess charges. First, attention is paid to SCL drift of carriers with a thermally activated mobility. For a *uniform* spatial distribution of excess charges, the non-linear partial differential equations (PDE's) could be solved in a straightforward way, as was concurrently done for isothermal experiments by Calderwood and Scaife, and independently by Wintle. For more general charge distributions we solved the PDE's on a digital computer, using finite-difference methods. We evaluated unipolar and bipolar excess-charge distributions. The best results were obtained by the central Wendroff-Thomée scheme, but the two-step Lax-Wendroff-Richtmyer scheme also functioned rather well. We have shown that one can measure *only a fraction* of the charge initially stored, because the carriers move *bi*directionally, i.e. to both electrodes, where they are neutralized. For a uniform charging up to a relative depth $r_o/1$ we found a release ratio of $q_r(\infty)/q_o \simeq r_o/2\ 1$, if $r_o < 0.25\ 1$. This formula was used to calculate the penetration depth of electrons in electron-bombarded Teflon FEP foil of 25 μm; we found for instance $r_o/1 = 0.15$ for 20 keV. The equation given holds only for non-conducting polymers. The formula for current release in the presence of ohmic conduction, when part of the excess charges is consumed unnoticed, is also given. Calculated thermograms for SCL drift turned out to be broader than those of a Debye relaxation for $r_o < 0.5\ 1$, and their shape depends on the initial penetration depth. However, their initial slope is solely dependent on the activation energy. Furthermore, the current *peaks* increase almost linearly with the initial charge stored, and the maximum emerges the sooner the higher the charge.

In discussing the excess-charge motion by diffusion, we stress that this generates a current only if the electrodes are *blocking*, i.e. if they prevent the excess charges from recombining with the image charges. We obtained experimental evidence that this imperfect recombination may occur for evaporated electrodes. To calculate the model thermograms for diffusion we have adapted to TSD the theory of Jaffé and Lemay for isothermal experiments.

To obtain a qualitative insight into the current TSD of heterogeneous polymers, such as partially crystalline ones, we focus in Chap. 6 on two-layer structures. We show that the released charge of such Maxwell-Wagner *series* models is less than the interfacial charges originally stored, because the internal current flow is *bi*directional. Current efficiency is 100 % only if one of the two components is a perfect insulator (air gap). The unnoticed charge loss may, according to Gross, cause the ultimately released charge of heterogeneous or stratified dielectrics to vary with heating rate, unless the components are put in parallel. In studying experimentally the MW charging and discharging of two polar polymers with an adjacent air gap, two current

peaks were revealed, one due to dipole orientation (α) and the other to ohmic conduction (ρ_c). Interestingly, the conduction peak coincided neatly with the TSD ρ peak of shorted metallized hetero-electrets. This supports the view that this peak originates from the motion of the excess charges.

In Chap. 7 we analyze current TSD of electrets shorted together with an adjacent air gap. This method allows the measurement of the excess-charge decay by ohmic conduction and is of major importance for investigations on homocharge decay. Moreover, it was of much help in assigning the molecular origin of the TSD ρ peak of shorted metallized hetero-electrets. Apparently, the simultaneous decay of dipoles and excess charges complicates the mathematics and to obtain quantitative results, we had to solve the pertinent ordinary differential equations (ODE's) numerically. Experimentally, however, we found in most air gap thermograms the dipole peak (α) and conduction peak (ρ_c) well separated. This enabled us to calculate the activation energy of the ρ_c peak; the value obtained agreed well with the activation energy of the ohmic conductivity.

In Chap. 8 we turn to the theoretical aspects of charge TSD of the much used homo-electret foils. As mentioned before, this measurement is done in open circuit, i.e. $j_r = 0$, because the external field of the electret is kept zero; this considerably simplifies the mathematics. Again, dipole reorientation, SCL drift, and ohmic conduction are considered as the main decay mechanisms. Salient differences between charge and current TSD are pointed out and the effect of penetration depth and height of the initial charge are analyzed. It is shown that the decay by SCL drift diminishes after a preheating; this effect enables one to make homo-electrets more stable.

In the experimental part, Chap. 9 describes the equipment used. The set-up for current TSD is fully automated, and covers a temperature range from -185° to 250 °C. As a rule a heating rate of 1 °C/min was chosen. The apparatus consists of a thermostat, two electrode systems for measurements with and without an air gap, a vibrating capacitor electrometer as an ammeter and some interface equipment to print and punch the data on a Teletype. The tape with data was evaluated on a IBM 360 Computer. The apparatus developed for charge TSD on electret foils, based on the cancellation of the external field of the electret by a known bias voltage, also works automatically.

In Chap. 10 experimental results are discussed, and current thermograms of several methacrylic homo- and copolymers are given and interpreted. The interpretation was often facilitated by published work on conventional dielectric and mechanical measurements. It is shown that the TSD α peak is located at the glass-rubber transition T_g known from dilatometric measurements. Accordingly, TSD may be applied to determine T_g points. On account of the low frequency involved, there is a

high resolution between the TSD peaks of the main-chain and side-group relaxations of a polymer, and to reveal the latter we had to cool to -185 °C. Nearly all polymers exhibit a ρ peak above T_g, due to the motion of the excess charges. This peak is sensitive to the presence of impurities, such as absorbed water. Since copolymers display marked ρ peaks, they can store higher charges than homopolymers. In relating the hetero-charging of three polymers to the formation conditions, the forming temperature T_f was found to have the largest effect on the current thermograms, and to obtain a representative thermogram T_f should be chosen above T_g; these findings agree with the theoretical predictions of Chap. 2. Relationships between the thermograms and the storage conditions were also established.

The coexistence of a hetero- and homocharge on bare electrets of polar polymers was proved unambigiously by the air-gap technique. We invariably found first a heterocurrent which reversed to a homocurrent above T_g. Investigating the TSD of sectioned hetero-electrets, we observed that the internal charge is unequally distributed. Most of the charge is accumulated close to the electrodes, which points to a significant excess-charge polarization. The excess charges even contribute considerably to the α peak. Our results contradict those of Gross et al. on carnauba wax; the disagreement may be due to differences in storage time. Gross stored his carnauba wax electrets up to 7 weeks before sectioning.

In the last section of Chap. 10 thermograms of the persisting charge of various homo-electret foils and electron-bombarded Teflon FEP foils are presented. We found that the striking stability of Teflon FEP homoelectrets can be further improved by preheating; this is interesting for the practical use of electrets. This phenomenon indicates also that the injected carriers are trapped at sites of different depths. This view is supported by the finding that current thermograms of electron-bombarded Teflon FEP foil show two peaks. Moreover, we observed large differences between the transition temperatures of current and charge TSD of Teflon FEP. It therefore seems likely that electrons released from their traps are soon retrapped rather than being lost in recombination centres. We finally noted that negatively charged Teflon FEP is much more stable than positively charged Teflon FEP.

The appendixes deal with the theory of some other topics. In App. I we discuss the solution of the PDE's that describe current TSD by the thermal release of electrons from traps, which we have seen to occur in negatively homocharged and electron-bombarded polymer foils. Following a method outlined by Monteith and Hauser for isothermal experiments and assuming that $n_t > > n$, the PDE's are worked out as a set of ODE's, by means of a 2nd order Runge-Kutta method. A case that conforms to the description on thermally activated SCL drift in Chap. 5 is that of strong retrapping at a single energy level. For intermediate cases of

retrapping, however, the spreading of the carriers was found to differ from that without traps. The magnitude of the charge measured, is again small compared with the charge originally trapped. We also review the theory of Creswell and Perlman which assumes fast recombination instead of fast retrapping, as it occurs in Teflon-FEP electrets. In Chap. 5 two plots, viz. the BFG plot and the charge-ratio plot, have been discussed for singling out the occurrence of these processes in actual data.

Supplements to Chaps 2, 5, 6 and 7 are collected in App. II. This describes, e.g., the finite-difference schemes used to solve the PDE's for SCL drift of nonuniform excess charge distributions. We also discuss homocharging by Townsend breakdown, visualizing this process as a Maxwell-Wagner charging.

Although we managed to elucidate part of the underlying molecular mechanisms of polymer electrets, much work remains to be done. It seems worthwhile to extend the theory of charge TSD to include trapping at various energy levels. For the unravelling of the molecular decay mechanism of injected homocharges, the TSD of ion implanted polymers appear to be of importance. Another objective is to ascertain the cryogenic relaxations of polymers by freezing them down to liquid helium temperature. The air-gap method should be investigated more extensively and research on sectioned electrets should be continued. Finally, TSD is not restricted to electrets. It can also be applied to dielectrics charged by friction or corona. At our research institute work is in progress that aims at studying the effects of antistatics with TSD.

SAMENVATTING

De thermisch gestimuleerde ontlading (TSD) van semi-permanent geladen polymeren (elektreten) werd theoretisch en experimenteel bestudeerd. Enerzijds om meer inzicht te krijgen in de moleculaire processen die het elektreeteffect veroorzaken en anderzijds om het niet-isothermische, diëlektrische laagfrekwent gedrag van polymeren te onderzoeken.

Ter inleiding wordt in hoofdst. 1 de opzet van het werk besproken, o.a. worden de gebruikte meettechnieken toegelicht, de mogelijke ontlaadprocessen beschreven en methoden aangegeven om deze processen van elkaar te onderscheiden. De volgende meetmethoden werden toegepast:

1. De gebruikelijke stroommeting aan tweezijdig gemetalliseerde *kortgesloten* elektreten (normale stroom-TSD) en twee nieuwe technieken:
2. Stroommeting aan een- en tweezijdig gemetalliseerde elektreten die via een *luchtspleet* worden *kortgesloten* (stroom-TSD met luchtspleet).
3. *Stroomloze* continumeting van de persisterende lading aan eenzijdig gemetalliseerde elektreetfilms (lading-TSD).

De tweezijdig gemetalliseerde elektreten waren meestal heteropolair geladen en bevatten, naast georiënteerde dipolen, meestentijds bij de elektroden opgezamelde intrinsieke excesladingen. De eenzijdig gemetalliseerde elektreten waren homopolair geladen. Deze bevatten voornamelijk excesladingen, die extrinsiek waren, omdat ze via Townsend-ontladingen werden geïnjekteerd. De homo-elektreten zijn wegens hun betere stabiliteit het belangrijkst voor de toepassingen. De meeste hetero-elektreten werden geformeerd uit homo- en copolymeren van methylmethacrylaatderivaten, die gepolymeriseerd waren op het Centraal Laboratorium TNO, terwijl de meeste homo-elektreten werden geformeerd uit handelsfilms, zoals Mylar, Makrofol en Teflon-FEP. Deze films waren gedeeltelijk kristallijn en dus niet homogeen. Daarnaast werden bewust stoffen bijgemengd om niet-homogene strukturen te krijgen.

Voor de uit polaire polymeren gevormde hetero-elektreten vonden we met normale stroom-TSD in het algemeen drie stroompieken: β, α en ρ. Hiervan waren de eerste twee reeds bekend uit gewone diëlektrische metingen; ze ontstaan door de relaxatiebeweging van de polaire zijgroepen en hoofdketensegmenten, waardoor de uitgerichte permanente *dipolen* zich heroriënteren. De ρ piek, die altijd boven het glaspunt wordt gevonden, was tot nu toe onbekend. Door een stroom-TSD met luchtspleet uit te voeren, konden we bewijzen dat deze piek wordt teweeggebracht door de *beweging van de excesladingen* zelf. In de normale stroom-TSD van homo-elektreten werd deze ρ piek eveneens waargenomen. Ook de α piek kon worden aangetoond, ofschoon deze elektreten waren gevormd uit *niet polaire* polymeren. Blijkbaar initieert de beweging van de polymeerketens die van de extrinsieke ladingen.

In de ladingsthermogrammen nam de lading gestadig af, deze vertoonden dus minder struktuur. De twee-traps lading-TSD van door elektronen bombardement geladen Teflon-FEP was evenwel markant, omdat gedurende de tweede opwarming de lading praktisch konstant bleef tot de eindtemperatuur van de eerste opwarming werd bereikt. Dit illustreert dat de beweging van de geïnjekteerde elektronen gepaard gaat met vrijmaking uit en herinvanging in vangcentra van verschillend energieniveau. Daar elektronen in hoog gelegen centra het eerst worden vrijgemaakt, blijven na de eerste opwarming voornamelijk stabiele elektronen over die in dieper gelegen centra zitten.

Om bovengenoemde verschijnselen te verklaren wordt in het theoretische deel een gedetailleerde, fenomenologische beschrijving van stroom- en lading-TSD gegeven. Aan de volgende ontlaadprocessen werd aandacht besteed:

1. heroriëntatie van permanente dipolen;
2. beweging van excesladingen naar de op de elektroden geïnduceerde beeldladingen, of naar tegengestelde ladingen in het polymeer;
3. neutralisatie van de excesladingen met de door de ohmse geleiding van het polymeer aangevoerde ladingen.(In de normale stroom-TSD blijft deze ontlading verborgen, doch niet in de stroom-TSD met luchtspleet).

De beweging van de excesladingen onder sub 2 wordt toegeschreven aan:

a. drift van de excesladingen in het elektrische veld dat ze zelf opwekken; deze beweging is ruimteladingsbegrensd en wordt daarom SCL drift genoemd. (We vermeldden reeds dat deze drift gepaard kan gaan met vrijmaking en herinvanging in vangcentra.);
b. diffusie, deze ontstaat ten gevolge van koncentratiegradiënten.

In heterogene polymeren kan daarnaast nog een ander ontlaadproces tot de ρ piek bijdragen, nl.:

4. het Maxwell-Wagner (MW) effect.

In zulke polymeren worden de excesladingen niet bij de elektroden opgeslagen, maar bij de *grensvlakken* van de twee komponenten, mits deze een verschillend geleidingsvermogen hebben. De grensladingen brengen tijdens TSD ongelijke geleidingsstromen in de twee komponenten teweeg, die nieuwe ladingen aanvoeren, welke de bestaande neutraliseren. De in komposieten optredende MW-ontlading is blijkbaar een indirekt gevolg van proces 3. Kortgesloten inhomogene elektreten wekken dus daarom een TSD stroom op, omdat hun geleidingsvermogen *niet* uniform is.(In kortgesloten *homogene* elektreten daarentegen wordt de ohmse neutralisatie niet opgemerkt, omdat daarin het geleidingsvermogen wel uniform is.)

Daar alle ontlaadprocessen thermisch zijn geaktiveerd, worden ze tijdens TSD aanzienlijk versneld. In het algemeen werd aangenomen dat deze aktivering aan een Arrhenius-vergelijking voldoet.

Beschouwen we vervolgens de inhoud van de resterende hoofdstukken afzonderlijk. De stroomopwekking ten gevolge van heroriëntatie van dipolen wordt in hoofdst. 2 behandeld. Onafhankelijk van Gross hebben we de theorie van Bucci c.s., die slechts voor één Debije-relaxatie geldt, uitgebreid tot een dipoolpolarisatie met een kontinue verdeling van relaxatietijden. Dit leek gewenst omdat de waargenomen TSD β en α pieken soms extreem breed waren. Aan de hand van modelthermogrammen laten we zien dat de TSD-stroom van een verdeelde polarisatie wordt *vervormd* als de formatie onvolkomen is. De vereiste integraties werden uitgevoerd op een digitale rekenmachine voor vijf distributies, nl. die van Gevers, Gross, Cole-Cole, Fuoss-Kirkwood en Wagner. Gevonden werd bijvoorbeeld dat bij lage formatietemperaturen T_f, wanneer de langzame subpolarisaties onvolledig worden gevuld, de stroomthermogrammen aan de hoge temperatuurkant worden afgesneden. In dit geval wordt het resulterende stroommaximum juist boven T_f waargenomen en is dus *niet* meer representatief voor het polymeer. Als de elektreet anderzijds te lang wordt bewaard, dan zullen de snelle subpolarisaties zijn gerelaxeerd en aan de lage temperatuurkant van het TSD stroomthermogram ontbreken. De opgenomen thermogrammen zullen dus alleen dan karakteristiek zijn voor het onderzochte polymeer, als dit *volledig* wordt geladen, hetgeen praktisch gemakkelijk is te verwezenlijken.

Met modelberekeningen aan volledig geladen polymeren werd vastgesteld, dat de verdelingen van Cole-Cole en Fuoss-Kirkwood het geschiktst zijn om TSD-gegevens te beschrijven. De verdeling van Wagner is minder geschikt, daar deze een te hoge beginhelling geeft. De doosvormige verdelingen van Gevers en Gross, die sterk op elkaar lijken, geven onrealistisch brede stroompieken; bovendien geven ze een te hoge beginhelling. In hoofdst. 2 beschouwen we ook de resolutie van TSD voor nabijgelegen dipoolrelaxaties en wijzen we op het nut van meer-traps TSD om een verdeling in "omklapfrekwenties" van de dipoolgroepen te *onderscheiden* van een verdeling in aktiveringsenergieën.

In hoofdst. 3, waarin de evaluatie van TSD gegevens van dipoolrelaxaties wordt besproken, leiden we een eenvoudige formule af om de aktiveringsenergie van een verdeelde polarisatie te berekenen uit de beginhelling en halfwaardetemperatuur van de stroomthermogrammen. We beschrijven ook een methode om de verdelingsfunktie uit TSD gegevens te berekenen. De methode, die voor het eerst werd gesuggereerd door Schwarzl en Staverman, is gebaseerd op de inversie van een Laplacetransformatie. Ter toetsing van de voorgestelde methoden werd de evaluatie van de γ piek van PcHMA, die een gevolg is van een stoel-stoel omklapping van de flexibele cyclohexylring, nader toegelicht. We vonden dat deze piek kan worden beschreven met een Fuoss-Kirkwood verde-

ling met verdelingsfaktor m = 0,44 en aktiveringsenergie van 9 kcal/mol. Deze resultaten stemmen goed overeen met die van Heijboer aan torsiekruipmetingen.

In hoofdst. 4 vergelijken we stroom-TSD door dipoolheroriëntatie met konventionele diëlektrische metingen. Door konversieformules van Schwarzl en Struik om te werken, konden we onze TSD gegevens in diëlektrische verliezen omrekenen. We laten zien dat TSD nagenoeg isochroon werkt bij een zeer *lage* frekwentie van ca 10^{-3} Hz. Bij de omrekening van de β en α piek van PMMA vielen de berekende diëlektrische verliezen van de α piek hoger uit dan de gemeten waarden. Blijkbaar wordt deze TSD dipoolpiek dus versterkt door de beweging van ruimteladingen; dit werd later met doorsnijdingsproeven bevestigd (hoofdst. 10). We vermeldden al dat alleen TSD pieken met een dipool karakter in diëlektrische metingen worden teruggevonden, de ρ piek was onbekend. We konden echter aantonen, dat deze piek wel kan worden waargenomen met isothermische stap-responsiemetingen. Dit werd onlangs ook aangetoond door Adamec.

In hoofdst. 5 bespreken we nieuw werk aan stroom-TSD door de beweging van excesladingen. Eerst wordt aandacht besteed aan de SCL drift van vrije ladingen met een thermisch geaktiveerde beweeglijkheid. Voor een uniforme ladingsverdeling konden de niet-lineaire partiële differentiaalvergelijkingen analytisch worden opgelost, zoals onlangs ook Calderwood en Scaife en later Wintle hebben gedaan. Voor niet-uniforme ladingsverdelingen losten we de partiële differentiaalvergelijkingen, met een digitale rekenmachine, op met behulp van differentievergelijkingen. Unipolaire en bipolaire ladingsverdelingen werden doorgerekend. De beste resultaten werden met het centrale Wendroff-Thomée schema verkregen, doch ook het twee-staps Lax-Wendroff-Richtmyer schema funktioneerde goed. We vonden dat men extern slechts een *fraktie* waarneemt van de oorspronkelijk opgeslagen lading, dit komt omdat de excesladingen in twee richtingen bewegen; ze bewegen immers naar *beide* elektroden, waar ze uiteindelijk worden geneutraliseerd. Voor een uniforme oplading leidden we af dat $q_r(\infty) \simeq r_o/21$, indien de relatieve penetratiediepte $r_o/1 \leq 0{,}25$. Met deze formule berekenden we de penetratie van in Teflon-FEP ingeschoten elektronen en vonden bijv. $r_o/1 = 0{,}15$ voor een bombarderingsenergie van 20 keV, wat goed overeenkomt met de uit de literatuur bekende waarde. De gegeven formule voor de vrijgemaakte lading $q_r(\infty)$ geldt voor niet-geleidende polymeren. De formule voor SCL drift in geleidende polymeren, waarin een deel van de excesladingen ongemerkt wordt gedissipeerd, werd eveneens afgeleid. Voor $r_o \leq 0{,}5$ 1 bleken de modelthermogrammen voor SCL drift breder te zijn dan die van een Debije-dipoolrelaxatie, bovendien hangt hun vorm van de penetratiediepte af. Alleen de beginhelling wordt uitsluitend door de aktiveringsenergie bepaald. Daarnaast bleek dat het stroommaximum *ongeveer lineair* met de beginlading aangroeit en dat het maximum eerder verschijnt, naarmate de lading hoger is.

Uit de diskussie over het ladingstransport door diffusie blijkt, dat diffusie alleen dan een stroom genereert als de elektroden blokkeren, d.w.z. als deze de excesladingen beletten met de beeldladingen te rekombineren. Incidenteel vonden we dat een dergelijke onvolkomen rekombinatie voorkomt bij opgedampte elektroden. Om de modelthermogrammen voor diffusie te berekenen werd Jaffé en LeMay's theorie voor isothermische metingen uitgebreid tot TSD.

In hoofdst. 6 besteden we aandacht aan twee-lagen strukturen om kwalitatief inzicht te krijgen in de stroom-TSD door het MW-effekt van heterogene polymeren, zoals amorf-kristallijne films. We laten zien dat de vrijgemaakte lading van zulke MW seriemodellen *kleiner* is dan de oorspronkelijk opgeslagen grenslading, doordat de interne ontlaadstroom in twee richtingen vloeit. Alleen als één der komponenten perfekt isoleert, is de stroomefficiëntie 100 %. In verband met het onopgemerkte interne ladingsverlies zal, volgens Gross, de maximaal vrijkomende lading van heterogene systemen met de opwarmsnelheid variëren; we laten zien dat de variaties evenwel klein zijn. Van twee polaire polymeren werd met het luchtspleetsysteem de MW op- en ontlading onderzocht. Er werden twee stroompieken waargenomen, hiervan ontstaat de ene door dipool(re)oriëntatie (α) en de andere door ohmse geleiding (ρ_c). Interessant was, dat de geleidingspiek overeen kwam met de ρ piek van kortgesloten, gemetalliseerde hetero-elektreten. Dit bevestigde onze mening dat deze piek zijn oorsprong vindt in de beweging van excesladingen.

In hoofdst. 7 analyseren we de stroom-TSD van elektreten in het elektrodesysteem met luchtspleet. Zoals eerder opgemerkt, maakt deze methode de meting van het verval van excesladingen door ohmse geleiding mogelijk; ze is daarom van groot belang voor de bestudering van de ontlading van homoladingen. Bovendien is ze van nut bij de vaststelling van de molekulaire herkomst van de ρ piek van kortgesloten gemetalliseerde hetero-elektreten. De gelijktijdige ontlading van dipolen en excesladingen maakt echter de wiskunde gekompliceerder en om kwantitatieve resultaten te krijgen moesten de desbetreffende gewone differentiaalvergelijkingen in het algemeen numeriek worden opgelost. Experimenteel vonden we evenwel de meeste dipool- en geleidingspieken goed gescheiden. In dit geval werden de simultane differentiaalvergelijkingen ontkoppeld en kon de aktiveringsenergie van de geleidingspiek eenvoudig worden berekend; de verkregen waarde stemde inderdaad met die van de ohmse geleiding goed overeen.

Hoofdst. 8 is gewijd aan de theorie van de ladings-TSD van de veel gebruikte homopolaire films. Deze meting gebeurt stroomloos, omdat het externe veld van de elektreet tot nul wordt gereduceerd; dit vereenvoudigt de wiskunde aanzienlijk. Opnieuw werden dipoolreoriëntatie, SCL drift en ohmse geleiding als de voornaamste ontlaadbronnen aangemerkt. Op markante verschillen tussen lading- en stroom-TSD wordt gewezen en het effekt van de penetratiediepte en de hoogte van de oplading worden

bestudeerd. Uit modelberekeningen bleek dat de ontlading door SCL drift afneemt na een voorverwarming; dit effekt maakt het mogelijk om homo-elektreten stabieler te maken.

In het experimentele deel dat begint bij hoofdst. 9, wordt de apparatuur beschreven. De opstelling voor stroom-TSD is volledig geautomatiseerd. De apparatuur bestaat uit: een thermostaat die een temperatuurgebied van -185° tot 250 °C kan bestrijken, twee elektrodesystemen voor metingen met en zonder luchtspleet, een trilplaatelektrometer als ampèremeter en enige acquisitie-apparatuur om de gegevens op een Teletype uit te typen en te ponsen. De ponsband met meetgegevens werd geevalueerd op een digitale rekenmachine (IBM-360). De nieuw ontwikkelde apparatuur voor ladings-TSD aan elektreetfilms, die is gebaseerd op de kompensatie van het externe veld van de elektreet met een voorgeschreven gelijkspanning, werkt eveneens automatisch. De opwarmsnelheid werd in beide meetopstellingen meestal 1 °C/min gekozen.

In hoofdst. 10 worden de experimentele resultaten beschreven. Eerst worden de stroomthermogrammen van verschillende methacrylaat homo- en copolymeren besproken. Voor de interpretatie van de thermogrammen konden we vaak terugvallen op de interpretatie van konventionele diëlektrische en mechanische meetresultaten. We laten zien dat de ligging van de TSD α piek overeenkomt met het glaspunt, zoals dat bijv. dilatometrisch wordt gemeten. TSD kan daarom omgekeerd worden toegepast om glaspunten te bepalen. Als gevolg van de lage meetfrekwentie, was er een *grote resolutie* tussen de TSD pieken van de hoofdketen- en zijgroeprelaxaties van het polymeer, en om de laatste waar te nemen, werd afgekoeld tot -185 °C. Voor bijna alle polymeren werd, als gevolg van de beweging van excesladingen, boven T_g een ρ piek waargenomen. Deze piek is overigens gevoelig voor verontreinigingen, zoals geabsorbeerd water. Aangezien copolymeren vaak een uitgesproken grote ρ piek bezitten, kan men hierin *meer* lading opslaan dan in homopolymeren. Uit een onderzoek naar het verband van de hetero-oplading met de formatiekondities, vonden we dat de formatietemperatuur T_f het grootste effekt had op de stroomthermogrammen en om een representatief thermogram te krijgen moest T_f boven T_g worden gekozen. Deze bevindingen stemmen overeen met onze theoretische voorspellingen van hoofdst. 2. De afhankelijkheid met de bewaarkondities werd ook nagegaan.

Door middel van stroom-TSD met luchtspleet werd de coëxistentie van een hetero- en homolading op niet bedampte elektreten van polaire polymeren vastgesteld. Steeds namen we eerst een heterostroom waar, die bij hogere temperatuur, t.w. boven T_g, in een homostroom overging. Door de stroom-TSD van doorgezaagde hetero-elektreten te onderzoeken, konden we aantonen, dat de interne lading *ongelijk* was verdeeld. De meeste lading is dicht bij de elektroden opgeslagen, wat wijst op een signifikante *ruimteladingspolarisatie*. De ruimteladingen dragen zelfs aanzienlijk bij tot de α piek. Onze resultaten zijn in tegenspraak met die van

Gross c.s. aan carnaubawas. De gevonden diskrepantie zou een gevolg kunnen zijn van een verschil in bewaartijd. Gross c.s. bewaarden hun elektreten tot zelfs 7 weken toe, voordat ze tot de doorsnijding en de TSD overgingen.

In het laatste deel van hoofdst. 10 worden de ladingsthermogrammen van verschillende homo-elektreten en van met elektronen gebombardeerd Teflon-FEP behandeld. De markante stabiliteit van Teflon-FEP kon nog verder worden verbeterd door een voorverwarming, dit is interessant voor het praktisch gebruik van elektreten. Dit stabilisatieverschijnsel wijst er overigens op, dat de geïnjecteerde ladingen in centra van verschillende diepte worden ingevangen. Deze zienswijze werd gestaafd door de stroomthermogrammen van met elektronen gebombardeerd Teflon-FEP, die twee pieken vertoonden. Bovendien namen we voor Teflon-FEP grote verschillen waar tussen de overgangstemperatuur in stroom- en ladings-TSD. Het lijkt daarom waarschijnlijk dat de thermisch vrijgemaakte elektronen weer snel worden ingevangen in plaats van verloren te gaan in rekombinatiecentra. Ten slotte merkten we op, dat negatief geladen Teflon-FEP veel stabieler is dan positief geladen Teflon-FEP.

In de appendices komen enige aanvullingen op de theorie aan de orde. In appendix I bespreken we de stroom-TSD ten gevolge van thermische vrijmaking van elektronen uit vangcentra en wordt de oplossing van de betreffende partiële differentiaalvergelijkingen aangegeven. Deze theorie is o.a. van belang voor negatief geladen homo-elektreten en met elektronen gebombardeerde polymeerfilms. In navolging van Monteith c.s. losten we, gebruikmakend van de voorwaarde $n_t >> n$, de partiële differentiaalvergelijkingen op als gewone differentiaalvergelijkingen met behulp van een 2e orde Runge-Kutta-methode. Aangetoond wordt dat sterke herinvanging in een enkel energieniveau overeenkomt met de in hoofdst. 5 behandelde thermisch gestimuleerde SCL drift van "vrije" ladingen. Voor minder sterke herinvanging vonden we echter een verschil in ruimtelijke spreiding met de vrije ladingen. De extern vrijkomende lading bedroeg opnieuw slechts een fraktie van de oorspronkelijk ingevangen lading. Kort wordt ingegaan op de theorie van Creswell c.s. die snelle rekombinatie in plaats van snelle herinvanging vooropstellen. Overigens werd in hoofdst. 5 aangegeven hoe deze processen met de zgn. BFG-grafiek en ladingsverhoudingsgrafiek van elkaar zijn te onderscheiden. Appendix II ten slotte bevat enige aanvullingen op hoofdst. 2, 5, 6 en 7. Hierin worden o.a. de differentieschema's beschreven om de partiële differentiaalvergelijkingen voor SCL drift van niet-uniforme ladingsverdelingen op te lossen. Verder behandelen we de homo-oplading door Townsend-ontlading, waarbij we dit proces als een MW-oplading opvatten.

Ofschoon we een deel van de molekulaire processen die de ontlading van polymeerelectreten bepalen, hebben kunnen ophelderen, valt er nog veel werk te doen. Zo lijkt het gewenst om de theorie over ladings-TSD

uit te breiden tot de thermische vrijmaking van ladingen uit vangcentra van verschillend energieniveau. Om de molekulaire ontlaadprocessen van geïnjecteerde homoladingen vast te stellen lijkt de TSD van polymeren die met ionen zijn geïmplanteerd van belang. Ook het bepalen van de cryogene relaxaties van polymeren door invriezing tot de temperatuur van vloeibaar helium lijkt interessant. Ten slotte dient meer aandacht te worden besteed aan de luchtspleetmethode en lijkt het gewenst om de TSD onderzoekingen aan doorgezaagde elektreten voort te zetten. TSD kan niet alleen worden toegepast op elektreten, maar ook op bijvoorbeeld door wrijving of corona opgeladen diëlektrika. Op het Centraal Laboratorium TNO worden momenteel met TSD de effekten van antistatica bestudeerd.

LEVENSLOOP

Voordat ik in 1957 Technische Natuurkunde aan de Technische Hogeschool te Delft ging studeren, doorliep ik van 1949 tot '53 de ULO-B en van 1953 tot '57 de afdeling Fysische Techniek van de HTS te Dordrecht.

In hetzelfde jaar dat ik mijn studie begon, trad ik in dienst bij het Centraal Laboratorium TNO te Delft. Daar verrichtte ik, onder leiding van Dr P. Dekking en Dr Ir J. Heijboer, mechanische metingen aan polymeren. Van 1959 tot '62 was ik gedetacheerd op het FOM-Instituut voor Plasma Fysica te Jutphaas, alwaar ik voor mijn candidaats- en ingenieursexamen werkte aan "doorslag in ijle gassen met hoogfrekwent velden" en aan "golfverschijnselen in een gemagnetiseerd plasma". Hierbij was Prof. Dr L.J.F. Broer mijn hoogleraar-mentor, terwijl Prof. Dr C.M. Braams en wijlen Dr H.C. Brinkman optraden als supervisors. In 1962 studeerde ik af.

Daarna keerde ik terug naar de Fysische Afdeling van het Centraal Laboratorium TNO te Delft, waar ik nu, met drie medewerkers, de onderwerpen: elektreten en elektrostatica behandel.